TECHNISCHE UNIVERSITÄT MÜNCHEN

TUM School of Engineering and Design

Modeling and control of deep geothermal electric submersible pump systems

Julian Kullick, M.Sc.

Vollständiger Abdruck der von der TUM School of Engineering and Design der Technischen Universität München zur Erlangung des akademischen Grades eines

Doktors der Ingenieurwissenschaften

genehmigten Dissertation.

Vorsitzender:		Prof. Dr. Carlo L. Bottasso
Prüfer der Dissertation:	1.	Prof. Dr.-Ing. habil. Christoph M. Hackl
	2.	Prof. Dr. Thomas Hamacher
	3.	Prof. Dr. Roberto Cárdenas Dobson

Die Dissertation wurde am 18.06.2020 bei der Technischen Universität München eingereicht und durch die TUM School of Engineering and Design am 08.11.2021 angenommen.

This document is typeset with LaTeX/TeX.

Danksagung

Zum Gelingen dieser Arbeit haben einige Personen in besonderem Maße beigetragen, denen ich an dieser Stelle meinen Dank aussprechen möchte.

Zuallererst bedanke ich mich ganz herzlich bei meinem Doktorvater, Prof. Dr.-Ing. habil. Christoph Hackl. Du hast mir damals ermöglicht, mit der Promotion zu beginnen, obwohl die finanzielle Situation unklar war. Du hast dich immer für deine Doktoranden eingesetzt, Gelder aufgetrieben, wo keine waren, großes fachliches Interesse gezeigt und geweckt, kritisch nachgehakt und hinterfragt, und motiviert weiterzumachen, auch wenn es einmal Rückschläge gab. Und du hast mich so manches Mal ins kalte Wasser geschubst, wofür ich rückblickend ebenfalls sehr dankbar bin. Vor allem aber hattest du immer ein offenes Ohr und viel Verständnis für persönliche Belange. Danke Christoph!

Des Weiteren möchte ich mich bei Prof. Dr. Thomas Hamacher für die Erstellung des Zweitgutachtens, sowie für das stets wohlwollende Auge auf unsere Forschungsgruppe bedanken. Ohne die Förderung der Nachwuchsforschungsgruppen im Rahmen der MSE wäre diese Promotion so nicht möglich gewesen. Außerdem danke ich Prof. Dr. Roberto Cárdenas Dobson für die Übernahme des Drittgutachtens und Prof. Dr. Carlo Botasso für die Übernahme des Prüfungsvorsitzes sowie für die zur Verfügungstellung der Räumlichkeiten und die Gastfreundschaft am Lehrstuhl für Windenergie zu Beginn meiner Promotion.

Ein großer Dank gilt auch meinen Freunden und ehemaligen Kollegen der CRES Gruppe - Christian, Korbinian, Hisham und Markus - für die vielen spannenden Gespräche, Kreativmeetings und den guten Zusammenhalt innerhalb der Gruppe. Gleichsam danke ich meinen Freunden und ehemaligen Kollegen vom EAL - Hannes, Eyke, Peter, Sascha und Dirk - für die lustigen Mittwochrunden, die erhellenden Diskussionen, aber auch für den fachlichen Rat, der mir immer sehr wichtig war. Darüber hinaus danke ich Hannes, Eyke und Korbinian sehr für das Korrekturlesen dieser Arbeit.

Ganz besonders möchte ich auch meinen Eltern und meiner Familie für die Liebe und Unterstützung, den Zuspruch und das Vertrauen in mich und meine Arbeit danken.

Mein allergrößter Dank gilt Dir, liebste Janna. Dafür dass du mir immer den Rücken freigehalten und gestärkt, mich unterstützt und meine Launen ertragen hast. Vor allem aber dafür, dass du mich immer wieder daran erinnert hast, was wirklich wichtig ist, und dass nach dem Tief auch wieder ein Hoch kommt. Alba, die Vorfreude auf deine Geburt hat mir einen besonderen Ansporn gegeben, diese Arbeit rechtzeitig abzuschließen.

München, Februar 2022 Julian Kullick

Contents

Abstract

This thesis deals with the modeling, simulation and efficient control of deep geothermal electric submersible pump (ESP) systems. First, a modular state-space model of an ESP system and its components is derived, covering the electrical, mechanical and hydraulic subsystems. Special emphasis is put on the particular properties of the ESP components regarding geothermal applications. Moreover, a realistic set of parameters is provided and software-based simulations of a start-up procedure are carried out. Secondly, an experimental machine identification method for induction machines is presented, which results in maximum efficiency torque control look-up tables (LUTs). The key idea is to define unique and reproducible operating points in an arbitrarily rotating reference frame and acquire characteristic machine maps, which are used to extract the maximum efficiency trajectories. It is shown that, particularly in part-load operation or at very high speeds, the machine efficiency can be increased compared to the standard control method of geothermal ESPs. Lastly, a speed-sensorless control system for the electric drive of an ESP is derived, which is based on a state-feedback stator current controller and a speed-adaptive full order observer. Due to the low switching frequencies in medium voltage applications, the derivation is conducted in the discrete-time domain. The control system is validated in simulations and experiments on a down-scaled drive system for all critical modes of operation.

Kurzzusammenfassung

Diese Arbeit befasst sich mit der Modellierung, Simulation und effizienten Regelung von tiefengeothermischen Tauchkreiselpumpen (TKPn) Systemen. Zunächst wird ein modulares Zustandsraummodell einer TKP und ihren Komponenten hergeleitet, welches die elektrischen, mechanischen und hydraulischen Teilsysteme berücksichtigt. Besonderes Augenmerk ist dabei auf die spezifischen Eigenschaften von TKP Komponenten für den Einsatz in der Geothermie gerichtet. Darüber hinaus werden mittels eines realistischen Parametersatzes numerische Simulationen eines Anfahrvorgangs durchgeführt. Anschließend, wird eine experimentelle Methode zur Identifikation von Asynchronmaschinen vorgestellt, welche zur Erzeugung von Referenztabellen für den Betrieb bei maximaler Effizienz verwendet wird. Die Grundidee besteht darin, einzigartige und reproduzierbare Arbeitspunkte in einem beliebig rotierenden Koordinatensystem zu definieren und charakteristische Maschinenkarten aufzunehmen, welche zur Extraktion der Referenztabellen verwendet werden können. Es kann gezeigt werden, dass die Effizienz im Vergleich zum Standardregelverfahren von geothermischen TKPn, insbesondere im Teillastbetrieb und bei hohen Geschwindigkeiten, erhöht wird. Schließlich wird ein drehgeberloses Regelverfahren für den elektrischen Antrieb einer TKP hergeleitet, welches auf einem Statorstrom-Zustandsregler und einem adaptiven Beobachter basiert. Durch die niedrigen Schaltfrequenzen bei Mittelspannungsantrieben, wird die Herleitung im diskreten Zeitbereich durchgeführt. Abschließend wird das Regelungssystem simulativ und experimentell an einem skalierten Maschinenprüfstand mit geringer Leistung für alle kritischen Betriebsmodi validiert.

List of Publications

The following publications were written during my employment at

- the Technical University of Munich (TUM) as a member of the Munich School of Engineering (MSE) research group "Control of Renewable Energy Systems (CRES)" from Oct. 2016 to Dec. 2018, and
- the Munich University of Applied Science (MUAS) as a member of the "Laboratory for Mechatronic and Renewable Energy Systems (LMRES)" from Jan. 2019 to Feb. 2020.

Funding from the Bavarian State Ministry of Education, Science and the Arts in the frame of the projects "Geothermie-Allianz Bayern (GAB)" and "Energy Valley Bavaria (EVB)" is gratefully acknowledged.

Journal publications (peer-reviewed)

- (∗) J. Kullick and C. M. Hackl. "Speed-Sensorless Control of Induction Machines with LC Filter for Geothermal Electric Submersible Pumping Systems". In: *Machines* 10.2 (Jan. 2022), p. 87
- J. Kullick and C. M. Hackl. "Nonlinear Modeling, Identification and Optimal Feedforward Torque Control of Induction Machines Using Steady-State Machine Maps". In: *IEEE Transactions on Industrial Electronics* (2022)
- A. Zanelli, J. Kullick, H. M. Eldeeb, G. Frison, C. M. Hackl, and M. Diehl. "Continuous Control Set Nonlinear Model Predictive Control of Reluctance Synchronous Machines". In: *IEEE Transactions on Control Systems Technology* 30.1 (2022), pp. 130–141
- H. M. Eldeeb, A. S. Abdel-Khalik, J. Kullick, and C. M. Hackl. "Pre- and Postfault Current Control of Dual Three-Phase Reluctance Synchronous Drives". In: *IEEE Transactions on Industrial Electronics* 67.5 (May 2020), pp. 3361–3373
- J. Kullick and C. M. Hackl. "Dynamic Modeling and Simulation of Deep Geothermal Electric Submersible Pumping Systems". In: *Energies* 10.10 (2017)
- (∗) H. Eldeeb, C. M. Hackl, L. Horlbeck, and J. Kullick. "A Unified Theory for Optimal Feedforward Torque Control of Anisotropic Synchronous Machines". In: *International Journal of Control* (2017), pp. 1–30

Conference publications

- C. Hackl, J. Kullick, and N. Monzen. "Generic Loss Minimization for Nonlinear Synchronous Machines by Analytical Computation of Optimal Reference Currents Considering Copper and Iron Losses". In: *2021 22nd IEEE International Conference on Industrial Technology (ICIT)*. vol. 1. 2021, pp. 1348–1355
- (∗) H. Eldeeb, C. M. Hackl, L. Horlbeck, and J. Kullick. "Analytical Solutions for the Optimal Reference Currents for MTPC/MTPA, MTPV and MTPF Control of Anisotropic Synchronous Machines". In: *2017 IEEE Int. Electr. Mach. Drives Conf.* IEEE, May 2017, pp. 1–6
- C. M. Hackl, J. Kullick, H. Eldeeb, and L. Horlbeck. "Analytical Computation of the Optimal Reference Currents for MTPC/MTPA, MTPV and MTPF Operation of Anisotropic Synchronous Machines Considering Stator Resistance and Mutual Inductance". In: *2017 19th European Conference on Power Electronics and Applications (EPE'17 ECCE Europe)*. Warsaw, 2017, P.1–P.10
- (∗) H. Eldeeb, C. M. Hackl, and J. Kullick. "Efficient Operation of Anisotropic Synchronous Machines for Wind Energy Systems". In: *Journal of Physics: Conference Series* 753.11 (2016), p. 112009
- C. M. Hackl, J. Kullick, M. J. Kamper, and J. C. Mitchell. "Current Control of Reluctance Synchronous Machines with Online Adjustment of the Controller Parameters". In: *2016 IEEE 25th International Symposium on Industrial Electronics (ISIE)*. June 2016

Book chapters

- C. M. Hackl, J. Kullick, and N. Monzen. "Optimale Betriebsführung von nichtlinearen Synchronmaschinen". de. In: *Elektrische Antriebe - Regelung von Antriebssystemen (5. Auflage)*. Springer, 2020
- C. M. Hackl, J. Kullick, and P. Landsmann. "Nichtlineare Stromregelverfahren für Reluktanz-Synchronmaschinen". de. In: *Elektrische Antriebe - Regelung von Antriebssystemen (5. Auflage)*. Springer, 2020

(∗) *All authors contributed equally and are listed in alphabetical order.*

Nomenclature

General notation

The following mathematical symbols, functions and definitions are used:

$\mathbb{R}, \mathbb{C}, \mathbb{N}$	Sets of real, complex and natural numbers.
$\mathbb{X} = \{x \mid \ldots\}$	Set of feasible values for quantity x.
$x \in \mathbb{R}$	Real scalar variable
$\boldsymbol{x} \in \mathbb{R}^n$	Real (column) vector of dimension n
$\boldsymbol{A} \in \mathbb{R}^{n \times m}$	Real matrix with n rows and m columns
$\boldsymbol{\mathcal{A}} \in \mathbb{R}^{n \times m}$	Real matrix with n rows and m columns referring to a discrete-time system.
$\|\boldsymbol{x}\| = \sqrt{\boldsymbol{x}^\top \boldsymbol{x}} = \sqrt{x_1^2 + \ldots + x_n^2}$	Euclidian norm of vector $\boldsymbol{x} = (x_1, \ldots, x_n)^\top \in \mathbb{R}^n$.
$\mathbf{o}_n$	Zero (column) vector of dimension n.
$\mathrm{diag}(\boldsymbol{x}) \in \mathbb{R}^{n \times n}$	Diagonal (square) matrix of dimension n, with vector $\boldsymbol{x} \in \mathbb{R}^n$ on its main diagonal.
$\boldsymbol{\imath}_n = (1, \ldots, 1)^\top$	Unity (column) vector of dimension n.
$\mathbf{0}_{n \times m}$	Zero matrix of n rows and m columns.
$\boldsymbol{I}_n := \mathrm{diag}(\boldsymbol{\imath}_n)$	Identity (square) matrix of dimension n.
$\boldsymbol{J} := \left[\begin{smallmatrix} 0 & -1 \\ 1 & 0 \end{smallmatrix}\right]$	Rotation matrix describing a rotation by $\frac{\pi}{2}$.
$x := y$	x is defined as y.
$x \stackrel{!}{=} y$	x must be equal to y (used for other relational operators, too).
$x^\star$	Reference (set-point) value for variable x.
x_{nom}	Nominal (rated) value for quantity x.
x_{sat}	Quantity x after saturation is applied.
$\hat{x}$	Magnitude $\|\boldsymbol{x}\|$ of vector $\boldsymbol{x}$ *or* estimate of quantity x (depending on context).
$\boldsymbol{A} \succ 0 \quad (\boldsymbol{A} \succcurlyeq 0)$	Positive (semi-) definite Matrix $\boldsymbol{A} \in \mathbb{R}^{n \times n}$, i.e. given some column vector $\boldsymbol{x} \in \mathbb{R}^n$, $\boldsymbol{x}^\top \boldsymbol{A} \boldsymbol{x} > 0$ ($\boldsymbol{x}^\top \boldsymbol{A} \boldsymbol{x} \geq 0$) holds true. Negative (semi-) definiteness follows analogously.
$n = \lfloor x \rfloor \quad (= \lceil x \rceil)$	Floor (ceil) operator, rounds the real number $x \in \mathbb{R}$ down (up) to the greatest (lowest) integer n less (greater) or equal x.
$\wedge$, $\vee$	Logical 'and' and 'or'.

Reference frames

A signal vector $\boldsymbol{x}$ may be assigned to difference reference frames, which are denoted by superscript terms ($\boldsymbol{x}^{\square}$):

Signal vector	**Assigned reference frame**
$\boldsymbol{x}^{\mathrm{abc}} = (x^{\mathrm{a}}, x^{\mathrm{b}}, x^{\mathrm{c}})^\top$	Three-phase signal, assigned to the abc-reference frame.
$\boldsymbol{x}^{\mathrm{abcn}} = (x^{\mathrm{an}}, x^{\mathrm{bn}}, x^{\mathrm{c}})^\top$	Line-to-neutral signal, assigned to the abcn-reference frame.
$\boldsymbol{x}^{\mathrm{a\text{-}b\text{-}c}} = (x^{\mathrm{a\text{-}b}}, x^{\mathrm{b\text{-}c}}, x^{\mathrm{c\text{-}a}})^\top$	Line-to-line signal, assigned to the a-b-c-reference frame.
$\boldsymbol{x}^{\alpha\beta} = (x^{\alpha}, x^{\beta})^\top$	Two-phase signal, assigned to the stationary and orthogonal $\alpha\beta$-reference frame.
$\boldsymbol{x}^{\alpha\beta\gamma} = (x^{\alpha}, x^{\beta}, x^{\gamma})^\top$	Three-phase signal, assigned to the stationary and orthogonal $\alpha\beta\gamma$-reference frame.
$\boldsymbol{x}^{\mathrm{dq}} = (x^{\mathrm{d}}, x^{\mathrm{q}})^\top$	Two-phase signal, assigned to the rotating and orthogonal dq-reference frame.
$\boldsymbol{x}^{\mathrm{dq0}} = (x^{\mathrm{d}}, x^{\mathrm{q}}, x^{0})^\top$	Three-phase signal, assigned to the rotating and orthogonal dq0-reference frame.

Location / component indices

A signal or paramater x may be related to a certain component or 'location', which is denoted by subscript letters ($x_{\square}$):

Index	**Component / Location**
'v'	Voltage source inverter
'dc'	DC-link
'f'	Filter (LC filter)
'c'	Cable (or *core*)
'm'	Machine (or *mechanical*, or *main*)
's'	Stator
'r'	Rotor
'p'	Pump
'i'	Impeller
'h'	Hydraulic system
'w'	Water
'wh'	Wellhead
'rv'	Reservoir
'it'	Intake

Other components or locations may occur, which are explained in the text. Furthermore, double subscripts 'i' and 'o' indicate inputs and outputs of a component.

Chapter 1

Introduction

In the *Paris Agreement* from 12 December 2015, parties of the United Nations Framework Convention on Climate Change (UNFCCC) agreed on keeping the global temperature rise due to climate change below two degrees Celsius above pre-industrial levels by the end of this century [14]. Even more ambitious plans were presented by the European Commission on 11 December 2019 with its *European Green Deal*, aiming to become the first climate-neutral continent by 2050 [15]. Such plans exemplify the global consent, that the transition from fossil fuels to renewables is crucial, in order to limit the impact of climate change. Technologies such as wind, solar, hydro-electric or geothermal energy systems could pave the way for a carbon neutral energy supply in the future. Among the mentioned technologies geothermal energy systems have two major advantages: (i) They provide base load power since they are not depending on volatile environmental conditions such as wind or sunlight, and (ii) they are versatile as both heat and electricity may be produced [16, p. 2].

The following chapter gives an introduction to this thesis. In Sec. 1.1, the use of geothermal energy systems in Germany is motivated and the inherent challenges concerning the pump system are identified. Moreover, the main objectives of this thesis are formulated. In Sec. 1.2, a brief state-of-the-art analysis is carried out, covering the main topics of this thesis. Lastly, in Sec. 1.3, the main contributions are summarized and an outline is given.

1.1 Motivation and problem statement

The term 'geothermal energy' describes the usable thermal energy contained in the interior of the Earth [17]. The main sources of geothermal energy are (i) convectional heat flow from the Earth's core to its surface, and (ii) radioactive decay in the Earth's mantle [17] (see Fig. 1.1). These ongoing physical processes make geothermal energy a *renewable* source of energy, which is considered unlimited from a human perspective [16, p. 26, 62].

Geothermal reservoirs are classified as *hydrothermal*, i.e. naturally permeable geological structures conducting geothermal fluid or steam, or *petrothermal*[1], i.e. impermeable deep rock formations which are artificially cracked by hydraulic stimulation (hydrofracturing / fracking) [18, Ch. 4.4]. In Germany, mainly hydrothermal systems are found, e.g. in the Upper Rhine Valley, the Northern Basin and the Bavarian Molasse Basin [18, Ch. 18.4]. These so-called low enthalpy[2] fields with reservoir temperatures below 200 °C [16, p. 32], are particularly suited for geothermal direct-use

[1] Also known as enhanced geothermal systems (EGS), or formerly as hot-dry rock systems (HDR).
[2] In thermodynamics, the term 'enthalpy' describes the heat content of material [16, p. 32].

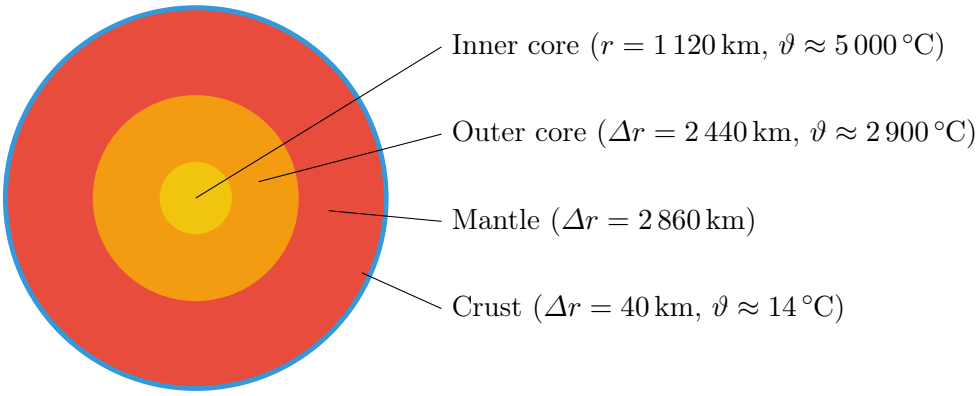

Figure 1.1: *Simplified 4-layer model of the Earth [16, Sec. 1.2].*

(thermal power for district heating systems) [18, Ch. 16.2]. Nevertheless, electric power production is made possible by employing Organic Rankine Cycle (OCR) or Kalina technology[3]. In order to efficiently and economically produce electric power with state-of-the-art technology, a fluid temperature of at least 120 °C is indispensible [16, p. 43]. With an average temperature gradient of 3 °C per 100 m depths [16, p. 8], the drilling depths in low enthalpy regions may reach several hundreds to thousands of meters in order to meet the temperature requirements. E.g. in the Bavarian Molasse Basin, a drilling depth of 3 500 m and more is required, in order to reach a water temperature beyond 120 °C [18]. In these areas, deep geothermal systems (more than 400 m depths [16]) are used.

In a frequently cited study from 2003, the geothermal potential for electrical power production in Germany was estimated at 6.4 $\mathrm{GW_e}$ for the year 2050 [19]. However, as of today, with an installed electrical capacity of 37 $\mathrm{MW_e}$ in 2018, this goal seems unlikely to be reached. A possible reason is that 90 % of the forecasted technical potential was attributed to petrothermal exploration, which is a controversial topic in Germany, as potential risks for the environment (e.g. chemical contamination or triggering of seismic activity) are weighed against the benefits of a high availability [18, Ch. 6.5][20]. Since the temperature requirements for geothermal direct-use are lower, a trend towards this kind of exploration has been observed recently [21]. As an example, the local energy supplier of the city of Munich (Germany) is working to provide the entire district heating demand from renewable energy systems by 2040, with major contributions coming from geothermal sources [21].

Fig. 1.2 shows a geothermal doublet which is the standard topology for hydrothermal systems. Two wellbores connect the deep groundwater aquifer with the geothermal power station. Through the production well hot fluid is lifted to the surface, whereas the injection well is used for reinjecting the cooled fluid after it has passed the heat exchanger. The heat exchanger transfers some of the heat of the geothermal fluid to a secondary medium, which is either used for electricity production or supplied directly to the district heating system [16, Ch. 8]. Due to the high pressure in the geothermal reservoir, the geothermal fluid is pushed upwards in the production well, settling at its idle water level closely beneath the surface. The remaining height difference must be overcome using a downhole pump. The so-called drawdown during pump operation needs to be considered in the pump dimensioning, as the water level further drops when fluid is extracted from the reservoir (dynamic water level). Moreover, an additional pressure reserve is required in order to avoid cavitation in the pump components [22, p. 45] and reduce the accumulation of mineral scales (scalings) [16,

[3] In order to increase the thermal efficiency, the heat content of the geothermal fluid is transferred to a working fluid with a lower vapor temperature, see also *Carnot efficiency* [17, p. 4260].

p. 271]. In total, the required pump head[4] for deep geothermal systems can be in the range of 700 m, at volume flow rates of up to 200 L s^{-1} [23]. For this purpose, multistage centrifugal pumps in the megawatt range are used.

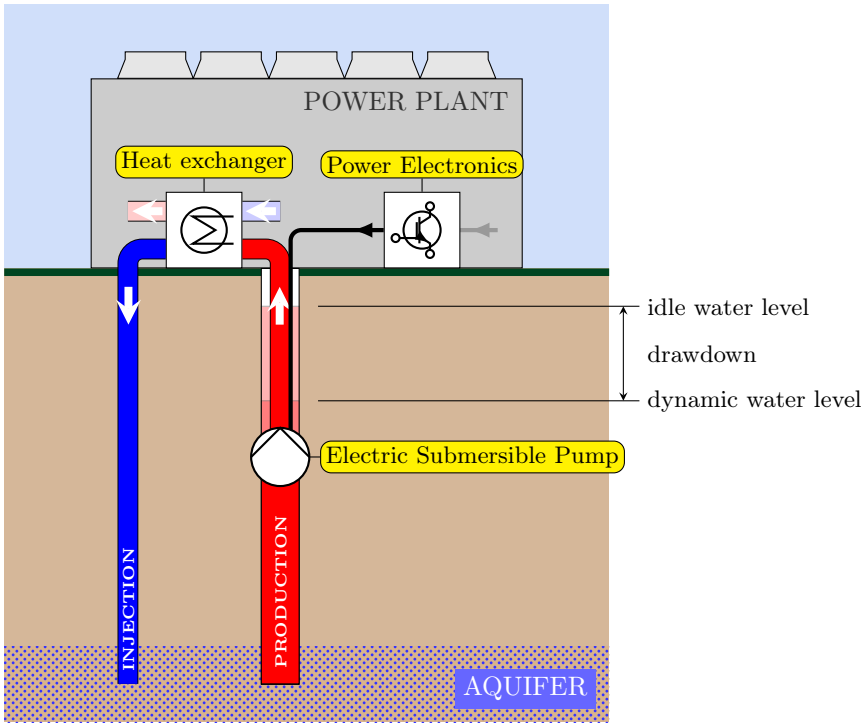

Figure 1.2: *Geothermal doublet for hydrothermal applications.*

Due to their high power outputs and great setting depths electric submersible pumps (ESPs) are used in most geothermal installations in Germany. An ESP consists of a hydraulic unit (pump) and a driving unit (motor), which are interconnected through the shaft and the protector (seal) [17, p. 4367]. The latter serves as an axial bearing and an oil reservoir for the oil-filled motor. The motor is electrically connected to the power source via a three-phase cable, which runs through the space between production tubing and casing. Due to the limited space in the borehole, the motor of a geothermal ESP has a long axial expansion of up to 22 m, whereas its diameter is comparably small with about 0.2 m [24]. If more power is required, a tandem configuration may be used, i.e. two motors are connected in series (mechanically). The unconventional dimensions are illustrated in Fig. 1.3, showing photographs of a dismounted geothermal ESP motor, taken at the geothermal power station in Unterhaching, Germany.
As an alternative to the ESP, a line-shaft pump (LSP) may be used, whose motor is located at the surface while the pump is located downhole, connected via a long driveshaft assembly. Although, LSPs have many advantages compared to ESPs (better cooling options, easy maintenance due to direct access, higher efficiency), their deployment is limited to geothermal systems with lower volume flow rates and limited setting depths. The maximum setting depths for LSP systems varies from approx. 250 to 300 m [16, 17] to 600 to 800 m [18] in the literature.

Since the ESP technology was predominantly adopted from the oil industry, the systems were not originally designed to withstand the harsh downhole conditions and high volume flow rates of deep geothermal power applications [25]. Although ESP manufacturers increased research activity and developed improved designs with higher power and temperature ratings in recent years [23, 26],

[4]For constant fluid density, pressure can be expressed as *head*, which is measured in meter.

(a) (b) (c)

Figure 1.3: *Photographs of the pump removal from the geothermal power station in Unterhaching, Germany: (a) ESP motor on a crane, showing its axial expansion, (b) zoom-in on the motor, showing its diameter and (c) the hydraulic part of the pump.*

average lifetimes of a few month to two years—referring to current installations in Germany—remain the bottleneck of the technology [27, p. 62][18, p. 681][25]. Maintenance and repair services are generally costly, as the entire production tubing needs to be removed from the borehole in order to set free the ESP, which requires specially trained personnel and expensive equipment. For unscheduled repair, additional costs are caused due to energy supply contracts and loss of revenue. Therefore, reliable and long term operation of the pump is key to the economical operation of the power plant [18]. The most relevant problems of the geothermal ESP are identified as follows:

- **Environmental and constructional aspects**:
  Due to the extreme ambient temperature and high power output, geothermal ESPs are constantly operated close to their thermal limits. The only way of cooling is to use the hot geothermal fluid passing along the motor casing. Overheating of the motor may lead to insulation failure and an increased power demand [26]. Moreover, chemical aspects such as corrosion or the accumulation of carbonate structures (scalings) may cause long-term damage to the system components [18, p. 681]. Due to its unfavourable constructional form (long axial expansion, small diameter, small shaft diameter), the ESP is further subject to high mechanical strain. Sudden load changes, e.g. due to solid parts entering the pump, can cause severe damage to the mechanical system [18, p. 672].
- **Limited availability of sensor data**:
  Condition monitoring of the ESP requires reliable and high quality sensor data of the remote system. Most manufacturers provide sensor units, which are attached to the ESP and transmit temperature, pressure, vibration or insulation measurements via the power cable (modulated onto the voltages) to the surface [28]. However, in case of sensor failure, there is no way of replacing the respective component, unless the ESP is removed from the borehole. Moreover, the transmission rate of the sensor data is very low (according to [28], sensor data is transmitted every 6 to 31 s, depending on the parameter). Other sensors, such as speed or torque sensors, are not installed at all.

- **Outdated and inefficient control**:
  Speed control of the ESP is typically realized by using a simple feedforward control scheme. Although the dynamic requirements on the control system are low for the given application, system start-up and sudden load changes will lead to very high currents and torque pulsations. Moreover, due to the lack of speed feedback, accurate tracking of the speed is not possible, which might lead to suboptimal operating conditions (e.g. deviations on the pump curve).

The success of the technology depends mainly on the question, whether power can be produced at costs comparable to other renewable energy systems. While hardware modifications such as enhanced materials, better machine designs or improved pump layouts are clearly necessary, focus of this work is on control and monitoring aspects, which do not require additional hardware, nor modification of existing hardware. The main goals of this thesis can be summarized as follows:

- Provide a better understanding of the physical processes taking place in the geothermal ESP system by means of a **dynamic model** which is suitable for simulations in e.g. Simulink®(or comparable numerical simulation tools).
- Improve the **efficiency** of the electrical machine, as to reduce heat production within the motor casing and minimize the electric power demand.
- Develop an enhanced **control** system which allows for accurate tracking of the optimum pump operating points and better disturbance rejection during sudden load changes or start-up and shut-down procedures. Moreover, incorporate a model-based reconstruction of relevant, yet non-measurable system states of the electromechanical parts of the ESP, required for the control and as a supplement for the condition monitoring system.

1.2 State-of-the-art

Concerning the previously stated objectives, relevant publications in the respective field of research are listed in the following.

1.2.1 Dynamic modeling of geothermal ESP systems

Publications dealing with the modeling and simulation of ESP systems are rarely found. Most of the available literature dealing with ESP systems is related to oil field applications, providing a limited scope on single subsystems of the ESP only.

For instance, in [29] an oil field ESP is described and simulated. The inherent motor geometry, the mechanical coupling between motor and load and the power transmission through the cable are accounted for. Although the electrical and mechanical components are described in detail and model sketches are presented, no equations are provided, nor is the hydraulic subsystem contained in the model. Similarly, in [30] simulations of an ESP for subsea applications are presented. Although some ESP specific characteristics are considered (e.g. multi-rotor induction machine, multi-level converter, long cable), details on the underlying models are not provided.
A detailed electromechanical model of an ESP is presented in [31], putting special emphasis on the mechanical resonance in the load torque, due to elastic coupling between the pump stages. In a recent study, a more sophisticated model of an oil field ESP is presented, which considers also mechanical resonance on the motor side, including a multi-rotor mechanical model for torsional stress and vibration analysis [32]. In both publications the hydraulic part is not considered, though.

In [33, 34] an ESP systems for subsea oil applications is analyzed, with focus on load filter design methods. Furthermore, the electric power transmission via downhole cables is analyzed in [35]. Simulation and experimental results from field studies are provided, yet the exact models underlying those results are not presented.
On the contrary, a general state-space model of an induction motor coupled with a multistage centrifugal pump is derived in [36]. The hydraulic part of the pump is derived by assuming an average streamline and applying basic laws from fluid dynamics. In the hydraulic model of the pump, the transient part of the pressure (head) created by the pump and subsequently the flow dynamics resulting from it are omitted, though. In fact, the transient model of the pump pressure is hardly found in literature. The only exceptions are [37, 38], where focus is solely on the hydraulic modeling of a centrifugal pump.
A simplified state-space model of a centrifugal pump system is proposed in [39], taking into account also the reservoir. The electrical system components, however, are not included.

In short, many publications are found related to the modeling of single parts of the ESP system, some of which even combining multiple components. However, a comprehensive model, featuring the electrical, mechanical and hydraulic components of a geothermal ESP, has not been published[5].

1.2.2 Efficient torque control of induction machines

Most publications dealing with maximum efficiency operation (or *loss minimizing control*) of electrical machines distinguish between (i) loss-model-based controllers (LMC, e.g. [40–48]), and (ii) search-based controllers (SC, e.g. [49–51]). Combinations of both (hybrid controllers) have also been reported [52]. For the LMC approach, an analytical expression of the power losses as a function of the control variables (e.g. reference currents or flux linkages) is derived and used for optimization. While the LMC method converges fast, it is also highly parameter and model dependent [43, 44, 53]. For the SC approach, on the other hand, the input power is measured and the control variables are iteratively changed until a minimum amount of input power is reached for a given torque and speed reference. This method does not depend on exact parameters, but the convergence rate is slow and torque pulsations may occur [46, 54].

In general, the electromagnetic torque output of an electrical machine is determined by the cross product of the current flowing through the stator windings and the magnetic field (linked flux) which is generated in the rotor. For induction machines (IMs), stator current and rotor flux can be controlled (almost) separately, i.e. the same torque output can be achieved for different combinations of currents and flux linkages. This degree of freedom gives room for efficiency enhancement.
Different torque control strategies may be pursued, depending on the machine speed (or applied frequency) and the commanded torque [6]. The corresponding optimization problems are typically stated using steady-state model equations (exceptions are e.g. [48, 55]). A unified framework for solving *analytically* the optimization problem has been presented in [6, 12] (with preliminary results in [8–10]); even though stated for synchronous machines, the concept may be applied to asynchronous machines as well. The fundamental idea is to reformulate the constraints (voltage ellipse, current circle, torque hyperbola) and the control strategies (MTPX hyperbolas) implicitly as *quadrics*[6] (or quadric surfaces) and solve an intersection problem, which narrows down to solving a fourth-order polynomial. With the presented framework, even anisotropic machines can be considered. Although iron losses are not included in [6], the extension is straightforward, i.e. by reformulation of the model equations considering iron losses (to be published in [12]). It is further

[5] With the exception of [5], which is the basis for the presented model in this work.

[6] A *quadric* is a vector-wise quadratic equation of the form $\boldsymbol{x}^\top \boldsymbol{M}\boldsymbol{x} + 2\boldsymbol{m}^\top \boldsymbol{x} + \mu = 0$, for some vectors $\boldsymbol{x} \in \mathbb{R}^2, \boldsymbol{m} \in \mathbb{R}^2$, matrix $\boldsymbol{M} \in \mathbb{R}^{2\times 2}$ and scalar $\mu \in \mathbb{R}$ [6].

shown, how magnetic saturation can be included, i.e. by linearization of the machine model at the current operating point and solving the optimization problem for the linearized system in each control step. It remains to chose the correct model and fit it into the existing framework, i.e. by formulating the respective quadrics. Moreover, accurate identification of the iron loss resistance and the magnetic saturation curve (or *flux maps*) are essential.

As opposed to synchronous machines, where all relevant quantities are accessible by measurement, squirrel-cage induction machines (SCIMs) have the disadvantage of the rotor currents and flux linkages not being directly accessible. As a consequence, flux estimation needs to be incorporated as to reconstruct the respective quantities. Naturally, the flux estimator is highly parameter dependent, too, which leads to deviations in the flux angle estimation. Moreover, the nonlinear effect of magnetic saturation needs to be considered. In order to cope with these practical issues, look-up table (LUT) based solutions have been proposed, either based on measurements [56, 57] or finite element analysis (FEA) [58, 59]. This way, the efficiency (or losses) can be calculated for various operating points and the optimal trajectories can be extracted from the acquired data. While iron losses are neglected in [56, 59], the standard iron loss model is incorporated in [57, 58], requiring LUT recordings for different speeds. A major drawback of all LUT-based approaches, is its dependency from the motor temperature. While it is proposed in [57] that the LUTs should be recorded for different temperatures, too, the question of *how* the temperature can be kept constant is not answered. In [60], a possible temperature compensation strategy is proposed for synchronous machines; however, under the assumption of negligible iron losses.

In summary, numerous publications dealing with LUT-based efficiency optimization of synchronous machines and IMs are found in literature. However, for IMs, most publications employ an explicit loss model for the efficiency calculation, which may suffer from modeling and parameter errors. A more generic approach, calculating directly the efficiency using input and output power measurements or estimates, while at the same time covering iron losses and temperature variations during the identification procedure, has not been published to the best knowledge of the author.

1.2.3 Speed-sensorless control of induction machines with LC filter

In medium voltage (MV) variable speed drive applications with long power cables (e.g. large pump systems), an inverter output (load) LC filter is often employed as to (i) decrease voltage deflection at the motor terminals, due to impedance imbalance between the cable and the motor, and to (ii) reduce steep voltage slopes which might damage the motor insulation and bearings due to high capacitive discharge [34, 61, 62]. However, the additional hardware comes at cost of electric coupling between the filter and motor currents and voltages, respectively, which in turn complicates the design of the control system.

Only few publications deal with the control of IMs with LC filter. Typically, a system of cascaded proportional-integral (PI) or dead-beat controllers is proposed [63–67]. These controllers, however, require individual and unintuitive tuning based on heuristic tuning rules or trial-and-error. Among the few publications further incorporating a *speed-sensorless* approach (i.e. [64, 65, 67]), the contribution of [64] stands out due to its minimal requirements on the measurement system, an extensive stability analysis and the provision of experimental results for all critical operation regions. The method, which has been patented [68], extends the (IM-only) full-order adaptive observer of [69] to the given drive system of IM and LC filter and has not been revisited ever since.

Generally, sensorless control of induction machines (without LC filter) using speed-adaptive reduced and full-order observers is a mature research topic which has been subject to extensive research in the past. First publications dealing with this topic appeared in the early nineties, with the pioneering

work of [70] (using the model reference adaptive system (MRAS) approach) and [71] (using the adaptive observer approach); it was shown only later, that the MRAS observer is a special case of the adaptive observer, which is at best marginally stable [72]. While in [70] the concept of *hyperstability* is applied—which was thoroughly derived for general MRAS systems in [73–75]—, the proof of global asymptotic stability in [71] is based on *Lyapunov's direct method*. Moreover, in [76] the hyperstability concept is transferred to the adaptive observer case. While the Lyapunov-based proof in [71] is flawed due to a neglected and non-measurable flux term in the adaption law, the hyperstability proof in [76] is based on false assumptions about the *positive-realness* property of the adaptive observer system [77]. In [78], a general observability study on induction machines is conducted, revealing the limitations of observer-based speed estimation schemes and highlighting the stability issues in the low-speed regeneration operation mode. As a consequence, research focus shifted towards tackling this low-speed instability phenomenom, e.g. [69, 72, 78–82]. First analytical designs for so-called *complete stability*— i.e. stability under all operating conditions except DC excitation—were proposed in [83–85]. In [83], a Lyapunov-based design is presented. However, it is shown in [86], that the proof is flawed and any such proof will fail, unless either the speed or the rotor flux are measured. In [84], the results of [83] are generalized by revisiting the hyperstability approach; it is shown that—even though not fulfilled by default—the positive realness property can be imposed by appropriate selection of the observer gains. A similar selection of observer gains is presented in [85] which is, however, obtained by performing a linearization analysis of the estimation error. A comprehensive survey on stabilizing methods for speed-adaptive reduced and full-order observers is presented in [87]. More recent results focus on performance improvements and robustness against parameter errors, i.e. by adaption of the stator and rotor resistances [88–92].

In conclusion, publications dealing with the control of an IM with LC filter almost exclusively employ a cascaded controller structure, which requires individual tuning of each controller. From the few publications using a *sensorless* approach, only the observer-based approach presented in [64] is applicable to the given drive system. However, it does not provide reasoning for the choice of observer gains and is derived for the continuous-time case only; for the low switching frequencies in large geothermal pump systems, a discrete-time approach is advisable, though.

1.3 Contribution & Outline

So far, a comprehensive dynamic model of a deep geothermal ESP system has not been published. In this work, a nonlinear state-space model is derived, covering all relevant components of a geothermal ESP. The multidisciplinary modeling approach (hydraulics, mechanics, electronics) results in a modular mathematical description of the identified system components, stated as a system of (coupled) first-order differential equations with specified interfaces. Due to its state-space form, the dynamic model is particularly suited for simulations in Simulink® (or similar software). Moreover, the modular structure allows for a simple exchange of components. The model is validated in simulations for different configurations and with a set of realistic system parameters. The *modeling* contributions can be summarized as follows:

1. A dynamic state-space model of a deep geothermal ESP system, comprising hydraulic, mechanical and electrical components is derived and validated in simulations.

   (a) An elastically coupled multi-rotor electrical machine and multi-stage centrifugal pump model is derived and evaluated against an ordinary lumped parameters model.

   (b) Various aspects like the impact of the power cable, the inverter output filter and the multi-level converter topology are analyzed in the given context.

(c) A realistic set of carefully balanced system parameters is provided, which allows for simulating a generic deep geothermal ESP system.

Regarding the efficient operation of IMs, it was found that LUT-based approaches often use explicit loss models, which are prone to modeling and parameter errors and do not consider temperature variations during the LUT recordings. In this work, an experimental method of identifying (and reproducing) the maximum efficiency operating points of an induction machine is presented, which is based on generic model equations and which is almost invariant to parameter uncertainties. In addition, by comparing the proposed method with the standard ESP control method the implementation of a more sophisticated control system is motivated. The *efficiency* contributions can be stated as follows

2. An experimental identification method for LUT-based maximum efficiency operation of an induction machine is presented.

   (a) The identification is conducted in an arbitrarily rotating coordinate system, i.e. it does not depend on the correct estimation of the rotor flux orientation.

   (b) Nonlinear machine maps, such as flux linkage or efficiency maps are shown.

   (c) An improved compensation strategy for temperature variations during the identification process is proposed.

3. A quantitative assessment of the maximum efficiency control strategy and the standard control strategy is carried out, revealing that, particularly in part-load, major energy savings can be achieved.

Lastly, a closed-loop speed control system for the electric drive system of an ESP is developed. Instead of the cascaded controller structure found in the literature, the control system is based on a gain-scheduled state-feedback current controller and superimposed proportional-integral speed and flux controllers. Since the speed cannot be measured in real-time due to the remote deployment of the electrical machine, a speed-sensorless approach needs to be realized. Using the concept of a speed-adaptive observer, the relevant system states and parameters can be reconstructed. Unlike the approach found in the literature, a deterministic tuning approach is used here, which can be fitted better to the parameters of the electric drive system. Both, controller and observer, are designed in the discrete-time domain. The proposed control system is validated experimentally on a down-scaled testbench and in simulations. The main *control* contributions are

4. A gain-scheduled state-feedback current controller with proportional-integral set-point tracking is derived for an induction machine with LC filter.

   (a) The control system is derived in the discrete-time domain as to account for the low switching frequencies and the inverter delay of large geothermal pump systems.

   (b) A deterministic and well-established tuning method from optimal control theory is applied and the impact of the tuning factors is analyzed.

5. A speed-adaptive observer for an induction machine with LC filter is derived.

   (a) Observability of the drive system is analyzed and critical operating points are identified.

   (b) It is shown that an analytical tuning rule as exists for the IM-only case cannot be derived if an LC filter is used. Instead tuning is likewise based on the optimal control approach and gain-scheduling is applied.

(c) The speed-adaptive observer is derived in the discrete-time domain, putting special emphasis on the correlation between continuous-time and discrete-time designs, e.g. by deriving the discretization error or describing respective gain transformations.

The thesis is structured as follows. In Chapter 2, the dynamic model of the ESP is derived and evaluated. Chapter 3 deals with the experimental efficiency optimization of the induction machine, while Chapter 4 concerns the closed-loop speed control system and speed-adaptive observer. Finally, in Chapter 5 the results are summarized and an outlook is given.

Chapter 2

Dynamic modeling and simulation of deep geothermal electric submersible pump systems

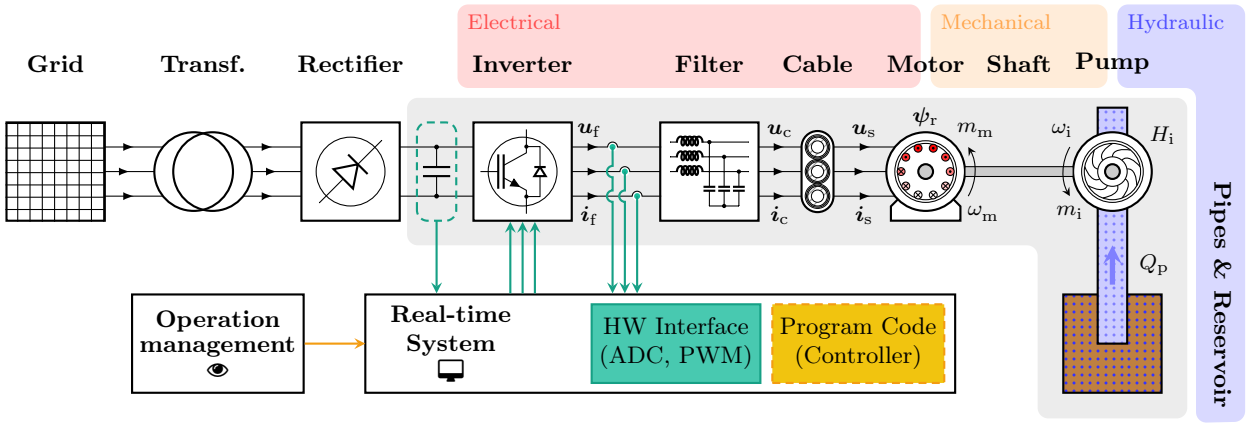

Figure 2.1: *Topology of an electric submersible pump (ESP) system in deep geothermal energy applications.*

A nonlinear state-space model of a geothermal ESP system is derived, which is prerequisite for simulations, system analysis and control system design. The main objective of this chapter is to provide a *modular* system model that can easily be implemented and extended in simulation software (e.g. Simulink® or similar software). Each component is modeled separately, thus allowing for convenient replacement of individual components.

An overview of the system components of a typical geothermal ESP system is shown in Fig. 2.1. The ESP model derived in this chapter is constrained to the gray shaded components. The remaining components are examplarily shown, but are outside the scope of this work. The ESP system can be divided into three physical subsystems, i.e. the electrical (red), the mechanical (orange) and the hydraulic subsystem (blue).

The ESP components are identified as follows (see e.g. [26, 29, 34]):

1. **Voltage source inverter** (VSI, see Sec. 2.1.1)
   → Produces variable frequency and amplitude output voltages.
2. **Filter** (see Sec. 2.1.2)
   → Smooths the pulsed VSI output voltages.
3. **Cable** (see Sec. 2.1.3)
   → Transmits the electrical power to the downhole motor.
4. **Motor** (see Sec. 2.1.4)
   → Drives the pump by converting electrical into mechanical power.
5. **Protector (Seal)**
   → Serves as an axial bearing and oil reservoir, located between motor and pump.
6. **Shaft** (see Sec. 2.3)
   → Conveys the mechanical power from the motor to the pump.
7. **Pump** (see Sec. 2.2.1)
   → Generates pressure by converting mechanical into hydraulic power.
8. **Pipes & reservoir** (see Sec. 2.2.2)
   → Determines the hydraulic load.

In the derived model, the protector is considered as a part (extension) of the shaft and is therefore included in the shaft model, without further elaborating on axial forces acting on the motor and pump, respectively. Based on the component selection, the nonlinear state-space models of the geothermal ESP system will be derived in the following.

Parts of this chapter have been published in [5]. The main extensions are: (i) A comparison between two-level and multi-level inverters, (ii) a deeper analysis of the LC filter impact, (iii) a multi-sectional cable model, (iv) an electromechanical multi-rotor induction machine model and (v) a hydromechanical multi-stage pump model.

Remark 1 (Thermal subsystem)**.** *As the term 'geothermal' indicates, the* thermal *subsystem might also be considered in the model. However, since the temperature varies slowly, its dynamics are assumed negligible. Nevertheless, the thermal impact on the other subsystems can be accounted for by introducing temperature dependent model parameters.*

For the sake of readability, the time dependency (argument t) of system states and time-varying parameters is not explicitly stated throughout this chapter.

2.1 Modeling of the electrical subsystem

The electrical subsystem comprises voltage source inverter (VSI), filter, cable and motor. Based on the three-phase description derived for each component, an equivalent two-phase description in stationary coordinates is obtained by applying the *amplitude invariant* Clarke transformation (see App. A.1.1). The phase voltages are stated with respect to the reference potential measured at the motor star point $\mathtt{Y_m}$, which is further specified in the motor section (see Sec. 2.1.4). Moreover, signal vectors which are assigned to a specific reference frame are introduced without explicitly stating the vector elements, e.g. the vector $\boldsymbol{x}^{\mathrm{abc}} = (x^{\mathrm{a}}, x^{\mathrm{b}}, x^{\mathrm{c}})^{\top}$ is introduced stating $\boldsymbol{x}^{\mathrm{abc}}$ only.

2.1.1 Voltage source inverter

The power converter links the grid with the electrical drive system and is typically given in back-to-back configuration, with a grid-side VSI, a shared DC-link and a motor-side VSI. The grid-side VSI (active front end) allows for bidirectional power flow. If the electrical power is supposed to flow from the grid to the machine only, a diode bridge rectifier may alternatively be used. In this work a charged DC-link capacitance with a constant voltage is assumed (see Ass. 2), hence the grid-side device is not relevant and the model is limited to the motor side only. The motor-side VSI serves as a voltage and power source for the electrical machine of the pump. Its pulsed (modulated) output voltages are generated such that their respective fundamental waveforms are sinusoids of variable frequency and amplitude, according to a specified reference voltage.

For MV applications with long power cables, multilevel converters are often preferred over two-level converters, since the steep voltage slopes of the output voltage can be reduced considerably. Moreover, the total harmonic distortion (THD) of the multilevel inverter output is reduced compared to the two-level inverter, as will be shown later in this section. Therefore, in this work a five-level active neutral-point clamped (5L-ANPC) inverter as described briefly in [93] (and in more detail in [94, Ch. 2.4.2]) is employed, which is well-suited for MV drive applications. For VSI related voltages and currents, subscript 'v' is used in the following.

2.1.1.1 Simplified model of a 5L-ANPC inverter

The schematic of a single phase $k \in \{\mathrm{a}, \mathrm{b}, \mathrm{c}\}$ of the inverter is depicted in Fig. 2.2. Each phase a, b and c of the inverter consists of three cascaded cells with a total of eight power switches per phase. The input is accessed via the terminals $\mathtt{D}+$ and $\mathtt{D}-$ while the output voltages are tapped from the terminals $\mathtt{T_k}$, respectively. Moreover, the phase current i_{v}^{k} flows out of the inverter. The power switches of phase k—typically insulated-gate bipolar transistor (IGBT) are employed here—are controlled by the three switching signals $s^{\mathrm{k1}}, s^{\mathrm{k2}}, s^{\mathrm{k3}} \in \{0, 1\}$ (the respective inverse signals are denoted by $\bar{s}^{\mathrm{k1}} = 1 - s^{\mathrm{k1}}$, $\bar{s}^{\mathrm{k2}} = 1 - s^{\mathrm{k2}}$ and $\bar{s}^{\mathrm{k3}} = 1 - s^{\mathrm{k3}}$). Cell 1 is controlled by switching signal s^{k1}, with switches 1 and 3 (counted from top to bottom) and switches 2 and 4 controlled in pairs. Cell 2 consists of two complementary switches controlled by s^{k2}, as does cell 3 which in turn is controlled by s^{k3}.

Assumption 1 (Ideal switches)**.** *The inverter IGBTs are assumed to be ideal switches with logical levels '1' (closed) and '0' (open), i.e.*

- *no current may flow if the switch is open,*
- *bidirectional current may flow (without voltage drop), if the switch is closed and*
- *the switching takes place instantaneously (no switching delay).*

The input DC-link capacitances $C_{\mathrm{dc_1}}$ are shared between the three phases, whereas the capacitance $C_{\mathrm{dc_2}}$ is assigned to each phase individually [93]. While $C_{\mathrm{dc_1}}$ is charged by the grid-side rectifier or VSI, $C_{\mathrm{dc_2}}$ is charged by exploiting redundant switching states; different switching combinations may lead to the same output voltage, but change the direction of the current flowing into or out of the capacitance (i.e. 'voltage balancing'). As sophisticated inverter control algorithms are beyond the scope of this work, the following assumption is made.

Assumption 2 (VSI capacitances)**.** *The inverter capacitances $C_{\mathrm{dc_1}}$ and $C_{\mathrm{dc_2}}$ are charged to defined voltage levels $\frac{u_{\mathrm{dc}}}{2}$ and $\frac{u_{\mathrm{dc}}}{4}$, respectively.*

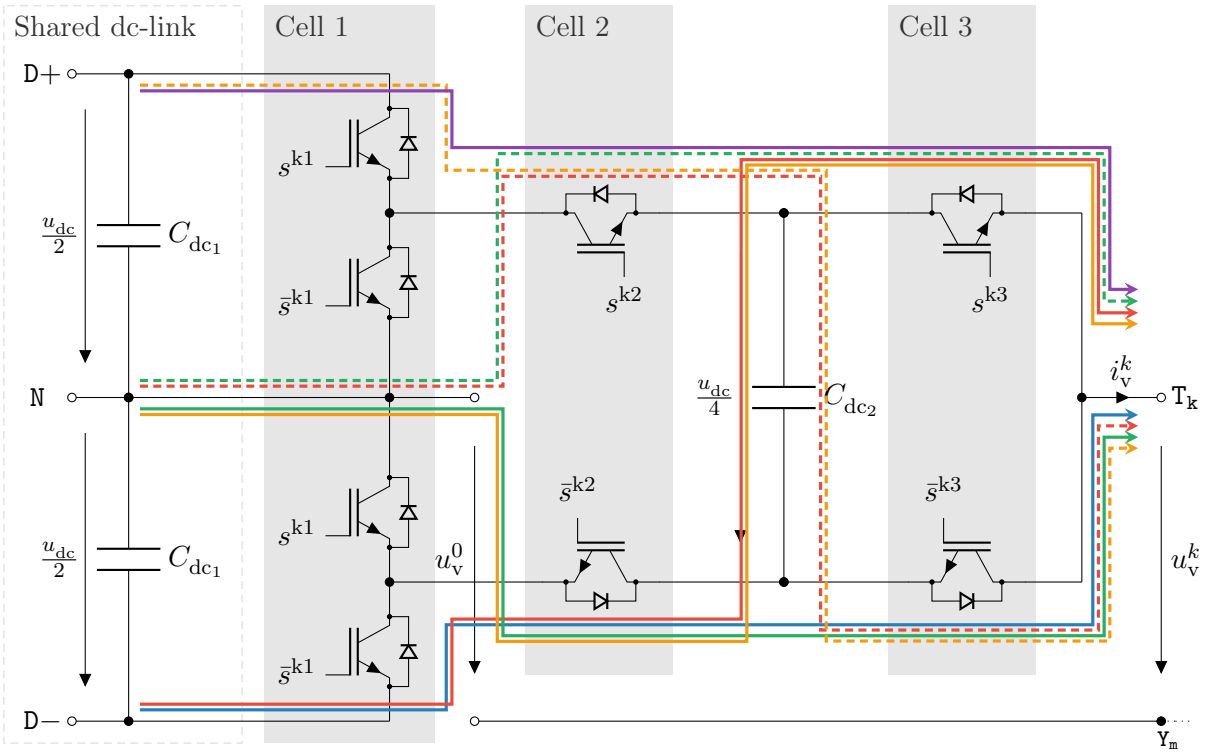

Figure 2.2: *Schematic of a single phase* $k \in \{a, b, c\}$ *of a 5L-ANPC inverter. The current paths (colored graphs) depend on the inverter switching levels.*

The line-to-neutral voltages u_v^{kn}, measured between output terminal T_k and inverter neutral point N, are given by

$$u_v^{kn} = u_v^k - u_v^0, \tag{2.1}$$

where u_v^k is the respective phase voltage measured between the output terminal T_k and the motor star point Y_m, and u_v^0 is the voltage measured between neutral point N and motor star point Y_m. The switching combinations and resulting line-to-neutral voltages of phase k are listed in Tab. 2.1. In Fig. 2.2 the corresponding current paths are indicated by the colored lines, which comply with the background colors of the table rows. Although three switches allow for eight different switching combinations, the line-to-neutral voltage can attain five distinct voltage levels only, i.e. $u_v^{kn} \in \{-\frac{u_{dc}}{2}, -\frac{u_{dc}}{4}, 0, \frac{u_{dc}}{4}, \frac{u_{dc}}{2}\}$. As the exact switching combinations leading to the different voltage levels are irrelevant for the presented model, the switching signal $s^k \in \{0, 1, 2, 3, 4\}$ is used to summarize and describe the overall switching state and its respective output voltage level for phase k.

Hence, the overall three-phase switching vector $\boldsymbol{s}^{abc} \in \{0, 1, 2, 3, 4\}^3$ can be introduced such that the line-to-neutral voltages $\boldsymbol{u}_v^{abcn}$ may be written as

$$\boldsymbol{u}_v^{abcn} = \frac{1}{4} u_{dc} \boldsymbol{s}^{abc} - \frac{1}{2} \mathbf{1}_3 u_{dc}. \tag{2.2}$$

Remark 2 (Inverter neutral point)**.** *The neutral point of the inverter is typically selected as the midpoint potential between the terminals* $D+$ *and* $D-$*. However, this choice is arbitrary and any other potential might be selected, e.g. the potential at terminal* $D-$*.*

The line-to-line voltages $\boldsymbol{u}_v^{a\text{-}b\text{-}c}$ measured between the inverter outputs T_a, T_b and T_c (see Fig. 2.2)

Table 2.1: *Switching states and output voltage levels of a single five-level ANPC inverter phase.*

State s^{k}	**Switch** $\mathbf{s}^{\mathrm{k1}}$	**Switch** s^{k2}	**Switch** s^{k2}	**Output voltage** $u_{\mathrm{v}}^{\mathrm{kn}}$
0	0	0	0	$-\frac{u_{\mathrm{dc}}}{2}$
1	0	0	1	$-\frac{u_{\mathrm{dc}}}{4}$
1	0	1	0	$-\frac{u_{\mathrm{dc}}}{4}$
2	1	0	0	0
2	0	1	1	0
3	1	0	1	$\frac{u_{\mathrm{dc}}}{4}$
3	1	1	0	$\frac{u_{\mathrm{dc}}}{4}$
4	1	1	1	$\frac{u_{\mathrm{dc}}}{2}$

can in turn be expressed in terms of the line-to-neutral voltages as

$$\boldsymbol{u}_{\mathrm{v}}^{\mathrm{a\text{-}b\text{-}c}} = \begin{pmatrix} u_{\mathrm{v}}^{\mathrm{an}} - u_{\mathrm{v}}^{\mathrm{bn}} \\ u_{\mathrm{v}}^{\mathrm{bn}} - u_{\mathrm{v}}^{\mathrm{cn}} \\ u_{\mathrm{v}}^{\mathrm{cn}} - u_{\mathrm{v}}^{\mathrm{an}} \end{pmatrix} = \underbrace{\begin{bmatrix} 1 & -1 & 0 \\ 0 & 1 & -1 \\ -1 & 0 & 1 \end{bmatrix}}_{=:\boldsymbol{T}_{\mathrm{V}}} \boldsymbol{u}_{\mathrm{v}}^{\mathrm{abcn}}, \tag{2.3}$$

yielding nine different output voltage levels, i.e. $\boldsymbol{u}_{\mathrm{v}}^{\mathrm{a\text{-}b\text{-}c}} \in u_{\mathrm{dc}} \cdot \{-1, -\frac{3}{4}, -\frac{1}{2}, -\frac{1}{4}, 0, \frac{1}{4}, \frac{1}{2}, \frac{3}{4}, 1\}^3$. In the remainder of this chapter, the motor star point $\mathtt{Y_m}$ is considered the reference point for the phase quantities. Hence, the phase voltages $\boldsymbol{u}_{\mathrm{v}}^{\mathrm{abc}}$, measured between the output terminals $\mathtt{T_k}$ of the inverter and $\mathtt{Y_m}$, are expressed in terms of the inverter variables as

$$\boldsymbol{u}_{\mathrm{v}}^{\mathrm{abc}} = \boldsymbol{u}_{\mathrm{v}}^{\mathrm{abcn}} - \boldsymbol{1}_3 u_{\mathrm{v}}^0 \overset{(2.2)}{=} \tfrac{1}{4} u_{\mathrm{dc}} \boldsymbol{s}^{\mathrm{abc}} - \left(\tfrac{1}{2} u_{\mathrm{dc}} + u_{\mathrm{v}}^0\right) \boldsymbol{1}_3. \tag{2.4}$$

Applying the reduced amplitude invariant Clarke transformation (as defined in (A.4) with $\kappa = \frac{2}{3}$), the phase voltages and currents at the inverter output can be stated in $\alpha\beta$-coordinates as

$$\boldsymbol{u}_{\mathrm{v}}^{\alpha\beta} = \boldsymbol{T}_{\mathrm{C,red}} \boldsymbol{u}_{\mathrm{v}}^{\mathrm{abc}} \overset{(2.4)}{=} \tfrac{1}{4} \boldsymbol{T}_{\mathrm{C,red}} u_{\mathrm{dc}} \boldsymbol{s}^{\mathrm{abc}} \quad \text{and} \tag{2.5}$$

$$\boldsymbol{i}_{\mathrm{v}}^{\alpha\beta} = \boldsymbol{T}_{\mathrm{C,red}} \boldsymbol{i}_{\mathrm{v}}^{\mathrm{abc}}. \tag{2.6}$$

Note that the term $\frac{1}{2} u_{\mathrm{dc}} + u_{\mathrm{v}}^0$ in (2.4) is cancelled out when using the reduced Clarke transformation. In the $\alpha\beta$-reference frame, the feasible phase voltages can be visualized by the voltage hexagon as shown in Fig. 2.3. The switching combinations $\boldsymbol{s}^{\mathrm{abc}}$ yielding the respective nodes are given in the circles attached to them (e.g. $\boldsymbol{s}^{\mathrm{abc}} = (2, 1, 4)^\top$).

In general, the objective of the VSI is to reproduce a given reference voltage vector $\boldsymbol{u}_{\mathrm{v}}^{\alpha\beta\star}$ at its output terminals. In order to achieve this goal, the desired voltage is sampled with sampling frequency f_{S} and translated into the time domain by modulation of the switching signal, using e.g. sinusoidal pulse-width modulation (SPWM) or space vector modulation (SVM). As a result, the sliding time integral (moving average) of the output voltages over a defined sampling period $T_{\mathrm{S}} = \frac{1}{f_{\mathrm{S}}}$ matches the reference voltage sample [95, Ch. 11.2.4], i.e.

$$\boldsymbol{u}_{\mathrm{v}}^{\alpha\beta\star}(nT_{\mathrm{S}}) = \frac{1}{T_{\mathrm{S}}} \int_{nT_{\mathrm{S}}}^{(n+1)T_{\mathrm{S}}} \boldsymbol{u}_{\mathrm{v}}^{\alpha\beta}(t)\mathrm{d}t, \qquad \text{for} \quad n \in \mathbb{N}. \tag{2.7}$$

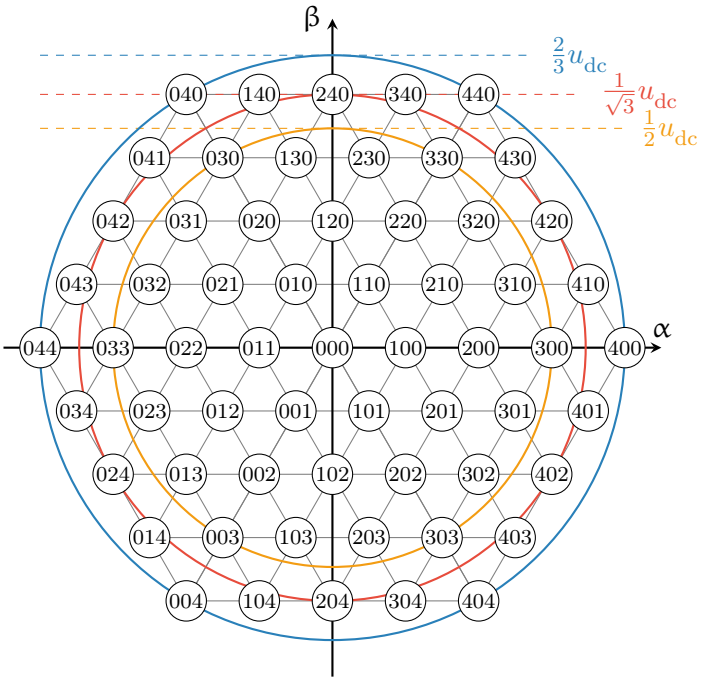

Figure 2.3: *Voltage hexagon of a five-level inverter with redundant switching states.*

An SVM algorithm for five-level inverters has been implemented based on [96]. The idea is to (i) find the sub-hexagon, which contains the reference voltage vector, (ii) perform a standard (two-level) SVM, and (iii) add the respective offset of the sub-hexagon, in order to obtain the correct switching vectors and timings. Note that, due to Ass. 2, redundant switching combinations are summarized by a single switching combination per node, simplifying significantly the implementation.

2.1.1.2 Comparison of 2L/5L inverter output waveforms

In order to exemplify the superiority of a five-level (5L) inverter over a two-level (2L) inverter, the raw inverter output line-to-line (LTL-RAW), line-to-neutral (LTN-RAW), phase (PHA-RAW) and zero-sequence components (ZER)—defined as $u_{\mathrm{v}}^{0} = \frac{1}{3}(u_{\mathrm{v}}^{\mathrm{an}} + u_{\mathrm{v}}^{\mathrm{bn}} + u_{\mathrm{v}}^{\mathrm{cn}})$ under the assumption of a balanced load [95, Ch. 4.2]—are plotted exemplarily for a single phase in Fig. 2.4, given a sinusoidal reference voltage (REF) of fundamental frequency $f = 50\,\mathrm{Hz}$ and an inverter sampling frequency of $f_{\mathrm{S}} = 1\,000\,\mathrm{Hz}$. It can be clearly observed that the 5L voltages are 'more sinusoidal' than the 2L outputs. Moreover, a time delay between the given reference and the respective filtered[1] line-to-line (LTL-LPF) and line-to-neutral (LTN-LPF) voltages is apparent. In Fig. 2.5, the fast Fourier transform (FFT) of the 5L and 2L phase voltages are compared, revealing that the fundamental components are comparable, but the high frequency side-band components are more distinct for the 2L inverter. As a result, the total harmonic distortion (THD) of the 5L inverter (THD = 11.86 %) is much smaller compared to the THD of the 2L inverter (THD = 40.1 %), with

$$\mathrm{THD} := \frac{\sum_{n=2}^{\infty} (\hat{u}^{(n)})^2}{\hat{u}^{(1)}}, \tag{2.8}$$

where $\hat{u}^{(n)}$ represents the n^{th} voltage harmonic's amplitude (see e.g. [97, p. 3.1.2.1]).

[1] Filtering has been carried out using the `filtfilt(...)` function of MATLAB® (Signal Processing Toolbox) and a third-order IIR digital low-pass filter (LPF) with cut-off frequency $0.5 f_{\mathrm{S}}$.

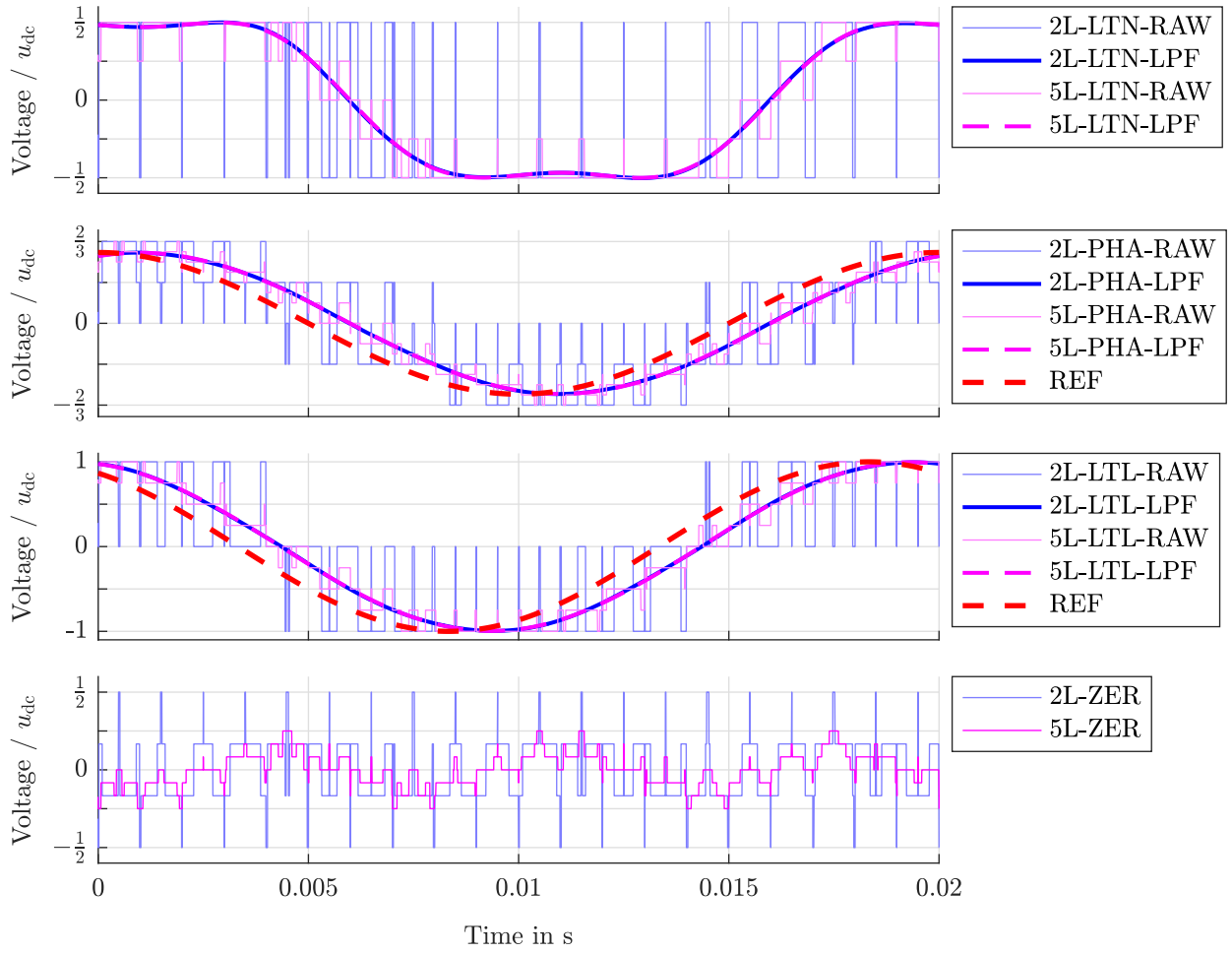

Figure 2.4: *Exemplary output voltage waveform comparison of a two-level (2L) and a five-level (5L) inverter, with raw output (RAW), filtered output (LPF) and reference (REF), generated at fundamental frequency* $f = 50\,\mathrm{Hz}$ *and with inverter sampling frequency* $f_\mathrm{S} = 1\,000\,\mathrm{Hz}$. *From top to bottom: Line-to-neutral voltages (LTN), phase voltages (PHA), line-to-line voltages (LTL), zero-sequence components (ZER).*

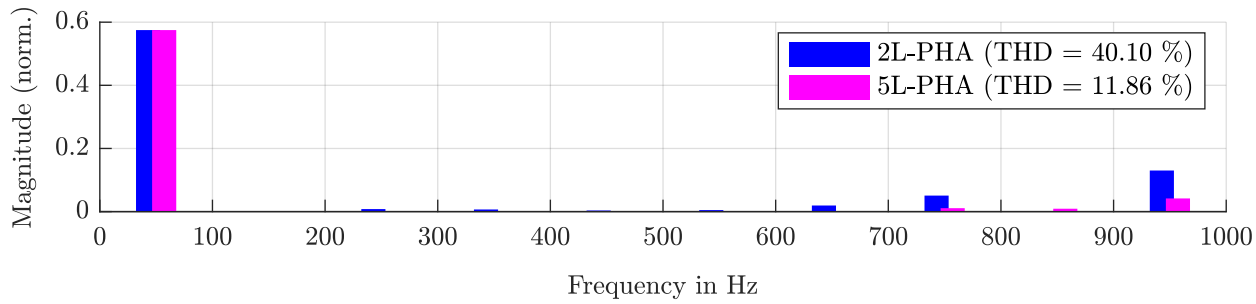

Figure 2.5: *FFT and THD comparison of the phase voltages (PHA) of a two-level (2L) and a five-level (5L) inverter, generated at fundamental frequency* $f = 50\,\mathrm{Hz}$ *and inverter sampling frequency* $f_\mathrm{S} = 1\,000\,\mathrm{Hz}$).

2.1.2 Filter (LC filter)

The VSI generates voltage pulses with steep slopes (high $\frac{\mathrm{d}}{\mathrm{d}t}\boldsymbol{u}_\mathrm{v}^{\alpha\beta}$) which (i) increase harmonic losses and (ii) put high stress on the insulation due to parasitic cable and motor capacitances [98]. Moreover, the high inductance of the motor windings causes (iii) wave reflection at the machine terminals with a reflection factor close to one [99]; since the reflected voltage may reach twice the original amplitude, a voltage derating is required [99]. An effective way of avoiding the mentioned effects is to employ an inverter output filter (LC lowpass filter) which smooths the output voltages, and thus reduces steep voltage slopes. The LC filter is located at the VSI output, linking the VSI with the power cable (see Fig. 2.1). Related quantities are denoted by subscript 'f'.

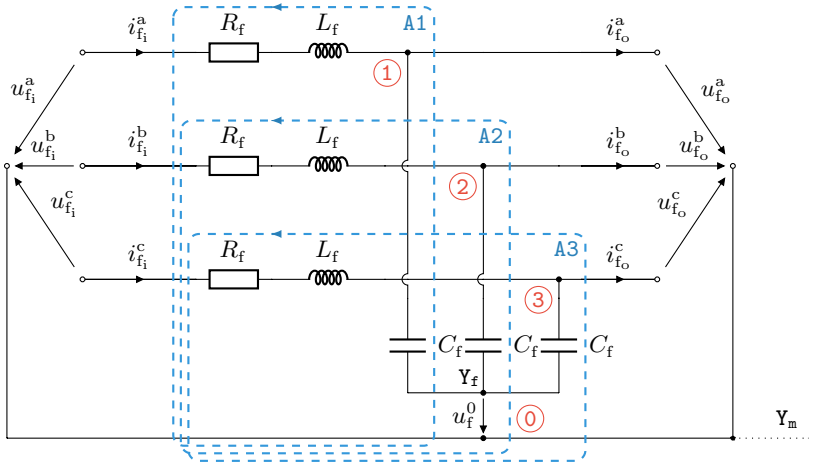

Figure 2.6: *Schematic of an LC filter with non-negligible series resistance.*

The schematic of an LC filter with non-negligible series resistance is shown in Fig. 2.6, with filter resistance R_f, filter inductance L_f and filter capacitance C_f. The star point $\mathtt{Y_f}$ of the wye-connected capacitors is not grounded, and hence floating with voltage u_f^0 between $\mathtt{Y_f}$ and the motor star point $\mathtt{Y_m}$. Moreover, the input voltages are denoted by $\boldsymbol{u}_{\mathrm{f_i}}^{\mathrm{abc}}$, the input currents by $\boldsymbol{i}_{\mathrm{f_i}}^{\mathrm{abc}}$, the output voltages by $\boldsymbol{u}_{\mathrm{f_o}}^{\mathrm{abc}}$ and the output currents by $\boldsymbol{i}_{\mathrm{f_o}}^{\mathrm{abc}}$.

Applying Kirchhoff's current law (KCL) on nodes ⓪ to ③ and Kirchhoff's voltage law (KVL) on meshes A1 to A3, respectively, yields

$$\frac{\mathrm{d}}{\mathrm{d}t}\begin{pmatrix}\boldsymbol{i}_{\mathrm{f_i}}^{\mathrm{abc}}\\ \boldsymbol{u}_{\mathrm{f_o}}^{\mathrm{abc}}\end{pmatrix} = \begin{bmatrix}-\frac{1}{T_\mathrm{f}}\boldsymbol{I}_3 & -\frac{1}{L_\mathrm{f}}\boldsymbol{I}_3\\ \frac{1}{C_\mathrm{f}}\boldsymbol{I}_3 & \boldsymbol{0}_{3\times3}\end{bmatrix}\begin{pmatrix}\boldsymbol{i}_{\mathrm{f_i}}^{\mathrm{abc}}\\ \boldsymbol{u}_{\mathrm{f_o}}^{\mathrm{abc}}\end{pmatrix} + \begin{bmatrix}\frac{1}{L_\mathrm{f}}\boldsymbol{I}_3 & \boldsymbol{0}_{3\times3}\\ \boldsymbol{0}_{3\times3} & -\frac{1}{C_\mathrm{f}}\boldsymbol{I}_3\end{bmatrix}\begin{pmatrix}\boldsymbol{u}_{\mathrm{f_i}}^{\mathrm{abc}}\\ \boldsymbol{i}_{\mathrm{f_o}}^{\mathrm{abc}}\end{pmatrix} + \underbrace{\begin{bmatrix}\boldsymbol{0}_3\\ \boldsymbol{1}_3\end{bmatrix}\frac{\mathrm{d}}{\mathrm{d}t}u_\mathrm{f}^0}_{\circledast}, \tag{2.9}$$

where $T_\mathrm{f} = \frac{L_\mathrm{f}}{R_\mathrm{f}}$ denotes the filter time constant. Since $\boldsymbol{T}_{\mathrm{C,red}}\boldsymbol{1}_3\frac{\mathrm{d}}{\mathrm{d}t}u_\mathrm{f}^0 = \boldsymbol{0}_2$, the $\circledast$ term in (2.9) vanishes if the reduced Clarke transformation is applied, thus yielding the reduced state-space representation

$$\frac{\mathrm{d}}{\mathrm{d}t}\begin{pmatrix}\boldsymbol{i}_{\mathrm{f_i}}^{\alpha\beta}\\ \boldsymbol{u}_{\mathrm{f_o}}^{\alpha\beta}\end{pmatrix} = \underbrace{\begin{bmatrix}-\frac{1}{T_\mathrm{f}}\boldsymbol{I}_2 & -\frac{1}{L_\mathrm{f}}\boldsymbol{I}_2\\ \frac{1}{C_\mathrm{f}}\boldsymbol{I}_2 & \boldsymbol{0}_{2\times2}\end{bmatrix}}_{=:\boldsymbol{A}_\mathrm{f}}\underbrace{\begin{pmatrix}\boldsymbol{i}_{\mathrm{f_i}}^{\alpha\beta}\\ \boldsymbol{u}_{\mathrm{f_o}}^{\alpha\beta}\end{pmatrix}}_{=:\boldsymbol{x}_\mathrm{f}} + \underbrace{\begin{bmatrix}\frac{1}{L_\mathrm{f}}\boldsymbol{I}_2 & \boldsymbol{0}_{2\times2}\\ \boldsymbol{0}_{2\times2} & -\frac{1}{C_\mathrm{f}}\boldsymbol{I}_2\end{bmatrix}}_{=:\boldsymbol{B}_\mathrm{f}}\underbrace{\begin{pmatrix}\boldsymbol{u}_{\mathrm{f_i}}^{\alpha\beta}\\ \boldsymbol{i}_{\mathrm{f_o}}^{\alpha\beta}\end{pmatrix}}_{=:\boldsymbol{u}_\mathrm{f}} \tag{2.10}$$

in the $\alpha\beta$-reference frame, with state vector $\boldsymbol{x}_\mathrm{f} \in \mathbb{R}^4$, input vector $\boldsymbol{u}_\mathrm{f} \in \mathbb{R}^4$, system matrix $\boldsymbol{A}_\mathrm{f} \in \mathbb{R}^{4\times4}$ and input matrix $\boldsymbol{B}_\mathrm{f} \in \mathbb{R}^{4\times4}$. Note, that the input voltage vector $\boldsymbol{u}_{\mathrm{f_i}}^{\alpha\beta}$ is equal to the VSI output vector $\boldsymbol{u}_\mathrm{v}^{\alpha\beta}$ and the output current vector $\boldsymbol{i}_{\mathrm{f_o}}^{\alpha\beta}$ depends on the load connected to the filter output.

In the following, the filtering capabilities of the LC filter are examined exemplarily for phase a. For the analysis, the filter parameters stated in Tab. 2.2 are assumed. The transfer function from the filter input voltage $u^{\mathrm{a}}_{\mathrm{f_i}}$ (= VSI output) to the filter output voltage $u^{\mathrm{a}}_{\mathrm{f_o}}$ is derived from (2.9) as that of a second-order system, i.e.

$$G_{\mathrm{f}}(s) = \frac{u^{\mathrm{a}}_{\mathrm{f_o}}(s)}{u^{\mathrm{a}}_{\mathrm{f_i}}(s)} = \frac{1}{\frac{1}{\omega_0^2}s^2 + 2\frac{\zeta}{\omega_0}s + 1} \qquad \text{with} \quad \omega_0 = \frac{1}{\sqrt{L_{\mathrm{f}}C_{\mathrm{f}}}} \quad \text{and} \quad \zeta = \frac{1}{2}\frac{R_{\mathrm{f}}C_{\mathrm{f}}}{\sqrt{L_{\mathrm{f}}C_{\mathrm{f}}}}, \tag{2.11}$$

where ω_0 is the filter resonant frequency and ζ denotes the damping coefficient. It can be deduced that, by variation of the filter series resistance R_{f}, different levels of damping of the filter resonance can be achieved. Defining R_{f0} as reference resistance (as stated in Tab. 2.2), variation of the filter resistance

- by $R_{\mathrm{f}} = 0.2R_{\mathrm{f0}}$ (0.2R) yields $\zeta = 0.002$,
- by $R_{\mathrm{f}} = R_{\mathrm{f0}}$ (1.0R) yields $\zeta = 0.009$ and
- by $R_{\mathrm{f}} = 5R_{\mathrm{f0}}$ (5.0R) yields $\zeta = 0.047$, respectively.

Figure 2.7 shows the filter impact from the phase voltage (PHA) at the inverter output (VSI) to the filter output (LC) for the no-load case, i.e. for $i^{\mathrm{a}}_{\mathrm{f_o}} = 0\,\mathrm{A}$ and for the aforementioned resistance variations. In Fig. 2.7a the transient behavior of the filter, excited at $t = 0\,\mathrm{s}$ with a step from zero to rated[2] voltage $\hat{u}_{\mathrm{f}} = \hat{u}_{\mathrm{s,nom}}$ (at rated frequency $f = \frac{\omega_{\mathrm{k,nom}}}{2\pi}$) is shown, revealing that—even for a five-level VSI—the filter resonance is excited in all cases. For very small filter resistance values (0.2R) the damping is extremely low, whereas for the default value (1.0R) the damping is improved and for a large resistance (5.0R) an almost sinusoidal output is achieved after two periods only. Figure 2.7b shows a zoom plot of Fig. 2.7a, where the filter impact can be observed in more detail; the time delay caused by the large filter time constant in the high resistance (5.0R) case is clearly visible. Moreover, Fig. 2.7c shows an FFT plot of the zoomed-in area, where the filter resonance frequency $f_{\mathrm{R1}} = \frac{\omega_0}{2\pi} = 272\,\mathrm{s}^{-1}$ stands out for the low (0.2R) and default resistance (1.0R) case, respectively. The last plot (Fig. 2.7d) is a magnitude (Bode) plot of the transfer function $G_{\mathrm{f}}(s)$, which confirms the previous statements with respective peaks at resonance frequency f_{R1}.

[2]The terms ‘rated’ and ‘nominal’ are used synonymously here.

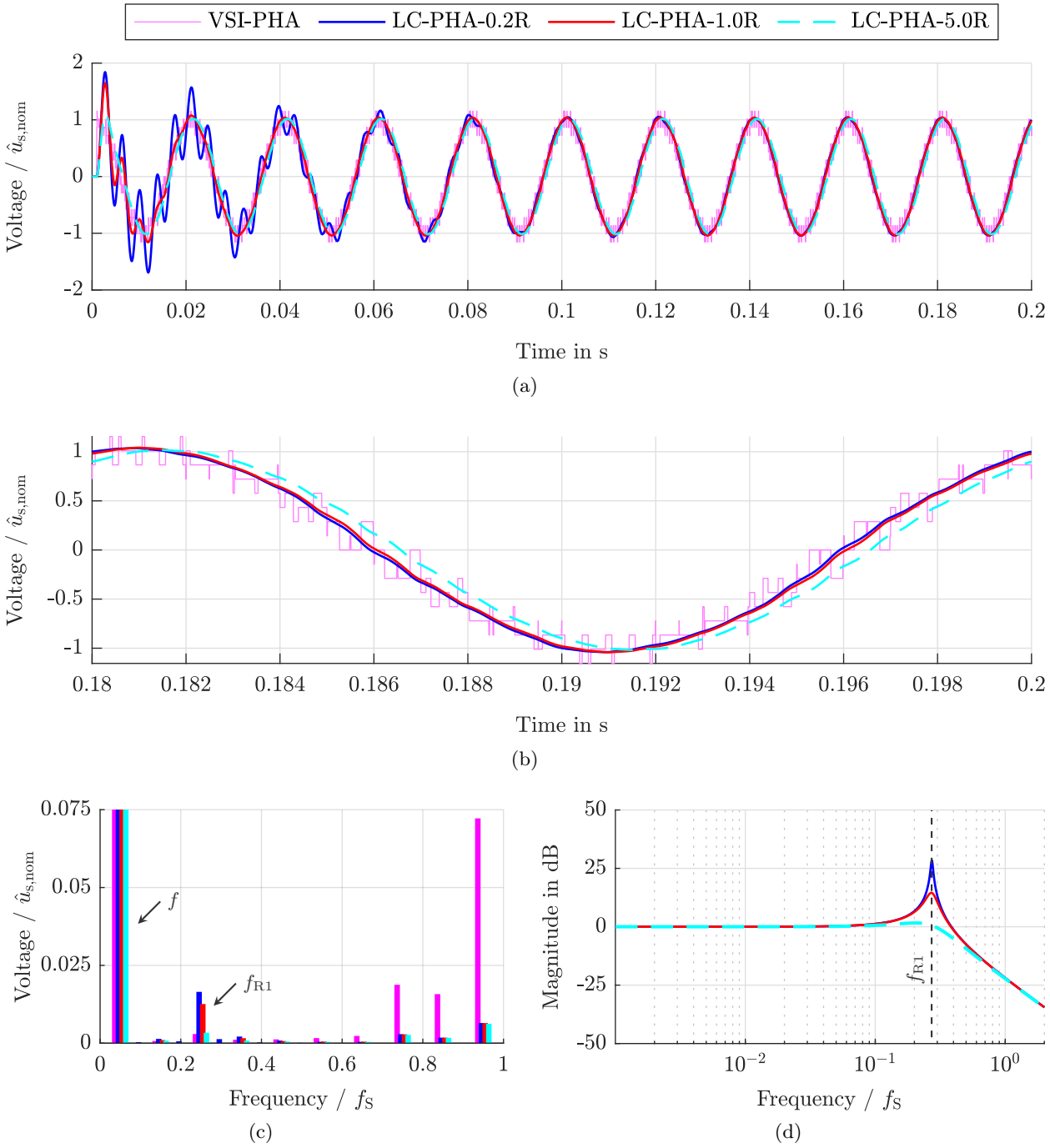

Figure 2.7: *Impact of the LC filter (LC) on the inverter (VSI) output phase voltage (PHA) under no-load conditions, for nominal reference voltage (nominal voltage* $\hat{u}_f = \hat{u}_{s,nom}$ *and frequency* $f = \frac{\omega_{k,nom}}{2\pi}$*) and for different values of* R_f *(*$0.2R \mathrel{\widehat{=}} 0.2R_{f0}$*,* $1.0R \mathrel{\widehat{=}} R_{f0}$*,* $5.0R \mathrel{\widehat{=}} 5R_{f0}$*), exemplary shown for phase* a*: (a) Transient response after step change at* $t = 0\,s$*, (b) Zoom plot of transient response, (c) FFT of zoomed area and (d) magnitude (Bode) plot.*

2.1.3 Cable

The power cable connects the filter output with the electrical machine and runs through the space between well-bore and production tubing. As it spans over the entire distance, from the filter output to the motor, the cable length l_c is a crucial parameter regarding the electromagnetic properties of the cable, i.e. resistance, inductance and capacitance, also known as *line parameters* and typically stated in per-unit-length (PUL). The line parameters further depend on the geometry and the selected materials of the cable. In the following subscript 'c' is used to denote cable quantities.

2.1.3.1 Layout and geometry

Figure 2.8 shows two different cable layouts: The flat-type cable as depicted in (a) and the trefoil cable as depicted in (b). Both cable types are widely used in industry and have advantages and disadvantages. While the trefoil cable reduces power imbalances due to the symmetric arrangement of the conductors, the flat-type cable is better suited if space is limited—e.g. in geothermal applications. However, due to its asymmetric structure, it leads to current and voltage imbalances in the system.

Although standardized in the IEEE Std 1018-2013 [100], a wide variety of ESP cables can be found. A typical conductor layout comprises the following layers:

1. conducting core (e.g. copper),
2. first insulation layer (e.g. Ethylen-Propylen-Dien-Kautschuk, EPDM),
3. metallic sheath for grounding and chemical protection (e.g. lead),
4. second insulation layer and/or jacket, and
5. metallic armor for mechanical protection (e.g. stainless steel).

Some cables are additionally equipped with thin layers of semiconducting tape between conducting and insulation layers and filling material (jacket) between armor and insulation. Depending on the selected materials and cable layout, the line parameters of the cable can be calculated e.g. using finite element method (FEM).

2.1.3.2 Cable model using a single π-segment

The standard models for power transmission lines are derived by using a distributed parameters approach, which allows modeling an infinitesimally short fraction of the cable as a combination of PUL series impedance (series connection of inductance and resistance) and shunt admittance (parallel connection of capacitance and conductance).

Assumption 3 (Cable shunt conductance)**.** *It is assumed that the shunt conductance of the power cable is negligible [101, p. 430], i.e. the leakage current of the cable towards ground and among conductors is zero.*

The line parameters of a three-phase line with trefoil or flat conductor arrangement are given by

$$\boldsymbol{R}_\mathrm{c}^{\prime\mathrm{abc}} = \begin{bmatrix} R_\mathrm{c}^{\prime\mathrm{a}} & 0 & 0 \\ 0 & R_\mathrm{c}^{\prime\mathrm{b}} & 0 \\ 0 & 0 & R_\mathrm{c}^{\prime\mathrm{c}} \end{bmatrix}, \quad \boldsymbol{L}_\mathrm{c}^{\prime\mathrm{abc}} = \begin{bmatrix} L_\mathrm{c}^{\prime\mathrm{aa}} & L_\mathrm{c}^{\prime\mathrm{ab}} & L_\mathrm{c}^{\prime\mathrm{ac}} \\ L_\mathrm{c}^{\prime\mathrm{ab}} & L_\mathrm{c}^{\prime\mathrm{bb}} & L_\mathrm{c}^{\prime\mathrm{bc}} \\ L_\mathrm{c}^{\prime\mathrm{ac}} & L_\mathrm{c}^{\prime\mathrm{bc}} & L_\mathrm{c}^{\prime\mathrm{cc}} \end{bmatrix} \quad \text{and} \quad \boldsymbol{C}_\mathrm{c}^{\prime\mathrm{abc}} = \begin{bmatrix} C_\mathrm{c}^{\prime\mathrm{aa}} & C_\mathrm{c}^{\prime\mathrm{ab}} & C_\mathrm{c}^{\prime\mathrm{ac}} \\ C_\mathrm{c}^{\prime\mathrm{ab}} & C_\mathrm{c}^{\prime\mathrm{bb}} & C_\mathrm{c}^{\prime\mathrm{bc}} \\ C_\mathrm{c}^{\prime\mathrm{ac}} & C_\mathrm{c}^{\prime\mathrm{bc}} & C_\mathrm{c}^{\prime\mathrm{cc}} \end{bmatrix}, \tag{2.12}$$

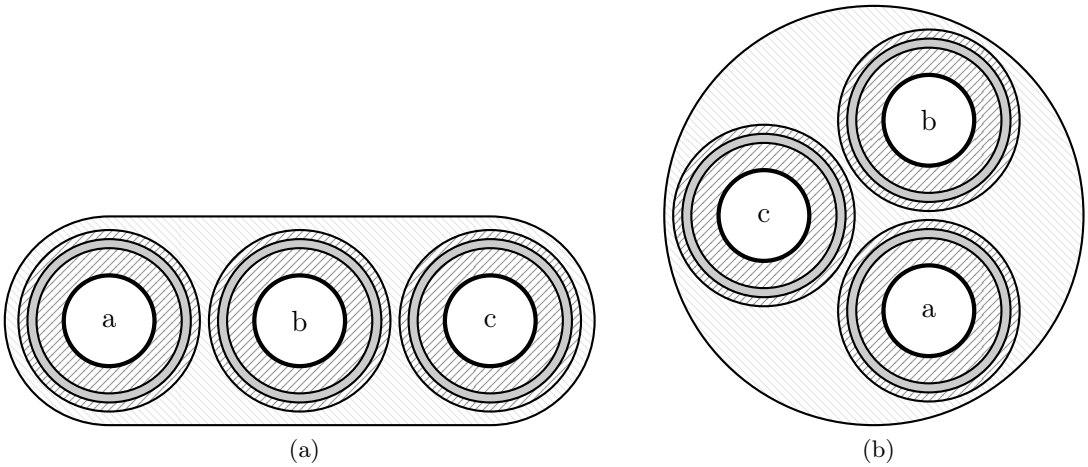

Figure 2.8: *Cross-section views of three-phase ESP power cables in (a) flat and (b) trefoil configuration.*

where $\boldsymbol{R}_{\mathrm{c}}^{\prime\mathrm{abc}}, \boldsymbol{L}_{\mathrm{c}}^{\prime\mathrm{abc}}$ and $\boldsymbol{C}_{\mathrm{c}}^{\prime\mathrm{abc}} \in \mathbb{R}^{3\times3}$ denote the PUL cable resistance, inductance and capacitance matrix, respectively. The PUL resistance matrix accounts for ohmic losses (voltage drop) along the power line, whereas the PUL inductance matrix describes the magnetic coupling among the three conductors, with self inductances $L_{\mathrm{c}}^{\prime kk}$ and mutual inductances $L_{\mathrm{c}}^{\prime kj}$, for $k, j \in \{\mathrm{a}, \mathrm{b}, \mathrm{c}\}, k \neq j$, respectively. Moreover, the PUL capacitance matrix describes the electric coupling among the conductors, with self capacitances $C_{\mathrm{c}}^{\prime kk}$ and mutual capacitances $C_{\mathrm{c}}^{\prime kj}$, for $k, j \in \{\mathrm{a}, \mathrm{b}, \mathrm{c}\}$ and $k \neq j$. Note that $\boldsymbol{L}_{\mathrm{c}}^{\prime\mathrm{abc}} = \boldsymbol{L}_{\mathrm{c}}^{\prime\mathrm{abc}\top} \succ 0$ and $\boldsymbol{C}_{\mathrm{c}}^{\prime\mathrm{abc}} = \boldsymbol{C}_{\mathrm{c}}^{\prime\mathrm{abc}\top} \succ 0$ are both symmetric and positive definite (see [102, Sec. 3.5]), and hence invertible. Furthermore, since the surrounding material is (mostly) non-magnetic, the inductances do not depend on the currents.

The distributed parameters approach leads to a set of partial differential equations called *Telegrapher's equations*, whose solution are time and space dependent wave functions for voltages and currents, respectively (see e.g. [103, Sec. 3.2]). As the distributed parameters approach results in an infinitely large number of states, discretization of the model using lumped parameters and a finite set of cable segments is performed. For sufficiently short segments, the space dependency can be neglected and the cable can be approximated by equivalent π- or T- circuits. A cable is classified short if the wavelength λ of the voltage and current waveforms is at least 60 times larger than the cable length, i.e. $\lambda \geq 60 \cdot l_{\mathrm{c}}$ holds true [101, p. 426]. Given the vacuum speed of light $c_0 \approx 300 \cdot 10^6\,\mathrm{m\,s^{-1}}$, the relative permittivity of the cable insulation $\epsilon_{\mathrm{r,EPDM}} \approx 2.4$ and the frequency of the driving signals f, the condition can be refined to (see [101, p. 410])

$$\lambda = \frac{c_0}{\sqrt{\epsilon_{\mathrm{r,EPDM}}}\, f} \overset{!}{\geq} 60 \cdot l_{\mathrm{c}} \quad \Longrightarrow \quad l_{\mathrm{c,max}} = 1\,580\,\mathrm{m}. \tag{2.13}$$

It can be concluded from (2.13) that, even without a sine filter and switching harmonics of up to 2 kHz, the maximum cable length of $l_{\mathrm{c,max}} = 1\,580\,\mathrm{m}$ covers most geothermal power applications, and hence a single T- or π-segment is sufficient for the modeling of the cable. In this work, the π-equivalent model is used which requires that, when combined with the LC filter, the output capacitances of the filter are added to the parallel cable input capacitances.

Remark 3. *Note that the T-equivalent circuit might be used just as well, requiring that the cable output inductances and resistances are added to the stator inductances and resistances (see App. C.3).*

The equivalent circuit of a single π-segment is shown in Fig. 2.9, with input voltages $\boldsymbol{u}_{\mathrm{c_i}}^{\mathrm{abc}}$, input currents $\boldsymbol{i}_{\mathrm{c_i}}^{\mathrm{abc}}$, output voltages $\boldsymbol{u}_{\mathrm{c_o}}^{\mathrm{abc}}$, output currents $\boldsymbol{i}_{\mathrm{c_o}}^{\mathrm{abc}}$ and currents through the inductances $\boldsymbol{i}_{\mathrm{c}}^{\mathrm{abc}}$. Magnetic coupling is represented in terms of flux linkage in the figure, i.e.

$$\tfrac{\mathrm{d}}{\mathrm{d}t}\boldsymbol{\psi}_{\mathrm{c}}^{\mathrm{abc}} = \boldsymbol{L}_{\mathrm{c}}^{\mathrm{abc}}\tfrac{\mathrm{d}}{\mathrm{d}t}\boldsymbol{i}_{\mathrm{c}}^{\mathrm{abc}}. \tag{2.14}$$

Moreover, line-to-ground capacitances $C_{\mathrm{c}}^{k\text{-}0}$ and line-to-line capacitances $C_{\mathrm{c}}^{k\text{-}j}$, for $k, j \in \{\mathrm{a}, \mathrm{b}, \mathrm{c}\}$ and $k \neq j$, are used instead of self and mutual capacitances as in (2.12). It can be shown that the PUL capacitance matrix can be written in terms of PUL line-to-ground and line-to-line capacitances (see derivation in App. C.2), i.e.

$$\boldsymbol{C}_{\mathrm{c}}^{\prime\mathrm{abc}} = \begin{bmatrix} C_{\mathrm{c}}^{\prime\mathrm{a}\text{-}0} + C_{\mathrm{c}}^{\prime\mathrm{a}\text{-}\mathrm{b}} + C_{\mathrm{c}}^{\prime\mathrm{c}\text{-}\mathrm{a}} & -C_{\mathrm{c}}^{\prime\mathrm{b}\text{-}\mathrm{c}} & -C_{\mathrm{c}}^{\prime\mathrm{c}\text{-}\mathrm{a}} \\ -C_{\mathrm{c}}^{\prime\mathrm{a}\text{-}\mathrm{b}} & C_{\mathrm{c}}^{\prime\mathrm{b}\text{-}0} + C_{\mathrm{c}}^{\prime\mathrm{a}\text{-}\mathrm{b}} + C_{\mathrm{c}}^{\prime\mathrm{b}\text{-}\mathrm{c}} & -C_{\mathrm{c}}^{\prime\mathrm{b}\text{-}\mathrm{c}} \\ -C_{\mathrm{c}}^{\prime\mathrm{c}\text{-}\mathrm{a}} & -C_{\mathrm{c}}^{\prime\mathrm{b}\text{-}\mathrm{c}} & C_{\mathrm{c}}^{\prime\mathrm{c}\text{-}0} + C_{\mathrm{c}}^{\prime\mathrm{b}\text{-}\mathrm{c}} + C_{\mathrm{c}}^{\prime\mathrm{c}\text{-}\mathrm{a}} \end{bmatrix}. \tag{2.15}$$

The π-model parameters are given by multiplying the PUL line parameters by the segment length l_{c} and splitting the capacitance into two equal parts, i.e.

$$\boldsymbol{R}_{\mathrm{c}}^{\mathrm{abc}} = l_{\mathrm{c}}\boldsymbol{R}_{\mathrm{c}}^{\prime\mathrm{abc}}, \qquad \boldsymbol{L}_{\mathrm{c}}^{\mathrm{abc}} = l_{\mathrm{c}}\boldsymbol{L}_{\mathrm{c}}^{\prime\mathrm{abc}} \text{and} \qquad \boldsymbol{C}_{\mathrm{c}}^{\mathrm{abc}} = \frac{1}{2}l_{\mathrm{c}}\boldsymbol{C}_{\mathrm{c}}^{\prime\mathrm{abc}}. \tag{2.16}$$

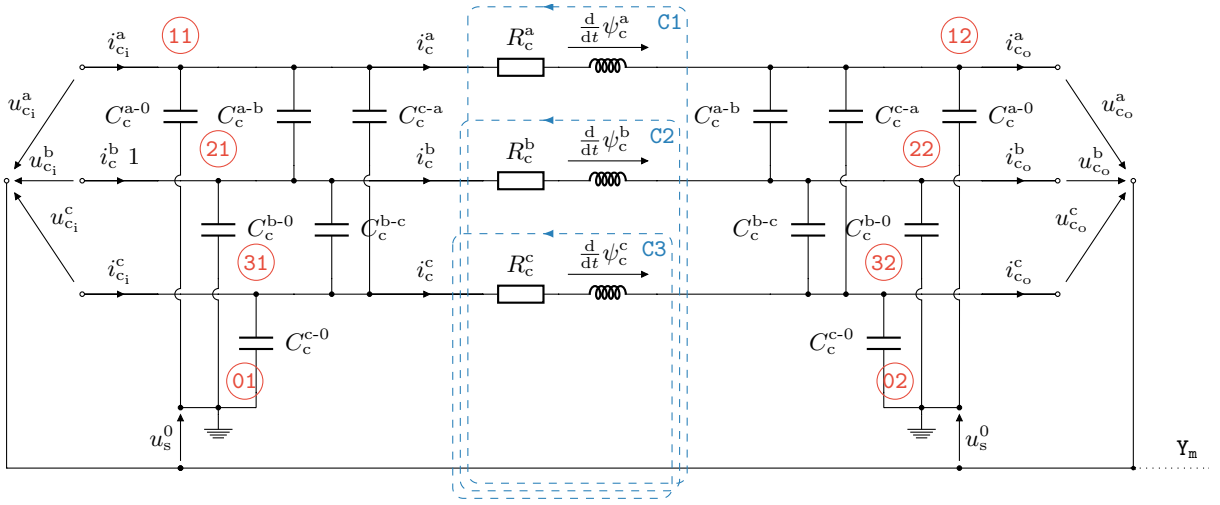

Figure 2.9: *Equivalent circuit of the power cable π-segment.*

The system description is obtained by evaluating meshes C1 to C3, nodes 01 to 31 and 02 to 32, i.e.

$$\begin{aligned} \tfrac{\mathrm{d}}{\mathrm{d}t}\begin{pmatrix} \boldsymbol{u}_{\mathrm{c_i}}^{\mathrm{abc}} \\ \boldsymbol{i}_{\mathrm{c}}^{\mathrm{abc}} \\ \boldsymbol{u}_{\mathrm{c_o}}^{\mathrm{abc}} \end{pmatrix} &= \begin{bmatrix} \boldsymbol{0}_{3\times3} & -(\boldsymbol{C}_{\mathrm{c}}^{\mathrm{abc}})^{-1} & \boldsymbol{0}_{3\times3} \\ (\boldsymbol{L}_{\mathrm{c}}^{\mathrm{abc}})^{-1} & -(\boldsymbol{L}_{\mathrm{c}}^{\mathrm{abc}})^{-1}\boldsymbol{R}_{\mathrm{c}}^{\mathrm{abc}} & -(\boldsymbol{L}_{\mathrm{c}}^{\mathrm{abc}})^{-1} \\ \boldsymbol{0}_{3\times3} & (\boldsymbol{C}_{\mathrm{c}}^{\mathrm{abc}})^{-1} & \boldsymbol{0}_{3\times3} \end{bmatrix} \begin{pmatrix} \boldsymbol{u}_{\mathrm{c_i}}^{\mathrm{abc}} \\ \boldsymbol{i}_{\mathrm{c}}^{\mathrm{abc}} \\ \boldsymbol{u}_{\mathrm{c_o}}^{\mathrm{abc}} \end{pmatrix} \\ &\quad + \begin{bmatrix} (\boldsymbol{C}_{\mathrm{c}}^{\mathrm{abc}})^{-1} & \boldsymbol{0}_{3\times3} \\ \boldsymbol{0}_{3\times3} & \boldsymbol{0}_{3\times3} \\ \boldsymbol{0}_{3\times3} & -(\boldsymbol{C}_{\mathrm{c}}^{\mathrm{abc}})^{-1} \end{bmatrix} \begin{pmatrix} \boldsymbol{i}_{\mathrm{c_i}}^{\mathrm{abc}} \\ \boldsymbol{i}_{\mathrm{c_o}}^{\mathrm{abc}} \end{pmatrix} - \underbrace{\begin{pmatrix} \boldsymbol{1}_3 \\ \boldsymbol{0}_3 \\ \boldsymbol{1}_3 \end{pmatrix}}_{\circledast} \tfrac{\mathrm{d}}{\mathrm{d}t}u_{\mathrm{s}}^{0}. \end{aligned} \tag{2.17}$$

Applying the reduced Clarke transformation (A.4), the ⊛ term is eliminated, i.e. $\boldsymbol{T}_{\mathrm{C,red}}\mathbf{1}_3\frac{\mathrm{d}}{\mathrm{d}t}u_{\mathrm{s}}^0 = \mathbf{o}_2$, and the state-space description for the π-segment in the αβ-coordinate system is obtained as

$$\frac{\mathrm{d}}{\mathrm{d}t}\begin{pmatrix}\boldsymbol{u}_{\mathrm{c_i}}^{\alpha\beta}\\ \hline \boldsymbol{i}_{\mathrm{c}}^{\alpha\beta}\\ \boldsymbol{u}_{\mathrm{c_o}}^{\alpha\beta}\end{pmatrix} = \left[\begin{array}{ccc}\mathbf{0}_{2\times2} & -\left(\boldsymbol{C}_{\mathrm{c}}^{\alpha\beta}\right)^{-1} & \mathbf{0}_{2\times2}\\ \hline \left(\boldsymbol{L}_{\mathrm{c}}^{\alpha\beta}\right)^{-1} & -\left(\boldsymbol{L}_{\mathrm{c}}^{\alpha\beta}\right)^{-1}\boldsymbol{R}_{\mathrm{c}}^{\alpha\beta} & -\left(\boldsymbol{L}_{\mathrm{c}}^{\alpha\beta}\right)^{-1}\\ \mathbf{0}_{2\times2} & \left(\boldsymbol{C}_{\mathrm{c}}^{\alpha\beta}\right)^{-1} & \mathbf{0}_{2\times2}\end{array}\right]\begin{pmatrix}\boldsymbol{u}_{\mathrm{c_i}}^{\alpha\beta}\\ \hline \boldsymbol{i}_{\mathrm{c}}^{\alpha\beta}\\ \boldsymbol{u}_{\mathrm{c_o}}^{\alpha\beta}\end{pmatrix} + \left[\begin{array}{cc}\left(\boldsymbol{C}_{\mathrm{c}}^{\alpha\beta}\right)^{-1} & \mathbf{0}_{2\times2}\\ \hline \mathbf{0}_{2\times2} & \mathbf{0}_{2\times2}\\ \mathbf{0}_{2\times2} & -\left(\boldsymbol{C}_{\mathrm{c}}^{\alpha\beta}\right)^{-1}\end{array}\right]\begin{pmatrix}\boldsymbol{i}_{\mathrm{c_i}}^{\alpha\beta}\\ \hline \boldsymbol{i}_{\mathrm{c_o}}^{\alpha\beta}\end{pmatrix} \tag{2.18}$$

where

$$\boldsymbol{R}_{\mathrm{c}}^{\alpha\beta} = \boldsymbol{T}_{\mathrm{C,red}}\boldsymbol{R}_{\mathrm{c}}^{\mathrm{abc}}\boldsymbol{T}_{\mathrm{C,red}}^{-1},\quad \boldsymbol{L}_{\mathrm{c}}^{\alpha\beta} = \boldsymbol{T}_{\mathrm{C,red}}\boldsymbol{L}_{\mathrm{c}}^{\mathrm{abc}}\boldsymbol{T}_{\mathrm{C,red}}^{-1}\quad\text{and}\quad \boldsymbol{C}_{\mathrm{c}}^{\alpha\beta} = \boldsymbol{T}_{\mathrm{C,red}}\boldsymbol{C}_{\mathrm{c}}^{\mathrm{abc}}\boldsymbol{T}_{\mathrm{C,red}}^{-1}. \tag{2.19}$$

2.1.3.3 Cable model using multiple π-sections

If the cable is longer than $l_{\mathrm{c,max}}$, or the LC filter is omitted, the model accuracy can be increased by connecting n_{c} π-sections in series, as depicted in Fig. 2.10. As a consequence, the input and output voltages of adjacent segments are combined in the states $\boldsymbol{u}_{\mathrm{c},k}^{\alpha\beta}$, for $k \in \{1,\dots,n_{\mathrm{c}}\}$. Moreover, the model parameters have to be adjusted, as the length of each segment is reduced, i.e.

$$\boldsymbol{R}_{\mathrm{c}}^{\mathrm{abc}} = \tfrac{l_{\mathrm{c}}}{n_{\mathrm{c}}}\boldsymbol{R}_{\mathrm{c}}^{\prime\mathrm{abc}},\qquad \boldsymbol{L}_{\mathrm{c}}^{\mathrm{abc}} = \tfrac{l_{\mathrm{c}}}{n_{\mathrm{c}}}\boldsymbol{L}_{\mathrm{c}}^{\prime\mathrm{abc}}\qquad\text{and}\qquad \boldsymbol{C}_{\mathrm{c}}^{\mathrm{abc}} = \tfrac{l_{\mathrm{c}}}{2n_{\mathrm{c}}}\boldsymbol{C}_{\mathrm{c}}^{\prime\mathrm{abc}}. \tag{2.20}$$

Transforming the parameter matrices into the αβ-reference frame, the resulting cable model is given by

$$\frac{\mathrm{d}}{\mathrm{d}t}\begin{pmatrix}\boldsymbol{u}_{\mathrm{c_i}}^{\alpha\beta}\\ \hline \boldsymbol{i}_{\mathrm{c},1}^{\alpha\beta}\\ \boldsymbol{u}_{\mathrm{c},1}^{\alpha\beta}\\ \vdots\\ \boldsymbol{i}_{\mathrm{c},k}^{\alpha\beta}\\ \boldsymbol{u}_{\mathrm{c},k}^{\alpha\beta}\\ \vdots\\ \boldsymbol{i}_{\mathrm{c},n_{\mathrm{c}}}^{\alpha\beta}\\ \boldsymbol{u}_{\mathrm{c},n_{\mathrm{c}}}^{\alpha\beta}\end{pmatrix} = \begin{pmatrix}\left(\boldsymbol{C}_{\mathrm{c}}^{\alpha\beta}\right)^{-1}\boldsymbol{i}_{\mathrm{c_i}}^{\alpha\beta} - \left(\boldsymbol{C}_{\mathrm{c}}^{\alpha\beta}\right)^{-1}\boldsymbol{i}_{\mathrm{c},1}^{\alpha\beta}\\ \hline \left(\boldsymbol{L}_{\mathrm{c}}^{\alpha\beta}\right)^{-1}\boldsymbol{u}_{\mathrm{c_i}}^{\alpha\beta} - \left(\boldsymbol{L}_{\mathrm{c}}^{\alpha\beta}\right)^{-1}\boldsymbol{R}_{\mathrm{c}}^{\alpha\beta}\boldsymbol{i}_{\mathrm{c},1}^{\alpha\beta} - \left(\boldsymbol{L}_{\mathrm{c}}^{\alpha\beta}\right)^{-1}\boldsymbol{u}_{\mathrm{c},1}^{\alpha\beta}\\ \frac{1}{2}\left(\boldsymbol{C}_{\mathrm{c}}^{\alpha\beta}\right)^{-1}\boldsymbol{i}_{\mathrm{c},1}^{\alpha\beta} - \frac{1}{2}\left(\boldsymbol{C}_{\mathrm{c}}^{\alpha\beta}\right)^{-1}\boldsymbol{i}_{\mathrm{c},2}^{\alpha\beta}\\ \vdots\\ \left(\boldsymbol{L}_{\mathrm{c}}^{\alpha\beta}\right)^{-1}\boldsymbol{u}_{\mathrm{c},k-1}^{\alpha\beta} - \left(\boldsymbol{L}_{\mathrm{c}}^{\alpha\beta}\right)^{-1}\boldsymbol{R}_{\mathrm{c}}^{\alpha\beta}\boldsymbol{i}_{\mathrm{c},k}^{\alpha\beta} - \left(\boldsymbol{L}_{\mathrm{c}}^{\alpha\beta}\right)^{-1}\boldsymbol{u}_{\mathrm{c},k}^{\alpha\beta}\\ \frac{1}{2}\left(\boldsymbol{C}_{\mathrm{c}}^{\alpha\beta}\right)^{-1}\boldsymbol{i}_{\mathrm{c},k}^{\alpha\beta} - \frac{1}{2}\left(\boldsymbol{C}_{\mathrm{c}}^{\alpha\beta}\right)^{-1}\boldsymbol{i}_{\mathrm{c},k+1}^{\alpha\beta}\\ \vdots\\ \left(\boldsymbol{L}_{\mathrm{c}}^{\alpha\beta}\right)^{-1}\boldsymbol{u}_{\mathrm{c},n_{\mathrm{c}}-1}^{\alpha\beta} - \left(\boldsymbol{L}_{\mathrm{c}}^{\alpha\beta}\right)^{-1}\boldsymbol{R}_{\mathrm{c}}^{\alpha\beta}\boldsymbol{i}_{\mathrm{c},n_{\mathrm{c}}}^{\alpha\beta} - \left(\boldsymbol{L}_{\mathrm{c}}^{\alpha\beta}\right)^{-1}\boldsymbol{u}_{\mathrm{c},n_{\mathrm{c}}}^{\alpha\beta}\\ \left(\boldsymbol{C}_{\mathrm{c}}^{\alpha\beta}\right)^{-1}\boldsymbol{i}_{\mathrm{c},n_{\mathrm{c}}}^{\alpha\beta} - \left(\boldsymbol{C}_{\mathrm{c}}^{\alpha\beta}\right)^{-1}\boldsymbol{i}_{\mathrm{c_o}}^{\alpha\beta}\end{pmatrix}, \tag{2.21}$$

where $\boldsymbol{u}_{\mathrm{c_o}}^{\alpha\beta} = \boldsymbol{u}_{\mathrm{c},n_{\mathrm{c}}}^{\alpha\beta}$ is the cable output voltage and $\boldsymbol{i}_{\mathrm{c_o}}^{\alpha\beta}$ the cable output current, which is equal to the current flowing into the load. Note that for the π-segment the output current $\boldsymbol{i}_{\mathrm{c_o}}^{\alpha\beta}$ is determined by the load.

2.1.3.4 Linking the cable with the filter

On the load side of the cable, the dynamics of the output voltage are exclusively determined by the cable model, whereas on the filter side, the parallel capacitances impose an equality constraint on the filter output and cable input voltage. The differential equations of the filter output voltage and the cable input voltage (generic case of multiple π-segments) are given by

$$C_{\mathrm{f}}\,\tfrac{\mathrm{d}}{\mathrm{d}t}\boldsymbol{u}_{\mathrm{f_o}}^{\alpha\beta} \overset{(2.10)}{=} \boldsymbol{i}_{\mathrm{f_i}}^{\alpha\beta} - \boldsymbol{i}_{\mathrm{f_o}}^{\alpha\beta}\qquad\text{and} \tag{2.22}$$

$$\boldsymbol{C}_{\mathrm{c}}^{\alpha\beta}\,\tfrac{\mathrm{d}}{\mathrm{d}t}\boldsymbol{u}_{\mathrm{c_i}}^{\alpha\beta} \overset{(2.21)}{=} \boldsymbol{i}_{\mathrm{c_i}}^{\alpha\beta} - \boldsymbol{i}_{\mathrm{c},1}^{\alpha\beta}. \tag{2.23}$$

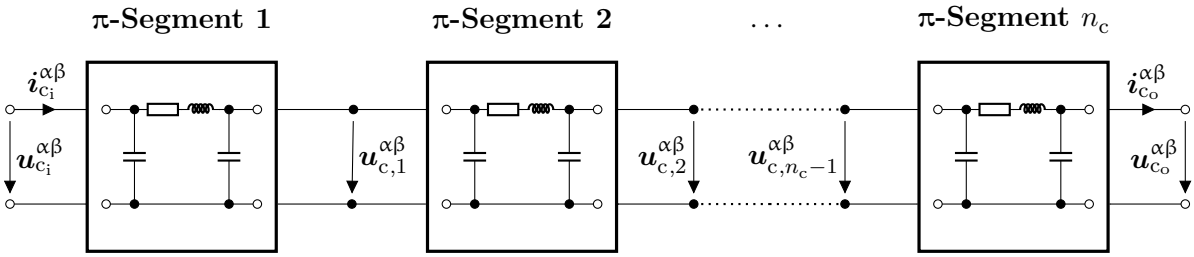

Figure 2.10: *Cable approximation by series connection of n_c π-circuits.*

Linking the filter with the cable requires that the filter output voltage is equal to the cable input voltage, i.e. $\boldsymbol{u}_{f_o}^{\alpha\beta} = \boldsymbol{u}_{c_i}^{\alpha\beta}$, and the filter output current is equal to the cable input current, i.e. $\boldsymbol{i}_{f_o}^{\alpha\beta} = \boldsymbol{i}_{c_i}^{\alpha\beta}$. As a consequence, taking the sum of (2.22) and (2.23) and solving for $\boldsymbol{u}_{f_o}^{\alpha\beta}$ yields

$$\tfrac{\mathrm{d}}{\mathrm{d}t}\boldsymbol{u}_{f_o}^{\alpha\beta} = (\boldsymbol{C}_{f,\mathrm{mod}}^{\alpha\beta})^{-1}\boldsymbol{i}_{f_i}^{\alpha\beta} - (\boldsymbol{C}_{f,\mathrm{mod}}^{\alpha\beta})^{-1}\boldsymbol{i}_{c,1}^{\alpha\beta}, \tag{2.24}$$

where the modified filter capacitance matrix $\boldsymbol{C}_{f,\mathrm{mod}}^{\alpha\beta} := C_f\,\boldsymbol{I}_2 + \boldsymbol{C}_c^{\alpha\beta}$ is introduced. Hence, the first rows of (2.21), respectively (2.18), and the last row of (2.10) need to be replaced by (2.24) when the submodels are combined.

2.1.4 Electrical machine (induction machine)

The electrical machine drives the pump to which it is mechanically linked via the shaft. In order to achieve a higher power output, two separate machines may be connected in series, which is known as *tandem* configuration [104]. Typically, squirrel-cage induction machines (SCIMs) are used, as this type of machine is robust and inexpensive to manufacture. However, as high currents flow through the rotor bars and resistive losses (heat) are proportional to the current squared, induction machines tend to heat up quickly. Moreover, the only feasible way to dissipate the heat is to use the *hot* geothermal fluid flowing along the machine casing. Therefore, the current rating has to be kept at a minimum level, which requires a higher voltage rating of the machine in order to guarantee the desired mechanical output power.

Due to space limitations within the borehole, the motor dimensions have to be adapted, resulting in a long axial expansion and a small diameter. While the stator windings typically expand over the whole length of the motor, the rotor on the other hand is segmented, with each segment being isolated from each other and equipped with its own bearings [105]. Moreover, the space between rotor and stator is filled with oil to (i) prevent water from entering the machine, (ii) adapt with the high ambient pressure and (iii) improve the heat transfer from the rotor to the motor surface in radial direction [105].

Remark 4. *Using an oil-filled 'air gap' results in additional windage losses in the motor, which are proportional to the rotational speed squared. As the flow of the oil is laminar for low temperatures, windage losses are significantly higher compared to high temperatures, where the flow becomes turbulent [106]. For the sake of simplicity, a constantly high temperature is assumed for geothermal applications. Hence, the temperature dependency of the windage losses is omitted in the presented model.*

For the modeling, it is assumed in a first step, that the ESP motor is short and hence equipped with a single rotor only, which is referred to as single-rotor/single-stator (`SR/SS`) configuration in the

following. Based on the SR/SS model, in a second step, a generic multi-rotor/single stator (MR/SS) model is derived by expanding the length of the stator and employing multiple short rotor segments with the same magnetic and electric properties as the SR/SS rotor. Furthermore, elasticity between adjacent rotor segments is considered. Finally, a simplified MR/SS model is derived, assuming that elasticity can be neglected. In addition, the following assumptions are imposed:

Assumption 4 (Induction machine modeling)**.** *It is assumed that*

- *the induction machine is* star-connected*, i.e. the secondary ends of the phase windings are interconnected at the motor star point* $\mathtt{Y_m}$*,*
- *iron losses in both, stator and rotor, can be neglected, and*
- *temperature dependencies of the resistive components can be neglected.*

Signals and parameters related to the stator, rotor and the machine in general are denoted by subscripts 's', 'r' and 'm', respectively.

2.1.4.1 Single-rotor/single-stator (SR/SS) model in the stationary αβ-reference frame

Figure 2.11 shows two cross-section views of the electrical machine in SR/SS configuration, (a) from the side and (b) from the front, respectively. Except for the oil-filled 'air gap', this configuration is that of a standard industrial SCIM.

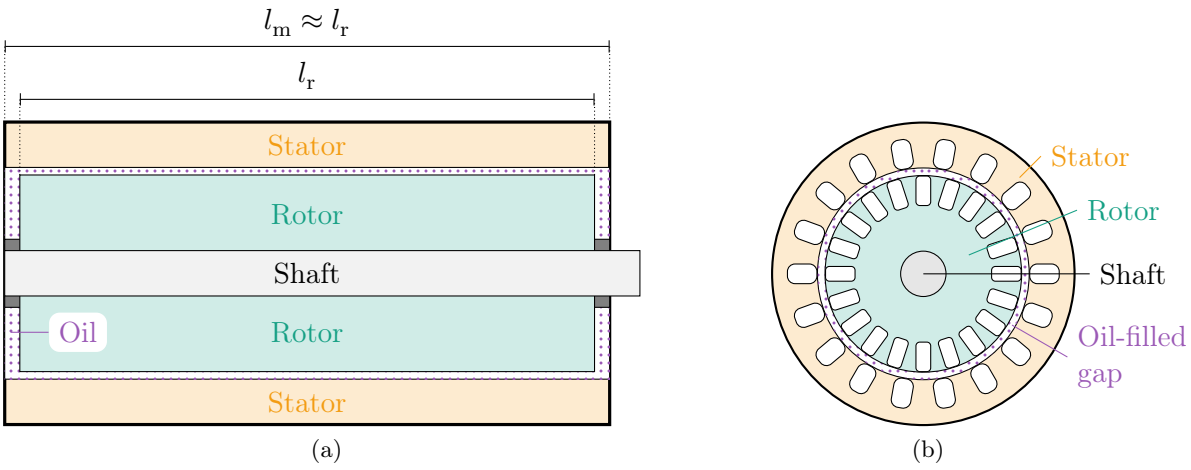

Figure 2.11: *Cross-section views of the single-rotor/single stator (SR/SS) ESP motor: (a) side view and (b) front view.*

The corresponding three-phase equivalent circuit for the fault-free case (i.e. all phases have identical electromagnetic properties) is shown in Fig. 2.12, with stator voltages $\boldsymbol{u}_\mathrm{s}^\mathrm{abc}$, stator currents $\boldsymbol{i}_\mathrm{s}^\mathrm{abc}$ and stator flux linkages $\boldsymbol{\psi}_\mathrm{s}^\mathrm{abc}$, rotor currents $\boldsymbol{i}_\mathrm{r}^\mathrm{abc}$, rotor flux linkages $\boldsymbol{\psi}_\mathrm{r}^\mathrm{abc}$ and rotor angular velocity ω_r, respectively. The rotor variables are related to the stator [107] and expressed in the stator-fixed abc-reference frame.

The stator windings (phases) are composed of the stator resistances R_s and the stator inductance L_s, where L_s can be split into the stator stray inductance $L_\mathrm{s\sigma}$ and the main inductance L_m, i.e. $L_\mathrm{s} = L_\mathrm{s\sigma} + L_\mathrm{m}$ [108, Sec. 8.3.1]. The main inductance causes magnetic coupling between the rotor and stator phases which can be expressed in terms of the stator and rotor flux linkages.

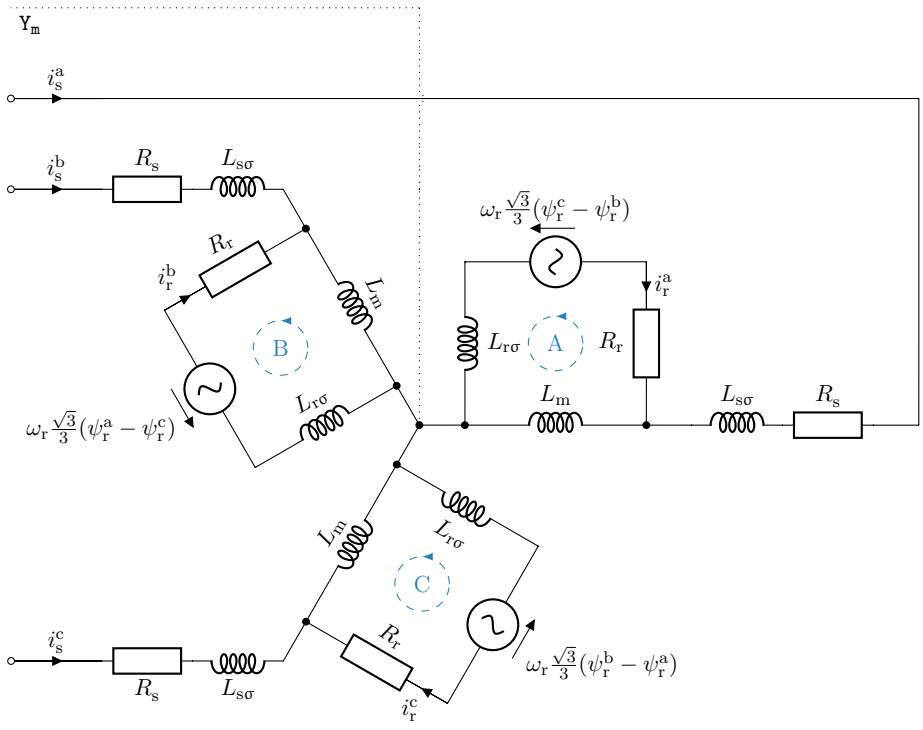

Figure 2.12: *Three-phase equivalent circuit of a squirrel-cage induction machine.*

Assumption 5 (Magnetic linearity)**.** *It is assumed that magnetic saturation can be neglected, and hence the stator and rotor flux linkages are affine functions of the stator and rotor currents, respectively, i.e.*

$$\boldsymbol{\psi}_\mathrm{s}^\mathrm{abc} = L_\mathrm{s}\boldsymbol{i}_\mathrm{s}^\mathrm{abc} + L_\mathrm{m}\boldsymbol{i}_\mathrm{r}^\mathrm{abc} \qquad \textit{and} \qquad \boldsymbol{\psi}_\mathrm{r}^\mathrm{abc} = L_\mathrm{m}\boldsymbol{i}_\mathrm{s}^\mathrm{abc} + L_\mathrm{r}\boldsymbol{i}_\mathrm{r}^\mathrm{abc}. \tag{2.25}$$

Remark 5. *It is shown in Ch. 3, that Ass. 5 becomes inadmissible for high levels of excitation. However, as the IM parameters are typically identified for the linear model and FEM data of a geothermal ESP electrical machine is not available, the linear model shall suffice in this chapter.*

Considering Ass. 5, the stator voltages, measured between the input terminals and the motor star point $\mathtt{Y_m}$, are given by

$$\boldsymbol{u}_\mathrm{s}^\mathrm{abc} = R_\mathrm{s}\boldsymbol{i}_\mathrm{s}^\mathrm{abc} + \tfrac{\mathrm{d}}{\mathrm{d}t}\boldsymbol{\psi}_\mathrm{s}^\mathrm{abc} \overset{(2.25)}{=} R_\mathrm{s}\boldsymbol{i}_\mathrm{s}^\mathrm{abc} + L_\mathrm{s}\tfrac{\mathrm{d}}{\mathrm{d}t}\boldsymbol{i}_\mathrm{s}^\mathrm{abc} + L_\mathrm{m}\tfrac{\mathrm{d}}{\mathrm{d}t}\boldsymbol{i}_\mathrm{r}^\mathrm{abc}. \tag{2.26}$$

Applying the reduced Clarke transformation (A.4) yields the corresponding representation

$$\boldsymbol{u}_\mathrm{s}^{\alpha\beta} = R_\mathrm{s}\boldsymbol{i}_\mathrm{s}^{\alpha\beta} + L_\mathrm{s}\tfrac{\mathrm{d}}{\mathrm{d}t}\boldsymbol{i}_\mathrm{s}^{\alpha\beta} + L_\mathrm{m}\tfrac{\mathrm{d}}{\mathrm{d}t}\boldsymbol{i}_\mathrm{r}^{\alpha\beta} \tag{2.27}$$

in the $\alpha\beta$-reference frame. On the rotor side, the conducting bars of the rotor cage are likewise modeled as a three-phase system, with rotor resistance R_r and rotor inductance L_r, composed of the rotor leakage inductance $L_{\mathrm{r}\sigma}$ and the main inductance L_m, i.e. $L_\mathrm{r} = L_{\mathrm{r}\sigma} + L_\mathrm{m}$ [108, Sec. 8.3.1]. Moreover, the rotor magnetic field induces a voltage in the rotor cage depending on the flux linkage $\boldsymbol{\psi}_\mathrm{r}^\mathrm{abc}$ and the electrical (synchronous) speed $\omega_\mathrm{r} := n_\mathrm{p}\omega_\mathrm{m}$, where ω_m is the mechanical speed and n_p is the number of pole pairs. Evaluating meshes (A), (B) and (C) yields the following dependency

$$-R_\mathrm{r}\boldsymbol{i}_\mathrm{r}^\mathrm{abc} - \underbrace{\left(L_\mathrm{r}\tfrac{\mathrm{d}}{\mathrm{d}t}\boldsymbol{i}_\mathrm{r}^\mathrm{abc} + L_\mathrm{m}\tfrac{\mathrm{d}}{\mathrm{d}t}\boldsymbol{i}_\mathrm{s}^\mathrm{abc}\right)}_{\overset{(2.25)}{=}\frac{\mathrm{d}}{\mathrm{d}t}\boldsymbol{\psi}_\mathrm{r}^\mathrm{abc}} + \omega_\mathrm{r}\underbrace{\frac{\sqrt{3}}{3}\begin{bmatrix}0 & -1 & 1\\ 1 & 0 & -1\\ -1 & 1 & 0\end{bmatrix}}_{=:\boldsymbol{J}^*}\boldsymbol{\psi}_\mathrm{r}^\mathrm{abc} = \mathbf{o}_3, \tag{2.28}$$

which, transformed to αβ-coordinates, becomes

$$-R_\mathrm{r}\boldsymbol{i}_\mathrm{r}^{\alpha\beta} - (L_\mathrm{r}\tfrac{\mathrm{d}}{\mathrm{d}t}\boldsymbol{i}_\mathrm{r}^{\alpha\beta} + L_\mathrm{m}\tfrac{\mathrm{d}}{\mathrm{d}t}\boldsymbol{i}_\mathrm{s}^{\alpha\beta}) + \omega_\mathrm{r}\boldsymbol{J}\boldsymbol{\psi}_\mathrm{r}^{\alpha\beta} = \mathbf{o}_2, \tag{2.29}$$

as $\boldsymbol{J} = \boldsymbol{T}_{\mathrm{C,red}}\boldsymbol{J}^*\boldsymbol{T}_{\mathrm{C,red}}^{-1}$ and

$$\boldsymbol{\psi}_\mathrm{r}^{\alpha\beta} = L_\mathrm{m}\boldsymbol{i}_\mathrm{s}^{\alpha\beta} + L_\mathrm{r}\boldsymbol{i}_\mathrm{r}^{\alpha\beta}. \tag{2.30}$$

Solving (2.30) for $\boldsymbol{i}_\mathrm{r}^{\alpha\beta}$ allows eliminating the rotor currents from (2.27) and (2.29), and hence the overall system can be summarized as follows

$$\tfrac{\mathrm{d}}{\mathrm{d}t}\begin{pmatrix}\boldsymbol{i}_\mathrm{s}^{\alpha\beta}\\ \boldsymbol{\psi}_\mathrm{r}^{\alpha\beta}\end{pmatrix} = \underbrace{\begin{bmatrix}-\frac{1}{T_\sigma}\boldsymbol{I}_2 & -\frac{1}{L_\mu}(\omega_\mathrm{r}\boldsymbol{J} - \frac{1}{T_\mathrm{r}}\boldsymbol{I}_2)\\ \frac{L_\mathrm{m}}{T_\mathrm{r}}\boldsymbol{I}_2 & \omega_\mathrm{r}\boldsymbol{J} - \frac{1}{T_\mathrm{r}}\boldsymbol{I}_2\end{bmatrix}}_{=:\boldsymbol{A}_\mathrm{m}(\omega_\mathrm{r})}\underbrace{\begin{pmatrix}\boldsymbol{i}_\mathrm{s}^{\alpha\beta}\\ \boldsymbol{\psi}_\mathrm{r}^{\alpha\beta}\end{pmatrix}}_{=:\boldsymbol{x}_\mathrm{m}} + \underbrace{\begin{bmatrix}\frac{1}{\sigma L_\mathrm{s}}\boldsymbol{I}_2\\ \mathbf{0}_{2\times 2}\end{bmatrix}}_{=:\boldsymbol{B}_\mathrm{m}}\underbrace{\boldsymbol{u}_\mathrm{s}^{\alpha\beta}}_{=:\boldsymbol{u}_\mathrm{m}}, \tag{2.31}$$

where $\sigma := 1 - \frac{L_\mathrm{m}^2}{L_\mathrm{s}L_\mathrm{r}}$ is the leakage factor, $T_\sigma := \frac{\sigma L_\mathrm{s}}{R_\mathrm{s}+L_\mathrm{m}^2/L_\mathrm{r}^2 R_\mathrm{r}}$ is the stator time constant, $T_\mathrm{r} := \frac{L_\mathrm{r}}{R_\mathrm{r}}$ is the rotor time constant and $L_\mu := \frac{\sigma L_\mathrm{s}L_\mathrm{r}}{L_\mathrm{m}}$ is an auxiliary inductance term, respectively. Moreover, for further analysis, the state vector $\boldsymbol{x}_\mathrm{m} \in \mathbb{R}^4$, the input vector $\boldsymbol{u}_\mathrm{m} \in \mathbb{R}^2$, the speed dependent system matrix $\boldsymbol{A}_\mathrm{m}(\omega_\mathrm{r}) \in \mathbb{R}^{4\times 4}$ and the input matrix $\boldsymbol{B}_\mathrm{m} \in \mathbb{R}^{4\times 2}$ of the SR/SS model are defined.

Note that the rotational speed ω_r describes an additional system state, which will be further elucidated in the mechanical subsystem derived in Sec. 2.3. In anticipation of said chapter, the electromagnetic torque m_m produced by the motor can be described in terms of the electrical system states, i.e. (see e.g. [109, Ch. 14], where $\kappa = \frac{2}{3}$)

$$m_\mathrm{m} = \tfrac{3}{2}n_\mathrm{p}\big(\boldsymbol{i}_\mathrm{s}^{\alpha\beta}\big)^\top\boldsymbol{J}\boldsymbol{\psi}_\mathrm{s}^{\alpha\beta} \overset{(2.30)}{=} \tfrac{3}{2}n_\mathrm{p}\tfrac{L_\mathrm{m}}{L_\mathrm{r}}\big(\boldsymbol{i}_\mathrm{s}^{\alpha\beta}\big)^\top\boldsymbol{J}\boldsymbol{\psi}_\mathrm{r}^{\alpha\beta}, \tag{2.32}$$

2.1.4.2 Multi-rotor/single-stator (MR/SS) machine model (elastic)

Due to unfavourable electromagnetic properties of IMs with a large rotor length-to-diameter ratio, the multi-rotor concept has become established for high power ESP motors [106]. Figure 2.13 shows two cross-section views of the multi-rotor/single stator (MR/SS) induction machine, likewise (a) from the side and (b) from the front. The respective two-phase equivalent circuit is depicted in Fig. 2.14.

Assumption 6. *It is assumed in the following, that the space between adjacent rotor segments is negligible, compared to the total rotor segment width. As a consequence, the length of the stator is considered equal to the number of rotors segments times the rotor segment length.*

While the stator windings span over the entire length $l_\mathrm{m} = l_\mathrm{r}n_\mathrm{r}$ of the motor, the rotor is segmented into n_r parts of equal length l_r, connected via a single shaft and equipped with individual bearings. Opposite of the rotor bearings, non-steel laminations are used to reduce magnetic flux channeling in the respective sections [106]. Since the stator winding resistance is proportional to the winding length, the total stator resistance—compared to the single-rotor system—increases to $n_\mathrm{r}R_\mathrm{s} =: R_{\mathrm{s}_\Sigma}$. Likewise, the stator leakage inductance increases proportionally to the motor (stator) length, i.e. $n_\mathrm{r}L_{\mathrm{s}\sigma} =: L_{\mathrm{s}\sigma_\Sigma}$.

The i-th rotor voltage is described by the following voltage equation

$$\boldsymbol{u}_{\mathrm{r},i}^{\alpha\beta} = \mathbf{o}_2 = R_\mathrm{r}\boldsymbol{i}_{\mathrm{r},i}^{\alpha\beta} + \tfrac{\mathrm{d}}{\mathrm{d}t}\boldsymbol{\psi}_{\mathrm{r},i}^{\alpha\beta} - \omega_{\mathrm{r},i}\boldsymbol{J}\boldsymbol{\psi}_{\mathrm{r},i}^{\alpha\beta}, \quad \text{for} \quad i \in \{1,\dots,n_\mathrm{r}\} \tag{2.33}$$

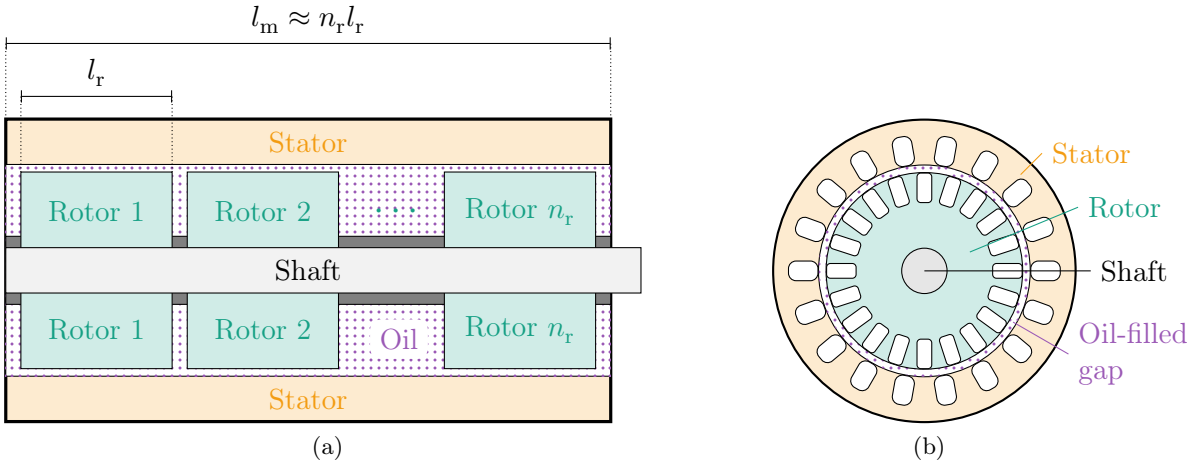

Figure 2.13: *Cross-section views of the multi-rotor/single stator (`MR/SS`) ESP motor: (a) side view and (b) front view.*

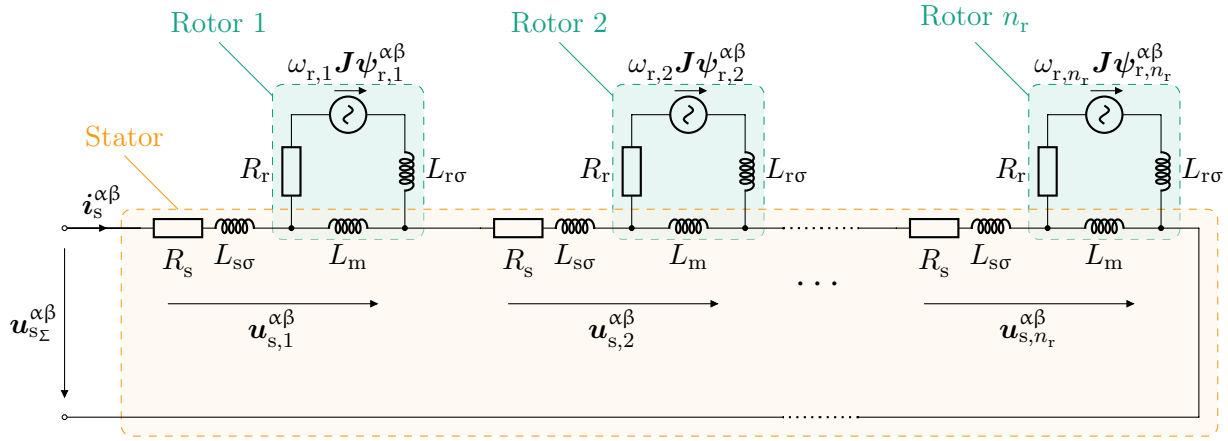

Figure 2.14: *Two-phase equivalent circuit of a multi-rotor/single-stator (`MR/SS`) induction machine.*

where $\omega_{\mathrm{r},i}$ is the angular velocity of the respective rotor segment, which is determined by a multi-mass mechanical model (see Sec. 2.3.1) and $\boldsymbol{i}^{\alpha\beta}_{\mathrm{r},i}$ and $\boldsymbol{\psi}^{\alpha\beta}_{\mathrm{r},i}$ are the i-th rotor current and flux linkage, respectively.

The linked flux between the stator and the i-th rotor depends on the area surrounded by the respective windings and rotor bars, as illustrated in Fig. 2.15. Since the flux impinged area *per rotor* does not change for the multi-rotor configuration (considering Ass. 6), the main inductance—compared to the single-rotor system—does not change, and hence the rotor flux linkage can be stated as

$$\boldsymbol{\psi}^{\alpha\beta}_{\mathrm{r},i} = L_\mathrm{m}\boldsymbol{i}^{\alpha\beta}_\mathrm{s} + L_\mathrm{r}\boldsymbol{i}^{\alpha\beta}_{\mathrm{r},i} \quad \Longrightarrow \quad \boldsymbol{i}^{\alpha\beta}_{\mathrm{r},i} = \tfrac{1}{L_\mathrm{r}}\boldsymbol{\psi}^{\alpha\beta}_{\mathrm{r},i} - \tfrac{L_\mathrm{m}}{L_\mathrm{r}}\boldsymbol{i}^{\alpha\beta}_\mathrm{s}. \tag{2.34}$$

Moreover, stating the overall stator flux linkage and inserting (2.34) yields

$$\boldsymbol{\psi}^{\alpha\beta}_{\mathrm{s}\Sigma} = \underbrace{n_\mathrm{r}(L_\mathrm{m} + L_\mathrm{s\sigma})}_{=:L_{\mathrm{s}\Sigma}}\boldsymbol{i}^{\alpha\beta}_\mathrm{s} + \sum_{i=1}^{n_\mathrm{r}} L_\mathrm{m}\boldsymbol{i}^{\alpha\beta}_{\mathrm{r},i} \overset{(2.34)}{=} \sigma L_{\mathrm{s}\Sigma}\boldsymbol{i}^{\alpha\beta}_\mathrm{s} + \tfrac{L_\mathrm{m}}{L_\mathrm{r}}\sum_{i=1}^{n_\mathrm{r}}\boldsymbol{\psi}^{\alpha\beta}_{\mathrm{r},i}. \tag{2.35}$$

Consequently, the multi-rotor stator current and rotor flux linkage dynamics are given in a more

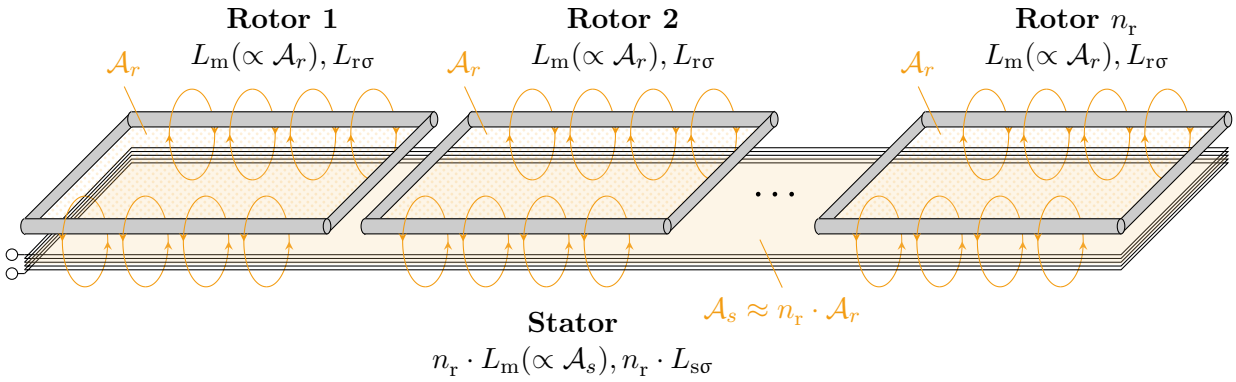

Figure 2.15: *Illustration of multi-rotor/single-stator flux impinged surfaces.*

compact form as

$$\frac{\mathrm{d}}{\mathrm{d}t}\begin{pmatrix} \boldsymbol{i}_{\mathrm{s}}^{\alpha\beta} \\ \boldsymbol{\psi}_{\mathrm{r},i}^{\alpha\beta} \end{pmatrix} = \begin{pmatrix} -\frac{1}{T_{\mathrm{s}}}\boldsymbol{i}_{\mathrm{s}}^{\alpha\beta} - \frac{1}{n_{\mathrm{r}}L_{\mu}}\sum_{i=1}^{n_{\mathrm{r}}}(\omega_{\mathrm{r},i}\boldsymbol{J} - \frac{1}{T_{\mathrm{r}}}\boldsymbol{I}_2)\boldsymbol{\psi}_{\mathrm{r},i}^{\alpha\beta} \\ \frac{L_{\mathrm{m}}}{T_{\mathrm{r}}}\boldsymbol{i}_{\mathrm{s}}^{\alpha\beta} + (\omega_{\mathrm{r},i}\boldsymbol{J} - \frac{1}{T_{\mathrm{r}}}\boldsymbol{I}_2)\boldsymbol{\psi}_{\mathrm{r},i}^{\alpha\beta} \end{pmatrix} + \begin{pmatrix} \frac{1}{\sigma L_{\mathrm{s}\Sigma}}\boldsymbol{I}_2\boldsymbol{u}_{\mathrm{s}\Sigma}^{\alpha\beta} \\ \boldsymbol{0}_{2\times 2} \end{pmatrix}, \tag{2.36}$$

where $\boldsymbol{u}_{\mathrm{s}\Sigma}^{\alpha\beta} := \sum_{i=1}^{n_{\mathrm{r}}} \boldsymbol{u}_{\mathrm{s},i}^{\alpha\beta}$. The driving torque of the i-th rotor segment is given in analogy to (2.32) by

$$m_{\mathrm{m},i} = \tfrac{3}{2}n_{\mathrm{p}}\tfrac{L_{\mathrm{m}}}{L_{\mathrm{r}}}\left(\boldsymbol{i}_{\mathrm{s}}^{\alpha\beta}\right)^{\top}\boldsymbol{J}\boldsymbol{\psi}_{\mathrm{r},i}^{\alpha\beta}. \tag{2.37}$$

For further comparison with the non-elastic case, the total motor torque, flux linkage and average rotor speed are defined as

$$m_{\mathrm{m}_\Sigma} := \sum_{i=1}^{n_{\mathrm{r}}} m_{\mathrm{m},i}, \qquad \boldsymbol{\psi}_{\mathrm{r}_\Sigma}^{\alpha\beta} := \sum_{i=1}^{n_{\mathrm{r}}} \boldsymbol{\psi}_{\mathrm{r},i}^{\alpha\beta} \qquad \text{and} \qquad \omega_{\mathrm{r}_\Pi} := \frac{1}{n_{\mathrm{r}}}\sum_{i=1}^{n_{\mathrm{r}}} \omega_{\mathrm{r},i}. \tag{2.38}$$

2.1.4.3 Multi-rotor/single-stator (MR/SS) machine model (non-elastic)

It can be deduced from (2.36) that, if

$$\omega_{\mathrm{r}} = \omega_{\mathrm{r},1} = \omega_{\mathrm{r},2} = \ldots = \omega_{\mathrm{r},n_{\mathrm{r}}}, \tag{2.39}$$

i.e. elasticity in the mechanical system is neglected, and $\boldsymbol{\psi}_{\mathrm{r}_\Sigma}^{\alpha\beta}$ is used as an auxiliary state, the system reduces to

$$\frac{\mathrm{d}}{\mathrm{d}t}\begin{pmatrix} \boldsymbol{i}_{\mathrm{s}}^{\alpha\beta} \\ \boldsymbol{\psi}_{\mathrm{r}_\Sigma}^{\alpha\beta} \end{pmatrix} = \begin{pmatrix} -\frac{1}{T_{\mathrm{s}}}\boldsymbol{i}_{\mathrm{s}}^{\alpha\beta} - \frac{1}{n_{\mathrm{r}}L_{\mu_\Sigma}}(\omega_{\mathrm{r}}\boldsymbol{J} - \frac{1}{T_{\mathrm{r}}}\boldsymbol{I}_2)\boldsymbol{\psi}_{\mathrm{r}_\Sigma}^{\alpha\beta} \\ \frac{L_{\mathrm{m}_\Sigma}}{T_{\mathrm{r}}}\boldsymbol{i}_{\mathrm{s}}^{\alpha\beta} + (\omega_{\mathrm{r}}\boldsymbol{J} - \frac{1}{T_{\mathrm{r}}}\boldsymbol{I}_2)\boldsymbol{\psi}_{\mathrm{r}_\Sigma}^{\alpha\beta} \end{pmatrix} + \begin{pmatrix} \frac{1}{\sigma L_{\mathrm{s}\Sigma}}\boldsymbol{I}_2\boldsymbol{u}_{\mathrm{s}\Sigma}^{\alpha\beta} \\ \boldsymbol{0}_{2\times 2} \end{pmatrix} \tag{2.40}$$

with $L_{\mathrm{m}_\Sigma} = n_{\mathrm{r}}L_{\mathrm{m}}$ and $L_{\mu_\Sigma} = n_{\mathrm{r}}L_{\mu}$ (consequently, also $L_{\mathrm{r}_\Sigma} = n_{\mathrm{r}}L_{\mathrm{r}}$ and $R_{\mathrm{r}_\Sigma} = n_{\mathrm{r}}R_{\mathrm{r}}$ hold). Considering further, that the time constants T_{s} and T_{r} do not change if both, resistances and inductances, are scaled with a factor n_{r} (e.g. $\frac{L_{\mathrm{r}_\Sigma}}{R_{\mathrm{r}_\Sigma}} = \frac{n_{\mathrm{r}}L_{\mathrm{r}}}{n_{\mathrm{r}}R_{\mathrm{r}}} = \frac{L_{\mathrm{r}}}{R_{\mathrm{r}}}$), the system is identical to the SR/SS system,

albeit with scaled (i.e. lumped) parameters. The overall driving torque and average rotor speed of the stiff multi-rotor system are given by

$$m_{\mathrm{m}_\Sigma} \overset{(2.38)}{=} \tfrac{3}{2} n_\mathrm{p} \tfrac{L_\mathrm{m}}{L_\mathrm{r}} \left(\boldsymbol{i}_\mathrm{s}^{\alpha\beta}\right)^\top \boldsymbol{J} \boldsymbol{\psi}_{\mathrm{r}_\Sigma}^{\alpha\beta}, \qquad \omega_{\mathrm{r}_\Pi} \overset{(2.38),(2.39)}{=} \omega_\mathrm{r}. \tag{2.41}$$

Note that the torque expression is easily derived by combining (2.37) and (2.38), i.e.

$$m_{\mathrm{m}_\Sigma} \overset{(2.37)}{=} \sum_{i=1}^{n_\mathrm{r}} \tfrac{3}{2} n_\mathrm{p} \tfrac{L_\mathrm{m}}{L_\mathrm{r}} \left(\boldsymbol{i}_\mathrm{s}^{\alpha\beta}\right)^\top \boldsymbol{J} \boldsymbol{\psi}_{\mathrm{r},i}^{\alpha\beta} = \tfrac{3}{2} n_\mathrm{p} \tfrac{L_\mathrm{m}}{L_\mathrm{r}} \left(\boldsymbol{i}_\mathrm{s}^{\alpha\beta}\right)^\top \boldsymbol{J} \sum_{i=1}^{n_\mathrm{r}} \boldsymbol{\psi}_{\mathrm{r},i}^{\alpha\beta} \overset{(2.38)}{=} \tfrac{3}{2} n_\mathrm{p} \tfrac{L_\mathrm{m}}{L_\mathrm{r}} \left(\boldsymbol{i}_\mathrm{s}^{\alpha\beta}\right)^\top \boldsymbol{J} \boldsymbol{\psi}_{\mathrm{r}_\Sigma}^{\alpha\beta}.$$

2.1.4.4 On the effect of self-excitation

Self-excitation of induction machines is a long known phenomenon [110] which occurs when a capacitor—e.g. from the LC filter—is connected in parallel with the machine windings and the electrical frequency ω_k is in the range of the resonance frequency $\omega_{\mathrm{R}2} := 1/\sqrt{C_\mathrm{f} L_\mathrm{s}}$ of the filter capacitance and the stator inductance. While this effect may be beneficial in applications, where the filter is placed near the machine—losses may be reduced as the reactive current has to overcome a small electric resistance due to the short distance between filter and machine—such benefits cannot be exploited in geothermal power plants as the power cable separates the filter from the motor. Moreover, self-excitation complicates the controller design, because the respective resonance frequency may lie within the band of feasible operation frequencies and must be considered accordingly.

Neglecting the power cable for the time being and assuming the rotor speed to be a slowly varying parameter (instead of a state), the following linear parameter varying system of an `SR/SS` induction machine connected to an LC filter is obtained

$$\frac{\mathrm{d}}{\mathrm{d}t} \begin{pmatrix} \boldsymbol{x}_\mathrm{f} \\ \boldsymbol{x}_\mathrm{m} \end{pmatrix} = \underbrace{\left[\begin{array}{c|c|c} \boldsymbol{A}_\mathrm{f} & \left[\boldsymbol{B}_{\mathrm{f},2} \mid \mathbf{o}_2\right] \\ \hline \left[\mathbf{o}_2 \mid \boldsymbol{B}_\mathrm{m}\right] & \boldsymbol{A}_\mathrm{m}(\omega_\mathrm{r}) \end{array}\right]}_{=:\boldsymbol{A}_\mathrm{se}} \underbrace{\begin{pmatrix} \boldsymbol{x}_\mathrm{f} \\ \boldsymbol{x}_\mathrm{m} \end{pmatrix}}_{=:\boldsymbol{x}_\mathrm{se}} + \underbrace{\left[\begin{array}{c} \boldsymbol{B}_{\mathrm{f},1} \\ \hline \mathbf{o}_2 \end{array}\right]}_{=:\boldsymbol{B}_\mathrm{se}} \underbrace{\boldsymbol{u}_{\mathrm{f_i}}^{\alpha\beta}}_{=:\boldsymbol{u}_\mathrm{se}}, \tag{2.42}$$

where the filter input matrix $\boldsymbol{B}_\mathrm{f} = [\boldsymbol{B}_{\mathrm{f},1}, \boldsymbol{B}_{\mathrm{f},2}]$ was split into two equal-sized submatrices $\boldsymbol{B}_{\mathrm{f},1}, \boldsymbol{B}_{\mathrm{f},2} \in \mathbb{R}^{4\times 2}$. The overall system is described by the state vector $\boldsymbol{x}_\mathrm{se} \in \mathbb{R}^8$, input vector $\boldsymbol{u}_\mathrm{se} \in \mathbb{R}^2$, the system matrix $\boldsymbol{A}_\mathrm{se} \in \mathbb{R}^{8\times 8}$ and the output matrix $\boldsymbol{B}_\mathrm{se} \in \mathbb{R}^{8\times 2}$.

The transfer functions from the VSI output to the filter and stator currents, respectively, are given by (see [111, Ch. 2.9.3])

$$G_{\mathrm{se,f}}(s) = \frac{i_\mathrm{f}^\alpha(s)}{u_{\mathrm{f_i}}^\alpha(s)} = \frac{i_\mathrm{f}^\beta(s)}{u_{\mathrm{f_i}}^\beta(s)} = \begin{pmatrix} 1 & \mathbf{o}_7^\top \end{pmatrix} (s\boldsymbol{I}_8 - \boldsymbol{A}_\mathrm{se})^{-1} \begin{pmatrix} \frac{1}{L_\mathrm{f}} \\ \mathbf{o}_7 \end{pmatrix}, \tag{2.43}$$

$$G_{\mathrm{se,s}}(s) = \frac{i_\mathrm{s}^\alpha(s)}{u_{\mathrm{f_i}}^\alpha(s)} = \frac{i_\mathrm{s}^\beta(s)}{u_{\mathrm{f_i}}^\beta(s)} = \begin{pmatrix} \mathbf{o}_4^\top & 1 & \mathbf{o}_3^\top \end{pmatrix} (s\boldsymbol{I}_8 - \boldsymbol{A}_\mathrm{se})^{-1} \begin{pmatrix} \frac{1}{L_\mathrm{f}} \\ \mathbf{o}_7 \end{pmatrix}. \tag{2.44}$$

Figure 2.16 shows magnitude and phase plots of the transfer functions $G_{\mathrm{se,f}}(s)$ and $G_{\mathrm{se,s}}(s)$ using the parameters in Tab. 2.2. The plots were generated for different, yet constant load conditions (indicated by the line style), i.e. $\omega_\mathrm{k} - \omega_\mathrm{r} = \text{const.}$, where ω_k is the electrical frequency of the applied voltage. Furthermore, the resonant frequencies $\omega_{\mathrm{R}1} = 5.45$ p.u. and $\omega_{\mathrm{R}2} = 0.82$ p.u. are marked, with the latter being located within the band of feasible operation frequencies. At this particular frequency—and for low-loads—reactive power is exchanged between the filter capacitance and the machine inductance, while the inverter supplies active power to the system only (unit power factor).

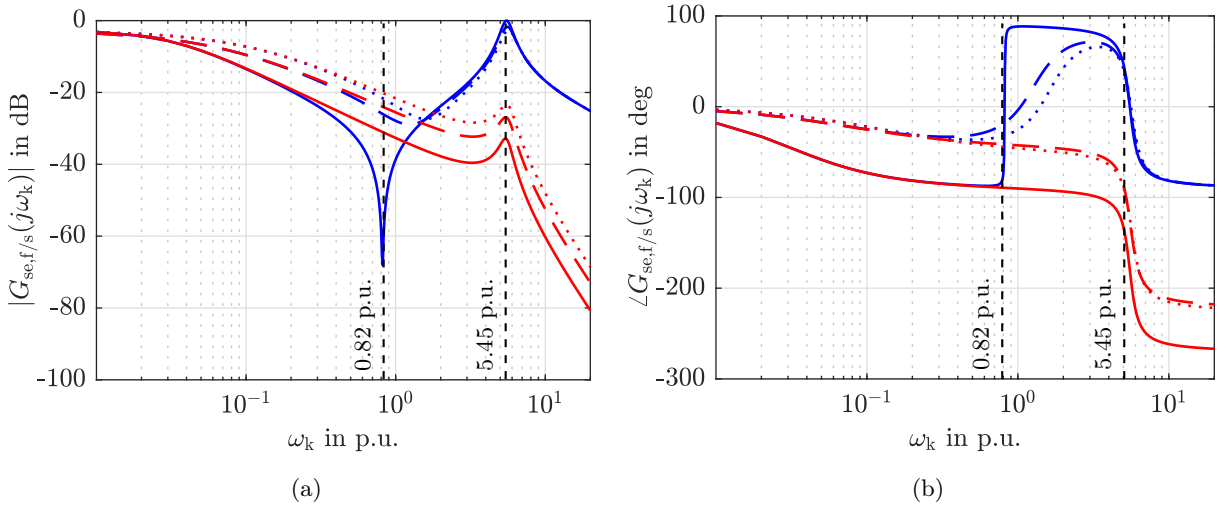

Figure 2.16: *Magnitude (a) and phase (b) plots for* $G_{\mathrm{se,f}}(s) = i_\mathrm{f}^\alpha(s)/u_{\mathrm{f_i}}^\alpha(s)$ *[——] and* $G_{\mathrm{se,s}}(s) = i_\mathrm{s}^\alpha(s)/u_{\mathrm{f_i}}^\alpha(s)$ *[——], assuming constant slip (i.e.* $\omega_\mathrm{k} - \omega_\mathrm{r} = \text{const.}$*). Plotted for different loads, i.e. the line styles solid [——], dashed [- - -] and dotted [····] refer to no-load, half rated load and rated load conditions, respectively.*

2.2 Modeling of the hydraulic subsystem

The hydraulic subsystem comprises pump, geothermal reservoir and pipe system. The former serves as an hydraulic source, while at the same time being a mechanical load. In turn, the latter two constitute the hydraulic load. The generated volume flow results from the net head applied to the fluid, i.e. the head difference between hydraulic source and load.

Remark 6 (Head)**.** *For hydraulic systems, the pressure exerted on a fluid of constant density is often expressed in terms of* head *(or pressure head), where head describes the height of a fluid column which would create an equivalent amount of pressure [112, p. 69].*

2.2.1 Pump

The pump is used to lift the geothermal fluid from the deep well to the surface. In order to produce the required volume flow rates—despite the strict space limitations in geothermal power applications—multi-stage centrifugal pumps are employed [106] (see Fig. 1.3c). Each stage of the pump consists of a rotating part, the impeller, and a fixed part, the diffuser. The fluid enters the pump stage through the impeller eye and is accelerated by the rotational movement of the impeller blades. The so obtained kinetic energy is converted into pressure energy in the diffuser. In the following, expressions for the load torque and the produced head of a single impeller are presented. Based on the single impeller model, a multi-stage pump model is derived. Impeller and pump quantities are denoted by subscripts ‘i’ and ‘p’, respectively.

2.2.1.1 Single impeller model

Figure 2.17a examplary shows the 2D cross-section of a centrifugal pump impeller, which defines the control volume $\mathcal{V}(\mathcal{A}, h_\mathrm{i})$ as a function of the cross-section area $\mathcal{A}$ and the uniform impeller

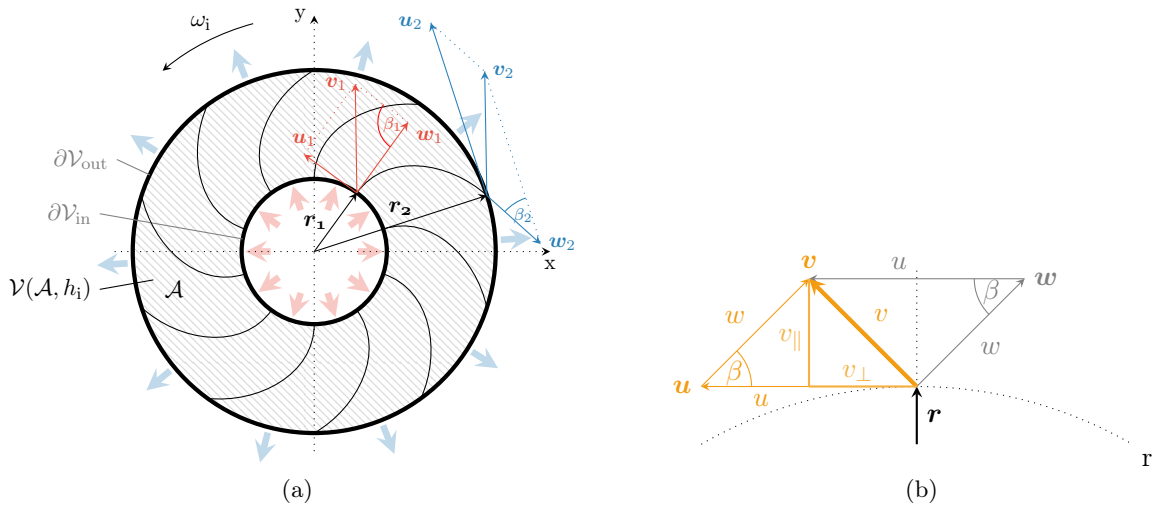

Figure 2.17: *Impeller geometry: (a) 2D impeller cross-section and (b) velocity triangle.*

height h_i—for reasons of simplicity a *radial* impeller is considered in the modeling. The fluid enters the impeller through the inlet area $\partial\mathcal{V}_\mathrm{in}$ at radius r_1 and leaves the impeller through the outlet area $\partial\mathcal{V}_\mathrm{out}$ at radius r_2. Due to its axisymmetric design, the shape of the blades depends on the radius r only and is described by its angle $\beta(r)$, with inlet angle $\beta_1 := \beta(r_1)$ and outlet angle $\beta_2 := \beta(r_2)$, respectively. The movement of the fluid particles is described by the velocity triangle (see Fig. 2.17b) at every point in $\mathcal{V}$, where u, w and v are tangential, relative and absolute speed, respectively.

Assumption 7 (1D streamline)**.** *The velocity distribution of the fluid particles within the control volume $\mathcal{V}$ (see Fig. 2.17a) is assumed* uniform *with respect to the angle, i.e. the velocity triangle depends only on the radius r, but not on the angle φ [22, Sec. 3.1].*

The impeller rotates at angular velocity ω_i, imposed by the motor through the shaft. Moreover, the total volume flowing through the pump stage is described by the volume flow Q_i and is the result of the produced head H_i, describing the height of the water column potentially produced in the pump stage.

Assumption 8 (Incompressible flow)**.** *The geothermal fluid is assumed to be* incompressible*, i.e. the density $\rho > 0$ of the fluid is constant.*

Due to Ass. 8, the impeller head is proportional to the static pressure created in the pump stage. Furthermore, the impeller creates a load torque m_i acting on the shaft. Both, load torque and head, depend on the rotational speed and the volume flow. The respective hydromechanical model of the pump is derived in Appendices C.1.1 and C.1.2.

The load torque created by a single stage of the impeller is derived in App. C.1.1 as

$$m_\mathrm{i} = \vartheta \tfrac{\mathrm{d}}{\mathrm{d}t} Q_\mathrm{i} + \Theta_\mathrm{w} \tfrac{\mathrm{d}}{\mathrm{d}t} \omega_\mathrm{i} + a_1 Q_\mathrm{i}^2 + a_2 Q_\mathrm{i} \omega_\mathrm{i} + a_3 \omega_\mathrm{i}^2, \tag{2.45}$$

with geometry dependent constants ϑ, Θ_w, a_1 and a_2 as defined in (C.7) and a_3 accounting for disk friction losses. Moreover, Θ_w describes the moment of inertia of the fluid contained in the impeller, whereas ϑ describes the impact of flow rate variations on the load torque.

The impeller head produced in a single pump stage is derived in App. C.1.2 as

$$H_\mathrm{i} = -\Gamma_\mathrm{w} \tfrac{\mathrm{d}}{\mathrm{d}t} Q_\mathrm{i} + \gamma \tfrac{\mathrm{d}}{\mathrm{d}t} \omega_\mathrm{i} + b_1 Q_\mathrm{i}^2 + b_2 \omega_\mathrm{i} Q_\mathrm{i} + b_3 \omega_\mathrm{i}^2, \tag{2.46}$$

with constants Γ_w, γ, b_1, b_2 and b_3. While Γ_w is the (head related) water inertia, γ describes the impact of change of the rotational speed on the produced head. The steady-state parameters b_1, b_2 and b_3 depend on the geometry, but also account for hydraulic losses such as hydraulic friction, shock losses and the slip factor [36]. Further information on the hydraulic loss mechanisms are given in App. C.1.2.

A qualitative H-Q-curve of an impeller for constant ω_i is depicted in Fig. 2.18: In the lossless case, the pump produces the theoretical (Euler) head, which is drawn as a bold black line. Due to the finite number of impeller vanes and flow deviations from the mean line, the theoretical head is decreased by a constant factor (slip factor), indicated by the hatched blue area. Incidence (hatched yellow area) and skin friction (hatched green area) losses depend quadratically on the volume flow, resulting in the parabolic shape of the curve. At the best efficiency point (BEP), the pump operates at designed conditions and the losses are minimal.

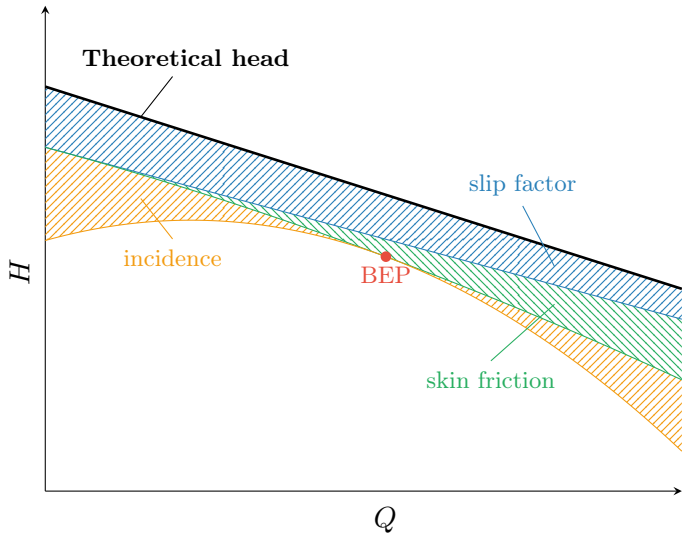

Figure 2.18: *Qualitative H-Q curve of a single pump stage, with theoretical head, slip losses, friction losses and shock (incidence) losses.*

Remark 7 (Pump type)**.** *In this section (and App. C.1), polynomial impeller head and torque expressions have been derived for a* radial *centrifugal pump. However, for geothermal applications, pump stages are typically of* mixed-flow *type [22, p. 49]. For this kind of pumps, analytical calculations become more complicated, since the fluid velocity has an additional z-component. Moreover, the polynomial head and torque approximations are not applicable in the part load region as can be concluded by inspecting the characteristic pump curves of both pump types [22, Sec. 4.1.6]. As part-load operation is tried to be avoided, though, the derived polynomial models can be fitted nonetheless for the feasible operation region near the BEP, provided that the pump curves are supplied by the pump manufacturer.*

2.2.1.2 Multi-stage pump model (with elastic shaft)

Deep geothermal ESP systems are deployed at great depths, such that the required head cannot be produced by a single pump stage anymore. For this reason, multi-stage pumps are typically employed [26, 28]. Assuming n_s pump stages of equal construction and connected via a single shaft,

each stage $j \in \{1, \ldots, n_\mathrm{s}\}$ adds to the total pump head H_{i_Σ} and load torque m_{i_Σ}, i.e.

$$H_{\mathrm{i}_\Sigma} = \sum_{j=1}^{n_\mathrm{s}} H_{\mathrm{i},j} \overset{(2.46)}{=} \sum_{j=1}^{n_\mathrm{s}} -\Gamma_\mathrm{w} \tfrac{\mathrm{d}}{\mathrm{d}t} Q_{\mathrm{i},j} + \gamma \tfrac{\mathrm{d}}{\mathrm{d}t} \omega_{\mathrm{i},j} + b_1 Q_{\mathrm{i},j}^2 + b_2 \omega_{\mathrm{i},j} Q_{\mathrm{i},j} + b_3 \omega_{\mathrm{i},j}^2 \qquad \text{and} \tag{2.47}$$

$$m_{\mathrm{i}_\Sigma} = \sum_{j=1}^{n_\mathrm{s}} m_{\mathrm{i},j} \overset{(2.45)}{=} \sum_{j=1}^{n_\mathrm{s}} \vartheta \tfrac{\mathrm{d}}{\mathrm{d}t} Q_{\mathrm{i},j} + \Theta_\mathrm{w} \tfrac{\mathrm{d}}{\mathrm{d}t} \omega_{\mathrm{i},j} + a_1 Q_{\mathrm{i},j}^2 + a_2 Q_{\mathrm{i},j} \omega_{\mathrm{i},j} + a_3 \omega_{\mathrm{i},j}^2, \tag{2.48}$$

where $H_{\mathrm{i},j}$ and $m_{\mathrm{i},j}$ denote the impeller head and load torque of stage j, respectively [113, Ch. 5.8.4]. Ideally, the volume flow $Q_{\mathrm{i},j}$ through the impeller stages should be the same as the flow Q_p leaving the pump discharge. However, due to leakage in the seals, wearing rings, bushings and axial thrust balancing devices a small portion of the flow is lost [22, Sec. 3.6.2]. Leakage flow occurs particularly at part-load as the high pressure fluid cannot exit the pump through the outlet, and hence flows back through narrow passages to the lower pressure regions. For the sake of simplicity the following assumption shall hold.

Assumption 9 (Leakage flow)**.** *It is assumed that the leakage flow is much smaller than the main flow and thus negligible, i.e.* $Q_\mathrm{p} = Q_{\mathrm{i},1} = \ldots = Q_{\mathrm{i},n_\mathrm{s}}$ *holds.*

Considering Ass. 9, the total pump head and load torque are given by

$$H_{\mathrm{i}_\Sigma} = -n_\mathrm{s} \Gamma_\mathrm{w} \tfrac{\mathrm{d}}{\mathrm{d}t} Q_\mathrm{p} + n_\mathrm{s} b_1 Q_\mathrm{p}^2 + \sum_{j=1}^{n_\mathrm{s}} \gamma \tfrac{\mathrm{d}}{\mathrm{d}t} \omega_{\mathrm{i},j} + b_2 \omega_{\mathrm{i},j} Q_\mathrm{p} + b_3 \omega_{\mathrm{i},j}^2 \qquad \text{and} \tag{2.49}$$

$$m_{\mathrm{i}_\Sigma} = n_\mathrm{s} \vartheta \tfrac{\mathrm{d}}{\mathrm{d}t} Q_\mathrm{p} + n_\mathrm{s} a_1 Q_\mathrm{p}^2 + \sum_{j=1}^{n_\mathrm{s}} \Theta_\mathrm{w} \tfrac{\mathrm{d}}{\mathrm{d}t} \omega_{\mathrm{i},j} + a_2 Q_\mathrm{p} \omega_{\mathrm{i},j} + a_3 \omega_{\mathrm{i},j}^2. \tag{2.50}$$

Moreover, the average impeller speed is defined as

$$\omega_{\mathrm{i}_\Pi} = \tfrac{1}{n_\mathrm{s}} \sum_{j=1}^{n_\mathrm{s}} \omega_{\mathrm{i},j}. \tag{2.51}$$

Remark 8 (Stiff system)**.** *If elasticity of the shaft is neglected in the mechanical system, each impeller stage contributes equally to the overall pump head and load torque, i.e.* $H_{\mathrm{i}_\Sigma} = n_\mathrm{s} H_\mathrm{i}$ *and* $m_{\mathrm{i}_\Sigma} = n_\mathrm{s} m_\mathrm{i}$*, since the angular velocities of the impellers are equal, i.e.* $\omega_\mathrm{i} = \omega_{\mathrm{i},1} = \omega_{\mathrm{i},2} = \ldots = \omega_{\mathrm{i},n_\mathrm{s}}$*. Consequently,* $\omega_{\mathrm{i}_\Pi} = \omega_\mathrm{i}$ *holds, too.*

2.2.2 Pipe system and geothermal reservoir

The hydraulic system (denoted by subscript 'h') between pump intake and wellhead defines the hydraulic load of the model. It is depicted in Fig. 2.19 and comprises the production pipe of radius r_pipe, pressures at both pipe ends (intake pressure p_it and wellhead pressure p_wh) and the water level h_w.

Assumption 10. *The production pipe radius* r_pipe *is assumed constant, such that the (steady-state) flow velocity can be considered uniform along the production path.*

In view of Ass. 10, the system head H_h (hydraulic load) can be described by the dynamic (transient) Bernoulli equation for incompressible, inviscid flow along a streamline as [114, Ch. 6.6]

$$H_\mathrm{h} = \Gamma_\mathrm{h}(h_\mathrm{w}) \tfrac{\mathrm{d}}{\mathrm{d}t} Q_\mathrm{h} + H_\mathrm{g}(h_\mathrm{w}, p_\mathrm{wh}, Q_\mathrm{h}) + K_\mathrm{fh}(h_\mathrm{w}) Q_\mathrm{h}^2 \tag{2.52}$$

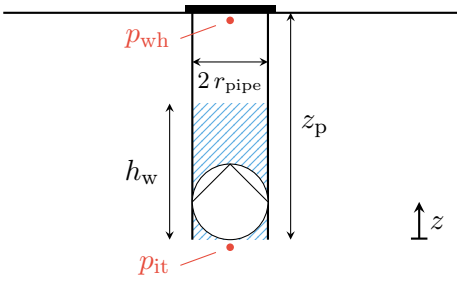

Figure 2.19: *Hydraulic system of the geothermal production well.*

with system flow $Q_{\mathrm{h}} = Q_{\mathrm{p}}$ (equal to the pump flow) and an additional loss term $K_{\mathrm{fh}}(h_{\mathrm{w}})Q_{\mathrm{h}}^2$ accounting for frictional losses in the piping system. The variable parameter $\Gamma_{\mathrm{h}}(h_{\mathrm{w}})$ denotes the inertia of the fluid in the piping system, whereas $K_{\mathrm{fh}}(h_{\mathrm{w}})$ is the combined hydraulic friction coefficient. Both coefficients, K_{fh} and Γ_{h}, linearly depend on the water level h_{w} and thus dynamically change during system start-up. The friction coefficient is derived using the Darcy-Weisbach Equation (see e.g. [22, Sec. 1.5.1]), i.e.

$$K_{\mathrm{fh}}(h_{\mathrm{w}}) = h_{\mathrm{w}} \frac{\lambda_{\mathrm{D}}}{4\pi^2 g\, r_{\mathrm{pipe}}^5} \tag{2.53}$$

where λ_{D} (dimensionless) denotes the Darcy friction factor depending on the Reynolds number[3] of the pipe system. The inertia on the other hand is given by

$$\Gamma_{\mathrm{h}}(h_{\mathrm{w}}) = h_{\mathrm{w}} \frac{1}{\pi g r_{\mathrm{pipe}}^2} \tag{2.54}$$

and follows from the integral along the streamline of the water (see e.g. [114, Ch. 6.6]). The term

$$H_{\mathrm{g}}(h_{\mathrm{w}}, p_{\mathrm{wh}}, Q_{\mathrm{p}}) = h_{\mathrm{w}} + \frac{p_{\mathrm{wh}} - p_{\mathrm{it}}(Q_{\mathrm{p}})}{\rho g} \tag{2.55}$$

denotes the part of the system head which consists of the (limited) water column h_{w} weighing on the pump, and the scaled pressure gradient between wellhead pressure p_{wh} and intake pressure p_{it}. While the wellhead pressure is typically kept constant once it reaches a defined value, the intake pressure changes throughout the operation of the system, resulting in a lower idle water level (drawdown). The drawdown is characterized by the productivity index δ of the geothermal reservoir and the idle pressure p_{it0} and changes with the volume flow Q_{p}. According to [18, Sec. 14.1.2] the intake pressure can be stated as

$$p_{\mathrm{it}}(Q_{\mathrm{p}}) = p_{\mathrm{it0}} - \frac{1}{\delta} Q_{\mathrm{p}}. \tag{2.56}$$

Moreover, the dynamics of the water level h_{w} can be described by the following equation

$$\tfrac{\mathrm{d}}{\mathrm{d}t} h_{\mathrm{w}} = \bar{k}_{h_{\mathrm{w}}}(h_{\mathrm{w}}, Q_{\mathrm{p}}) \frac{1}{\pi r_{\mathrm{pipe}}^2} Q_{\mathrm{p}}, \tag{2.57}$$

where

$$\bar{k}_{h_{\mathrm{w}}}(h_{\mathrm{w}}, Q_{\mathrm{p}}) = \begin{cases} 0\,, & \text{for} \quad (h_{\mathrm{w}} \le 0 \wedge Q_{\mathrm{p}} \le 0) \vee (h_{\mathrm{w}} \ge z_{\mathrm{p}} \wedge Q_{\mathrm{p}} \ge 0) \\ 1\,, & \text{else} \end{cases} \tag{2.58}$$

toggles the integration in (2.57).

[3] Named after its inventor, the physicist Osborne Reynolds (⋆1842, Belfast, Northern Ireland), the *Reynolds number* is a dimensionless quantity, describing the ratio of inertial forces to viscous forces in a fluid. For low values, the flow tends to be *laminar*, whereas for higher values it becomes *turbulent* [112, Sec. 8.2].

Assumption 11 (Wellhead pressure)**.** *In idle state, the water column on the pump reaches its idle water level. The remaining (upper) part of the production tubing is filled with air. For the sake of simplicity, it is assumed that the air can escape without resistance, until the lifted water reaches the wellhead.*

Due to Ass. 11, the wellhead pressure p_{wh} builds-up only if the water column reaches the wellhead. Moreover it is saturated by a defined (and constant) value $p^{\star}_{\mathrm{wh}}$, according to the employed pressure valve. The dynamics of the wellhead pressure can be described by

$$\tfrac{\mathrm{d}}{\mathrm{d}t} p_{\mathrm{wh}} = \bar{k}_{h_{\mathrm{w}}}(h_{\mathrm{w}}, Q_{\mathrm{p}}, p_{\mathrm{wh}}) \frac{\rho g}{\pi r_{\mathrm{pipe}}^2} Q_{\mathrm{p}}, \tag{2.59}$$

with decision function

$$\bar{k}_{p_{\mathrm{wh}}}(h_{\mathrm{w}}, Q_{\mathrm{p}}, p_{\mathrm{wh}}) = \begin{cases} 0\,, & \text{for} \quad h_{\mathrm{w}} \neq z_{\mathrm{p}} \vee (p_{\mathrm{wh}} \leq 0 \wedge Q_{\mathrm{p}} \leq 0) \vee (p_{\mathrm{wh}} \geq p^{\star}_{\mathrm{wh}} \wedge Q_{\mathrm{p}} \geq 0) \\ 1\,, & \text{else,} \end{cases} \tag{2.60}$$

toggling the integration in (2.59).

The equilibrium condition of the hydraulic system is obtained by enforcing $H_{\mathrm{h}} \overset{!}{=} H_{\mathrm{i}_\Sigma}$, yielding

$$H_{\mathrm{h}} \overset{(2.55),(2.56)}{=} \Gamma_{\mathrm{h}}(h_{\mathrm{w}}) \tfrac{\mathrm{d}}{\mathrm{d}t} Q_{\mathrm{h}} + \overbrace{h_{\mathrm{w}} + \frac{p_{\mathrm{wh}} - p_{\mathrm{it0}}}{\rho g}}^{=:\widehat{H}_{\mathrm{g}}(h_{\mathrm{w}}, p_{\mathrm{wh}})} + \frac{1}{\rho g \delta} Q_{\mathrm{p}} + K_{\mathrm{fh}}(h_{\mathrm{w}}) Q_{\mathrm{h}}^2 \tag{2.61}$$

$$\overset{!}{=} -n_{\mathrm{s}} \Gamma_{\mathrm{w}} \tfrac{\mathrm{d}}{\mathrm{d}t} Q_{\mathrm{p}} + n_{\mathrm{s}} b_1 Q_{\mathrm{p}}^2 + \sum_{j=1}^{n_{\mathrm{s}}} \left(\gamma \tfrac{\mathrm{d}}{\mathrm{d}t} \omega_{\mathrm{i},j} + b_2 \omega_{\mathrm{i},j} Q_{\mathrm{p}} + b_3 \omega_{\mathrm{i},j}^2 \right) \overset{(2.49)}{=} H_{\mathrm{i}_\Sigma}, \tag{2.62}$$

where $\widehat{H}_{\mathrm{g}}$ is the static head. Defining $\Gamma_{\mathrm{t}}(h_{\mathrm{w}}) = \Gamma_{\mathrm{h}}(h_{\mathrm{w}}) + n_{\mathrm{s}} \Gamma_{\mathrm{w}} > 0$ as overall inertia of the water column over the pump (always positive as the pump should be submersed), and for $Q_{\mathrm{p}} = Q_{\mathrm{h}}$, the flow dynamics are obtained as

$$\begin{aligned} \tfrac{\mathrm{d}}{\mathrm{d}t} Q_{\mathrm{p}} \;=\; & \frac{n_{\mathrm{s}} b_1 - K_{\mathrm{fh}}(h_{\mathrm{w}})}{\Gamma_{\mathrm{t}}(h_{\mathrm{w}})} Q_{\mathrm{p}}^2 - \frac{1}{\rho g \delta \Gamma_{\mathrm{t}}(h_{\mathrm{w}})} Q_{\mathrm{p}} - \frac{\widehat{H}_{\mathrm{g}}(h_{\mathrm{w}}, p_{\mathrm{wh}})}{\Gamma_{\mathrm{t}}(h_{\mathrm{w}})} \\ & + \sum_{j=1}^{n_{\mathrm{s}}} \left(\gamma \tfrac{\mathrm{d}}{\mathrm{d}t} \omega_{\mathrm{i},j} + \frac{b_2}{\Gamma_{\mathrm{t}}(h_{\mathrm{w}})} \omega_{\mathrm{i},j} Q_{\mathrm{p}} + \frac{b_3}{\Gamma_{\mathrm{t}}(h_{\mathrm{w}})} \omega_{\mathrm{i},j}^2 \right). \end{aligned} \tag{2.63}$$

Note that the amount of water in the production tubing is typically much higher than the water contained in the pump and thus the overall fluid inertia can be approximated by $\Gamma_{\mathrm{t}}(h_{\mathrm{w}}) \approx \Gamma_{\mathrm{h}}(h_{\mathrm{w}})$, i.e. $\Gamma_{\mathrm{w}} \approx 0$ (the inertia of the fluid is negligible). The equation above fully describes the dynamics of the hydraulic system. However, as it depends on the derivative of the rotational speed, the dynamics of Q_{p} and $\omega_{\mathrm{i},j}$ need to be decoupled. This can be achieved in two ways: (i) By defining $\gamma := 0$, leading to the default steady-state pump head used in most text books, see e.g. [115–117], or (ii) by deriving the governing equations of the mechanical system, which also depend on both derivative terms. Since the complexity of the system increases significantly if the speed derivative is considered in (2.63), and the (speed change induced) temporary head peaks have a negligible effect on the slowly changing hydraulic system, the first option is chosen.

Assumption 12 (Speed derivative impact on pump head)**.** *It is assumed that the impact of speed derivatives on the hydraulic system dynamics in* (2.63) *is negligible, i.e.* $\gamma = 0$ *holds.*

Finally, considering Ass. 12, the nonlinear hydraulic system dynamics can be stated as

$$\tfrac{\mathrm{d}}{\mathrm{d}t} Q_{\mathrm{p}} = \tfrac{n_{\mathrm{s}} b_1 - K_{\mathrm{fh}}(h_{\mathrm{w}})}{\Gamma_{\mathrm{t}}(h_{\mathrm{w}})} Q_{\mathrm{p}}^2 - \tfrac{1}{\rho g \delta \Gamma_{\mathrm{t}}(h_{\mathrm{w}})} Q_{\mathrm{p}} - \tfrac{\widehat{H}_{\mathrm{g}}(h_{\mathrm{w}}, p_{\mathrm{wh}})}{\Gamma_{\mathrm{t}}(h_{\mathrm{w}})} + \sum_{j=1}^{n_{\mathrm{s}}} \left(\tfrac{b_2}{\Gamma_{\mathrm{t}}(h_{\mathrm{w}})} \omega_{\mathrm{i},j} Q_{\mathrm{p}} + \tfrac{b_3}{\Gamma_{\mathrm{t}}(h_{\mathrm{w}})} \omega_{\mathrm{i},j}^2 \right). \tag{2.64}$$

2.3 Modeling of the mechanical subsystem (shaft)

The mechanical subsystem links the electrical with the hydraulic subsystem as it transfers the motor torque via the shaft to the pump, which in turn imposes a load torque on the shaft. According to Newton's second law, the shaft is accelerated in proportion to the net torque applied. As proposed by [29] and [31], the shaft is modeled as an elastic spring-damper-system due to its high length-to-diameter ratio. For the sake of simplicity lumped parameters are used to describe the multi-body system [118, Ch. 2.1], i.e. the following assumptions hold:

Assumption 13 (Inertia-free shaft)**.** *The shaft is assumed an inertia-free (massless) interconnection between two rotating (rigid) masses, subject to torsion and damping effects.*

Assumption 14 (Concentrated flywheel)**.** *The rotating masses (i.e. rotor segments or pump stages) are considered rigid flywheels without spatial extent along the shaft, located in the center of gravity of the respective segment. It is further assumed that any distributed accelerating or braking torque applied to the rotating mass, acts as a lumped torque at the location of the respective flywheel.*

Depending on the desired level of accuracy (and complexity), the rotor of the electrical machine and the rotating parts of the pump are modelled as single- or multi-mass systems. In this section, the generic multi-mass mechanical system is derived. It is further shown, that the generic model can be reduced to single-mass systems independently for both, motor and pump side, by adapting the respective parameters. In either case, the shaft section linking pump and motor is subject to elasticity.

2.3.1 Generic multi-mass mechanical system

The free-body diagram of the multi-mass mechanical system is depicted in Fig. 2.20: The electrical machine is composed of n_r rotors with moment of inertia Θ_r and friction coefficient $\nu_{\mathrm{r},i}, i \in \{1, \dots, n_\mathrm{r}\}$, coupled by shaft segments of length l_r, stiffness $k_{\mathrm{r,t}}$ and damping coefficient $k_{\mathrm{r,d}}$. Analogously, the pump consists of n_s stages, with combined water and impeller moment of inertia Θ_iw, friction coefficient $\nu_{\mathrm{i},j}, j \in \{1, \dots, n_\mathrm{s}\}$, and shaft segments of length l_i, stiffness $k_{\mathrm{i,t}}$ and damping coefficient $k_{\mathrm{i,d}}$, respectively. The shaft section interconnecting motor and pump is described by length l_mp, stiffness k_t and damping coefficient k_d.

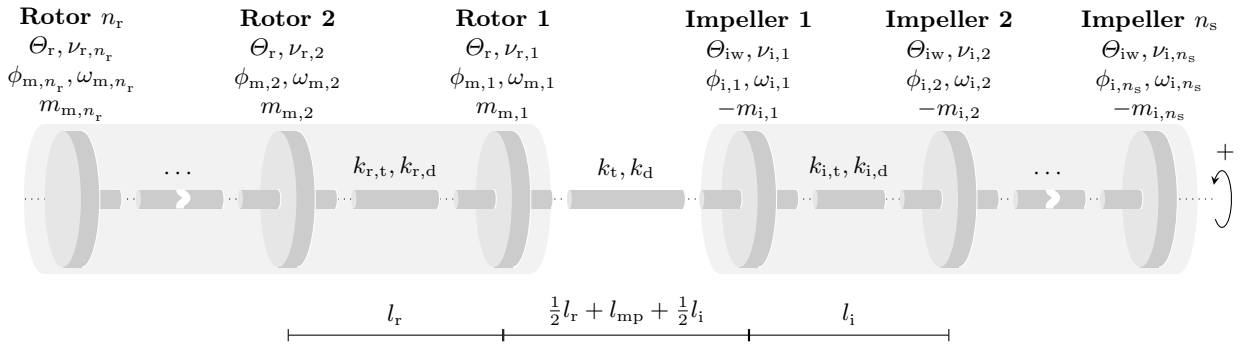

Figure 2.20: *Free-body diagram of the multi-mass mechanical system of the motor-pump unit.*

Assumption 15 (Shaft radius)**.** *It is assumed that the shaft has a uniform radius. As a consequence, the stiffness and damping coefficients are inversely proportional to the shaft length.*

Remark 9 (Viscous friction)**.** *Note that due to scalings, mechanical wear or constructional differences, the friction coefficients $\nu_{\mathrm{r},i}$ and $\nu_{\mathrm{i},j}$ may differ and/or change over time in the most general case. For most applications, it is sufficient though, to assume equal coefficients for each rotor and pump stage, respectively.*

Applying Newton's second law (sum of torques equals accelerating torque) and considering electromagnetic, torsion and damping torques, the *motor-side* mechanical system is described by

$$\left.\begin{aligned}
m_{\mathrm{m},1} &\overset{(2.37)}{=} \tfrac{3}{2} n_{\mathrm{p}} \tfrac{L_{\mathrm{m}}}{L_{\mathrm{r}}} \left(\boldsymbol{i}_{\mathrm{s}}^{\alpha\beta}\right)^{\top} \boldsymbol{J} \boldsymbol{\psi}_{\mathrm{r},1}^{\alpha\beta} \\
&\overset{!}{=} \Theta_{\mathrm{r}} \tfrac{\mathrm{d}}{\mathrm{d}t} \omega_{\mathrm{m},1} + k_{\mathrm{r,t}}(\phi_{\mathrm{m},1} - \phi_{\mathrm{m},2}) + k_{\mathrm{t}}(\phi_{\mathrm{m},1} - \phi_{\mathrm{i},1}) + k_{\mathrm{r,d}}(\omega_{\mathrm{m},1} - \omega_{\mathrm{m},2}) \\
&\quad + k_{\mathrm{d}}(\omega_{\mathrm{m},1} - \omega_{\mathrm{i},1}) + \nu_{\mathrm{r},1}\omega_{\mathrm{m},1} \\
&\quad \vdots \\
m_{\mathrm{m},i} &\overset{(2.37)}{=} \tfrac{3}{2} n_{\mathrm{p}} \tfrac{L_{\mathrm{m}}}{L_{\mathrm{r}}} \left(\boldsymbol{i}_{\mathrm{s}}^{\alpha\beta}\right)^{\top} \boldsymbol{J} \boldsymbol{\psi}_{\mathrm{r},i}^{\alpha\beta} \\
&\overset{!}{=} \Theta_{\mathrm{r}} \tfrac{\mathrm{d}}{\mathrm{d}t} \omega_{\mathrm{m},i} + k_{\mathrm{r,t}}(2\phi_{\mathrm{m},i} - \phi_{\mathrm{m},i-1} - \phi_{\mathrm{m},i+1}) + k_{\mathrm{r,d}}(2\omega_{\mathrm{m},i} - \omega_{\mathrm{m},i-1} - \omega_{\mathrm{m},i+1}) \\
&\quad + \nu_{\mathrm{r},i}\omega_{\mathrm{m},i} \\
&\quad \vdots \\
m_{\mathrm{m},n_{\mathrm{r}}} &\overset{(2.37)}{=} \tfrac{3}{2} n_{\mathrm{p}} \tfrac{L_{\mathrm{m}}}{L_{\mathrm{r}}} \left(\boldsymbol{i}_{\mathrm{s}}^{\alpha\beta}\right)^{\top} \boldsymbol{J} \boldsymbol{\psi}_{\mathrm{r},n_{\mathrm{r}}}^{\alpha\beta} \\
&\overset{!}{=} \Theta_{\mathrm{r}} \tfrac{\mathrm{d}}{\mathrm{d}t} \omega_{\mathrm{m},i} + k_{\mathrm{r,t}}(\phi_{\mathrm{m},n_{\mathrm{r}}} - \phi_{\mathrm{m},n_{\mathrm{r}}-1}) + k_{\mathrm{r,d}}(\omega_{\mathrm{m},n_{\mathrm{r}}} - \omega_{\mathrm{m},n_{\mathrm{r}}-1}) + \nu_{\mathrm{r},n_{\mathrm{r}}}\omega_{\mathrm{m},i}
\end{aligned}\right\} \tag{2.65}$$

Solving for the $\frac{\mathrm{d}}{\mathrm{d}t}\omega_{\mathrm{m},i}$ terms and using $\frac{\mathrm{d}}{\mathrm{d}t}\phi_{\mathrm{m},i} = \omega_{\mathrm{m},i}$ yields the motor-side mechanical system

$$\frac{\mathrm{d}}{\mathrm{d}t}\begin{pmatrix} \phi_{\mathrm{m},1} \\ \omega_{\mathrm{m},1} \\ \vdots \\ \phi_{\mathrm{m},i} \\ \omega_{\mathrm{m},i} \\ \vdots \\ \phi_{\mathrm{m},n_{\mathrm{r}}} \\ \omega_{\mathrm{m},n_{\mathrm{r}}} \end{pmatrix} \overset{(2.37),(2.65)}{=} \begin{pmatrix} \omega_{\mathrm{m},1} \\ \frac{3n_{\mathrm{p}}L_{\mathrm{m}}}{2\Theta_{\mathrm{r}}L_{\mathrm{r}}} \left(\boldsymbol{i}_{\mathrm{s}}^{\alpha\beta}\right)^{\top} \boldsymbol{J} \boldsymbol{\psi}_{\mathrm{r},1}^{\alpha\beta} - \frac{k_{\mathrm{r,t}}}{\Theta_{\mathrm{r}}}(\phi_{\mathrm{m},1} - \phi_{\mathrm{m},2}) - \frac{k_{\mathrm{t}}}{\Theta_{\mathrm{r}}}(\phi_{\mathrm{m},1} - \phi_{\mathrm{i},1}) \\ \quad - \frac{k_{\mathrm{r,d}}}{\Theta_{\mathrm{r}}}(\omega_{\mathrm{m},1} - \omega_{\mathrm{m},2}) - \frac{k_{\mathrm{d}}}{\Theta_{\mathrm{r}}}(\omega_{\mathrm{m},1} - \omega_{\mathrm{i},1}) - \frac{\nu_{\mathrm{r},1}}{\Theta_{\mathrm{r}}}\omega_{\mathrm{m},1} \\ \vdots \\ \omega_{\mathrm{m},i} \\ \frac{3n_{\mathrm{p}}L_{\mathrm{m}}}{2\Theta_{\mathrm{r}}L_{\mathrm{r}}} \left(\boldsymbol{i}_{\mathrm{s}}^{\alpha\beta}\right)^{\top} \boldsymbol{J} \boldsymbol{\psi}_{\mathrm{r},i}^{\alpha\beta} - \frac{k_{\mathrm{r,t}}}{\Theta_{\mathrm{r}}}(2\phi_{\mathrm{m},i} - \phi_{\mathrm{m},i-1} - \phi_{\mathrm{m},i+1}) \\ \quad - \frac{k_{\mathrm{r,d}}}{\Theta_{\mathrm{r}}}(2\omega_{\mathrm{m},i} - \omega_{\mathrm{m},i-1} - \omega_{\mathrm{m},i+1}) - \frac{\nu_{\mathrm{r},i}}{\Theta_{\mathrm{r}}}\omega_{\mathrm{m},i} \\ \vdots \\ \omega_{\mathrm{m},n_{\mathrm{r}}} \\ \frac{3n_{\mathrm{p}}L_{\mathrm{m}}}{2\Theta_{\mathrm{r}}L_{\mathrm{r}}} \left(\boldsymbol{i}_{\mathrm{s}}^{\alpha\beta}\right)^{\top} \boldsymbol{J} \boldsymbol{\psi}_{\mathrm{r},n_{\mathrm{r}}}^{\alpha\beta} - \frac{k_{\mathrm{r,t}}}{\Theta_{\mathrm{r}}}(\phi_{\mathrm{m},n_{\mathrm{r}}} - \phi_{\mathrm{m},n_{\mathrm{r}}-1}) \\ \quad - \frac{k_{\mathrm{r,d}}}{\Theta_{\mathrm{r}}}(\omega_{\mathrm{m},n_{\mathrm{r}}} - \omega_{\mathrm{m},n_{\mathrm{r}}-1}) - \frac{\nu_{\mathrm{r},n_{\mathrm{r}}}}{\Theta_{\mathrm{r}}}\omega_{\mathrm{m},n_{\mathrm{r}}} \end{pmatrix}. \tag{2.66}$$

In general, the number of states for the motor-side mechanical system is $2 \cdot n_{\mathrm{r}}$.

Remark 10 (Single motor / tandem configuration)**.** *Note that the electrical machine is modelled as a single unit, whereas in real plants the so-called tandem configuration is frequently used. In tandem configuration, two motors are mechanically connected in series, while being electrically in parallel. An extension of the presented model is easily realized by adding a second, identical set of rotor segments, controlled by the same voltage and coupled through the same shaft.*

Conversely, the *pump-side* torque balance can be stated as

$$\left.\begin{aligned}
-m_{\mathrm{i},1} &\overset{(2.45)}{=} -\vartheta\tfrac{\mathrm{d}}{\mathrm{d}t}Q_\mathrm{p} - \Theta_\mathrm{w}\tfrac{\mathrm{d}}{\mathrm{d}t}\omega_{\mathrm{i},1} - a_1 Q_\mathrm{p}^2 - a_2 Q_\mathrm{p}\omega_{\mathrm{i},1} - a_3{\omega_{\mathrm{i},1}}^2 \\
&\overset{!}{=} \Theta_\mathrm{i}\tfrac{\mathrm{d}}{\mathrm{d}t}\omega_{\mathrm{i},1} + k_{\mathrm{i,t}}(\phi_{\mathrm{i},1} - \phi_{\mathrm{i},2}) + k_\mathrm{t}(\phi_{\mathrm{i},1} - \phi_{\mathrm{m},1}) + k_{\mathrm{i,d}}(\omega_{\mathrm{i},1} - \omega_{\mathrm{i},2}) \\
&\quad + k_\mathrm{d}(\omega_{\mathrm{i},1} - \omega_{\mathrm{m},1}) + \nu_{\mathrm{i},1}\omega_{\mathrm{i},1} \\
&\quad \vdots \\
-m_{\mathrm{i},j} &\overset{(2.45)}{=} -\vartheta\tfrac{\mathrm{d}}{\mathrm{d}t}Q_\mathrm{p} - \Theta_\mathrm{w}\tfrac{\mathrm{d}}{\mathrm{d}t}\omega_{\mathrm{i},j} - a_1 Q_\mathrm{p}^2 - a_2 Q_\mathrm{p}\omega_{\mathrm{i},j} - a_3{\omega_{\mathrm{i},j}}^2 \\
&\overset{!}{=} \Theta_\mathrm{i}\tfrac{\mathrm{d}}{\mathrm{d}t}\omega_{\mathrm{i},j} + k_{\mathrm{i,t}}(2\phi_{\mathrm{i},j} - \phi_{\mathrm{i},j-1} - \phi_{\mathrm{i},j+1}) + k_{\mathrm{i,d}}(2\omega_{\mathrm{i},j} - \omega_{\mathrm{i},j-1} - \omega_{\mathrm{i},j+1}) \\
&\quad + \nu_{\mathrm{i},j}\omega_{\mathrm{i},j} \\
&\quad \vdots \\
-m_{\mathrm{i},n_\mathrm{s}} &\overset{(2.45)}{=} -\vartheta\tfrac{\mathrm{d}}{\mathrm{d}t}Q_\mathrm{p} - \Theta_\mathrm{w}\tfrac{\mathrm{d}}{\mathrm{d}t}\omega_{\mathrm{i},n_\mathrm{s}} - a_1 Q_\mathrm{p}^2 - a_2 Q_\mathrm{p}\omega_{\mathrm{i},n_\mathrm{s}} - a_3{\omega_{\mathrm{i},n_\mathrm{s}}}^2 \\
&\overset{!}{=} \Theta_\mathrm{i}\tfrac{\mathrm{d}}{\mathrm{d}t}\omega_{\mathrm{i},n_\mathrm{s}} + k_{\mathrm{i,t}}(\phi_{\mathrm{i},n_\mathrm{s}} - \phi_{\mathrm{i},n_\mathrm{s}-1}) + k_{\mathrm{i,d}}(\omega_{\mathrm{i},n_\mathrm{s}} - \omega_{\mathrm{i},n_\mathrm{s}-1}) \\
&\quad + \nu_{\mathrm{i},n_\mathrm{s}}\omega_{\mathrm{i},n_\mathrm{s}}
\end{aligned}\right\} \tag{2.67}$$

Since both derivative terms $\frac{\mathrm{d}}{\mathrm{d}t}Q_\mathrm{p}$ and $\frac{\mathrm{d}}{\mathrm{d}t}\omega_\mathrm{i} = \frac{\mathrm{d}}{\mathrm{d}t}\omega_{\mathrm{i},j}$ with $j \in \{1, \dots, n_\mathrm{s}\}$ appear in (2.67), the pump-side mechanical system cannot be reformulated in state-space form (i.e. $\frac{\mathrm{d}}{\mathrm{d}t}\boldsymbol{x} = \boldsymbol{f}(\boldsymbol{x}, \boldsymbol{u})$). However, the following assumption is legitimate (see [36]), especially for large pump systems.

Assumption 16 (Flow dynamics)**.** *The hydraulic system is considerably slower than the mechanical system, i.e.*

$$\left.\begin{aligned}
|-\vartheta\tfrac{\mathrm{d}}{\mathrm{d}t}Q_\mathrm{p}| &\ll |(\Theta_\mathrm{i} + \Theta_\mathrm{w})\tfrac{\mathrm{d}}{\mathrm{d}t}\omega_{\mathrm{i},1} + k_{\mathrm{i,t}}(\phi_{\mathrm{i},1} - \phi_{\mathrm{i},2}) + k_\mathrm{t}(\phi_{\mathrm{i},1} - \phi_{\mathrm{m},1}) + k_{\mathrm{i,d}}(\omega_{\mathrm{i},1} - \omega_{\mathrm{i},2}) \\
&\quad + k_\mathrm{d}(\omega_{\mathrm{i},1} - \omega_{\mathrm{m},1}) + \nu_{\mathrm{i},1}\omega_{\mathrm{i},1} + a_1 Q_\mathrm{p}^2 + a_2 Q_\mathrm{p}\omega_{\mathrm{i},1} + a_3{\omega_{\mathrm{i},1}}^2| \\
&\quad \vdots \\
|-\vartheta\tfrac{\mathrm{d}}{\mathrm{d}t}Q_\mathrm{p}| &\ll |(\Theta_\mathrm{i} + \Theta_\mathrm{w})\tfrac{\mathrm{d}}{\mathrm{d}t}\omega_{\mathrm{i},j} + k_{\mathrm{i,t}}(2\phi_{\mathrm{i},j} - \phi_{\mathrm{i},j-1} - \phi_{\mathrm{i},j+1}) \\
&\quad + k_{\mathrm{i,d}}(2\omega_{\mathrm{i},j} - \omega_{\mathrm{i},j-1} - \omega_{\mathrm{i},j+1}) + \nu_{\mathrm{i},j}\omega_{\mathrm{i},j} + a_1 Q_\mathrm{p}^2 + a_2 Q_\mathrm{p}\omega_{\mathrm{i},j} + a_3{\omega_{\mathrm{i},j}}^2| \\
&\quad \vdots \\
|-\vartheta\tfrac{\mathrm{d}}{\mathrm{d}t}Q_\mathrm{p}| &\ll |(\Theta_\mathrm{i} + \Theta_\mathrm{w})\tfrac{\mathrm{d}}{\mathrm{d}t}\omega_{\mathrm{i},n_\mathrm{s}} + k_{\mathrm{i,t}}(\phi_{\mathrm{i},n_\mathrm{s}} - \phi_{\mathrm{i},n_\mathrm{s}-1}) \\
&\quad + k_{\mathrm{i,d}}(\omega_{\mathrm{i},n_\mathrm{s}} - \omega_{\mathrm{i},n_\mathrm{s}-1}) + \nu_{\mathrm{i},n_\mathrm{s}}\omega_{\mathrm{i},n_\mathrm{s}} + a_1 Q_\mathrm{p}^2 + a_2 Q_\mathrm{p}\omega_{\mathrm{i},n_\mathrm{s}} + a_3{\omega_{\mathrm{i},n_\mathrm{s}}}^2|
\end{aligned}\right\} \tag{2.68}$$

holds.

As a consequence of Ass. 16, the $\frac{\mathrm{d}}{\mathrm{d}t}Q_\mathrm{p}$ terms in (2.67) are negligible and the pump side mechanical

system can be written as

$$\frac{\mathrm{d}}{\mathrm{d}t}\begin{pmatrix}\phi_{\mathrm{i},1}\\ \omega_{\mathrm{i},1}\\ \\ \vdots\\ \phi_{\mathrm{i},j}\\ \omega_{\mathrm{i},j}\\ \\ \vdots\\ \phi_{\mathrm{i},n_\mathrm{s}}\\ \omega_{\mathrm{i},n_\mathrm{s}}\end{pmatrix} = \begin{pmatrix} \omega_{\mathrm{i},1} \\ -\frac{k_{\mathrm{i,t}}}{\Theta_{\mathrm{iw}}}(\phi_{\mathrm{i},1}-\phi_{\mathrm{i},2}) - \frac{k_{\mathrm{t}}}{\Theta_{\mathrm{iw}}}(\phi_{\mathrm{i},1}-\phi_{\mathrm{m},1}) - \frac{k_{\mathrm{i,d}}}{\Theta_{\mathrm{iw}}}(\omega_{\mathrm{i},1}-\omega_{\mathrm{i},2}) \\ -\frac{k_{\mathrm{d}}}{\Theta_{\mathrm{iw}}}(\omega_{\mathrm{i},1}-\omega_{\mathrm{m},1}) - \frac{\nu_{\mathrm{i},1}}{\Theta_{\mathrm{iw}}}\omega_{\mathrm{i},1} - \frac{a_1}{\Theta_{\mathrm{iw}}}Q_\mathrm{p}^2 - \frac{a_2}{\Theta_{\mathrm{iw}}}Q_\mathrm{p}\omega_{\mathrm{i},1} - \frac{a_3}{\Theta_{\mathrm{iw}}}{\omega_{\mathrm{i},1}}^2 \\ \vdots \\ \omega_{\mathrm{i},j} \\ -\frac{k_{\mathrm{i,t}}}{\Theta_{\mathrm{iw}}}(2\phi_{\mathrm{i},j}-\phi_{\mathrm{i},j-1}-\phi_{\mathrm{i},j+1}) - \frac{k_{\mathrm{i,d}}}{\Theta_{\mathrm{iw}}}(2\omega_{\mathrm{i},j}-\omega_{\mathrm{i},j-1}-\omega_{\mathrm{i},j+1}) \\ -\frac{\nu_{\mathrm{i},j}}{\Theta_{\mathrm{iw}}}\omega_{\mathrm{i},j} - \frac{a_1}{\Theta_{\mathrm{iw}}}Q_\mathrm{p}^2 - \frac{a_2}{\Theta_{\mathrm{iw}}}Q_\mathrm{p}\omega_{\mathrm{i},j} - \frac{a_3}{\Theta_{\mathrm{iw}}}{\omega_{\mathrm{i},j}}^2 \\ \vdots \\ \omega_{\mathrm{i},n_\mathrm{s}} \\ -\frac{k_{\mathrm{i,t}}}{\Theta_{\mathrm{iw}}}(\phi_{\mathrm{i},n_\mathrm{s}}-\phi_{\mathrm{i},n_\mathrm{s}-1}) - \frac{k_{\mathrm{i,d}}}{\Theta_{\mathrm{iw}}}(\omega_{\mathrm{i},n_\mathrm{s}}-\omega_{\mathrm{i},n_\mathrm{s}-1}) \\ -\frac{\nu_{\mathrm{i},n_\mathrm{s}}}{\Theta_{\mathrm{iw}}}\omega_{\mathrm{i},n_\mathrm{s}} - \frac{a_1}{\Theta_{\mathrm{iw}}}Q_\mathrm{p}^2 - \frac{a_2}{\Theta_{\mathrm{iw}}}Q_\mathrm{p}\omega_{\mathrm{i},n_\mathrm{s}} - \frac{a_3}{\Theta_{\mathrm{iw}}}{\omega_{\mathrm{i},n_\mathrm{s}}}^2 \end{pmatrix}, \tag{2.69}$$

where $\Theta_{\mathrm{iw}} = \Theta_\mathrm{i} + \Theta_\mathrm{w}$ is the combined moment of inertia of the solid impeller parts and the water contained in the impeller stage. The number of states for the pump-side mechanical system is $2 \cdot n_\mathrm{s}$.

2.3.2 Two-mass mechanical system (lumped parameters)

A more simple mechanical model is obtained, if elasticity of the shaft is considered only for the shaft segment between motor and pump, but not among the rotors and pump stages themselves. Figure 2.21 shows the free-body diagram of the simplified two-mass mechanical system with lumped parameters on the motor and pump side, respectively.

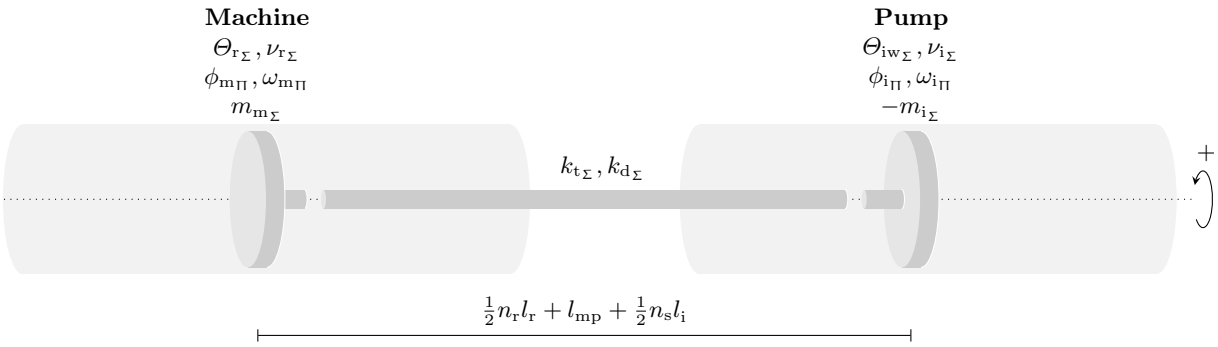

Figure 2.21: *Free-body diagram of the two-mass (lumped parameters) mechanical system of the motor-pump unit.*

For the two-mass system, the motor-side mechanical model (2.66) simplifies as follows

$$\frac{\mathrm{d}}{\mathrm{d}t}\begin{pmatrix}\phi_{\mathrm{m}_\Pi}\\ \omega_{\mathrm{m}_\Pi}\end{pmatrix} \overset{(2.37),(2.65)}{=} \begin{pmatrix} \omega_{\mathrm{m}_\Pi} \\ \frac{3n_\mathrm{p}L_\mathrm{m}}{2\Theta_{\mathrm{r}_\Sigma}L_\mathrm{r}}\left(\boldsymbol{i}_\mathrm{s}^{\alpha\beta}\right)^\top \boldsymbol{J}\boldsymbol{\psi}_{\mathrm{r}_\Sigma}^{\alpha\beta} - \frac{k_{\mathrm{t}_\Sigma}}{\Theta_{\mathrm{r}_\Sigma}}(\phi_{\mathrm{m}_\Pi}-\phi_{\mathrm{i}_\Pi}) - \frac{k_{\mathrm{d}_\Sigma}}{\Theta_{\mathrm{r}_\Sigma}}(\omega_{\mathrm{m}_\Pi}-\omega_{\mathrm{i}_\Pi}) - \frac{\nu_{\mathrm{r}_\Sigma}}{\Theta_{\mathrm{r}_\Sigma}}\omega_{\mathrm{m}_\Pi} \end{pmatrix}, \tag{2.70}$$

which has two states only, namely the motor angle $\phi_{\mathrm{m}_\Pi} = \phi_\mathrm{m}$ and the motor speed $\omega_{\mathrm{m}_\Pi} = \omega_\mathrm{m}$. Moreover stiffness, damping and friction coefficients are given as lumped parameters $k_{\mathrm{t}_\Sigma}, k_{\mathrm{d}_\Sigma}$ and

ν_{r_Σ}, respectively. Likewise, the pump-side mechanical system (2.69) simplifies to

$$\frac{\mathrm{d}}{\mathrm{d}t}\begin{pmatrix}\phi_{\mathrm{i}_\Pi}\\ \omega_{\mathrm{i}_\Pi}\end{pmatrix} = \begin{pmatrix}\omega_{\mathrm{i}_\Pi}\\ -\frac{n_\mathrm{s}a_1}{\Theta_{\mathrm{iw}_\Sigma}}Q_\mathrm{p}^2 - \frac{n_\mathrm{s}a_2}{\Theta_{\mathrm{iw}_\Sigma}}Q_\mathrm{p}\omega_{\mathrm{i}_\Pi} - \frac{n_\mathrm{s}a_3}{\Theta_{\mathrm{iw}_\Sigma}}{\omega_{\mathrm{i}_\Pi}}^2 - \frac{\nu_{\mathrm{i}_\Sigma}}{\Theta_{\mathrm{iw}_\Sigma}}\omega_{\mathrm{i}_\Pi}\\ -\frac{k_{\mathrm{t}_\Sigma}}{\Theta_{\mathrm{iw}_\Sigma}}(\phi_{\mathrm{i}_\Pi}-\phi_{\mathrm{m}_\Pi}) - \frac{k_{\mathrm{d}_\Sigma}}{\Theta_{\mathrm{iw}_\Sigma}}(\omega_{\mathrm{i}_\Pi}-\omega_{\mathrm{m}_\Pi})\end{pmatrix}, \tag{2.71}$$

with pump angle ϕ_{i_Π}, pump angular velocity ω_{i_Π}, total moment of inertia $\Theta_{\mathrm{iw}_\Sigma} = n_\mathrm{s}\Theta_\mathrm{iw}$ and friction coefficient $\nu_{\mathrm{i}_\Sigma} = n_\mathrm{s}\nu_\mathrm{i}$.

2.4 Overall system model

In the preceding sections, submodels for the electrical, hydraulic and mechanical subsystems have been derived. In the following the derived models are connected and described as nonlinear state-space equations, which can be used for implementation. Two different systems are presented and compared, namely a multi-rotor/multi-stage elastic system and a two-mass lumped system. Colors indicate the subsystem of the respective state variables, i.e. electrical (red), mechanical (orange) and hydraulic (blue) subsystem.

2.4.1 Multi-rotor/multi-stage elastic system (MMES)

Connecting the electrical components and observing that (see Fig. 2.1)

$$\boldsymbol{u}_\mathrm{f}^{\alpha\beta} = \boldsymbol{u}_{\mathrm{f_i}}^{\alpha\beta} = \boldsymbol{u}_\mathrm{v}^{\alpha\beta}, \qquad \boldsymbol{i}_\mathrm{f}^{\alpha\beta} = \boldsymbol{i}_{\mathrm{f_i}}^{\alpha\beta} \qquad \boldsymbol{u}_\mathrm{c}^{\alpha\beta} = \boldsymbol{u}_{\mathrm{c_i}}^{\alpha\beta} \qquad \boldsymbol{u}_{\mathrm{c_o}}^{\alpha\beta} = \boldsymbol{u}_{\mathrm{s}_\Sigma}^{\alpha\beta} \qquad \text{and} \qquad \boldsymbol{i}_{\mathrm{c_o}}^{\alpha\beta} = \boldsymbol{i}_\mathrm{s}^{\alpha\beta},$$

the multi-rotor electrical system, described by (2.10), (2.18) and (2.36), is summarized as follows

$$\frac{\mathrm{d}}{\mathrm{d}t}\underbrace{\begin{pmatrix}\boldsymbol{i}_\mathrm{f}^{\alpha\beta}\\ \boldsymbol{u}_\mathrm{c}^{\alpha\beta}\\ \hline \boldsymbol{i}_{\mathrm{c},1}^{\alpha\beta}\\ \boldsymbol{u}_{\mathrm{c},1}^{\alpha\beta}\\ \vdots\\ \boldsymbol{i}_{\mathrm{c},k}^{\alpha\beta}\\ \boldsymbol{u}_{\mathrm{c},k}^{\alpha\beta}\\ \vdots\\ \boldsymbol{i}_{\mathrm{c},n_\mathrm{c}}^{\alpha\beta}\\ \boldsymbol{u}_{\mathrm{s}_\Sigma}^{\alpha\beta}\\ \hline \boldsymbol{i}_\mathrm{s}^{\alpha\beta}\\ \boldsymbol{\psi}_{\mathrm{r},i}^{\alpha\beta}\end{pmatrix}}_{\boldsymbol{x}_\mathrm{el}} = \underbrace{\begin{pmatrix}-\frac{1}{T_\mathrm{f}}\boldsymbol{i}_\mathrm{f}^{\alpha\beta} - \frac{1}{L_\mathrm{f}}\boldsymbol{u}_\mathrm{c}^{\alpha\beta}\\ (\boldsymbol{C}_{\mathrm{f,mod}}^{\alpha\beta})^{-1}\boldsymbol{i}_\mathrm{f}^{\alpha\beta} - (\boldsymbol{C}_{\mathrm{f,mod}}^{\alpha\beta})^{-1}\boldsymbol{i}_{\mathrm{c},1}^{\alpha\beta}\\ \hline (\boldsymbol{L}_\mathrm{c}^{\alpha\beta})^{-1}\boldsymbol{u}_\mathrm{c}^{\alpha\beta} - (\boldsymbol{L}_\mathrm{c}^{\alpha\beta})^{-1}\boldsymbol{R}_\mathrm{c}^{\alpha\beta}\boldsymbol{i}_{\mathrm{c},1}^{\alpha\beta} - (\boldsymbol{L}_\mathrm{c}^{\alpha\beta})^{-1}\boldsymbol{u}_{\mathrm{c},1}^{\alpha\beta}\\ \frac{1}{2}(\boldsymbol{C}_\mathrm{c}^{\alpha\beta})^{-1}\boldsymbol{i}_{\mathrm{c},1}^{\alpha\beta} - \frac{1}{2}(\boldsymbol{C}_\mathrm{c}^{\alpha\beta})^{-1}\boldsymbol{i}_{\mathrm{c},2}^{\alpha\beta}\\ \vdots\\ (\boldsymbol{L}_\mathrm{c}^{\alpha\beta})^{-1}\boldsymbol{u}_{\mathrm{c},k-1}^{\alpha\beta} - (\boldsymbol{L}_\mathrm{c}^{\alpha\beta})^{-1}\boldsymbol{R}_\mathrm{c}^{\alpha\beta}\boldsymbol{i}_{\mathrm{c},k}^{\alpha\beta} - (\boldsymbol{L}_\mathrm{c}^{\alpha\beta})^{-1}\boldsymbol{u}_{\mathrm{c},k}^{\alpha\beta}\\ \frac{1}{2}(\boldsymbol{C}_\mathrm{c}^{\alpha\beta})^{-1}\boldsymbol{i}_{\mathrm{c},k}^{\alpha\beta} - \frac{1}{2}(\boldsymbol{C}_\mathrm{c}^{\alpha\beta})^{-1}\boldsymbol{i}_{\mathrm{c},k+1}^{\alpha\beta}\\ \vdots\\ (\boldsymbol{L}_\mathrm{c}^{\alpha\beta})^{-1}\boldsymbol{u}_{\mathrm{c},n_\mathrm{c}-1}^{\alpha\beta} - (\boldsymbol{L}_\mathrm{c}^{\alpha\beta})^{-1}\boldsymbol{R}_\mathrm{c}^{\alpha\beta}\boldsymbol{i}_{\mathrm{c},n_\mathrm{c}}^{\alpha\beta} - (\boldsymbol{L}_\mathrm{c}^{\alpha\beta})^{-1}\boldsymbol{u}_{\mathrm{s}_\Sigma}^{\alpha\beta}\\ (\boldsymbol{C}_\mathrm{c}^{\alpha\beta})^{-1}\boldsymbol{i}_{\mathrm{c},n_\mathrm{c}}^{\alpha\beta} - (\boldsymbol{C}_\mathrm{c}^{\alpha\beta})^{-1}\boldsymbol{i}_\mathrm{s}^{\alpha\beta}\\ \hline -\frac{1}{T_\mathrm{s}}\boldsymbol{i}_\mathrm{s}^{\alpha\beta} + \frac{1}{n_\mathrm{r}L_\mu}\frac{1}{T_\mathrm{r}}\sum_{i=1}^{n_\mathrm{r}}\boldsymbol{\psi}_{\mathrm{r},i}^{\alpha\beta} + \frac{1}{\sigma L_{\mathrm{s}_\Sigma}}\boldsymbol{u}_{\mathrm{s}_\Sigma}^{\alpha\beta}\\ \frac{L_\mathrm{m}}{T_\mathrm{r}}\boldsymbol{i}_\mathrm{s}^{\alpha\beta} - \frac{1}{T_\mathrm{r}}\boldsymbol{\psi}_{\mathrm{r},i}^{\alpha\beta}\end{pmatrix}}_{\boldsymbol{f}_\mathrm{el}(\boldsymbol{x}_\mathrm{el})} + \underbrace{\begin{pmatrix}\frac{1}{L_\mathrm{f}}\boldsymbol{u}_\mathrm{f}^{\alpha\beta}\\ \boldsymbol{0}_2\\ \hline \boldsymbol{0}_2\\ \boldsymbol{0}_2\\ \vdots\\ \boldsymbol{0}_2\\ \boldsymbol{0}_2\\ \vdots\\ \boldsymbol{0}_2\\ \boldsymbol{0}_2\\ \hline -\frac{1}{n_\mathrm{r}L_\mu}\sum_{i=1}^{n_\mathrm{r}} n_\mathrm{p}\omega_{\mathrm{m},i}\boldsymbol{J}\boldsymbol{\psi}_{\mathrm{r},i}^{\alpha\beta}\\ n_\mathrm{p}\omega_{\mathrm{m},i}\boldsymbol{J}\boldsymbol{\psi}_{\mathrm{r},i}^{\alpha\beta}\end{pmatrix}}_{\boldsymbol{g}_\mathrm{el}(\boldsymbol{x}_\mathrm{el},\boldsymbol{x}_\mathrm{me})}, \tag{2.72}$$

with state vector $\boldsymbol{x}_\mathrm{el} \in \mathbb{R}^{2\cdot(2+2\cdot n_\mathrm{c}+1+n_\mathrm{r})}$, system function $\boldsymbol{f}_\mathrm{el} \in \mathbb{R}^{2\cdot(2+2\cdot n_\mathrm{c}+1+n_\mathrm{r})}$ and input function $\boldsymbol{g}_\mathrm{el} \in \mathbb{R}^{2\cdot(2+2\cdot n_\mathrm{c}+1+n_\mathrm{r})}$. The mechanical system states $\boldsymbol{x}_\mathrm{me}$ serve as inputs, thus nonlinearly interconnecting the electrical with the mechanical subsystem.

The hydraulics system, described in Eqs. (2.57), (2.59) and (2.64), is given by

$$\frac{\mathrm{d}}{\mathrm{d}t}\underbrace{\begin{pmatrix} Q_\mathrm{p} \\ h_\mathrm{w} \\ p_\mathrm{wh} \end{pmatrix}}_{\boldsymbol{x}_\mathrm{hy}} = \underbrace{\begin{pmatrix} \frac{n_\mathrm{s} b_1 - K_\mathrm{fh}(h_\mathrm{w})}{\Gamma_\mathrm{t}(h_\mathrm{w})} Q_\mathrm{p}^2 - \frac{1}{\rho g \delta \Gamma_\mathrm{t}(h_\mathrm{w})} Q_\mathrm{p} - \frac{\widehat{H}_\mathrm{g}(h_\mathrm{w}, p_\mathrm{wh})}{\Gamma_\mathrm{t}(h_\mathrm{w})} \\ \bar{k}_{h_\mathrm{w}}(h_\mathrm{w}, Q_\mathrm{p}) \frac{1}{\pi r_\mathrm{pipe}^2} Q_\mathrm{p} \\ \bar{k}_{p_\mathrm{wh}}(h_\mathrm{w}, Q_\mathrm{p}, p_\mathrm{wh}) \frac{\rho g}{\pi r_\mathrm{pipe}^2} Q_\mathrm{p} \end{pmatrix}}_{\boldsymbol{f}_\mathrm{hy}(\boldsymbol{x}_\mathrm{hy})} + \underbrace{\begin{pmatrix} \sum_{j=1}^{n_\mathrm{s}} \left(\frac{b_2}{\Gamma_\mathrm{t}(h_\mathrm{w})} \omega_{\mathrm{i},j} Q_\mathrm{p} + \frac{b_3}{\Gamma_\mathrm{t}(h_\mathrm{w})} \omega_{\mathrm{i},j}^2 \right) \\ 0 \\ 0 \end{pmatrix}}_{\boldsymbol{g}_\mathrm{hy}(\boldsymbol{x}_\mathrm{hy}, \boldsymbol{x}_\mathrm{me})} \tag{2.73}$$

with state vector $\boldsymbol{x}_\mathrm{hy} \in \mathbb{R}^3$, system function $\boldsymbol{f}_\mathrm{hy} \in \mathbb{R}^3$ and input function $\boldsymbol{g}_\mathrm{hy} \in \mathbb{R}^3$. Again, the mechanical system states $\boldsymbol{x}_\mathrm{me}$ serve as inputs, which nonlinearly interconnect the hydraulic with the mechanical subsystem.

Lastly, the multi-rotor mechanical system can be stated based on Eqs. (2.66) and (2.69) as

$$\frac{\mathrm{d}}{\mathrm{d}t}\underbrace{\begin{pmatrix} \phi_{\mathrm{m},1} \\ \omega_{\mathrm{m},1} \\ \vdots \\ \phi_{\mathrm{m},i} \\ \omega_{\mathrm{m},i} \\ \vdots \\ \phi_{\mathrm{m},n_\mathrm{r}} \\ \omega_{\mathrm{m},n_\mathrm{r}} \\ \phi_{\mathrm{i},1} \\ \omega_{\mathrm{i},1} \\ \vdots \\ \phi_{\mathrm{i},j} \\ \omega_{\mathrm{i},j} \\ \vdots \\ \phi_{\mathrm{i},n_\mathrm{s}} \\ \omega_{\mathrm{i},n_\mathrm{s}} \end{pmatrix}}_{\boldsymbol{x}_\mathrm{me}} = \underbrace{\begin{pmatrix} \omega_{\mathrm{m},1} \\ -\frac{k_{\mathrm{r,t}}}{\Theta_\mathrm{r}}(\phi_{\mathrm{m},1} - \phi_{\mathrm{m},2}) - \frac{k_\mathrm{t}}{\Theta_\mathrm{r}}(\phi_{\mathrm{m},1} - \phi_{\mathrm{i},1}) \\ -\frac{k_{\mathrm{r,d}}}{\Theta_\mathrm{r}}(\omega_{\mathrm{m},1} - \omega_{\mathrm{m},2}) - \frac{k_\mathrm{d}}{\Theta_\mathrm{r}}(\omega_{\mathrm{m},1} - \omega_{\mathrm{i},1}) - \frac{\nu_{\mathrm{r},1}}{\Theta_\mathrm{r}}\omega_{\mathrm{m},1} \\ \vdots \\ \omega_{\mathrm{m},i} \\ -\frac{k_{\mathrm{r,t}}}{\Theta_\mathrm{r}}(2\phi_{\mathrm{m},i} - \phi_{\mathrm{m},i-1} - \phi_{\mathrm{m},i+1}) \\ -\frac{k_{\mathrm{r,d}}}{\Theta_\mathrm{r}}(2\omega_{\mathrm{m},i} - \omega_{\mathrm{m},i-1} - \omega_{\mathrm{m},i+1}) - \frac{\nu_{\mathrm{r},i}}{\Theta_\mathrm{r}}\omega_{\mathrm{m},i} \\ \vdots \\ \omega_{\mathrm{m},n_\mathrm{r}} \\ -\frac{k_{\mathrm{r,t}}}{\Theta_\mathrm{r}}(\phi_{\mathrm{m},n_\mathrm{r}} - \phi_{\mathrm{m},n_\mathrm{r}-1}) \\ -\frac{k_{\mathrm{r,d}}}{\Theta_\mathrm{r}}(\omega_{\mathrm{m},n_\mathrm{r}} - \omega_{\mathrm{m},n_\mathrm{r}-1}) - \frac{\nu_{\mathrm{r},n_\mathrm{r}}}{\Theta_\mathrm{r}}\omega_{\mathrm{m},n_\mathrm{r}} \\ \omega_{\mathrm{i},1} \\ -\frac{k_{\mathrm{i,t}}}{\Theta_\mathrm{iw}}(\phi_{\mathrm{i},1} - \phi_{\mathrm{i},2}) - \frac{k_\mathrm{t}}{\Theta_\mathrm{iw}}(\phi_{\mathrm{i},1} - \phi_{\mathrm{m},1}) - \frac{k_{\mathrm{i,d}}}{\Theta_\mathrm{iw}}(\omega_{\mathrm{i},1} - \omega_{\mathrm{i},2}) \\ -\frac{k_\mathrm{d}}{\Theta_\mathrm{iw}}(\omega_{\mathrm{i},1} - \omega_{\mathrm{m},1}) - \frac{\nu_{\mathrm{i},1}}{\Theta_\mathrm{iw}}\omega_{\mathrm{i},1} - \frac{a_3}{\Theta_\mathrm{iw}}\omega_{\mathrm{i},1}^2 \\ \vdots \\ \omega_{\mathrm{i},j} \\ -\frac{k_{\mathrm{i,t}}}{\Theta_\mathrm{iw}}(2\phi_{\mathrm{i},j} - \phi_{\mathrm{i},j-1} - \phi_{\mathrm{i},j+1}) - \frac{k_{\mathrm{i,d}}}{\Theta_\mathrm{iw}}(2\omega_{\mathrm{i},j} - \omega_{\mathrm{i},j-1} - \omega_{\mathrm{i},j+1}) \\ -\frac{\nu_{\mathrm{i},j}}{\Theta_\mathrm{iw}}\omega_{\mathrm{i},j} - \frac{a_3}{\Theta_\mathrm{iw}}\omega_{\mathrm{i},j}^2 \\ \vdots \\ \omega_{\mathrm{i},n_\mathrm{s}} \\ -\frac{k_{\mathrm{i,t}}}{\Theta_\mathrm{iw}}(\phi_{\mathrm{i},n_\mathrm{s}} - \phi_{\mathrm{i},n_\mathrm{s}-1}) - \frac{k_{\mathrm{i,d}}}{\Theta_\mathrm{iw}}(\omega_{\mathrm{i},n_\mathrm{s}} - \omega_{\mathrm{i},n_\mathrm{s}-1}) \\ -\frac{\nu_{\mathrm{i},n_\mathrm{s}}}{\Theta_\mathrm{iw}}\omega_{\mathrm{i},n_\mathrm{s}} - \frac{a_3}{\Theta_\mathrm{iw}}\omega_{\mathrm{i},n_\mathrm{s}}^2 \end{pmatrix}}_{\boldsymbol{f}_\mathrm{me}(\boldsymbol{x}_\mathrm{me})} + \underbrace{\begin{pmatrix} 0 \\ \frac{3 n_\mathrm{p} L_\mathrm{m}}{2\Theta_\mathrm{r} L_\mathrm{r}} \left(\boldsymbol{i}_\mathrm{s}^{\alpha\beta}\right)^\top \boldsymbol{J} \boldsymbol{\psi}_{\mathrm{r},1}^{\alpha\beta} \\ \vdots \\ 0 \\ \frac{3 n_\mathrm{p} L_\mathrm{m}}{2\Theta_\mathrm{r} L_\mathrm{r}} \left(\boldsymbol{i}_\mathrm{s}^{\alpha\beta}\right)^\top \boldsymbol{J} \boldsymbol{\psi}_{\mathrm{r},i}^{\alpha\beta} \\ \vdots \\ 0 \\ \frac{3 n_\mathrm{p} L_\mathrm{m}}{2\Theta_\mathrm{r} L_\mathrm{r}} \left(\boldsymbol{i}_\mathrm{s}^{\alpha\beta}\right)^\top \boldsymbol{J} \boldsymbol{\psi}_{\mathrm{r},n_\mathrm{r}}^{\alpha\beta} \\ 0 \\ -\frac{a_1}{\Theta_\mathrm{iw}} Q_\mathrm{p}^2 - \frac{a_2}{\Theta_\mathrm{iw}} Q_\mathrm{p} \omega_{\mathrm{i},1} \\ \vdots \\ 0 \\ -\frac{a_1}{\Theta_\mathrm{iw}} Q_\mathrm{p}^2 - \frac{a_2}{\Theta_\mathrm{iw}} Q_\mathrm{p} \omega_{\mathrm{i},j} \\ \vdots \\ 0 \\ -\frac{a_1}{\Theta_\mathrm{iw}} Q_\mathrm{p}^2 - \frac{a_2}{\Theta_\mathrm{iw}} Q_\mathrm{p} \omega_{\mathrm{i},n_\mathrm{s}} \end{pmatrix}}_{\boldsymbol{g}_\mathrm{me}(\boldsymbol{x}_\mathrm{el}, \boldsymbol{x}_\mathrm{el}, \boldsymbol{x}_\mathrm{hy})} \tag{2.74}$$

with state vector $\boldsymbol{x}_\mathrm{me} \in \mathbb{R}^{2(n_\mathrm{r}+n_\mathrm{s})}$, system function $\boldsymbol{f}_\mathrm{me} \in \mathbb{R}^{2(n_\mathrm{r}+n_\mathrm{s})}$ and input function $\boldsymbol{g}_\mathrm{me} \in \mathbb{R}^{2(n_\mathrm{r}+n_\mathrm{s})}$. Inputs are the electrical states $\boldsymbol{x}_\mathrm{el}$ and the hydraulic states $\boldsymbol{x}_\mathrm{hy}$. Likewise, the mechanical subsystem is interconnected with the electrical and the hydraulic subsystem by those 'inputs'.

2.4.2 Two-mass lumped system (2MLS)

If elasticity of the shaft within the multi-rotor electrical machine and the multi-stage pump is neglected, torsional effects may occur only between the lumped masses of electrical machine and pump, respectively. The electric system is simplified subject to (2.40), yielding

$$\frac{\mathrm{d}}{\mathrm{d}t}\underbrace{\begin{pmatrix} \boldsymbol{i}_{\mathrm{f}}^{\alpha\beta} \\ \boldsymbol{u}_{\mathrm{c}}^{\alpha\beta} \\ \hline \boldsymbol{i}_{\mathrm{c},1}^{\alpha\beta} \\ \boldsymbol{u}_{\mathrm{c},1}^{\alpha\beta} \\ \vdots \\ \boldsymbol{i}_{\mathrm{c},k}^{\alpha\beta} \\ \boldsymbol{u}_{\mathrm{c},k}^{\alpha\beta} \\ \vdots \\ \boldsymbol{i}_{\mathrm{c},n_\mathrm{c}}^{\alpha\beta} \\ \boldsymbol{u}_{\mathrm{s}\Sigma}^{\alpha\beta} \\ \hline \boldsymbol{i}_{\mathrm{s}}^{\alpha\beta} \\ \boldsymbol{\psi}_{\mathrm{r}\Sigma}^{\alpha\beta} \end{pmatrix}}_{\boldsymbol{x}_{\mathrm{el}}} = \underbrace{\begin{pmatrix} -\frac{1}{T_\mathrm{f}}\boldsymbol{i}_{\mathrm{f}}^{\alpha\beta} - \frac{1}{L_\mathrm{f}}\boldsymbol{u}_{\mathrm{c}}^{\alpha\beta} \\ (\boldsymbol{C}_{\mathrm{f,mod}}^{\alpha\beta})^{-1}\boldsymbol{i}_{\mathrm{f}}^{\alpha\beta} - (\boldsymbol{C}_{\mathrm{f,mod}}^{\alpha\beta})^{-1}\boldsymbol{i}_{\mathrm{c},1}^{\alpha\beta} \\ \hline (\boldsymbol{L}_{\mathrm{c}}^{\alpha\beta})^{-1}\boldsymbol{u}_{\mathrm{ci}}^{\alpha\beta} - (\boldsymbol{L}_{\mathrm{c}}^{\alpha\beta})^{-1}\boldsymbol{R}_{\mathrm{c}}^{\alpha\beta}\boldsymbol{i}_{\mathrm{c},1}^{\alpha\beta} - (\boldsymbol{L}_{\mathrm{c}}^{\alpha\beta})^{-1}\boldsymbol{u}_{\mathrm{c},1}^{\alpha\beta} \\ \frac{1}{2}(\boldsymbol{C}_{\mathrm{c}}^{\alpha\beta})^{-1}\boldsymbol{i}_{\mathrm{c},1}^{\alpha\beta} - \frac{1}{2}(\boldsymbol{C}_{\mathrm{c}}^{\alpha\beta})^{-1}\boldsymbol{i}_{\mathrm{c},2}^{\alpha\beta} \\ \vdots \\ (\boldsymbol{L}_{\mathrm{c}}^{\alpha\beta})^{-1}\boldsymbol{u}_{\mathrm{c},k-1}^{\alpha\beta} - (\boldsymbol{L}_{\mathrm{c}}^{\alpha\beta})^{-1}\boldsymbol{R}_{\mathrm{c}}^{\alpha\beta}\boldsymbol{i}_{\mathrm{c},k}^{\alpha\beta} - (\boldsymbol{L}_{\mathrm{c}}^{\alpha\beta})^{-1}\boldsymbol{u}_{\mathrm{c},k}^{\alpha\beta} \\ \frac{1}{2}(\boldsymbol{C}_{\mathrm{c}}^{\alpha\beta})^{-1}\boldsymbol{i}_{\mathrm{c},k}^{\alpha\beta} - \frac{1}{2}(\boldsymbol{C}_{\mathrm{c}}^{\alpha\beta})^{-1}\boldsymbol{i}_{\mathrm{c},k+1}^{\alpha\beta} \\ \vdots \\ (\boldsymbol{L}_{\mathrm{c}}^{\alpha\beta})^{-1}\boldsymbol{u}_{\mathrm{c},n_\mathrm{c}-1}^{\alpha\beta} - (\boldsymbol{L}_{\mathrm{c}}^{\alpha\beta})^{-1}\boldsymbol{R}_{\mathrm{c}}^{\alpha\beta}\boldsymbol{i}_{\mathrm{c},n_\mathrm{c}}^{\alpha\beta} - (\boldsymbol{L}_{\mathrm{c}}^{\alpha\beta})^{-1}\boldsymbol{u}_{\mathrm{s}\Sigma}^{\alpha\beta} \\ (\boldsymbol{C}_{\mathrm{c}}^{\alpha\beta})^{-1}\boldsymbol{i}_{\mathrm{c},n_\mathrm{c}}^{\alpha\beta} - (\boldsymbol{C}_{\mathrm{c}}^{\alpha\beta})^{-1}\boldsymbol{i}_{\mathrm{s}}^{\alpha\beta} \\ \hline -\frac{1}{T_\mathrm{s}}\boldsymbol{i}_{\mathrm{s}}^{\alpha\beta} + \frac{1}{n_\mathrm{r}L_\mu}\frac{1}{T_\mathrm{r}}\sum_{i=1}^{n_\mathrm{r}}\boldsymbol{\psi}_{\mathrm{r},i}^{\alpha\beta} + \frac{1}{\sigma L_{\mathrm{s}\Sigma}}\boldsymbol{u}_{\mathrm{s}\Sigma}^{\alpha\beta} \\ \frac{L_{\mathrm{m}\Sigma}}{T_\mathrm{r}}\boldsymbol{i}_{\mathrm{s}}^{\alpha\beta} + -\frac{1}{T_\mathrm{r}}\boldsymbol{\psi}_{\mathrm{r}\Sigma}^{\alpha\beta} \end{pmatrix}}_{\boldsymbol{f}_{\mathrm{el}}(\boldsymbol{x}_{\mathrm{el}})} + \underbrace{\begin{pmatrix} \frac{1}{L_\mathrm{f}}\boldsymbol{u}_{\mathrm{f}}^{\alpha\beta} \\ \mathbf{o}_2 \\ \hline \mathbf{o}_2 \\ \mathbf{o}_2 \\ \vdots \\ \mathbf{o}_2 \\ \mathbf{o}_2 \\ \vdots \\ \mathbf{o}_2 \\ \mathbf{o}_2 \\ \hline -\frac{1}{L_\mu}n_\mathrm{p}\omega_{\mathrm{m}\Pi}\boldsymbol{J}\boldsymbol{\psi}_{\mathrm{r}\Sigma}^{\alpha\beta} \\ n_\mathrm{p}\omega_{\mathrm{m}\Pi}\boldsymbol{J}\boldsymbol{\psi}_{\mathrm{r}\Sigma}^{\alpha\beta} \end{pmatrix}}_{\boldsymbol{g}_{\mathrm{el}}(\boldsymbol{x}_{\mathrm{el}},\boldsymbol{x}_{\mathrm{me}})}, \tag{2.75}$$

with state vector $\boldsymbol{x}_{\mathrm{el}} \in \mathbb{R}^{2\cdot(4+2\cdot n_\mathrm{c})}$, system function $\boldsymbol{f}_{\mathrm{el}} \in \mathbb{R}^{2\cdot(4+2\cdot n_\mathrm{c})}$ and input function $\boldsymbol{g}_{\mathrm{el}} \in \mathbb{R}^{2\cdot(4+2\cdot n_\mathrm{c})}$. As before, the mechanical system states $\boldsymbol{x}_{\mathrm{me}}$ serve as inputs.

If elastic coupling among the impeller stages of the pump is neglected (see also Remark 8), the hydraulic system is described by

$$\frac{\mathrm{d}}{\mathrm{d}t}\underbrace{\begin{pmatrix} Q_\mathrm{p} \\ h_\mathrm{w} \\ p_\mathrm{wh} \end{pmatrix}}_{\boldsymbol{x}_{\mathrm{hy}}} = \underbrace{\begin{pmatrix} \frac{n_\mathrm{s}b_1 - K_\mathrm{fh}(h_\mathrm{w})}{\Gamma_\mathrm{t}(h_\mathrm{w})}Q_\mathrm{p}^2 - \frac{1}{\rho g \delta \Gamma_\mathrm{t}(h_\mathrm{w})}Q_\mathrm{p} - \frac{\widehat{H}_\mathrm{g}(h_\mathrm{w},p_\mathrm{wh})}{\Gamma_\mathrm{t}(h_\mathrm{w})} \\ \bar{k}_{h_\mathrm{w}}(h_\mathrm{w},Q_\mathrm{p})\frac{1}{\pi r_\mathrm{pipe}^2}Q_\mathrm{p} \\ \bar{k}_{p_\mathrm{wh}}(h_\mathrm{w},Q_\mathrm{p},p_\mathrm{wh})\frac{\rho g}{\pi r_\mathrm{pipe}^2}Q_\mathrm{p} \end{pmatrix}}_{\boldsymbol{f}_{\mathrm{hy}}(\boldsymbol{x}_{\mathrm{hy}})} + \underbrace{\begin{pmatrix} \frac{n_\mathrm{s}b_2}{\Gamma_\mathrm{t}(h_\mathrm{w})}\omega_{\mathrm{i}\Pi}Q_\mathrm{p} + \frac{n_\mathrm{s}b_3}{\Gamma_\mathrm{t}(h_\mathrm{w})}\omega_{\mathrm{i}\Pi}^2 \\ 0 \\ 0 \end{pmatrix}}_{\boldsymbol{g}_{\mathrm{hy}}(\boldsymbol{x}_{\mathrm{hy}},\boldsymbol{x}_{\mathrm{me}})} \tag{2.76}$$

with state vector $\boldsymbol{x}_{\mathrm{hy}} \in \mathbb{R}^3$, system function $\boldsymbol{f}_{\mathrm{hy}} \in \mathbb{R}^3$ and input function $\boldsymbol{g}_{\mathrm{hy}} \in \mathbb{R}^3$. Likewise, the mechanical system states $\boldsymbol{x}_{\mathrm{me}}$ serve as inputs.

Lastly, the mechanical system with lumped parameters is described by (2.70) and (2.71), yielding

$$\frac{\mathrm{d}}{\mathrm{d}t}\underbrace{\begin{pmatrix}\phi_{\mathrm{m}\Pi}\\ \omega_{\mathrm{m}\Pi}\\ \phi_{\mathrm{i}\Pi}\\ \omega_{\mathrm{i}\Pi}\end{pmatrix}}_{\boldsymbol{x}_{\mathrm{me}}} = \underbrace{\begin{pmatrix}\omega_{\mathrm{m}\Pi}\\ -\frac{k_{\mathrm{t}\Sigma}}{\Theta_{\mathrm{r}\Sigma}}(\phi_{\mathrm{m}\Pi}-\phi_{\mathrm{i}\Pi})-\frac{k_{\mathrm{d}\Sigma}}{\Theta_{\mathrm{r}\Sigma}}(\omega_{\mathrm{m}\Pi}-\omega_{\mathrm{i}\Pi})-\frac{\nu_{\mathrm{r}\Sigma}}{\Theta_{\mathrm{r}\Sigma}}\omega_{\mathrm{m}\Pi}\\ \omega_{\mathrm{i}\Pi}\\ -\frac{n_{\mathrm{s}}a_3}{\Theta_{\mathrm{iw}\Sigma}}{\omega_{\mathrm{i}\Pi}}^2-\frac{\nu_{\mathrm{i}\Sigma}}{\Theta_{\mathrm{iw}\Sigma}}\omega_{\mathrm{i}\Pi}-\frac{k_{\mathrm{t}\Sigma}}{\Theta_{\mathrm{iw}\Sigma}}(\phi_{\mathrm{i}\Pi}-\phi_{\mathrm{m}\Pi})\\ -\frac{k_{\mathrm{d}\Sigma}}{\Theta_{\mathrm{iw}\Sigma}}(\omega_{\mathrm{i}\Pi}-\omega_{\mathrm{m}\Pi})\end{pmatrix}}_{\boldsymbol{f}_{\mathrm{me}}(\boldsymbol{x}_{\mathrm{me}})} + \underbrace{\begin{pmatrix}0\\ \frac{3n_{\mathrm{p}}L_{\mathrm{m}}}{2\Theta_{\mathrm{r}\Sigma}L_{\mathrm{r}}}\left(\boldsymbol{i}_{\mathrm{s}}^{\alpha\beta}\right)^{\top}\boldsymbol{J}\boldsymbol{\psi}_{\mathrm{r}\Sigma}^{\alpha\beta}\\ 0\\ -\frac{n_{\mathrm{s}}a_1}{\Theta_{\mathrm{iw}\Sigma}}Q_{\mathrm{p}}^2-\frac{n_{\mathrm{s}}a_2}{\Theta_{\mathrm{iw}\Sigma}}Q_{\mathrm{p}}\omega_{\mathrm{i}\Pi}\end{pmatrix}}_{\boldsymbol{g}_{\mathrm{me}}(\boldsymbol{x}_{\mathrm{el}},\boldsymbol{x}_{\mathrm{el}},\boldsymbol{x}_{\mathrm{hy}})} \tag{2.77}$$

with state vector $\boldsymbol{x}_{\mathrm{me}} \in \mathbb{R}^4$, system function $\boldsymbol{f}_{\mathrm{me}} \in \mathbb{R}^4$ and input function $\boldsymbol{g}_{\mathrm{me}} \in \mathbb{R}^4$. Inputs are the electrical states $\boldsymbol{x}_{\mathrm{el}}$ and the hydraulic states $\boldsymbol{x}_{\mathrm{hy}}$.

2.5 Simulation

Simulations have been carried out for two different systems, namely

- the multi-rotor/multi-stage elastic system, described by (2.72), (2.73) and (2.74), referred to as `MMES`, and
- the two-mass system with lumped parameters, described by (2.75), (2.76) and (2.77), referred to as `2MLS`.

The models have been implemented in MATLAB®/ Simulink®R2018b using the parameters given in Tables 2.2, 2.3 and 2.4. The parameters were either calculated based on estimated geometry and system data (e.g. inverter, filter, cable) or provided by local energy suppliers[4] (e.g. hydraulic system, pump, motor, shaft). The simulations have been performed using the `ode4` solver with a fixed step time of 1 µs for the duration of 100 s. The simulation data was sampled at the end of each PWM cycle (sampling rate f_{S}), since at this point the voltage over time integral of the inverter output voltage equals the voltage over time integral of the sampled reference voltage.

Input to the system is the inverter output / filter input reference voltage $\boldsymbol{u}_{\mathrm{f}}^{\alpha\beta\star}(=\boldsymbol{u}_{\mathrm{v}}^{\alpha\beta\star})$, which is used to control the system. Speed control is realized using a simple open-loop V/Hz controller, which is widely used in industry and inherently sensorless, since no feedback is required. The main idea of V/Hz control is to achieve a constant excitation of the IM, while the motor torque is set as required by the load. This is achieved by keeping the voltage amplitude over frequency ratio $\xi := \|\boldsymbol{u}_{\mathrm{v}}^{\alpha\beta\star}\|/\omega_{\mathrm{k}}$ constant (here $\xi = 96.2\,\mathrm{V\,s}$) and setting the desired speed by adjusting the electrical frequency ω_{k}. Note that in general and depending on the applied load, the mechanical speed differs from the electric speed for *asynchronous* machines.

[4] As to avoid conflicts with existing nondisclosure agreements, the suppliers' data has been modified in such a way that the values remain realistic yet do not represent real values.

Table 2.2: *Simulation parameters of the electrical subsystem.*

	Parameter	**Variable**	**Value**	**Unit**
VSI	DC-link voltage	u_{dc}	$10 \cdot 10^3$	V
	Switching frequency	f_{S}	$1 \cdot 10^3$	Hz
Filter	Filter inductance	L_{f}	$3.1 \cdot 10^{-3}$	H
	Filter capacitance	C_{f}	$0.11 \cdot 10^{-3}$	F
	Filter resistance	R_{f}	1	Ω
	Resonant frequency	f_{R1}	272.5	Hz
Cable	Length	l_{c}	997.5	m
	Number of segments	n_{c}	2	
	Line resistances	$R'^{\mathrm{a}}_{\mathrm{c}}, R'^{\mathrm{b}}_{\mathrm{c}}, R'^{\mathrm{c}}_{\mathrm{c}}$	$0.38 \cdot 10^{-3}$	$\Omega\,\mathrm{m}^{-1}$
	Line self inductances	$L'^{\mathrm{aa}}_{\mathrm{c}}, L'^{\mathrm{bb}}_{\mathrm{c}}, L'^{\mathrm{cc}}_{\mathrm{c}}$	$1.15 \cdot 10^{-6}$	$\mathrm{H}\,\mathrm{m}^{-1}$
	Line mutual inductances	$L^{\mathrm{ab}}_{\mathrm{c}}, L^{\mathrm{bc}}_{\mathrm{c}}$	$0.86 \cdot 10^{-6}$	$\mathrm{H}\,\mathrm{m}^{-1}$
		$L^{\mathrm{ac}}_{\mathrm{c}}$	$0.69 \cdot 10^{-6}$	$\mathrm{H}\,\mathrm{m}^{-1}$
	Line self capacitances	$C'^{\mathrm{aa}}_{\mathrm{c}}, C'^{\mathrm{bb}}_{\mathrm{c}}, C'^{\mathrm{cc}}_{\mathrm{c}}$	$82.5 \cdot 10^{-12}$	$\mathrm{F}\,\mathrm{m}^{-1}$
	Line mutual capacitances	$C'^{\mathrm{ab}}_{\mathrm{c}}, C'^{\mathrm{bc}}_{\mathrm{c}}$	$-32.2 \cdot 10^{-12}$	$\mathrm{F}\,\mathrm{m}^{-1}$
		$C'^{\mathrm{ac}}_{\mathrm{c}}$	$-32.2 \cdot 10^{-12}$	$\mathrm{F}\,\mathrm{m}^{-1}$
Motor	Rated voltage (phase-peak)	$\hat{u}_{\mathrm{s,nom}}$	$5.75 \cdot 10^3$	V
	Rated current (phase-peak)	$\hat{i}_{\mathrm{s,nom}}$	190	A
	Rated frequency (phase-peak)	$\omega_{\mathrm{k,nom}}$	$60 \cdot 2\pi$	$\mathrm{rad}\,\mathrm{s}^{-1}$
	Number of pole pairs	n_{p}	1	
	Stator resistance	$R_{\mathrm{s}_\Sigma} (= n_{\mathrm{r}} R_{\mathrm{s}})$	0.37	Ω
	Rotor resistance	$R_{\mathrm{r}_\Sigma} (= n_{\mathrm{r}} R_{\mathrm{r}})$	0.47	Ω
	Main inductance	$L_{\mathrm{m}_\Sigma} (= n_{\mathrm{r}} L_{\mathrm{m}})$	$129.5 \cdot 10^{-3}$	H
	Stator leakage inductance	$L_{\mathrm{s}\sigma_\Sigma} (= n_{\mathrm{r}} L_{\mathrm{s}\sigma})$	$8.7 \cdot 10^{-3}$	H
	Rotor leakage inductance	$L_{\mathrm{r}\sigma_\Sigma} (= n_{\mathrm{r}} L_{\mathrm{r}\sigma})$	$11.5 \cdot 10^{-3}$	H

Table 2.3: *Simulation parameters of the mechanical subsystem.*

	Parameter	Variable	Value	Unit
Shaft	Spring constant (2MLS)	k_{t_Σ}	$1.5 \cdot 10^3$	$\mathrm{N\,m\,rad^{-1}}$
	Spring constant (MMES)	k_t	$7.195 \cdot 10^3$	$\mathrm{N\,m\,rad^{-1}}$
	Damping factor (2MLS)	k_{d_Σ}	0.294	$\mathrm{N\,m\,s\,rad^{-1}}$
	Damping factor (MMES)	k_d	0.171	$\mathrm{N\,m\,s\,rad^{-1}}$
	Shaft length	l_{mp}	2	m
Motor	Moment of inertia	$\Theta_{r_\Sigma} (= n_r \Theta_r)$	0.059	$\mathrm{kg\,m^{-2}}$
	Visc. friction coefficient	$\nu_{r_\Sigma} (= n_r \nu_r)$	$1.5 \cdot 10^{-3}$	N m s
	Spring constant (rot-rot)	$k_{r,t}$	$1.418 \cdot 10^4$	$\mathrm{N\,m\,rad^{-1}}$
	Damping factor (rot-rot)	$k_{r,d}$	$1.913 \cdot 10^{-1}$	$\mathrm{N\,m\,s\,rad^{-1}}$
	Motor length	l_m	20	m
	Number of rotors	n_r	14	
Pump	Moment of inertia	$\Theta_{iw_\Sigma} (= n_s \Theta_{iw})$	0.233	$\mathrm{kg\,m^{-2}}$
	Visc. friction coefficient	$\nu_{i_\Sigma} (= n_s \nu_i)$	$1.5 \cdot 10^{-3}$	N m s
	Spring constant (imp-imp)	$k_{i,t}$	$101.25 \cdot 10^{-3}$	$\mathrm{N\,m\,rad^{-1}}$
	Damping factor (imp-imp)	$k_{i,d}$	0.982	$\mathrm{N\,m\,s\,rad^{-1}}$
	Pump length	l_p	3	m
	Number of stages	n_s	15	

Table 2.4: *Simulation parameters of the hydraulic subsystem.*

	Parameter	Variable	Value	Unit
Pump	Head parameters (fitted)	γ	0	$\mathrm{m\,s^{-2}}$
		b_1	$-7.87 \cdot 10^2$	$\mathrm{kg\,m^{-4}}$
		b_2	$2.5 \cdot 10^{-1}$	$\mathrm{s^2\,m^{-2}}$
		b_3	$2.875 \cdot 10^{-4}$	$\mathrm{m\,s^{-2}}$
	Torque parameters (fitted)	ϑ	0	$\mathrm{kg\,m^{-2}}$
		a_1	$2.518 \cdot 10^3$	$\mathrm{kg\,m^{-5}}$
		a_2	$3.34 \cdot 10^{-1}$	$\mathrm{kg\,m^{-2}}$
		a_3	$8.331 \cdot 10^{-4}$	$\mathrm{kg\,m^2}$
System	Fluid inertia (full load)	Γ_h	$3.082 \cdot 10^3$	$\mathrm{s^2\,m^{-2}}$
	Required wellhead pressure	$p^\star_{wh}$	$10 \cdot 10^5$	Pa
	Setting depth	z_p	950	m
	Pipe radius	r_{pipe}	0.1	m
	Darcy factor	λ_D	0.12	
	Reservoir pressure (idle)	p_{it0}	$70 \cdot 10^5$	Pa
	Reservoir production index	δ	$8.06 \cdot 10^{-8}$	$\mathrm{m^5\,N^{-1}\,s^{-1}}$
	Ambient and water temperature	T_0	140	°C

2.5.1 Simulation scenario

The system is assumed to be in idle state initially. The geothermal reservoir lifts the fluid to its idle water level of approximately 180 m below surface level and the ESP system is at standstill with zero voltage applied. The start-up phase is split into two regions: In *Region 1a* ($t \leq 30\,\mathrm{s}$), a major frequency and magnitude step from 0 to 30 Hz, respectively 0 to 2 900 V is performed (at $t = 2\,\mathrm{s}$). In *Region 1b* ($40\,\mathrm{s} < t \leq 60\,\mathrm{s}$), minor steps of 5 Hz and 480 V every 5 s are applied. Once the maximum values are reached, the voltage magnitude and frequency are kept constant. In *Region 2* ($60\,\mathrm{s} < t \leq 82\,\mathrm{s}$), the hydraulic system is still in transient state; while in *Region 3* ($t > 82\,\mathrm{s}$), the overall system is in steady-state.

2.5.2 Results and discussion

The results presented in this section refer to the more general `MMES`-case if no difference between the two cases is noticeable. Otherwise, results are presented for both cases.

An overview plot of the system responses is shown in Fig. 2.22. In addition, the characteristic pump curves including the hydraulic system trajectories are shown in Fig. 2.23. The corresponding power and efficiency plots are shown in Fig. 2.24, whereas detailed views on the electrical, mechanical and hydraulic subsystems at specified instants in time are presented in Figs. 2.26 and 2.27 for steady-state conditions, and in Figs. 2.28, 2.29 and 2.30 for transients (i.e. step changes), respectively.

2.5.2.1 Overall system

The simulation results of the overall system are shown in Fig. 2.22. In the first plot (from top to bottom), the voltage magnitudes measured at the inputs of the different electric system components are plotted, i.e. the filter input (inverter output) reference voltage $\hat{u}_\mathrm{f}^\star = \|\boldsymbol{u}_\mathrm{f}^{\alpha\beta\star}\|$, the cable input (filter output) voltage $\hat{u}_\mathrm{c} = \|\boldsymbol{u}_\mathrm{c}^{\alpha\beta}\|$ and the machine input (cable output) voltage $\hat{u}_\mathrm{s} = \|\boldsymbol{u}_\mathrm{s}^{\alpha\beta}\|$. As described in Sec. 2.1.1, the inverter output (filter input) voltage switches between discrete voltage levels, varying around the desired reference voltage yet matching on average per sampling period. As the data sampling time (1 ms) is much bigger than the simulation step time (1 µs), the filter input voltage is represented by the sampled and delayed (for one switching period) reference voltage. As prescribed by the V/Hz controller, the filter input voltage magnitude is increased stepwise during start-up (Regions 1a and 1b) and equals $u_\mathrm{dc}/\sqrt{3} \approx 5\,770\,\mathrm{V}$ in Regions 2 and 3. The damping resistor of the filter and the resistive part of the power cable lead to voltage drops which can be observed in the slightly smaller magnitudes of the cable and stator voltages, respectively.

The second plot shows the corresponding current magnitudes, with filter input current $\hat{i}_\mathrm{f} = \|\boldsymbol{i}_\mathrm{f}^{\alpha\beta}\|$, cable input current $\hat{i}_\mathrm{c} = \|\boldsymbol{i}_\mathrm{c}^{\alpha\beta}\|$, stator current $\hat{i}_\mathrm{s} = \|\boldsymbol{i}_\mathrm{s}^{\alpha\beta}\|$ and rotor currents $\hat{i}_{\mathrm{r},i} = \|\boldsymbol{i}_{\mathrm{r},i}^{\alpha\beta}\|$, with $i \in \{1, \ldots, n_\mathrm{r}\}$. The first observation is that the cable and stator currents almost perfectly coincide, which leads to the conclusion that the influence of the cable on the dynamic system narrows down to a mere voltage drop, assuming that a filter is employed. Another important observation is that the filter current is smaller in magnitude than the stator current, which implies that current is circulating between the filter output and the motor. This effect was introduced as *self-excitation* and explained in Sec. 2.1.4.4. It should be taken into account when designing the filter, since higher currents than measured at the inverter output terminals will flow into the filter capacitors and the stator.

The third plot of Fig. 2.22 shows the average motor and pump speeds ω_{m_Π} and ω_{i_Π}. Due to

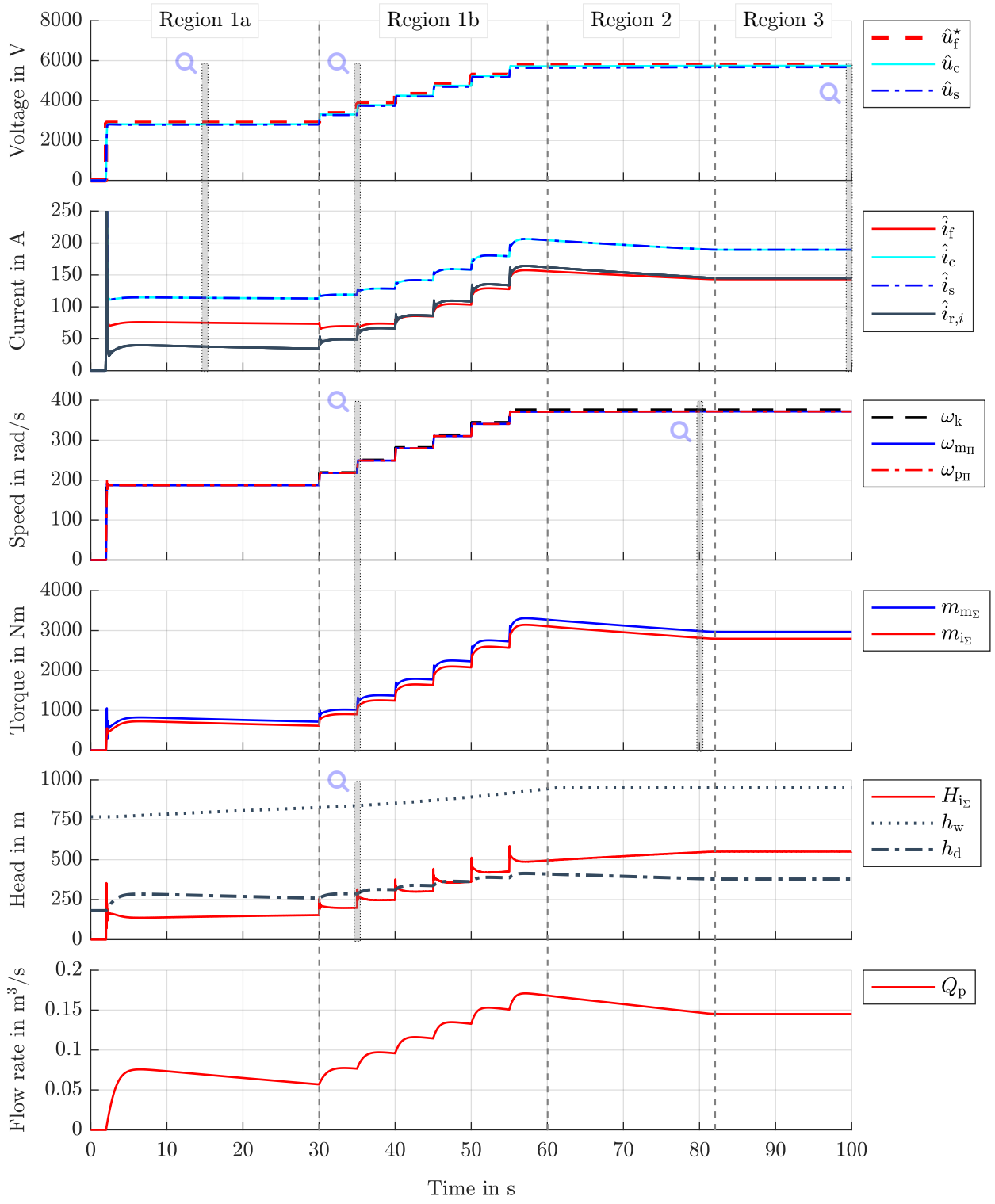

Figure 2.22: *ESP Simulation results (overview): Filtered system states of the electrical, mechanical and hydraulic subsystem.*

the frequency steps, the machine speeds up during Region 1, reaching a final value slightly below $377\,\mathrm{rad\,s^{-1}}$ (60 Hz), which is due to the slip of the induction machine.

In the fourth plot, the total machine torque m_{m_Σ} produced by the motor and the total load torque m_{i_Σ} of the pump are shown, where m_{m_Σ} is the sum of all rotor driving torques $m_{\mathrm{m},i}, i \in \{1,\dots,n_\mathrm{r}\}$ and m_{i_Σ} is the sum of all impeller load torques $m_{\mathrm{i},j}, j \in \{1,\dots,n_\mathrm{s}\}$. It can be observed that the load torque is directly related to the volumetric flow rate Q_p (6th plot), which increases during start-up, then slightly reduces and finally reaches steady-state at $t \approx 82\,\mathrm{s}$. Due to friction and damping in the mechanical system, the motor must provide a higher torque than actually required by the load which can be observed in the plot.

The fifth plot shows the pump pressure expressed as head H_{i_Σ} (being the sum of all impeller head portions $H_{\mathrm{i},j}, j \in \{1,\dots,n_\mathrm{s}\}$), the water column h_w resting on the pump, and the drawdown h_d. Since the pump head depends on both, speed and volume flow rate, any changes in the respective quantities lead to a change in the pump head. When the flow finally settles at $t = 82\,\mathrm{s}$ (Region 3), the pump head reaches its final value of 550 m and the overall pump system is in steady-state. The corresponding pump flow Q_p is shown in the sixth (last) plot, settling at $0.145\,\mathrm{m^3\,s^{-1}}$ (or $145\,\mathrm{L\,s^{-1}}$).

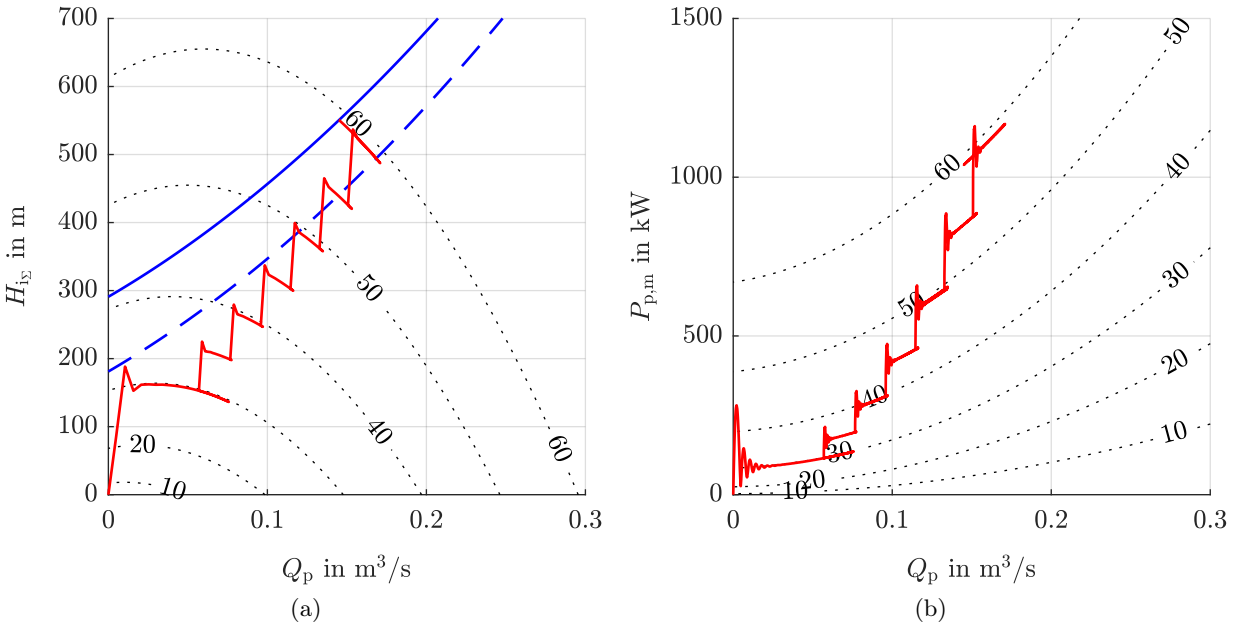

Figure 2.23: *ESP Simulation results (refer to Fig. 2.22): (a) HQ-curves (pump head over flow rate) for different (constant) speed values [····], with hydraulic system curve, for* $p_\mathrm{wh} = 0$ *[- - -] and* $p_\mathrm{wh} = p^\star_\mathrm{wh}$ *[—], respectively, and simulated trajectory* $(H_\mathrm{p}(\cdot), Q_\mathrm{p}(\cdot))$ *[—] and (b) PQ-curves (pump input power over flow rate) for different (constant) speed values [····], with simulated trajectory* $(P_\mathrm{p,m}(\cdot), Q_\mathrm{p}(\cdot))$ *[—].*

In addition, Fig. 2.23 shows contour plots of the simulated pump system, with (a) the trajectory of the pump operating points [—] over the HQ-contour plot of the simulated pump and (b) its respective input power as defined in (2.79) (PQ-contour plot). The dashed blue line [- - -] in (a) represents the hydraulic system curve for the initial wellhead pressure (i.e. $p_\mathrm{wh} = 1 \cdot 10^5\,\mathrm{Pa}$), whereas the solid blue line [—] represents the nominal wellhead pressure $p_\mathrm{wh} = p^\star_\mathrm{wh}$. The pump trajectory [—] in (a) clearly exhibits the speed steps. Furthermore, as the flow builds up, the trajectory finally approaches the hydraulic system curve for initial wellhead pressure [- - -]. When the trajectory crosses the dashed line the height difference between pump and wellhead is overcome. Finally, the

trajectory reaches the hydraulic system curve for nominal wellhead pressure [—]. In (b), the stepwise increase of input power during the acceleration phase (Region 1) is also clearly visible, whereas the power reduction due to the flow reduction in Region 2 is hard to identify. In Region 3, the pump input power reaches its final value of $P_{\mathrm{p,m}} \approx 1.05\,\mathrm{MW}$ (compare also with the first subplot in Fig. 2.24).

2.5.2.2 Power and efficiency

In the following, electrical power terms such as apparent, active and reactive power will be used. For voltage and current vectors $\boldsymbol{u}^{\alpha\beta}$ and $\boldsymbol{i}^{\alpha\beta}$, the averaged power terms are defined as[5]

$$P := \tfrac{3}{2}\tfrac{1}{T_\mathrm{S}} \int_{t-T_\mathrm{S}}^{t} (\boldsymbol{u}^{\alpha\beta})^\top \boldsymbol{i}^{\alpha\beta} \mathrm{d}\tau, \quad Q := \tfrac{3}{2}\tfrac{1}{T_\mathrm{S}} \int_{t-T_\mathrm{S}}^{t} (\boldsymbol{u}^{\alpha\beta})^\top \boldsymbol{J}\boldsymbol{i}^{\alpha\beta} \mathrm{d}\tau, \quad S := \tfrac{3}{2}\tfrac{1}{T_\mathrm{S}} \int_{t-T_\mathrm{S}}^{t} \|\boldsymbol{u}^{\alpha\beta}\| \|\boldsymbol{i}^{\alpha\beta}\| \mathrm{d}\tau, \quad (2.78)$$

with sampling period T_S, active power P, reactive power Q and apparent power S. Moreover the power factor is defined as $\cos(\phi) := \frac{P}{S}$.

The first plot of Fig. 2.24 (likewise from top to bottom) shows various power terms related to the pump system, i.e. the motor electrical input power $P_{\mathrm{m,e}}$, the motor mechanical output power $P_{\mathrm{m,m}}$, the pump mechanical input power $P_{\mathrm{p,m}}$ and the pump hydraulic output power $P_{\mathrm{p,h}}$, i.e.

$$P_{\mathrm{m,e}} \overset{(2.78)}{:=} P, \qquad P_{\mathrm{m,m}} := m_{\mathrm{m}_\Sigma} \omega_{\mathrm{m}_\Pi}, \qquad P_{\mathrm{p,m}} := m_{\mathrm{i}_\Sigma} \omega_{\mathrm{i}_\Pi} \qquad \text{and} \qquad P_{\mathrm{p,h}} := \rho g Q_\mathrm{p} H_{\mathrm{i}_\Sigma}. \quad (2.79)$$

As power is flowing in the aforementioned order—from the motor input to the pump output—and losses occur in each subsystem a steady decrease in power can be observed (see Fig. 2.25). The corresponding efficiencies are shown in the second plot, with $\eta_\mathrm{m} := P_{\mathrm{m,m}}/P_{\mathrm{m,e}}$ denoting the motor efficiency and $\eta_\mathrm{p} := P_{\mathrm{p,h}}/P_{\mathrm{p,m}}$ denoting the pump efficiency, respectively. The motor efficiency reaches values of over 90 %, while the pump efficiency is much lower with a maximum value of about 70 %. The total efficiency of the system is given by $\eta_\mathrm{t} := P_\mathrm{f}/P_{\mathrm{p,h}}$ with a maximum value of approximately 60 %, where P_f denotes the active power at the filter input.

Remark 11 (Motor efficiency)**.** *Note that the motor efficiency is typically stated* including *friction and windage losses, whereas in the presented results only the electromagnetic conversion process is evaluated. Moreover, iron losses (see Ch. 3) have not been included in the machine model, which results in a higher motor efficiency than one would normally expect for an ESP motor.*

Plots 3–5 show the apparent, active and reactive power components, measured at the filter input (subscript 'f'), cable input (subscript 'c') and machine stator (subscript 's'), respectively. The apparent power shows similar characteristics as the current magnitudes depicted in Fig. 2.22, with a higher apparent power in motor and cable, compared to the filter. On the contrary, the active power is steadily reduced from filter to motor, as resistive components in the system dissipate power. Looking at the reactive power, it can be observed that the inverter supplies reactive power to the system until the frequency is increased from 40 to 45 Hz at $t = 40\,\mathrm{s}$; the self-excitation frequency of the given setup is $\omega_{\mathrm{R2}} = 1/(2\pi\sqrt{L_\mathrm{s} C_\mathrm{f}}) \approx 40.8\,\mathrm{Hz}$, i.e. at this point, reactive power starts circulating

[5] The instantaneous apparent power is calculated by $s = \sqrt{p^2 + q^2}$, where p and q are the instantaneous active and reactive power, respectively. For further details see App. A.4 and [119].

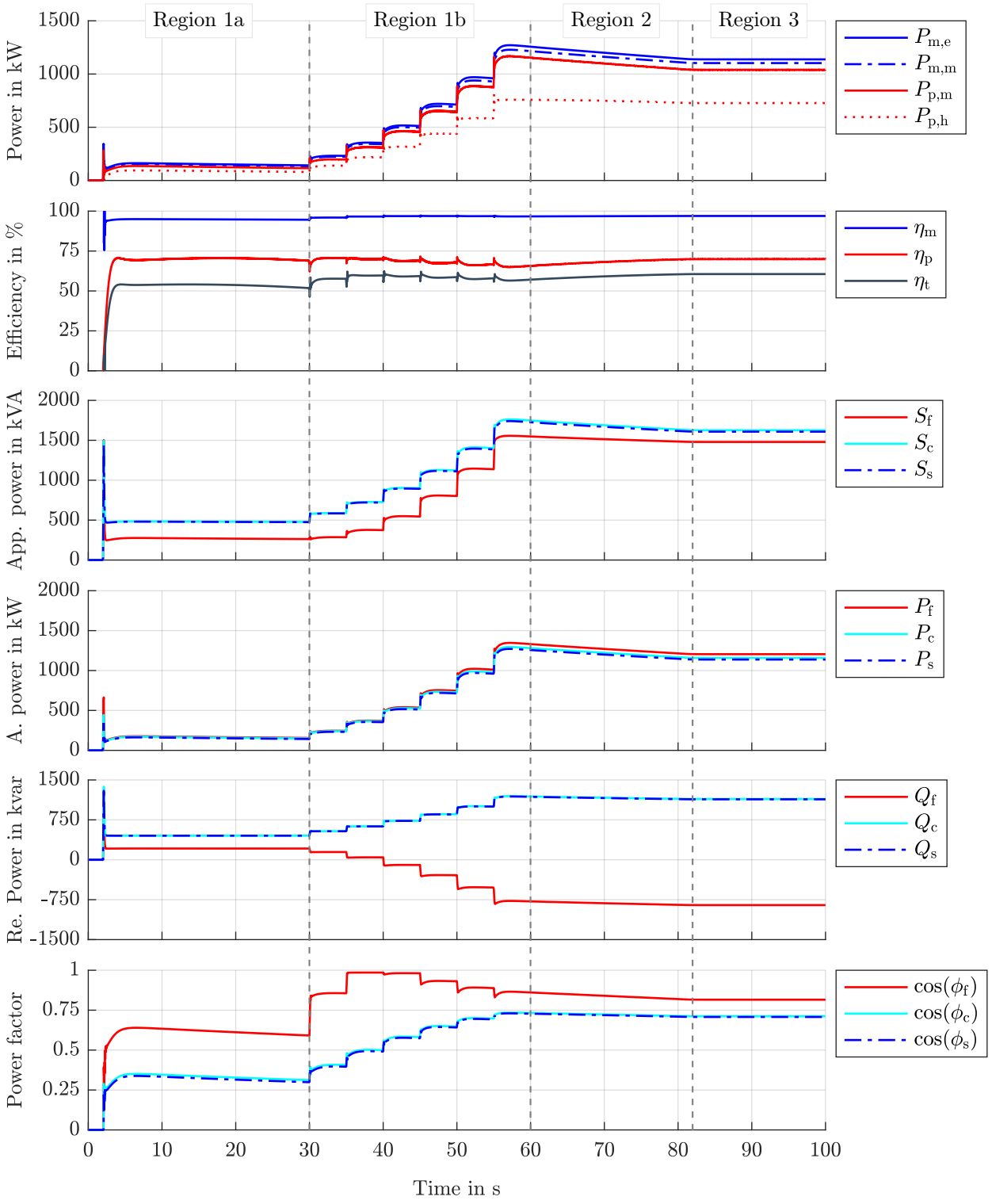

Figure 2.24: *ESP Simulation results: Power and efficiency related data.*

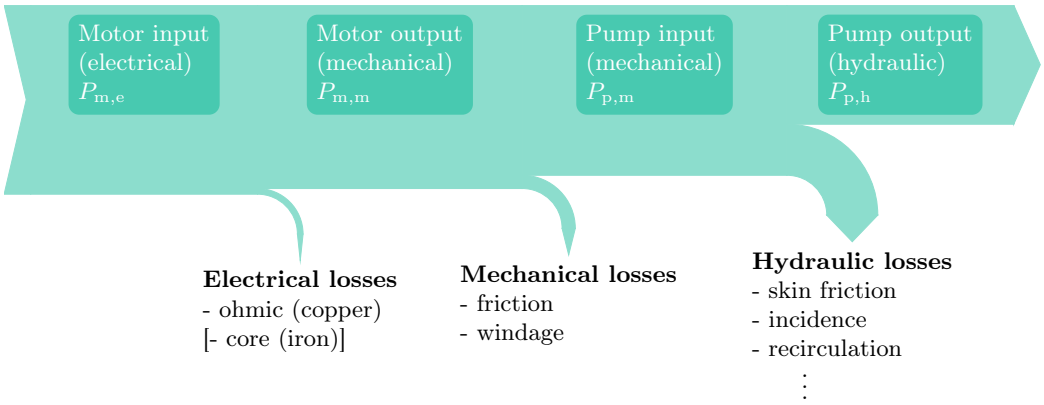

Figure 2.25: *Power flow graph (Sankey diagram) of the geothermal ESP.*

between the filter capacitance and the stator inductance, thus reducing the required reactive power supplied by the inverter (see Sec. 2.1.4.4).

In the sixth plot, the corresponding power factors are depicted. As expected, the filter power factor $\cos(\phi_f)$ approaches 1 in the vicinity of the self-excitation frequency (i.e. $t = 40\,s$), since the reactive power flow is zero at this stage.

2.5.2.3 Detailed views (zoom-in) during steady-state

In addition to the overview plots of Fig. 2.22, detailed views on the electrical (see Figs. 2.26 and 2.28), mechanical (see Figs. 2.27 and 2.29) and hydraulic (see Fig. 2.30) subsystems are provided. In the detailed views, a comparison between the `MMES` and `2MLS` simulation data is reasonable, since differences become apparent.

In Fig. 2.26, the α-components of the relevant electrical system states are depicted for two-different time instants, i.e. for $t = 15\,s$ and $t = 99.955\,s$, and for the respective duration of 45 ms. Plots (a) and (b) refer to the `MMES`-case, whereas plots (c) and (d) are related to the `2MLS`-case. At both time instants, the electrical system is in quasi steady-state, since the load changes slowly and the excitation frequency of $\omega_k = 30\,Hz$ in (a) and (c) and $\omega_k = 60\,Hz$ in (b) and (d) is constant.
The upper plots of (a) and (b) show the α-components of the voltages, namely the reference voltage $u_f^{\alpha\star}$, the filter input voltage u_f^{α}, the cable input voltage u_c^{α} and the stator voltage u_s^{α}, with amplitudes of about 2.8 kV and 5.7 kV in (a) and (b), respectively. It can be observed that the produced output voltage of the inverter is smoothed by the filter in both cases. The cable itself, however, does not have a noticeable impact on the voltages (as motivated above).
The mid plots of (a) and (b) show the filter input current i_f^{α}, the cable input current i_c^{α}, the stator current i_s^{α} and the numerous rotor currents $i_{r,i}^{\alpha}, i \in \{1, \ldots, n_r\}$. In both plots, the filter input currents are distorted, whereas the stator currents are smoothed by the large inductance of the motor. The effect of self-excitation can be seen clearly in (a), where the amplitude of i_s^{α} is higher than that of i_f^{α}. Moreover, a slight phase shift between stator and filter currents can be observed. Since the load is still low in the presented interval (compare with Fig. 2.22), the amplitude of the rotor current remains comparably small. The rotor current is clearly shifted in phase, however. In Region 3, i.e. plot (b), the amplitudes of both, filter and stator currents, are nearly doubled compared to (a). Moreover, the stator current is subject to a phase shift of about $\pi/2$ compared to the filter input current, whereas the phase shift of the rotor current is even larger. Since the load is much higher in Region 3, the amplitude of the rotor current is increased notably compared to (a). In

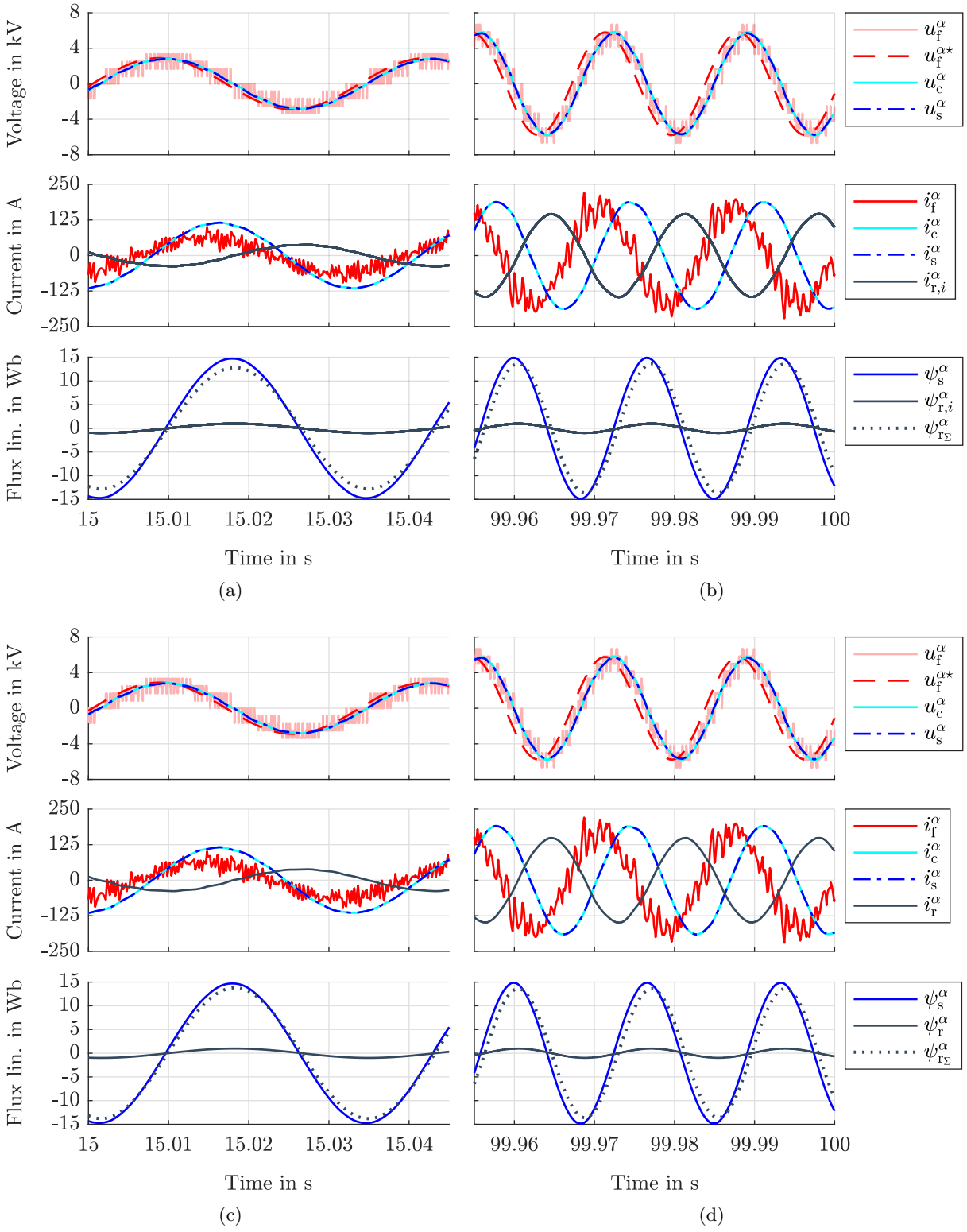

Figure 2.26: *Detailed view (steady-state) on electrical system for two different time intervals (Zoom 1 & 2), zoom-in from Fig. 2.22: (a) Multi-rotor/multi-stage elastic system (Zoom 1), (b) multi-rotor/multi-stage elastic system (Zoom 2), (c) two-mass lumped system (Zoom 1) and (d) two-mass lumped system (Zoom 2).*

both cases, the cable does not influence the current waveforms.
The lower plots of (a) and (b) show the α-components of the stator flux linkages $\psi_{\mathrm{s}}^{\alpha}$, the numerous rotor flux linkages $\psi_{\mathrm{r},i}^{\alpha}, i \in \{1,\dots,n_{\mathrm{r}}\}$ and the sum of rotor flux linkages $\psi_{\mathrm{r}_{\Sigma}}^{\alpha}$, respectively. Although the rotor flux is slightly shifted in phase and reduced in amplitude in (b), both plots give evidence that, once magnetized, the flux linkages do not change significantly.
The current and flux linkage plots of the `MMES`-case can be compared to the `2MLS` data shown in (c) and (d). It can be deduced from the plots, that the elastic coupling between adjacent rotor segments does not have a significant impact on the electric system, at least concerning steady-state. Only in the flux linkage plots of (a) and (c), a slight difference in magnitude is observed between the sums of rotor flux linkages $\psi_{\mathrm{r}_{\Sigma}}^{\alpha}$.

In Fig. 2.27, further insight on the mechanical system (steady-state) is provided for time instant $t = 80\,\mathrm{s}$ and duration $\Delta t = 20\,\mathrm{ms}$; the `MMES` data is depicted in (a), whereas the `2MLS` data is shown in (b). The upper plots of (a) and (b) show the angular velocities $\omega_{\mathrm{m},i}, i \in \{1,\dots,n_{\mathrm{r}}\}$ and $\omega_{\mathrm{i},j}, j \in \{1,\dots,n_{\mathrm{s}}\}$ and the lower plots the torques $m_{\mathrm{m},i}, i \in \{1,\dots,n_{\mathrm{r}}\}$ and $m_{\mathrm{i},j}, j \in \{1,\dots,n_{\mathrm{s}}\}$ of motor and pump, respectively. In (a) it can be observed that—on the motor side—elasticity of the shaft has a notable impact, since the individual rotor velocities $\omega_{\mathrm{m},i}$ mutually vary up to $2\,\mathrm{rad\,s^{-1}}$. On the pump-side, however, a marginal impact of shaft elasticity is observed. Regarding torque, the difference for both, driving torques and load torques, is insignificant, although general variations in the motor torque can be observed, whereas the load torque of the pump is almost constant. In comparison, the angular velocity in (b) resembles an average value of the multiple rotor speeds in (a), while the torques depicted in (b) are almost identical to those in (a).

2.5.2.4 Detailed views (zoom-in) during transient response

The transient behavior of the various subsystems is analyzed for a step change in the reference frequency and amplitude at time instant $t = 35\,\mathrm{s}$ and durations $\Delta t = 0.1\,\mathrm{s}$ for Fig. 2.28 and $\Delta t = 0.2\,\mathrm{s}$ for Figs. 2.29 and 2.30, respectively.

In Fig. 2.28, the electrical system is shown. Signal description and order are identical to those of Fig. 2.26. The difference between the `MMES`-case depicted in (a) and the `2MLS`-case shown in (b) is relatively minor and to be found in the rotor currents $i_{\mathrm{r},i}^{\alpha}$, which deviate slightly around some mean value in (a)—in particular after the step change. Again, also the sum of rotor flux linkages $\psi_{\mathrm{r}_{\Sigma}}^{\alpha}$ in (a) is marginally smaller compared to (b).

In Fig. 2.29, the mechanical system is shown for the transient case, where again signal description and order are identical to the steady-state case shown in Fig. 2.27. For both cases, `MMES` (see Fig. 2.29a) and `2MLS` (see Fig. 2.29b), the frequency change results in a major oscillation of angular velocities and torques, on either side of the shaft, i.e. motor and pump. In (a) it can be seen that the speed variation on the motor side is up to $55\,\mathrm{rad\,s^{-1}}$ right after the step, whereas on the pump side variations are limited to $10\,\mathrm{rad\,s^{-1}}$. As for the torque, variations are in the range of $25\,\mathrm{N\,m}$ on the motor side, and relatively small on the pump side. The dominating shapes of speed and torque waveforms in (a) and (b) are comparable, nonetheless.

The transient behavior of the hydraulic system is shown in Fig. 2.30—the pump head is sufficient to show here, as the flow rate varies comparably slow (compare with Fig. 2.22). In both cases, the `MMES`-case shown in (a) and the `2MLS`-case shown in (b), the mean impeller head $H_{\mathrm{i}_{\Sigma}}/n_{\mathrm{s}}$ oscillates after the step change, as it is proportional to the impeller speed squared [see (2.46)], which is depicted in Fig. 2.29a. In (a), a minor oscillation of the individual impeller head components around the mean value can be observed, which does not have a significant impact on the flow rate, due to the high inertia of the water column.

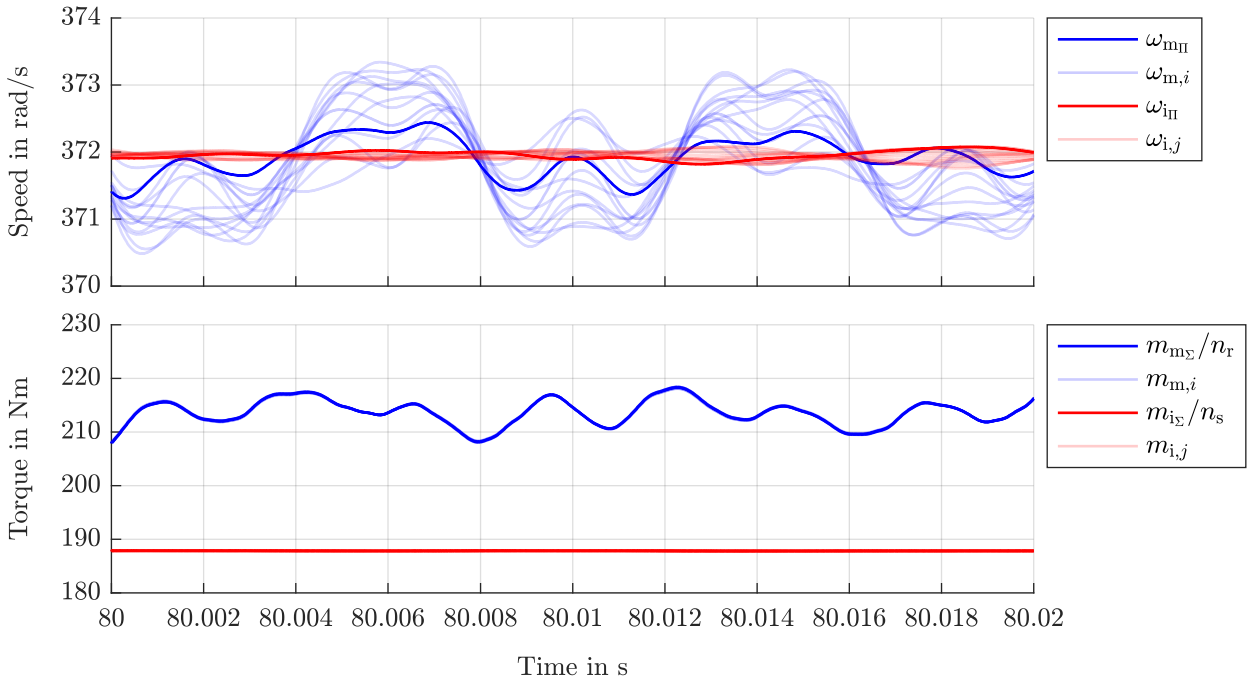

(a)

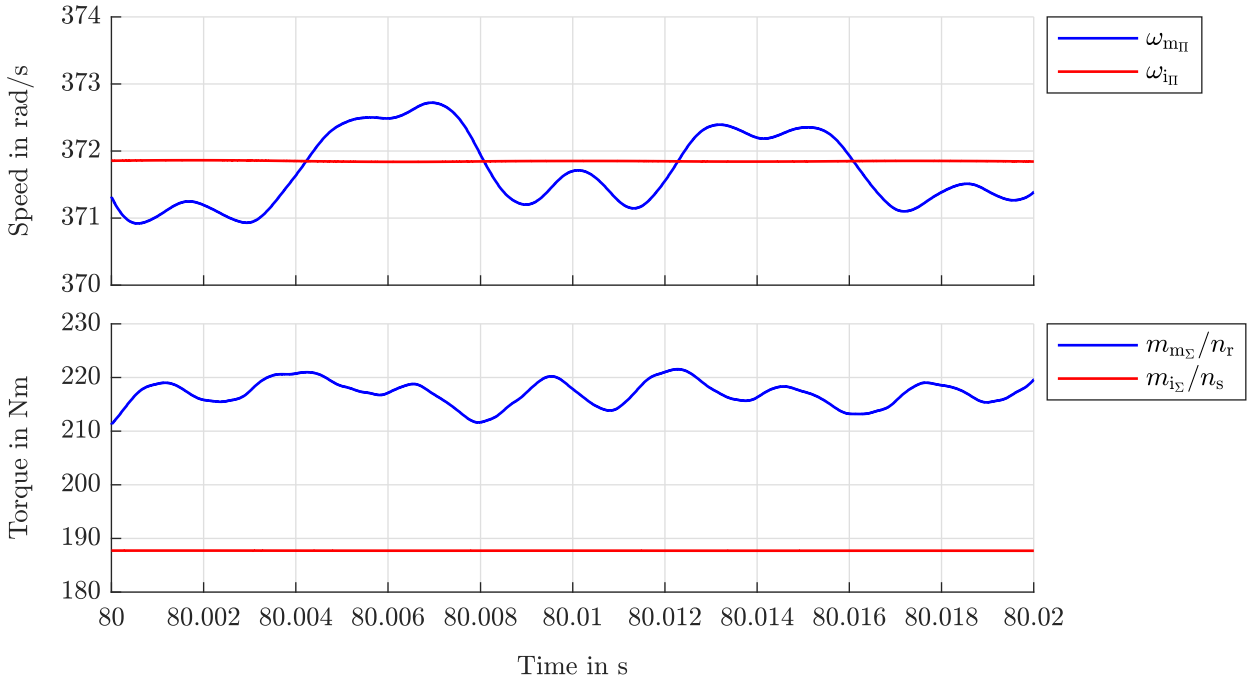

(b)

Figure 2.27: *Detailed view (steady-state) on mechanical system, zoom-in from Fig. 2.22: (a) Multi-rotor/multi-stage elastic system and (b) two-mass lumped system.*

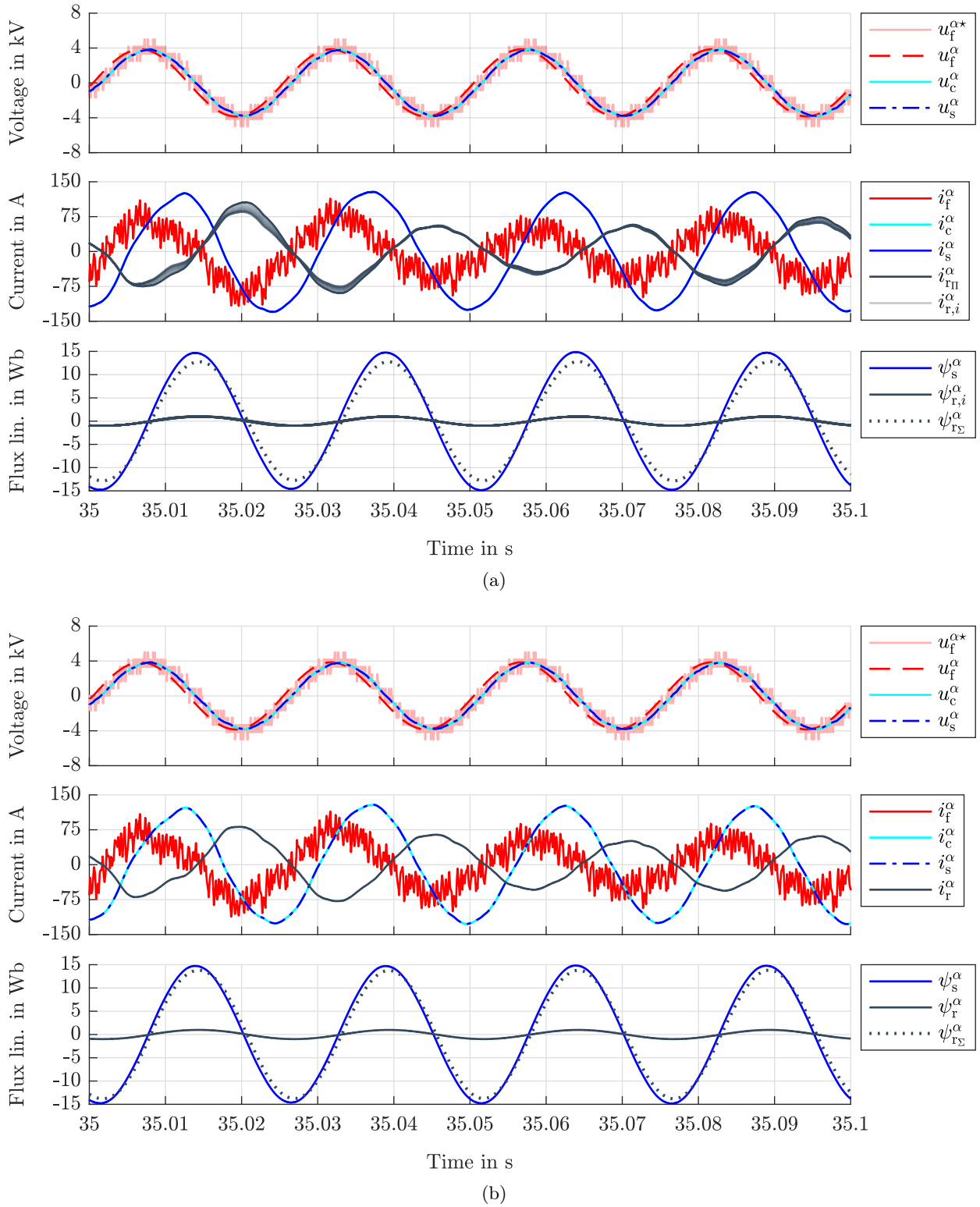

Figure 2.28: *Detailed view (transient response) on electrical system, zoom-in from Fig. 2.22: (a) Multi-rotor/multi-stage elastic system and (b) two-mass lumped system.*

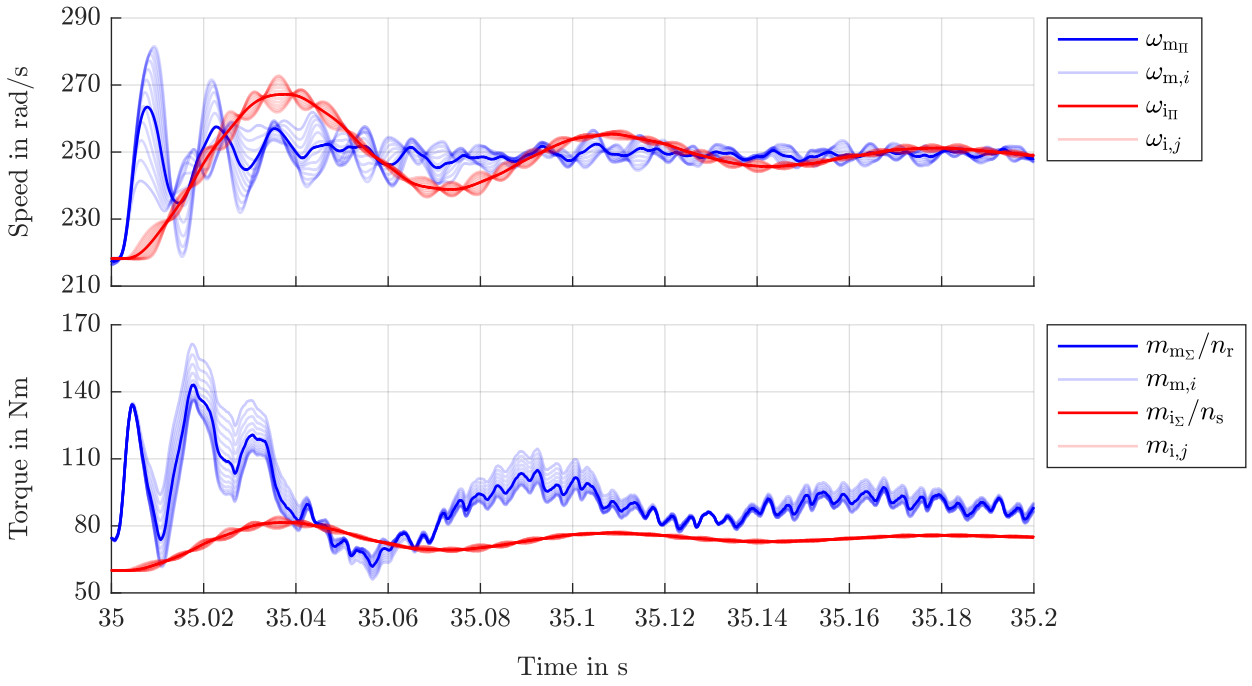

(a)

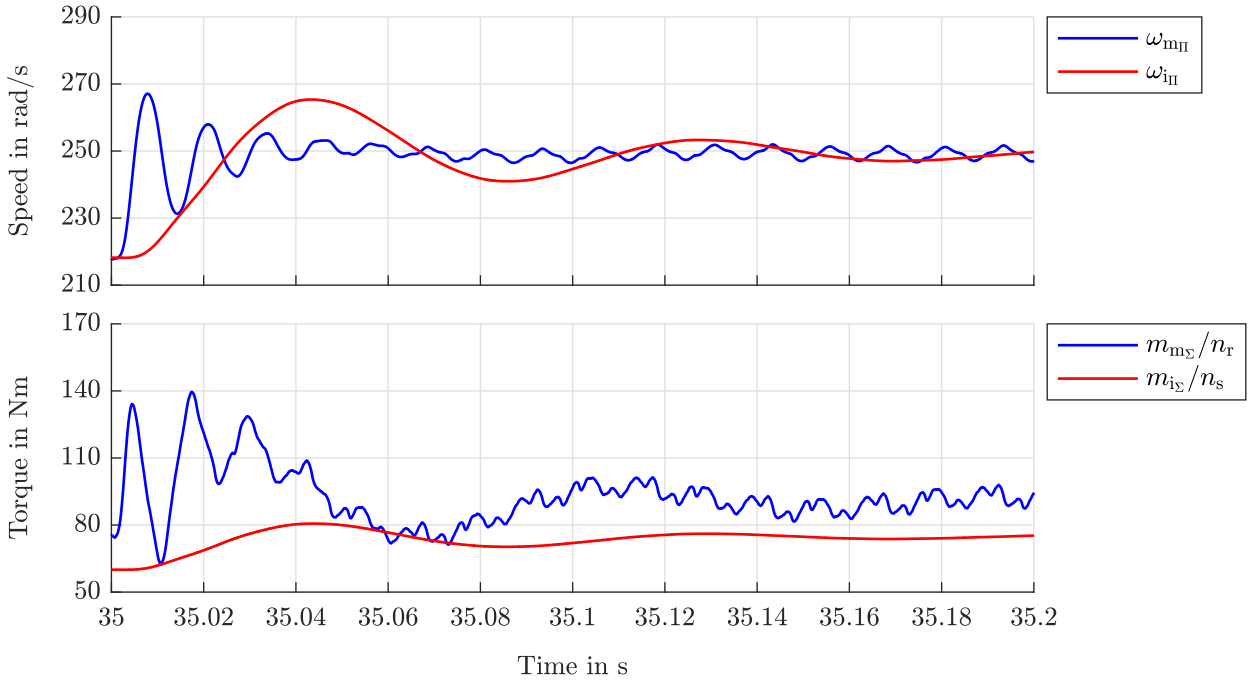

(b)

Figure 2.29: *Detailed view (transient response) on mechanical system, zoom-in from Fig. 2.22: (a) Multi-rotor/multi-stage elastic system and (b) two-mass lumped system.*

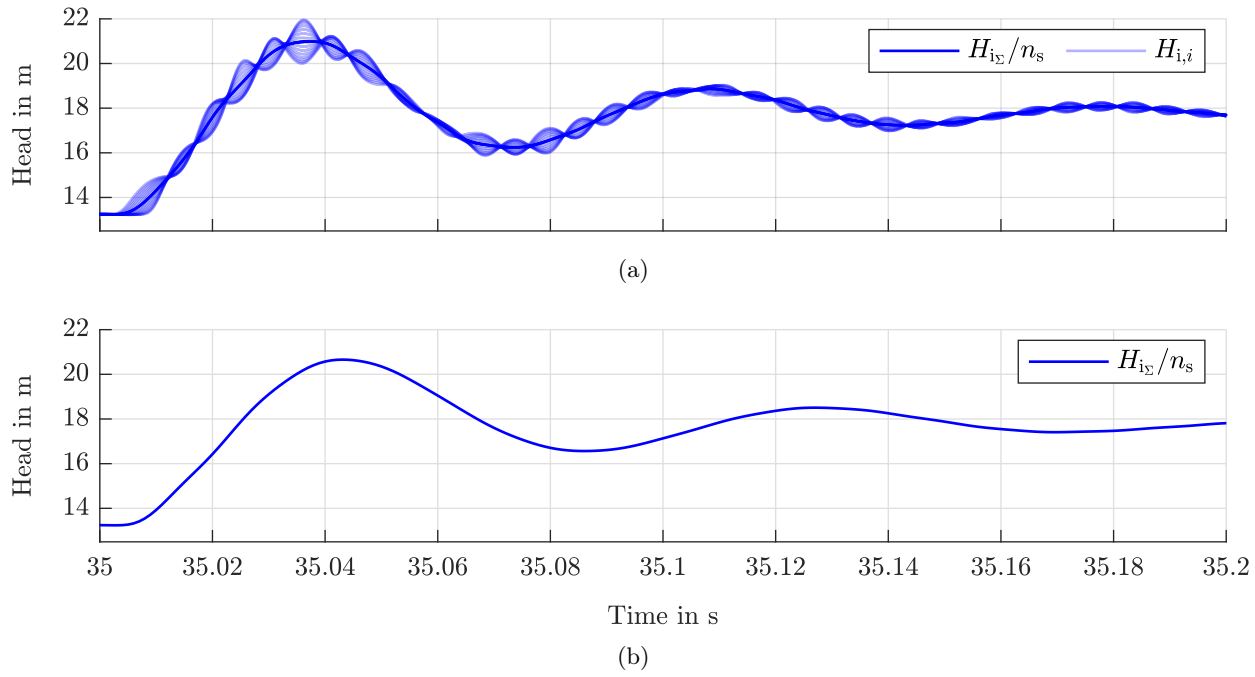

Figure 2.30: *Detailed view (transient response) on hydraulic system, zoom-in from Fig. 2.22: (a) Multi-rotor/multi-stage elastic system and (b) two-mass lumped system.*

2.6 Summary

A detailed state-space model of a deep geothermal ESP system has been derived, comprising electrical, mechanical and hydraulic subsystems. Based on the model, simulations have been performed for a megawatt ESP system located at 950 m below surface level, lifting geothermal fluid of 140 °C temperature. During start-up the electrical frequency has been increased step-wise from 0 to 60 Hz and the voltage amplitude from 0 to 5 750 V, respectively. It could be observed that—once the start-up procedure was completed—the system reached steady-state.

Besides reaching stable conditions it could be observed that the cable does not have a significant impact on the system dynamics as the relevant frequencies are located far beyond both fundamental and switching frequencies. On the other hand, the effect of motor self-excitation resulting from the large filter capacitance became apparent when looking at the power factor, reactive power and currents. It should be taken into account when selecting the ESP components, as the motor currents may be considerably higher than the inverter output currents. The mechanical system was modeled in two-ways, (i) as a generic multi-rotor/multi-stage elastic system (`MMES`) and (ii) as a two-mass lumped system (`2MLS`). It was observed in the results section, that—for the given set of parameters—elasticity of the shaft does not have a major effect on the overall system, due to the high-inertia electrical and hydraulic properties of motor currents and geothermal fluid, respectively. In conclusion, simulation results have shown that the model is able to emulate a realistic behavior for the tested scenario, the realistic system parameters and the chosen system dimensions.

Chapter 3

Efficient feedforward torque control of induction machines

Speed control of ESP systems is typically realized by means of simple V/Hz control, which is well suited for applications where a straightforward and cost-effective solution is preferred over a highly dynamic control. In particular regarding geothermal power systems, where the use of rotational encoders is aggravated due to the remote deployment and harsh environment of the motor, V/Hz control is a simple and cheap *sensorless* control solution. Besides its slow dynamics, major drawbacks of this *open-loop* control method (no speed feedback is used) are

(i) inaccurate motor speed 'tracking' due to the slip of induction machines (the mechanical frequency does not comply with the electrical frequency),

(ii) a potentially lower efficiency, especially in part-load operation and for a *constant* V/Hz ratio [120], and

(iii) current overshooting and potential loss of control for sudden load changes [108, Sec. 9.1].

The following chapter experimentally motivates for the use of a *closed-loop* speed control system, based on an underlying field-oriented control (FOC)-like stator current controller (more details provided in Sec. 3.1.2). Apart from the fact that a closed-loop controller may prevent excessive currents (thermal limits are not exceeded) and reduce torque oscillations (mechanical strain is reduced), its advantage over the V/Hz controller in terms of efficiency per torque will be shown. As a means to extract the machine characteristics and assess different torque control strategies, a machine identification method for IMs is presented, which is appealing to industry since being generic and straightforward to replicate. Furthermore, it will be shown that maximum efficiency operation can be achieved, even without the use of expensive lab equipment such as a torque sensor or high-bandwidth voltage sensors. Parts of this chapter have already been published in [121].

The chapter is structured as follows: In Sec. 3.1, a generic induction machine model in an arbitrarily rotating coordinate system is presented. In addition, a simple FOC-like current control scheme and the superimposed LUT-based feedforward torque controller are briefly presented. Moreover, in preparation of the evaluation of the identified machine data, a steady-state system analysis is conducted and the impact of iron losses[1] is investigated. In Sec. 3.2, the machine identification procedure is presented, comprising the sub-tasks of (i) data acquisition, (ii) machine map extraction and (iii) LUT generation. Finally, in Sec. 3.3, the results of the identification procedure are

[1] The terms 'iron ...' and 'core ...' are used synonymously throughout this chapter, e.g. the term 'iron loss' describes the same thing as 'core loss'.

discussed, confirming that—in particular for geothermal power applications—an FOC-like control system is beneficial in terms of efficiency for most operating conditions.

3.1 Generic machine model and control system

In this section a generic electromechanical model of a squirrel-cage induction machine (SCIM) is stated and the implemented control system is briefly described (see Fig. 3.3). While the generic model is used for the machine identification and the extraction of torque control LUTs, the underlying current control system is based on a simplified model as it serves as a mere tool for the identification procedure and for the realization of the commanded torque control outputs (stator current set-points).

3.1.1 Dynamic SCIM model in arbitrarily rotating coordinates

The generic SCIM model can be considered a generalized version of the SR/SS-model, which was derived for the stationary αβ-reference frame in Ch. 2. Major modifications are

(i) the consideration of iron (core) losses in the stator,

(ii) generic magnetic flux modeling without the use of constant inductances (only applied where indicated, e.g. in the control system and for illustrative purposes),

(iii) transformation into an arbitrarily rotating reference frame, and

(iv) modeling of temperature dependencies.

Figure 3.1 shows a cross-section view of an SCIM, illustrating the orientation of the stationary αβ-reference frame and the rotating dq-reference frame, respectively. The dq-reference frame rotates at angular velocity ω_k, while $\phi_\mathrm{k} = \int \omega_\mathrm{k} \mathrm{d}t$ denotes the respective (Park) transformation angle (see App. A.1.2).

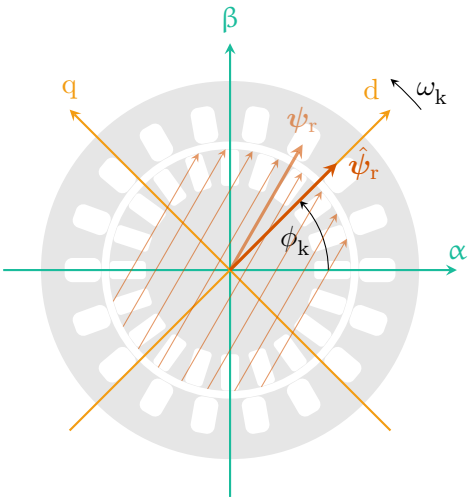

Figure 3.1: *Cross-section view of an induction machine, with stationary* αβ*-reference frame and arbitrarily rotating* dq*-reference frame (aligned here with the estimated rotor flux linkage* $\hat{\boldsymbol{\psi}}_\mathrm{r}^\mathrm{dq}$*), shifted by the offset angle* $\phi_\mathrm{k} = \int \omega_\mathrm{k} \mathrm{d}t$ *and rotating at angular velocity* ω_k.

Remark 12 (Reference frame)**.** *Typically, for field-oriented control of IMs, the* dq*-reference frame is aligned with the rotor, stator or air-gap flux linkage space vector. However, for* indirect *rotor flux oriented controllers, where the rotor flux linkage is estimated ($\hat{\boldsymbol{\psi}}_\mathrm{r}^\mathrm{dq}$), alignment errors are inevitable. Therefore, speaking of an 'arbitrarily rotating' instead of a 'rotor flux oriented' reference frame seems more appropriate.*

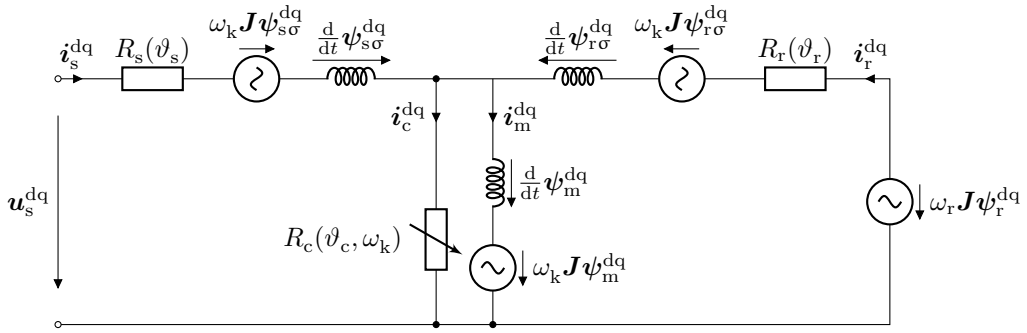

Figure 3.2: *Vectorial T-equivalent circuit (including core losses) of the SCIM in arbitrarily rotating* dq*-coordinates (see e.g. [122]).*

The corresponding vectorial equivalent circuit in the arbitrarily rotating dq-reference frame is depicted in Fig. 3.2. Applying KVL and Newton's second law, respectively, the governing equations can be stated as (argument t dropped for the sake of brevity)

$$\left.\begin{aligned}
\boldsymbol{u}_\mathrm{s}^\mathrm{dq} &= R_\mathrm{s}(\vartheta_\mathrm{s})\boldsymbol{i}_\mathrm{s}^\mathrm{dq} + \tfrac{\mathrm{d}}{\mathrm{d}t}\boldsymbol{\psi}_\mathrm{s}^\mathrm{dq} + \omega_\mathrm{k}\boldsymbol{J}\boldsymbol{\psi}_\mathrm{s}^\mathrm{dq},\\
\mathbf{o}_2 &= R_\mathrm{r}(\vartheta_\mathrm{r})\boldsymbol{i}_\mathrm{r}^\mathrm{dq} + \tfrac{\mathrm{d}}{\mathrm{d}t}\boldsymbol{\psi}_\mathrm{r}^\mathrm{dq} + (\omega_\mathrm{k}-\omega_\mathrm{r})\boldsymbol{J}\boldsymbol{\psi}_\mathrm{r}^\mathrm{dq},\\
\mathbf{o}_2 &= R_\mathrm{c}(\vartheta_\mathrm{c},\omega_\mathrm{k})\boldsymbol{i}_\mathrm{c}^\mathrm{dq} - \tfrac{\mathrm{d}}{\mathrm{d}t}\boldsymbol{\psi}_\mathrm{m}^\mathrm{dq} - \omega_\mathrm{k}\boldsymbol{J}\boldsymbol{\psi}_\mathrm{m}^\mathrm{dq},\\
\Theta_\mathrm{m}\tfrac{\mathrm{d}}{\mathrm{d}t}\omega_\mathrm{m} &= m_\mathrm{m} + m_\mathrm{f} + m_\mathrm{l},\\
\tfrac{\mathrm{d}}{\mathrm{d}t}\phi_\mathrm{k} &= \omega_\mathrm{k},
\end{aligned}\right\} \tag{3.1}$$

with stator voltage $\boldsymbol{u}_\mathrm{s}^\mathrm{dq}$, stator, rotor and core loss currents $\boldsymbol{i}_\mathrm{s}^\mathrm{dq}, \boldsymbol{i}_\mathrm{r}^\mathrm{dq}$ and $\boldsymbol{i}_\mathrm{c}^\mathrm{dq}$—where by means of KCL

$$\boldsymbol{i}_\mathrm{s}^\mathrm{dq} = \boldsymbol{i}_\mathrm{c}^\mathrm{dq} + \boldsymbol{i}_\mathrm{m}^\mathrm{dq} - \boldsymbol{i}_\mathrm{r}^\mathrm{dq} \tag{3.2}$$

holds—and stator and rotor flux linkages

$$\boldsymbol{\psi}_\mathrm{s}^\mathrm{dq} = \boldsymbol{\psi}_\mathrm{m}^\mathrm{dq} + \boldsymbol{\psi}_{\mathrm{s}\sigma}^\mathrm{dq} \qquad \text{and} \qquad \boldsymbol{\psi}_\mathrm{r}^\mathrm{dq} = \boldsymbol{\psi}_\mathrm{m}^\mathrm{dq} + \boldsymbol{\psi}_{\mathrm{r}\sigma}^\mathrm{dq}. \tag{3.3}$$

Furthermore, $\boldsymbol{\psi}_\mathrm{m}^\mathrm{dq}$ denotes the main (air gap) flux linkage, while $\boldsymbol{\psi}_{\mathrm{s}\sigma}^\mathrm{dq}$ and $\boldsymbol{\psi}_{\mathrm{r}\sigma}^\mathrm{dq}$ denote the stator and rotor stray flux linkages, respectively. The temperature dependent stator, rotor and (additionally frequency dependent) core resistance are denoted by $R_\mathrm{s}(\vartheta_\mathrm{s}), R_\mathrm{r}(\vartheta_\mathrm{r})$ and $R_\mathrm{c}(\vartheta_\mathrm{c},\omega_\mathrm{k})$ with respective temperatures $\vartheta_\mathrm{s}, \vartheta_\mathrm{r}$ and ϑ_c. Moreover, $\omega_\mathrm{r} = n_\mathrm{p}\omega_\mathrm{m}$ is the electrical rotor speed, ω_m the mechanical rotor speed, n_p the number of pole pairs, Θ_m the total moment of inertia, and m_m, m_f and m_l denote machine, friction and load torque, respectively.

The stator-side torque expression $m_{\mathrm{m,s}}$ is given by (see e.g. [123, Sec. 15.18])

$$\begin{aligned}
\overbrace{\tfrac{3}{2}n_\mathrm{p}\boldsymbol{i}_\mathrm{s}^{\mathrm{dq}\top}\boldsymbol{J}\boldsymbol{\psi}_\mathrm{s}^\mathrm{dq}}^{=:m_{\mathrm{m,s}}} &\overset{(3.3)}{=} \tfrac{3}{2}n_\mathrm{p}\boldsymbol{i}_\mathrm{s}^{\mathrm{dq}\top}\boldsymbol{J}(\boldsymbol{\psi}_\mathrm{m}^\mathrm{dq}+\boldsymbol{\psi}_{\mathrm{s}\sigma}^\mathrm{dq}) = \tfrac{3}{2}n_\mathrm{p}\boldsymbol{i}_\mathrm{s}^{\mathrm{dq}\top}\boldsymbol{J}\boldsymbol{\psi}_\mathrm{m}^\mathrm{dq} + \overbrace{\tfrac{3}{2}n_\mathrm{p}\boldsymbol{i}_\mathrm{s}^{\mathrm{dq}\top}\boldsymbol{J}\boldsymbol{\psi}_{\mathrm{s}\sigma}^\mathrm{dq}}^{=0}\\
&\overset{(3.2)}{=} \tfrac{3}{2}n_\mathrm{p}(\boldsymbol{i}_\mathrm{c}^\mathrm{dq}+\boldsymbol{i}_\mathrm{m}^\mathrm{dq}-\boldsymbol{i}_\mathrm{r}^\mathrm{dq})^\top\boldsymbol{J}\boldsymbol{\psi}_\mathrm{m}^\mathrm{dq} = \underbrace{\tfrac{3}{2}n_\mathrm{p}\boldsymbol{i}_\mathrm{c}^{\mathrm{dq}\top}\boldsymbol{J}\boldsymbol{\psi}_\mathrm{m}^\mathrm{dq}}_{=:m_{\mathrm{m,c}}} + \underbrace{-\tfrac{3}{2}n_\mathrm{p}\boldsymbol{i}_\mathrm{r}^{\mathrm{dq}\top}\boldsymbol{J}\boldsymbol{\psi}_\mathrm{r}^\mathrm{dq}}_{=:m_{\mathrm{m,r}}}.
\end{aligned} \tag{3.4}$$

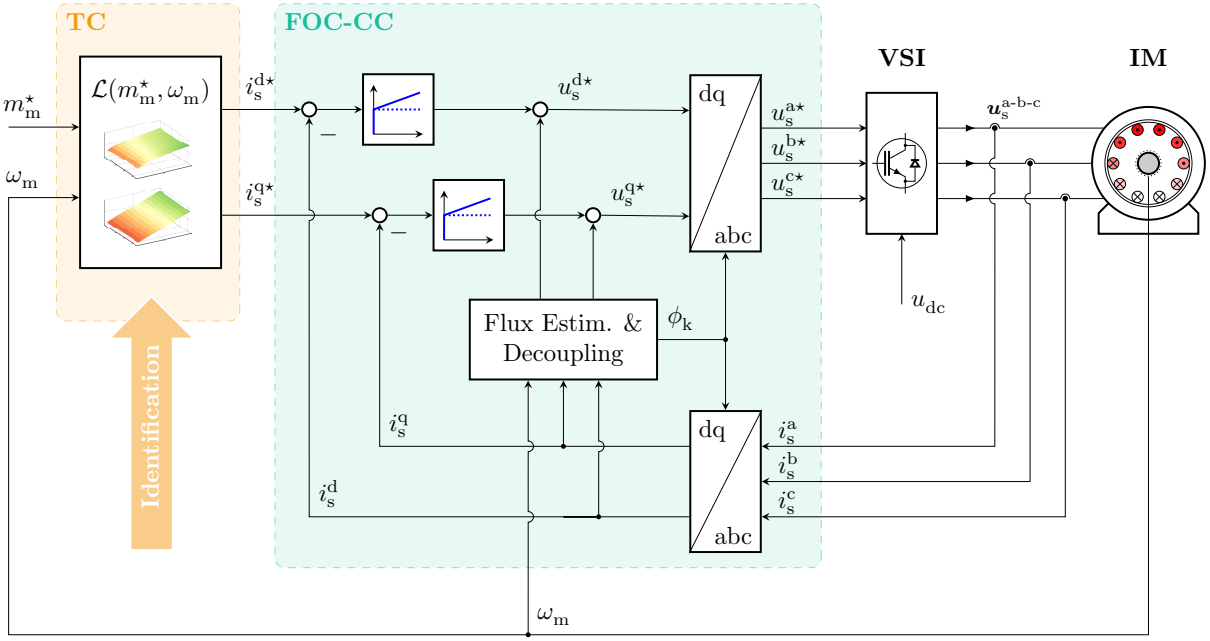

Figure 3.3: *Overview of the cascaded control system for the machine identification and maximum efficiency operation, with LUT-based torque controller (TC) and FOC-like current controller (FOC-CC).*

Note that in the equation above $\boldsymbol{i}_\mathrm{s}^{\mathrm{dq}\top}\boldsymbol{J}\boldsymbol{\psi}_{\mathrm{s}\sigma}^{\mathrm{dq}} = 0$, $\boldsymbol{i}_\mathrm{m}^{\mathrm{dq}\top}\boldsymbol{J}\boldsymbol{\psi}_\mathrm{m}^{\mathrm{dq}} = 0$ and $\boldsymbol{i}_\mathrm{r}^{\mathrm{dq}\top}\boldsymbol{J}\boldsymbol{\psi}_{\mathrm{r}\sigma}^{\mathrm{dq}} = 0$ were used, as flux linkage and current of an isotropic inductor point into the same direction. It can be deduced from the torque balance (3.4) that the rotor-side torque $m_\mathrm{m,r}$ is reduced with respect to the stator-side torque $m_\mathrm{m,s}$ by the core loss related torque expression $m_\mathrm{m,c}$. The rotor side torque $m_\mathrm{m,r} = m_\mathrm{m}$, however, is the *effective* (or *usable*) machine torque m_m which causes any rotor acceleration. The effect of torque detuning due to core losses was thoroughly investigated in [122].

3.1.2 Torque and current control system

An overview of the FOC-like control system is given in Fig. 3.3: A LUT-based feedforward torque controller ('TC' in the figure) is employed, which translates a given reference torque $m_\mathrm{m}^\star$ and the actual speed ω_m into the stator reference currents $i_\mathrm{s}^{\mathrm{d}\star}$ and $i_\mathrm{s}^{\mathrm{q}\star}$. The LUTs are obtained from the machine identification procedure described in Sec. 3.2. Different torque control strategies can be used, which are further elaborated in Sec. 3.2.3. The respective stator reference currents are fed to the underlying current control system ('FOC-CC' in the figure), which is implemented as a standard (indirect) rotor-flux oriented FOC controller (refer to e.g. [108, Sec. 9.2] and [124, Sec. 13.4.4] for more details). The current controller comprises (i) two proportional-integral (PI) controllers with anti-windup (conditional integration, see e.g. [125, Sec. 4.1]) for zero offset reference tracking of both current components, and (ii) a feedforward disturbance compensation (decoupling network) which compensates for the back electromotive force (EMF), thus improving the transient response. Output of the current controller is the stator reference voltage $\boldsymbol{u}_\mathrm{s}^{\mathrm{dq}\star}$.

Since the rotor flux linkage $\boldsymbol{\psi}_\mathrm{r}^{\mathrm{dq}}$ is not measured, a flux observer is used. As the main goal is to obtain a *fixed* and *reproducible* orientation rather than an accurate rotor flux estimate, a simple open-loop flux observer meets the requirements (other types of observers are feasible, too), i.e.

$$\frac{\mathrm{d}}{\mathrm{d}t}\hat{\psi}_\mathrm{r}^\mathrm{d} = \alpha\, i_\mathrm{s}^\mathrm{d} - \beta\, \hat{\psi}_\mathrm{r}^\mathrm{d}, \tag{3.5}$$

where $\hat{\psi}_\mathrm{r}^\mathrm{d}$ denotes the estimated rotor flux linkage and $\alpha, \beta > 0$ are machine constants. Moreover, *estimated* rotor flux orientation is obtained by selecting the electrical frequency as

$$\omega_\mathrm{k} = \omega_\mathrm{r} + \alpha\, \frac{i_\mathrm{s}^\mathrm{q}}{\hat{\psi}_\mathrm{r}^\mathrm{d}}, \tag{3.6}$$

which is feasible for all $\hat{\psi}_\mathrm{r}^\mathrm{d} \neq 0$. The resulting (Park) transformation angle $\phi_\mathrm{k} = \int \omega_\mathrm{k} \mathrm{d}t$ aligns the dq-reference frame with the estimated rotor flux linkage $\hat{\psi}_\mathrm{r}^\mathrm{d}$ (see Fig. 3.1). Based on the *linear* machine model (2.31), the parameters are selected as $\alpha = \frac{L_\mathrm{m}}{T_\mathrm{r}}$ and $\beta = \frac{1}{T_\mathrm{r}}$, where $T_\mathrm{r} = \frac{L_\mathrm{r}}{R_\mathrm{r}}$ is the rotor time constant, L_r is the rotor self inductance and L_m is the main inductance. Since the inductances vary with the saturation level of the main flux and the rotor resistance depends on the rotor temperature ϑ_r, the estimated values for α and β are typically inaccurate. As a consequence, the dq-reference frame is not perfectly aligned with the *actual* rotor flux linkage (hence the term 'FOC-like', see Fig. 3.1). However, a key aspect of the presented approach is that, for arbitrary values of α, reproducible operating points can be generated, which can be evaluated with respect to efficiency and do not rely on an accurate rotor flux orientation. It will be shown that this assumption holds only partially true, since the varying temperature affects the reproducibility of the operating points. Nevertheless, if the machine identification is performed on a pre-heated machine, the results can be considered valid and reproducible.

Remark 13. *Note that, in steady-state ($\frac{\mathrm{d}}{\mathrm{d}t}\hat{\psi}_\mathrm{r}^\mathrm{d} = 0$ in (3.5)), the electrical frequency can be stated as*

$$\omega_\mathrm{k} = \omega_\mathrm{r} + \beta \frac{i_\mathrm{s}^\mathrm{q}}{i_\mathrm{s}^\mathrm{d}} = \omega_\mathrm{r} + \beta \tan\varphi_i, \tag{3.7}$$

where φ_i is the angle of the current vector $(i_\mathrm{s}^\mathrm{d}, i_\mathrm{s}^\mathrm{q})$ in the dq*-reference frame. As a consequence, the steady-state slip frequency $\omega_\mathrm{k} - \omega_\mathrm{r}$ is fully determined by the stator currents and the (constant) scaling factor β. Vice versa, any pair of $(i_\mathrm{s}^\mathrm{d}, i_\mathrm{s}^\mathrm{q})$-currents produces a specific ω_k for a given speed ω_r and, hence, a unique operating point $(\omega_\mathrm{k} - \omega_\mathrm{r}, \|\boldsymbol{i}_\mathrm{s}^\mathrm{dq}\|)$. Note further that ω_k should be limited as it tends to infinity for $i_\mathrm{s}^\mathrm{d} = 0$ or $\varphi_i = \frac{\pi}{2}$.*

3.1.3 Steady-state model and system analysis

The machine identification is based on steady-state measurements at unique operating points $(i_\mathrm{s}^{\mathrm{d}\star}, i_\mathrm{s}^{\mathrm{q}\star}) = (i_\mathrm{s}^\mathrm{d}, i_\mathrm{s}^\mathrm{q})$, tracked by the current controllers as described in the preceding section. Prior to the detailed description of the identification procedure, an analysis of the steady-state system is conducted, emphasizing the difficulties of estimating the machine torque when core losses are taken into account.

The steady-state electrical system with vectorial T-equivalent circuit as depicted in Fig. 3.4 is derived from (3.1) by assuming all derivative terms zero, i.e.

$$\left.\begin{aligned} \boldsymbol{u}_\mathrm{s}^\mathrm{dq} &= R_\mathrm{s}(\vartheta_\mathrm{s})\boldsymbol{i}_\mathrm{s}^\mathrm{dq} + \omega_\mathrm{k}\boldsymbol{J}\boldsymbol{\psi}_\mathrm{s}^\mathrm{dq}, \\ \mathbf{o}_2 &= R_\mathrm{r}(\vartheta_\mathrm{r})\boldsymbol{i}_\mathrm{r}^\mathrm{dq} + (\omega_\mathrm{k} - \omega_\mathrm{r})\boldsymbol{J}\boldsymbol{\psi}_\mathrm{r}^\mathrm{dq}, \\ \mathbf{o}_2 &= R_\mathrm{c}(\vartheta_\mathrm{c}, \omega_\mathrm{k})\boldsymbol{i}_\mathrm{c}^\mathrm{dq} - \omega_\mathrm{k}\boldsymbol{J}\boldsymbol{\psi}_\mathrm{m}^\mathrm{dq}. \end{aligned}\right\} \tag{3.8}$$

Without loss of generality, it is assumed for the remainder of this analysis that the main flux linkage can be described as the product of magnetizing current and main inductance $L_\mathrm{m}(\boldsymbol{i}_\mathrm{m}^\mathrm{dq})$, i.e. $\boldsymbol{\psi}_\mathrm{m}^\mathrm{dq} = L_\mathrm{m}(\boldsymbol{i}_\mathrm{m}^\mathrm{dq})\boldsymbol{i}_\mathrm{m}^\mathrm{dq}$.

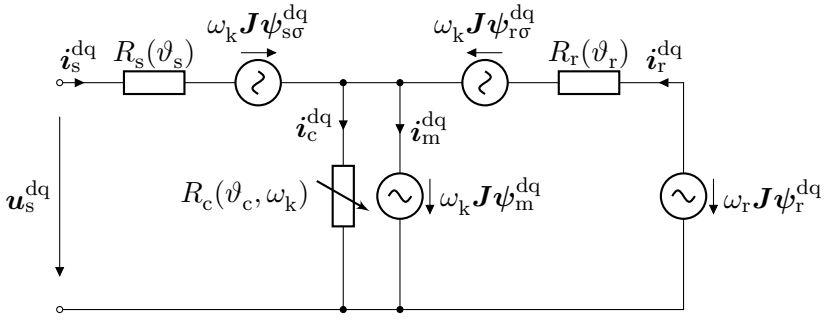

Figure 3.4: *Vectorial steady-state T-equivalent circuit (including core losses) of the SCIM in arbitrarily rotating* dq*-coordinates.*

Remark 14. *The temporary assumption of linear flux linkages is imposed for illustrative purposes. Without this assumption, stating the magnetizing current as a function of the stator current (or vice versa) and drawing the vector diagram is not possible. In the nonlinear case, the main inductance changes due to magnetic saturation. However, as the magnetizing inductance can be assigned any positive number in the analysis, the results are transferable to the nonlinear case and the assumption does not affect the generality of the presented analysis.*

As a consequence of the linear flux assumption, the last equation of (3.8) can be solved for the core loss current, i.e.

$$\boldsymbol{i}_\mathrm{c}^{\mathrm{dq}} = \underbrace{\frac{\omega_\mathrm{k} L_\mathrm{m}(\boldsymbol{i}_\mathrm{m}^{\mathrm{dq}})}{R_\mathrm{c}(\vartheta_\mathrm{c},\omega_\mathrm{k})}\boldsymbol{J}}_{=:\boldsymbol{M}_\mathrm{c}(\boldsymbol{i}_\mathrm{m}^{\mathrm{dq}})}\boldsymbol{i}_\mathrm{m}^{\mathrm{dq}}. \tag{3.9}$$

Assuming further that the rotor stray flux linkage can be stated as $\boldsymbol{\psi}_{\mathrm{r}\sigma}^{\mathrm{dq}} = L_{\mathrm{r}\sigma}\boldsymbol{i}_\mathrm{r}^{\mathrm{dq}}$, the rotor flux linkage $\boldsymbol{\psi}_\mathrm{r}^{\mathrm{dq}} = L_\mathrm{m}(\boldsymbol{i}_\mathrm{m}^{\mathrm{dq}})\boldsymbol{i}_\mathrm{m}^{\mathrm{dq}} + L_{\mathrm{r}\sigma}\boldsymbol{i}_\mathrm{r}^{\mathrm{dq}}$ is obtained. Inserting this expression into the second equation of (3.8) and solving for $\boldsymbol{i}_\mathrm{r}^{\mathrm{dq}}$ gives

$$\boldsymbol{i}_\mathrm{r}^{\mathrm{dq}} = \underbrace{L_\mathrm{m}(\boldsymbol{i}_\mathrm{m}^{\mathrm{dq}})\left(-L_{\mathrm{r}\sigma}\boldsymbol{I}_2 + \frac{R_\mathrm{r}(\vartheta_\mathrm{r})}{(\omega_\mathrm{k}-\omega_\mathrm{r})}\boldsymbol{J}\right)^{-1}}_{=:\boldsymbol{M}_\mathrm{r}(\boldsymbol{i}_\mathrm{m}^{\mathrm{dq}})}\boldsymbol{i}_\mathrm{m}^{\mathrm{dq}}. \tag{3.10}$$

For the steady-state analysis, it was assumed that the main inductance is constant, which allows expressing the magnetizing current as a function of the stator current, i.e.

$$\boldsymbol{i}_\mathrm{s}^{\mathrm{dq}} \overset{(3.2)}{=} \boldsymbol{i}_\mathrm{m}^{\mathrm{dq}} + \boldsymbol{i}_\mathrm{c}^{\mathrm{dq}} - \boldsymbol{i}_\mathrm{r}^{\mathrm{dq}} \overset{(3.9),(3.10)}{=} (\boldsymbol{I}_2 + \boldsymbol{M}_\mathrm{c} - \boldsymbol{M}_\mathrm{r})\,\boldsymbol{i}_\mathrm{m}^{\mathrm{dq}} \quad\Longrightarrow\quad \boldsymbol{i}_\mathrm{m}^{\mathrm{dq}} = (\boldsymbol{I}_2 + \boldsymbol{M}_\mathrm{c} - \boldsymbol{M}_\mathrm{r})^{-1}\,\boldsymbol{i}_\mathrm{s}^{\mathrm{dq}}. \tag{3.11}$$

This explicit expression in combination with the model equations of the preceding sections and Remark 13 finally allows drawing the steady-state vector diagrams. In the following let $\boldsymbol{I}^* := \left[\begin{smallmatrix}1 & 0\\ 0 & -1\end{smallmatrix}\right]$ denote a matrix which, when multiplied with a vector, produces a vector with equal d-component and q-component of opposing sign (similar to the 'complex conjugate'). All quantities have been normalized to their respective base values (parameters given in Tab. B.1). Moreover, the estimated machine parameter $\widehat{\alpha} = 0.7\,\alpha$ is assumed for the calculation of ω_k as in (3.6), i.e. an angle misalignment is deliberately provoked. Figure 3.5 shows two different vector diagrams, (a) neglecting and (b) considering iron losses. In order to stress the impact of iron losses, two different operating points have been plotted for constant speed of $\omega_\mathrm{r} = \omega_{\mathrm{r,nom}}$, i.e. $\boldsymbol{i}_\mathrm{s}^{\mathrm{dq}+} = (0.2, 0.6)^\top \cdot \hat{i}_{\mathrm{s,nom}}$ (superscript '+', motoring mode) and $\boldsymbol{i}_\mathrm{s}^{\mathrm{dq}-} = (0.2, -0.6)^\top \cdot \hat{i}_{\mathrm{s,nom}} = \boldsymbol{I}^*\boldsymbol{i}_\mathrm{s}^{\mathrm{dq}+}$ (superscript '−', generating mode).

Remark 15. *Note that the core resistance R_c depends on the frequency ω_k, which differs in general for motoring and generating mode, i.e. $\omega_\mathrm{k}^+ \neq \omega_\mathrm{k}^-$. However, for the sake of simplicity, equal core resistances have been assumed for the two operating points (motoring and generating mode), which is reasonable as the difference between the two frequencies is small, and hence the difference between the core resistance values is small, too.*

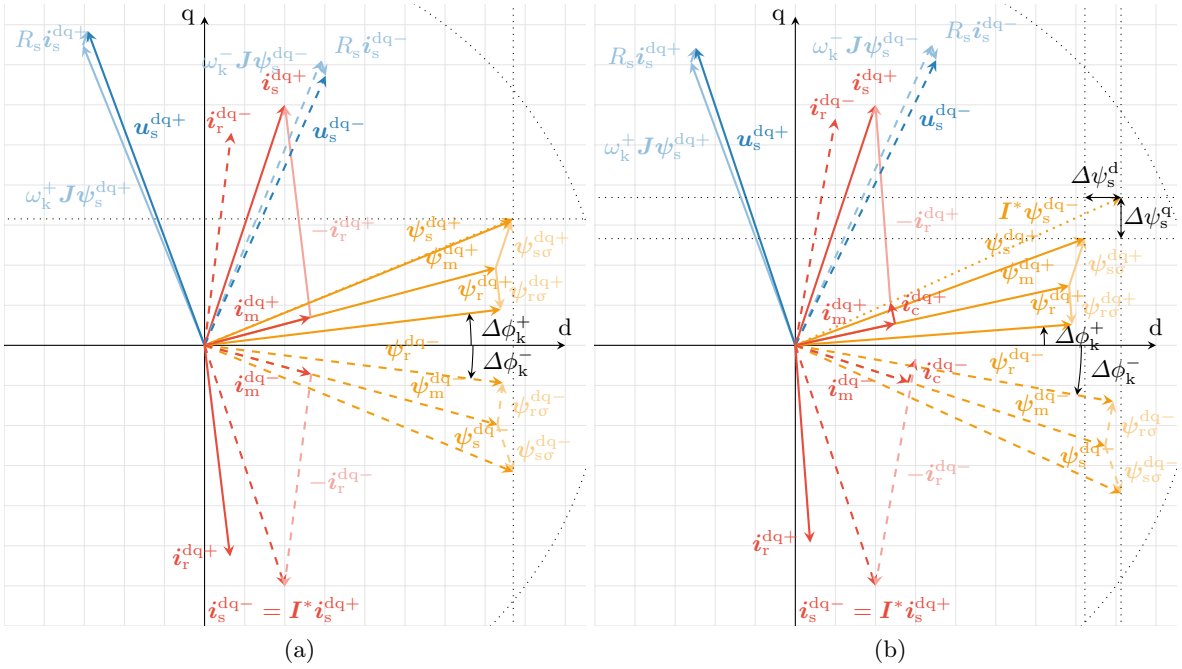

Figure 3.5: *Vector diagrams of the SCIM for operating points $\boldsymbol{i}_\mathrm{s}^{\mathrm{dq}+} = (0.2, 0.6)^\top \cdot \hat{i}_{\mathrm{s,nom}}$ (motoring mode) and $\boldsymbol{i}_\mathrm{s}^{\mathrm{dq}-} = (0.2, -0.6)^\top \cdot \hat{i}_{\mathrm{s,nom}}$ (generating mode) at $\omega_\mathrm{r} = \omega_{\mathrm{r,nom}}$: (a) iron losses neglected and (b) iron losses considered.*

An important observation for the case when iron losses are neglected (Fig. 3.5a) is, that the flux linkages and currents are symmetric with respect to the d-axis; in particular $\boldsymbol{\psi}_\mathrm{s}^{\mathrm{dq}+} = \boldsymbol{I}^*\boldsymbol{\psi}_\mathrm{s}^{\mathrm{dq}-}$ holds. Moreover, the angle offset is equal for motoring and generating mode, i.e. $\Delta\phi_\mathrm{k}^+ = -\Delta\phi_\mathrm{k}^-$. For the second case, when iron losses are considered (Fig. 3.5b), the following conclusions can be drawn:

- The flux linkage symmetry of motoring and generating conditions declines, in particular $\boldsymbol{\psi}_\mathrm{s}^{\mathrm{dq}+} \neq \boldsymbol{I}^*\boldsymbol{\psi}_\mathrm{s}^{\mathrm{dq}-}$.
- The alignment error $\Delta\phi_\mathrm{k}$ differs for motoring and generating conditions, i.e. $\Delta\phi_\mathrm{k}^+ \neq -\Delta\phi_\mathrm{k}^-$.

The symmetry property of the stator flux linkages is a useful tool which allows for remedying stator resistance variations, i.e. due to a change of the winding temperature, or voltage reconstruction errors, i.e. due to voltage drops in the power electronic devices of the VSI. Therefore, if iron losses are neglected, a good estimate of the stator-side torque $m_{\mathrm{m,s}}$, and—assuming $m_{\mathrm{m,c}} \approx 0$—of the rotor-side machine torque $m_{\mathrm{m,r}}$ can be obtained [see (3.4)]. However, if the stator resistance can be tracked online by measurement, the effect of iron losses can be considered in the calculations and the flux imbalance can be determined exactly.

3.2 Machine identification procedure

In this section, the machine identification procedure is described, which produces the look-up tables $\mathcal{L}^{\mathrm{M}}_{i_\mathrm{s}^{\mathrm{d}\star}}(m^\star_\mathrm{m}, \omega_\mathrm{m})$ and $\mathcal{L}^{\mathrm{M}}_{i_\mathrm{s}^{\mathrm{q}\star}}(m^\star_\mathrm{m}, \omega_\mathrm{m})$, mapping a given reference torque $m^\star_\mathrm{m}$ and the actual machine speed ω_m to the reference currents $i_\mathrm{s}^{\mathrm{d}\star}$ and $i_\mathrm{s}^{\mathrm{q}\star}$, subject to some torque control strategy 'M'. The procedure itself is split into the three sub-tasks (see also process chart in Fig. 3.6), namely

(i) data acquisition (see Sec. 3.2.1),

(ii) postprocessing and machine map extraction (see Sec. 3.2.2) and

(iii) look-up table generation (see Sec. 3.2.3).

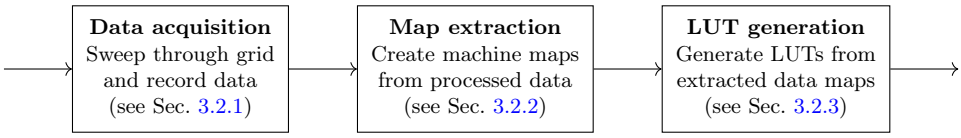

Figure 3.6: *Generic machine identification process chart.*

3.2.1 Data acquisition

In order to be able to calculate the machine efficiency (with or without the use of a torque sensor), the following data is acquired:

- stator currents $\boldsymbol{i}_\mathrm{s}^{\mathrm{dq}}$ and references $\boldsymbol{i}_\mathrm{s}^{\mathrm{dq}\star}$ (dq-reference frame),
- stator reference voltages $\boldsymbol{u}_\mathrm{s}^{\alpha\beta\star}$ ($\alpha\beta$-reference frame, as inverter delay needs to be compensated),
- electrical speed ω_k and angle ϕ_k,
- mechanical speed ω_m,
- rotor-side machine torque $m_\mathrm{m} = m_\mathrm{m,r}$ (optional), and
- stator resistance R_s / winding temperature ϑ_s (optional, not available here).

A current control system as described in Sec. 3.1.2 is prerequisite for the data acquisition. The controller implementation requires basic parameter knowledge (see Tab. B.1), e.g. obtained from the standard no-load and locked-rotor tests (refer to e.g. [124, Sec. 13.6.2]). At the same time the prime mover is speed controlled enforcing a constant shaft speed of $\omega_\mathrm{m} = \omega^\star_\mathrm{m}$. Measurements are conducted for different speeds, i.e. the entire current grid is covered before the reference speed is changed.

3.2.1.1 Reference current sweeping

Since a constant speed is enforced by the prime mover, the induction machine currents can be set arbitrarily without accelerating or decelerating the rotor. The fundamental idea is that each combination of stator currents $\boldsymbol{i}_\mathrm{s}^{\mathrm{dq}} = (i_\mathrm{s}^\mathrm{d}, i_\mathrm{s}^\mathrm{q})$ represents a *reproducible* and *unique* operating point. Hence, the objective is to gather information for each pair of currents within the feasible range, i.e.

$$\boldsymbol{i}_\mathrm{s}^{\mathrm{dq}} \in \mathbb{I}_\mathrm{s} = \{\boldsymbol{i}_\mathrm{s}^{\mathrm{dq}} \,|\, {i_\mathrm{s}^\mathrm{d}}^2 + {i_\mathrm{s}^\mathrm{q}}^2 \leq \hat{i}^2_{\mathrm{s,nom}}\}. \tag{3.12}$$

This is achieved by sampling the current plane on a regular grid and sweeping through each grid point, while logging the measured data (see list above). For reasons of redundancy, only the positive

Table 3.1: *Parameters of the machine identification procedure.*

Parameter	Variable	Value	Unit
Window length		1.2	s
Grid dimensions	m	16	
	n	16	
Current limits	$i^{\mathrm{d}}_{\mathrm{s,min}}$	0.05	p.u.
	$i^{\mathrm{d}}_{\mathrm{s,max}}$	0.5	p.u.
	$i^{\mathrm{q}}_{\mathrm{s,max}}$	1	p.u.

d-axis is covered, i.e. measurements are recorded for the first and fourth quadrant of the current plane only.

The first quadrant of the generated current grid is depicted in Fig. 3.7a. A minimum amount of excitation current $i^{\mathrm{d}}_{\mathrm{s,min}} > 0$ is required for the rotor flux orientation to operate properly (recall Remark 13). On the other hand, magnetic saturation sets in for high values of $i^{\mathrm{d}}_{\mathrm{s}}$, which motivates for an upper limit $i^{\mathrm{d}}_{\mathrm{s,max}}$ (e.g. half rated current), i.e. $i^{\mathrm{d}\star}_{\mathrm{s}} \in [i^{\mathrm{d}}_{\mathrm{s,min}}, i^{\mathrm{d}}_{\mathrm{s,max}}]$. In turn, the absolute value of the q-current is varied from zero to some defined maximum value $i^{\mathrm{q}}_{\mathrm{s,max}}$, i.e. $|i^{\mathrm{q}\star}_{\mathrm{s}}| \in [0, i^{\mathrm{q}}_{\mathrm{s,max}}]$. The resulting grid vectors (orange dots in the figure) are given by

$$\left.\begin{aligned} \bar{\boldsymbol{i}}^{\mathrm{d}}_{\mathrm{s}} &:= \left(\bar{i}^{\mathrm{d}}_{\mathrm{s}}[1] = i^{\mathrm{d}}_{\mathrm{s,min}}, \quad \dots \quad , \bar{i}^{\mathrm{d}}_{\mathrm{s}}[m] = i^{\mathrm{d}}_{\mathrm{s,max}}\right) \\ \text{and} \quad \bar{\boldsymbol{i}}^{\mathrm{q}}_{\mathrm{s}} &:= \left(\bar{i}^{\mathrm{q}}_{\mathrm{s}}[1] = 0, \quad \dots \quad , \bar{i}^{\mathrm{q}}_{\mathrm{s}}[n] = i^{\mathrm{q}}_{\mathrm{s,max}}\right), \end{aligned}\right\} \tag{3.13}$$

where the variables m and n determine the grid size and should be a trade-off between accuracy and effort. Note that the grid corners may be located outside of $\mathbb{I}_{\mathrm{s}}$, i.e. the stator currents may exceed the current limit if all pairs of $\boldsymbol{i}^{\mathrm{dq}\star}_{\mathrm{s}} \in \{\bar{\boldsymbol{i}}^{\mathrm{d}}_{\mathrm{s}} \times \bar{\boldsymbol{i}}^{\mathrm{q}}_{\mathrm{s}}\}$ are used (gray dots in the figure). The respective grid points may be skipped or recorded nonetheless, if sufficient cooling is provided.

The measurement is performed in analogy to the procedure described in [60]. For each combination of $i \in \{1, \dots, m\}$ and $j \in \{1, \dots, n\}$, measurements are recorded as illustrated in Fig. 3.7b: The *active period* consists of a motoring subperiod $(\bar{i}^{\mathrm{d}}_{\mathrm{s}}[i], \bar{i}^{\mathrm{q}}_{\mathrm{s}}[j])$ [Mot. 1], a braking subperiod $(\bar{i}^{\mathrm{d}}_{\mathrm{s}}[i], -\bar{i}^{\mathrm{q}}_{\mathrm{s}}[j])$ [Gen.] and a second motoring subperiod [Mot. 2], in order to compensate for temperature variations (by averaging over two motoring subperiods). In contrast to the *idle period* introduced after the active period in [60], a basic *temperature control* [ϑ-control] period is introduced, which can be used to heat up (full braking torque [- - -]) or cool down the machine (zero torque [——]), and thus to regulate the temperature (to a limited extent). Finally, a short idle period [Idle] is added for the q-current to be reset to zero.

In order to avoid accumulations of high or low current periods, the reference indices are resorted as depicted in Fig. 3.7c: Instead of following the ascending order $0, 1, 2, \dots, n$ (examplary for index j) , the reference index order is changed to $0, n, 1, n-1, \dots$, i.e. the current is toggling between low and high values.

An exemplary measurement window is shown in Fig. 3.8, recorded at $\omega^{\star}_{\mathrm{m}} \approx 149\,\mathrm{rad\,s^{-1}}$ (half rated speed) and with $\boldsymbol{i}^{\mathrm{dq}\star}_{\mathrm{s}} = (1.4\,\mathrm{A}, 5.4\,\mathrm{A})$ for motoring mode and $\boldsymbol{i}^{\mathrm{dq}\star}_{\mathrm{s}} = (1.4\,\mathrm{A}, -5.4\,\mathrm{A})$ for generating mode, respectively. It can be seen that after each step in the q-reference current, a short transient time occurs, during which the steady-state assumption does not hold. The shaded areas [▒] mark the used steady-state intervals for the average value calculation. Note that the settling time may vary, depending on the speed controller tuning and the amount of (load torque) perturbation. Therefore, the averaging interval may appear rather short in Fig. 3.8 as a conservative guess of the settling time was used.

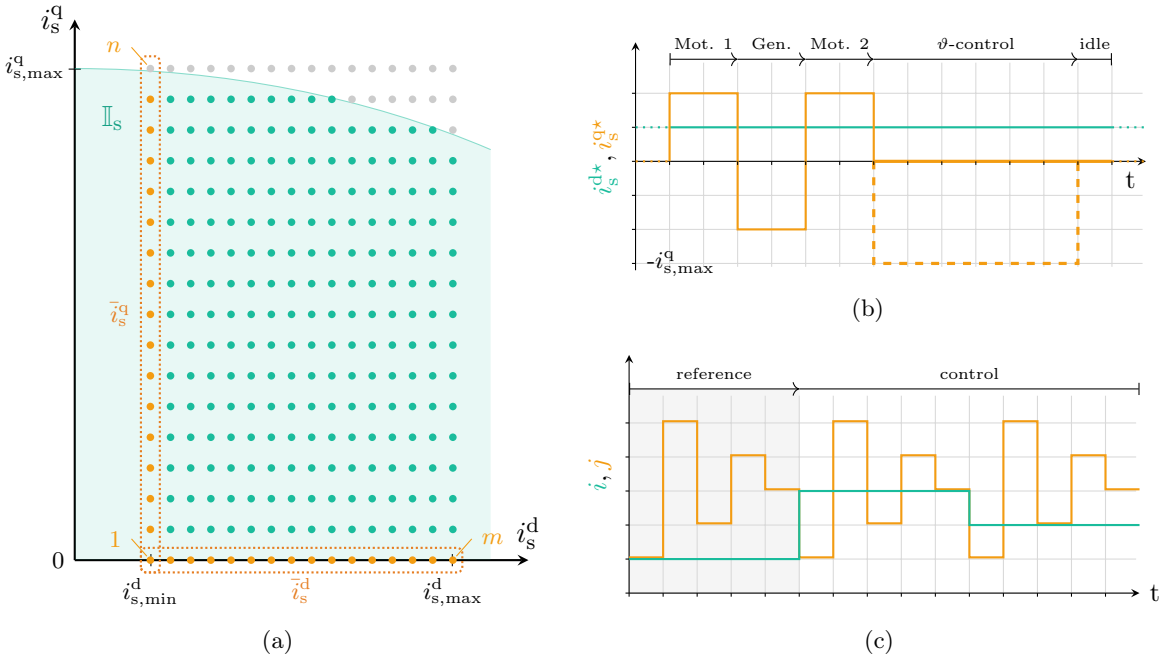

Figure 3.7: *Data acquisition subtask: (a) Current grid (first quadrant), (b) subperiods of a single measurement sequence with ϑ-control and for constant (i, j) and (c) illustration of the reference current index sweeping (i, j).*

3.2.1.2 Active temperature regulation

The ϑ-controller, which is implemented as a simple hysteresis controller, uses the measurements from the preceding motoring and braking periods, in order to select the respective control action (*heat-up* or *cool-down*). In anticipation of Sec. 3.2.2.2 and assuming steady-state, the stator d-flux linkage can be calculated using (3.8) as

$$\psi_s^d = \frac{1}{\omega_k}\left(u_s^q - R_s(\vartheta_s) i_s^q\right) \quad \Longrightarrow \quad \begin{cases} \psi_s^{d+} = \frac{1}{\omega_k^+}(u_s^{q+} - R_s(\vartheta)|i_s^q|), & i_s^q \geq 0, \\ \psi_s^{d-} = \frac{1}{\omega_k^-}(u_s^{q-} + R_s(\vartheta)|i_s^q|), & i_s^q < 0, \end{cases} \tag{3.14}$$

where superscripts '+' and '−' indicate motoring and generating mode, respectively. In the steady-state analysis it was shown that $\psi_s^{d+} = \psi_s^{d-} - \Delta\psi_s^d$ holds, if iron losses are considered (see Fig. 3.5b). If $\Delta\psi_s^d \ll \psi_s^{d-}$ is assumed, i.e. $\psi_s^{d+} \approx \psi_s^{d-}$ holds, the stator resistance can be approximated by

$$\hat{R}_s \approx \frac{\frac{u_s^{q+}}{\omega_k^+} - \frac{u_s^{q-}}{\omega_k^-}}{\left(\frac{1}{\omega_k^+} + \frac{1}{\omega_k^-}\right)|i_s^q|}. \tag{3.15}$$

Note that the approximation (3.15) becomes inaccurate for higher speeds and large amounts of excitation, where iron losses become more significant. However, if the stator winding temperature cannot be measured directly, the estimated resistance value constitutes a decent approximation.

Since two motoring mode measurements are available, the average values can be calculated for ω_k^+ and u_s^{q+}, respectively, in order to account for temperature variations during the active measurement period. The stator winding temperature is approximated by (e.g. [103, p. 4])

$$\hat{\vartheta}_s = \vartheta_{s0} + \frac{1}{\alpha_{Cu}}\left(\frac{\hat{R}_s}{R_{s0}} - 1\right), \tag{3.16}$$

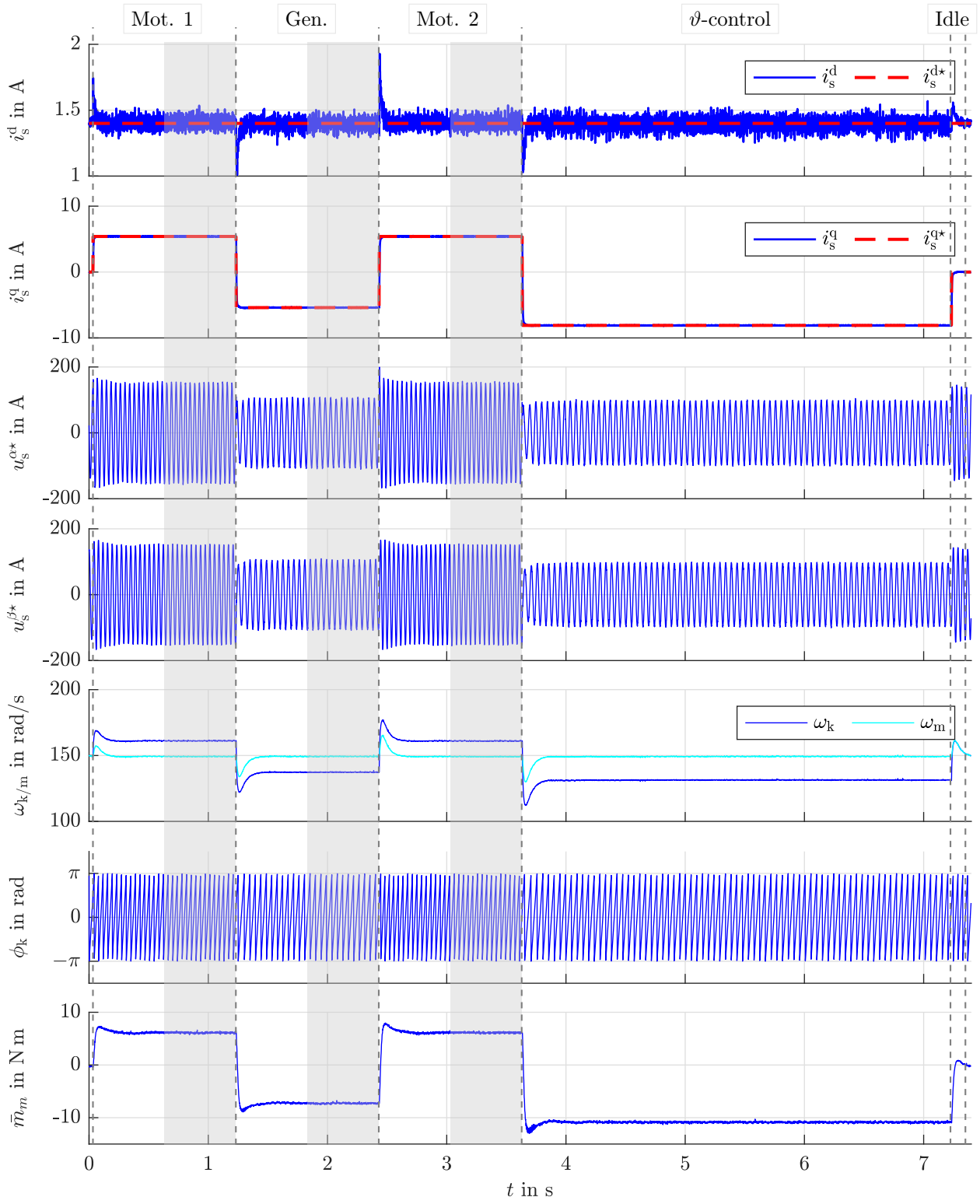

Figure 3.8: *Exemplary measurement window during the machine identification procedure for* $\omega_m^\star \approx 149\,\mathrm{rad\,s^{-1}}$ *and with* $\boldsymbol{i}_s^{dq\star} = (1.4\,\mathrm{A}, 5.4\,\mathrm{A})$ *for motoring mode and* $\boldsymbol{i}_s^{dq\star} = (1.4\,\mathrm{A}, -5.4\,\mathrm{A})$ *for generating mode, respectively. The averaging windows are marked by [ ].*

where $\alpha_{\mathrm{Cu}} = 3.93 \cdot 10^{-3}\,\mathrm{K}^{-1}$ [126] is the temperature coefficient of copper and ϑ_{s0} is the reference temperature for the reference stator resistance R_{s0}.

The objective of the ϑ-controller is to maintain a constant temperature. Therefore, in the first cycle of constant $i_{\mathrm{s}}^{\mathrm{d}\star}$ ($i = 1$, see shaded area in Fig. 3.7c), the resistance values are stored for each pair of q-currents, in order to collect resistance reference values. In the following cycles ($2 \leq i \leq m$), the updated resistance value is compared to its reference value (i.e. $i = 1$ and equal j). If the value increased, zero torque is applied. If it decreased, an active period of full braking torque is imposed. The length of the ϑ-control interval is equal to the active interval (Mot. 1, Gen., Mot. 2) length.

3.2.2 Postprocessing and machine map extraction

The conversion from time series data to machine maps requires various postprocessing steps. After a general description of the postprocessing steps, the most relevant maps are presented exemplary for a data set recorded at $\omega_{\mathrm{m}} = 0.5\,\mathrm{p.u.}$

3.2.2.1 Postprocessing steps

The raw data maps are created from the time series data (recorded at constant speed) and postprocessed afterwards, in order to refine the grid, expand the range, repair missing parts and smooth the map. In the following, the mapping procedure as implemented is explained and illustrated for the stator d-flux linkage $\psi_{\mathrm{s}}^{\mathrm{d}}$ and the efficiency η.

1. **Extract raw maps from time series data:**
   The recorded time series data of the measured, reconstructed or estimated signals is converted to machine maps by extracting the mean values at each operating point and storing them in respective raw data maps. Since the (controlled) physical system requires some time to reach steady-state as it enters a new operating point, a defined fraction of each measurement window is cut off and the averaging is performed for the remaining part only (illustrated by the shaded areas [ ] in Fig. 3.8). The raw maps of the stator flux linkage $\psi_{\mathrm{s}}^{\mathrm{d}}$ and the efficiency η are shown in Figs. 3.9a and 3.10a, respectively.

2. **Symmetrize flux linkages and recalculate dependent maps:**
   The calculated (raw) flux maps depend on an estimate of the stator resistance and the reconstructed (not measured) stator voltages, which are both prone to parameter or reconstruction errors. Deviations from the actual values introduce a flux linkage imbalance (between motoring and generating mode), in addition to the imbalance caused by iron losses. Any such imbalance can be removed by imposing $\boldsymbol{\psi}_{\mathrm{s}}^{\mathrm{dq}+} \stackrel{!}{=} \boldsymbol{I}^{*}\boldsymbol{\psi}_{\mathrm{s}}^{\mathrm{dq}-}$ [60], i.e. calculating the average values
   $$\psi_{\mathrm{s,avg}}^{\mathrm{d}} = 0.5(\psi_{\mathrm{s}}^{\mathrm{d}+} + \psi_{\mathrm{s}}^{\mathrm{d}-}) \qquad \text{and} \qquad \psi_{\mathrm{s,avg}}^{\mathrm{q}} = 0.5(\psi_{\mathrm{s}}^{\mathrm{q}+} - \psi_{\mathrm{s}}^{\mathrm{q}-}), \tag{3.17}$$
   for motoring and generating mode, respectively. Note that the symmetry assumption of the stator flux linkage only holds true though, if iron losses are negligible (see Sec. 3.1.3). Hence, a trade-off between the iron loss induced flux estimation error and the error caused by stator resistance or voltage misestimations has to be made. In this work, the elimination of stator resistance and voltage estimation errors is favoured over the consideration of iron losses, whose impact on the flux linkages is considered negligible. If the symmetrization is applied, all dependent quantities, such as the estimated torque and efficiency have to be recalculated. The resulting flux map is depicted in Fig. 3.9b. As the measured efficiency does not depend on the flux linkages, the respective efficiency map in Fig. 3.10b remains unchanged.

3. **Repair data in vicinity of $i_s^q = 0\,A$:**
   When changing from motoring to generating mode, i.e. at the transition from positive to negative i_s^q (and constant i_s^d) and at the reversal of active power flow, the estimated d-flux linkage shows an elevation along the d-axis. Independent of the cause, in terms of efficiency this area is rather irrelevant, since almost no power is transferred. In fact, the machine is in an ill-defined state, alternating between motoring and generating mode. Therefore, a minimum q-current $i_{s,min}^q$ is introduced, below which the measurements are discarded and 'repaired' by means of a 1D spline interpolation in q-direction. The interpolated areas are illustrated by the transparent areas in the map plots. The resulting flux map is depicted in Fig. 3.9c. Note that the efficiency is zero along the d-axis (isotropic machine), so that, for the efficiency map, interpolation is performed quadrant-wise, starting from the zeros at $i_s^q = 0$ and moving into ±q-direction. The result is shown in Fig. 3.10c.

4. **Refine grid:**
   When defining the base vectors for the data acquisition, it is reasonable to chose a logarithmic scale for the d-current. The d-current is directly associated with the stator flux linkage, which typically has a steep slope for low values of i_s^d, and becomes flatter for higher values of i_s^d, as magnetic saturation sets in. Independent of the initial grid size and shape, a grid refinement is performed using surface fitting tools [e.g. 2D linear interpolation in MATLAB®(Curve Fitting Toolbox), `interp2(...)` command]. The refined maps have equidistant base vectors and are shown in Figs. 3.9d and 3.10d.

5. **Expand map to four quadrants:**
   As four quadrant machine maps are typically used for synchronous machines (see e.g. [6, 11]), the redundant second and third quadrants are added by exploiting the symmetry properties of the respective quantities. As an example, the torque map is point-symmetric with respect to the origin. The resulting maps are depicted in Figs. 3.9e and 3.10e. Note that the additional quadrants are not relevant for the LUT generation as they contain redundant information only; for induction machines, typically some positive rotor d-flux linkage is set, as choosing a negative d-flux linkage would merely require swapping the sign of the q-current, in order to achieve the same behavior (e.g. torque output).

6. **Repair data in the vicinity of $i_s^d = 0\,A$:**
   As a minimum d-current $i_{s,min}^d$ has been defined for the data acquisition, the existing gap for $|i_s^d| < i_{s,min}^d$ is closed by applying surface fitting methods in the respective range. Again, the efficiency map is forced to be zero at $i_s^d = 0\,A$. Furthermore, in order to smooth the map and remove outliers or measurement noise, locally weighted linear regression surface fitting is applied to the whole map, which is accomplished in MATLAB® (Curve Fitting Toolbox, `fit(...)` command) using the 'loess' fitting option ('locally weighted scatter plot smooth'). Other fitting options, e.g. linear or cubic interpolation, are also feasible. Note that fitting the maps further allows for the extrapolation of data, such that for higher speeds, where the voltage limit becomes more relevant, the maps can be extended into the infeasible measurement range. The finalized maps are used for the torque control LUT generation and are shown in Figs. 3.9f and 3.10f, respectively.

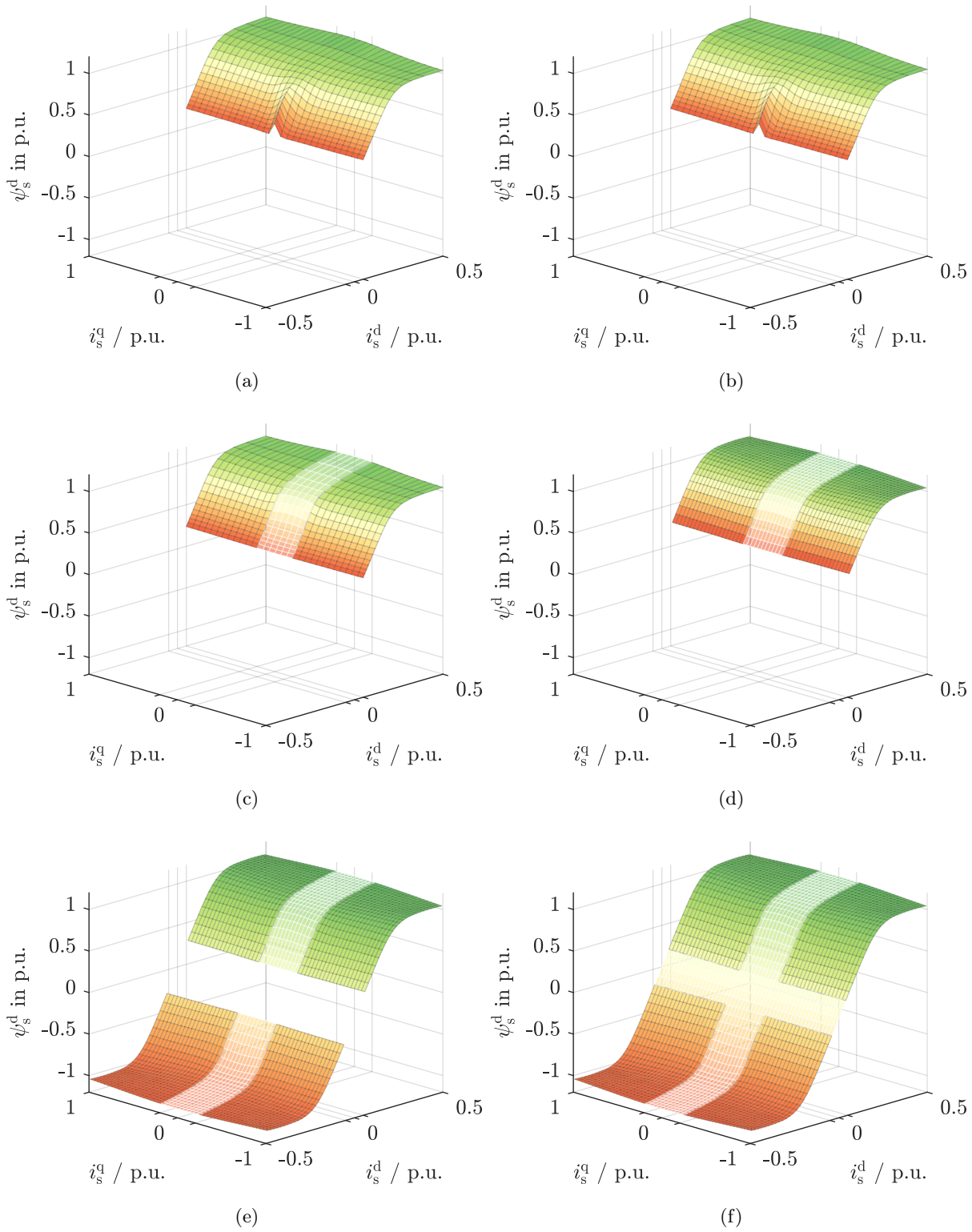

Figure 3.9: *Postprocessing of the stator* d*-flux linkage map: (a) Raw data, (b) symmetrized raw data, (c) repaired raw data in* i_s^q *direction near* $i_s^q = 0\,\mathrm{A}$*, (d) refined grid, (e) four quadrant expansion and (f) interpolation in* d*-direction near* $i_s^d = 0\,\mathrm{A}$.

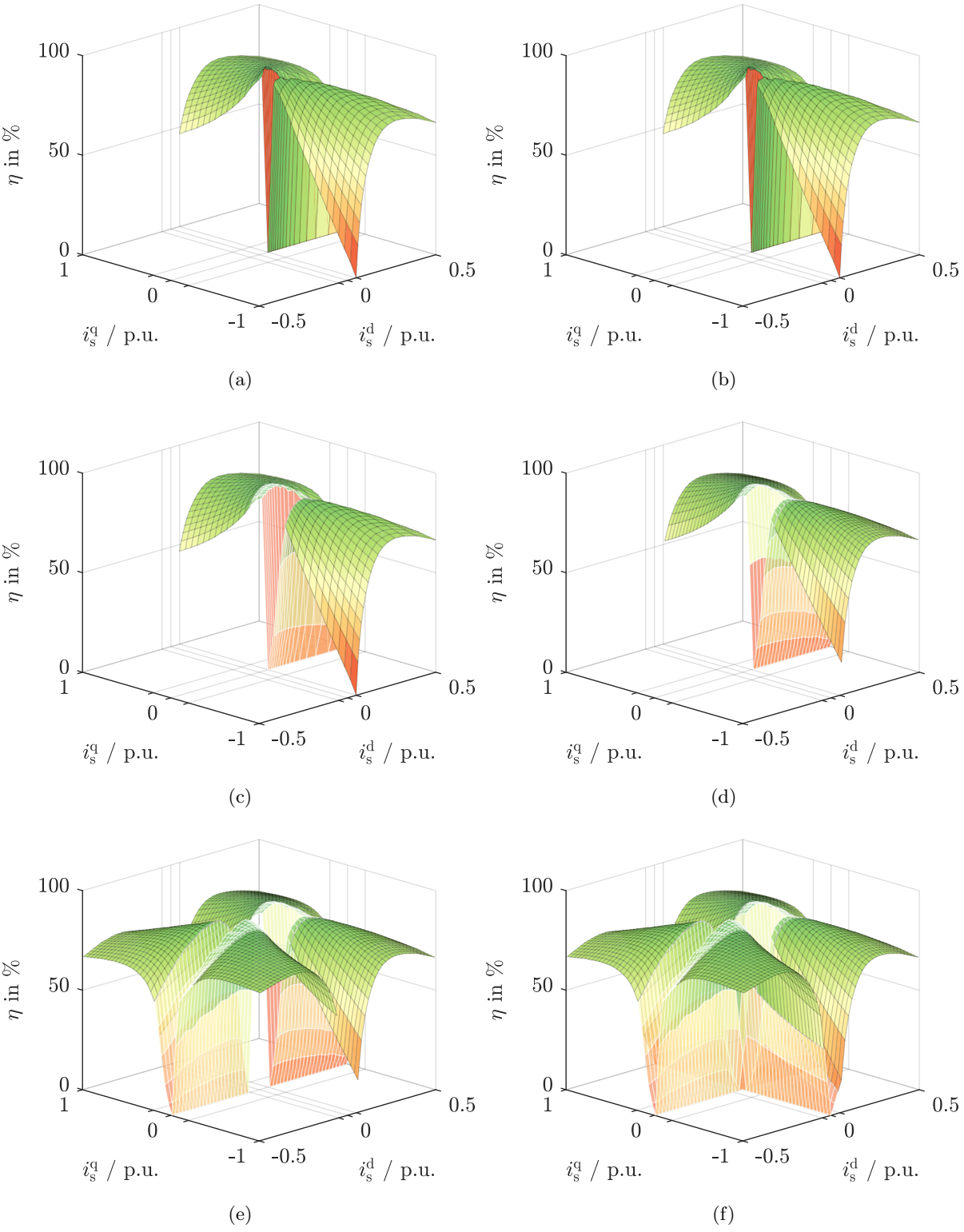

Figure 3.10: *Postprocessing of the efficiency map: (a) Raw data, (b) symmetrized raw data, (c) repaired raw data in* i_s^q *direction near* $i_s^q = 0\,\mathrm{A}$*, (d) refined grid, (e) four quadrant expansion and (f) interpolation in* d*-direction near* $i_s^d = 0\,\mathrm{A}$.

3.2.2.2 Mapping results

Applying the mapping procedure described above, machine maps are created for various quantities. As not all relevant quantities can be measured directly, they have to be reconstructed or estimated based on system knowledge or model equations. Reconstructed or estimated quantities are indicated by $\hat{\square}$ in the following list. The plotted maps are normalized to their respective base values (per unit system with base values in Tab. B.1). Moreover, for reasons of redundancy, only two quadrants (first and fourth) are shown.

- **Stator voltages maps [$\hat{\boldsymbol{u}}_\mathrm{s}^\mathrm{dq}$ (reconstruction)]:**

  The applied stator voltage is typically not measured, as the pulsed output of the inverter requires voltage sensors of very high bandwidth. Therefore, it is reconstructed from the reference voltage in stationary coordinates $\boldsymbol{u}_\mathrm{s}^{\alpha\beta\star}$ as follows (see Ch. 4.1.1 for a detailed derivation)

$$\hat{\boldsymbol{u}}_\mathrm{s}^{\alpha\beta}[k] = \int_{(k-1)\,T_\mathrm{S}}^{k\,T_\mathrm{S}} \boldsymbol{u}_\mathrm{s}^{\alpha\beta}(t)\mathrm{d}t \approx \frac{T_\delta}{T_\mathrm{S}}\boldsymbol{u}_\mathrm{s}^{\alpha\beta\star}[k-2] + \frac{T_\mathrm{S}-T_\delta}{T_\mathrm{S}}\boldsymbol{u}_\mathrm{s}^{\alpha\beta\star}[k-1], \tag{3.18}$$

  where T_S is the inverter sampling time, T_δ is the time shift between the beginning of the pulse-width modulation (PWM) cycle and the measurement trigger and $k\,T_\mathrm{S}$ is the current time instant. For *symmetric* PWM, T_δ is typically restricted to $\{\frac{1}{2}T_\mathrm{S}, T_\mathrm{S}\}$, since the current measurement has to be triggered during an active zero vector, thus reducing the measurement distortion. The reconstructed voltage is transformed into the dq-reference frame, using the inverse Park transformation with the current angle $\phi_\mathrm{k}[k]$, i.e. $\hat{\boldsymbol{u}}_\mathrm{s}^\mathrm{dq}[k] = \boldsymbol{T}_\mathrm{p}(\phi_\mathrm{k}[k])^{-1}\hat{\boldsymbol{u}}_\mathrm{s}^{\alpha\beta}[k]$. The stator voltage maps are depicted in Fig. 3.11. Clearly, the d-component in (a) is smaller than the q-component in (b), since the latter is mainly used to compensate for the induced back electromotive force (BEMF), whereas u_s^d is strongly dependent on the q-current.

Remark 16 (Inverter nonlinearity)**.** *Note that the series voltage drop of the inverter is compensated for by calculating the mean value over at least one electrical revolution [60]. Moreover, the effect of inverter dead-time is assumed negligible.*

Remark 17 (Reference frames)**.** *Instead of using the stationary* αβ*-reference voltages, Eq.* (3.18) *may also be applied for the* dq*-reference voltages. However, due to the continuous rotation of the* dq*-reference frame (for $\omega_\mathrm{k} \neq 0$), the angle difference $\Delta\phi_\mathrm{k} \approx \omega_\mathrm{k}T_\mathrm{S}$ between the reference frames of two consecutive control instants needs to be compensated for by appropriate pre-rotation of the reference vector (see also [109, Ch. 14.3.1]).*

- **Voltage over frequency (V/Hz) map [ξ (reconstruction/measurement)]:**

  The V/Hz ratio, in the following denoted by ξ, is defined as

$$\xi := \frac{2\pi\|\boldsymbol{u}_\mathrm{s}^\mathrm{dq}\|}{\omega_\mathrm{k}}. \tag{3.19}$$

  The V/Hz map, which is shown in Fig. 3.11c, is close to—but not exactly—symmetric with respect to the d-axis. This is due to the fact, that the electrical frequency ω_k increases for positive q-currents (positive slip frequency, motoring mode), whereas it decreases for negative q-currents (negative slip frequency, generating mode). The V/Hz map is similar in shape to the rotor flux linkage magnitude (see Fig. 3.12c).

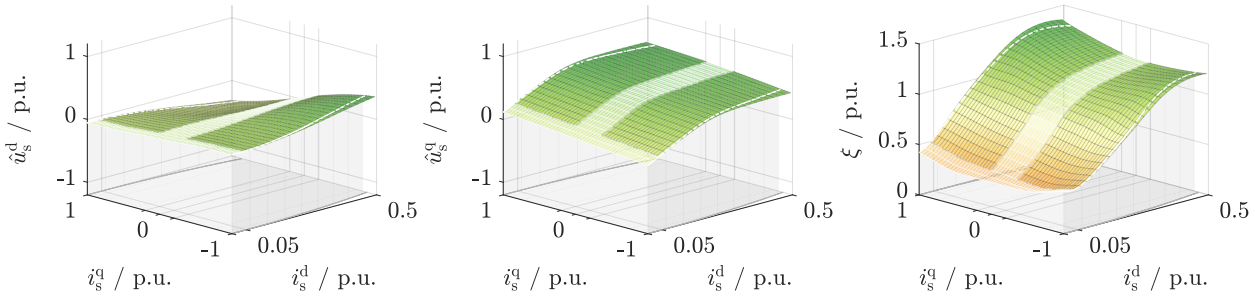

Figure 3.11: *Machine maps (1st & 4th quadrant) recorded at* $\omega_\mathrm{m} = 0.5\,\mathrm{p.u.}$*: (a) Stator* d*-voltage, (b) stator* q*-voltage and (c) V/Hz ratio.*

- **Stator flux linkage maps [$\hat{\boldsymbol{\psi}}_\mathrm{s}^\mathrm{dq}$ (estimate)]:**

  An *estimate* of the stator flux linkage is obtained from the steady-state stator voltage equation (3.8), i.e.

  $$\hat{\boldsymbol{\psi}}_\mathrm{s}^\mathrm{dq} \overset{(3.8)}{=} \frac{1}{\omega_\mathrm{k}} \boldsymbol{J}^{-1} \left(\hat{\boldsymbol{u}}_\mathrm{s}^\mathrm{dq} - \hat{R}_\mathrm{s} \boldsymbol{i}_\mathrm{s}^\mathrm{dq} \right), \tag{3.20}$$

  where $\hat{R}_\mathrm{s}$ is the estimated stator resistance, e.g. obtained by a DC test or using a multimeter. Note that (3.20) is valid for $\omega_\mathrm{k} \neq 0$ only, i.e. DC excitation is not covered. Recall that, if the stator resistance cannot be tracked continuously by measurement, flux symmetrization may be applied in order to eliminate the effect of resistance variations due to temperature changes, i.e. by calculating the average value for motoring and generating modes using (3.17). However, if iron losses are not negligible (e.g. for high speeds), the actual flux linkage map becomes non-symmetric and an additional error is introduced by the symmetrization.

  The resulting stator flux linkage maps are shown in Fig. 3.12. It can be seen in the d-component in (a), that at $i_\mathrm{s}^\mathrm{d} = 0.3\,\mathrm{p.u.}$, the flux linkage saturates almost completely. Moreover, it can be observed in the q-component in (b) that it becomes almost zero in close vicinity of zero excitation (around $i_\mathrm{s}^\mathrm{d} = 0\,\mathrm{A}$), because the rotor flux linkage is in line with the stator flux linkage. Only for higher loads, there is an angle difference between the rotor and stator flux linkages, which causes a significant q-component of the stator flux linkage.

  Using the stator flux linkage maps, the differential inductances may further be calculated. However, as the inductances are not relevant for the efficiency optimization, the derivation is found in App. D.1.

- **Rotor flux linkage (magnitude) map [$\|\hat{\boldsymbol{\psi}}_\mathrm{r}^\mathrm{dq}\|$ (estimate)]:**

  Although not relevant for the LUT generation, an estimate of the rotor flux linkage magnitude can be calculated for illustrative purposes, if the machine torque $m_\mathrm{m} = m_\mathrm{m,r}$ is measured. Solving the steady-state rotor voltage equation for $\boldsymbol{\psi}_\mathrm{r}^\mathrm{dq}$ yields

  $$\boldsymbol{\psi}_\mathrm{r}^\mathrm{dq} \overset{(3.8)}{=} -\frac{R_\mathrm{r}(\vartheta_\mathrm{r})}{(\omega_\mathrm{k} - \omega_\mathrm{r})} \boldsymbol{J}^{-1} \boldsymbol{i}_\mathrm{r}^\mathrm{dq}. \tag{3.21}$$

  Furthermore, multiplying both sides from the left with ${\boldsymbol{\psi}_\mathrm{r}^\mathrm{dq}}^\top$ yields

  $$\|\boldsymbol{\psi}_\mathrm{r}^\mathrm{dq}\|^2 = -\frac{R_\mathrm{r}(\vartheta_\mathrm{r})}{\omega_\mathrm{k} - \omega_\mathrm{r}} {\boldsymbol{\psi}_\mathrm{r}^\mathrm{dq}}^\top \boldsymbol{J}^{-1} \boldsymbol{i}_\mathrm{r}^\mathrm{dq}, \tag{3.22}$$

  which is proportional to the machine torque $m_\mathrm{m,r}$ [see (3.4)]. Hence, taking the square root and inserting $m_\mathrm{m,r}$ gives the rotor flux linkage magnitude. As the rotor resistance is not

exactly known, the *estimated* rotor flux linkage magnitude is given by

$$\|\hat{\boldsymbol{\psi}}_{\mathrm{r}}^{\mathrm{dq}}\| \overset{(3.4)}{=} \sqrt{\frac{\hat{R}_{\mathrm{r}}}{\omega_{\mathrm{k}}-\omega_{\mathrm{r}}}\frac{2}{3n_{\mathrm{p}}}m_{\mathrm{m,r}}}, \tag{3.23}$$

where $\hat{R}_{\mathrm{r}}$ is an estimate of the rotor resistance, e.g. obtained from the locked-rotor test.

The resulting map is depicted in Fig. 3.12c. Similar to the stator d-component, the effect of magnetic saturation can be clearly observed in d-direction. Ideally, the q-current should not influence the rotor flux linkage. However, a slight variation is observed also in q-direction, which might be caused by misalignment of the dq-reference frame (e.g. due to parameter errors or iron losses).

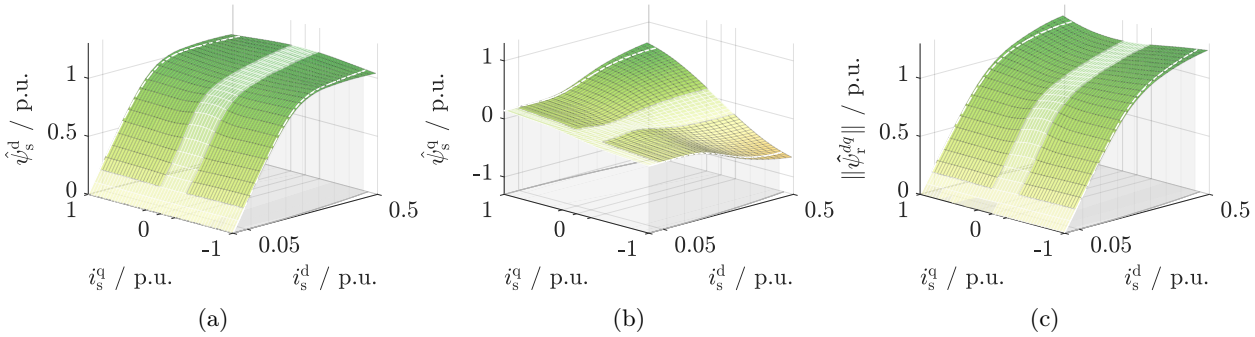

Figure 3.12: *Machine maps (1st & 4th quadrant) recorded at* $\omega_{\mathrm{m}} = 0.5\,\mathrm{p.u.}$*: (a) Stator* d*-flux linkage, (b) stator* q*-flux linkage and (c) rotor flux linkage magnitude.*

- **Torque map [$\hat{m}_{\mathrm{m}}$ (estimate) *or* m_{m} (measurement)]:**

  Since rotor current and rotor flux linkage are not measured, the machine torque $m_{\mathrm{m}} = m_{\mathrm{m,r}}$ has to be either measured using a torque sensor, or approximated by $m_{\mathrm{m,s}}$—see (3.4), assuming $m_{\mathrm{c}} = 0\,\mathrm{N\,m}$—i.e.

  $$\hat{m}_{\mathrm{m}} = \tfrac{3}{2}n_{\mathrm{p}}\boldsymbol{i}_{\mathrm{s}}^{\mathrm{dq}\top}\boldsymbol{J}\hat{\boldsymbol{\psi}}_{\mathrm{s}}^{\mathrm{dq}} \approx m_{\mathrm{m,s}}. \tag{3.24}$$

  If, in turn, a torque sensor is available, the measured torque $\bar{m}_{\mathrm{m}}$ will be biased due to friction, which is purely speed-dependent and cannot be removed by means of torque control. Since only the electromagnetic conversion process is assessed, friction needs to be removed from the measurement: For reference currents $(i_{\mathrm{s,min}}^{\mathrm{d}}, 0)$, the machine torque is very close to zero, yielding a good approximation of the friction torque $m_{\mathrm{f}} \approx \bar{m}_{\mathrm{m}}$. Hence, calculating

  $$m_{\mathrm{m}} = \bar{m}_{\mathrm{m}} - m_{\mathrm{f}} \tag{3.25}$$

  gives the corrected machine torque.

  Figure 3.13 shows the torque machine maps, with (a) measured and (b) estimated torque. Moreover, (c) shows the difference $\Delta m_{\mathrm{m}} := m_{\mathrm{m}} - \hat{m}_{\mathrm{m}}$ between the two. Note that $-\Delta m_{\mathrm{m}}$ is plotted so as to improve the presentation of the map. A noticeable observation is that the maximum difference with $|\Delta m_{\mathrm{m}}| \approx 0.035\,\mathrm{p.u.}$ is much smaller in motoring mode (first quadrant), compared to the maximum difference $|\Delta m_{\mathrm{m}}| \approx 0.056\,\mathrm{p.u.}$ in generating mode (fourth quadrant). In order to explain this effect, it is meaningful to take a closer look into the estimated torque calculation. If the stator resistance is estimated using flux symmetrization, the actual stator flux linkage can be stated as $\boldsymbol{\psi}_{\mathrm{s}}^{\mathrm{dq}} = \hat{\boldsymbol{\psi}}_{\mathrm{s}}^{\mathrm{dq}} \pm \frac{1}{2}\Delta\boldsymbol{\psi}_{\mathrm{s}}^{\mathrm{dq}}$ (see Fig. 3.5b), where

$\hat{\boldsymbol{\psi}}_\mathrm{s}^\mathrm{dq} = \boldsymbol{\psi}_\mathrm{s,avg}^\mathrm{dq}$ is the mean value of the motoring and generating mode estimates $\hat{\boldsymbol{\psi}}_\mathrm{s}^\mathrm{dq+}$ and $\hat{\boldsymbol{\psi}}_\mathrm{s}^\mathrm{dq-}$, calculated by (3.17). Hence, the stator-side torque equation becomes

$$m_\mathrm{m,s} = \tfrac{3}{2} n_\mathrm{p} \boldsymbol{i}_\mathrm{s}^{\mathrm{dq}\top} \boldsymbol{J} \boldsymbol{\psi}_\mathrm{s}^\mathrm{dq} = \tfrac{3}{2} n_\mathrm{p} \boldsymbol{i}_\mathrm{s}^{\mathrm{dq}\top} \boldsymbol{J} \hat{\boldsymbol{\psi}}_\mathrm{s}^\mathrm{dq} \pm \tfrac{3}{4} n_\mathrm{p} \boldsymbol{i}_\mathrm{s}^{\mathrm{dq}\top} \boldsymbol{J} \Delta\boldsymbol{\psi}_\mathrm{s}^\mathrm{dq} = \hat{m}_\mathrm{m} \pm \Delta m_\mathrm{m,s}, \tag{3.26}$$

where $\Delta m_\mathrm{m,s} > 0$ represents an additional torque error term, which is added or subtracted, depending on the current mode of operation. Calculating the torque difference using (3.4) and (3.26) yields

$$\Delta m_\mathrm{m} = m_\mathrm{m} - \hat{m}_\mathrm{m} \overset{(3.4),(3.26)}{=} m_\mathrm{m,s} - m_\mathrm{m,c} - (m_\mathrm{m,s} \mp \Delta m_\mathrm{m,s}) = -m_\mathrm{m,c} \pm \Delta m_\mathrm{m,s}. \tag{3.27}$$

As $m_\mathrm{m,c} \geq 0$ (see e.g. cross product of $\boldsymbol{i}_\mathrm{c}^\mathrm{dq}$ and $\boldsymbol{\psi}_\mathrm{m}^\mathrm{dq}$ in Fig. 3.5a) and $\Delta m_\mathrm{m,s}$ is added or subtracted, the measured torque difference between the first and fourth quadrant in Fig. 3.13c can be explained.

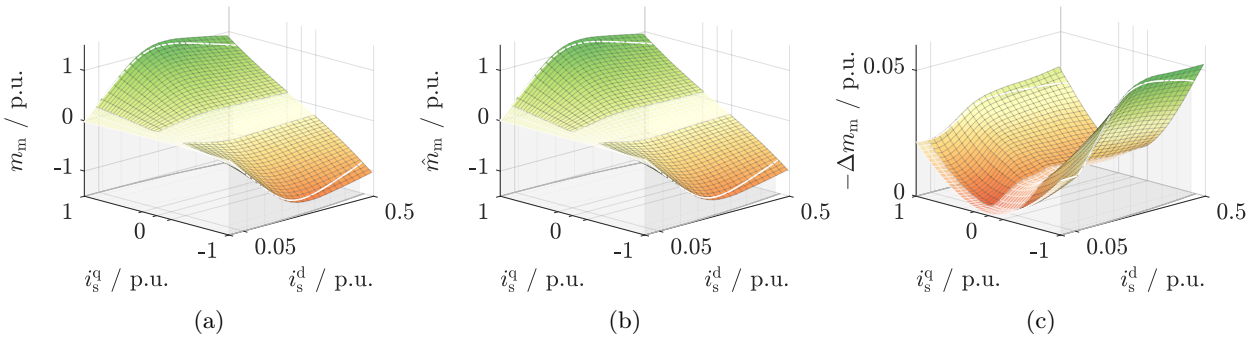

Figure 3.13: *Machine maps (1st & 4th quadrant) recorded at* $\omega_\mathrm{m} = 0.5\,\mathrm{p.u.}$*: (a) Measured torque, (b) estimated torque and (c) difference between measured and estimated torque.*

- **Electrical power map [$\hat{p}_\mathrm{e}$ (estimate/measurement)]:**

  The instantaneous active power supplied by the VSI is prerequisite for calculating the machine efficiency. It is given by (see e.g. [124, Ch. 24.2.2.1])

  $$\hat{p}_\mathrm{e} = \tfrac{3}{2} \hat{\boldsymbol{u}}_\mathrm{s}^{\mathrm{dq}\top} \boldsymbol{i}_\mathrm{s}^\mathrm{dq}. \tag{3.28}$$

  The electrical power map is depicted in Fig. 3.14a. Since the machine is operated at half rated speed, the electrical power reaches values above 0.5 p.u. in motoring mode (first quadrant), as the electrical side provides the power losses. Since the power flow is reversed in generating mode (fourth quadrant), its sign is reversed, too. In generating mode, the electrical power is clearly beyond −0.5 p.u. as the power losses are provided by the mechanical side.

- **Mechanical power maps [$\hat{p}_\mathrm{m}$ (estimate) *or* p_m (measurement)]:**

  The mechanical power p_m, transmitted via the machine shaft, and its estimate $\hat{p}_\mathrm{m}$ are given by

  $$p_\mathrm{m} = m_\mathrm{m} \omega_\mathrm{m} \qquad \text{and} \qquad \hat{p}_\mathrm{m} = \hat{m}_\mathrm{m} \omega_\mathrm{m}, \tag{3.29}$$

  with respective maps plotted in Figs. 3.14b and 3.14c. Apart from the fact, that both maps are almost identical (as estimated and measured torque are almost the same), it can be observed that values of about 0.5 p.u. are reached in either mode of operation.

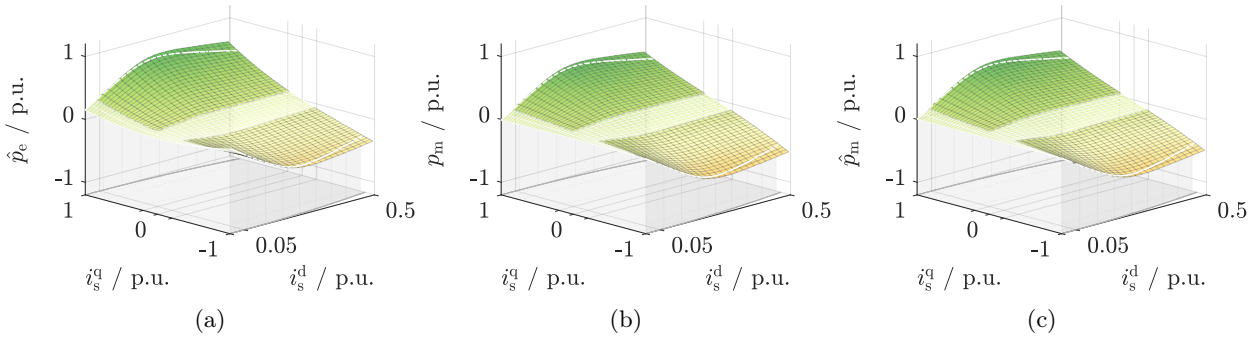

Figure 3.14: *Machine maps (1st & 4th quadrant) recorded at* $\omega_\mathrm{m} = 0.5\,\mathrm{p.u.}$*: (a) Active (electrical) power, (b) measured mechanical power and (c) estimated mechanical power.*

- **Efficiency maps [$\hat{\eta}$ (estimate) or η (estimate/measurement)]:**

  If $p_\mathrm{e} \geq 0$, the machine operates in motoring mode (passive sign convention), while for $p_\mathrm{e} < 0$ it operates as a generator. Hence, the efficiency η and its estimate $\hat{\eta}$ are defined as

$$\hat{\eta} = \begin{cases} \frac{\hat{p}_\mathrm{m}}{\hat{p}_\mathrm{e}} & , \ldots \\ \frac{\hat{p}_\mathrm{e}}{\hat{p}_\mathrm{m}} & , \ldots \end{cases} \qquad \eta = \begin{cases} \frac{p_\mathrm{m}}{\hat{p}_\mathrm{e}} & , \quad \text{for} \quad \hat{p}_\mathrm{e} \geq 0 \quad \text{and} \quad p_\mathrm{m} \geq 0 \\ \frac{\hat{p}_\mathrm{e}}{p_\mathrm{m}} & , \quad \text{for} \quad \hat{p}_\mathrm{e} < 0 \quad \text{and} \quad p_\mathrm{m} < 0. \end{cases} \tag{3.30}$$

  Figure 3.15 shows the (a) measured and (b) estimated efficiencies. Both maps feature a steep slope towards the d- and q-axis and a comparably flat plateau in the remaining areas. In addition the (negative) efficiency difference $\Delta\eta := \eta - \hat{\eta}$ is plotted in (c).

  Note that power losses do not need to be specified for the presented method, as η is calculated directly from the net input and output power terms. However, calculating the power loss terms is possible, nevertheless. The respective calculation steps and the resulting maps are presented in App. D.2.

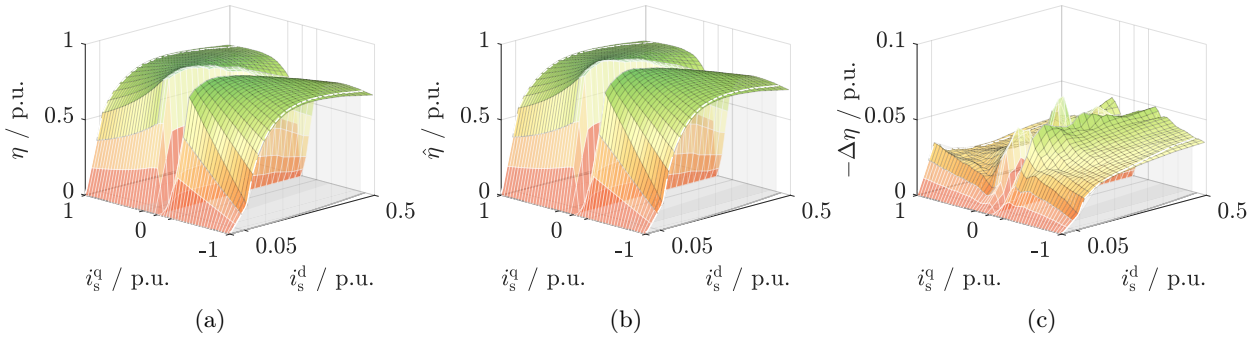

Figure 3.15: *Machine maps (1st & 4th quadrant) recorded at* $\omega_\mathrm{m} = 0.5\,\mathrm{p.u.}$*: (a) Measured efficiency, (b) estimated efficiency and (c) difference between measured and estimated efficiency.*

3.2.3 Look-up table generation

Since the mapping of machine torque m_m to stator currents $\boldsymbol{i}_\mathrm{s}^\mathrm{dq}$ is ambiguous (assuming constant speed), different torque control strategies may be pursued, achieving equal torque output while being subject to either an equality constraint or an optimization problem (see e.g. [6, 12]). The *optimal*

stator reference currents $i_\mathrm{s}^{\mathrm{d}\star}$ and $i_\mathrm{s}^{\mathrm{q}\star}$ are stored in the corresponding LUTs $\mathcal{L}^{\mathrm{M}}_{i_\mathrm{s}^{\mathrm{d}\star}}$ and $\mathcal{L}^{\mathrm{M}}_{i_\mathrm{s}^{\mathrm{q}\star}}$ for the considered feedforward torque control strategy 'M' (e.g. M=MTPC, M=MTPV, ...). The following description refers to the extraction of the torque control strategies for a single set of machine maps, i.e. recorded at some constant speed $\omega_\mathrm{m} = \text{const}$. Repeating the procedure for data sets recorded at different speeds and adding the results to the tables yields the 2D LUTs $\mathcal{L}^{\mathrm{M}}_{i_\mathrm{s}^{\mathrm{d}\star}}(m_\mathrm{m}^\star, \omega_\mathrm{m})$ and $\mathcal{L}^{\mathrm{M}}_{i_\mathrm{s}^{\mathrm{q}\star}}(m_\mathrm{m}^\star, \omega_\mathrm{m})$.

Defining the torque contour line related to the reference torque $m_\mathrm{m}^\star$ as

$$\boldsymbol{i}_\mathrm{s}^{\mathrm{dq}\blacktriangle}(m_\mathrm{m}^\star) \in \mathbb{I}_\mathrm{m}(m_\mathrm{m}^\star) = \{\boldsymbol{i}_\mathrm{s}^{\mathrm{dq}} \quad | \quad m_\mathrm{m}(\boldsymbol{i}_\mathrm{s}^{\mathrm{dq}}) = m_\mathrm{m}^\star\}, \tag{3.31}$$

the control strategies 'M' can be stated as either of the following two types of problems:

- The *minimization problem*
$$\boldsymbol{i}_\mathrm{s}^{\mathrm{dq}\star} = \operatorname{argmin} y_1(\boldsymbol{i}_\mathrm{s}^{\mathrm{dq}\blacktriangle}) \tag{3.32}$$
directly yields the optimal solution that minimizes $y_1 \in \mathbb{R}$, e.g. $y_1 = \|\boldsymbol{i}_\mathrm{s}^{\mathrm{dq}\blacktriangle}\|$ (maximum torque per current) or $y_1 = \|\boldsymbol{u}_\mathrm{s}^{\mathrm{dq}}(\boldsymbol{i}_\mathrm{s}^{\mathrm{dq}\blacktriangle})\|$ (maximum torque per voltage).

- The *equality constraint* on $x(\boldsymbol{i}_\mathrm{s}^{\mathrm{dq}\blacktriangle}) = x^\star$ is first converted into a minimization problem
$$\boldsymbol{i}_\mathrm{s}^{\mathrm{dq}\star} = \operatorname{argmin} |x(\boldsymbol{i}_\mathrm{s}^{\mathrm{dq}\blacktriangle}) - x^\star| = \operatorname{argmin} y_2(\boldsymbol{i}_\mathrm{s}^{\mathrm{dq}\blacktriangle}) \tag{3.33}$$
with $y_2(\boldsymbol{i}_\mathrm{s}^{\mathrm{dq}\blacktriangle}) := |x(\boldsymbol{i}_\mathrm{s}^{\mathrm{dq}\blacktriangle}) - x^\star| \in \mathbb{R}$. Its solution are the currents which solve best the equality constraint, e.g. $x = \xi$, $x^\star = \xi^\star$ and $y_2 = |\xi(\boldsymbol{i}_\mathrm{s}^{\mathrm{dq}\blacktriangle}) - \xi^\star|$ (constant V/Hz ratio).

As the acquired machine maps are discrete data sets instead of continuous functions, the optimization problems need to be solved numerically for numerous values of $m_\mathrm{m}^\star \in [-m_{\mathrm{m,nom}}, m_{\mathrm{m,nom}}]$ in order to obtain the desired LUT data. Finding the numerical solution for torque strategy 'M' and given reference torque $m_\mathrm{m}^\star$ can be achieved by carrying out the following steps in MATLAB®:

1. Calculate the torque contour line using the `contourc(...)` command.
2. Remove infeasible data points, e.g. grid points exceeding the current limit.
3. Look up the optimization variable $y = y_{1/2}$ (depending on the control strategy 'M') from the machine maps using the `interp2(...)` command for all data points of the contour line.
4. Find the current vector $\boldsymbol{i}_\mathrm{s}^{\mathrm{dq}\star}$ which minimizes the optimization variable y.

Note that for the last step, polynomial fitting of the discrete data points (e.g. y over $i_\mathrm{s}^{\mathrm{d}\blacktriangle}$) using the `fit(...)` command (Curve Fitting Toolbox) and subsequent analytical calculation of the solution $i_\mathrm{s}^{\mathrm{d}\star}$ ($i_\mathrm{s}^{\mathrm{q}\star}$ results from interpolation on the contour line), yields a better result than mere selection of the best fit out of the available (discrete) data points.

Various optimization problems and equality constraints may be formulated, out of which the most commonly used strategies are specified in the following.

1. **Constant V/Hz (M=VHz):**
The V/Hz control strategy prescribes that the voltage magnitude $\|\boldsymbol{u}_\mathrm{s}^{\mathrm{dq}}\|$ is constant with respect to the excitation frequency ω_k, i.e. $\xi = \text{const}$. (equality constraint with $y_2 = |\xi(\boldsymbol{i}_\mathrm{s}^{\mathrm{dq}}) - \xi^\star|$). In fact, it does not describe a torque control strategy in the classical sense, but rather a scalar, open-loop speed control scheme, which would normally be difficult to compare with a closed-loop vector controlled system in terms of efficiency. However, the presented method allows for

a quantitative assessment, nonetheless. Given a constant V/Hz ratio—e.g. for rated voltage and frequency $\xi^\star = \xi_{\mathrm{nom}} = 2\pi\hat{u}_{\mathrm{s,nom}}/\omega_{\mathrm{k,nom}}$ is calculated in accordance with (3.19)—the corresponding LUTs $\mathcal{L}^{\mathrm{VHz}}_{i_{\mathrm{s}}^{\mathrm{d}\star}}(m^\star_{\mathrm{m}}, \omega_{\mathrm{m}})$ and $\mathcal{L}^{\mathrm{VHz}}_{i_{\mathrm{s}}^{\mathrm{q}\star}}(m^\star_{\mathrm{m}}, \omega_{\mathrm{m}})$ are obtained (see Fig. 3.16a & 3.16b). It can be shown that, using a different ξ, a different (better) result in terms of efficiency can be obtained for rated torque. Moreover, it should be noted that if $\xi > \xi_{\mathrm{nom}}$ the machine cannot reach nominal speed under full load, due to the voltage constraint.

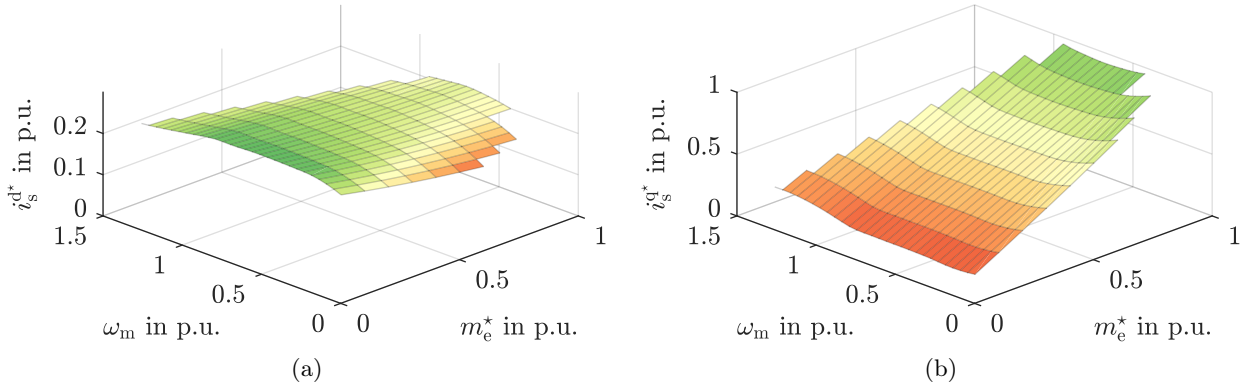

Figure 3.16: *Torque control LUTs for* Constant V/Hz *(M=VHz): (a)* d- *and (b)* q-*reference currents as functions of reference torque* $m^\star_{\mathrm{m}}$ *and speed* ω_{m}.

2. **Constant Flux (M=CF):**
   In the range below rated speed, the constant flux (CF) strategy prescribes a constant excitation current $i_{\mathrm{s}}^{\mathrm{d}\star} = \text{const.}$ (equality constraint with $y_2 = |i_{\mathrm{s}}^{\mathrm{d}} - i_{\mathrm{s}}^{\mathrm{d}\star}|$), where, for example, $i_{\mathrm{s}}^{\mathrm{d}\star}$ is selected as the no-load current at rated speed. At the same time, $i_{\mathrm{s}}^{\mathrm{q}\star}$ is used to control the machine torque. The corresponding LUTs $\mathcal{L}^{\mathrm{CF}}_{i_{\mathrm{s}}^{\mathrm{d}\star}}(m^\star_{\mathrm{m}}, \omega_{\mathrm{m}})$ and $\mathcal{L}^{\mathrm{CF}}_{i_{\mathrm{s}}^{\mathrm{q}\star}}(m^\star_{\mathrm{m}}, \omega_{\mathrm{m}})$ (see Figs. 3.17a & 3.17b) are obtained by evaluating the equality constraint.

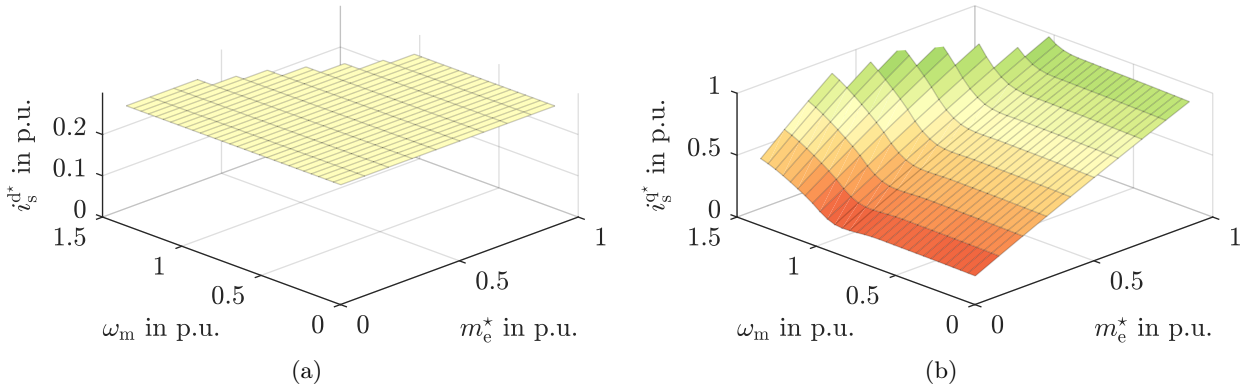

Figure 3.17: *Torque control LUTs for* Constant Flux *(M=CF): (a)* d- *and (b)* q-*reference currents as functions of reference torque* $m^\star_{\mathrm{m}}$ *and speed* ω_{m}.

3. **Maximum Torque per Current (M=MTPC):**
   In order to minimize the ohmic losses of the machine (in fact, only in the stator resistance R_{s}), MTPC control may be preferred over CF control. Here, evaluating the optimization problem of minimizing the stator current magnitude (i.e. $y_1 = \|\boldsymbol{i}_{\mathrm{s}}^{\mathrm{dq}}\|$) yields the corresponding LUTs $\mathcal{L}^{\mathrm{MTPC}}_{i_{\mathrm{s}}^{\mathrm{d}\star}}(m^\star_{\mathrm{m}}, \omega_{\mathrm{m}})$ and $\mathcal{L}^{\mathrm{MTPC}}_{i_{\mathrm{s}}^{\mathrm{q}\star}}(m^\star_{\mathrm{m}}, \omega_{\mathrm{m}})$ (see Figs. 3.18a & 3.18b).

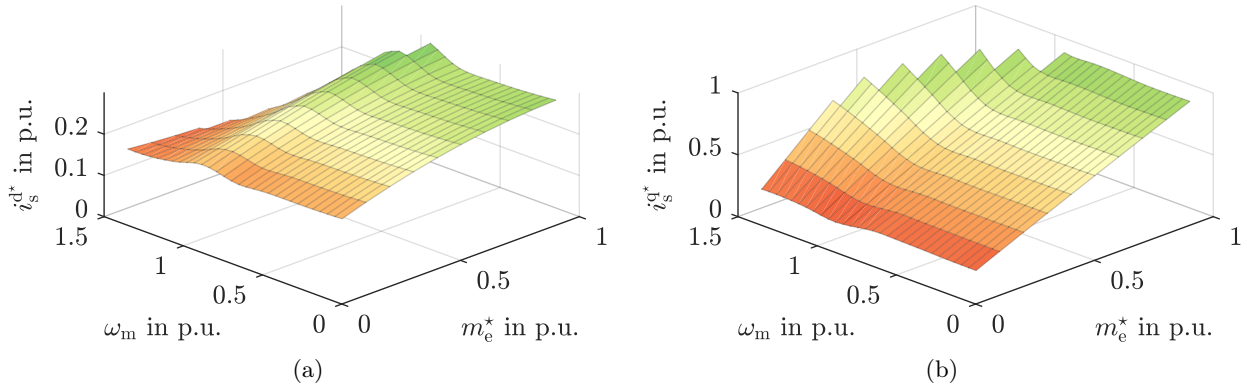

Figure 3.18: *Torque control LUTs for* Maximum Torque per Current *(M=MTPC): (a)* d- *and (b)* q-*reference currents as functions of reference torque* $m_m^\star$ *and speed* ω_m.

4. **Maximum Torque per Loss (M=MTPL):**
   As an extension to MTPC, the MTPL control strategy not only reduces stator losses, but also rotor and iron losses. For the LUT generation, the equivalent optimization goal of maximizing the efficiency is evaluated [i.e. $y_1 = -\eta(\boldsymbol{i}_s^{dq})$], yielding $\mathcal{L}_{i_s^{d\star}}^{MTPL}(m_m^\star, \omega_m)$ and $\mathcal{L}_{i_s^{q\star}}^{MTPL}(m_m^\star, \omega_m)$ (see Figs. 3.19a & 3.19b).

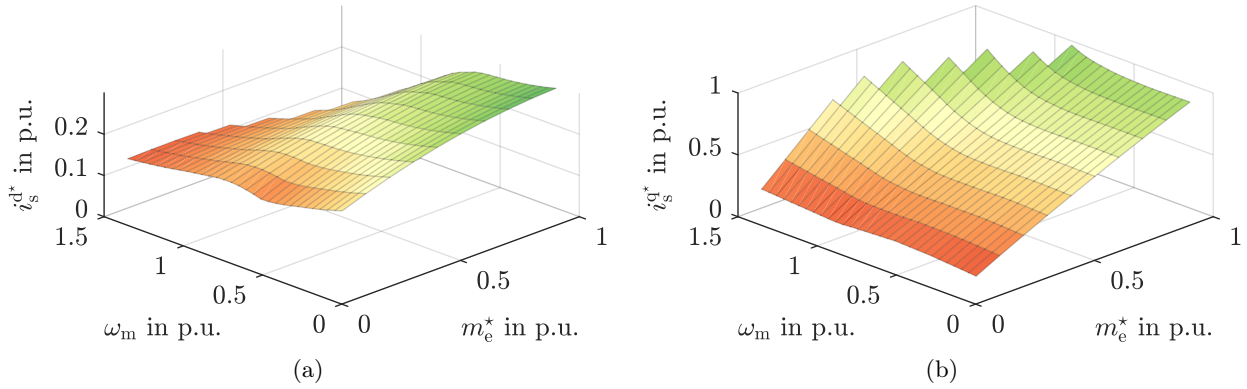

Figure 3.19: *Torque control LUTs for* Maximum Torque per Loss *(M=MTPL): (a)* d- *and (b)* q-*reference currents as functions of reference torque* $m_m^\star$ *and speed* ω_m.

5. **Maximum Torque per Voltage (M=MTPV):**
   The MTPV strategy allows setting the maximum achievable torque if the voltage constraint becomes active, i.e. the optimization goal of minimizing the voltage magnitude is evaluated (i.e. $y_1 = \|\boldsymbol{u}_s^{dq}(\boldsymbol{i}_s^{dq})\|$), yielding $\mathcal{L}_{i_s^{d\star}}^{MTPV}(m_m^\star, \omega_m)$ and $\mathcal{L}_{i_s^{q\star}}^{MTPV}(m_m^\star, \omega_m)$ (see Fig. 3.20a & Fig. 3.20b). Note that the MTPV strategy is strongly dependent of the machine speed ω_m.

3.3 Discussion of results

Figures 3.16–3.20 show the reference current LUTs for the different control strategies, measured for $\omega_m \in \{0.1, \ldots, 1.5\} \cdot \omega_{m,nom}$, i.e. including the field-weakening range. It is observed that for higher

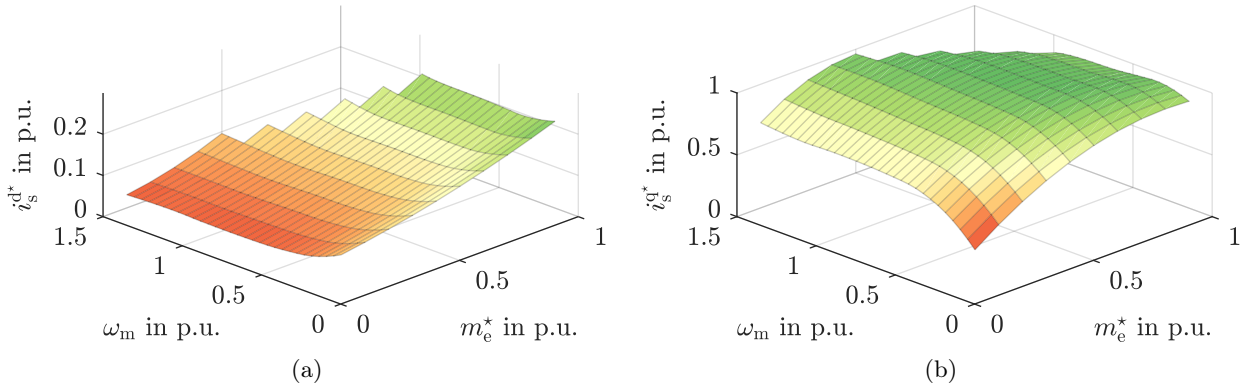

Figure 3.20: *Torque control LUTs,* Maximum Torque per Voltage *(M=MTPV): (a)* d- *and (b)* q- *reference currents as functions of reference torque* $m_m^\star$ *and speed* ω_m.

speeds, the LUTs are partially clipped. This is due to the voltage limit, which denies operating the machine in the respective operating point. In the rated speed range ($\omega_m \leq \omega_{m,nom}$), $i_s^{q\star}$ does not vary with ω_m and is almost linear in $m_m^\star$ for all strategies except for VHz (see Fig. 3.16); differences are found mainly in the $i_s^{d\star}$ LUTs: For VHz an almost constant $i_s^{d\star}$ can be observed (since the excitation is supposed to be constant), for CF (see Fig. 3.17) $i_s^{d\star}$ is perfectly constant, and for MTPC (see Fig. 3.18) and MTPL (see Fig. 3.19) a nonlinear relation in $m_m^\star$ is observed. In addition, for MTPL, a slight variation in ω_m direction is observed. Beyond rated speed, which is only feasible for MTPC and MTPL, the $i_s^{d\star}$ values are reduced, whereas $i_s^{q\star}$ increases. For MTPV (see Fig. 3.20), it is observed that a very high $i_s^{q\star}$ is needed in the entire operation range, whereas $i_s^{d\star}$ remains low compared to the other strategies. As expected, with the MTPV strategy, a very low excitation is aimed at, which is confirmed by the LUTs.

Figure 3.21 shows 2D contour plots of the machine efficiency (with colored layers) [——]) and torque [····] for first quadrant operation (motoring mode). Additionally, the respective torque control trajectories are plotted on top. Note that an additional V/Hz curve [- - -] is added, which represents an optimized voltage-over-frequency ratio $\xi_{opt} = \text{argmax}\,\eta(\xi)$ s.t. $m_m = m_{m,nom}$ that maximizes the efficiency for rated torque. Each plot shows results for one specific mechanical speed (left to right, top-down: $\omega_m \in \{0.1, \ldots, 1\} \cdot \omega_{m,nom}$), which is kept constant by the prime mover. MTPC, MTPL and MTPV trajectories are shown for both, measured torque (argument m_m) and estimated torque (argument $\hat{m}_m$), with the sample points indicated by respective markers (see legend above the plots). Note that the contour lines are drawn for the measured torque; hence, only the markers of the corresponding measured torque trajectories are actually located on the contour lines, whereas the markers of the estimated torque trajectories are slightly off, due to the torque estimation error. For higher speeds, the controller is incapable of covering the whole current plane, which is why some regions are reconstructed by extrapolation of the data maps. These areas are marked by a transparent white layer (see plots 8, 9 and 10, i.e. for $\omega_m = \{0.8, 0.9, 1\} \cdot \omega_{m,nom}$). Comparing the plots, it can be seen that the efficiency generally increases with the speed. Moreover, it can be observed that, for the selected speeds, measured and estimated curves almost perfectly coincide, even though a torque difference has been identified in Fig. 3.13c.

The variation of the MTPC and MTPL trajectories due to speed changes is shown in Fig. 3.22a for three different speeds, i.e. $\omega_m = 0.3\,\text{p.u.}$ [——], $\omega_m = 0.5\,\text{p.u.}$ [- - -] and $\omega_m = 0.7\,\text{p.u.}$ [- · -]. The respective curves have been acquired on a pre-heated machine. For MTPC [——], the trajectory is only slightly shifted in $-i_s^d$ direction with increasing speed. This can be explained with the effect of torque detuning due to iron losses, which increase with the speed and the induced voltage. For

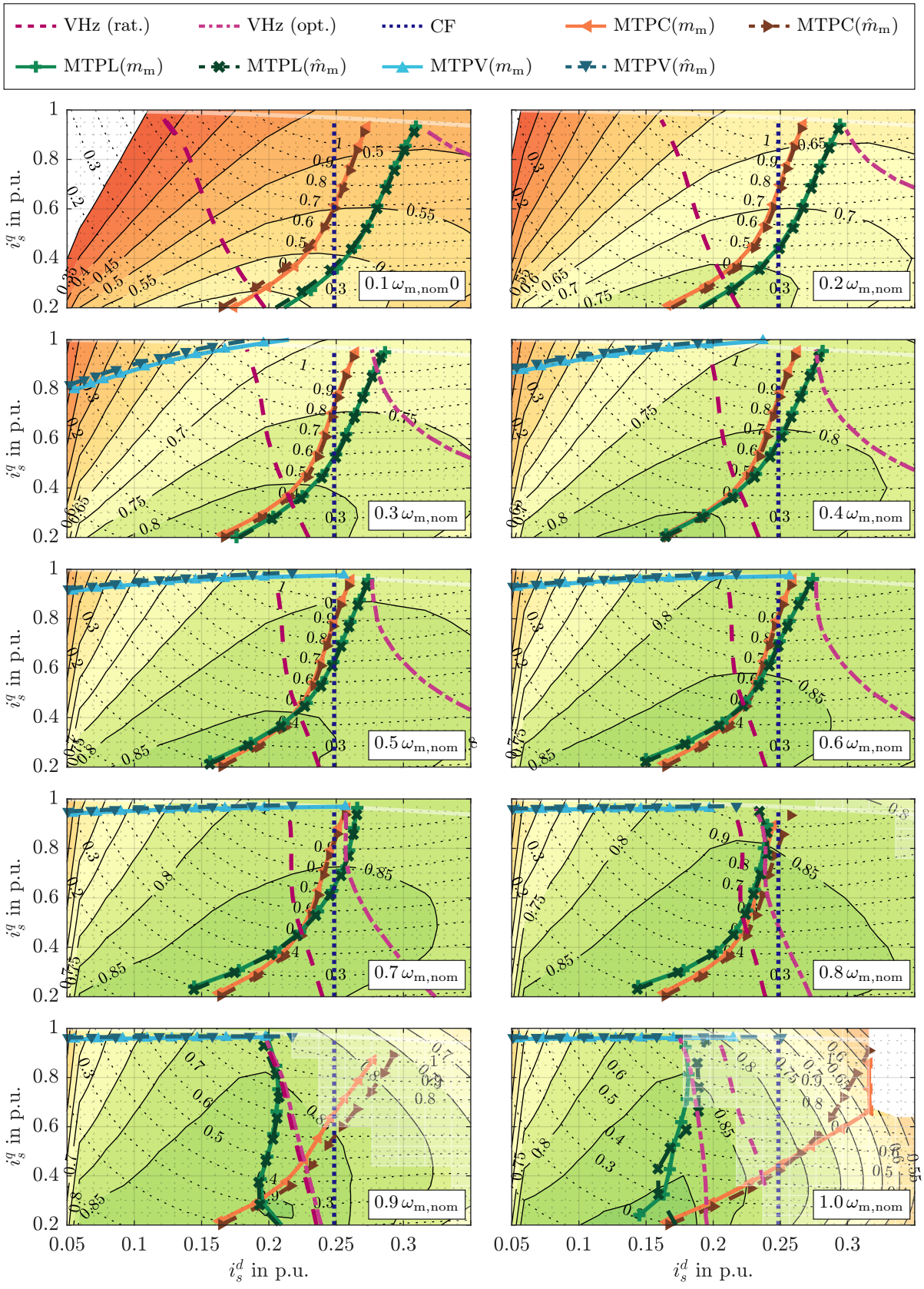

Figure 3.21: *Efficiency (colored layers) [——] and torque [·····] contour plots over the first quadrant (motoring mode) of the current plane, for different speeds* $\{0.1, \ldots, 1\} \cdot \omega_{\mathrm{m,nom}}$.

MTPL [—] on the other hand, it can be observed that the trajectory is clearly shifted towards the q-axis with increasing speeds due to the iron resistance growing with the speed. Hence, weakening the flux leads to a higher efficiency, as iron losses can be reduced effectively.

Similarly, Fig. 3.22b shows the temperature impact on the MTPC and MTPL trajectories, recorded at constant speed $\omega_\mathrm{m} = 0.5\,\mathrm{p.u.}$ (half rated speed). The first recording was conducted on a cold machine [—] with a casing temperature of approximately 20 °C, whereas the second recording was carried out on a hot machine [- - -] after sufficient pre-heating at full load. Due to the cooling fan, it is expected that the measured casing temperature of approximately 50 °C was much lower than the actual temperature inside the machine. Note that the winding temperature limit is specified as 135 °C by the manufacturer. It is observed that both, MTPC [—] and MTPL [—] trajectories, are shifted in $-i_\mathrm{s}^\mathrm{d}$-direction by almost the same amount. A possible explanation is that the actual rotor flux linkage diverges further from the d-axis of the arbitrarily rotating coordinate system, as the actual parameter β in (3.7) increases with a growing rotor resistance, whereas the assumed (and implemented) value remains constant. Hence, an increasing part of the q-current is used for flux production instead of torque production. Irrespective of its cause, the trajectory shift implicates that the temperature effect is not negligible and measurements should be conducted on a machine with almost constant temperature only, in order to obtain reproducible results. Note that, for geothermal power applications, the temperature is generally high, but the overall temperature variation is comparably low.

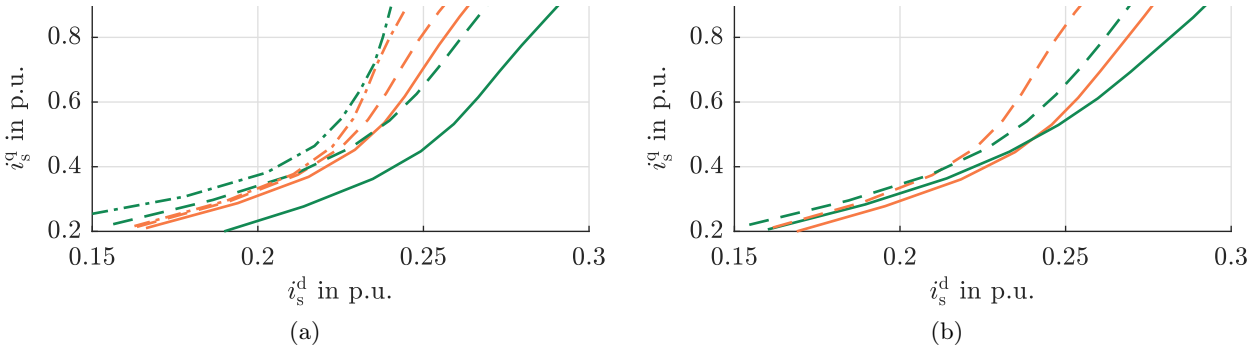

Figure 3.22: *Impact analysis: (a) Impact of* speed *variation for* $\omega_\mathrm{m} = 0.3\,\mathrm{p.u.}$ *[—],* $\omega_\mathrm{m} = 0.5\,\mathrm{p.u.}$ *[- - -] and* $\omega_\mathrm{m} = 0.7\,\mathrm{p.u.}$ *[- · -] (for hot machine) on the MTPC [—] and MTPL [—] trajectories, and (b) impact of* temperature *variation for measurements on a cold machine [—] and a hot machine [- - -] (at constant speed* $\omega_\mathrm{m} = 0.5\,\mathrm{p.u.}$*), respectively.*

Figure 3.23 shows the impact of the ϑ-controller compared to the passive cooling as proposed in [60]. The results are averaged over several i_s^q values and show the estimated temperature $\hat{\vartheta}_\mathrm{s}$ (left axis) and resistance $\hat{R}_\mathrm{s}$ (right axis), respectively, over i_s^d. If the ϑ-controller is used, the variation with respect to some mean value [· · · ·] is only about 2 °C for $i_\mathrm{s}^\mathrm{d} < 0.25\,\mathrm{p.u.}$ On the other hand, if the ϑ-controller is not used, the variation is much higher (about 7 °C). The observed temperature rise for higher i_s^d-currents (shaded area [ ]) is caused by (i) insufficient cooling at higher loads (i.e. the cooling period is too short) and (ii) a resistance estimation error, due to a flux inbalance with increasing iron losses. Prolonging the cooling period is possible in theory, but due to the large thermal time constant, the consumed time for the entire identification procedure is increased significantly. Moreoever, as no direct temperature feedback (in terms of measurement) is used, the duration of the required cooling period is difficult to determine.

Lastly, Fig. 3.24 shows the efficiencies of the different control strategies plotted versus the machine torque for different mechanical speeds (left to right, top-down: $\omega_\mathrm{m} \in \{0.1, \ldots, 1\} \cdot \omega_\mathrm{m,nom}$). In

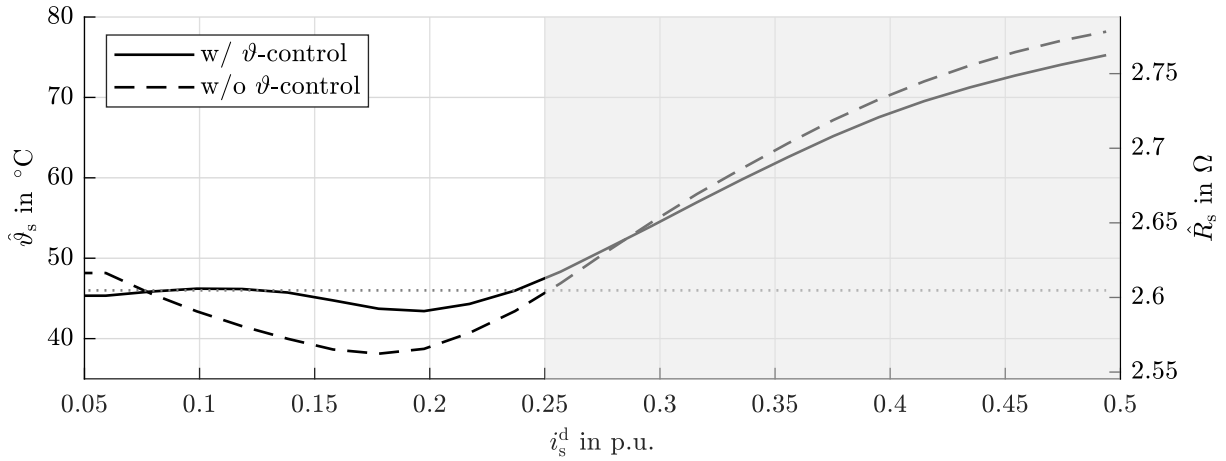

Figure 3.23: *Impact of ϑ-control on estimated stator winding temperature $\hat{\vartheta}_\mathrm{s}$ and resistance $\hat{R}_\mathrm{s}$, measured at $\omega_\mathrm{m} = 0.5\,\mathrm{p.u.}$.*

addition, for plots 1–9, zoomed views for the interval $m_\mathrm{m} \in [0.95, 1] \cdot m_\mathrm{m,nom}$ are plotted on top of the figures, as the lines are barely distinguishable in that area. The previous observation of the efficiency increasing for higher speeds is confirmed, as the plotted lines move in $+\eta$ direction, up to about $\omega_\mathrm{m} = 0.8\,\mathrm{p.u.}$, where a maximum efficiency of $\eta \approx 94\,\%$ for rated torque is reached. Naturally, the MTPL(m_m) curve [—] marks the upper limit for all curves and is considered the benchmark for the other strategies, which are being compared to the MTPL curve in the following:

- The rated VHz curve [- - -] is considerably worse than MTPL for low speeds, reaching its optimum efficiency only in partload, i.e. where the VHz (rat.) crosses the MTPL trajectory (see Fig. 3.21). With increasing speed, the curve gets closer to the MTPL and at $\omega_\mathrm{m} = 0.8\,\mathrm{p.u.}$, a difference exists only for very low torque values. For higher speeds, the partload performance becomes worse again.
- The optimized VHz [- · -] is designed to maximize the efficiency for rated torque, which is confirmed by the zoomed views. However, this comes at cost of partload efficiency, which is lower compared to the rated VHz. Nevertheless, the optimized VHz approaches MTPL for higher speeds, as the rated VHz does, yet performs better at rated speed as the trajectories in Fig. 3.21 (last plot) almost coincide.
- The CF curve [····] is comparable with the rated VHz curve, since the general idea of keeping the flux on a constant level is the same for both strategies. Differences between the two can be spotted in the low torque region for low speeds and beyond $\omega_\mathrm{m} = 0.8\,\mathrm{p.u.}$, where the impact of iron losses becomes more apparent; as CF for the selected $i_\mathrm{s}^{\mathrm{d}\star}$ uses a higher d-current than VHz (rat.) (see Fig. 3.21), the efficiency is lower at high speeds. Note that a different choice of $i_\mathrm{s}^{\mathrm{d}\star}$ might produce a different result.
- The MTPC curve [—] is very close to the MTPL curve except for speeds $\omega_\mathrm{m} \geq 0.9\,\mathrm{p.u.}$, where the trajectory diverges into positive d-direction (see Fig. 3.21) and, hence, becomes less efficient due to increasing iron losses. The zoom plots reveal, that for low speeds, too, a small difference between MTPC and MTPL can be identified, which is reduced with increasing speed. In general, the estimated torque MTPC curve [- - -] matches well with the measured one, except for $\omega_\mathrm{m} = \{0.1, 0.8\} \cdot \omega_\mathrm{m,nom}$, where the curves are slightly off.
- The MTPV curve [—] clearly fails to compete with the other strategies in terms of efficiency. However, since it is only relevant for very high speeds, as it allows producing the maximum

amount of torque under a given voltage constraint, the focus is not on efficiency optimization here. Nevertheless, for higher torques, MTPV gets close to MTPL. Likewise to MTPC, the estimated torque MTPV curve [- - -] is very close the measured torque MTPV.

In conclusion, at low speeds MTPL is superior to VHz (rat.), while MTPC performs only slightly worse. At $\omega_{\mathrm{m}} = 0.8\,\mathrm{p.u.}$, except for MTPV, all strategies reach similar efficiencies and perform equally fine, whereas for higher speeds, iron losses become significant, such that the MTPC performance drops.

3.4 Summary

An experimental induction machine identification method has been presented, which allows for calculating speed-dependent torque control look-up tables, whose outputs—the dq-reference currents—are fed to an FOC-like current control system. Although, the arbitrarily rotating dq-reference frame does not coincide exactly with the actual rotor flux linkage space vector, reproducible and unique operating points can be set, which is key when using an LUT-based approach. It was shown that maximum efficiency ('maximum torque per loss') operation can be achieved, by estimating the stator flux linkages, machine torque and efficiency, respectively, and calculating the optimized trajectories based on those quantities; expensive laboratory equipment such as a torque sensor is not needed. The results have been verified by measuring the torque and comparing the estimated and measured torque trajectories. Different torque control strategies have been assessed, revealing that MTPL operation—in summary—outperforms the other control strategies, although near $\omega_{\mathrm{m}} = 0.8\,\mathrm{p.u.}$ all tested strategies showed equally good performance. Comparing MTPL with VHz, it was shown that for both, low and very high speeds, efficiency could be increased by using MTPL. For geothermal power applications, rated speed operation seems the most relevant case. Since the pump might not run at full load (part load conditions) for various reasons, e.g.

(i) the electrical machine is over-dimensioned,

(ii) the pump is detuned to prevent overheating, or

(iii) the system curve changes over time (scalings, productivity of the reservoir, etc.) reducing the volume flow and hence the load,

an efficiency increase of up to several percent can be achieved by using MTPL instead of VHz.

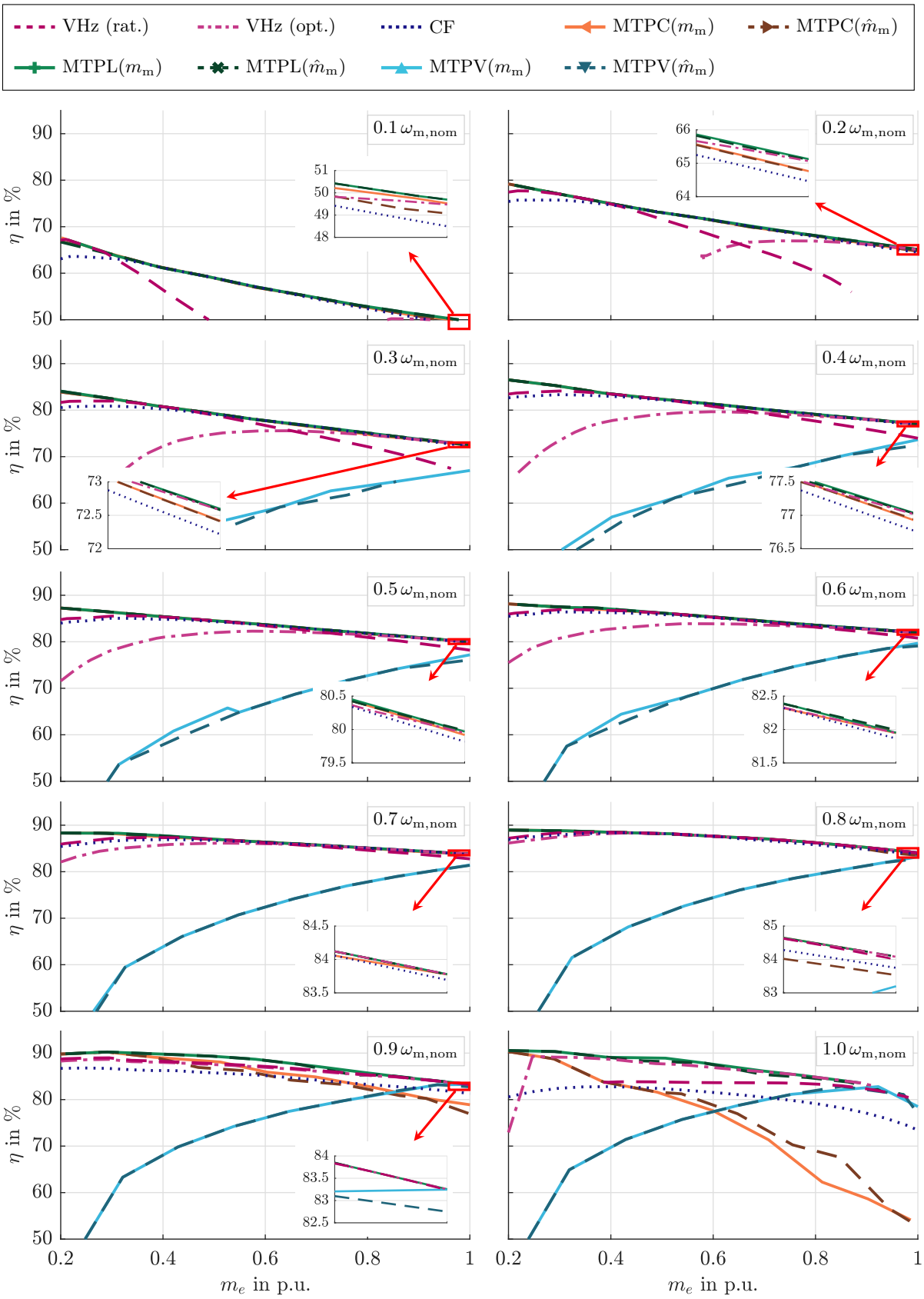

Figure 3.24: *Efficiency (colored layers) [——] and torque [- - -] contour plots over first quadrant (motoring mode) current plane for different speeds* $\{0.1, \ldots, 1\} \cdot \omega_{\mathrm{m,nom}}$.

Chapter 4

Discrete-time speed-sensorless state-feedback-based control of induction machines with LC filter

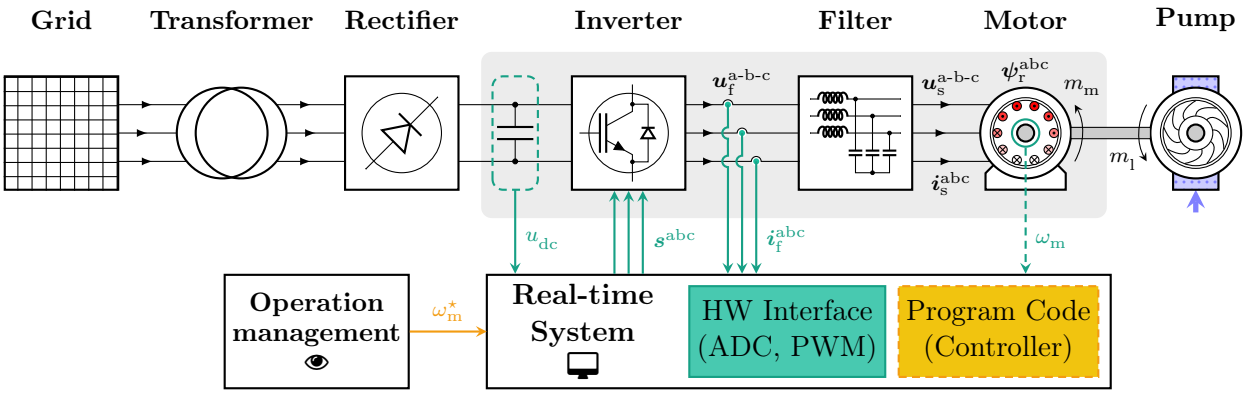

Figure 4.1: *Simplified topology of a geothermal ESP system.*

A closed-loop (sensorless) speed control system is derived for the electric drive system of a geothermal ESP. As opposed to the typically employed *open-loop* V/Hz control method, the *closed-loop* speed controller allows for accurate tracking of a given speed set-point. This, in turn, improves the tracking accuracy of the the pump's BEP. Moreover, using a FOC-like current controller—which is part of the proposed control scheme—helps increasing the efficiency of the electrical machine (as was shown in the preceding chapter). Furthermore, it improves the dynamic behavior (less torque ripple, faster settling times) and avoids excessive currents which might damage the components. Conversely, the proposed method requires a higher computational effort, which needs to be weighed against the benefits of a higher efficiency (decreasing cost and increasing lifetime of the components) and better speed tracking.

The (simplified) topology of the ESP system is depicted in Fig. 4.1, where the relevant components of the electric drive system (inverter, filter and electrical machine) are highlighted. As to restrain the complexity of the control system to a manageable degree, the dynamics of the power cable are neglected as motivated in Ch. 2; ohmic losses in the cable may be considered nonetheless, by adding the electric resistance of the power cable to the stator winding resistance. The hydraulic system is

considered an external system, mechanically acting (with load torque m_l) on the electrical machine via the shaft. Moreover, torsional and frictional effects in- or outside of the electrical machine are neglected for the speed controller design (friction is considered part of the load torque).

The control system is implemented on a real-time system [digital signal processor (DSP)], which is equipped with various interface boards, e.g. a PWM output generation module, translating the controller output into switching signals $\boldsymbol{s}^\mathrm{abc}$, or analog-to-digital converter (ADC) modules, processing sensor data of the filter currents $\boldsymbol{i}_\mathrm{f}^\mathrm{abc}$ and the DC-link voltage u_dc.

An overview of the control system components is given in Fig. 4.2. The main objective of the control system is to make the motor speed ω_m follow a defined set-point $\omega_\mathrm{m}^\star$, which is commanded by the operation management. The machine torque m_m is controlled using the concept of (indirect) rotor flux-oriented *stator current control*; by performing a coordinate transformation from the stationary $\alpha\beta$-reference frame to the rotating dq-reference frame—aligned with the (estimated) rotor flux linkage—magnetic flux and torque can be controlled (almost) separately by the stator current d- and q-components, respectively. The superimposed *speed and flux controllers* produce the respective reference currents. The control system requires information about the electrical and mechanical system states. As not all states can be measured, a *state observer* is used, reconstructing the system states and supplying the estimated values to the control system. The observer itself is fed with the reference voltage produced by the current controller. In addition, as the speed is typically not measured in geothermal ESP systems, the observer is extended by a *speed estimation* module, reconstructing the speed ω_m. Furthermore, *flux orientation* needs to be incorporated.

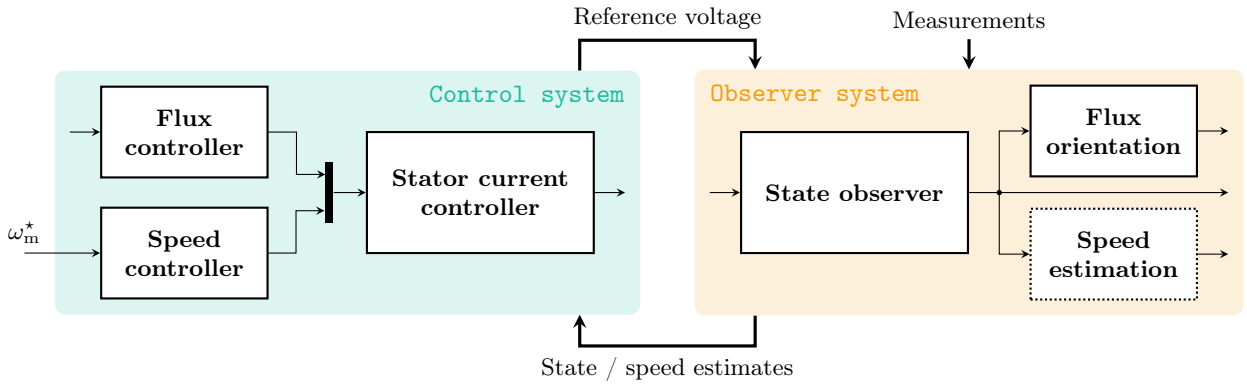

Figure 4.2: *Overview of the control and observer system components.*

Since large geothermal ESPs are typically located in the MV range, the inverter switching frequency is kept low, in order to reduce switching losses in the power modules [61]. As a consequence, the control system is derived in the discrete-time domain to account for the reduced switching and sampling times.

The chapter is structured as follows. In Sec. 4.1, the dynamics of the controlled drive system (inverter, filter and electrical machine) are isolated from the overall ESP system and transformed from the continuous-time (CT) into the discrete-time (DT) domain. Based on the DT system model, the control system is derived in Sec. 4.2: First, the system is augmented by two additional states, in order to realize integral set-point tracking of the stator currents. Then, using the augmented system, the cascaded control system consisting of an inner-loop state-feedback stator current controller and superimposed speed and flux PI controllers is designed. In Sec. 4.3, the full-order state observer is derived, where initially the speed is assumed to be measured. In the next step, the observer is extended by a speed estimation module (speed-adaptive observer), reconstructing the speed and

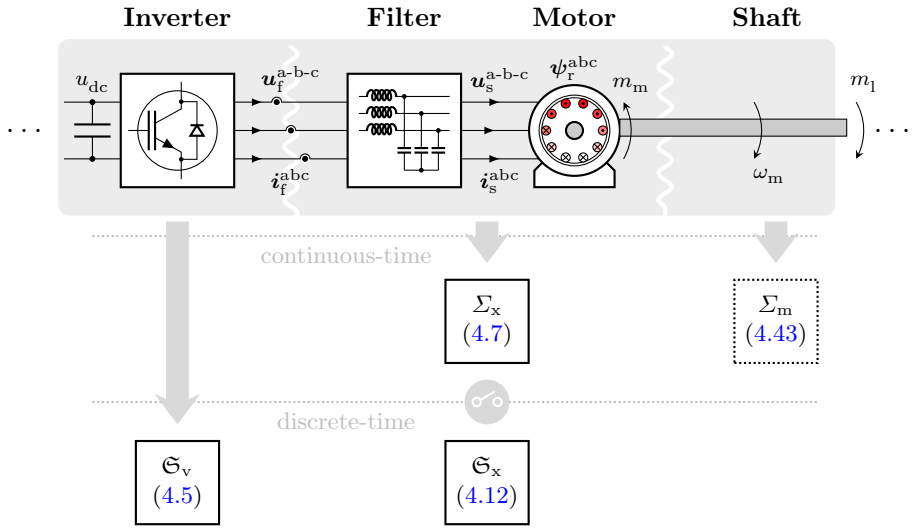

Figure 4.3: *Discrete-time system abstraction of the drive system.*

allowing for speed-sensorless operation. Practical extensions regarding the implementation are further presented. Finally, in Sec. 4.4, the proposed control scheme is validated by simulations and experiments on a down-scaled drive system. Parts of this chapter have been published in [127].

Remark 18 (Notation)**.** *In order to unify the notation, the following formalism is introduced. The system description is split into three different subsystems, namely*

- *the* ***voltage source inverter*** *subsystem (subscript* ‘v’*),*
- *the subsystem of* ***filter and electrical machine*** *(subscript* ‘x’*) and*
- *the* ***integral-action*** *subsystem (subscript* ‘i’*).*

Let $\mathrm{a}, \mathrm{b} \in \{\mathrm{v}, \mathrm{x}, \mathrm{i}\}$ *denote subscripts allocating any of the three subsystems* ‘v’*,* ‘x’ *and* ‘i’ *to scalars, vectors or matrices. Then* states *of subsystem* ‘a’ *are denoted by* $\boldsymbol{x}_\mathrm{a}$*. Similarly, for the* system matrices *which map states of subsystem* ‘a’ *to states of subsystem* ‘b’ *the notation* $\boldsymbol{A}_{\mathrm{a}\to\mathrm{b}}$ *is used; the simplified notation* $\boldsymbol{A}_\mathrm{a} = \boldsymbol{A}_{\mathrm{a}\to\mathrm{a}}$ *is used for mappings between the same subsystems* ‘a’*. In addition* input matrices $\boldsymbol{B}_\mathrm{a}$ *relate the subsystem inputs to the states of subsystem* ‘a’ *and* output matrices $\boldsymbol{C}_\mathrm{a}$ *map the states of subsystem* ‘a’ *to the outputs of the respective subsystem. The benefit of this notation is that combinations of systems may be defined, whose state vectors and matrices are denoted using subscript* ‘ab’*, i.e. combining subsystem* ‘a’ *with subsystem* ‘b’*. Moreover, ‘normal’ font bold capital letters (e.g.* $\boldsymbol{A}$*) are used for* continuous-time *matrices, whereas calligraphic bold capital letters (e.g.* $\boldsymbol{\mathcal{A}}$*) are used to indicate* discrete-time *matrices. Lastly, CT (sub-)* systems, controllers *and* observers *are denoted by* $\Sigma_\square$*,* $\tilde{\Sigma}_\square$ *and* $\hat{\Sigma}_\square$*, while its DT counterparts are denoted using* $\mathfrak{S}_\square$*,* $\tilde{\mathfrak{S}}_\square$ *and* $\hat{\mathfrak{S}}_\square$*, respectively.*

4.1 System definition

In the following, the discrete-time system model of the controlled system comprising VSI, LC filter and IM is derived. The abstraction procedure is shown in Fig. 4.3. While for the inverter, it is reasonable to state the DT system $\mathfrak{S}_\mathrm{v}$ straightaway, the subsystem of LC filter and IM is stated as CT system Σ_x first, and discretized afterwards yielding the DT system $\mathfrak{S}_\mathrm{x}$.

Throughout this chapter, the following assumptions shall hold.

Assumption 17 (Quasi-constant speed)**.** *It is assumed that the mechanical system is considerably 'slower' than the electrical system, such that the rotational speed* $\omega_\mathrm{r} = n_\mathrm{p}\omega_\mathrm{m}$ *can be considered a time-varying parameter.*

Assumption 18 (Electrical frequency)**.** *The rate of change* $\omega_\mathrm{k} = \frac{\mathrm{d}}{\mathrm{d}t}\phi_\mathrm{k}$ *of the Park transformation angle* ϕ_k *is prescribed by the rotor flux orientation (see Sec. 4.3.2.3). For asynchronous machines, it is closely related to the mechanical speed* ω_r*, deviating only by the applied slip which is proportional to the (limited) torque. As a consequence, it can be considered a time-varying parameter, too.*

For the sake of completeness, a fourth subsystem, namely the **mechanical** subsystem (subscript 'm'), is mentioned in Fig. 4.3. Due to Ass. 17, its dynamics are decoupled from the other subsystems, though. However, the corresponding continuous-time mechanical system Σ_m is required for the tuning of the speed controller and will be revisited in the respective section (see Sec. 4.2.2.3).

4.1.1 Discrete-time inverter model

Considering a low switching frequency (e.g. $f_\mathrm{sw} \leq 1\,\mathrm{kHz}$), the VSI dynamics are important for the controller design, since the reference voltages cannot be supplied instantaneously at the inverter outputs. The delay introduced by the inverter depends on the employed modulation scheme, the switching frequency f_sw of the inverter and the sampling delay T_δ.

Assumption 19 (Inverter properties)**.** *Considering the output modulation (i.e. PWM) of the VSI, the following properties shall hold*

1. *The inverter switching frequency* f_sw *is equal to the sampling frequency* f_S *of the measurement, i.e.* $f_\mathrm{sw} = f_\mathrm{S}$ *(and* $T_\mathrm{sw} = T_\mathrm{S}$*).*
2. *Space-vector modulation is used to calculate the timings of the PWM output generation module, hence producing symmetric (mid centered) pulse patterns.*
3. *The current measurement is triggered with a delay of* T_δ *with respect to the beginning of the PWM period.*
4. *The effect of inverter dead-time (see [108, Sec. 2.5]) and voltage drops in the power devices are negligible (Nevertheless, a compensation strategy is proposed as an extension in Sec. 4.3.4.5).*

As the system model Σ_x is discretized for the controller design, the system input is subject to the zero-order hold (ZOH) assumption [128, Sec. 11.1.6], i.e. the input is assumed to be constant from the present time instant $k\,T_\mathrm{S}$ to the succeeding time instant $(k+1)\,T_\mathrm{S}$. Hence, the mean output voltage $\boldsymbol{u}_\mathrm{f,zoh}^{\alpha\beta}$ between time instants $k\,T_\mathrm{S}$ and $(k+1)\,T_\mathrm{S}$ needs to be stated, i.e.

$$\boldsymbol{u}_\mathrm{f,zoh}^{\alpha\beta}(k\,T_\mathrm{S}) = \tfrac{1}{T_\mathrm{S}} \int_{k\,T_\mathrm{S}}^{(k+1)\,T_\mathrm{S}} \boldsymbol{u}_\mathrm{f}^{\alpha\beta}(t)\,\mathrm{d}t = \tfrac{1}{T_\mathrm{S}} \int_{k\,T_\mathrm{S}}^{k\,T_\mathrm{S}+T_\delta} \boldsymbol{u}_\mathrm{f}^{\alpha\beta}(t)\,\mathrm{d}t + \tfrac{1}{T_\mathrm{S}} \int_{k\,T_\mathrm{S}+T_\delta}^{(k+1)\,T_\mathrm{S}} \boldsymbol{u}_\mathrm{f}^{\alpha\beta}(t)\,\mathrm{d}t. \tag{4.1}$$

Typically—for pulse centered PWM—the current measurement is triggered either in the middle or at the end of the PWM period, i.e. the measurement delay is $T_\delta \in \{\frac{1}{2}, 1\} \cdot T_\mathrm{S}$. This way it is ensured that the measurement is performed during an active zero vector, thus minimizing the measurement distortion. In Fig. 4.4, the voltage reconstruction is illustrated for both cases, (a) $T_\delta = \frac{1}{2}T_\mathrm{S}$ and

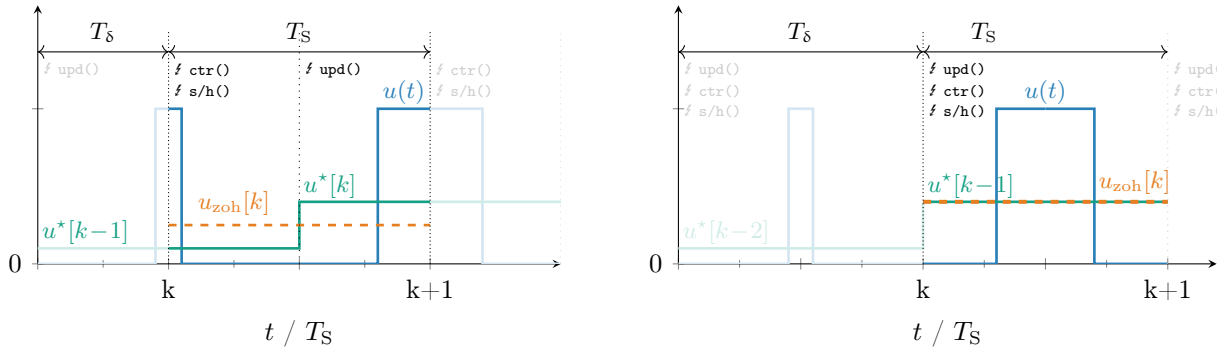

Figure 4.4: *Illustration of the zero-order hold approximation* $u^\star_{\text{zoh}}$ *[- - -] of an exemplary phase voltage* $u(t)$ *[—], using the reference voltage [—], for (a)* $T_\delta = \frac{1}{2}T_S$ *and (b)* $T_\delta = T_S$*. During the controller routine* `ctr()`*, the new reference* $u^\star_{\text{zoh}}$ *is calculated, which is applied in the subsequent update routine* `upd()`*; sampling occurs in the sample-and-hold routine* `s/h()`*.*

(b) $T_\delta = T_S$, which are examined in the following. Considering the two options for the choice of T_δ, Eq. (4.1) can be stated explicitly as:

$$\underline{T_\delta = \tfrac{1}{2}T_S:} \quad \boldsymbol{u}^{\alpha\beta}_{\text{f,zoh}}(k\,T_S) \overset{(4.1)}{=} \frac{1}{T_S}\int_{k\,T_S}^{(k+0.5)\,T_S} \boldsymbol{u}^{\alpha\beta}_{\text{f}}(t)\,\mathrm{d}t + \frac{1}{T_S}\int_{(k+0.5)\,T_S}^{(k+1)\,T_S} \boldsymbol{u}^{\alpha\beta}_{\text{f}}(t)\,\mathrm{d}t$$
$$\overset{(2.7)}{=} \tfrac{1}{2}\boldsymbol{u}^{\alpha\beta\star}_{\text{f}}((k-1)\,T_S) + \tfrac{1}{2}\boldsymbol{u}^{\alpha\beta\star}_{\text{f}}(k\,T_S),$$

$$\underline{T_\delta = T_S:} \quad \boldsymbol{u}^{\alpha\beta}_{\text{f,zoh}}(k\,T_S) \overset{(4.1)}{=} \frac{1}{T_S}\int_{k\,T_S}^{(k+1)\,T_S} \boldsymbol{u}^{\alpha\beta}_{\text{f}}(t)\,\mathrm{d}t + \overbrace{\frac{1}{T_S}\int_{(k+1)\,T_S}^{(k+1)\,T_S} \boldsymbol{u}^{\alpha\beta}_{\text{f}}(t)\,\mathrm{d}t}^{=0} \overset{(2.7)}{=} \boldsymbol{u}^{\alpha\beta\star}_{\text{f}}((k-1)\,T_S),$$

where Assumption 19.2 (symmetric pulses) was used in the first case. Using the discrete notation $x[k] = x(k\,T_S)$, the average voltage can be summarized as

$$\boldsymbol{u}^{\alpha\beta}_{\text{f,zoh}}[k] = \tfrac{T_\delta}{T_S}\boldsymbol{u}^{\alpha\beta\star}_{\text{f}}[k-1] + \tfrac{T_S-T_\delta}{T_S}\boldsymbol{u}^{\alpha\beta\star}_{\text{f}}[k], \tag{4.2}$$

where $\boldsymbol{u}^{\alpha\beta\star}_{\text{f}}[k]$ is the control input and $\boldsymbol{u}^{\alpha\beta\star}_{\text{f}}[k-1]$ is the control input of the previous time step. Note that (4.2) only holds for $T_\delta \in \{\frac{1}{2}, 1\} \cdot T_S$, as otherwise the mean value assumption of (2.7) is not satisfied. Based on (4.2), the dq-equivalent of the ZOH approximation can be derived as follows

$$\begin{aligned} \boldsymbol{u}^{\text{dq}}_{\text{f,zoh}}[k] &= \boldsymbol{T}_{\text{p}}^{-1}(\phi_{\text{k}}[k])\boldsymbol{u}^{\alpha\beta}_{\text{f,zoh}}[k] \\ &\overset{(4.2)}{=} \boldsymbol{T}_{\text{p}}^{-1}(\phi_{\text{k}}[k])\left(\tfrac{T_\delta}{T_S}\boldsymbol{u}^{\alpha\beta\star}_{\text{f}}[k-1] + \tfrac{T_S-T_\delta}{T_S}\boldsymbol{u}^{\alpha\beta\star}_{\text{f}}[k]\right) \\ &= \tfrac{T_\delta}{T_S}\boldsymbol{x}_{\text{v}}[k] + \tfrac{T_S-T_\delta}{T_S}\boldsymbol{u}^{\text{dq}\star}_{\text{f}}[k], \end{aligned} \tag{4.3}$$

where $\boldsymbol{u}^{\text{dq}\star}_{\text{f}}[k]$ is the control input and

$$\begin{aligned} \boldsymbol{x}_{\text{v}}[k] &= \boldsymbol{T}_{\text{p}}^{-1}(\phi_{\text{k}}[k])\boldsymbol{u}^{\alpha\beta\star}_{\text{f}}[k-1] \\ &= \boldsymbol{T}_{\text{p}}^{-1}(\phi_{\text{k}}[k])\boldsymbol{T}_{\text{p}}(\phi_{\text{k}}[k-1])\boldsymbol{u}^{\text{dq}\star}_{\text{f}}[k-1] \\ &= \boldsymbol{T}_{\text{p}}(-T_S\omega_{\text{k}}[k-1])\boldsymbol{u}^{\text{dq}\star}_{\text{f}}[k-1] \end{aligned} \tag{4.4}$$

constitutes a discrete state of the inverter subsystem. Note that the reference voltage handed over to the modulator is given by $\boldsymbol{u}_\mathrm{f}^{\alpha\beta\star}[k] = \boldsymbol{T}_\mathrm{p}(\phi_\mathrm{k}[k])\boldsymbol{u}_\mathrm{f}^{\mathrm{dq}\star}[k]$, i.e. no pre-rotation of the reference vector is needed. Moreover, in anticipation of the following sections, the reference voltage is saturated, as its magnitude is limited to $u_\mathrm{dc}/\sqrt{3}$. Hence, $\boldsymbol{u}_\mathrm{f}^{\mathrm{dq}\star}$ is replaced by $\boldsymbol{u}_\mathrm{f,sat}^{\mathrm{dq}\star}$ in the model.

In conclusion, the discrete-time inverter subsystem in dq-coordinates is given by

$$\mathfrak{S}_\mathrm{v}: \quad \begin{cases} \boldsymbol{x}_\mathrm{v}[k+1] & = \overbrace{\boldsymbol{T}_\mathrm{p}(-T_\mathrm{S}\,\omega_\mathrm{k}[k])}^{=:\boldsymbol{\mathcal{B}}_\mathrm{v}[k]}\boldsymbol{u}_\mathrm{f,sat}^{\mathrm{dq}\star}[k], \\ \boldsymbol{u}_\mathrm{f,zoh}^{\mathrm{dq}}[k] & = \frac{T_\delta}{T_\mathrm{S}}\boldsymbol{x}_\mathrm{v}[k] + \frac{T_\mathrm{S}-T_\delta}{T_\mathrm{S}}\boldsymbol{u}_\mathrm{f,sat}^{\mathrm{dq}\star}[k] \end{cases} \tag{4.5}$$

with state $\boldsymbol{x}_\mathrm{v}$ (shifting ahead (4.4) by one time step), saturated input $\boldsymbol{u}_\mathrm{f,sat}^{\mathrm{dq}\star}$, (known) output $\boldsymbol{u}_\mathrm{f,zoh}^{\mathrm{dq}}$ and input matrix $\boldsymbol{\mathcal{B}}_\mathrm{v} \in \mathbb{R}^{2\times 2}$. The corresponding block diagram is depicted in Fig. 4.5. The states $\boldsymbol{x}_\mathrm{v}$ of the $\mathfrak{S}_\mathrm{v}$ subsystem are known and can be used for state-feedback.

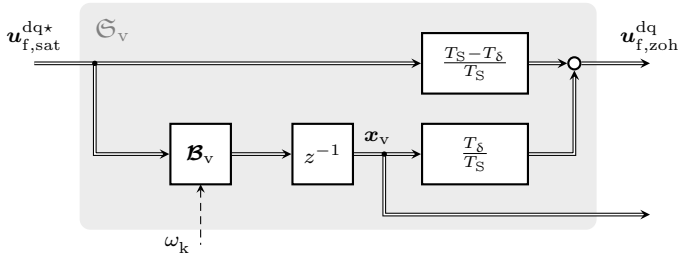

Figure 4.5: *Block diagram of the discrete-time inverter system* $\mathfrak{S}_\mathrm{v}$.

4.1.2 Continuous-time system model

Recalling the results from Ch. 2 and considering Ass. 17, the dynamics of the filter currents $\boldsymbol{i}_\mathrm{f}^{\alpha\beta}$, the stator voltages $\boldsymbol{u}_\mathrm{s}^{\alpha\beta}$, the stator currents $\boldsymbol{i}_\mathrm{s}^{\alpha\beta}$ and the rotor flux linkage $\boldsymbol{\psi}_\mathrm{r}^{\alpha\beta}$ are given by

$$\left.\begin{aligned} \tfrac{\mathrm{d}}{\mathrm{d}t}\boldsymbol{i}_\mathrm{f}^{\alpha\beta}(t) &= -\tfrac{1}{T_\mathrm{f}}\boldsymbol{i}_\mathrm{f}^{\alpha\beta}(t) - \tfrac{1}{L_\mathrm{f}}\boldsymbol{u}_\mathrm{s}^{\alpha\beta}(t) + \tfrac{1}{L_\mathrm{f}}\boldsymbol{u}_\mathrm{f}^{\alpha\beta}(t) \\ \tfrac{\mathrm{d}}{\mathrm{d}t}\boldsymbol{u}_\mathrm{s}^{\alpha\beta}(t) &= \tfrac{1}{C_\mathrm{f}}\boldsymbol{i}_\mathrm{f}^{\alpha\beta}(t) - \tfrac{1}{C_\mathrm{f}}\boldsymbol{i}_\mathrm{s}^{\alpha\beta}(t) \\ \tfrac{\mathrm{d}}{\mathrm{d}t}\boldsymbol{i}_\mathrm{s}^{\alpha\beta}(t) &= \tfrac{1}{\sigma L_\mathrm{s}}\boldsymbol{u}_\mathrm{s}^{\alpha\beta}(t) - \tfrac{1}{T_\mathrm{s}}\boldsymbol{i}_\mathrm{s}^{\alpha\beta}(t) - \tfrac{1}{L_\mu}\left(\omega_\mathrm{r}(t)\boldsymbol{J} - \tfrac{1}{T_\mathrm{r}}\boldsymbol{I}_2\right)\boldsymbol{\psi}_\mathrm{r}^{\alpha\beta}(t) \\ \tfrac{\mathrm{d}}{\mathrm{d}t}\boldsymbol{\psi}_\mathrm{r}^{\alpha\beta}(t) &= \tfrac{L_\mathrm{m}}{T_\mathrm{r}}\boldsymbol{i}_\mathrm{s}^{\alpha\beta}(t) + \left(\omega_\mathrm{r}(t)\boldsymbol{J} - \tfrac{1}{T_\mathrm{r}}\boldsymbol{I}_2\right)\boldsymbol{\psi}_\mathrm{r}^{\alpha\beta}(t) \end{aligned}\right\}, \tag{4.6}$$

where, as opposed to Ch. 3, the simplified model of the IM is considered, i.e. iron losses are neglected (see Ass. 4) and the linear flux model with constant inductances is assumed (see Ass. 5).

The system equations (4.6), stated in αβ-coordinates, are transformed into the arbitrarily rotating dq-reference frame by applying the Park transformation (see App. A.1.2) with transformation angle $\phi_\mathrm{k} = \int \omega_\mathrm{k}\mathrm{d}t$. Considering Ass. 17 and 18, the continuous-time linear parameter-varying (LPV) system can be stated as

$$\Sigma_\mathrm{x}: \quad \begin{cases} \tfrac{\mathrm{d}}{\mathrm{d}t}\boldsymbol{x}_\mathrm{x}(t) = \boldsymbol{A}_\mathrm{x}(\omega_\mathrm{r},\omega_\mathrm{k})\boldsymbol{x}_\mathrm{x}(t) + \boldsymbol{B}_\mathrm{x}\boldsymbol{u}_\mathrm{f}^{\mathrm{dq}}(t) \\ \boldsymbol{i}_\mathrm{f}^{\mathrm{dq}}(t) = \boldsymbol{C}_\mathrm{x}\boldsymbol{x}_\mathrm{x}(t) \\ \boldsymbol{i}_\mathrm{s}^{\mathrm{dq}}(t) = \boldsymbol{F}_\mathrm{x}\boldsymbol{x}_\mathrm{x}(t) \end{cases} \tag{4.7}$$

with state vector $\boldsymbol{x}_\mathrm{x} := (\boldsymbol{i}_\mathrm{f}^{\mathrm{dq}\top}, \boldsymbol{u}_\mathrm{s}^{\mathrm{dq}\top}, \boldsymbol{i}_\mathrm{s}^{\mathrm{dq}\top}, \boldsymbol{\psi}_\mathrm{r}^{\mathrm{dq}\top})^\top \in \mathbb{R}^8$, input $\boldsymbol{u}_\mathrm{f}^\mathrm{dq}$, measured output $\boldsymbol{i}_\mathrm{f}^\mathrm{dq}$ and control output $\boldsymbol{i}_\mathrm{s}^\mathrm{dq}$; the 'control output' is an auxiliary output, which is used as feedback for the control system. The parameter-varying state matrix $\boldsymbol{A}_\mathrm{x}(\omega_\mathrm{r}, \omega_\mathrm{k}) \in \mathbb{R}^{8\times8}$, the input matrix $\boldsymbol{B}_\mathrm{x} \in \mathbb{R}^{8\times2}$ and the output matrices $\boldsymbol{C}_\mathrm{x}$ and $\boldsymbol{F}_\mathrm{x} \in \mathbb{R}^{2\times8}$, are defined as

$$\left.\begin{aligned} \boldsymbol{A}_\mathrm{x}(\omega_\mathrm{r}, \omega_\mathrm{k}) &:= \boldsymbol{A}_0 + \boldsymbol{A}_\mathrm{r}\omega_\mathrm{r}(t) + \boldsymbol{A}_\mathrm{k}\omega_\mathrm{k}(t), & \boldsymbol{B}_\mathrm{x} &:= \begin{bmatrix} \frac{1}{L_\mathrm{f}}\boldsymbol{I}_2 & \boldsymbol{0}_{2\times2} & \boldsymbol{0}_{2\times2} & \boldsymbol{0}_{2\times2} \end{bmatrix}^\top, \\ \boldsymbol{C}_\mathrm{x} &:= \begin{bmatrix} \boldsymbol{I}_2 & \boldsymbol{0}_{2\times2} & \boldsymbol{0}_{2\times2} & \boldsymbol{0}_{2\times2} \end{bmatrix} \quad \text{and} & \boldsymbol{F}_\mathrm{x} &:= \begin{bmatrix} \boldsymbol{0}_{2\times2} & \boldsymbol{0}_{2\times2} & \boldsymbol{I}_2 & \boldsymbol{0}_{2\times2} \end{bmatrix}, \end{aligned}\right\} \tag{4.8}$$

with constant submatrices

$$\boldsymbol{A}_0 := \begin{bmatrix} -\frac{1}{T_\mathrm{f}}\boldsymbol{I}_2 & -\frac{1}{L_\mathrm{f}}\boldsymbol{I}_2 & \boldsymbol{0}_{2\times2} & \boldsymbol{0}_{2\times2} \\ \frac{1}{C_\mathrm{f}}\boldsymbol{I}_2 & \boldsymbol{0}_{2\times2} & -\frac{1}{C_\mathrm{f}}\boldsymbol{I}_2 & \boldsymbol{0}_{2\times2} \\ \boldsymbol{0}_{2\times2} & \frac{1}{\sigma L_\mathrm{s}}\boldsymbol{I}_2 & -\frac{1}{T_\mathrm{s}}\boldsymbol{I}_2 & \frac{1}{L_\mu}\frac{1}{T_\mathrm{r}}\boldsymbol{I}_2 \\ \boldsymbol{0}_{2\times2} & \boldsymbol{0}_{2\times2} & \frac{L_\mathrm{m}}{T_\mathrm{r}}\boldsymbol{I}_2 & -\frac{1}{T_\mathrm{r}}\boldsymbol{I}_2 \end{bmatrix} \tag{4.9}$$

and

$$\boldsymbol{A}_\mathrm{r} := \begin{bmatrix} \boldsymbol{0}_{2\times2} & \boldsymbol{0}_{2\times2} & \boldsymbol{0}_{2\times2} & \boldsymbol{0}_{2\times2} \\ \boldsymbol{0}_{2\times2} & \boldsymbol{0}_{2\times2} & \boldsymbol{0}_{2\times2} & \boldsymbol{0}_{2\times2} \\ \boldsymbol{0}_{2\times2} & \boldsymbol{0}_{2\times2} & \boldsymbol{0}_{2\times2} & -\frac{1}{L_\mu}\boldsymbol{J} \\ \boldsymbol{0}_{2\times2} & \boldsymbol{0}_{2\times2} & \boldsymbol{0}_{2\times2} & \boldsymbol{J} \end{bmatrix}, \qquad \boldsymbol{A}_\mathrm{k}, := \begin{bmatrix} -\boldsymbol{J} & \boldsymbol{0}_{2\times2} & \boldsymbol{0}_{2\times2} & \boldsymbol{0}_{2\times2} \\ \boldsymbol{0}_{2\times2} & -\boldsymbol{J} & \boldsymbol{0}_{2\times2} & \boldsymbol{0}_{2\times2} \\ \boldsymbol{0}_{2\times2} & \boldsymbol{0}_{2\times2} & -\boldsymbol{J} & \boldsymbol{0}_{2\times2} \\ \boldsymbol{0}_{2\times2} & \boldsymbol{0}_{2\times2} & \boldsymbol{0}_{2\times2} & -\boldsymbol{J} \end{bmatrix}, \tag{4.10}$$

respectively. The corresponding block diagram is depicted in Fig. 4.6a.

4.1.3 Discrete-time system model with ZOH input

Under the assumptions of a zero-order hold input and slowly varying parameters (see Ass. 17 & 18),

$$\forall\, k\, T_\mathrm{S} \le t \le (k+1)T_\mathrm{S}: \quad \boldsymbol{u}_{\mathrm{f,zoh}}^\mathrm{dq} = \text{const.}, \qquad \omega_\mathrm{k}(t) = \text{const.} \quad \text{and} \quad \omega_\mathrm{r}(t) = \text{const.} \tag{4.11}$$

hold true. Hence, the CT system Σ_x can be discretized subject to the discretization method described in App. E.1, yielding the DT system

$$\mathfrak{S}_\mathrm{x}: \quad \begin{cases} \boldsymbol{x}_\mathrm{x}[k+1] = \boldsymbol{\mathcal{A}}_\mathrm{x}[k]\boldsymbol{x}_\mathrm{x}[k] + \boldsymbol{\mathcal{B}}_\mathrm{x}^*[k]\overbrace{\left(\frac{T_\delta}{T_\mathrm{S}}\boldsymbol{x}_\mathrm{v}[k] + \frac{T_\mathrm{S}-T_\delta}{T_\mathrm{S}}\boldsymbol{u}_\mathrm{f}^{\mathrm{dq}\star}[k]\right)}^{=\boldsymbol{u}_{\mathrm{f,zoh}}^\mathrm{dq}[k]}, \\ \boldsymbol{i}_\mathrm{f}^\mathrm{dq}[k] = \boldsymbol{\mathcal{C}}_\mathrm{x}\boldsymbol{x}_\mathrm{x}[k], \qquad \boldsymbol{i}_\mathrm{s}^\mathrm{dq}[k] = \boldsymbol{\mathcal{F}}_\mathrm{x}\boldsymbol{x}_\mathrm{x}[k], \end{cases} \tag{4.12}$$

with discrete system, input and output matrices

$$\left.\begin{aligned} \boldsymbol{\mathcal{A}}_\mathrm{x}[k] &:= \boldsymbol{I}_8 + \boldsymbol{S}_{N_\delta}[k]\boldsymbol{A}_\mathrm{x}(\omega_\mathrm{r}[k], \omega_\mathrm{k}[k]), & \boldsymbol{\mathcal{B}}_\mathrm{x}^*[k] &:= \boldsymbol{S}_{N_\delta}[k]\boldsymbol{B}_\mathrm{x}, \\ \boldsymbol{\mathcal{C}}_\mathrm{x} &:= \boldsymbol{C}_\mathrm{x} & \text{and} \quad \boldsymbol{\mathcal{F}}_\mathrm{x} &:= \boldsymbol{F}_\mathrm{x}. \end{aligned}\right\} \tag{4.13}$$

The discretization matrix $\boldsymbol{S}_{N_\delta}$ and the respective residual matrix $\tilde{\boldsymbol{S}}_{N_\delta}$ are defined as (see App. E.1)

$$\left.\begin{aligned} \boldsymbol{S}_{N_\delta}[k] &:= \sum_{i=1}^{N_\delta} \frac{T_\mathrm{S}^i}{i!}\big(\boldsymbol{A}_\mathrm{x}(\omega_\mathrm{r}[k], \omega_\mathrm{k}[k])\big)^{i-1} \quad \text{and} \quad \tilde{\boldsymbol{S}}_{N_\delta}[k] := \sum_{i=N_\delta+1}^{\infty} \frac{T_\mathrm{S}^i}{i!}\big(\boldsymbol{A}_\mathrm{x}(\omega_\mathrm{r}[k], \omega_\mathrm{k}[k])\big)^{i-1}, \end{aligned}\right\} \tag{4.14}$$

where N_δ is the discretization order. The respective block diagram of the DT inverter subsystem is depicted in Fig. 4.6b, where $\{\cdot\}$ indicates the discretization order of respective matrices.

Remark 19 (Discretization order)**.** *Unlike for software implemented systems where a finite discretization order must be chosen—e.g. control or observer systems—the discretization order of the real system is $N_\delta = \infty$, i.e. yielding $\boldsymbol{S}_{N_\delta} = \boldsymbol{S}_\infty$ and $\tilde{\boldsymbol{S}}_\infty = \boldsymbol{0}_{8\times8}$.*

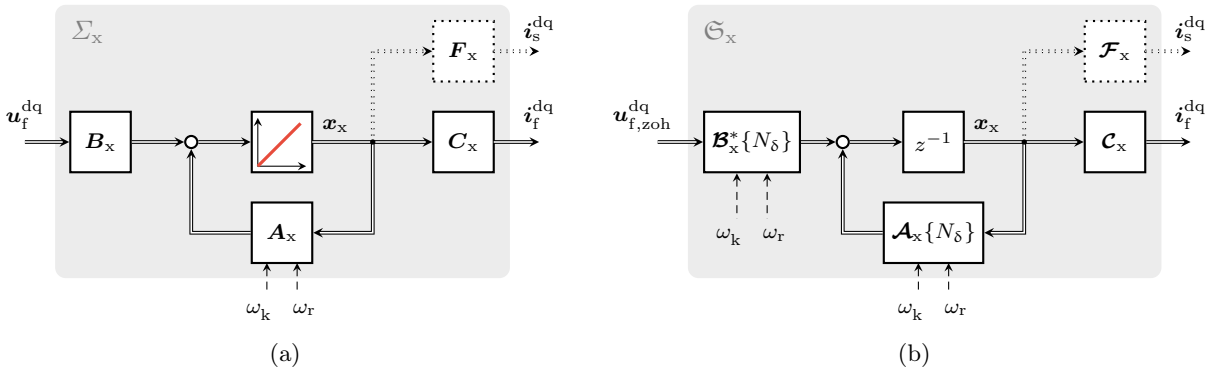

Figure 4.6: *Block diagrams of the (a) continuous-time drive system Σ_x and the (b) discrete-time drive system $\mathfrak{S}_x$.*

4.2 Control system

The closed-loop speed control system is realized using a cascaded controller structure as depicted in Fig. 4.7. The outer-loop proportional-integral (PI) flux and speed controllers produce the (saturated) stator reference currents $i_{s,sat}^{d\star}$ and $i_{s,sat}^{q\star}$, which are forwarded to the inner-loop state-feedback stator current controller. In order to be able to reach higher-than-rated speed, a field-weakening LUT produces the flux reference $\psi_r^{d\star}$ based on the actual frequency ω_k. The state-feedback controller is derived assuming total knowledge of the actual system states $\boldsymbol{x}_x$. However, for the implementation, the estimated states $\hat{\boldsymbol{x}}_x$ will be used, which is feasible due to the so-called *separation principle* (see e.g. [129, p. 56]). The separation principle states that the eigenvalues of controller and observer can be prescribed *separately*, without affecting each other.

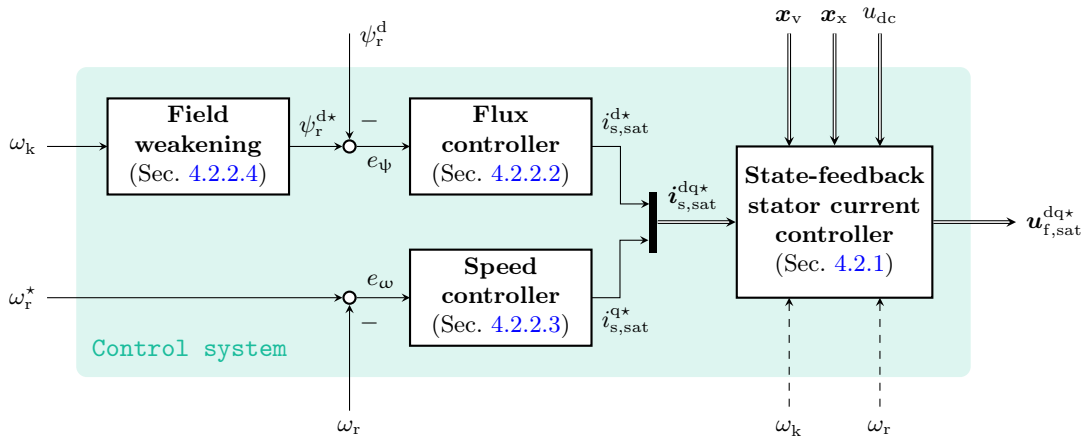

Figure 4.7: *Overview of the closed-loop speed control system.*

4.2.1 State-feedback current control system with proportional-integral (PI) set-point tracking

Due to the series connection of LC filter and induction machine, the stator currents can only be controlled indirectly through the LC filter output. In the literature, this problem is typically solved by using a low-level cascade of PI or dead-beat controllers for the filter currents, stator voltages and

stator currents, respectively (e.g. [64, 67, 130]). This approach, however, requires individual tuning of the controllers, which is often based on rules of thumb, trial-and-error and rough approximations of the system dynamics. In this chapter, the electrical system of LC filter and induction machine (and VSI) is considered as a whole, controlled by a single state-feedback controller. This way, the controller tuning becomes more robust and intuitive as e.g. the linear quadratic regulator (LQR) tuning approach can be used. For the controller design, it is assumed that the drive system is fully controllable (which is shown for the continuous-time system Σ_x in App. E.4).

The state-feedback stator current control system constitutes the inner-loop of the cascaded control system. Main requirements are (i) fast tracking of the reference currents $\boldsymbol{i}_\mathrm{s,sat}^\mathrm{dq\star}$ and (ii) asymptotic reference tracking, i.e. $\lim_{t\to\infty} \boldsymbol{i}_\mathrm{s,sat}^\mathrm{dq\star} - \boldsymbol{i}_\mathrm{s}^\mathrm{dq} = \mathbf{o}_2$. As a plain state-feedback controller is not able to track a given set-point, integral-action (I) is introduced in terms of two additional system states (integrals over the control error) which are considered in the state-feedback design, leading to an augmented system. In addition, a feedforward (proportional) term (P) is added to achieve a faster transient response.

In view of the implementation, it is advisable to design the control system in the discrete-time domain in order account for the typically low switching frequencies of MV drives in geothermal ESP applications.

4.2.1.1 Discrete-time integral-error states with anti-windup and ZOH input

The system is augmented by two additional (virtual) states $\boldsymbol{x}_\mathrm{i} \in \mathbb{R}^2$, which represent the integral over the control error $\boldsymbol{i}_\mathrm{s,sat}^\mathrm{dq\star} - \boldsymbol{i}_\mathrm{s}^\mathrm{dq}$ (control input). As the integration should be disabled if the voltage limit is exceeded, an anti-windup decision function $f_\mathrm{awu,sf}$ (see below for more details) is further incorporated in the state-feedback control system [109, Sec. 10.4.1], yielding the CT integral subsystem

$$\Sigma_\mathrm{i}: \quad \tfrac{\mathrm{d}}{\mathrm{d}t}\boldsymbol{x}_\mathrm{i}(t) = f_\mathrm{awu,sf}(\boldsymbol{u}_\mathrm{f}^\mathrm{dq\star})\left(\boldsymbol{i}_\mathrm{s,sat}^\mathrm{dq\star}(t) - \boldsymbol{F}_\mathrm{x}\boldsymbol{x}_\mathrm{x}(t)\right). \tag{4.15}$$

Discretization of the integrator dynamics should be performed in combination with the discretization of the continuous-time plant model Σ_x, i.e. considering the combined system

$$\tfrac{\mathrm{d}}{\mathrm{d}t}\begin{pmatrix}\boldsymbol{x}_\mathrm{x}(t)\\ \boldsymbol{x}_\mathrm{i}(t)\end{pmatrix} = \overbrace{\left[\begin{array}{c|c}\boldsymbol{A}_\mathrm{x}(\omega_\mathrm{r},\omega_\mathrm{k}) & \mathbf{0}_{8\times2}\\ \hline -\boldsymbol{F}_\mathrm{x} & \mathbf{0}_{2\times2}\end{array}\right]}^{=:\boldsymbol{A}_\mathrm{xi}(\omega_\mathrm{r},\omega_\mathrm{k})\in\mathbb{R}^{10\times10}}\begin{pmatrix}\boldsymbol{x}_\mathrm{x}(t)\\ \boldsymbol{x}_\mathrm{i}(t)\end{pmatrix} + \overbrace{\begin{bmatrix}\boldsymbol{B}_\mathrm{x}\\ \mathbf{0}_{2\times2}\end{bmatrix}}^{=:\boldsymbol{B}_\mathrm{xi}\in\mathbb{R}^{10\times2}}\boldsymbol{u}_\mathrm{f}^\mathrm{dq}(t) + \overbrace{\begin{bmatrix}\mathbf{0}_{8\times2}\\ \boldsymbol{I}_2\end{bmatrix}}^{=:\boldsymbol{E}_\mathrm{xi}\in\mathbb{R}^{10\times2}}\boldsymbol{i}_\mathrm{s,sat}^\mathrm{dq\star}(t). \tag{4.16}$$

The respective discretization matrix $\boldsymbol{S}_{N_\delta}^*$ is derived as

$$\boldsymbol{S}_{N_\delta}^*[k] = \sum_{i=1}^{N_\delta}\frac{T_\mathrm{S}^i}{i!}\boldsymbol{A}_\mathrm{xi}^{i-1}(\omega_\mathrm{r}[k],\omega_\mathrm{k}[k]) = \ldots = \begin{bmatrix}\boldsymbol{S}_{N_\delta}[k] & \mathbf{0}_{2\times2}\\ -\boldsymbol{F}_\mathrm{x}(\boldsymbol{S}_{N_\delta}[k] - T_\mathrm{S}\boldsymbol{I}_8)\boldsymbol{A}_\mathrm{xi}^{-1}(\omega_\mathrm{r}[k],\omega_\mathrm{k}[k]) & T_\mathrm{S}\boldsymbol{I}_2\end{bmatrix} \tag{4.17}$$

and can be used to calculate the discrete-time system, input and control input matrices as follows

(for more details see App. E.1)

$$\left.\begin{aligned}
\boldsymbol{\mathcal{A}}_{\mathrm{xi}}[k] &= \left[\begin{array}{c|c} \boldsymbol{\mathcal{A}}_{\mathrm{x}}[k] & \boldsymbol{\mathcal{A}}_{\mathrm{i}\to\mathrm{x}}[k] \\ \hline \boldsymbol{\mathcal{A}}_{\mathrm{x}\to\mathrm{i}}[k] & \boldsymbol{\mathcal{A}}_{\mathrm{i}}[k] \end{array}\right] := \boldsymbol{I}_{10} + \boldsymbol{S}^{*}_{N_\delta}[k]\boldsymbol{A}_{\mathrm{xi}}(\omega_{\mathrm{r}}[k],\omega_{\mathrm{k}}[k]) = \left[\begin{array}{c|c} \boldsymbol{\mathcal{A}}_{\mathrm{x}}[k] & \boldsymbol{0}_{8\times 2} \\ \hline -\boldsymbol{F}_{\mathrm{x}}\boldsymbol{S}_{N_\delta}[k] & \boldsymbol{I}_2 \end{array}\right], \\
\boldsymbol{\mathcal{B}}^{*}_{\mathrm{xi}}[k] &= \left[\begin{array}{c} \boldsymbol{\mathcal{B}}^{*}_{\mathrm{x}}[k] \\ \hline \boldsymbol{\mathcal{B}}^{*}_{\mathrm{i}}[k] \end{array}\right] := \boldsymbol{S}^{*}_{N_\delta}[k]\boldsymbol{B}_{\mathrm{xi}} = \left[\begin{array}{c} \boldsymbol{\mathcal{B}}^{*}_{\mathrm{x}}[k] \\ \hline -\boldsymbol{F}_{\mathrm{x}}(\boldsymbol{S}_{N_\delta}[k] - T_{\mathrm{S}}\boldsymbol{I}_8)\boldsymbol{A}_{\mathrm{x}}^{-1}(\omega_{\mathrm{r}}[k],\omega_{\mathrm{k}}[k])\boldsymbol{B}_{\mathrm{x}} \end{array}\right] \\
\text{and} \quad \boldsymbol{\mathcal{E}}_{\mathrm{xi}} &= \left[\begin{array}{c} \boldsymbol{\mathcal{E}}_{\mathrm{x}}[k] \\ \hline \boldsymbol{\mathcal{E}}_{\mathrm{i}}[k] \end{array}\right] := \boldsymbol{S}^{*}_{N_\delta}[k]\boldsymbol{E}_{\mathrm{xi}} = \left[\begin{array}{c} \boldsymbol{0}_{8\times 2} \\ \hline T_{\mathrm{S}}\boldsymbol{I}_2 \end{array}\right].
\end{aligned}\right\} \tag{4.18}$$

Apparently, the DT system $\mathfrak{S}_{\mathrm{x}}$ does not change by introducing the two additional states. However, due to the approximated exact discretization, the system input $\boldsymbol{u}_{\mathrm{f}}^{\mathrm{dq}}$ is acting on the states $\boldsymbol{x}_{\mathrm{i}}$, as $\boldsymbol{\mathcal{B}}^{*}_{\mathrm{i}}$ is unequal to zero.

In the context of integral-action, integrator windup is an important topic. The windup effect occurs, when the reference cannot be applied by the actuator—e.g. due to physical limitations—and the controller, in the attempt of counteracting the increasing integral error, produces an even higher reference. Typical consequences are a deteriorated performance or even instability. As a countermeasure, the integration needs to be interrupted, if the voltage limit is exceeded [109, Sec. 10.4.1.1]. The resulting DT dynamics of the integral states with anti-windup are given by

$$\begin{aligned}
\mathfrak{S}_{\mathrm{i}}: \quad \boldsymbol{x}_{\mathrm{i}}[k+1] = \boldsymbol{\mathcal{A}}_{\mathrm{i}}\boldsymbol{x}_{\mathrm{i}}[k] + f_{\mathrm{awu,sf}}(\boldsymbol{u}_{\mathrm{f}}^{\mathrm{dq}\star}[k])\Big(&\boldsymbol{\mathcal{A}}_{\mathrm{x}\to\mathrm{i}}[k]\boldsymbol{x}_{\mathrm{x}}[k] + \boldsymbol{\mathcal{E}}_{\mathrm{i}}\boldsymbol{i}_{\mathrm{s,sat}}^{\mathrm{dq}\star}[k] \\
&+ \boldsymbol{\mathcal{B}}^{*}_{\mathrm{i}}[k]\underbrace{\left[\tfrac{T_\delta}{T_{\mathrm{S}}}\boldsymbol{x}_{\mathrm{v}}[k] + \tfrac{T_{\mathrm{S}}-T_\delta}{T_{\mathrm{S}}}\boldsymbol{u}_{\mathrm{f}}^{\mathrm{dq}\star}[k]\right]}_{=\boldsymbol{u}_{\mathrm{f,zoh}}^{\mathrm{dq}}[k]}\Big),
\end{aligned} \tag{4.19}$$

with matrices as defined in (4.18) and anti-windup decision function

$$f_{\mathrm{awu,sf}}(\boldsymbol{u}_{\mathrm{f}}^{\mathrm{dq}\star}) = \begin{cases} 1, & \text{for } \|\boldsymbol{u}_{\mathrm{f}}^{\mathrm{dq}\star}\| \leq \hat{u}_{\mathrm{f,nom}}, \\ 0, & \text{else.} \end{cases} \tag{4.20}$$

The corresponding block diagrams are depicted in Fig. 4.8, showing (a) the CT and (b) DT integral subsystems, respectively. In the latter, $\{\cdot\}$ indicates the discretization order of respective matrices.

4.2.1.2 State-feedback control law and closed-loop system

For the controller design, it is assumed that anti-windup is inactive, i.e. $f_{\mathrm{awu,sf}} = 1$ holds true. Thus, the nonlinearity in subsystem $\mathfrak{S}_{\mathrm{i}}$ caused by $f_{\mathrm{awu,sf}}$ is removed. Combining the subsystems $\mathfrak{S}_{\mathrm{v}}, \mathfrak{S}_{\mathrm{x}}$ and $\mathfrak{S}_{\mathrm{i}}$, yields the overall DT augmented system

$$\left.\begin{aligned}
\mathfrak{S}_{\mathrm{vxi}}: \quad \begin{pmatrix} \boldsymbol{x}_{\mathrm{v}}[k+1] \\ \boldsymbol{x}_{\mathrm{x}}[k+1] \\ \boldsymbol{x}_{\mathrm{i}}[k+1] \end{pmatrix} &= \overbrace{\left[\begin{array}{c|c|c} \boldsymbol{0}_{2\times 2} & \boldsymbol{0}_{2\times 8} & \boldsymbol{0}_{2\times 2} \\ \hline \boldsymbol{\mathcal{A}}_{\mathrm{v}\to\mathrm{x}}[k] & \boldsymbol{\mathcal{A}}_{\mathrm{x}}[k] & \boldsymbol{0}_{2\times 2} \\ \hline \boldsymbol{\mathcal{A}}_{\mathrm{v}\to\mathrm{i}}[k] & \boldsymbol{\mathcal{A}}_{\mathrm{x}\to\mathrm{i}}[k] & \boldsymbol{\mathcal{A}}_{\mathrm{i}} \end{array}\right]}^{=:\boldsymbol{\mathcal{A}}_{\mathrm{vxi}}[k]} \overbrace{\begin{pmatrix} \boldsymbol{x}_{\mathrm{v}}[k] \\ \boldsymbol{x}_{\mathrm{x}}[k] \\ \boldsymbol{x}_{\mathrm{i}}[k] \end{pmatrix}}^{=:\boldsymbol{x}_{\mathrm{vxi}}} + \overbrace{\begin{bmatrix} \boldsymbol{\mathcal{B}}_{\mathrm{v}}[k] \\ \boldsymbol{\mathcal{B}}_{\mathrm{x}}[k] \\ \boldsymbol{\mathcal{B}}_{\mathrm{i}}[k] \end{bmatrix}}^{=:\boldsymbol{\mathcal{B}}_{\mathrm{vxi}}[k]} \boldsymbol{u}_{\mathrm{f}}^{\mathrm{dq}\star}[k] + \overbrace{\begin{bmatrix} \boldsymbol{0}_{2\times 2} \\ \boldsymbol{0}_{8\times 2} \\ \boldsymbol{\mathcal{E}}_{\mathrm{i}} \end{bmatrix}}^{=:\boldsymbol{\mathcal{E}}_{\mathrm{vxi}}[k]} \boldsymbol{i}_{\mathrm{s,sat}}^{\mathrm{dq}\star}[k], \\
\boldsymbol{i}_{\mathrm{f}}^{\mathrm{dq}}[k] &= \underbrace{\begin{bmatrix} \boldsymbol{0}_{2\times 2} & \boldsymbol{\mathcal{C}}_{\mathrm{x}} & \boldsymbol{0}_{2\times 2} \end{bmatrix}}_{=:\boldsymbol{\mathcal{C}}_{\mathrm{vxi}}} \boldsymbol{x}_{\mathrm{vxi}}[k], \qquad \boldsymbol{i}_{\mathrm{s}}^{\mathrm{dq}}[k] = \underbrace{\begin{bmatrix} \boldsymbol{0}_{2\times 2} & \boldsymbol{\mathcal{F}}_{\mathrm{x}} & \boldsymbol{0}_{2\times 2} \end{bmatrix}}_{=:\boldsymbol{\mathcal{F}}_{\mathrm{vxi}}} \boldsymbol{x}_{\mathrm{vxi}}[k],
\end{aligned}\right. \tag{4.21}$$

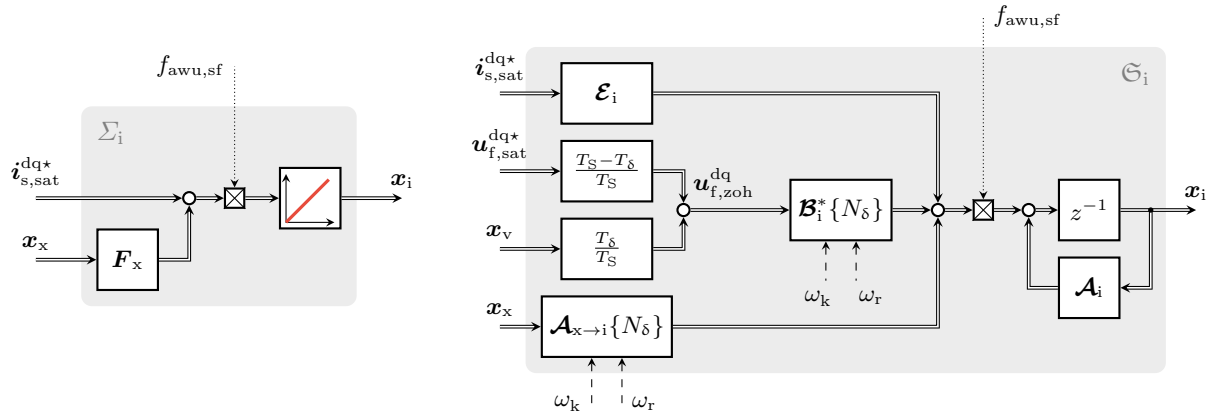

Figure 4.8: *Block diagrams of the (a) continuous-time integral error subsystem Σ_{i} and (b) the discrete-time integral error subsystem $\mathfrak{S}_{\mathrm{i}}$.*

with augmented state vector $\boldsymbol{x}_{\mathrm{vxi}} \in \mathbb{R}^{12}$, control input $\boldsymbol{u}^{\mathrm{dq}\star}_{\mathrm{f}}$, auxiliary input $\boldsymbol{i}^{\mathrm{dq}\star}_{\mathrm{s,sat}}$, measured output $\boldsymbol{i}^{\mathrm{dq}}_{\mathrm{f}}$, control output $\boldsymbol{i}^{\mathrm{dq}}_{\mathrm{s}}$, system matrix $\boldsymbol{\mathcal{A}}_{\mathrm{vxi}} \in \mathbb{R}^{12\times12}$, input matrix $\boldsymbol{\mathcal{B}}_{\mathrm{vxi}} \in \mathbb{R}^{12\times2}$, auxiliary input matrix $\boldsymbol{\mathcal{E}}_{\mathrm{vxi}} \in \mathbb{R}^{12\times2}$ and control output matrix $\boldsymbol{\mathcal{F}}_{\mathrm{vxi}} \in \mathbb{R}^{2\times12}$. Note that the ZOH input $\boldsymbol{u}^{\mathrm{dq}}_{\mathrm{f,zoh}}$ is split into two parts in (4.21), such that the part related to the states $\boldsymbol{x}_{\mathrm{v}}$ is moved to the system matrix, whereas the part related to $\boldsymbol{u}^{\mathrm{dq}\star}_{\mathrm{f}}$ constitutes the input matrix of the system, i.e.

$$\begin{bmatrix}\boldsymbol{\mathcal{A}}_{\mathrm{v}\to\mathrm{x}}[k]\\ \boldsymbol{\mathcal{A}}_{\mathrm{v}\to\mathrm{i}}[k]\end{bmatrix} := \tfrac{T_{\delta}}{T_{\mathrm{S}}}\begin{bmatrix}\boldsymbol{\mathcal{B}}^{*}_{\mathrm{x}}[k]\\ \boldsymbol{\mathcal{B}}^{*}_{\mathrm{i}}[k]\end{bmatrix} \qquad \text{and} \qquad \begin{bmatrix}\boldsymbol{\mathcal{B}}_{\mathrm{x}}[k]\\ \boldsymbol{\mathcal{B}}_{\mathrm{i}}[k]\end{bmatrix} := \tfrac{T_{\mathrm{S}}-T_{\delta}}{T_{\mathrm{S}}}\begin{bmatrix}\boldsymbol{\mathcal{B}}^{*}_{\mathrm{x}}[k]\\ \boldsymbol{\mathcal{B}}^{*}_{\mathrm{i}}[k]\end{bmatrix}. \tag{4.22}$$

The corresponding state-feedback control law with proportional-integral (PI) set-point tracking is given by (see [129, Ch. 8.6])

$$\tilde{\mathfrak{S}}_{\mathrm{sf,i}}: \quad \boldsymbol{u}^{\mathrm{dq}\star}_{\mathrm{f}}[k] = -\boldsymbol{\mathcal{K}}_{\mathrm{vxi}}\boldsymbol{x}_{\mathrm{vxi}}[k] + \boldsymbol{\mathcal{K}}_{\mathrm{p}}\boldsymbol{i}^{\mathrm{dq}\star}_{\mathrm{s,sat}}[k], \tag{4.23}$$

with feedback gain matrix $\boldsymbol{\mathcal{K}}_{\mathrm{vxi}} = \left[\boldsymbol{\mathcal{K}}_{\mathrm{v}} \,\middle|\, \boldsymbol{\mathcal{K}}_{\mathrm{x}} \,\middle|\, \boldsymbol{\mathcal{K}}_{\mathrm{i}}\right] \in \mathbb{R}^{2\times12}$ and feedfoward (proportional) gain matrix $\boldsymbol{\mathcal{K}}_{\mathrm{p}} \in \mathbb{R}^{2\times2}$. Integral-action is realized by the feedback gain component $\boldsymbol{\mathcal{K}}_{\mathrm{i}} \in \mathbb{R}^{2\times2}$ and states $\boldsymbol{x}_{\mathrm{i}}$.

Remark 20 (Proportional gain)**.** *In the control law (4.23), the feedforward gain matrix $\boldsymbol{\mathcal{K}}_{\mathrm{p}}$ is labelled* proportional *gain, although only the stator reference current $\boldsymbol{i}^{\mathrm{dq}\star}_{\mathrm{s,sat}}$ is multiplied by $\boldsymbol{\mathcal{K}}_{\mathrm{p}}$ (not the control error $\boldsymbol{i}^{\mathrm{dq}\star}_{\mathrm{s,sat}} - \boldsymbol{i}^{\mathrm{dq}}_{\mathrm{s}}$). However, rewriting the state-feedback gain as $\boldsymbol{\mathcal{K}}_{\mathrm{x}} = \boldsymbol{\mathcal{K}}^{*}_{\mathrm{x}} + \boldsymbol{\mathcal{K}}_{\mathrm{p}}\boldsymbol{\mathcal{F}}_{\mathrm{x}}$, the control law can be expressed as*

$$\boldsymbol{u}^{\mathrm{dq}\star}_{\mathrm{f}}[k] = -\left[\boldsymbol{\mathcal{K}}_{\mathrm{v}} \,\middle|\, \boldsymbol{\mathcal{K}}^{*}_{\mathrm{x}} - \boldsymbol{\mathcal{K}}_{\mathrm{p}}\boldsymbol{\mathcal{F}}_{\mathrm{x}} \,\middle|\, \boldsymbol{\mathcal{K}}_{\mathrm{i}}\right]\boldsymbol{x}_{\mathrm{vxi}}[k] + \boldsymbol{\mathcal{K}}_{\mathrm{p}}(\boldsymbol{i}^{\mathrm{dq}\star}_{\mathrm{s,sat}}[k] - \boldsymbol{i}^{\mathrm{dq}}_{\mathrm{s}}[k]), \tag{4.24}$$

featuring a proportional term in the classical sense.

Finally, the controller output $\boldsymbol{u}^{\mathrm{dq}\star}_{\mathrm{f}}$ needs to be limited, as the inverter can produce voltages with a maximum magnitude of $u_{\mathrm{dc}}/\sqrt{3}$ only, i.e.

$$\boldsymbol{u}^{\mathrm{dq}\star}_{\mathrm{f,sat}} = f_{\mathrm{sat,sf}}(\boldsymbol{u}^{\mathrm{dq}\star}_{\mathrm{f}}, u_{\mathrm{dc}}) = \begin{cases}\boldsymbol{u}^{\mathrm{dq}\star}_{\mathrm{f}}, & \|\boldsymbol{u}^{\mathrm{dq}\star}_{\mathrm{f}}\| \le \frac{u_{\mathrm{dc}}}{\sqrt{3}}\\ \boldsymbol{u}^{\mathrm{dq}\star}_{\mathrm{f}} \cdot \frac{u_{\mathrm{dc}}}{\sqrt{3}\,\|\boldsymbol{u}^{\mathrm{dq}\star}_{\mathrm{f}}\|}, & \text{else.}\end{cases} \tag{4.25}$$

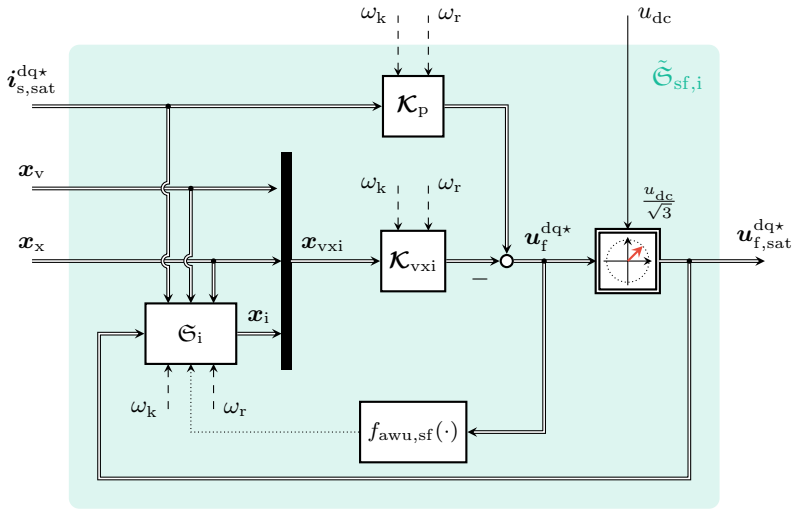

Figure 4.9: *Block diagram of the discrete-time state-feedback stator current controller* $\tilde{\mathfrak{S}}_\mathrm{sf,i}$ *with proportional-integral set-point tracking and anti-windup.*

Remark 21 (Nonlinear behavior)**.** *Note that both, conditional integration (anti-windup) and output saturation, are nonlinearities in the system which potentially affect the stability of the system as the controller deviates from its designated behavior. However, in most cases, operation close to the voltage limit can be avoided.*

Inserting the unsaturated control law (4.23) into (4.21) yields the closed-loop system dynamics

$$\mathfrak{S}_\mathrm{vxi,cl}: \begin{cases} \boldsymbol{x}_\mathrm{vxi}[k+1] = \overbrace{(\boldsymbol{\mathcal{A}}_\mathrm{vxi}[k] - \boldsymbol{\mathcal{B}}_\mathrm{vxi}[k]\boldsymbol{\mathcal{K}}_\mathrm{vxi})}^{=:\boldsymbol{\mathcal{A}}_\mathrm{vxi,cl}[k]}\boldsymbol{x}_\mathrm{vxi}[k] + \overbrace{(\boldsymbol{\mathcal{E}}_\mathrm{vxi}[k] + \boldsymbol{\mathcal{B}}_\mathrm{vxi}[k]\boldsymbol{\mathcal{K}}_\mathrm{p})}^{=:\boldsymbol{\mathcal{E}}_\mathrm{vxi,cl}[k]}\boldsymbol{i}_\mathrm{s,sat}^\mathrm{dq\star}[k], \\ \boldsymbol{i}_\mathrm{f}^\mathrm{dq}[k] = \boldsymbol{\mathcal{C}}_\mathrm{vxi}\boldsymbol{x}_\mathrm{vxi}[k], \qquad \boldsymbol{i}_\mathrm{s}^\mathrm{dq}[k] = \boldsymbol{\mathcal{F}}_\mathrm{vxi}\boldsymbol{x}_\mathrm{vxi}[k], \end{cases} \tag{4.26}$$

with closed-loop system matrix $\boldsymbol{\mathcal{A}}_\mathrm{vxi,cl} \in \mathbb{R}^{12\times 12}$ and auxiliary input matrix $\boldsymbol{\mathcal{E}}_\mathrm{vxi,cl} \in \mathbb{R}^{12\times 2}$.

4.2.1.3 Feedback gain selection (LQR) and controller gain scheduling

For the closed-loop system to be stable, the (complex) eigenvalues of the system matrix $\boldsymbol{\mathcal{A}}_\mathrm{vxi,cl}$ must be located within the unit circle of the complex plane [128, Ch. 11.5]. If the system is fully controllable, the eigenvalues can be shifted arbitrarily using the feedback gains $\boldsymbol{\mathcal{K}}_\mathrm{vxi}$, such that the desired dynamic behavior is achieved. However, as the question of a reasonable eigenvalue location might be difficult to answer, an alternative tuning method based on the *optimal control* idea may be preferred over the pole placement design. The so-called optimal controller gains are calculated using the linear quadratic regulator (LQR) approach (see e.g. [129, Ch. 9, 10]). For *discrete-time* linear time-invariant (LTI) systems (or LPV systems with slowly varying parameters), the idea is to select the feedback gains $\boldsymbol{\mathcal{K}}_\mathrm{vxi}$ such that the quadratic cost function

$$\mathcal{J} := \frac{1}{2}\sum_{i=0}^{\infty}(\boldsymbol{x}_\mathrm{vxi}[i])^\top \boldsymbol{Q}_\mathrm{K}\boldsymbol{x}_\mathrm{vxi}[i] + (\boldsymbol{u}_\mathrm{f}^\mathrm{dq\star}[i])^\top \boldsymbol{R}_\mathrm{K}\boldsymbol{u}_\mathrm{f}^\mathrm{dq\star}[i] \tag{4.27}$$

with *infinite horizon* is minimized, i.e. by solving the optimization problem

$$\arg\min_{\boldsymbol{\mathcal{K}}_\mathrm{vxi}} \frac{1}{2}\sum_{i=0}^{\infty}(\boldsymbol{x}_\mathrm{vxi}[i])^\top \left[\boldsymbol{Q}_\mathrm{K} + \boldsymbol{\mathcal{K}}_\mathrm{vxi}^\top \boldsymbol{R}_\mathrm{K}\boldsymbol{\mathcal{K}}_\mathrm{vxi}\right]\boldsymbol{x}_\mathrm{vxi}[i] \tag{4.28}$$

where $\boldsymbol{Q}_\mathrm{K} = \boldsymbol{Q}_\mathrm{K}^\top \succcurlyeq 0 \in \mathbb{R}^{12\times 12}$ is the weighting matrix for the states $\boldsymbol{x}_\mathrm{vxi}$, and $\boldsymbol{R}_\mathrm{K} = \boldsymbol{R}_\mathrm{K}^\top \succ 0 \in \mathbb{R}^{2\times 2}$ is the weighting matrix for the input $\boldsymbol{u}_\mathrm{f}^{\mathrm{dq}\star}$. It can be shown (see e.g. [129, Sec. 9.2.5]) that—if the system is *stabilizable* [109, Prop. 5.69]—the solution of the optimization problem is given by

$$\boldsymbol{\mathcal{K}}_\mathrm{vxi} = (\boldsymbol{R}_\mathrm{K} + \boldsymbol{\mathcal{B}}_\mathrm{vxi}^\top[k]\boldsymbol{P}_\mathrm{K}\boldsymbol{\mathcal{B}}_\mathrm{vxi}[k])^{-1}\boldsymbol{\mathcal{B}}_\mathrm{vxi}^\top[k]\boldsymbol{P}_\mathrm{K}\boldsymbol{\mathcal{A}}_\mathrm{vxi}[k], \tag{4.29}$$

where the matrix $\boldsymbol{P}_\mathrm{K} = \boldsymbol{P}_\mathrm{K}^\top \succ 0 \in \mathbb{R}^{12\times 12}$ is obtained by solving the *algebraic matrix Ricatti equation*

$$\boldsymbol{P}_\mathrm{K} = \boldsymbol{Q}_\mathrm{K} + \boldsymbol{\mathcal{A}}_\mathrm{vxi}^\top[k]\left[\boldsymbol{P}_\mathrm{K} - \boldsymbol{P}_\mathrm{K}\boldsymbol{\mathcal{B}}_\mathrm{vxi}[k](\boldsymbol{R}_\mathrm{K} + \boldsymbol{\mathcal{B}}_\mathrm{vxi}^\top[k]\boldsymbol{P}_\mathrm{K}\boldsymbol{\mathcal{B}}_\mathrm{vxi})^{-1}\boldsymbol{\mathcal{B}}_\mathrm{vxi}^\top[k]\boldsymbol{P}_\mathrm{K}\right]\boldsymbol{\mathcal{A}}_\mathrm{vxi}[k]. \tag{4.30}$$

Clearly, the solution of the optimization problem is parameter dependent, as the matrices $\boldsymbol{\mathcal{A}}_\mathrm{vxi}$ and $\boldsymbol{\mathcal{B}}_\mathrm{vxi}$ depend on ω_r and ω_k. Therefore, the gain matrix $\boldsymbol{\mathcal{K}}_\mathrm{vxi} = \boldsymbol{\mathcal{K}}_\mathrm{vxi}(\omega_\mathrm{r}, \omega_\mathrm{k})$ is calculated for different parameters and stored in look-up tables for each entry of $\boldsymbol{\mathcal{K}}_\mathrm{vxi}$. During operation, the values are looked-up for the actual values of $\omega_\mathrm{r}[k]$ and $\omega_\mathrm{k}[k]$ in each instant of the controller routine (gain-scheduling). The advantage of the look-up tables is, that the computationally expensive solution of the matrix Ricatti equation (4.29) does not need to be solved online in every control instant.

The LQR tuning is realized by choosing appropriate matrices $\boldsymbol{Q}_\mathrm{K}$ and $\boldsymbol{R}_\mathrm{K}$. In order to reduce the amount of tuning factors, the following matrices

$$\left.\begin{aligned}
\boldsymbol{Q}_\mathrm{K} &= \alpha_K \begin{bmatrix}
\frac{1}{\hat{u}_{\mathrm{f,nom}}^2}\boldsymbol{I}_2 & \boldsymbol{0}_{2\times2} & \boldsymbol{0}_{2\times2} & \boldsymbol{0}_{2\times2} & \boldsymbol{0}_{2\times2} & \boldsymbol{0}_{2\times2} \\
\boldsymbol{0}_{2\times2} & \frac{1}{\hat{i}_{\mathrm{f,nom}}^2}\boldsymbol{I}_2 & \boldsymbol{0}_{2\times2} & \boldsymbol{0}_{2\times2} & \boldsymbol{0}_{2\times2} & \boldsymbol{0}_{2\times2} \\
\boldsymbol{0}_{2\times2} & \boldsymbol{0}_{2\times2} & \frac{1}{\hat{u}_{\mathrm{s,nom}}^2}\boldsymbol{I}_2 & \boldsymbol{0}_{2\times2} & \boldsymbol{0}_{2\times2} & \boldsymbol{0}_{2\times2} \\
\boldsymbol{0}_{2\times2} & \boldsymbol{0}_{2\times2} & \boldsymbol{0}_{2\times2} & \frac{1}{\hat{i}_{\mathrm{s,nom}}^2}\boldsymbol{I}_2 & \boldsymbol{0}_{2\times2} & \boldsymbol{0}_{2\times2} \\
\boldsymbol{0}_{2\times2} & \boldsymbol{0}_{2\times2} & \boldsymbol{0}_{2\times2} & \boldsymbol{0}_{2\times2} & \frac{1}{\hat{\psi}_{\mathrm{r,nom}}^2}\boldsymbol{I}_2 & \boldsymbol{0}_{2\times2} \\
\boldsymbol{0}_{2\times2} & \boldsymbol{0}_{2\times2} & \boldsymbol{0}_{2\times2} & \boldsymbol{0}_{2\times2} & \boldsymbol{0}_{2\times2} & \beta_K\boldsymbol{I}_2
\end{bmatrix} \quad \text{and} \\
\boldsymbol{R}_\mathrm{K} &= (1-\alpha_K)\frac{1}{\hat{u}_{\mathrm{f,nom}}^2}\boldsymbol{I}_2,
\end{aligned}\right\} \tag{4.31}$$

are proposed, where the diagonal elements are divided by the squared nominal magnitudes of the respective state or input variables. This way, the squared states and inputs in the cost function (4.27) become more balanced. The factors $\alpha_K \in (0,1)$ and β_K are the only remaining tuning factors. While $\alpha_K \in (0,1)$ weighs the invested input energy, β_K weighs the integral-action of the control system. The DT controller gains are calculated using the MATLAB® (Control System Toolbox) function `dlqr(...)`.

Assuming that the proportional term is zero for the time being, i.e. $\boldsymbol{\mathcal{K}}_\mathrm{p} = \boldsymbol{0}_{2\times2}$ in (4.23), the impact of the two tuning factors can be analyzed by evaluating the step response of the closed-loop system $\mathfrak{S}_\mathrm{vxi,cl}$ for different tuning parameters α_K and β_K and constant ω_k and ω_r (e.g. using the `step(...)` function in MATLAB®). A trade-off should be found between fast transients and robustness against parameter uncertainties or noise. Figure 4.10 shows the (a) i_s^d and (b) i_s^q responses of a step in the d-reference current, assuming $\omega_\mathrm{r} = 0.5\,\omega_\mathrm{r,nom}$ and $\omega_\mathrm{k} = 0.5\omega_\mathrm{r,nom} + 0.5(\omega_\mathrm{k,nom} - \omega_\mathrm{r,nom})$ (half rated speed at half rated load), with gains calculated for $\alpha_K = 0.5$ and different $\beta_K \in \{10^4, 10^5, 10^7\}$. It is observed that, the larger β_K, the faster the system gets. However, overshooting occurs for too large values of β_K [····]. Figure 4.11 shows the respective responses of (a) i_s^d and (b) i_s^q for different $\alpha_K = \in \{0.005, 0.05, 0.5\}$ and $\beta_K = 5000$. Likewise, for increased α_K, the system settles faster and the coupling on i_s^q is reduced.

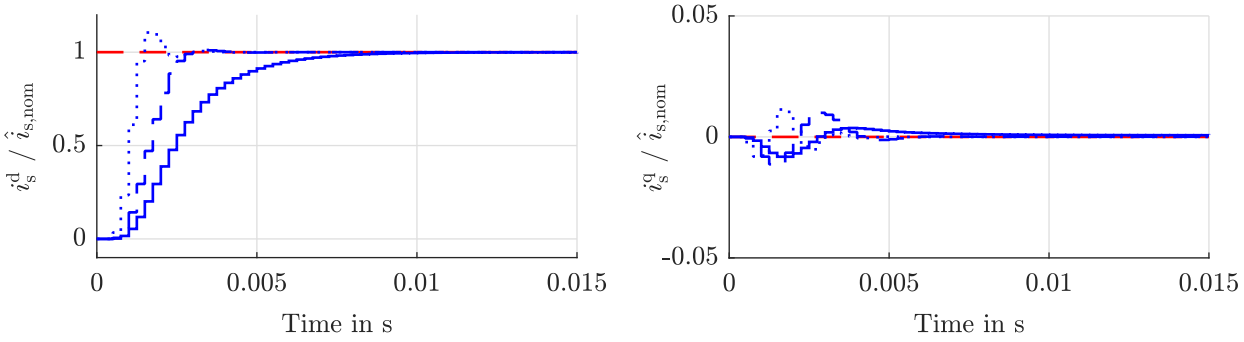

(a) (b)

Figure 4.10: *Step responses* $[\boldsymbol{i}_s^{dq\star} = (\hat{i}_{s,nom}, 0)^\top]$ *of the closed-loop current control system* $\mathfrak{S}_{vxi,cl}$ *for* $\beta_K = 1000$ [—], $\beta_K = 5000$ [- - -] *and* $\beta_K = 10000$ [····], *respectively, and* $\alpha_K = 0.5$*: Responses of the (a)* d*-current and (b)* q*-current.*

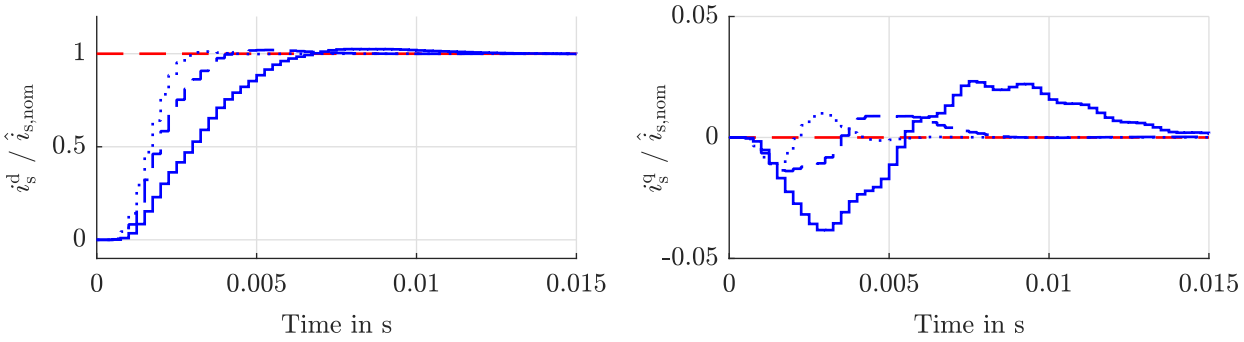

(a) (b)

Figure 4.11: *Step responses* $[\boldsymbol{i}_s^{dq\star} = (\hat{i}_{s,nom}, 0)^\top]$ *of the closed-loop current control system* $\mathfrak{S}_{vxi,cl}$ *for* $\alpha_K = 0.005$ [—], $\alpha_K = 0.05$ [- - -] *and* $\alpha_K = 0.5$ [····], *respectively, and* $\beta_K = 5000$*: Responses of the (a)* d*-current and (b)* q*-current.*

4.2.1.4 Feedforward (proportional) gain selection

The idea of the feedforward gain is to reduce the settling time of the set-point tracking by applying a first guess of the voltage that is presumably needed to achieve the given stator reference current if no integral control action was used; in turn, the integral-action is responsible for removing the remaining control error only. Therefore, for the time being, the steady-state solution of the system *without* integral-action is inspected, i.e. the 'vx' subsystem

$$\mathfrak{S}_{vx}: \begin{cases} \begin{pmatrix} \boldsymbol{x}_v[k+1] \\ \boldsymbol{x}_x[k+1] \end{pmatrix} = \overbrace{\left[\begin{array}{c|c} \boldsymbol{0}_{2\times 2} & \boldsymbol{0}_{2\times 8} \\ \hline \boldsymbol{\mathcal{A}}_{v\to x}[k] & \boldsymbol{\mathcal{A}}_x[k] \end{array}\right]}^{=:\boldsymbol{\mathcal{A}}_{vx}\in\mathbb{R}^{10\times 10}} \overbrace{\begin{pmatrix} \boldsymbol{x}_v[k] \\ \boldsymbol{x}_x[k] \end{pmatrix}}^{=:\boldsymbol{x}_{vx}\in\mathbb{R}^{10}} + \overbrace{\begin{bmatrix} \boldsymbol{\mathcal{B}}_v[k] \\ \boldsymbol{\mathcal{B}}_x[k] \end{bmatrix}}^{=:\boldsymbol{\mathcal{B}}_{vx}\in\mathbb{R}^{10\times 2}} \boldsymbol{u}_f^{dq\star}[k] \\ \boldsymbol{i}_f^{dq}[k] = \underbrace{\left[\boldsymbol{0}_{2\times 2} \mid \boldsymbol{\mathcal{C}}_x\right]}_{=:\boldsymbol{\mathcal{C}}_{vx}\in\mathbb{R}^{2\times 10}} \boldsymbol{x}_{vx}[k], \qquad \boldsymbol{i}_s^{dq}[k] = \underbrace{\left[\boldsymbol{0}_{2\times 2} \mid \boldsymbol{\mathcal{F}}_x\right]}_{=:\boldsymbol{\mathcal{F}}_{vx}\in\mathbb{R}^{2\times 10}} \boldsymbol{x}_{vx}[k]. \end{cases} \tag{4.32}$$

While in the CT domain, steady-state requires that $\frac{\mathrm{d}}{\mathrm{d}t}\boldsymbol{x}_{vxi} = 0$, in the DT domain $\boldsymbol{x}_{vxi}[k{+}1] = \boldsymbol{x}_{vxi}[k]$

must hold, i.e.

$$\lim_{k\to\infty} \boldsymbol{i}_{\mathrm{s}}^{\mathrm{dq}}[k] =: \boldsymbol{i}_{\mathrm{s},\infty}^{\mathrm{dq}} = \boldsymbol{\mathcal{F}}_{\mathrm{vx}}\boldsymbol{x}_{\mathrm{vx},\infty} = \boldsymbol{\mathcal{F}}_{\mathrm{vx}}\left[\boldsymbol{I}_{10} - \boldsymbol{\mathcal{A}}_{\mathrm{vx}}[k] + \boldsymbol{\mathcal{B}}_{\mathrm{vx}}[k]\boldsymbol{\mathcal{K}}_{\mathrm{vx}}[k]\right]^{-1}\boldsymbol{\mathcal{B}}_{\mathrm{vx}}[k]\boldsymbol{\mathcal{K}}_{\mathrm{p}}\boldsymbol{i}_{\mathrm{s,sat},\infty}^{\mathrm{dq}\star}, \tag{4.33}$$

with $\boldsymbol{i}_{\mathrm{s},\infty}^{\mathrm{dq}}$ and $\boldsymbol{i}_{\mathrm{s,sat},\infty}^{\mathrm{dq}\star}$ denoting the steady-state values of $\boldsymbol{i}_{\mathrm{s}}^{\mathrm{dq}}$ and $\boldsymbol{i}_{\mathrm{s,sat}}^{\mathrm{dq}}$, respectively. Solving

$$\boldsymbol{i}_{\mathrm{s,sat},\infty}^{\mathrm{dq}\star} - \boldsymbol{i}_{\mathrm{s},\infty}^{\mathrm{dq}} \overset{(4.33)}{=} \left[\boldsymbol{I}_{10} - \boldsymbol{\mathcal{F}}_{\mathrm{vxi}}\left[\boldsymbol{I}_{10} - \boldsymbol{\mathcal{A}}_{\mathrm{vx}}[k] + \boldsymbol{\mathcal{B}}_{\mathrm{vx}}[k]\boldsymbol{\mathcal{K}}_{\mathrm{vx}}[k]\right]^{-1}\boldsymbol{\mathcal{B}}_{\mathrm{vx}}[k]\boldsymbol{\mathcal{K}}_{\mathrm{p}}\right]\boldsymbol{i}_{\mathrm{s,sat},\infty}^{\mathrm{dq}\star} \overset{!}{=} \mathbf{o}_2 \tag{4.34}$$

for $\boldsymbol{\mathcal{K}}_{\mathrm{p}}$ yields the proportional gain candidate

$$\boldsymbol{\mathcal{K}}_{\mathrm{p}}^{*}[k] = \left[\boldsymbol{\mathcal{F}}_{\mathrm{vx}}\left(\boldsymbol{I}_{10} - \boldsymbol{\mathcal{A}}_{\mathrm{vx}}[k] + \boldsymbol{\mathcal{B}}_{\mathrm{vx}}[k]\boldsymbol{\mathcal{K}}_{\mathrm{vx}}[k]\right)^{-1}\boldsymbol{\mathcal{B}}_{\mathrm{vx}}[k]\right]^{-1}, \tag{4.35}$$

which is parameter dependent, too, and needs to be recalculated in each control cycle. For practical implementations a third tuning factor, $\gamma_K \in [0,1]$, is introduced, weighting the proportional term

$$\boldsymbol{\mathcal{K}}_{\mathrm{p}}[k] = \gamma_K\boldsymbol{\mathcal{K}}_{\mathrm{p}}^{*}[k]. \tag{4.36}$$

Remark 22. *Note that for $\gamma_K = 0$, purely integral set-point tracking is realized, which might be slower and requires a sophisticated anti-windup strategy, as the proposed strategy will reach a locked-up situation once the integrator is disabled; on the other hand, the inversion of a 10-by-10 matrix in (4.35) can be circumvented. Conversely, for $\gamma_K = 1$, the step response of the closed-loop system $\mathfrak{S}_{\mathrm{vxi,cl}}$ tends to overshoot. Thus, an intermediate value seems a good compromise. The previous statements are confirmed in Fig. 4.12, showing again the step responses of (a) $i_{\mathrm{s}}^{\mathrm{d}}$ and (b) $i_{\mathrm{s}}^{\mathrm{q}}$ with varying $\gamma_K = \in \{0, 0.3, 1\}$ and constant $\alpha_K = 0.5$ and $\beta_K = 5000$.*

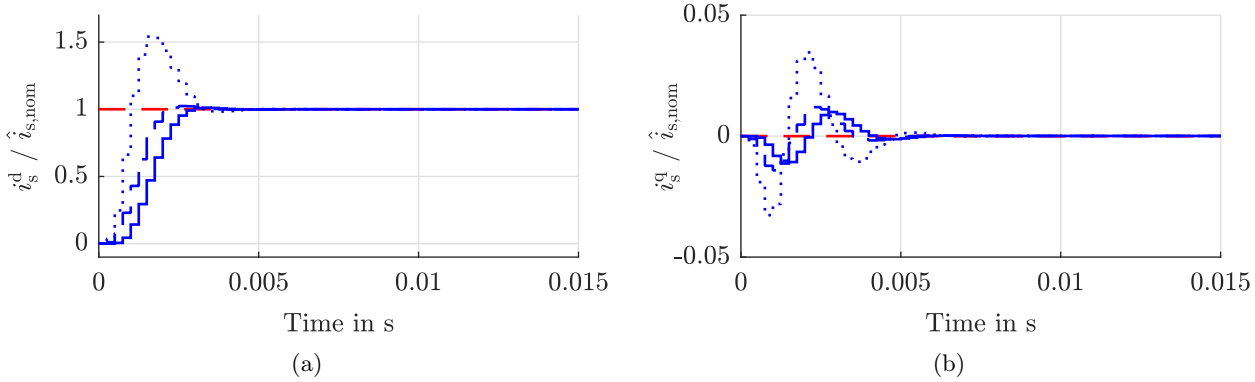

Figure 4.12: *Step responses $[\boldsymbol{i}_{\mathrm{s}}^{\mathrm{dq}\star} = (\hat{i}_{\mathrm{s,nom}}, 0)^{\top}]$ of the closed-loop current control system $\mathfrak{S}_{\mathrm{vxi,cl}}$ for $\gamma_K = 0$ [——], $\gamma_K = 0.3$ [- - -] and $\gamma_K = 1$ [····], respectively, and for $\alpha_K = 0.5$ and $\beta_K = 5000$: Responses of the (a) d-current and (b) q-current.*

4.2.2 Proportional-integral (PI) flux and speed controllers

Having stated the inner-loop current control system, the outer-loop flux and speed controllers can be designed, producing the reference currents $\boldsymbol{i}_{\mathrm{s}}^{\mathrm{dq}\star}$ (respectively the saturated references $\boldsymbol{i}_{\mathrm{s,sat}}^{\mathrm{dq}\star}$) for the underlying state-feedback current control system (see Fig. 4.7). For both control systems, PI controllers with anti-windup are employed. The discrete-time equivalents of the continuous-time controllers are obtained by applying the bilinear transform (Tustin's method, see e.g. [131]), which is more robust than the forward Euler method, particularly at low sampling frequencies. The (model-based) controller tuning requires a rough estimate of the underlying closed-loop current controller dynamics and the respective flux and speed dynamics.

4.2.2.1 Approximation of the closed-loop current dynamics

Since the state-feedback current controller constitutes the innermost control loop of the cascaded speed control system, its dynamics need to be estimated for the design of the outer-loop flux and speed controllers. The actual step response of the d-current [—] is depicted in Fig. 4.13. The closed-loop current dynamics can be approximated by a delay of $T_{\mathrm{i,dt}}$ and a first-order lag system with time constant $T_{\mathrm{i,cl}}$ [—]. Taking the sum of both time constants, i.e. $T_{\mathrm{i,cl}}^{*} := T_{\mathrm{i,cl}} + T_{\mathrm{i,dt}}$, yields a first-order lag system approximation [- - -] of the overall system (see e.g. [132, Ch. 5.7.2]), i.e.

$$\tfrac{\mathrm{d}}{\mathrm{d}t}\boldsymbol{i}_{\mathrm{s}}^{\mathrm{dq}}(t) \approx -\tfrac{1}{T_{\mathrm{i,cl}}}\boldsymbol{i}_{\mathrm{s}}^{\mathrm{dq}}(t) + \tfrac{1}{T_{\mathrm{i,cl}}}\boldsymbol{i}_{\mathrm{s}}^{\mathrm{dq}\star}(t - T_{\mathrm{i,dt}}) \approx -\tfrac{1}{T_{\mathrm{i,cl}}^{*}}\boldsymbol{i}_{\mathrm{s}}^{\mathrm{dq}}(t) + \tfrac{1}{T_{\mathrm{i,cl}}^{*}}\boldsymbol{i}_{\mathrm{s}}^{\mathrm{dq}\star}(t). \tag{4.37}$$

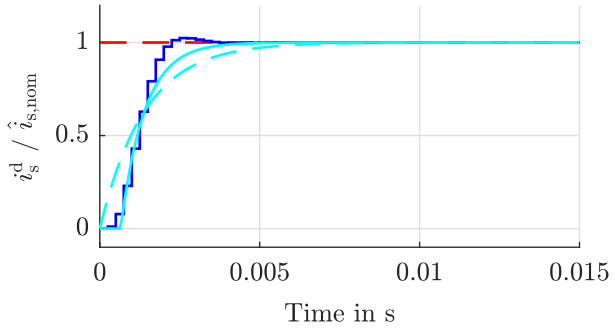

Figure 4.13: *Step response* $[\boldsymbol{i}_{\mathrm{s}}^{\mathrm{dq}\star} = (\hat{i}_{\mathrm{s,nom}}, 0)^{\top}]$ *of the closed-loop current control system* $\mathfrak{S}_{\mathrm{vxi,cl}}$ *for* $\alpha_K = 0.5$, $\beta_K = 5000$ *and* $\gamma_K = 0.3$ *[—]; Approximations using a combination of time delay* $T_{\mathrm{i,dt}}$ *and first-order lag system with time constant* $T_{\mathrm{i,cl}}$ *[—], and a first-order lag system approximation with time constant* $T_{\mathrm{i,cl}}^{*} := T_{\mathrm{i,cl}} + T_{\mathrm{i,dt}}$ *[- - -].*

4.2.2.2 Flux linkage control loop

The control objective is to set the d-component of the rotor flux linkage, i.e. $\psi_{\mathrm{r}}^{\mathrm{d}} = \psi_{\mathrm{r}}^{\mathrm{d}\star}$, where $\psi_{\mathrm{r}}^{\mathrm{d}\star}$ denotes the rotor flux linkage set-point; assuming rotor flux orientation, the q-component of the rotor flux linkage is zero. The dynamics of the rotor flux linkage are extracted from (4.7) and can be stated as a first-order lag system

$$\tfrac{\mathrm{d}}{\mathrm{d}t}\psi_{\mathrm{r}}^{\mathrm{d}}(t) \overset{\psi_{\mathrm{r}}^{\mathrm{q}}=0}{=} \tfrac{L_{\mathrm{m}}}{T_{\mathrm{r}}} i_{\mathrm{s}}^{\mathrm{d}}(t) - \tfrac{1}{T_{\mathrm{r}}}\psi_{\mathrm{r}}^{\mathrm{d}}(t) \tag{4.38}$$

with input $i_{\mathrm{s}}^{\mathrm{d}}$, time constant T_{r} and gain L_{m}. In combination with the approximation of the closed-loop current control system [see (4.37)], a second-order system with time constants T_{r} and $T_{\mathrm{i,cl}}^{*}$ and gain L_{m} is obtained. The continuous-time PI controller with anti-windup is given by

$$\tilde{\Sigma}_{\mathrm{pi},\psi}: \quad \begin{cases} \tfrac{\mathrm{d}}{\mathrm{d}t}\xi_{\psi}(t) = f_{\mathrm{awu},\psi}(i_{\mathrm{s}}^{\mathrm{d}\star}) e_{\psi}(t), \\ i_{\mathrm{s}}^{\mathrm{d}\star}(t) = K_{\mathrm{p},\psi} e_{\psi}(t) + K_{\mathrm{i},\psi}\xi_{\psi}(t), \end{cases} \tag{4.39}$$

with control error $e_{\psi} := \psi_{\mathrm{r}}^{\mathrm{d}\star} - \psi_{\mathrm{r}}^{\mathrm{d}}$ (input), reference d-current (output) $i_{\mathrm{s}}^{\mathrm{d}\star}$, integral error state ξ_{ψ}, proportional gain $K_{\mathrm{p},\psi}$, integral gain $K_{\mathrm{i},\psi}$ and anti-windup decision function

$$f_{\mathrm{awu},\psi}(i_{\mathrm{s}}^{\mathrm{d}\star}) = \begin{cases} 1, & |i_{\mathrm{s}}^{\mathrm{d}\star}| < i_{\mathrm{s,max}}^{\mathrm{d}}, \\ 0, & \text{else}, \end{cases} \tag{4.40}$$

where $i_{\mathrm{s,max}}^{\mathrm{d}}$ is the maximum allowable stator d-reference current.

Remark 23 (Anti-windup for outer-loop controllers)**.** *Unlike the anti-windup decision function of the current controller [see (4.20)], where the vector norm (magnitude) of the reference signal was evaluated, the absolute values of the individual vector components $|i_\mathrm{s}^{\mathrm{d}\star}|$ and $|i_\mathrm{s}^{\mathrm{q}\star}|$ are evaluated for the outer-loop controllers. Reasons for this choice of decision function are:*

(i) For currents $|i_\mathrm{s}^{\mathrm{d}\star}| > i_{\mathrm{s,max}}^{\mathrm{d}}$, the d*-current becomes basically ineffective (flux saturation), consuming valuable current reserves, which could otherwise be used by the* q*-current controller.*

(ii) Keeping up the magnetic excitation (rotor flux linkage) is of highest priority as a loss of control may result otherwise. However, if the vector norm was saturated instead, huge changes in the load torque or the speed (reference), respectively, might put the q*-current controller in favor, thus reducing the* d*-controller action.*

Moreover, the control output is limited by

$$i_{\mathrm{s,sat}}^{\mathrm{d}\star} = f_{\mathrm{sat},\psi}(i_\mathrm{s}^{\mathrm{d}\star}) = \begin{cases} i_\mathrm{s}^{\mathrm{d}\star}, & |i_\mathrm{s}^{\mathrm{d}\star}| < i_{\mathrm{s,max}}^{\mathrm{d}}, \\ \mathrm{sign}(i_\mathrm{s}^{\mathrm{d}\star}) \cdot i_{\mathrm{s,max}}^{\mathrm{d}}, & \text{else.} \end{cases} \tag{4.41}$$

Tuning of the controller is performed based on the *Symmetric Optimum* criterion [124, Ch. 3.1], selecting $K_{\mathrm{i},\psi}$ and $K_{\mathrm{p},\psi}$ as

$$K_{\mathrm{p},\psi} = \frac{T_\mathrm{r}}{2L_\mathrm{m}T_{\mathrm{i,cl}}^*} \qquad \text{and} \qquad K_{\mathrm{i},\psi} = \frac{2K_{\mathrm{p},\psi}}{4T_{\mathrm{i,cl}}^*}. \tag{4.42}$$

The discrete-time equivalent $\tilde{\mathfrak{S}}_{\mathrm{pi},\psi}$ of PI controller $\tilde{\Sigma}_{\mathrm{pi},\psi}$ is obtained according to App. E.3. The respective block diagram is shown in Fig. 4.14a.

4.2.2.3 Speed control loop

The objective of the speed control system is to track the reference speed $\omega_\mathrm{m}^\star$. The simplified dynamics of the mechanical system Σ_m are given by [see (3.1)]

$$\Sigma_\mathrm{m}: \quad \tfrac{\mathrm{d}}{\mathrm{d}t}\omega_\mathrm{m}(t) = \tfrac{1}{\Theta_\mathrm{m}}\big(\overbrace{\tfrac{3}{2}n_\mathrm{p}\tfrac{L_\mathrm{m}}{L_\mathrm{r}}i_\mathrm{s}^{\mathrm{q}}(t)\psi_\mathrm{r}^{\mathrm{d}}(t)}^{=m_\mathrm{m}(t)} - m_\mathrm{l}(t)\big), \tag{4.43}$$

where Θ_m is the overall moment of inertia of the mechanical system, $i_\mathrm{s}^{\mathrm{q}}$ is the input and m_l is the load torque, which is considered an unknown disturbance. The dynamics (4.43) show purely integral behavior since friction is included in the load torque. The integrator 'time constant' (which does not have the physical unit s) and gain are given by Θ_m and $\frac{3}{2}n_\mathrm{p}\frac{L_\mathrm{m}}{L_\mathrm{r}}\psi_\mathrm{r}^{\mathrm{d}}$, respectively. The flux linkage is assumed constant, i.e. $\psi_\mathrm{r}^{\mathrm{d}} = \hat{\psi}_{\mathrm{r,nom}}$, which is guaranteed by the flux controller for all operating conditions except for field-weakening operation (see Sec. 4.2.2.4). In analogy to the flux controller, the dynamics are coupled with the underlying first-order approximation of the closed-loop current controller, yielding a second-order system. The corresponding continuous-time PI controller can be stated as

$$\tilde{\Sigma}_{\mathrm{pi},\omega}: \quad \begin{cases} i_\mathrm{s}^{\mathrm{q}\star}(t) = K_{\mathrm{p},\omega}e_\omega(t) + K_{\mathrm{i},\omega}\xi_\omega(t), \\ \tfrac{\mathrm{d}}{\mathrm{d}t}\xi_\omega(t) = f_{\mathrm{awu},\omega}(i_\mathrm{s}^{\mathrm{q}\star})e_\omega(t), \end{cases} \tag{4.44}$$

with control error $e_\omega := \omega_\mathrm{m}^\star - \omega_\mathrm{m}$, integral error state ξ_ω, proportional gain $K_{\mathrm{p},\omega}$ and integral gain $K_{\mathrm{i},\omega}$. The anti-windup decision function is given by

$$f_{\mathrm{awu},\omega}(i_\mathrm{s}^{\mathrm{q}\star}) = \begin{cases} 1, & |i_\mathrm{s}^{\mathrm{q}\star}| < i_{\mathrm{s,max}}^{\mathrm{q}}, \\ 0, & \text{else,} \end{cases} \tag{4.45}$$

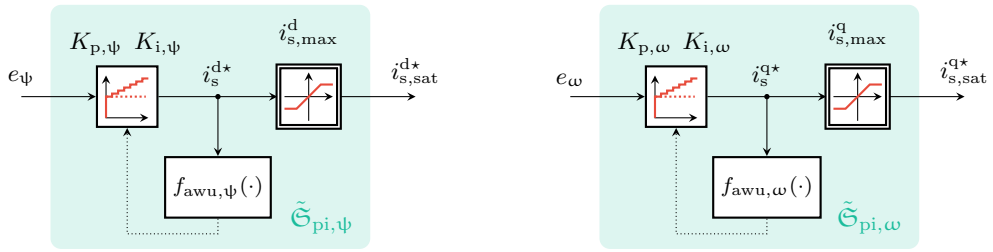

Figure 4.14: *Block diagrams of the discrete-time (a) flux PI controller* $\tilde{\mathfrak{S}}_{\mathrm{pi},\psi}$ *and (b) the speed PI controller* $\tilde{\mathfrak{S}}_{\mathrm{pi},\omega}$.

where $i_{\mathrm{s,max}}^{\mathrm{q}}$ denotes the maximum allowable reference q-current which should be chosen such that rated current is not exceeded, e.g.

$$i_{\mathrm{s,max}}^{\mathrm{q}} = \sqrt{\hat{i}_{\mathrm{s,nom}}^2 - i_{\mathrm{s,max}}^{\mathrm{d}2}}. \tag{4.46}$$

Finally, the control output is limited by

$$i_{\mathrm{s,sat}}^{\mathrm{q}\star} = f_{\mathrm{sat},\omega}(i_{\mathrm{s}}^{\mathrm{q}\star}) = \begin{cases} i_{\mathrm{s}}^{\mathrm{q}\star}, & |i_{\mathrm{s}}^{\mathrm{q}\star}| < i_{\mathrm{s,max}}^{\mathrm{q}}, \\ \mathrm{sign}(i_{\mathrm{s}}^{\mathrm{q}\star}) \cdot i_{\mathrm{s,max}}^{\mathrm{q}}, & \text{else.} \end{cases} \tag{4.47}$$

Again, tuning is performed according to the Symmetric Optimum criterion, yielding

$$K_{\mathrm{p},\omega} = \frac{\Theta_{\mathrm{m}}}{2T_{\mathrm{i,cl}}^* \frac{3}{2} n_{\mathrm{p}} \frac{L_{\mathrm{m}}}{L_{\mathrm{r}}} \psi_{\mathrm{r}}^{\mathrm{d}\star} T_{\mathrm{i,cl}}^*} \qquad \text{and} \qquad K_{\mathrm{i},\omega} = \frac{K_{\mathrm{p},\omega}}{4T_{\mathrm{i,cl}}^*}. \tag{4.48}$$

The discrete-time equivalent $\tilde{\mathfrak{S}}_{\mathrm{pi},\omega}$ of PI controller $\tilde{\Sigma}_{\mathrm{pi},\omega}$ is obtained according to App. E.3. The respective block diagram is shown in Fig. 4.14b.

4.2.2.4 Field-weakening operation

If the machine is to be operated at speeds higher than rated speed, the magnetic field needs to be reduced in order to decrease the induced voltage, and thus the voltage demand of the system. Although this mode of operation is irrelevant for geothermal ESP systems, the field-weakening reference curve is calculated, nevertheless, so as to cover the entire operating range of the drive system. The idea is briefly sketched in the following.

The aim is to find an expression $\psi_{\mathrm{r,fw}}^{\mathrm{d}}(\omega_{\mathrm{k}}, \hat{u}_{\mathrm{f,nom}}, \hat{i}_{\mathrm{s,nom}})$, which depends on the electrical frequency ω_{k} and the physical limits of the machine and the inverter, i.e. the current limit $\hat{i}_{\mathrm{s,nom}}$ and the voltage limit $\hat{u}_{\mathrm{f,nom}}$. Therefore, let

(i) the system be in steady-state,

(ii) the d-axis be aligned with the rotor flux linkage space vector, i.e.

$$\psi_{\mathrm{r}}^{\mathrm{q}} = 0\,\mathrm{Wb} \qquad \text{and} \qquad \omega_{\mathrm{r}} = \omega_{\mathrm{k}} - \frac{L_{\mathrm{m}} R_{\mathrm{r}}}{L_{\mathrm{r}}} \frac{i_{\mathrm{s}}^{\mathrm{q}}}{\psi_{\mathrm{r}}^{\mathrm{d}}} \tag{4.49}$$

hold, and

(iii) the maximum amount of stator current be applied, i.e.

$$\|\boldsymbol{i}_\mathrm{s}^\mathrm{dq}\| = \sqrt{{i_\mathrm{s}^\mathrm{d}}^2 + {i_\mathrm{s}^\mathrm{q}}^2} = \hat{i}_\mathrm{s,nom}. \tag{4.50}$$

From (i) it follows that the system equations (4.7) can be stated as (argument t dropped for the sake of brevity)

$$\left.\begin{aligned}
\mathbf{o}_2 &= -(R_\mathrm{f}\boldsymbol{I}_2 + \omega_\mathrm{k} L_\mathrm{f}\boldsymbol{J})\boldsymbol{i}_\mathrm{f}^\mathrm{dq} - \boldsymbol{u}_\mathrm{s}^\mathrm{dq} + \boldsymbol{u}_\mathrm{f}^\mathrm{dq},\\
\mathbf{o}_2 &= \boldsymbol{i}_\mathrm{f}^\mathrm{dq} - \omega_\mathrm{k} C_\mathrm{f}\boldsymbol{J}\boldsymbol{u}_\mathrm{s}^\mathrm{dq} - \boldsymbol{i}_\mathrm{s}^\mathrm{dq},\\
\mathbf{o}_2 &= \boldsymbol{u}_\mathrm{s}^\mathrm{dq} - (\tilde{R}_\mathrm{s}\boldsymbol{I}_2 + \omega_\mathrm{k}\sigma L_\mathrm{s}\boldsymbol{J})\boldsymbol{i}_\mathrm{s}^\mathrm{dq} - \tfrac{L_\mathrm{m}}{L_\mathrm{r}}(\omega_\mathrm{r}\boldsymbol{J} - \tfrac{R_\mathrm{r}}{L_\mathrm{r}}\boldsymbol{I}_2)\boldsymbol{\psi}_\mathrm{r}^\mathrm{dq},\\
\mathbf{o}_2 &= L_\mathrm{m} R_\mathrm{r}\boldsymbol{i}_\mathrm{s}^\mathrm{dq} - (R_\mathrm{r}\boldsymbol{I}_2 + (\omega_\mathrm{k} - \omega_\mathrm{r})L_\mathrm{r}\boldsymbol{J})\boldsymbol{\psi}_\mathrm{r}^\mathrm{dq},
\end{aligned}\right\} \tag{4.51}$$

where $\tilde{R}_\mathrm{s} = R_\mathrm{s} + \frac{L_\mathrm{m}^2}{L_\mathrm{r}^2}R_\mathrm{r}$ is an auxiliary resistance term. Using MATLAB® (Symbolic Math Toolbox), the third equation of (4.51) is solved for $\boldsymbol{u}_\mathrm{s}^\mathrm{dq}(\boldsymbol{i}_\mathrm{s}^\mathrm{dq}, \boldsymbol{\psi}_\mathrm{r}^\mathrm{dq}, \omega_\mathrm{k})$, which in turn is used to solve the second equation for $\boldsymbol{i}_\mathrm{f}^\mathrm{dq}(\boldsymbol{i}_\mathrm{s}^\mathrm{dq}, \boldsymbol{\psi}_\mathrm{r}^\mathrm{dq}, \omega_\mathrm{k})$. Using both expressions, the first equation can be solved for $\boldsymbol{u}_\mathrm{f}^\mathrm{dq}(\boldsymbol{\psi}_\mathrm{r}^\mathrm{dq}, \boldsymbol{i}_\mathrm{s}^\mathrm{dq}, \omega_\mathrm{k})$.

Moreover, from (ii) and (iii) it follows that the stator currents $\boldsymbol{i}_\mathrm{s}^\mathrm{dq}$ can be rewritten in terms of $\psi_\mathrm{r}^\mathrm{d}$ and the nominal stator current magnitude $\hat{i}_\mathrm{s,nom}$, i.e.

$$\boldsymbol{i}_\mathrm{s}^\mathrm{dq}(\hat{i}_\mathrm{s,nom}, \psi_\mathrm{r}^\mathrm{d}) = \begin{pmatrix} i_\mathrm{s}^\mathrm{d} \\ i_\mathrm{s}^\mathrm{q} \end{pmatrix} \overset{(4.49),(4.50),(4.51)}{=} \begin{pmatrix} \frac{1}{L_\mathrm{m}}\psi_\mathrm{r}^\mathrm{d} \\ \sqrt{\hat{i}_\mathrm{s,nom}^2 - \frac{1}{L_\mathrm{m}^2}{\psi_\mathrm{r}^\mathrm{d}}^2} \end{pmatrix}. \tag{4.52}$$

Inserting $\boldsymbol{i}_\mathrm{s}^\mathrm{dq}(\psi_\mathrm{r}^\mathrm{d}, \hat{i}_\mathrm{s,nom})$ in $\boldsymbol{u}_\mathrm{f}^\mathrm{dq}(\boldsymbol{\psi}_\mathrm{r}^\mathrm{dq}, \boldsymbol{i}_\mathrm{s}^\mathrm{dq}, \omega_\mathrm{k})$ yields $\boldsymbol{u}_\mathrm{f}^\mathrm{dq}(\psi_\mathrm{r}^\mathrm{d}, \hat{i}_\mathrm{s,nom}, \omega_\mathrm{k})$. The voltage constraint of the inverter requires that the filter voltage magnitude is smaller than or equal to its nominal value, i.e.

$$\|\boldsymbol{u}_\mathrm{f}^\mathrm{dq}\|^2 - \hat{u}_\mathrm{f,nom}^2 \overset{!}{\leq} 0. \tag{4.53}$$

When calculating the field-weakening reference curves, a commonly imposed assumption is that the resistive terms are negligible (e.g. [64]), i.e. $R_\mathrm{f} = 0\,\Omega, R_\mathrm{s} = 0\,\Omega$ and $R_\mathrm{r} = 0\,\Omega$, which allows for finding an analytic expression

$$\|\boldsymbol{u}_\mathrm{f}^\mathrm{dq}\|^2 - \hat{u}_\mathrm{f,nom}^2 = \omega_\mathrm{k}^2\gamma_1(\omega_\mathrm{k})^2\hat{i}_\mathrm{s,nom}^2 + \omega_\mathrm{k}^2\tfrac{1}{L_\mathrm{m}^2}(\gamma_2(\omega_\mathrm{k})^2 - \gamma_1(\omega_\mathrm{k})^2){\psi_\mathrm{r}^\mathrm{d}}^2 - \hat{u}_\mathrm{f,nom}^2, \tag{4.54}$$

with

$$\gamma_1(\omega_\mathrm{k}) := \sigma L_\mathrm{s} + L_\mathrm{f} - \omega_\mathrm{k}^2 C_\mathrm{f}\sigma L_\mathrm{s} L_\mathrm{f} \qquad \text{and} \qquad \gamma_2(\omega_\mathrm{k}) := L_\mathrm{s} + L_\mathrm{f} - \omega_\mathrm{k}^2 C_\mathrm{f} L_\mathrm{f} L_\mathrm{s}. \tag{4.55}$$

Solving for $\psi_\mathrm{r}^\mathrm{d}$ yields the condition

$$\psi_\mathrm{r}^\mathrm{d}(\omega_\mathrm{k}, \hat{u}_\mathrm{f,nom}, \hat{i}_\mathrm{s,nom}) \leq L_\mathrm{m}\sqrt{\frac{1}{\omega_\mathrm{k}^2(\gamma_2(\omega_\mathrm{k})^2 - \gamma_1(\omega_\mathrm{k})^2)}\hat{u}_\mathrm{f,nom}^2 - \frac{\gamma_1(\omega_\mathrm{k})^2}{\gamma_2(\omega_\mathrm{k})^2 - \gamma_1(\omega_\mathrm{k})^2}\hat{i}_\mathrm{s,nom}^2}. \tag{4.56}$$

It is reasonable to define an upper limit $\psi_\mathrm{r,max}^\mathrm{d} := \psi_\mathrm{r}^\mathrm{d}(\omega_\mathrm{k,nom}, \hat{u}_\mathrm{f,nom}, \hat{i}_\mathrm{s,nom})$, which finally leads to

$$\psi_\mathrm{r,fw}^\mathrm{d}(\omega_\mathrm{k}, \hat{u}_\mathrm{f,nom}, \hat{i}_\mathrm{s,nom}) = \begin{cases} \psi_\mathrm{r,max}^\mathrm{d}, & \text{for} \quad \omega_\mathrm{k} \leq \omega_\mathrm{k,nom} \\ \psi_\mathrm{r}^\mathrm{d}(\omega_\mathrm{k}, \hat{u}_\mathrm{f,nom}, \hat{i}_\mathrm{s,nom}), & \text{else.} \end{cases} \tag{4.57}$$

If the resistances are not assumed negligible, the analytic expression becomes lengthy and unreadable. However, using MATLAB®, the numeric values can be calculated, nonetheless. Figure 4.15a shows the respective curves with and without the consideration of resistances. In addition, Fig. 4.15b shows the corresponding block diagram. The output of the field-weakening block is fed as a reference value to the rotor flux controller, i.e. $\psi_{\mathrm{r}}^{\mathrm{d}\star} = \psi_{\mathrm{r,fw}}^{\mathrm{d}}(\omega_{\mathrm{k}}, \hat{u}_{\mathrm{f,nom}}, \hat{i}_{\mathrm{s,nom}})$.

Remark 24. *Due to parameter uncertainties and modeling errors (e.g. simple magnetic model), it is reasonable to relax the condition by reducing the voltage limit which is used for the calculation. As a result, the flux-weakening reference* $\psi_{\mathrm{r,fw}}^{\mathrm{d}}(\omega_{\mathrm{k}}, \hat{u}_{\mathrm{f,nom}}, \hat{i}_{\mathrm{s,nom}})$ *is slightly reduced.*

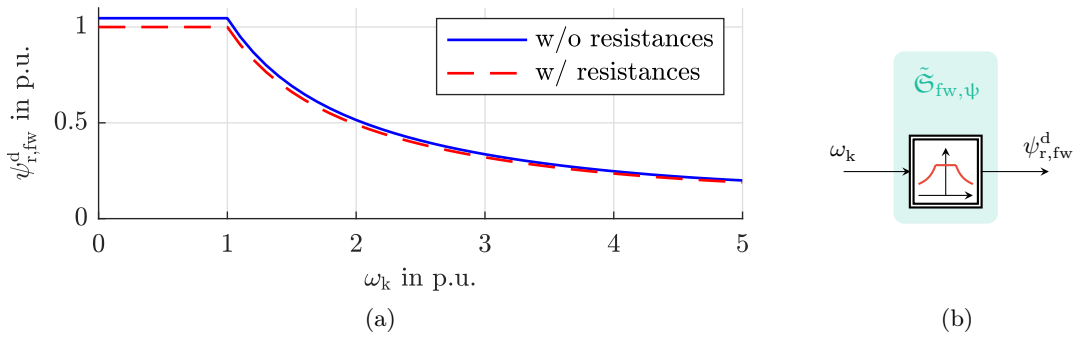

Figure 4.15: *(a) Field-weakening rotor flux reference curve as a function of the electrical frequency, considering [- - -] and neglecting [——] the resistance terms, and (b) block diagram of the field-weakening unit.*

4.3 Observer system

For the implementation of the proposed control system, full state-feedback is required. Since not all states are measured in geothermal energy systems, an observer must be employed to reconstruct the missing state measurements. First, it is shown under which conditions the system is *observable*; or rather, at which conditions observability is lost. Then, a full-order state observer is designed, assuming ideal parameter knowledge and available speed measurements. Tuning of the observer is, again, based on the LQR tuning method. As the mechanical speed of the electrical machine is typically not measured in geothermal ESP systems, the full-order observer is extended by a speed estimation scheme. Moreover, for performance reasons, several practical extensions are proposed.

4.3.1 On the observability of induction machines with LC filter

Prior to designing the observer, a structural analysis is conducted in order to determine under which conditions it is possible to reconstruct all system states for the given setup of induction machine *and* LC filter. The analysis of the continuous-time system Σ_{x} is based on the ideas presented in [133], where general conditions for the observability of induction machines (without LC filter) are derived subject to the concept of *weak observability* (see App. E.5). As the mentioned paper already thoroughly covers the 'IM-only' case, focus of this section is on validating that the observability conditions do not change when adding the LC filter.

Objective is to analyze the weak observability property of system Σ_{x} defined in (4.7), in order to identify critical operating points. As proposed in [133], and opposed to Ass. 17, the speed ω_{r} is

considered a state (instead of a slowly varying parameter) in the following analysis. Moreover, the load torque m_l is introduced as an additional state. The resulting system is described by

$$\Sigma_\mathrm{o}: \quad \begin{cases} \frac{\mathrm{d}}{\mathrm{d}t}\boldsymbol{x}_\mathrm{o}(t) = \boldsymbol{f}_\mathrm{o}(\boldsymbol{x}_\mathrm{o}, \boldsymbol{u}_\mathrm{f}^\mathrm{dq}, \omega_\mathrm{k}) \\ \boldsymbol{i}_\mathrm{f}^\mathrm{dq}(t) = \boldsymbol{g}_\mathrm{o}(\boldsymbol{x}_\mathrm{o}) \end{cases} \tag{4.58}$$

with state vector $\boldsymbol{x}_\mathrm{o} = (\boldsymbol{x}_\mathrm{x}^\top, \omega_\mathrm{r}, m_\mathrm{l})^\top \in \mathbb{R}^{10}$, input $\boldsymbol{u}_\mathrm{f}^\mathrm{dq} \in \mathbb{R}^2$, (measured) output $\boldsymbol{i}_\mathrm{f}^\mathrm{dq} \in \mathbb{R}^2$ and system and output functions $\boldsymbol{f}_\mathrm{o} \in \mathbb{R}^{10}$ and $\boldsymbol{g}_\mathrm{o} \in \mathbb{R}^2$ defined as

$$\boldsymbol{f}_\mathrm{o}(\boldsymbol{x}_\mathrm{o}, \boldsymbol{u}_\mathrm{f}^\mathrm{dq}, \omega_\mathrm{k}) := \begin{pmatrix} \boldsymbol{A}_\mathrm{x}(\omega_\mathrm{r}, \omega_\mathrm{k})\boldsymbol{x}_\mathrm{x}(t) + \boldsymbol{B}_\mathrm{x}\boldsymbol{u}_\mathrm{f}^\mathrm{dq}(t) \\ \frac{1}{\Theta_\mathrm{m}}(m_\mathrm{m}(\boldsymbol{x}_\mathrm{x}) - m_\mathrm{l}(t)) \\ 0 \end{pmatrix} \quad \text{and} \quad \boldsymbol{g}_\mathrm{o}(\boldsymbol{x}_\mathrm{o}) := \begin{bmatrix} \boldsymbol{C}_\mathrm{x} & \boldsymbol{0}_{2\times 2} \end{bmatrix} \boldsymbol{x}_\mathrm{o}(t), \tag{4.59}$$

respectively. Furthermore, $m_\mathrm{m}(\boldsymbol{x}_\mathrm{x}) = \frac{3}{2} n_\mathrm{p} \frac{L_\mathrm{m}}{L_\mathrm{r}} (\boldsymbol{i}_\mathrm{s}^\mathrm{dq})^\top \boldsymbol{J} \boldsymbol{\psi}_\mathrm{r}^\mathrm{dq}$ is the machine torque [as defined in (2.32)] and Θ_m denotes the total moment of inertia. The load torque m_l is assumed to be constant and friction is neglected. For the remainder of the analysis, the argument t is dropped for the sake of readability.

The *observability rank condition* (see App. E.5, Theorem 1), requires that the rank of the observability matrix (see App. E.5, Def. 2) is equal to the system order. However, as the given system has two outputs, the reduced observability matrix

$$\boldsymbol{S}_\mathrm{O}^*[\Sigma_\mathrm{o}] := \frac{\partial}{\partial \boldsymbol{x}_\mathrm{o}} \begin{pmatrix} \boldsymbol{g}_\mathrm{o}(\boldsymbol{x}_\mathrm{o}) \\ \frac{\mathrm{d}}{\mathrm{d}t}\boldsymbol{g}_\mathrm{o}(\boldsymbol{x}_\mathrm{o}) \\ \frac{\mathrm{d}^2}{\mathrm{d}t^2}\boldsymbol{g}_\mathrm{o}(\boldsymbol{x}_\mathrm{o}) \\ \frac{\mathrm{d}^3}{\mathrm{d}t^3}\boldsymbol{g}_\mathrm{o}(\boldsymbol{x}_\mathrm{o}) \\ \frac{\mathrm{d}^4}{\mathrm{d}t^4}\boldsymbol{g}_\mathrm{o}(\boldsymbol{x}_\mathrm{o}) \end{pmatrix} \in \mathbb{R}^{10\times 10} \tag{4.60}$$

may be used instead of the full matrix $\boldsymbol{S}_\mathrm{O}[\Sigma_\mathrm{o}] \in \mathbb{R}^{20\times 10}$ in (E.34) in order to prove full rank. The reduced observability matrix of system Σ_o is calculated symbolically using MATLAB® (Symbolic Math Toolbox). For the matrix to have full rank, its determinant must not be zero, i.e.

$$\det\left(\boldsymbol{S}_\mathrm{O}^*[\Sigma_\mathrm{o}]\right) \overset{!}{\neq} 0 \tag{4.61}$$

must hold [134, p. 92]. Defining

$$\alpha := \frac{{C_\mathrm{f}}^6 {L_\mathrm{f}}^8 L_\mathrm{r}^5 L_\mathrm{s} \Theta_\mathrm{m} \sigma^4}{L_\mathrm{m} R_\mathrm{r}} > 0 \qquad \text{and} \qquad \beta := \frac{L_\mathrm{m} R_\mathrm{r}}{L_\mathrm{r} L_\mathrm{s}} > 0, \tag{4.62}$$

the scaled determinant is given by[1]

$$\alpha \cdot \det\left(\boldsymbol{S}_\mathrm{O}^*[\Sigma_\mathrm{o}]\right) = \beta\left(1 + \tfrac{1}{\beta^2}\omega_\mathrm{r}^2\right)\left(\omega_\mathrm{r}\|\boldsymbol{\psi}_\mathrm{r}^\mathrm{dq}\|^2 + R_\mathrm{r}\tfrac{2}{3n_\mathrm{p}} m_\mathrm{m}(\boldsymbol{x}_\mathrm{x})\right) + \tfrac{1}{\Theta_\mathrm{m}}\left(m_\mathrm{m}(\boldsymbol{x}_\mathrm{x}) - m_\mathrm{l}\right)\|\boldsymbol{\psi}_\mathrm{r}^\mathrm{dq}\|^2. \tag{4.63}$$

Recalling the generic rotor voltage equation [see (3.1)]

$$\boldsymbol{i}_\mathrm{r}^\mathrm{dq} = -\tfrac{1}{R_\mathrm{r}}\left(\tfrac{\mathrm{d}}{\mathrm{d}t}\boldsymbol{\psi}_\mathrm{r}^\mathrm{dq} + (\omega_\mathrm{k} - \omega_\mathrm{r})\boldsymbol{J}\boldsymbol{\psi}_\mathrm{r}^\mathrm{dq}\right) \tag{4.64}$$

[1] Note that a similar condition is found in [133]. However, in the cited paper, an auxiliary speed term w is defined, which is possible here, too, by setting $w = \beta\omega_\mathrm{r}$. This way, the term $\frac{\mathrm{d}}{\mathrm{d}t} w/(1+w^2)$ (as in the paper) would be obtained.

the machine torque (neglecting iron losses, see Ch. 3.1) can be rewritten as

$$m_\mathrm{m} \overset{(3.4)}{=} -\tfrac{3}{2} n_\mathrm{p} (\boldsymbol{i}_\mathrm{r}^\mathrm{dq})^\top \boldsymbol{J} \boldsymbol{\psi}_\mathrm{r}^\mathrm{dq} \overset{(4.64)}{=} \tfrac{3}{2} n_\mathrm{p} \tfrac{1}{R_\mathrm{r}} (\tfrac{\mathrm{d}}{\mathrm{d}t} \boldsymbol{\psi}_\mathrm{r}^\mathrm{dq} + (\omega_\mathrm{k} - \omega_\mathrm{r}) \boldsymbol{J} \boldsymbol{\psi}_\mathrm{r}^\mathrm{dq})^\top \boldsymbol{J} \boldsymbol{\psi}_\mathrm{r}^\mathrm{dq}. \tag{4.65}$$

Inserting (4.43) and (4.65) into (4.63), and dividing the result by $\|\boldsymbol{\psi}_\mathrm{r}^\mathrm{dq}\|^2$ (the trivial case of $\boldsymbol{\psi}_\mathrm{r}^\mathrm{dq} = 0\,\mathrm{Wb}$ is not considered) yields

$$\frac{\alpha}{\|\boldsymbol{\psi}_\mathrm{r}^\mathrm{dq}\|^2} \det\left(\boldsymbol{S}_\mathrm{O}^*[\Sigma_\mathrm{o}]\right) = \beta(1 + \tfrac{1}{\beta^2}\omega_\mathrm{r}^2)\Big(\omega_\mathrm{k} + \overbrace{\frac{(\frac{\mathrm{d}}{\mathrm{d}t}\boldsymbol{\psi}_\mathrm{r}^\mathrm{dq})^\top \boldsymbol{J} \boldsymbol{\psi}_\mathrm{r}^\mathrm{dq}}{\|\boldsymbol{\psi}_\mathrm{r}^\mathrm{dq}\|^2}}^{\dagger}\Big) + \tfrac{\mathrm{d}}{\mathrm{d}t}\omega_\mathrm{r}. \tag{4.66}$$

The rotor flux linkage and its derivative can be rewritten in terms of polar coordinates as

$$\boldsymbol{\psi}_\mathrm{r}^\mathrm{dq} = \|\boldsymbol{\psi}_\mathrm{r}^\mathrm{dq}\| \begin{pmatrix}\cos(\phi_\psi)\\ \sin(\phi_\psi)\end{pmatrix} \quad \text{and} \quad \tfrac{\mathrm{d}}{\mathrm{d}t}\boldsymbol{\psi}_\mathrm{r}^\mathrm{dq} = \tfrac{\mathrm{d}}{\mathrm{d}t}\|\boldsymbol{\psi}_\mathrm{r}^\mathrm{dq}\| \begin{pmatrix}\cos(\phi_\psi)\\ \sin(\phi_\psi)\end{pmatrix} + \|\boldsymbol{\psi}_\mathrm{r}^\mathrm{dq}\|\omega_\psi \boldsymbol{J} \begin{pmatrix}\cos(\phi_\psi)\\ \sin(\phi_\psi)\end{pmatrix}, \tag{4.67}$$

where ϕ_ψ denotes the flux angle in the dq-reference frame, and $\omega_\psi = \frac{\mathrm{d}}{\mathrm{d}t}\phi_\psi$ is the speed of the flux angle relative to the dq-reference frame. Using (4.67), the †-term can be determined, i.e.

$$(\tfrac{\mathrm{d}}{\mathrm{d}t}\boldsymbol{\psi}_\mathrm{r}^\mathrm{dq})^\top \boldsymbol{J} \boldsymbol{\psi}_\mathrm{r}^\mathrm{dq} = \left[\tfrac{\mathrm{d}}{\mathrm{d}t}\|\boldsymbol{\psi}_\mathrm{r}^\mathrm{dq}\| \begin{pmatrix}\cos(\phi_\psi)\\ \sin(\phi_\psi)\end{pmatrix} + \|\boldsymbol{\psi}_\mathrm{r}^\mathrm{dq}\|\omega_\psi \boldsymbol{J} \begin{pmatrix}\cos(\phi_\psi)\\ \sin(\phi_\psi)\end{pmatrix}\right]^\top \boldsymbol{J} \|\boldsymbol{\psi}_\mathrm{r}^\mathrm{dq}\| \begin{pmatrix}\cos(\phi_\psi)\\ \sin(\phi_\psi)\end{pmatrix} = \|\boldsymbol{\psi}_\mathrm{r}^\mathrm{dq}\|^2 \omega_\psi. \tag{4.68}$$

Now, inserting (4.68) into (4.66), the final condition can be stated as

$$\frac{\alpha}{\|\boldsymbol{\psi}_\mathrm{r}^\mathrm{dq}\|^2} \det\left(\boldsymbol{S}_\mathrm{O}^*[\Sigma_\mathrm{o}]\right) = \beta(1 + \tfrac{1}{\beta^2}\omega_\mathrm{r}^2)(\omega_\mathrm{k} + \omega_\psi) + \tfrac{\mathrm{d}}{\mathrm{d}t}\omega_\mathrm{r} \overset{!}{\neq} 0. \tag{4.69}$$

For the arbitrarily rotating dq-reference frame, the angular velocity $\omega_\mathrm{k} + \omega_\psi$ describes the absolute rotational speed of the rotor flux linkage space vector with respect to the stationary $\alpha\beta$-reference frame. It follows from the condition above that for the system to be observable, either the rotor flux angle must not be constant ($\omega_\mathrm{k} + \omega_\psi \neq 0$, DC excitation) or the rate of change of the rotational speed is non-zero ($\frac{\mathrm{d}}{\mathrm{d}t}\tilde{\omega} \neq 0$, acceleration or deceleration). The results above match with the results in [133], where the authors derived observability conditions related to the $\alpha\beta$-reference frame for the IM-only case. In this section it was shown, that the LC filter, as well as the assigned reference frame, do not change the conditions under which observability is lost.

4.3.2 Full-order state observer (with speed measurement)

In this section, a state observer is derived for the case of available speed measurements. Moreover, the following assumption shall hold.

Assumption 20 (Ideal parameter knowledge)**.** *It is assumed that the parameters of the system and input matrices $\boldsymbol{A}_\mathrm{x}$ and $\boldsymbol{B}_\mathrm{x}$, respectively, are known exactly.*

A state observer is used to reconstruct the system states as not all states can be measured directly. An overview of the observer system assuming measured speed is given in Fig. 4.16. The principle idea is to run a model of the physical system in parallel to the actual system and feed it with the same inputs. The error between the measured output from the real system and the output produced by

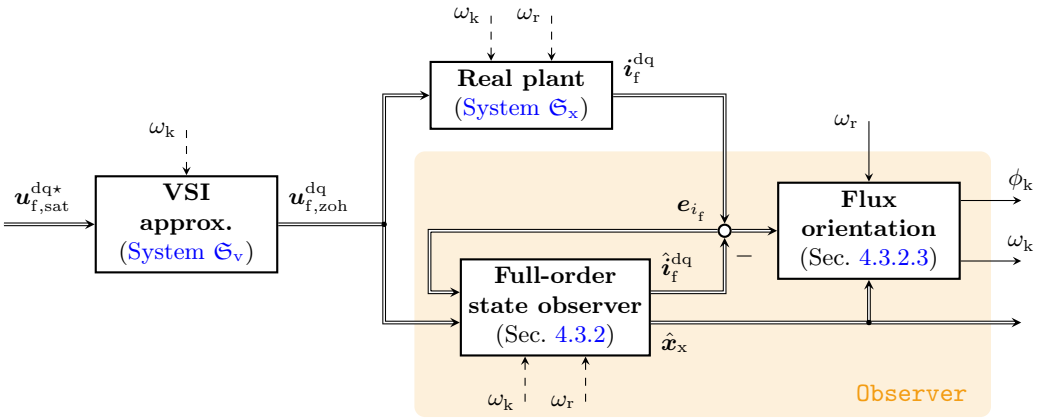

Figure 4.16: *Overview of the basic observer system assuming measured speed.*

the parallel model can be used as corrective feedback. Hence, given that the parameters are perfectly known (Ass. 20), the state estimation error decays exponentially. In analogy to the state-feedback controller design, the state observer is designed in the discrete-time domain. The estimated states, as well as the state estimation error are used for the (estimated) rotor flux orientation. As the input $\boldsymbol{u}_\mathrm{f,zoh}^\mathrm{dq}$ is reconstructed 'externally' and assumed to be known, the controller is designed for the system $\mathfrak{S}_\mathrm{x}$ only.

4.3.2.1 Observer structure

A full-order observer for system $\mathfrak{S}_\mathrm{x}$ [as defined in (4.12)] is given by

$$\hat{\mathfrak{S}}_\mathrm{x}: \quad \begin{cases} \hat{\boldsymbol{x}}_\mathrm{x}[k+1] = \boldsymbol{\mathcal{A}}_\mathrm{x}[k]\hat{\boldsymbol{x}}_\mathrm{x}[k] + \boldsymbol{\mathcal{B}}_\mathrm{x}^*[k]\boldsymbol{u}_\mathrm{f,zoh}^\mathrm{dq}[k] + \boldsymbol{\mathcal{L}}_\mathrm{x}\boldsymbol{e}_{i_\mathrm{f}}[k] \\ \hat{\boldsymbol{i}}_\mathrm{f}^\mathrm{dq}[k] = \boldsymbol{\mathcal{C}}_\mathrm{x}\hat{\boldsymbol{x}}_\mathrm{x}[k] \end{cases} \tag{4.70}$$

where $\hat{\boldsymbol{x}}_\mathrm{x} = ((\hat{\boldsymbol{i}}_\mathrm{f}^\mathrm{dq})^\top, (\hat{\boldsymbol{u}}_\mathrm{s}^\mathrm{dq})^\top, (\hat{\boldsymbol{i}}_\mathrm{s}^\mathrm{dq})^\top, (\hat{\boldsymbol{\psi}}_\mathrm{r}^\mathrm{dq})^\top)^\top \in \mathbb{R}^8$ are the estimated states, $\hat{\boldsymbol{i}}_\mathrm{f}^\mathrm{dq} \in \mathbb{R}^2$ is the estimated output and $\boldsymbol{e}_{i_\mathrm{f}} := \boldsymbol{i}_\mathrm{f}^\mathrm{dq} - \hat{\boldsymbol{i}}_\mathrm{f}^\mathrm{dq} \in \mathbb{R}^2$ is the output estimation error. Moreover, $\boldsymbol{\mathcal{L}}_\mathrm{x} \in \mathbb{R}^{8\times 2}$ denotes the discrete-time observer gain matrix. The corresponding block diagram is depicted in Fig. 4.17, where $\{\cdot\}$ after respective matrices indicates the discretization order used for their calculation.

Remark 25. *If continuous-time observer gains $\boldsymbol{L}_\mathrm{x} \in \mathbb{R}^{8\times 2}$ were given, the discrete-time equivalent could be calculated by $\boldsymbol{\mathcal{L}}_\mathrm{x} = \boldsymbol{S}_{N_\delta}\boldsymbol{L}_\mathrm{x}$. This equivalence may be useful when comparing observer gains derived for CT and DT systems, respectively.*

Assuming exact parameters (Ass. 20), the dynamics of the state estimation error $\boldsymbol{e}_\mathrm{x} := \boldsymbol{x}_\mathrm{x} - \hat{\boldsymbol{x}}_\mathrm{x}$ are given by

$$\boldsymbol{e}_\mathrm{x}[k+1] \overset{(4.12),(4.70)}{=} \left(\boldsymbol{\mathcal{A}}_\mathrm{x}[k] - \boldsymbol{\mathcal{L}}_\mathrm{x}\boldsymbol{\mathcal{C}}_\mathrm{x}\right)\boldsymbol{e}_\mathrm{x}[k] + \epsilon_{N_\delta}[k] \tag{4.71}$$

where $\boldsymbol{e}_{i_\mathrm{f}} = \boldsymbol{\mathcal{C}}_\mathrm{x}\boldsymbol{e}_\mathrm{x}$ was used and

$$\epsilon_{N_\delta}[k] := \overbrace{\tilde{\boldsymbol{S}}_{N_\delta}[k]}^{\text{see (4.14)}} \left(\boldsymbol{A}_\mathrm{x}[k]\boldsymbol{x}_\mathrm{x}[k] + \boldsymbol{B}_\mathrm{x}\boldsymbol{u}_\mathrm{f,zoh}^\mathrm{dq}[k]\right) \tag{4.72}$$

describes the discretization error due to a finite discretization order N_δ.

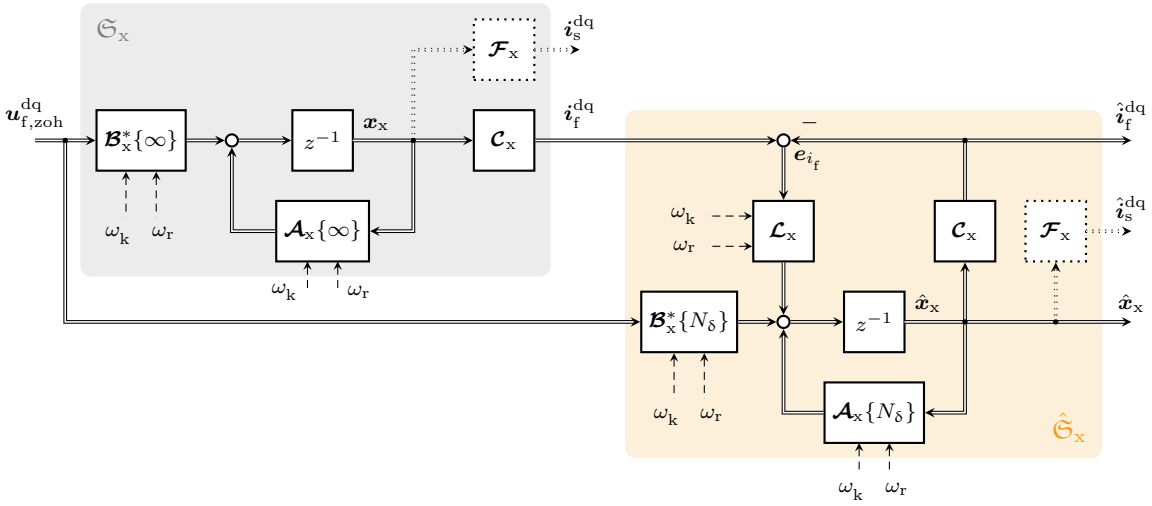

Figure 4.17: *Block diagram of the full-order observer* $\hat{\mathfrak{S}}_\mathrm{x}$ *(assuming measured speed).*

Assumption 21 (Observer discretization order)**.** *It is assumed that the discretization order* N_δ *is sufficiently high, such that the discretization error becomes negligible, i.e.* $\epsilon_{N_\delta}[k] \approx 0$ *holds true.*

Hence, if the eigenvalues of $\boldsymbol{\mathcal{A}}_\mathrm{x}[k] - \boldsymbol{\mathcal{L}}_\mathrm{x}\boldsymbol{\mathcal{C}}_\mathrm{x}$ are located within the unit circle of the complex plane, the state estimation error decays exponentially and

$$\lim_{k\to\infty} \boldsymbol{e}_\mathrm{x}[k] = 0 \tag{4.73}$$

holds true. Since the system is observable (for almost every operating point), the eigenvalues of $\boldsymbol{\mathcal{A}}_\mathrm{x}[k] - \boldsymbol{\mathcal{L}}_\mathrm{x}\boldsymbol{\mathcal{C}}_\mathrm{x}$ may be altered by applying state-feedback [128, Sec. 8.2.3].

4.3.2.2 Observer gain selection

For the state-feedback design approach, the structure of the closed-loop (observer) system matrix $\boldsymbol{\mathcal{A}}_\mathrm{x}[k] - \boldsymbol{\mathcal{L}}_\mathrm{x}\boldsymbol{\mathcal{C}}_\mathrm{x}$ is deficient in a sense that $\boldsymbol{\mathcal{L}}_\mathrm{x}$ and $\boldsymbol{\mathcal{C}}_\mathrm{x}$ are supposed to be in reverse order. However, since $\boldsymbol{\mathcal{A}}_\mathrm{x}[k] - \boldsymbol{\mathcal{L}}_\mathrm{x}\boldsymbol{\mathcal{C}}_\mathrm{x}$ has the same eigenvalues as its transpose $\boldsymbol{\mathcal{A}}_\mathrm{x}^\top[k] - \boldsymbol{\mathcal{C}}_\mathrm{x}^\top\boldsymbol{\mathcal{L}}_\mathrm{x}^\top$ [128, p. 344],[129, p. 114], the state-feedback observer problem reduces to an equivalent control problem for the *dual* system

$$\check{\boldsymbol{x}}_\mathrm{x}[k+1] = \boldsymbol{\mathcal{A}}_\mathrm{x}^\top[k]\check{\boldsymbol{x}}_\mathrm{x}[k] + \boldsymbol{\mathcal{C}}_\mathrm{x}^\top\check{\boldsymbol{u}}^\mathrm{dq}[k], \tag{4.74}$$

with dual state vector $\check{\boldsymbol{x}}_\mathrm{x} \in \mathbb{R}^8$ and dual 'state-feedback control' input $\check{\boldsymbol{u}}^\mathrm{dq} := -\boldsymbol{\mathcal{L}}_\mathrm{x}^\top\check{\boldsymbol{x}}_\mathrm{x}$.

In theory, the observer dynamics can be made arbitrarily fast by choosing large gains $\boldsymbol{\mathcal{L}}_\mathrm{x}$. However, considering the limited sampling rate, measurement noise and parameter errors, a trade-off must be found between fast dynamics and robustness against uncertainties [128, pp. 344-347]. If no particular requirements regarding the robustness against certain parameter errors (i.e. for speed estimation errors) are defined, a well-balanced compromise can be achieved by using—as for the controller tuning—the LQR approach, i.e. solving the optimization problem

$$\arg\min_{\boldsymbol{\mathcal{L}}_\mathrm{x}} \frac{1}{2}\sum_{i=0}^{\infty} \check{\boldsymbol{x}}_\mathrm{x}^\top[i]\left(\boldsymbol{Q}_\mathrm{L} + \boldsymbol{\mathcal{L}}_\mathrm{x}\boldsymbol{R}_\mathrm{L}\boldsymbol{\mathcal{L}}_\mathrm{x}^\top\right)\check{\boldsymbol{x}}_\mathrm{x}[i], \tag{4.75}$$

where $\boldsymbol{Q}_\mathrm{L} = \boldsymbol{Q}_\mathrm{L}^\top \succcurlyeq 0 \in \mathbb{R}^{8\times 8}$ is the weighting matrix for the dual states $\check{\boldsymbol{x}}_\mathrm{x}$, and $\boldsymbol{R}_\mathrm{L} = \boldsymbol{R}_\mathrm{L}^\top \succ 0 \in \mathbb{R}^{2\times 2}$ is the weighting matrix for the dual input $\check{\boldsymbol{u}}^\mathrm{dq}$. The respective gains solving (4.75) can be

stated as

$$\boldsymbol{\mathcal{L}}_{\mathrm{x}}^{\top} = (\boldsymbol{R}_{\mathrm{L}} + \boldsymbol{\mathcal{C}}_{\mathrm{x}}\boldsymbol{P}_{\mathrm{L}}\boldsymbol{\mathcal{C}}_{\mathrm{x}}^{\top})^{-1}\boldsymbol{\mathcal{C}}_{\mathrm{x}}\boldsymbol{P}_{\mathrm{L}}\boldsymbol{\mathcal{A}}_{\mathrm{x}}^{\top}[k], \tag{4.76}$$

where, in analogy to the controller design, the matrix $\boldsymbol{P}_{\mathrm{L}} = \boldsymbol{P}_{\mathrm{L}}^{\top} \succ 0 \in \mathbb{R}^{8\times 8}$ is obtained by solving the algebraic matrix Ricatti equation

$$\boldsymbol{P}_{\mathrm{L}} = \boldsymbol{Q}_{\mathrm{L}} + \boldsymbol{\mathcal{A}}_{\mathrm{x}}^{\top}[k]\left[\boldsymbol{P}_{\mathrm{L}} - \boldsymbol{P}_{\mathrm{L}}\boldsymbol{\mathcal{C}}_{\mathrm{x}}^{\top}(\boldsymbol{R}_{\mathrm{L}} + \boldsymbol{\mathcal{C}}_{\mathrm{x}}\boldsymbol{P}_{\mathrm{L}}\boldsymbol{\mathcal{C}}_{\mathrm{x}}^{\top})^{-1}\boldsymbol{\mathcal{C}}_{\mathrm{x}}\boldsymbol{P}_{\mathrm{L}}\right]\boldsymbol{\mathcal{A}}_{\mathrm{x}}[k]. \tag{4.77}$$

The solution of the optimization problem is parameter dependent, too, as the system matrix $\boldsymbol{\mathcal{A}}_{\mathrm{x}}$ depends on ω_{r} and ω_{k}. Therefore, the observer gain matrix $\boldsymbol{\mathcal{L}}_{\mathrm{x}} = \boldsymbol{\mathcal{L}}_{\mathrm{x}}(\omega_{\mathrm{r}}, \omega_{\mathrm{k}})$ is likewise calculated for different parameters and stored in look-up tables for each entry of $\boldsymbol{\mathcal{L}}_{\mathrm{x}}$. During operation the gains are looked-up for the actual parameters $\omega_{\mathrm{r}}[k]$ and $\omega_{\mathrm{k}}[k]$ in every instant of the observer routine.

As for the controller tuning, the weighting matrices $\boldsymbol{Q}_{\mathrm{L}}$ and $\boldsymbol{R}_{\mathrm{L}}$ are selected as

$$\boldsymbol{Q}_{\mathrm{L}} = \alpha_L \begin{bmatrix} \frac{1}{\hat{i}^2_{\mathrm{f,nom}}}\boldsymbol{I}_2 & \boldsymbol{0}_{2\times 2} & \boldsymbol{0}_{2\times 2} & \boldsymbol{0}_{2\times 2} \\ \boldsymbol{0}_{2\times 2} & \frac{1}{\hat{u}^2_{\mathrm{s,nom}}}\boldsymbol{I}_2 & \boldsymbol{0}_{2\times 2} & \boldsymbol{0}_{2\times 2} \\ \boldsymbol{0}_{2\times 2} & \boldsymbol{0}_{2\times 2} & \frac{1}{\hat{i}^2_{\mathrm{s,nom}}}\boldsymbol{I}_2 & \boldsymbol{0}_{2\times 2} \\ \boldsymbol{0}_{2\times 2} & \boldsymbol{0}_{2\times 2} & \boldsymbol{0}_{2\times 2} & \frac{1}{\hat{\psi}^2_{\mathrm{r,nom}}}\boldsymbol{I}_2 \end{bmatrix} \quad \text{and} \quad \boldsymbol{R}_{\mathrm{L}} = (1-\alpha_L)\frac{1}{\hat{i}^2_{\mathrm{f,nom}}}\boldsymbol{I}_2, \tag{4.78}$$

where the factor $\alpha_L \in (0, 1)$ constitutes the only tuning factor.

Remark 26. *Calculating the discrete-time observer gains can be performed using either* `lqrd(...)` *or* `dlqr(...)`*, provided by the Control System Toolbox of MATLAB®. The effective difference between the two functions is that* `lqrd(...)` *returns the gain matrix* $\boldsymbol{L}_{\mathrm{x}}$ *which needs to be discretized online (i.e. by* $\boldsymbol{\mathcal{L}}_{\mathrm{x}} = \boldsymbol{S}_{N_\delta}\boldsymbol{L}_{\mathrm{x}}$*), whereas* `dlqr(...)` *returns the discrete-time gain matrix* $\boldsymbol{\mathcal{L}}_{\mathrm{x}}$ *directly. For various reasons (as will become clear in the following), it may be beneficial to calculate the continuous-time gains first, and perform the discretization online. Hence, when using* `dlqr(...)`*, the CT gain matrix is obtained by* $\boldsymbol{L}_{\mathrm{x}} = \boldsymbol{S}_{N_\delta}^{-1}\boldsymbol{\mathcal{L}}_{\mathrm{x}}$*. Further details on the peculiarities of the gain calculation for discrete-time observer systems using MATLAB® are given in App. E.6.*

4.3.2.3 Estimated rotor flux orientation

The d-axis of the dq-reference frame is supposed to be aligned with the estimated rotor flux linkage $\hat{\boldsymbol{\psi}}_{\mathrm{r}}^{\mathrm{dq}}$, which is achieved if the electrical frequency ω_{k} is chosen such that $\hat{\psi}_{\mathrm{r}}^{\mathrm{q}} = 0\,\mathrm{Wb}$ holds true. Assuming that the observer gain can be written as $\boldsymbol{\mathcal{L}}_{\mathrm{x}} = \boldsymbol{S}_{N_\delta}\boldsymbol{L}_{\mathrm{x}}$ (see Remark 26), the observer system $\hat{\mathfrak{S}}_{\mathrm{x}}$ [as defined in (4.70)] can be stated as

$$\hat{\boldsymbol{x}}_{\mathrm{x}}[k+1] = \left[\boldsymbol{I}_8 + \boldsymbol{S}_{N_\delta}[k]\big(\boldsymbol{A}_{\mathrm{x}}[k] - \boldsymbol{L}_{\mathrm{x}}[k]\boldsymbol{C}_{\mathrm{x}}\big)\right]\hat{\boldsymbol{x}}_{\mathrm{x}}[k] + \boldsymbol{S}_{N_\delta}[k]\boldsymbol{B}_{\mathrm{x}}\boldsymbol{u}_{\mathrm{f,zoh}}^{\mathrm{dq}}[k] + \boldsymbol{S}_{N_\delta}[k]\boldsymbol{C}_{\mathrm{x}}\boldsymbol{x}_{\mathrm{x}}[k]. \tag{4.79}$$

Rewriting the equation yields

$$\boldsymbol{S}_{N_\delta}^{-1}[k]\big(\hat{\boldsymbol{x}}_{\mathrm{x}}[k+1] - \hat{\boldsymbol{x}}_{\mathrm{x}}[k]\big) = \big(\boldsymbol{A}_{\mathrm{x}}[k] - \boldsymbol{L}_{\mathrm{x}}[k]\boldsymbol{C}_{\mathrm{x}}\big)\hat{\boldsymbol{x}}_{\mathrm{x}}[k] + \boldsymbol{B}_{\mathrm{x}}\boldsymbol{u}_{\mathrm{f,zoh}}^{\mathrm{dq}}[k] + \boldsymbol{C}_{\mathrm{x}}\boldsymbol{x}_{\mathrm{x}}[k]. \tag{4.80}$$

Note that the term $\boldsymbol{S}_{N_\delta}^{-1}[k]\big(\hat{\boldsymbol{x}}_{\mathrm{x}}[k+1] - \hat{\boldsymbol{x}}_{\mathrm{x}}[k]\big)$ is the 'reverse discretization', representing the time derivative of $\hat{\boldsymbol{x}}_{\mathrm{x}}$ evaluated at time instants $k\,T_{\mathrm{S}}$, i.e.

$$\tfrac{\mathrm{d}}{\mathrm{d}t}\hat{\boldsymbol{x}}_{\mathrm{x}}(k\,T_{\mathrm{S}}) = \boldsymbol{S}_{N_\delta}^{-1}[k]\big(\hat{\boldsymbol{x}}_{\mathrm{x}}[k+1] - \hat{\boldsymbol{x}}_{\mathrm{x}}[k]\big). \tag{4.81}$$

Hence, for $\hat{\psi}_\mathrm{r}^\mathrm{q} = 0\,\mathrm{Wb}$ (and $\frac{\mathrm{d}}{\mathrm{d}t}\hat{\psi}_\mathrm{r}^\mathrm{q} = 0\,\mathrm{Wb}$) to hold true, the eighth row of (4.80), corresponding to the derivative of the q-component of the rotor flux linkage, is supposed to be zero. Recalling (4.7) and (4.8), it follows that

$$0 = \tfrac{Lm}{T_\mathrm{r}}\hat{i}_\mathrm{s}^\mathrm{q}[k] - (\omega_\mathrm{k}[k] - \omega_\mathrm{r}[k])\hat{\psi}_\mathrm{r}^\mathrm{d}[k] + \bar{l}_\psi[k](i_\mathrm{f}^\mathrm{q}[k] - \hat{i}_\mathrm{f}^\mathrm{q}[k]) + \tilde{l}_\psi[k](i_\mathrm{f}^\mathrm{d}[k] - \hat{i}_\mathrm{f}^\mathrm{d}[k]), \tag{4.82}$$

must hold, where the seventh and eighth row of $\boldsymbol{L}_\mathrm{x}$ are given by $\boldsymbol{L}_{\mathrm{x},\psi} = \bar{l}_\psi \boldsymbol{I}_2 + \tilde{l}_\psi \boldsymbol{J}$. Solving for ω_k yields

$$\omega_\mathrm{k}[k] = \omega_\mathrm{r}[k] + \frac{\overbrace{\tfrac{Lm}{T_\mathrm{r}}\hat{i}_\mathrm{s}^\mathrm{q}[k] + \bar{l}_\psi[k](i_\mathrm{f}^\mathrm{q}[k] - \hat{i}_\mathrm{f}^\mathrm{q}[k]) + \tilde{l}_\psi[k](i_\mathrm{f}^\mathrm{d}[k] - \hat{i}_\mathrm{f}^\mathrm{d}[k])}^{=:u_{\omega_\mathrm{k}}}}{\max\{\hat{\psi}_\mathrm{r}^\mathrm{d}[k], \epsilon\}}, \quad \epsilon > 0. \tag{4.83}$$

In general, the term $u_{\omega_\mathrm{k}} \in \mathbb{R}$ is subject to fast changes, e.g. due to noise or a small filter time constant T_f. Hence, Eq. (4.83) is not suited for practical implementation, as the fast changing ω_k would negatively affect the control system, leading to audible noise, vibrations and even instability. Moreover, Ass. 18 might be violated. On the other hand, discarding u_{ω_k} leads to an angle misalignment and possibly non-zero $\hat{\psi}_\mathrm{s}^\mathrm{q}$. Therefore, it is reasonable to use a LPF with filter time constant T_{ω_k} for the input u_{ω_k}, yielding the filtered signal y_{ω_k}. In summary, the field-orientation module $\hat{\mathfrak{S}}_\mathrm{fo}$ can be stated as

$$\hat{\mathfrak{S}}_\mathrm{fo}: \quad \begin{cases} \omega_\mathrm{k}[k] & = \omega_\mathrm{r}[k] + \frac{\frac{Lm}{T_\mathrm{r}}\hat{i}_\mathrm{s}^\mathrm{q}[k] + y_{\omega_\mathrm{k}}[k]}{\max\{\hat{\psi}_\mathrm{r}^\mathrm{d}[k], \epsilon\}}, \quad \epsilon > 0. \\ \phi_\mathrm{k}[k+1] & = \phi_\mathrm{k}[k] + T_\mathrm{S}\omega_\mathrm{k}[k], \end{cases} \tag{4.84}$$

where ϕ_k denotes the Park transformation angle.

4.3.3 Speed-adaptive observer (speed-sensorless)

In geothermal power applications, mounting a rotational encoder is typically omitted, due to the harsh environmental conditions within the bore hole. Moreover, as the standard V/Hz control method is an open-loop method, speed feedback is not essential for the operation of the system and, hence, operators may as well save the cost of an additional sensor system. Furthermore, returning the encoder signal via an additional cable along the production tube is risky, as the signal line might be damaged easily; a control system depending on such signal (feedback control) would be rather vulnerable, and hence not suited for industrial application. As the presented speed control system is a *closed-loop* control system, speed feedback is essential, though. For the mentioned reasons, a speed sensorless solution is preferred, as it is more robust and economic at the same time. The full-order state observer derived in the previous section is extended by a speed estimation module. An overview of the modified observer structure is given in Fig. 4.18, where the speed estimation module was added (compared to Fig. 4.16).

4.3.3.1 Speed estimation error and its impact on the state estimates

In the following, the mechanical speed ω_r is replaced by its estimated value $\hat{\omega}_\mathrm{r}$ in the system description (4.7). Defining the speed estimation error as

$$e_{\omega_\mathrm{r}}(t) := \omega_\mathrm{r}(t) - \hat{\omega}_\mathrm{r}(t), \tag{4.85}$$

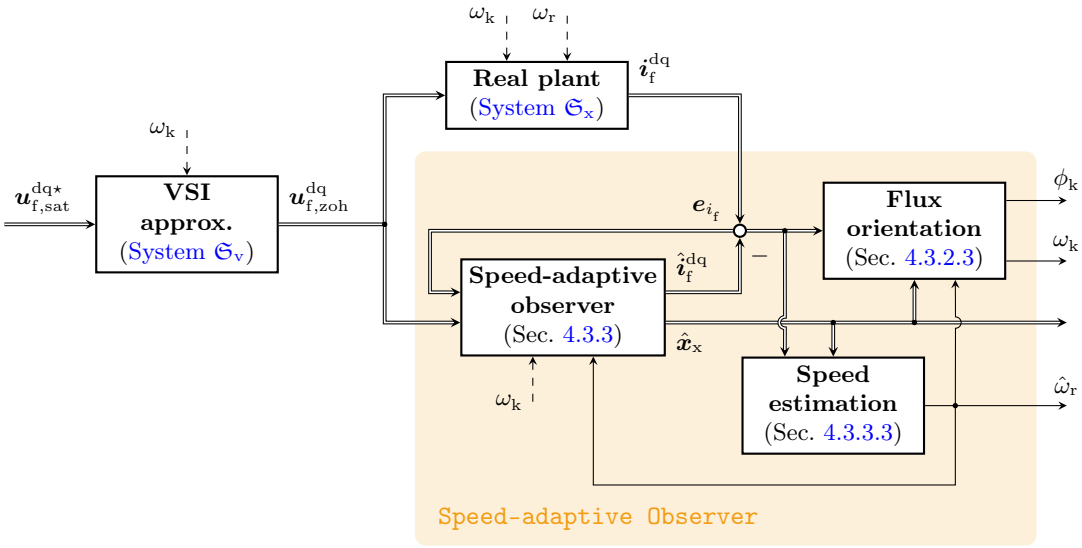

Figure 4.18: *Overview of the speed-adaptive observer system.*

and recalling (4.8) and (4.10), the continuous-time system matrix can be rewritten in terms of the speed estimation error, i.e.

$$\boldsymbol{A}_\mathrm{x}(\hat{\omega}_\mathrm{r},\omega_\mathrm{k}) \overset{(4.85)}{=} \boldsymbol{A}_\mathrm{x}(\omega_\mathrm{r},\omega_\mathrm{k}) - \boldsymbol{A}_\mathrm{r} e_{\omega_\mathrm{r}}(t) =: \hat{\boldsymbol{A}}_\mathrm{x}(\omega_\mathrm{r},\omega_\mathrm{k},e_{\omega_\mathrm{r}}). \tag{4.86}$$

Hence, the discretization matrix becomes

$$\hat{\boldsymbol{S}}_{N_\delta}[k] := \sum_{i=1}^{N_\delta} \frac{T_\mathrm{S}^i}{i!} \boldsymbol{A}_\mathrm{x}^{i-1}(\hat{\omega}_\mathrm{r}[k],\omega_\mathrm{k}[k]) \tag{4.87}$$

resulting in the discrete-time speed-adaptive observer system

$$\hat{\mathfrak{S}}_{\mathrm{x},\hat{\omega}}: \quad \begin{cases} \hat{\boldsymbol{x}}_\mathrm{x}[k+1] = \hat{\boldsymbol{\mathcal{A}}}_\mathrm{x}[k]\hat{\boldsymbol{x}}_\mathrm{x}[k] + \hat{\boldsymbol{\mathcal{B}}}_\mathrm{x}^*[k]\boldsymbol{u}_\mathrm{f,zoh}^\mathrm{dq}[k] + \hat{\boldsymbol{\mathcal{L}}}_\mathrm{x}[k]\boldsymbol{e}_{i_\mathrm{f}}[k] \\ \quad \hat{\boldsymbol{i}}_\mathrm{f}^\mathrm{dq}[k] = \boldsymbol{\mathcal{C}}_\mathrm{x}\hat{\boldsymbol{x}}_\mathrm{x}[k] \end{cases} \tag{4.88}$$

with discrete-time system matrix $\hat{\boldsymbol{\mathcal{A}}}_\mathrm{x} \in \mathbb{R}^{8\times 8}$, input matrix $\hat{\boldsymbol{\mathcal{B}}}_\mathrm{x}^* \in \mathbb{R}^{8\times 2}$ and observer gain matrix $\hat{\boldsymbol{\mathcal{L}}}_\mathrm{x} \in \mathbb{R}^{8\times 2}$ defined as

$$\left.\begin{aligned} \hat{\boldsymbol{\mathcal{A}}}_\mathrm{x}[k] &:= \boldsymbol{I}_8 + \hat{\boldsymbol{S}}_{N_\delta}[k]\boldsymbol{A}_\mathrm{x}(\hat{\omega}_\mathrm{r}[k],\omega_\mathrm{k}[k]), \\ \hat{\boldsymbol{\mathcal{B}}}_\mathrm{x}^*[k] &:= \hat{\boldsymbol{S}}_{N_\delta}[k]\boldsymbol{B}_\mathrm{x}, \\ \hat{\boldsymbol{\mathcal{L}}}_\mathrm{x}[k] &:= \hat{\boldsymbol{S}}_{N_\delta}[k]\boldsymbol{L}_\mathrm{x}(\hat{\omega}_\mathrm{r}[k],\omega_\mathrm{k}[k]). \end{aligned}\right\} \tag{4.89}$$

The block diagram of the speed-adaptive observer is depicted in Fig. 4.19, where (again) $\{\cdot\}$ indicates the discretization order which is used for the calculation of respective matrices.

It can be shown that—given a sufficiently high discretization order N_δ, a small sampling time T_S and a small speed estimation error e_{ω_r}—the error difference can be stated as (see App. E.2)

$$\boldsymbol{e}_\mathrm{x}[k+1] \approx \left(\boldsymbol{\mathcal{A}}_\mathrm{x}[k] - \hat{\boldsymbol{\mathcal{L}}}_\mathrm{x}[k]\boldsymbol{\mathcal{C}}_\mathrm{x}\right)\boldsymbol{e}_\mathrm{x}[k] + \boldsymbol{\mathcal{G}}_\mathrm{x}\hat{\psi}_\mathrm{r}^\mathrm{dq}[k]e_{\omega_\mathrm{r}}[k], \tag{4.90}$$

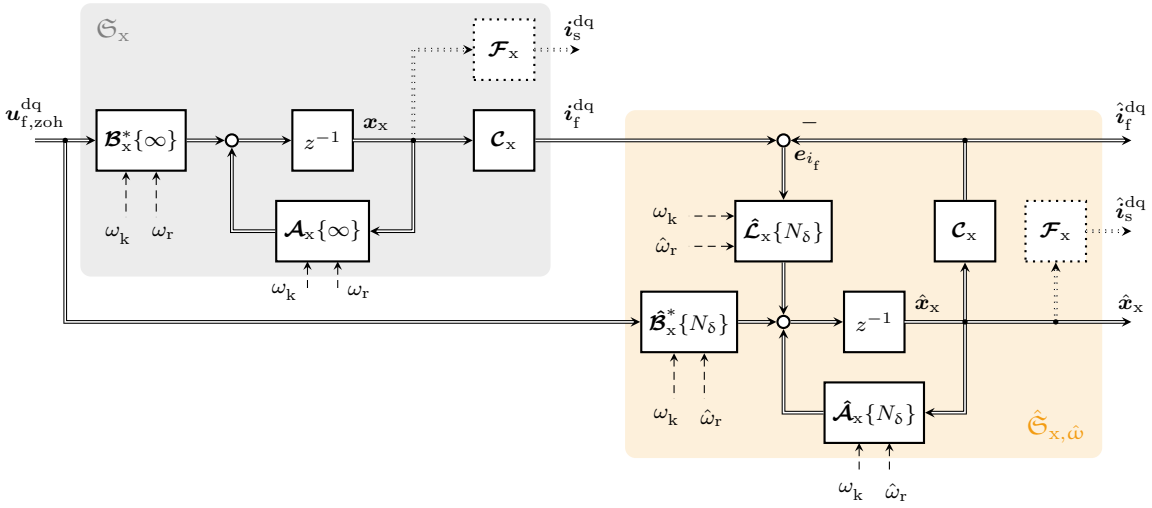

Figure 4.19: *Overview of the speed-adaptive observer system.*

with 'input' matrix $\boldsymbol{\mathcal{G}}_\mathrm{x} \in \mathbb{R}^{8\times 2}$ defined as

$$\boldsymbol{\mathcal{G}}_\mathrm{x} := T_\mathrm{S} \begin{bmatrix} \boldsymbol{0}_{2\times 2} \\ \boldsymbol{0}_{2\times 2} \\ -\frac{1}{L_\mu}\boldsymbol{J} \\ \boldsymbol{J} \end{bmatrix}. \tag{4.91}$$

It is evident from (4.90) that the speed estimation error e_{ω_r} directly affects the state estimation error, as it can be considered the input to the error system.

4.3.3.2 Lyapunov-based speed adaption law derivation (failed attempt)

Since the introduction of the speed-adaptive observer concept for induction machines in [71], many attempts have been made to find a generalized stability proof for global asymptotic stability of the speed-adaptive observer (see e.g. [71, 79, 83]). In [86] it was shown for IMs only, that a Lyapunov-based stability proof will eventually fail (at least for the commonly used Lyapunov candidate), unless either the rotor flux linkage or the speed are measured. However, marginally stable and good practical designs can be derived using this analytic approach (see e.g. [84, 85, 88]). In this section, the attempt of a Lyapunov-based stability proof is transferred to the induction machine with LC filter case. Although, eventually, this approach is not a fruitful one, it shows that the given problem requires a different solution as for the IM-only case.

In the following, in order to simplify the derivation, a speed-adaptive observer in the continuous-time domain (for system Σ_x) is considered, i.e.

$$\hat{\Sigma}_{\mathrm{x},\hat{\omega}_\mathrm{r}}: \quad \begin{cases} \frac{\mathrm{d}}{\mathrm{d}t}\hat{\boldsymbol{x}}_\mathrm{x}(t) = \overbrace{\left(\boldsymbol{A}_0 + \boldsymbol{A}_\mathrm{r}\hat{\omega}_\mathrm{r}(t) + \boldsymbol{A}_\mathrm{k}\omega_\mathrm{k}(t)\right)}^{=\boldsymbol{A}_\mathrm{x}(\hat{\omega}_\mathrm{r},\omega_\mathrm{k})}\hat{\boldsymbol{x}}_\mathrm{x}(t) + \boldsymbol{B}_\mathrm{x}\boldsymbol{u}_\mathrm{f}^{\mathrm{dq}\star}(t) + \boldsymbol{L}_\mathrm{x}\boldsymbol{C}_\mathrm{x}\boldsymbol{e}_\mathrm{x}(t), \\ \hat{\boldsymbol{i}}_\mathrm{f}^{\mathrm{dq}}(t) = \boldsymbol{C}_\mathrm{x}\hat{\boldsymbol{x}}_\mathrm{x}(t). \end{cases} \tag{4.92}$$

Recalling the state estimation error $\boldsymbol{e}_\mathrm{x} = \boldsymbol{x}_\mathrm{x} - \hat{\boldsymbol{x}}_\mathrm{x}$, the corresponding state estimation error system

can be written as

$$\hat{\Sigma}_\mathrm{e}: \quad \begin{cases} \frac{\mathrm{d}}{\mathrm{d}t}\boldsymbol{e}_\mathrm{x}(t) & \overset{(4.7),(4.92)}{=} & \boldsymbol{A}_{\mathrm{x,cl}}(\omega_\mathrm{r},\omega_\mathrm{k})\boldsymbol{e}_\mathrm{x}(t) + \boldsymbol{B}_{\mathrm{x,cl}}(\hat{\boldsymbol{x}}_\mathrm{x})e_{\omega_\mathrm{r}}(t), \\ \boldsymbol{e}_{i_\mathrm{f}}(t) & = & \boldsymbol{C}_\mathrm{x}\boldsymbol{e}_\mathrm{x}(t), \end{cases} \tag{4.93}$$

with closed-loop system matrix $\boldsymbol{A}_{\mathrm{x,cl}}(\omega_\mathrm{r},\omega_\mathrm{k}) := \boldsymbol{A}_\mathrm{x}(\omega_\mathrm{r},\omega_\mathrm{k}) - \boldsymbol{L}_\mathrm{x}\boldsymbol{C}_\mathrm{x} \in \mathbb{R}^{8\times 8}$ and input matrix $\boldsymbol{B}_{\mathrm{x,cl}}(\hat{\boldsymbol{x}}_\mathrm{x}) := \boldsymbol{A}_\mathrm{r}\hat{\boldsymbol{x}}_\mathrm{x} \in \mathbb{R}^{8\times 1}$. Note that e_{ω_r} is the system input, whereas the known vector $\hat{\boldsymbol{x}}_\mathrm{x}$ parametrizes the input matrix.

Now, the objective is to make the adaptive observer *asymptotically stable*, as this guarantees that the state estimation error $\boldsymbol{e}_\mathrm{x}$ decays to zero [111, p. 153]. A possible way of proving asymptotic stability is *Lyapunov's direct method* [111, p. 153]. The Lyapunov function candidate (LFC) is selected as proposed in literature (see e.g. [71, 86]), i.e.

$$V(t) = \boldsymbol{e}_\mathrm{x}(t)^\top \boldsymbol{P}\boldsymbol{e}_\mathrm{x}(t) + \rho e_{\omega_\mathrm{r}}(t)^2, \tag{4.94}$$

with matrix $\boldsymbol{P} = \boldsymbol{P}^\top \succ 0 \in \mathbb{R}^{8\times 8}$ and constant $\rho > 0 \in \mathbb{R}$.

Since the mechanical speed is assumed to change slowly compared to the electrical system states (see Ass. 17), its derivative can be considered zero, yielding the derivative of the speed estimation error

$$\tfrac{\mathrm{d}}{\mathrm{d}t}e_{\omega_\mathrm{r}}(t) = \tfrac{\mathrm{d}}{\mathrm{d}t}\omega_\mathrm{r}(t) - \tfrac{\mathrm{d}}{\mathrm{d}t}\hat{\omega}_\mathrm{r}(t) \overset{\text{Ass. } 17}{\approx} -\tfrac{\mathrm{d}}{\mathrm{d}t}\hat{\omega}_\mathrm{r}(t). \tag{4.95}$$

Using (4.95), the time derivative of V can be stated as

$$\tfrac{\mathrm{d}}{\mathrm{d}t}V(t) = -\underbrace{\boldsymbol{e}_\mathrm{x}(t)^\top \boldsymbol{Q}\boldsymbol{e}_\mathrm{x}(t)}_{\dagger} + \underbrace{2\boldsymbol{e}_\mathrm{x}(t)^\top \boldsymbol{P}\boldsymbol{B}_{\mathrm{x,cl}}(\hat{\boldsymbol{x}}_\mathrm{x})e_{\omega_\mathrm{r}}(t) - 2\rho e_{\omega_\mathrm{r}}(t)\tfrac{\mathrm{d}}{\mathrm{d}t}\hat{\omega}_\mathrm{r}(t)}_{\ddagger}. \tag{4.96}$$

with

$$\boldsymbol{Q} := -(\boldsymbol{A}_{\mathrm{x,cl}}(\omega_\mathrm{r},\omega_\mathrm{k})^\top \boldsymbol{P} + \boldsymbol{P}\boldsymbol{A}_{\mathrm{x,cl}}(\omega_\mathrm{r},\omega_\mathrm{k})^\top). \tag{4.97}$$

For the system to become asymptotically stable, $\frac{\mathrm{d}}{\mathrm{d}t}V(t) < 0$ must hold true for all $\boldsymbol{e}_\mathrm{x} \neq \boldsymbol{0}_8$ and $e_{\omega_\mathrm{r}} \neq 0$. The first part (†-term) is negative if the matrix $\boldsymbol{Q}$ is symmetric and positive definite ($\boldsymbol{Q} = \boldsymbol{Q}^\top \succ 0$), which holds true locally, if the eigenvalues of $\boldsymbol{A}_{\mathrm{x,cl}}$ have negative real parts [111, p. 153]. Since the system is fully observable, this condition can be guaranteed locally by proper selection of the observer gains $\boldsymbol{L}_\mathrm{x}$ and gain scheduling. It remains to show that the second part (‡-term) of (4.96) is smaller than or equal to zero. Intuitively, this can be achieved by selecting

$$\tfrac{\mathrm{d}}{\mathrm{d}t}\hat{\omega}_\mathrm{r}(t) = \tfrac{1}{\rho}\boldsymbol{e}_\mathrm{x}(t)^\top \boldsymbol{P}\boldsymbol{B}_{\mathrm{x,cl}}(\hat{\boldsymbol{x}}_\mathrm{x}), \tag{4.98}$$

where the factor ρ is a design parameter. However, the adaption law (4.98) cannot be implemented since the vector $\boldsymbol{e}_\mathrm{x}$ is not fully known. In fact, only the filter current estimation error $\boldsymbol{e}_{i_\mathrm{f}} = \boldsymbol{C}_\mathrm{x}\boldsymbol{e}_\mathrm{x}$ is known from measurements. Hence, if there existed a matrix $\boldsymbol{P}$ for which

$$\boldsymbol{P}\boldsymbol{B}_{\mathrm{x,cl}}(\hat{\boldsymbol{x}}_\mathrm{x}) = \boldsymbol{C}_\mathrm{x}^\top \tag{4.99}$$

held true, the lack of information could be ignored without affecting the stability of the adaptive observer. The so-called *Meyer-Kalman-Yakubovich Lemma* (see [135, Lemma 3.5.4]) states that such $\boldsymbol{P}$ exists, if and only if the transfer function from the input e_{ω_r} to the measurable output $\boldsymbol{e}_{i_\mathrm{f}}$ is *strictly positive real* (SPR)—a property from robust control theory which is not further elaborated here (for details refer to [135, Definition 3.5.1]). As the relative degree of the system $\hat{\Sigma}_\mathrm{e}$ is greater

than one[2], the SPR property is not satisfied (see [135, Corrolary 3.5.1]) and, hence, the matrix $\boldsymbol{P}$ satisfying (4.97) and (4.99) does not exist. As opposed to the IM-only case, where such $\boldsymbol{P}$ exists for some particular choice of $\boldsymbol{Q} \succcurlyeq 0$, and hence the SPR property can be enforced using the observer gains. However, for the given configuration of induction machine *and* LC filter, finding such stabilizing gains using the same approach is not possible. Therefore, a hands-on solution needs to be found, which is analyzed regarding its low-speed capabilities and stabilized by other means.

4.3.3.3 Speed adaption law

Although an adaption law guaranteeing asymptotic stability cannot be derived with the presented approach, some useful information can be drawn from the ideal adaption law (4.98). Expanding the equation yields

$$\begin{aligned}\frac{\mathrm{d}}{\mathrm{d}t}\hat{\omega}_\mathrm{r}(t) \overset{(4.98)}{=} \frac{1}{\rho}\Big[&\boldsymbol{e}_{i_\mathrm{f}}(t)^\top(-\tfrac{1}{L_\mu}\boldsymbol{P}_{13}+\boldsymbol{P}_{14}) + \boldsymbol{e}_{u_\mathrm{s}}(t)^\top(-\tfrac{1}{L_\mu}\boldsymbol{P}_{23}+\boldsymbol{P}_{24})\\ &+ \boldsymbol{e}_{i_\mathrm{s}}(t)^\top(-\tfrac{1}{L_\mu}\boldsymbol{P}_{33}+\boldsymbol{P}_{34}) + \boldsymbol{e}_{\psi_\mathrm{r}}(t)^\top(-\tfrac{1}{L_\mu}\boldsymbol{P}_{43}+\boldsymbol{P}_{44})\Big]\boldsymbol{J}\hat{\boldsymbol{\psi}}_\mathrm{r}^\mathrm{dq}(t). \end{aligned} \tag{4.100}$$

The sub-matrices $\boldsymbol{P}_{i3}$ and $\boldsymbol{P}_{i4}$, for $i = 1,\dots,4$, guarantee that the right-hand side of (4.100) is always proportional to the speed estimation error, thus 'pushing' the estimated speed $\hat{\omega}_\mathrm{r}$ towards the actual value ω_r by integration over the error term. However, for the given setup only the first term, namely $\frac{1}{\rho}\boldsymbol{e}_{i_\mathrm{f}}^\top(-\frac{1}{L_\mu}\boldsymbol{P}_{13}+\boldsymbol{P}_{14})\boldsymbol{J}\hat{\boldsymbol{\psi}}_\mathrm{r}^\mathrm{dq}$, can be used for speed adaption, as $\boldsymbol{e}_{u_\mathrm{s}}$, $\boldsymbol{e}_{i_\mathrm{s}}$ and $\boldsymbol{e}_{\psi_\mathrm{r}}$ are not known. Hence, the question arises, how the filter current estimation error $\boldsymbol{e}_{i_\mathrm{f}}$ relates to the speed estimation error e_{ω_r}, and how this information can be used to reduce the latter. Ideally, a substitute for (4.100) is found, which is directly proportional to the speed estimation error and only depends on measured or estimated quantities.

As the electrical system is considered much faster than the mechanical system (see Ass. 17), a steady-state evaluation of the state estimation error gives further insight into the relation between $\boldsymbol{e}_{i_\mathrm{f}}$ and e_{ω_r}. The steady-state solution of (4.90) is given by

$$\lim_{k\to\infty}\boldsymbol{e}_\mathrm{x}[k+1] =: \boldsymbol{e}_{\mathrm{x},\infty} = \overbrace{\left(\boldsymbol{I}_8 - \boldsymbol{\mathcal{A}}_\mathrm{x}(\omega_\mathrm{r},\omega_\mathrm{k}) + \boldsymbol{\mathcal{L}}_\mathrm{x}(\omega_\mathrm{r},\omega_\mathrm{k})\boldsymbol{\mathcal{C}}_\mathrm{x}\right)^{-1}\boldsymbol{\mathcal{G}}_\mathrm{x}}^{=:\boldsymbol{\Gamma}(\omega_\mathrm{r},\omega_\mathrm{k})}\hat{\boldsymbol{\psi}}_{\mathrm{r},\infty}^\mathrm{dq}e_{\omega_\mathrm{r},\infty}, \tag{4.101}$$

with 'static gain' matrix $\boldsymbol{\Gamma} = [\boldsymbol{\Gamma}_1^\top, \boldsymbol{\Gamma}_2^\top, \boldsymbol{\Gamma}_3^\top, \boldsymbol{\Gamma}_4^\top]^\top \in \mathbb{R}^{8\times 2}$ and steady-state state estimation error $\boldsymbol{e}_{\mathrm{x},\infty} \in \mathbb{R}^8$. Hence, the steady-state filter current estimation error $\boldsymbol{e}_{i_\mathrm{f},\infty}$ can be expressed as

$$\boldsymbol{e}_{i_\mathrm{f},\infty} = \boldsymbol{\mathcal{C}}_\mathrm{x}\boldsymbol{e}_{\mathrm{x},\infty} = \boldsymbol{\Gamma}_1(\omega_\mathrm{r},\omega_\mathrm{k})\hat{\boldsymbol{\psi}}_{\mathrm{r},\infty}^\mathrm{dq}e_{\omega_\mathrm{r},\infty}, \tag{4.102}$$

where $\boldsymbol{\Gamma}_1(\omega_\mathrm{r},\omega_\mathrm{k}) = \bar{\gamma}_1(\omega_\mathrm{r},\omega_\mathrm{k})\boldsymbol{I}_2 + \tilde{\gamma}_1(\omega_\mathrm{r},\omega_\mathrm{k})\boldsymbol{J}$ is the first submatrix of $\boldsymbol{\Gamma}$, and $\bar{\gamma}_1, \tilde{\gamma}_1 \in \mathbb{R}$ are respective operating point dependent scalars. Multiplying $\boldsymbol{e}_{i_\mathrm{f},\infty}^\top$ by $\boldsymbol{J}\hat{\boldsymbol{\psi}}_{\mathrm{r},\infty}^\mathrm{dq}$ as in the ideal adaption law (both terms are known) yields the 'error torque'

$$\tau_{\hat{\omega}} = \boldsymbol{e}_{i_\mathrm{f},\infty}^\top\boldsymbol{J}\hat{\boldsymbol{\psi}}_{\mathrm{r},\infty}^\mathrm{dq} = (\hat{\boldsymbol{\psi}}_{\mathrm{r},\infty}^\mathrm{dq})^\top(\bar{\gamma}_1\boldsymbol{I}_2 - \tilde{\gamma}_1\boldsymbol{J})\boldsymbol{J}\hat{\boldsymbol{\psi}}_{\mathrm{r},\infty}^\mathrm{dq}e_{\omega_\mathrm{r},\infty} = \tilde{\gamma}_1\|\hat{\boldsymbol{\psi}}_{\mathrm{r},\infty}^\mathrm{dq}\|^2 e_{\omega_\mathrm{r}}, \tag{4.103}$$

a measurable expression which is proportional to the speed estimation error e_{ω_r}, the squared magnitude of the estimated rotor flux linkage $\|\hat{\boldsymbol{\psi}}_{\mathrm{r},\infty}^\mathrm{dq}\|^2$ and the scalar $\tilde{\gamma}_1(\omega_\mathrm{r},\omega_\mathrm{k})$.

[2]The term *relative degree* describes the order of the output derivative of a system on which the input directly acts [109, Sec. 5.4.4]. Here, the input e_{ω_r} is not acting directly on the derivative of the measurable output $\boldsymbol{e}_{i_\mathrm{f}}$.

The impact of the speed estimation error on the different steady-state errors $\boldsymbol{e}_{\mathrm{x},\infty}$ is shown in Fig. 4.20 for different speeds (line styles) and loads (markers) and with observer gains calculated by the LQR tuning method described in the previous section. The flux linkage $\hat{\boldsymbol{\psi}}_{\mathrm{r}}^{\mathrm{dq}} = (\hat{\psi}_{\mathrm{r,nom}}, 0)$ and the speed estimation error $e_{\omega_{\mathrm{r}}} = 2\,\mathrm{rad\,s^{-1}}$ are assumed to be constant. It can be observed, that for all plotted steady-state error maps, the majority of state estimation errors is located in the positive q-axis half plane, i.e. the q-components of the state estimation errors have the same sign as the speed estimation error for most operating points; on the contrary, the negative q-axis half plane (red shaded area [ ]) can be considered the critical region, as corresponding q-components are not proportional to the speed estimation error, but to its negative value. While the rotor flux linkage estimation error is strictly positive in q-direction, the current and voltage errors are subject to a sign change for a small number of operating points. These operating points are located in the low-speed regenerating region, which is known to cause stability issues for most observer-based speed estimation schemes. Apart from that, it can be observed that the filter and stator current error maps are very similar (scaled), which leads to the conclusion that the filter current estimation error may as well be used for speed adaption.

Hence, using the measurable error torque ($\boldsymbol{e}_{i_{\mathrm{f}}}$ is measured, $\hat{\boldsymbol{\psi}}_{\mathrm{r}}^{\mathrm{dq}}$ is known)

$$\tau_{\hat{\omega}}[k] = \boldsymbol{e}_{i_{\mathrm{f}}}[k]^{\top} \boldsymbol{J} \hat{\boldsymbol{\psi}}_{\mathrm{r}}^{\mathrm{dq}}[k] \tag{4.104}$$

as an input, the speed estimation can be realized using a simple PI controller

$$\hat{\mathfrak{S}}_{\mathrm{pi},\hat{\omega}}: \quad \begin{cases} \hat{\omega}_{\mathrm{r}}[k] = L_{\mathrm{p},\hat{\omega}} \tau_{\hat{\omega}}[k] + L_{\mathrm{i},\hat{\omega}} \xi_{\hat{\omega}}[k], \\ \xi_{\hat{\omega}}[k] = \frac{T_{\mathrm{S}}}{2} (\tau_{\hat{\omega}}[k] + \tau_{\hat{\omega}}[k-1]) \xi_{\hat{\omega}}[k-1]. \end{cases} \tag{4.105}$$

This modification of the often called 'conventional' adaption law was first proposed in [64], where different observer gains were used, though.

4.3.3.4 Tuning based on linearized system

Tuning of the speed estimator $\hat{\mathfrak{S}}_{\mathrm{pi},\hat{\omega}}$ is based on a linearization analysis, which is conducted in the following. For the analysis it is assumed that the mechanical speed, electrical speed and estimated rotor flux linkage are constant, i.e. at fixed operating points

$$\omega_{\mathrm{k}}[k] = \omega_{\mathrm{k,op}}, \qquad \omega_{\mathrm{r}}[k] = \omega_{\mathrm{r,op}} \qquad \text{and} \qquad \hat{\boldsymbol{\psi}}_{\mathrm{r}}^{\mathrm{dq}}[k] = \hat{\boldsymbol{\psi}}_{\mathrm{r,op}}^{\mathrm{dq}}. \tag{4.106}$$

Concerning the speed terms, the assumption is justified by the different time scales of the electrical and mechanical system (see Ass. 17 and 18), whereas constant flux is ensured by the flux controller (similar assumptions e.g. as in [88]). The linearized system (linearization of discrete-time systems described in [136, pp. 399, 400]) is given by

$$\begin{pmatrix} \Delta \boldsymbol{e}_{\mathrm{x}}[k+1] \\ \Delta e_{\omega_{\mathrm{r}}}[k+1] \end{pmatrix} = \begin{bmatrix} \frac{\partial \boldsymbol{e}_{\mathrm{x}}[k+1]}{\partial \boldsymbol{e}_{\mathrm{x}}[k]} & \frac{\partial \boldsymbol{e}_{\mathrm{x}}[k+1]}{\partial e_{\omega_{\mathrm{r}}}[k]} \\ \frac{\partial e_{\omega_{\mathrm{r}}}[k+1]}{\partial \boldsymbol{e}_{\mathrm{x}}[k]} & \frac{\partial e_{\omega_{\mathrm{r}}}[k+1]}{\partial e_{\omega_{\mathrm{r}}}[k]} \end{bmatrix} \Bigg|_{\mathrm{op}} \cdot \begin{pmatrix} \Delta \boldsymbol{e}_{\mathrm{x}}[k] \\ \Delta e_{\omega_{\mathrm{r}}}[k] \end{pmatrix}, \tag{4.107}$$

where $[\cdot]|_{\mathrm{op}}$ indicates evaluation of the Jacobian matrix (linearized system matrix) at the operating point. The elements of the first row of the Jacobian are given by

$$\frac{\partial \boldsymbol{e}_{\mathrm{x}}[k+1]}{\partial \boldsymbol{e}_{\mathrm{x}}[k]}\Bigg|_{\mathrm{op}} \overset{(4.90)}{=} \boldsymbol{\mathcal{A}}_{\mathrm{x}}[k] - \boldsymbol{\mathcal{L}}_{\mathrm{x}}[k] \boldsymbol{\mathcal{C}}_{\mathrm{x}} \tag{4.108}$$

$$\frac{\partial \boldsymbol{e}_{\mathrm{x}}[k+1]}{\partial e_{\omega_{\mathrm{r}}}[k]}\Bigg|_{\mathrm{op}} \overset{(4.90)}{=} \boldsymbol{\mathcal{G}}_{\mathrm{x}}(\hat{\boldsymbol{\psi}}_{\mathrm{r,op}}^{\mathrm{dq}}). \tag{4.109}$$

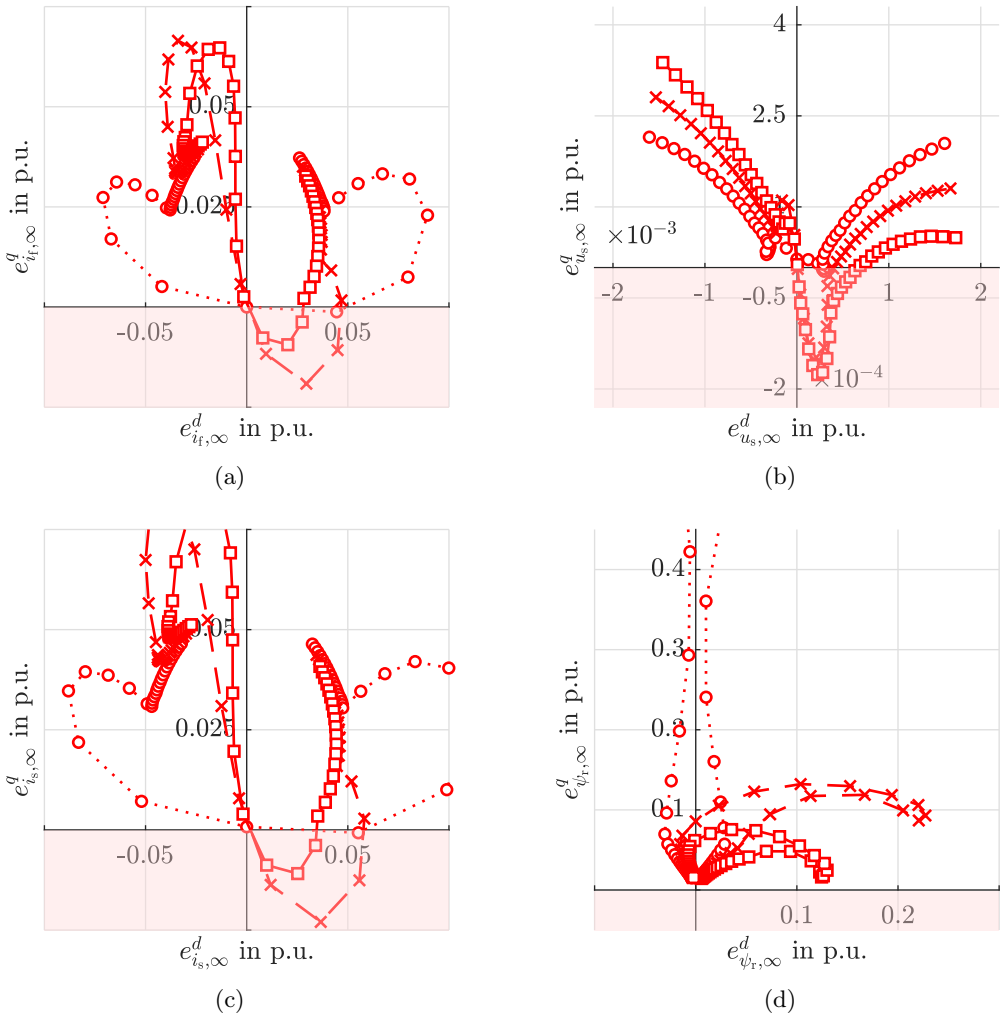

Figure 4.20: *Steady-state estimation error maps for constant rotor flux linkage* $\hat{\boldsymbol{\psi}}_\mathrm{r}^\mathrm{dq} = (\hat{\psi}_\mathrm{r,nom}, 0)^\top$, *constant speed estimation error* $e_{\omega_\mathrm{r}} = 2\,\mathrm{rad\,s^{-1}}$ *varying speeds* $\omega_\mathrm{r} = \{-1, \ldots, 1\} \cdot \omega_\mathrm{r,nom}$ *(represented by markers of the same style) and different loads* $\omega_\mathrm{k} - \omega_\mathrm{r} = \{0, 0.5, 1\} \cdot (\omega_\mathrm{k,nom} - \omega_\mathrm{r,nom})$, *indicated by different marker styles 'o', 'square' and 'x', respectively.*

In order to calculate the partial derivatives of $e_{\omega_\mathrm{r}}[k+1]$ an expression for $e_{\omega_\mathrm{r}}[k+1]$ is required. Assuming $\omega_\mathrm{r}[k+1] = \omega_\mathrm{r}[k] = \omega_\mathrm{r,op}$, the expression can be stated as

$$\begin{aligned} e_{\omega_\mathrm{r}}[k+1] &= \omega_\mathrm{r}[k+1] - \hat{\omega}_\mathrm{r}[k+1] \\ &\overset{(4.105),(4.104),(4.90)}{=} -(L_{\mathrm{i},\hat{\omega}}\tfrac{T_\mathrm{S}}{2} + L_{\mathrm{p},\hat{\omega}})\boldsymbol{e}_\mathrm{x}[k]^\top(\boldsymbol{\mathcal{A}}_\mathrm{x}[k] - \boldsymbol{\mathcal{L}}_\mathrm{x}[k]\boldsymbol{\mathcal{C}}_\mathrm{x})^\top\boldsymbol{\mathcal{C}}_\mathrm{x}^\top\boldsymbol{J}\hat{\boldsymbol{\psi}}_\mathrm{r}^\mathrm{dq}[k+1] \\ &\quad -(L_{\mathrm{i},\hat{\omega}}\tfrac{T_\mathrm{S}}{2} - L_{\mathrm{p},\hat{\omega}})\boldsymbol{e}_\mathrm{x}[k]^\top\boldsymbol{\mathcal{C}}_\mathrm{x}^\top\boldsymbol{J}\hat{\boldsymbol{\psi}}_\mathrm{r}^\mathrm{dq}[k] + e_{\omega_\mathrm{r}}[k], \end{aligned} \tag{4.110}$$

where $\boldsymbol{e}_{i_\mathrm{f}}^\top = \boldsymbol{e}_\mathrm{x}^\top\boldsymbol{\mathcal{C}}_\mathrm{x}^\top$ and $\boldsymbol{\mathcal{G}}_\mathrm{x}^\top\boldsymbol{\mathcal{C}}^\top = \mathbf{o}_2^\top$ were used. Now, the partial derivatives can be determined as

$$\left.\frac{\partial e_{\omega_\mathrm{r}}[k+1]}{\partial \boldsymbol{e}_\mathrm{x}[k]}\right|_\mathrm{op} \overset{(4.110)}{=} -(\hat{\boldsymbol{\psi}}_\mathrm{r,op}^\mathrm{dq})^\top\boldsymbol{J}\boldsymbol{\mathcal{C}}_\mathrm{x}\Big[(L_{\mathrm{i},\hat{\omega}}\tfrac{T_\mathrm{S}}{2} + L_{\mathrm{p},\hat{\omega}})(\boldsymbol{\mathcal{A}}_\mathrm{x}[k] - \boldsymbol{\mathcal{L}}_\mathrm{x}[k]\boldsymbol{\mathcal{C}}_\mathrm{x}) + (L_{\mathrm{i},\hat{\omega}}\tfrac{T_\mathrm{S}}{2} - L_{\mathrm{p},\hat{\omega}})\boldsymbol{I}_8\Big], \tag{4.111}$$

$$\left.\frac{\partial \boldsymbol{e}_\mathrm{x}[k+1]}{\partial e_{\omega_\mathrm{r}}[k]}\right|_\mathrm{op} \overset{(4.110)}{=} 1, \tag{4.112}$$

where $\hat{\boldsymbol{\psi}}_{\mathrm{r}}^{\mathrm{dq}}[k+1] \approx \hat{\boldsymbol{\psi}}_{\mathrm{r}}^{\mathrm{dq}}[k] = \hat{\boldsymbol{\psi}}_{\mathrm{r,op}}^{\mathrm{dq}}$ was used. For the linearized system to be stable, the eigenvalues of its system matrix must be located within the unit circle of the complex plane. Defining intervals for $L_{\mathrm{p},\hat{\omega}}$ and $L_{\mathrm{i},\hat{\omega}}$, the eigenvalues can be evaluated using MATLAB®. However, as the linearized system matrix depends on the operating point $\omega_{\mathrm{r,op}}$ and $\omega_{\mathrm{k,op}}$—the flux linkage $\hat{\boldsymbol{\psi}}_{\mathrm{r,op}}^{\mathrm{dq}} = (\hat{\psi}_{\mathrm{r,nom}}, 0)^{\top}$ is assumed to be constant as taken care of by the flux controller—the eigenvalues need to be evaluated for various operating points. Aim is to achieve stable conditions for as many operating points as possible. Therefore, each combination of speed adaption gains is evaluated for a pre-defined set of operating points $\omega_{\mathrm{r,op}}$ and $\omega_{\mathrm{k,op}}$. The total count of stable conditions for each pair of gains $L_{\mathrm{p},\hat{\omega}}$ and $L_{\mathrm{i},\hat{\omega}}$ is stored in a table. The resulting heat map for the given system, normalized with respect to the total count of operating points, is depicted in Fig. 4.21a. A reasonable choice of gains is the geometric center of the surface with the highest count number. Although very large integral gains are feasible in theory, experimental and simulative results show that noise amplification leads to unstable behavior. Therefore gains are selected as $L_{\mathrm{i},\hat{\omega}} = 1500$ and $L_{\mathrm{p},\hat{\omega}} = 0$, thus yielding a purely integral speed-adaption law.

In Fig. 4.21b, a Nyquist curve of the eigenvalues λ_i, $i \in \{1, \ldots, 9\}$ of the linearized system matrix is plotted for increasing $L_{\mathrm{i},\hat{\omega}} \in [0, 70000]$ ($L_{\mathrm{p},\hat{\omega}} = 0$) and operating point $\omega_{\mathrm{r,op}} = 0.5\,\omega_{\mathrm{r,nom}}$, $\omega_{\mathrm{k,op}} = 0.5\,\omega_{\mathrm{k,nom}}$ and $\hat{\boldsymbol{\psi}}_{\mathrm{r,op}}^{\mathrm{dq}} = (\hat{\psi}_{\mathrm{r,nom}}, 0)^{\top}$. The trajectories of the eigenvalues start at marking 'x' ($L_{\mathrm{i},\hat{\omega}} = 0$) and terminate at marking 'o' ($L_{\mathrm{i},\hat{\omega}} = 70000$). It can be seen that all eigenvalues, except $\lambda_{5/6}$ (corresponding to the stator currents estimation error $\boldsymbol{e}_{i_{\mathrm{s}}}$), remain within the unit circle for all values of $L_{\mathrm{i},\hat{\omega}}$. Hence, only the stator current estimate can become instable for too large values of $L_{\mathrm{i},\hat{\omega}}$, which implies a consecutive (slow) tuning of the speed adaption.

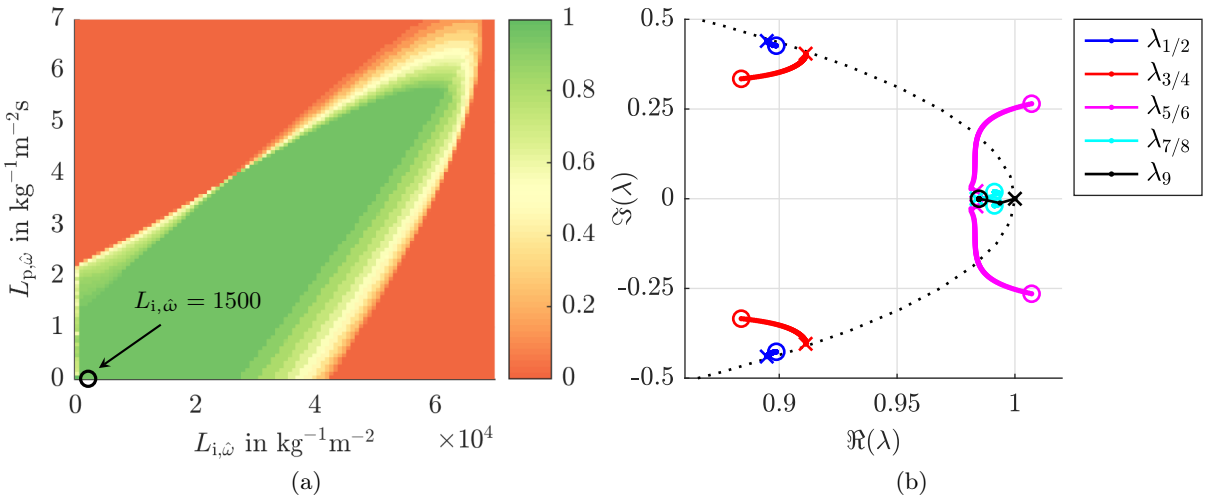

Figure 4.21: *Observer gain selection: (a) Heat map (normalized) of the total count of feasible operating points $\omega_{\mathrm{r,op}}$ and $\omega_{\mathrm{k,op}}$ for which the linearized system is stable; (b) Nyquist plot for eigenvalues λ_i of the linearized system matrix for increasing values of $L_{\mathrm{i},\hat{\omega}} \in [0, 70000]$ ($L_{\mathrm{p},\hat{\omega}} = 0$) and evaluated at operating point $\omega_{\mathrm{r,op}} = 0.5\,\omega_{\mathrm{r,nom}}$ and $\omega_{\mathrm{k,op}} = 0.5\,\omega_{\mathrm{k,nom}}$ ('o': $L_{\mathrm{i},\hat{\omega}} = 0$, 'x': $L_{\mathrm{i},\hat{\omega}} = 70000$).*

4.3.4 Extensions

The basic structure of the observer has been derived in the previous sections. In order to improve the observer performance and stability, in particular at low speeds, several modifications are proposed.

4.3.4.1 Doubling the observer sampling rate

So far, it has been assumed that the observer sampling frequency is equal to the PWM frequency, and, thus, equal to the controller sampling frequency. However, as the SVM modulated inverter output typically comprises *two* zero vectors, the observer sampling frequency can be doubled as the filter current measurement can be performed twice per period. Doubling the sampling frequency (half the sampling time) effectively reduces the discretization error ϵ_{N_δ} [recall (4.72)], as the residual matrix $\tilde{\boldsymbol{S}}_{N_\delta}$ [see (4.14)] becomes smaller: The factor $(\frac{1}{2}T_\mathrm{S})^i$ in the infinite sum tends faster to zero than T_S^i.

Although, theoretically, the observer sampling can be made arbitrary fast, it is not recommended to measure the filter currents at any other instants than the beginning or center of the switching period; the current sampling might occur during or shortly after an active switch of the output voltages, leading to oscillations and distorted measurements.

In the following, let $k_\mathrm{c}T_\mathrm{S}$ and $k_\mathrm{o}\frac{1}{2}T_\mathrm{S}$ denote the controller and observer sampling instants, respectively. The following modifications are necessary if the observer sampling rate is doubled:

1. **ZOH input calculation:** The ZOH input required for the observer is calculated by

$$\boldsymbol{u}_{\mathrm{f,zoh}}^{\mathrm{dq}}[k_\mathrm{o}] = \boldsymbol{T}_\mathrm{p}^{-1}(\phi_\mathrm{k}[k_\mathrm{o}])\boldsymbol{u}_{\mathrm{f,zoh}}^{\alpha\beta}[k_\mathrm{o}]. \tag{4.113}$$

   The input $\boldsymbol{u}_{\mathrm{f,zoh}}^{\alpha\beta}[k_\mathrm{o}]$ can be reconstructed from $\boldsymbol{u}_\mathrm{f}^{\alpha\beta\star}[k_\mathrm{c}]$ similar to the derivations in Sec. 4.1.1, given the control delay T_δ and the offset of the observer sampling with respect to the controller sampling (zero or $0.5T_\mathrm{S}$). Note that the reference voltage $\boldsymbol{u}_\mathrm{f}^{\alpha\beta\star}[k_\mathrm{c}]$ is changed every second observer step only, i.e. when the controller routine is executed at time instants $k_\mathrm{c}T_\mathrm{S} = 0.5k_\mathrm{o}T_\mathrm{S}$.

2. **Angle and frequency calculation:** The electrical angle $\phi_\mathrm{k}[k_\mathrm{o}]$ and frequency $\omega_\mathrm{k}[k_\mathrm{o}]$ need to be recalculated at every instant k_o, i.e. (4.84) becomes

$$\phi_\mathrm{k}[k_\mathrm{o}+1] = \phi_\mathrm{k}[k_\mathrm{o}] + \tfrac{1}{2}T_\mathrm{S}\omega_\mathrm{k}[k_\mathrm{o}]. \tag{4.114}$$

3. **Observer discretization:** The discrete-time observer system description is altered, as the discretization matrix becomes

$$\boldsymbol{S}_{N_{\delta,\mathrm{o}}}[k_\mathrm{o}] = \sum_{i=1}^{N_\delta} \frac{(\frac{1}{2}T_\mathrm{S})^i}{i!}\boldsymbol{A}_\mathrm{x}^{i-1}(\omega_\mathrm{r}[k_\mathrm{o}], \omega_\mathrm{k}[k_\mathrm{o}]). \tag{4.115}$$

Note that the controller uses the most recent state estimate only, i.e. the state estimate calculated at time instant $k_\mathrm{c}T_\mathrm{S} = k_\mathrm{o}\frac{1}{2}T_\mathrm{S}$.

4.3.4.2 Observer and controller gain LUT generation

As the system matrix $\boldsymbol{A}_\mathrm{x}(\omega_\mathrm{r}, \omega_\mathrm{k})$ depends on the electrical frequency ω_k and the mechanical speed ω_r, gain scheduling has been proposed in Secs. 4.2.1.3 and 4.3.2.2, i.e. the controller gain matrix

$\boldsymbol{\mathcal{K}}_{\mathrm{vxi}}$ and the observer gain matrix $\boldsymbol{\mathcal{L}}_{\mathrm{x}}$ are calculated for different values of ω_{r} and ω_{k} and the resulting gain elements are stored in look-up tables. However, although ω_{k} is a free variable that may be chosen arbitrarily, rotor flux orientation typically results in an electrical frequency in the vicinity of ω_{r}; given a constant stator current magnitude and steady-state conditions, the speed difference $\Delta\omega := \omega_{\mathrm{k}} - \omega_{\mathrm{r}}$ is proportional to the machine torque m_{m}, which is a bounded quantity. Therefore, instead of calculating the gain matrices over a grid of ω_{k} and ω_{r}, a higher resolution in the feasible operating range is obtained by selecting the speed difference $\Delta\omega$ and the mechanical speed ω_{r} as base values, i.e. calculating $\boldsymbol{\mathcal{K}}_{\mathrm{vxi}}(\Delta\omega, \omega_{\mathrm{r}})$ and $\boldsymbol{\mathcal{L}}_{\mathrm{x}}(\Delta\omega, \omega_{\mathrm{r}})$, respectively. Selecting appropriate boundaries for $\Delta\omega \in [\Delta\omega_{\min}, \Delta\omega_{\max}]$ and $\omega_{\mathrm{r}} \in [\omega_{\mathrm{r,min}}, \omega_{\mathrm{r,max}}]$, with lower boundaries $\Delta\omega_{\min}$ and $\omega_{\mathrm{r,min}}$ and upper boundaries $\Delta\omega_{\max}$ and $\omega_{\mathrm{r,max}}$, the look-up tables can be calculated.

4.3.4.3 Reducing the calculation effort by exploiting symmetry of the gain matrices

The equivalent two-phase electrical system description used throughout this thesis is based on a fundamental 2-by-2 block matrix structure, which stems from the close relation of the (vectorial) space-vector notation to the complex number description (see [95, Sec. 4.4] and App. A.2). As a result, each block matrix $\boldsymbol{A} \in \mathbb{R}^{2\times 2}$ may be written as $\boldsymbol{A} = \bar{a}\boldsymbol{I}_2 + \tilde{a}\boldsymbol{J}$, where $\bar{a} \in \mathbb{R}$ and $\tilde{a} \in \mathbb{R}$ are the block matrix equivalent 'real' and 'imaginary' parts, respectively. Apparently, the number of elements reduces from four to two. Transferring this property to the gain matrices $\boldsymbol{\mathcal{K}}_{\mathrm{vxi}} \in \mathbb{R}^{2\times 12}$ and $\boldsymbol{\mathcal{L}}_{\mathrm{x}} \in \mathbb{R}^{8\times 2}$, it can be concluded that, instead of storing $24 + 16 = 40$ elements in LUTs, it is sufficient to store $12 + 8 = 20$ elements only.

4.3.4.4 Variable main inductance

It was shown in Ch. 3 that the flux linkages are nonlinear functions of the respective magnetizing currents, due to the effect of magnetic saturation. Hence, the assumption of linear inductances is only valid for low levels of excitation. Figure 4.22a shows a qualitative plot of the magnetizing flux linkage $\psi_{\mathrm{m}}^{\mathrm{d}}$ and its linear approximation $\bar{\psi}_{\mathrm{m}}^{\mathrm{d}}$, both being functions of the magnetizing current $i_{\mathrm{m}}^{\mathrm{d}}$. The corresponding *secant* inductances L_{m} and $\bar{L}_{\mathrm{m}}$ are shown in Fig. 4.22b. Clearly, the parameter L_{m} varies with the excitation instead of being constant, which was assumed in the controller and observer derivation. This property becomes particularly relevant in the speed-sensorless case, since avoiding observer errors caused by parametric uncertainties (i.e. inductances) improves the speed-estimation accuracy and robustness. If the magnetic saturation curve is known (e.g. by means of machine identification as proposed in Ch. 3), a simple yet effective way of considering magnetic saturation is to adapt online the main inductance L_{m} subject to the estimated stator d-current $\hat{i}_{\mathrm{s}}^{\mathrm{d}}$ in the observer equations (as proposed e.g. in [88]). However, a drawback of this method is that the system gains are calculated assuming a possibly different magnetizing inductance and, hence, the system may become instable if the tuning is too aggressive.

4.3.4.5 Inverter nonlinearity correction

Another important aspect is the correct reconstruction of the VSI output voltage, which constitutes the primary input of the observer. At low speeds and, consequently, at low voltage levels, absolute errors in the voltage reconstruction become more apparent, corrupting the state and speed estimation alike. So far, it has been assumed that the inverter output voltage $\boldsymbol{u}_{\mathrm{v}}^{\mathrm{abc}}$—on average per PWM cycle–follows its sampled reference $\boldsymbol{u}_{\mathrm{v}}^{\mathrm{abc}\star}$ (see Ass. 19.4). However, an ideal inverter model was used in this assumption. In practical applications, nonlinear effects disturb the voltage reconstruction.

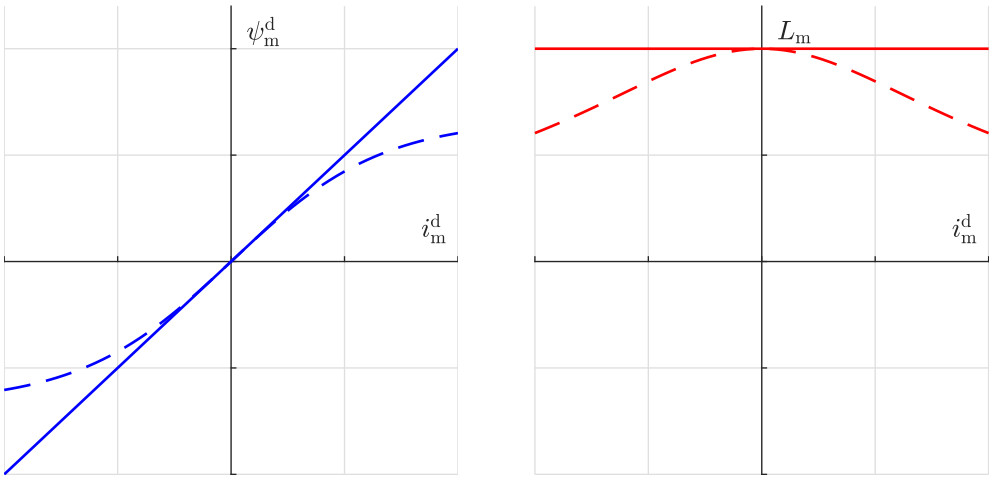

Figure 4.22: *The effect of magnetic saturation: (a) Qualitative flux linkage curves of the flux linkage* $\psi_\mathrm{m}^\mathrm{d}(i_\mathrm{m}^\mathrm{d})$ *[- - -] and its approximation* $\bar{\psi}_\mathrm{m}^\mathrm{d}(i_\mathrm{m}^\mathrm{d})$ *[——] and (b) the corresponding secant inductances* $L_\mathrm{m}(i_\mathrm{m}^\mathrm{d})$ *[- - -] and* $\bar{L}_\mathrm{m}(i_\mathrm{m}^\mathrm{d})$ *[——], being functions of the magnetizing current* i_m^d.

These nonlinear effects are well-documented e.g. in [137–141] and comprise

(i) a voltage drop in the power devices of the inverter (caused by the differential resistance and the forward voltage drop of the semiconductors[3]), and

(ii) the inverter dead-time effect[4].

While the differential resistance is typically accounted for by modifying the resistance term of the connected load (filter or stator), the threshold voltage and dead-time voltage drop need to be compensated differently. A compensation method for sensorless drives is proposed in [88, 142]: The duty cycle d^k of phase $k \in \{a, b, c\}$, which is fed to the PWM module of the real-time system is modified according to

$$d^k = d^{k\star} + \overbrace{\frac{2d_\delta}{\pi} \arctan\left(\frac{i_\mathrm{v}^k}{i_\delta}\right)}^{=:\Delta d}, \tag{4.116}$$

where $d^{k\star}$ is the reference duty cycle produced by the SVM, Δd is the duty cycle offset, i_v^k is the measured phase current (equal to the filter input current) and d_δ and i_δ are parameters, which need to be identified for the given setup. Fig. 4.23a shows the duty cycle offset for different values of i_v^k, while Fig. 4.23b illustrates the difference between the reference and the actual switching pattern for a single phase.

4.3.4.6 Stator resistance adaption (low speed)

At low speeds, the speed adaptive observer is very sensitive to parameter errors, in particular deviations in the stator resistance [85]. Besides, the stability issue of the speed-adaptive observer can

[3]The differential resistance describes the on-state slope resistance of the active switches and freewheeling diodes, whereas the forward voltage drop is the threshold voltage of the respective semiconducting devices [141].

[4]The dead-time effect describes the voltage distortion caused by the additional time, at which both switches of the inverter same leg are required to be in off-state in order to avoid *shoot-through* [108, Sec. 2.5].

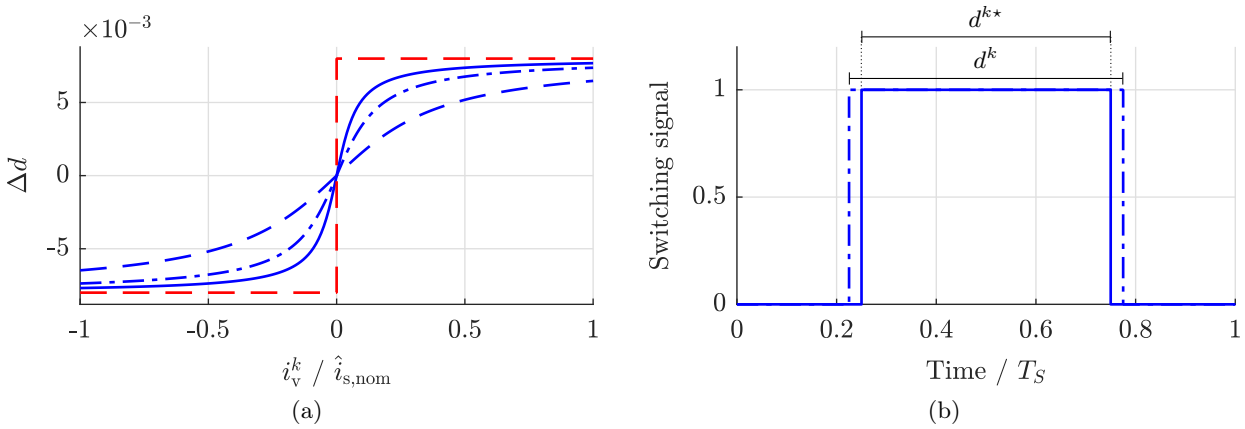

Figure 4.23: *Inverter nonlinearity correction: (a) Offset duty cycle Δd for $i_{\mathrm{v}}^k = 0.05\,\hat{i}_{\mathrm{s,nom}}$ [—], $i_{\mathrm{v}}^k = 0.1\,\hat{i}_{\mathrm{s,nom}}$ [- - -] and $i_{\mathrm{v}}^k = 0.25\,\hat{i}_{\mathrm{s,nom}}$ [-·-] as approximations of the* sign *function [- - -]; (b) Exemplary switching patterns for the reference duty cycle $d^{k\star}$ [—] and the actual duty cycle d^k [-·-].*

be remedied to some degree by simultaneous adaption of the stator resistance and the rotor speed. Therefore, a simple stator resistance adaption mechanism is proposed, replacing the the stator resistance R_{s} by its estimated value $\hat{R}_{\mathrm{s}}$. A detailed derivation is omitted, though, as the resistance adaption is considered an optional extension only, which is used as a low-speed stabilization measure, too, e.g. in [85, 87, 88, 92, 143].

As the q-component of the filter current estimation error is used for the speed adaption, the respective d-component may be used for the resistance adaption (as proposed e.g. in [88]), yielding the purely integral resistance adaption mechanism

$$\hat{\mathfrak{S}}_{\mathrm{i},\hat{\mathrm{R}}}: \quad \hat{R}_{\mathrm{s}}[k+1] = \hat{R}_{\mathrm{s}}[k] + L_{\mathrm{i},\hat{\mathrm{R}}} T_{\mathrm{S}} \tau_{\hat{\mathrm{R}}}[k], \tag{4.117}$$

with integral gain $L_{\mathrm{i},\hat{\mathrm{R}}} \in \mathbb{R}$ and input

$$\tau_{\hat{\mathrm{R}}}[k] := \operatorname{sign}(\omega_{\mathrm{k}}[k]) \boldsymbol{e}_{i_{\mathrm{f}}}[k]^{\top} \hat{\boldsymbol{\psi}}_{\mathrm{r}}^{\mathrm{dq}}[k]. \tag{4.118}$$

The output of the resistance adaption is limited by minimum and maximum values $R_{\mathrm{s,min}} \in \mathbb{R}$ and $R_{\mathrm{s,max}} \in \mathbb{R}$, respectively. Moreover, as the stator resistance adaption is known to produce stability issues at high electrical frequencies ω_{k} [87], the resistance adaption is enabled for low frequencies only, i.e. below a defined limit $|\omega_{\mathrm{k}}| < \omega_{\mathrm{k},\hat{\mathrm{R}}} \in \mathbb{R}$. This limitation also justifies the proposed adaption mechanism using the *filter* current estimation error instead of the *stator* current estimation error (as used for the IM-only case), since for low frequencies the filter current is almost identical to the stator current.

4.4 Implementation and results

Simulations and experiments have been conducted for two different scenarios:

(S_1) Speed control system with speed sensor and standard observer as derived in Sec. 4.3.2.

(S_2) Speed-sensorless case with speed-adaptive observer as presented in Sec. 4.3.3.

The closed-loop speed control system for both scenarios has been implemented in MATLAB®/ Simulink® and validated in simulations and experiments, respectively; an overview of the overall speed-sensorless implemented system with all its components (extensions are not illustrated, but have been considered, too) is shown in Fig. 4.24. For the experimental validation, the testbench used in Ch. 3 has been extended by a custom-built LC filter and a measurement board (see App. B.2), the latter being used to measure the stator currents and voltages, respectively.

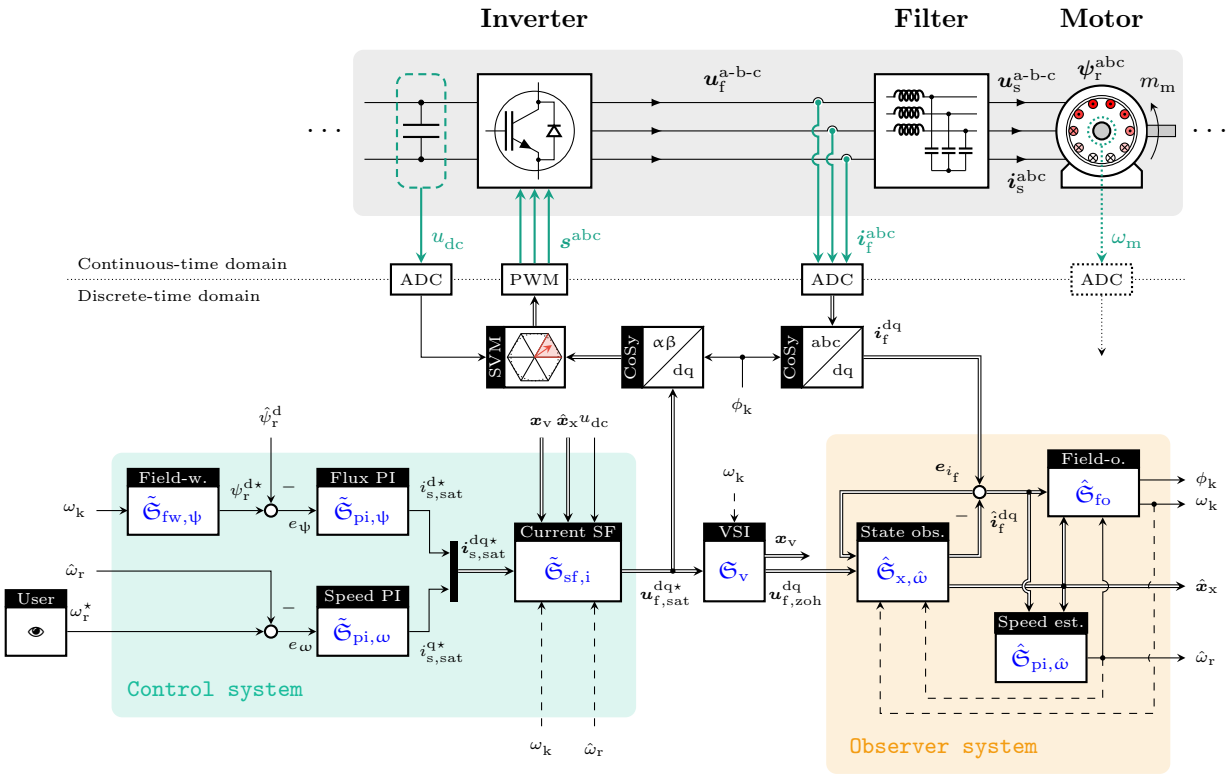

Figure 4.24: *Block diagram of the overall implemented speed-sensorless control system (without extensions).*

In order to evaluate the performance of the combined controller and observer system, both scenarios comprise four different operation regions:

- **REG. I – Speed reversal:** In the first region, a speed reversal is performed under full load in order to evaluate the low speed performance of the system. As was shown in Sec. 4.3.1, observability is lost for DC excitation (i.e. $\omega_\mathrm{k} = 0$), which occurs twice during the test. While the observer with speed sensor is comparably robust, the speed-adaptive observer is typically judged in terms of its zero-crossing capabilities.

- **REG. II – Stand-still:** The second region covers a stand-still test under varying load. After a short period of full load, the load is ramped down slowly to zero. Likewise, this test is conducted in order to evaluate the low-speed capabilities of the system, proving that stand-still operation at varying load is possible.

- **REG. III – Field-weakening:** In the third region, the high-speed capabilities of the control system are tested, by performing a no-load acceleration from zero to one-point-five times rated speed. After a brief period of high-speed operation, the speed is reset to stand-still by means of active braking (generating mode). For a constant magnetic field, the induced voltage

increases almost linearly with the speed, such that for rated excitation the voltage limit is reached for rated speed and load. Therefore, the magnetic field (rotor flux linkage) needs to be decreased in order to reach higher speeds than rated speed.

- **REG. IV – Load variations:** In the fourth region step-wise load variations are performed, while the speed is kept constant at its rated value. Apart from operating near the voltage limit and potentially triggering the anti-windup mechanism, the full controller bandwidth is evaluated during high speed operation.

The test run comprises the four described operation regions, as well as the transitions between the different regions. The parameters of the controller and observer systems are stated in Tab. 4.1 (where 'a.u.' means 'arbitrary unit'). Where necessary, the time series data has been digitally low-pass filtered in order to improve the readability of the results.

Table 4.1: *System parameters of the implemented control system.*

	Parameter	Variable	Value	Unit
Controller	Sampling time	T_S	$250 \cdot 10^{-6}$	s
	Sampling delay	$T_\delta\,(=0.5T_\mathrm{S})$	$125 \cdot 10^{-6}$	s
	LQR tuning factors	α_K, β_K	$0.5,\ 1 \cdot 10^4$	
	Proportional gain	γ_K	0.3	
	Discretization order	$N_{\delta,\mathrm{c}}$	3	
	Current control approximation	$T^*_{\mathrm{i,cl}}$	0.01	s
	Speed controller gains	$K_{\mathrm{p},\omega}, K_{\mathrm{i},\omega}$	0.3, 7.4	a.u.
	Flux controller gains	$K_{\mathrm{p},\psi}, K_{\mathrm{i},\psi}$	26.7, 670	a.u.
	Stator current limits	$i^\mathrm{d}_{\mathrm{s,max}}, i^\mathrm{q}_{\mathrm{s,max}}$	$0.5\,\hat{i}_{\mathrm{s,nom}}, 1.25\,\hat{i}_{\mathrm{s,nom}}$	A, A
	Inverter output correction	d_δ, i_δ	$0.008, 0.31\,\hat{i}_{\mathrm{s,nom}}$	a.u., A
Observer	Sampling time (half)	$0.5\,T_\mathrm{S}$	$125 \cdot 10^{-6}$	s
	LQR tuning factors	α_L	$2 \cdot 10^{-8}$	
	Discretization order	$N_{\delta,\mathrm{o}}$	3	
	Speed adaption gains	$L_{\mathrm{p},\hat{\omega}}, L_{\mathrm{i},\hat{\omega}}$	0, 1 500	
	Resistance adaption gains	$L_{\mathrm{p},\hat{\mathrm{R}}}, L_{\mathrm{i},\hat{\mathrm{R}}}$	0, 20	
	LPF filter time constant	T_{ω_k}	$20 \cdot 10^{-3}$	s

4.4.1 Scenario (S_1): State-feedback control system with full-order observer (measured speed)

Scenario (S_1) is considered first, serving as a reference for Scenario (S_2). The experimental results for the control system are shown in Fig. 4.25, with the operating regions marked by vertical lines [- - -] and unshaded areas (intermediate areas are shaded [ ]). Measured or sampled values are plotted as solid blue lines [——], whereas reference values are drawn as dashed red lines [- - -]. In the first plot from the top, the trajectory of the mechanical speed ω_m (first plot) is shown, which runs on a smooth line following its set-point value $\omega^\star_\mathrm{m}$ in all four regions with good accuracy. Moreover, the electrical frequency ω_k [- · -] is plotted, which (visibly) deviates from the mechanical speed for higher loads only. The rise-time of the speed has a lower limit due to the torque limitation, which becomes visible during the acceleration test in REG. III. In the second plot, the corresponding (measured) machine torque m_m is shown. The torque output of the speed-controlled IM is equal to the overall load and acceleration torque. Hence, by applying a friction compensated load torque

m_l subject to the reference $m_\mathrm{l}^\star$ [- - -], the desired machine torque can be set with good accuracy. Minor deviations are observed during stand-still operation only. The third and fourth plots show the estimated stator currents $\hat{i}_\mathrm{s}^\mathrm{d}$ and $\hat{i}_\mathrm{s}^\mathrm{q}$ and their respective set points $i_\mathrm{s}^{\mathrm{d}\star}$ and $i_\mathrm{s}^{\mathrm{q}\star}$ as commanded by the superimposed flux and speed controllers. Again, all references are tracked properly. While the d-current varies within a band of about 0.2 p.u. only, the q-current—which is proportional to the machine torque—varies from 1.25 times negative to positive rated current, which constitutes the upper limit of the speed controller output. The estimated rotor flux linkage $\hat{\psi}_\mathrm{r}^\mathrm{d}$ is shown in the fifth plot; as imposed by the flux controller, it is almost constant in all regions, following its reference $\psi_\mathrm{r}^{\mathrm{d}\star}$ with good accuracy. In REG. III, the excitation needs to be reduced, in order to reach speed values beyond rated speed (field-weakening). The last plot shows the magnitude of the VSI voltage command $\boldsymbol{u}_\mathrm{f}^{\mathrm{dq}\star}$ and the respective voltage limit $u_\mathrm{dc}/\sqrt{3}$ [- - -], which depends on the measured DC-link voltage u_dc. As expected, the required voltage is close to its maximum value only for higher speeds. The field-weakening operation in REG. III proves to work properly as the voltage limit is not exceeded. Braking from 1.5 times rated speed to stand-still causes the DC-link voltage u_dc to rise temporarily, until the chopper resistors become active. For rated (motor) torque and rated speed in REG. IV, the voltage limit is (almost) reached.

The observer performance for Scenario (S_1) is evaluated using Figs. 4.26 and 4.27, showing the observer states and the corresponding state estimation errors, respectively. The d- and q-components corresponding to the respective filter current, stator voltage, stator current and rotor flux linkage signals are arranged from top to bottom, again, shown for all four regions (REG. I–IV). In Fig. 4.26, the *measured* states are plotted as solid red [—] (simulation results) and solid blue [—] (experimental results) lines, whereas the *estimated* states are plotted as dashed red [- - -] (simulation results) and dashed blue [- - -] (experimental results) lines. In Fig. 4.27, the corresponding state estimation errors $\boldsymbol{e}_\mathrm{x} = \boldsymbol{x}_\mathrm{x} - \hat{\boldsymbol{x}}_\mathrm{x}$ are plotted for the simulation data [—] and the experimental data [—], respectively. For both figures, the plotted signals have been low-pass filtered in order to improve the clarity of the results. Since the rotor flux linkage could not been measured in the experiment, the respective data is missing in the results.

A major objective of the observer is to estimate correctly the system states $\boldsymbol{x}_\mathrm{x}$. Thus, the state estimation error $\boldsymbol{e}_\mathrm{x}$ constitutes a good performance measure for the assessment of the observer. Comparing the estimated and measured states from the experimental results ([—] and [- - -] in Fig. 4.26, [—] in Fig. 4.27), it can be observed that for most parts a good match (error below 0.05 p.u.) between the two signals is achieved by the observer. For the filter d-current, a deviation is observed, particularly in REG. I, whereas for the q-component, the error is generally higher in the vicinity of $\omega_\mathrm{m} = 0\,\mathrm{rad\,s^{-1}}$. Inverter nonlinearities and parameter errors in the resistive components are a possible explanation for the deviations. Note that due to the different scalings of the vertical axes, the difference between estimated and measured q-currents is barely visible in Fig. 4.26. The estimation of the stator currents is similar in quality to that of the filter currents. As for the stator voltage, the error is small for lower speeds, but increases slightly in the d-component at higher speeds, i.e. in REG. III and IV. The rotor flux linkage estimation can only be judged by the simulation results. Apparently, zero speed and non-zero load conditions are problematic for the rotor d-flux linkage estimation, i.e. in REG. I and II.

Except for the d-current components, a good overall match between simulated and measured states is achieved (see Fig. 4.26). The difference in the d-currents can be explained by the simplified magnetic model that was used in the simulations.

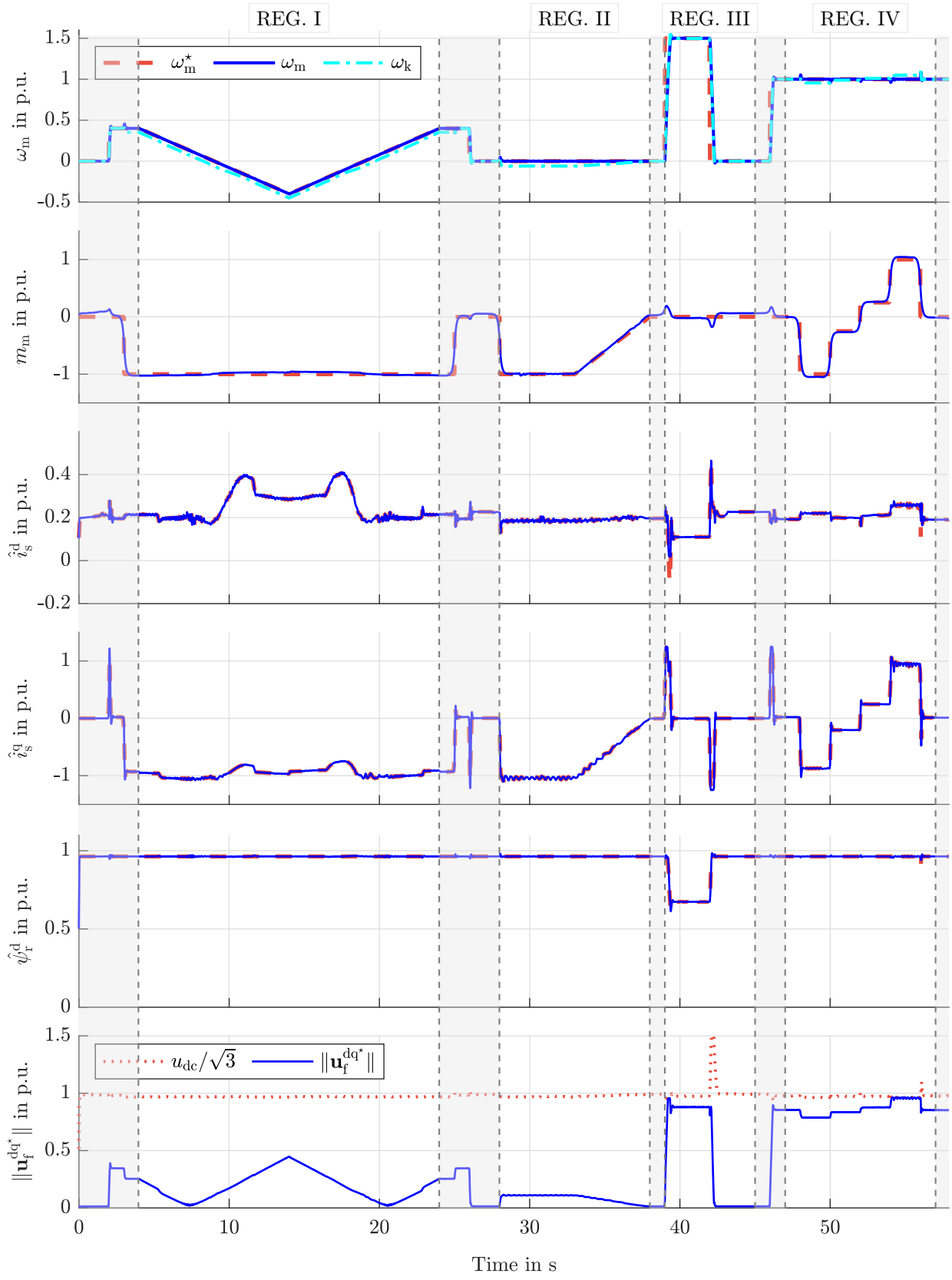

Figure 4.25: *Scenario (S_1): Experimental validation of the control system, with measured or estimated quantities [—] and respective reference values or limits [- - -].*

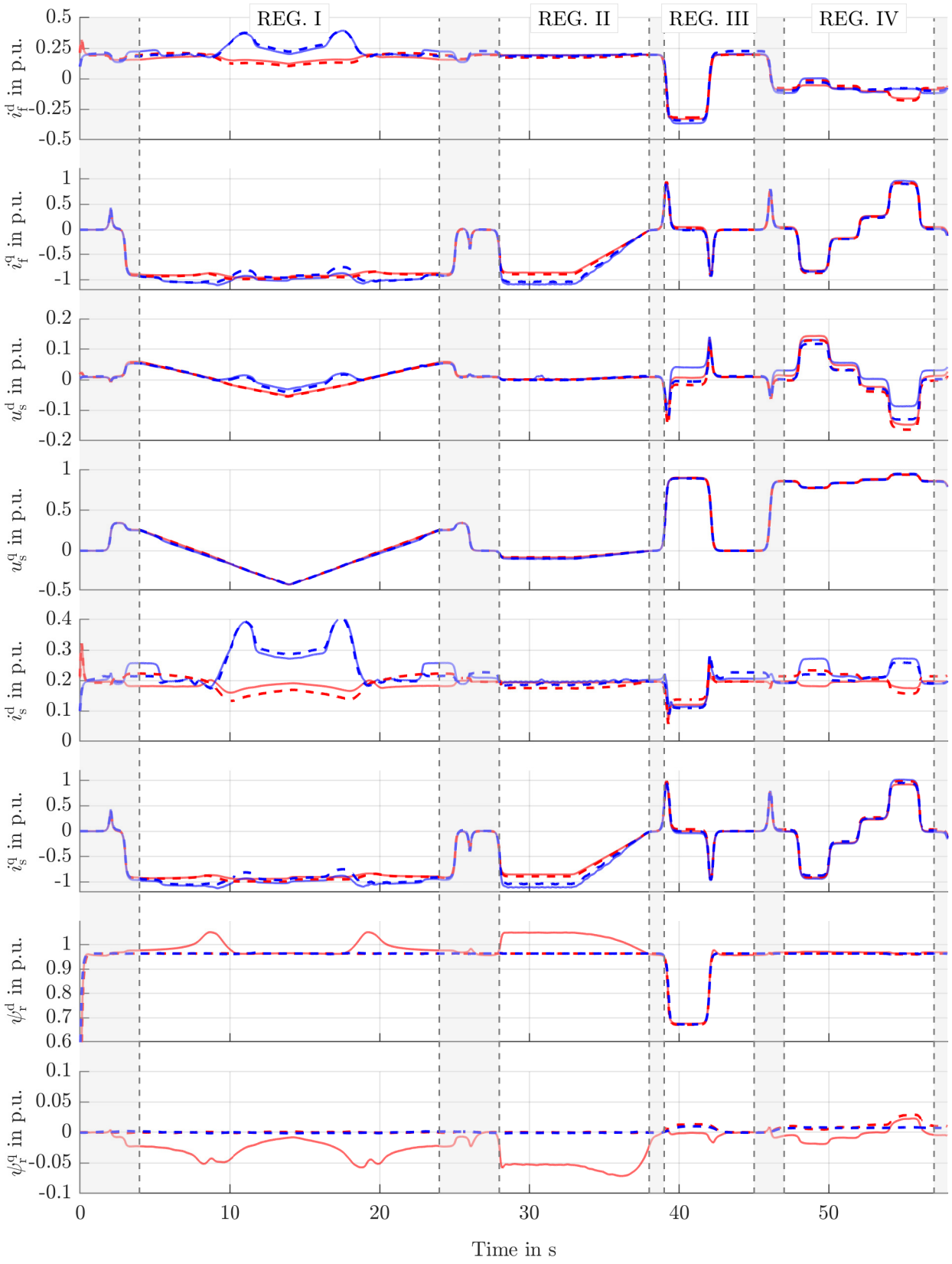

Figure 4.26: *Scenario* (S_1)*: Experimental and simulative validation of the observer system, part I (states). With measured [——] and estimated [- - -] experimental data and measured [——] and estimated [- - -] simulation data.*

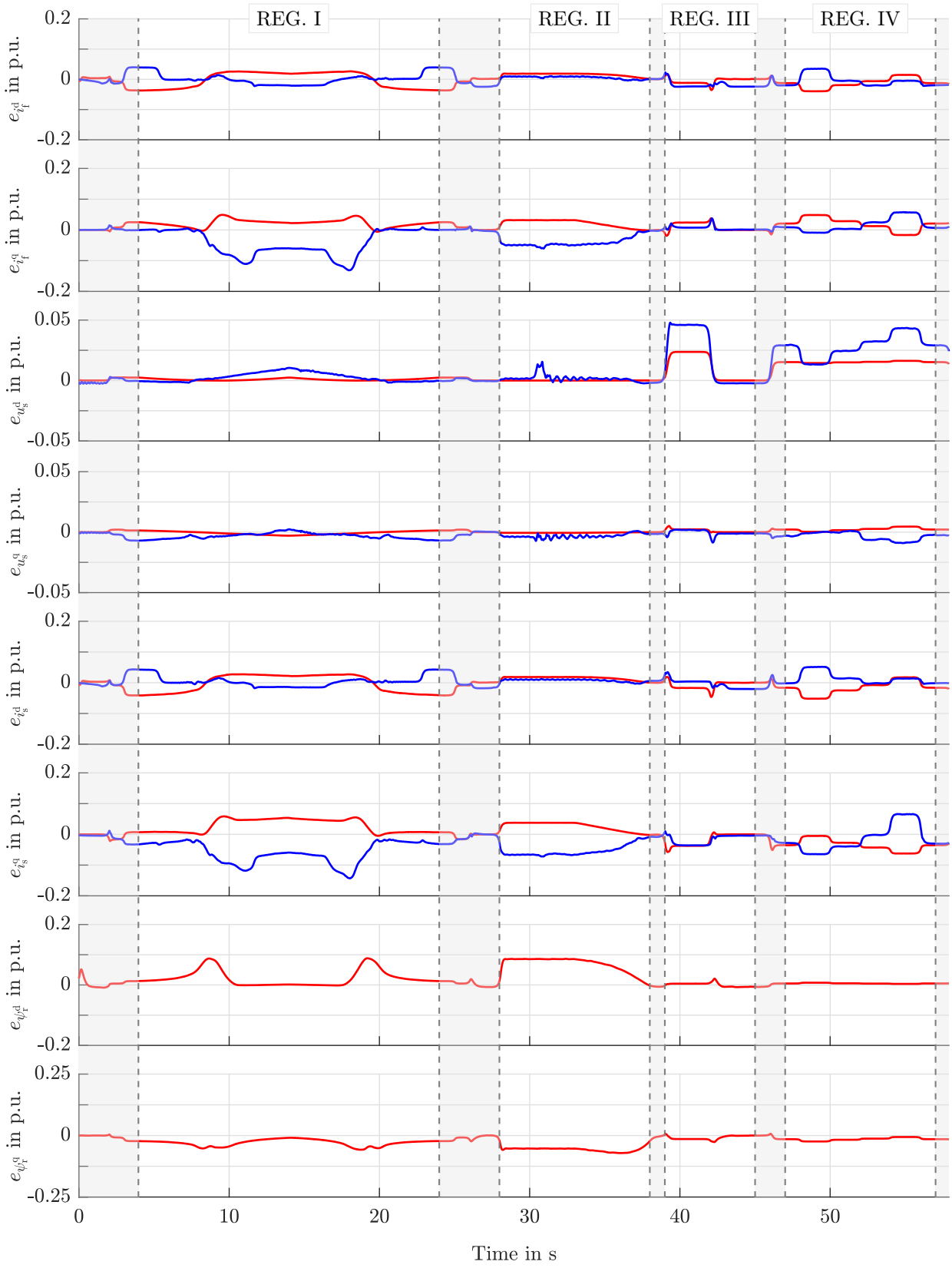

Figure 4.27: *Scenario (S_1): Experimental [—] and simulative [—] validation of the observer system, part II (state estimation error).*

4.4.2 Scenario (S_2): State-feedback control system speed-adaptive full-order observer (speed not measured)

The results for the speed-sensorless case, i.e. Scenario (S_2), are presented in the following.

Again, the control system is considered first. Its performance is evaluated using Fig. 4.28. The structure, line colors and line styles are the same as introduced in the previous section (and Fig. 4.25), with the only difference, that the estimated speed $\hat{\omega}_\mathrm{m} = n_\mathrm{p}\hat{\omega}_\mathrm{r}$ [—] is added in the first subplot. It can be seen that the speed is tracked properly by the speed controller, even though the estimated speed is used for feedback in the speed control loop. Moreover, the estimated speed matches the actual speed in all operation regions. The remaining subplots are almost identical with the plots of the Scenario (S_1) in Fig. 4.25, thus validating that the control system performs just as well in the sensorless.

The observer system for of Scenario (S_2) is, as before, evaluated separately using plots of the measured and estimated states (see Fig. 4.29) and the corresponding state estimation errors (see Fig. 4.30). In addition, the speed estimation error is shown in Fig. 4.31. Again, experimental [—] and simulation [—] results are presented in the plots. It can be seen in Fig. 4.29, that the experimental results match well with the simulation results; only for the stator d-current, during the low speed tests of REG. I and II, the measured (REG. I) and estimated (REG. II) values deviate. And, as in Scenario (S_1), the 'measured' value of the rotor flux linkage q-component drops in the simulated data (while its estimate remains constant) at $t \approx 26\,\mathrm{s}$ and $t \approx 42\,\mathrm{s}$, respectively. The reason for those dips is the applied DC excitation $\omega_\mathrm{k} = 0\,\mathrm{rad\,s^{-1}}$, which results from the no-load and stand-still operation at respective time instants.

Looking at the state estimation errors in Fig. 4.30, it is observed that the q-components of all states are estimated very well for both, simulations and experiments. In particular, the estimation error of the filter q-current (second plot from the top) is estimated almost perfectly, which is due to the speed estimation using the filter q-current estimation error as its input; as long as there exists a filter d-current estimation error, the speed is adapted, until the input of the adaption controller $\hat{\mathfrak{S}}_{\mathrm{pi},\hat{\omega}}$ eventually becomes zero. The downside of this effect is, that the parameter and discretization errors are 'pushed' into the d-components. Apparently, the d-component errors become larger for high loads (REG. I, II and III). Moreover, the stator d-voltage (third plot) exhibits larger errors for higher speeds, which is reasonable as errors in the linear magnetic model (even with L_m-adaption) will become more apparent at high speeds (the induced voltage increases with the speed). Furthermore, iron losses are neglected in the observer, which have a negative impact at higher speeds, too, and explain the difference between simulations and experiments.

Lastly, the speed estimation error e_{ω_r} is shown in Fig. 4.31. Except for very low-speed operation, the speed estimation error remains smaller than one percent. For comparison, if V/Hz control is used, the applied frequency ω_k and the (electrical) rotor speed ω_r typically differ about five percent at full load, proving the effectiveness of the closed-loop sensorless speed controller. Nevertheless, a rather big difference between simulation and experiment is observed, which is due to modeling and parameter errors in the simulation.

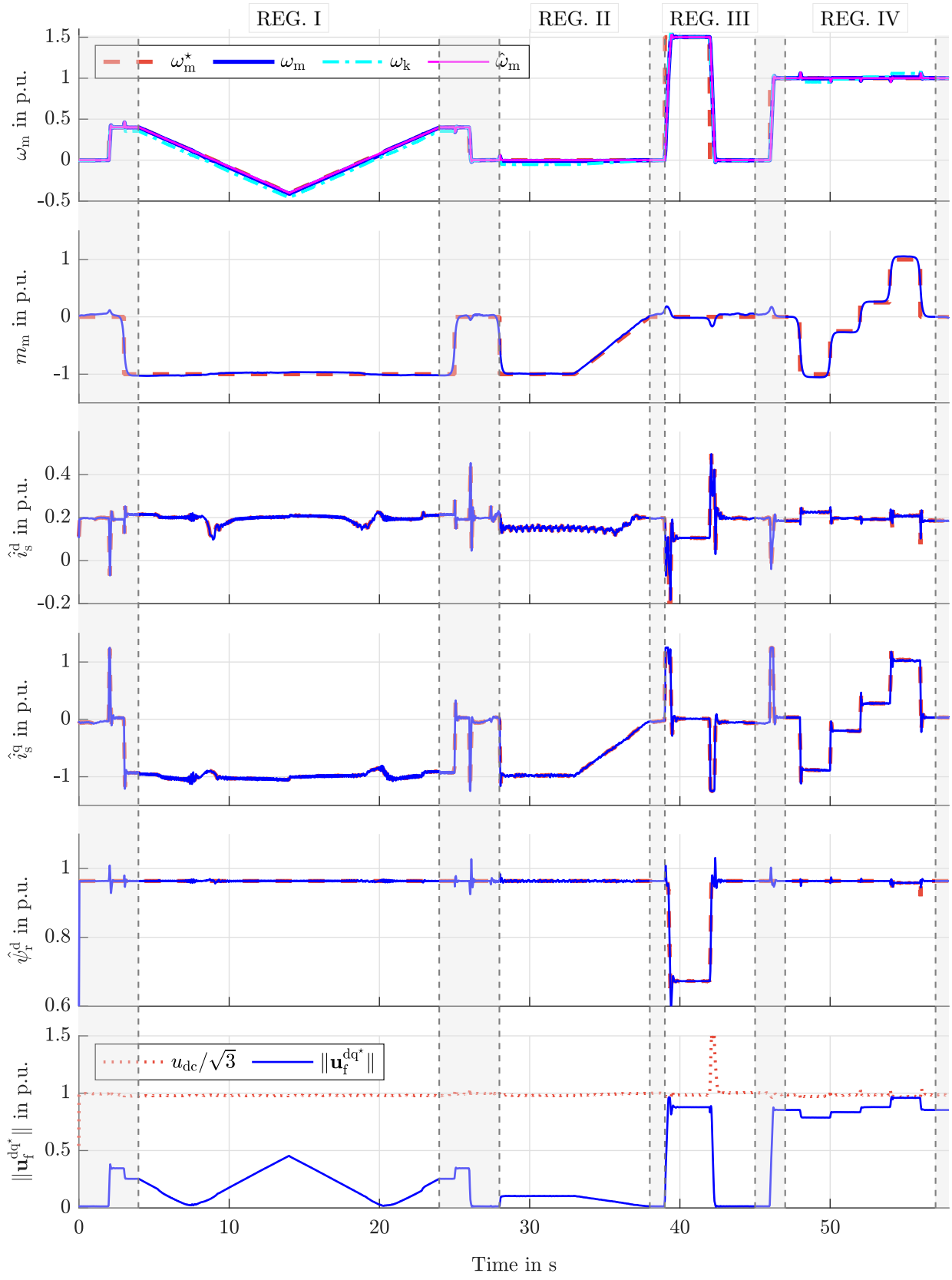

Figure 4.28: *Scenario (S_2): Experimental validation of the control system, with measured or estimated quantities [—] and respective reference values or limits [- - -].*

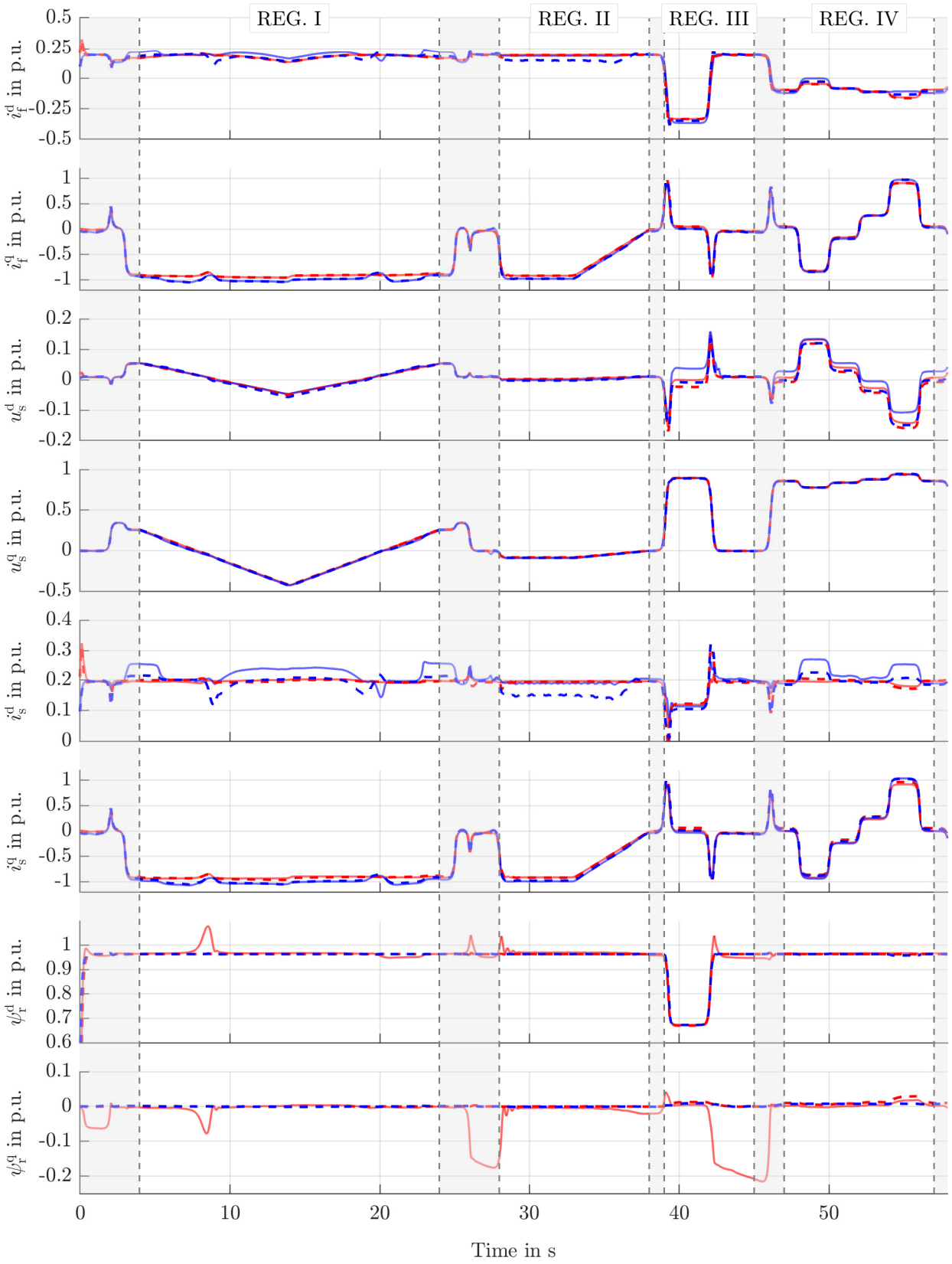

Figure 4.29: *Scenario (S_2): Experimental and simulative validation of the observer system, part I (states). With measured [——] and estimated [- - -] experimental data and measured [——] and estimated [- - -] simulation data.*

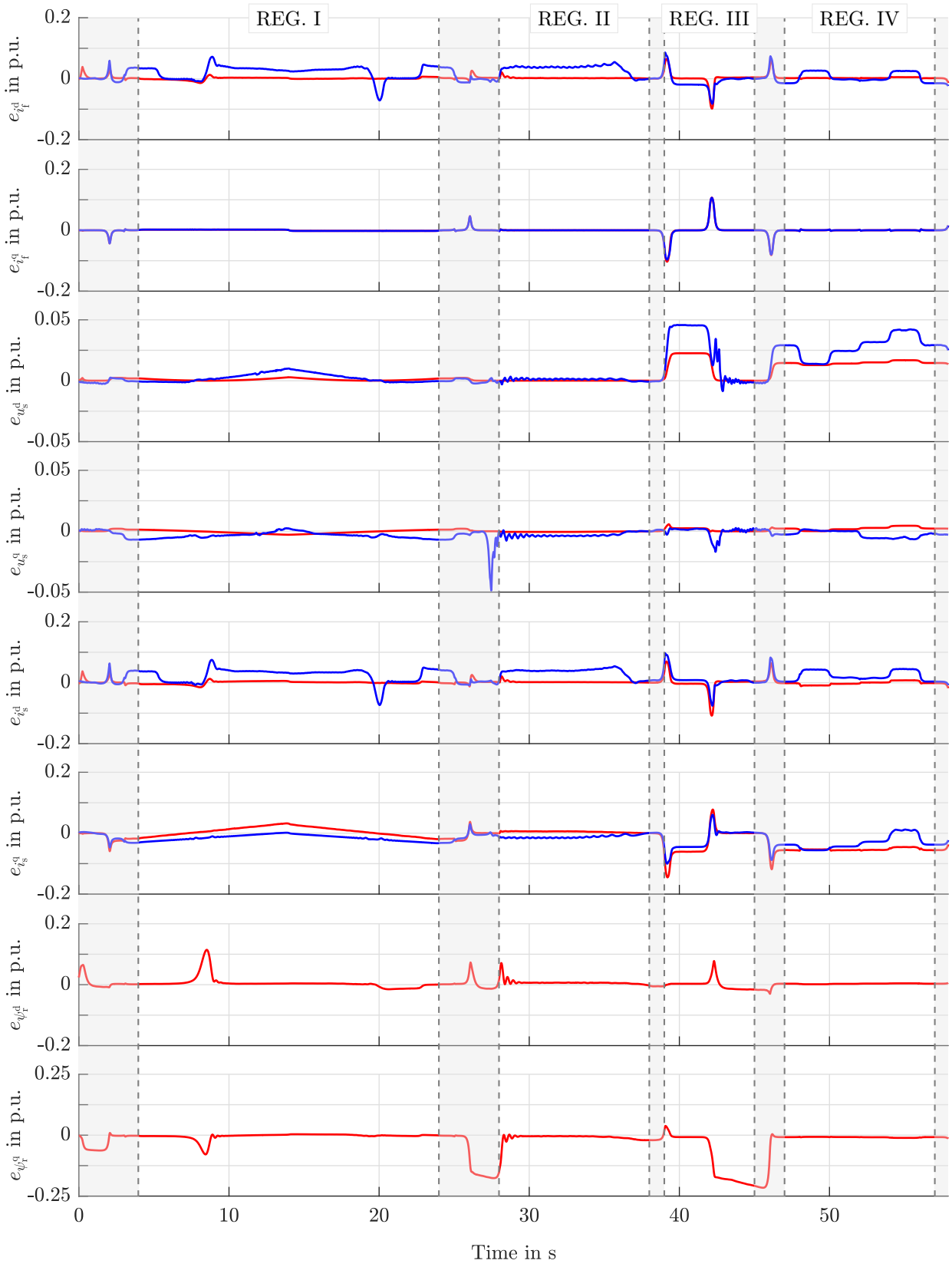

Figure 4.30: *Scenario (S_2): Experimental [—] and simulative [—] validation of the observer system, part IIa (state estimation error).*

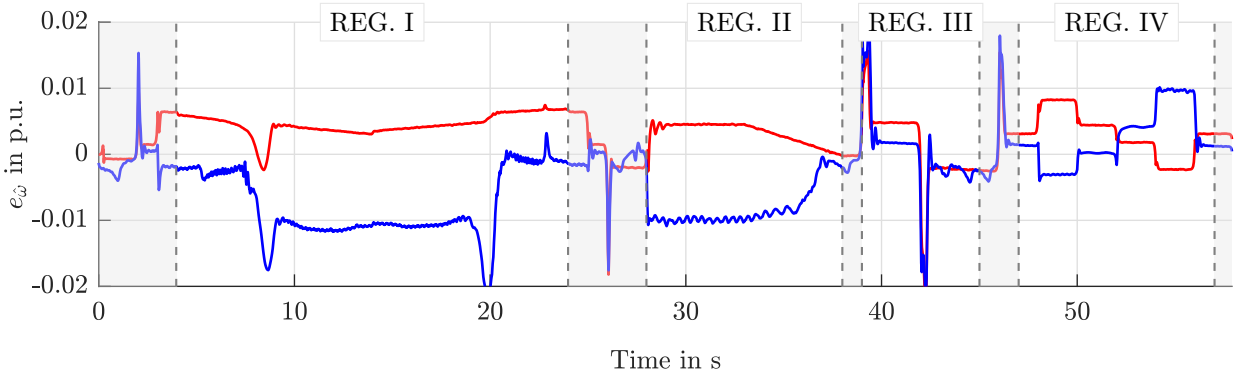

Figure 4.31: *Scenario (S_2): Experimental [—] and simulative [—] validation of the observer system, part III (speed estimation error).*

4.5 Summary

A closed-loop speed control system for the electric drive system of a geothermal ESP has been derived. In contrast to the methods described in literature, using cascaded PI controllers whose tuning is based on rules of thumb or trial-and-error, the proposed state-feedback current controller is tuned using the programmatic LQR approach, requiring a total of three tuning factors only. In addition a speed-adaptive observer has been proposed, which is tuned alike using the LQR approach; an analytic tuning rule guaranteeing complete stability has not been published yet for the combination of LC filter and IM—and probably does not exist at all. In order to account for the low switching frequencies in geothermal ESP systems, the controller and observer designs have been carried out in the discrete-time domain, considering also the time delay of the inverter. The presented approach has been validated experimentally and in simulations on a down-scaled drive system, showing very good overall performance, even in the critical operating regions like the low-speed regeneration mode (loss of observability), during stand-still or field-weakening operation (very high frequencies). It can be concluded, that the presented approach constitutes an alternative to the frequently used V/Hz control method, offering the benefits of a higher efficiency and reduced stress on the electrical and mechanical components.

Chapter 5

Conclusion

This thesis dealt with the modeling, simulation and enhanced control of a geothermal ESP and its electric drive unit. In the following, the main results are summarized and a brief outlook is given.

In Ch. 2, a modular nonlinear state-space model of a geothermal ESP and all relevant subcomponents was derived. In order to obtain a model in state-space form which is suitable for simulations in Simulink®(or similar software), simplifying assumptions had to be made. The benefits of using a multi-level inverter and the impact of the LC filter have been thoroughly analyzed. Moreover, the self-excitation effect occuring between the LC filter output capacitance and the stator inductance has been investigated. Furthermore, an electromechanical multi-rotor induction machine model in combination with a hydromechanical multi-stage pump model was derived. Its relation to the respective lumped parameters model was further elaborated. Finally, a start-up procedure of a geothermal ESP system was simulated in Simulink®. The required set of realistic model parameters was carefully balanced based on available literature, data sheets and in consultation with local operators. The simulation results were analyzed in terms of feasibility and the following observations were made:

- Simulation results validated that the model produced reasonable outputs, i.e. a realistic behavior of the pump system and its subcomponents could be replicated.
- The effect of self-excitation could be observed in the outputs, revealing that the motor currents may differ significantly from the inverter output currents. This might be a problem, if only the inverter output currents are measured.
- The impact of the cable on the voltage and current dynamics was limited to a mere resistive drop, since the LC filter removed critical frequencies.
- For the given set of parameters, the torsional effects in the multi-rotor/multi-stage pump model were almost negligible, such that the lumped parameters model yielded similar results. However, the elastic shaft model could be beneficial for vibration analysis, nonetheless.

In Ch. 3, it was investigated to what extent the efficiency of the ESP motor (induction machine) could be increased with respect to the standard V/Hz control method typically used in geothermal applications. For this purpose, an experimental machine identification procedure was proposed, which allowed for the derivation of essential machine maps, such as flux linkage, torque or efficiency maps. The maps were recorded for different speeds and over a grid of stator currents, expressed in an arbitrarily rotating, yet unique and reproducible reference frame. Assuming good knowledge of the inverter output voltage, only the temperature variation in the resistive components proved

critical, as the orientation may slightly vary for different temperatures. As an extension to an existing temperature compensation method for synchronous machines, an improved compensation scheme for induction machines was proposed. Based on the machine maps, trajectories for different torque control strategies were derived and compared against the benchmark method of maximum efficiency torque control. The main findings are summarized as follows:

- It was shown that maximum efficiency operation can be achieved, even without the use of expensive equipment such as a torque sensor.
- Compared to the standard V/Hz method, efficiency improvements of several percent can be achieved in part-load operation and at low speeds.

Maximizing the efficiency increases the pump lifetime and reduces cost as power can be saved. However, in order to be able to implement the proposed method, a field-oriented control (FOC)-based control system needs to implemented.

For this reason, in Ch. 4, a speed-sensorless FOC-based control scheme for the electric drive system of induction machine and LC filter was derived. Due to the low switching frequency in MV drives, the derivation was conducted in the discrete-time domain. The inverter delay was accounted for and PI set-point tracking was implemented. The tuning of the state-feedback current controller was achieved by using the linear quadratic regulator (LQR) method, which is deterministic and requires three tuning parameters only (instead of six, as required for cascaded PI controllers). Varying speeds and loads were accounted for by adopting gain-scheduling for the feedback gains. The outer-loop speed and flux controllers were tuned using the Symmetric Optimum criterion, which was based on an approximation of the inner control loop dynamics. As no additional hardware was supposed to be used, a full-order observer was employed in order to reconstruct the non-measurable system states. Similar to the state-feedback controller design, the observer was tuned using the LQR method with a single tuning factor only. Likewise, gain-scheduling was incorporated. Moreover, since the speed cannot be measured either in geothermal ESP systems (in real-time), a speed estimation scheme was implemented. Practical extensions for the implementation were further provided. Finally, the overall controller and observer performance were validated in simulations and experiments on a down-scaled electric drive system. The following results were obtained:

- Highly dynamic closed-loop speed control (with and without speed sensor) was possible for all operation modes, including zero-crossings, stand-still tests, load variations at rated speed and field-weakening operation.
- The speed estimation error could be reduced to one percent (worst case), compared to the V/Hz method, where an error of up to five percent is expected. Moreover, large current overshoots or torque pulsations were not observed, even during transient operation.

In conclusion, it was shown that a more efficient and robust control system can be implemented in geothermal power plants, without the need of additional sensors or other hardware. The efficiency gain and the improved disturbance attenuation make up for the increased computational effort. Moreover, using the speed-adaptive observer a model-based state reconstruction of the electromechanical system is obtained, supplementing existing condition monitoring systems.

Future work comprises the ESP model validation using experimental data from an existing power plant. Moreover, the efficiency optimization should be incorporated in the presented speed control system, i.e. by conducting the identification procedure using the speed-adaptive observer (instead of the open-loop observer) and calculating respective flux linkage references, which are then supplied to the flux controller. Lastly, implementing the control system on a large-scale setup should be tested, prior to running it in an actual geothermal pump application.

Bibliography

[1] J. Kullick and C. M. Hackl. "Speed-Sensorless Control of Induction Machines with LC Filter for Geothermal Electric Submersible Pumping Systems". In: *Machines* 10.2 (Jan. 2022), p. 87.

[2] J. Kullick and C. M. Hackl. "Nonlinear Modeling, Identification and Optimal Feedforward Torque Control of Induction Machines Using Steady-State Machine Maps". In: *IEEE Transactions on Industrial Electronics* (2022).

[3] A. Zanelli et al. "Continuous Control Set Nonlinear Model Predictive Control of Reluctance Synchronous Machines". In: *IEEE Transactions on Control Systems Technology* 30.1 (2022), pp. 130–141.

[4] H. M. Eldeeb, A. S. Abdel-Khalik, J. Kullick, and C. M. Hackl. "Pre- and Postfault Current Control of Dual Three-Phase Reluctance Synchronous Drives". In: *IEEE Transactions on Industrial Electronics* 67.5 (May 2020), pp. 3361–3373.

[5] J. Kullick and C. M. Hackl. "Dynamic Modeling and Simulation of Deep Geothermal Electric Submersible Pumping Systems". In: *Energies* 10.10 (2017).

[6] H. Eldeeb, C. M. Hackl, L. Horlbeck, and J. Kullick. "A Unified Theory for Optimal Feedforward Torque Control of Anisotropic Synchronous Machines". In: *International Journal of Control* (2017), pp. 1–30.

[7] C. Hackl, J. Kullick, and N. Monzen. "Generic Loss Minimization for Nonlinear Synchronous Machines by Analytical Computation of Optimal Reference Currents Considering Copper and Iron Losses". In: *2021 22nd IEEE International Conference on Industrial Technology (ICIT)*. Vol. 1. 2021, pp. 1348–1355.

[8] H. Eldeeb, C. M. Hackl, L. Horlbeck, and J. Kullick. "Analytical Solutions for the Optimal Reference Currents for MTPC/MTPA, MTPV and MTPF Control of Anisotropic Synchronous Machines". In: *2017 IEEE Int. Electr. Mach. Drives Conf.* IEEE, May 2017, pp. 1–6.

[9] C. M. Hackl, J. Kullick, H. Eldeeb, and L. Horlbeck. "Analytical Computation of the Optimal Reference Currents for MTPC/MTPA, MTPV and MTPF Operation of Anisotropic Synchronous Machines Considering Stator Resistance and Mutual Inductance". In: *2017 19th European Conference on Power Electronics and Applications (EPE'17 ECCE Europe)*. Warsaw, 2017, P.1–P.10.

[10] H. Eldeeb, C. M. Hackl, and J. Kullick. "Efficient Operation of Anisotropic Synchronous Machines for Wind Energy Systems". In: *Journal of Physics: Conference Series* 753.11 (2016), p. 112009.

[11] C. M. Hackl, J. Kullick, M. J. Kamper, and J. C. Mitchell. "Current Control of Reluctance Synchronous Machines with Online Adjustment of the Controller Parameters". In: *2016 IEEE 25th International Symposium on Industrial Electronics (ISIE)*. June 2016.

[12] C. M. Hackl, J. Kullick, and N. Monzen. “Optimale Betriebsführung von nichtlinearen Synchronmaschinen”. de. In: *Elektrische Antriebe - Regelung von Antriebssystemen (5. Auflage)*. Springer, 2020.

[13] C. M. Hackl, J. Kullick, and P. Landsmann. “Nichtlineare Stromregelverfahren für Reluktanz-Synchronmaschinen”. de. In: *Elektrische Antriebe - Regelung von Antriebssystemen (5. Auflage)*. Springer, 2020.

[14] *Paris Agreement*. Tech. rep. United Nations, Dec. 2015.

[15] *The European Green Deal*. Tech. rep. European Commission, Dec. 2019.

[16] I. Stober and K. Bucher. *Geothermal Energy*. Berlin, Heidelberg: Springer Berlin Heidelberg, 2013.

[17] R. A. Meyers, ed. *Encyclopedia of Sustainability Science and Technology*. en. New York, NY: Springer New York, 2012.

[18] M. Bauer and W. Freeden. *Handbuch Tiefe Geothermie*. 2014.

[19] H. Paschen, D. Oertel, and R. Grünwald. *Möglichkeiten Geothermischer Stromerzeugung in Deutschland - Sachstandsbericht*. Tech. rep. Arbeitsbericht Nr. 84. Büro für Technikfolgen-Abschätzung beim Deutschen Bundestag (TAB), Feb. 2003.

[20] W. Neumann, F. Auer, H. Barthel, and H.-H. Schmidt-Kanefendt. *Strom Und Wärme Aus Tiefengeothermie*. Tech. rep. Berlin: Bund für Umwelt und Naturschutz Deutschland e.V. (BUND), June 2019.

[21] *2018 Annual Report*. Tech. rep. New Zealand: IEA Geothermal, Nov. 2019.

[22] J. F. Gülich. *Centrifugal Pumps*. Springer Science + Business Media, 2010.

[23] Milles, Uwe. *Robuste Pumpen für die Geothermie entwickeln*. de. Mar. 2016.

[24] Baker Hughes Incorporated. *XP Series High Horsepower ESP System (Booklet)*. English. Jan. 2014.

[25] N. R. E. L. (NREL). *Electronic Submersible Pump (ESP) Technology and Limitations with Respect to Geothermal Systems*. en. Sept. 2014.

[26] J. Vandevier and B. Gould. “Application of Electrical Submersible Pumping Systems in High Temperature Geothermal Environments Use of ESP Systems In”. In: *Geotherm. Resour. Counc. Trans.* 33 (2009), pp. 649–682.

[27] A. Report. *2015 Annual Report*. en. Tech. rep. New Zealand: IEA Geothermal, Feb. 2017, p. 179.

[28] L. F. Lobianco and W. Wardani. “Electrical Submersible Pumps for Geothermal Applications”. In: *SECOND EUROPEAN GEOTHERMAL REVIEW – geothermal Energy for Power Production* (June 2010).

[29] A. Lima, R. Stephan, and A. Pedroso. “Modelling the Electrical Drive System for Oil Exploitation”. In: *International Power System Transients Conference*. 1997, pp. 234–239.

[30] J. R. Smith, D. M. Grant, A. Al-Mashgari, and R. D. Slater. “Operation of Subsea Electrical Submersible Pumps Supplied over Extended Length Cable Systems”. In: *IEE Proceedings - Electric Power Applications* 147.6 (Nov. 2000), pp. 544–552.

[31] O. V. Thorsen and M. Dalva. “Combined Electrical and Mechanical Model of Electric Submersible Pumps”. In: *IEEE Transactions on Industry Applications* 37.2 (Mar. 2001), pp. 541–547.

[32] S. F. Rabbi, J. T. Kahnamouei, X. Liang, and J. Yang. "Shaft Failure Analysis in Soft-Starter Fed Electrical Submersible Pump Systems". In: *IEEE Open Journal of Industry Applications* 1 (2020), pp. 1–10.

[33] X. Liang and R. Adedun. "Load Harmonics Analysis and Mitigation". In: *48th IEEE Industrial Commercial Power Systems Conference*. May 2012, pp. 1–8.

[34] X. Liang, N. C. Kar, and J. Liu. "Load Filter Design Method for Medium-Voltage Drive Applications in Electrical Submersible Pump Systems". In: *IEEE Trans. Ind. Appl.* 51.3 (May 2015), pp. 2017–2029.

[35] X. Liang, S. O. Faried, and O. Ilochonwu. "Subsea Cable Applications in Electrical Submersible Pump Systems". In: *IEEE Transactions on Industry Applications* 46.2 (Mar. 2010), pp. 575–583.

[36] C. S. Kallesøe. "Fault Detection and Isolation in Centrifugal Pumps". en. PhD thesis. Aalborg: Aalborg University, 2006.

[37] S. Saito. "The Transient Characteristics of a Pump during Start Up". In: *Bulletin of JSME* 25.201 (1982), pp. 372–379.

[38] A. Dazin, G. Caignaert, and G. Bois. "Transient Behavior of Turbomachineries: Applications to Radial Flow Pump Startups". In: *Journal of Fluids Engineering* 129.11 (2007), pp. 1436–1444.

[39] G. Janevska. "Mathematical Modeling of Pump System". In: *Proceedings in EIIC-The 2nd Electronic International Interdisciplinary Conference*. 2013, pp. 455–458.

[40] K. Matsuse, T. Yoshizumi, S. Katsuta, and S. Taniguchi. "High-Response Flux Control of Direct-Field-Oriented Induction Motor with High Efficiency Taking Core Loss into Account". In: *IEEE Trans. Ind. Appl.* 35.1 (1999), pp. 62–69.

[41] R. Leidhold, G. Garcia, and M. Valla. "Field-Oriented Controlled Induction Generator with Loss Minimization". In: *IEEE Trans. Ind. Electron.* 49.1 (Feb. 2002), pp. 147–156.

[42] G. Dong and O. Ojo. "Efficiency Optimizing Control of Induction Motor Using Natural Variables". In: *IEEE Transactions on Industrial Electronics* 53.6 (Dec. 2006), pp. 1791–1798.

[43] M. N. Uddin and S. W. Nam. "New Online Loss-Minimization-Based Control of an Induction Motor Drive". In: *IEEE Transactions on Power Electronics* 23.2 (Mar. 2008), pp. 926–933.

[44] M. N. Uddin and S. W. Nam. "Development of a Nonlinear and Model-Based Online Loss Minimization Control of an IM Drive". In: *IEEE Transactions on Energy Conversion* 23.4 (Dec. 2008), pp. 1015–1024.

[45] G. Pellegrino, R. I. Bojoi, and P. Guglielmi. "Unified Direct-Flux Vector Control for AC Motor Drives". In: *IEEE Transactions on Industry Applications* 47.5 (Sept. 2011), pp. 2093–2102.

[46] Z. Qu, M. Ranta, M. Hinkkanen, and J. Luomi. "Loss-Minimizing Flux Level Control of Induction Motor Drives". In: *IEEE Transactions on Industry Applications* 48.3 (May 2012), pp. 952–961.

[47] J. Rivera Dominguez et al. "Copper and Core Loss Minimization for Induction Motors Using High-Order Sliding-Mode Control". In: *IEEE Transactions on Industrial Electronics* 59.7 (July 2012), pp. 2877–2889.

[48] J.-F. Stumper, A. Dötlinger, and R. Kennel. "Loss Minimization of Induction Machines in Dynamic Operation". In: *IEEE Transactions on Energy Conversion* 28.3 (Sept. 2013), pp. 726–735.

[49] J. Moreira, T. Lipo, and V. Blasko. "Simple Efficiency Maximizer for an Adjustable Frequency Induction Motor Drive". In: *IEEE Transactions on Industry Applications* 27.5 (Sept. 1991), pp. 940–946.

[50] G. Sousa, B. Bose, and J. Cleland. "Fuzzy Logic Based On-Line Efficiency Optimization Control of an Indirect Vector-Controlled Induction Motor Drive". In: *IEEE Transactions on Industrial Electronics* 42.2 (Apr. 1995), pp. 192–198.

[51] Cao-Minh Ta and Y. Hori. "Convergence Improvement of Efficiency-Optimization Control of Induction Motor Drives". In: *IEEE Transactions on Industry Applications* 37.6 (Nov. 2001), pp. 1746–1753.

[52] C. Chakraborty and Y. Hori. "Fast Efficiency Optimization Techniques for the Indirect Vector-Controlled Induction Motor Drives". In: *IEEE Transactions on Industry Applications* 39.4 (July 2003), pp. 1070–1076.

[53] A. M. Bazzi and P. T. Krein. "Review of Methods for Real-Time Loss Minimization in Induction Machines". In: *IEEE Transactions on Industry Applications* 46.6 (Nov. 2010), pp. 2319–2328.

[54] S. Vukosavic and E. Levi. "Robust DSP-Based Efficiency Optimization of a Variable Speed Induction Motor Drive". In: *IEEE Transactions on Industrial Electronics* 50.3 (June 2003), pp. 560–570.

[55] A. Borisevich and G. Schullerus. "Energy Efficient Control of an Induction Machine Under Torque Step Changes". In: *IEEE Transactions on Energy Conversion* 31.4 (Dec. 2016), pp. 1295–1303.

[56] R. Bojoi et al. "Unified Direct-Flux Vector Control of Induction Motor Drives with Maximum Torque per Ampere Operation". In: *2013 IEEE Energy Conversion Congress and Exposition*. IEEE, Sept. 2013.

[57] S. A. Odhano et al. "Maximum Efficiency per Torque Direct Flux Vector Control of Induction Motor Drives". In: *IEEE Transactions on Industry Applications* 51.6 (Nov. 2015), pp. 4415–4424.

[58] O. Wallscheid, M. Meyer, and J. Böcker. "An Open-Loop Operation Strategy for Induction Motors Considering Iron Losses and Saturation Effects in Automotive Applications". In: *2015 IEEE 11th International Conference on Power Electronics and Drive Systems*. June 2015, pp. 981–985.

[59] H. Cai, L. Gao, and L. Xu. "Calculation of Maximum Torque Operating Conditions for Inverter-Fed Induction Machine Using Finite-Element Analysis". In: *IEEE Transactions on Industrial Electronics* 66.4 (Apr. 2019), pp. 2649–2658.

[60] E. Armando et al. "Experimental Identification of the Magnetic Model of Synchronous Machines". In: *IEEE Transactions on Industry Applications* 49.5 (Sept. 2013), pp. 2116–2125.

[61] H. Abu-Rub et al. "Medium-Voltage Drives: Challenges and Existing Technology". In: *IEEE Power Electronics Magazine* 3.2 (June 2016), pp. 29–41.

[62] M. Smochek, A. F. Pollice, M. Rastogi, and M. Harshman. "Long Cable Applications From a Medium-Voltage Drives Perspective". In: *IEEE Transactions on Industry Applications* 52.1 (Jan. 2016), pp. 645–652.

[63] M. Kojima et al. "Novel Vector Control System Using Deadbeat-Controlled PWM Inverter with Output LC Filter". In: *IEEE Transactions on Industry Applications* 40.1 (Jan. 2004), pp. 162–169.

[64] J. Salomäki, M. Hinkkanen, and J. Luomi. "Sensorless Control of Induction Motor Drives Equipped With Inverter Output Filter". In: *IEEE Transactions on Industrial Electronics* 53.4 (June 2006), pp. 1188–1197.

[65] S. Mukherjee and G. Poddar. "Fast Control of Filter for Sensorless Vector Control SQIM Drive With Sinusoidal Motor Voltage". In: *IEEE Transactions on Industrial Electronics* 54.5 (Oct. 2007), pp. 2435–2442.

[66] K. Hatua, A. K. Jain, D. Banerjee, and V. T. Ranganathan. "Active Damping of Output LC Filter Resonance for Vector-Controlled VSI-Fed AC Motor Drives". In: *IEEE Trans. Ind. Electron.* 59.1 (Jan. 2012), pp. 334–342.

[67] J. Guzinski and H. Abu-Rub. "Sensorless Induction Motor Drive with Voltage Inverter and Sine-Wave Filter". In: *2013 IEEE International Symposium on Sensorless Control for Electrical Drives and Predictive Control of Electrical Drives and Power Electronics (SLED/PRECEDE)*. Oct. 2013, pp. 1–8.

[68] J. Salomäki. "Speed Sensorless Control of an Induction Machine Using a PWM Inverter with Output LC Filter". en. US 7,084.604 B2 (Helsinki). Aug. 2006.

[69] M. Hinkkanen and J. Luomi. "Stabilization of Regenerating-Mode Operation in Sensorless Induction Motor Drives by Full-Order Flux Observer Design". In: *IEEE Transactions on Industrial Electronics* 51.6 (Dec. 2004), pp. 1318–1328.

[70] C. Schauder. "Adaptive Speed Identification for Vector Control of Induction Motors without Rotational Transducers". In: *IEEE Transactions on Industry Applications* 28.5 (Sept. 1992), pp. 1054–1061.

[71] H. Kubota, K. Matsuse, and T. Nakano. "DSP-Based Speed Adaptive Flux Observer of Induction Motor". In: *IEEE Transactions on Industry Applications* 29.2 (Mar. 1993), pp. 344–348.

[72] M. Hinkkanen. "Analysis and Design of Full-Order Flux Observers for Sensorless Induction Motors". In: *IEEE Transactions on Industrial Electronics* 51.5 (Oct. 2004), pp. 1033–1040.

[73] I. Landau. "A Hyperstability Criterion for Model Reference Adaptive Control Systems". In: *IEEE Transactions on Automatic Control* 14.5 (Oct. 1969), pp. 552–555.

[74] I. Landau. "A Survey of Model Reference Adaptive Techniques—Theory and Applications". In: *Automatica* 10.4 (1974), pp. 353–379.

[75] I. Landau and H. Silveira. "A Stability Theorem with Applications to Adaptive Control". In: *IEEE Transactions on Automatic Control* 24.2 (Apr. 1979), pp. 305–312.

[76] G. Yang and T. H. Chin. "Adaptive-Speed Identification Scheme for a Vector-Controlled Speed Sensorless Inverter-Induction Motor Drive". In: *IEEE Transactions on Industry Applications* 29.4 (July 1993), pp. 820–825.

[77] S. Suwankawin and S. Sangwongwanich. "A Speed-Sensorless IM Drive with Decoupling Control and Stability Analysis of Speed Estimation". In: *IEEE Transactions on Industrial Electronics* 49.2 (Apr. 2002), pp. 444–455.

[78] H. Hofmann and S. R. Sanders. "Speed-Sensorless Vector Torque Control of Induction Machines Using a Two-Time-Scale Approach". In: *IEEE Transactions on Industry Applications* 34.1 (Jan. 1998), pp. 169–177.

[79] J. Maes and J. A. Melkebeek. "Speed-Sensorless Direct Torque Control of Induction Motors Using an Adaptive Flux Observer". In: *IEEE Transactions on Industry Applications* 36.3 (May 2000), pp. 778–785.

[80] C.-M. Ta, T. Uchida, and Y. Hori. "MRAS-Based Speed Sensorless Control for Induction Motor Drives Using Instantaneous Reactive Power". In: *Industrial Electronics Society, 2001. IECON '01. The 27th Annual Conference of the IEEE.* Vol. 2. 2001, 1417–1422 vol.2.

[81] H. Tajima, G. Guidi, and H. Umida. "Consideration about Problems and Solutions of Speed Estimation Method and Parameter Tuning for Speed-Sensorless Vector Control of Induction Motor Drives". In: *IEEE Trans. Ind. Appl.* 38.5 (Sept. 2002), pp. 1282–1289.

[82] H. Kubota et al. "Regenerating-Mode Low-Speed Operation of Sensorless Induction Motor Drive with Adaptive Observer". In: *IEEE Transactions on Industry Applications* 38.4 (July 2002), pp. 1081–1086.

[83] S. Suwankawin and S. Sangwongwanich. "Design Strategy of an Adaptive Full-Order Observer for Speed-Sensorless Induction-Motor Drives-Tracking Performance and Stabilization". In: *IEEE Transactions on Industrial Electronics* 53.1 (Feb. 2006), pp. 96–119.

[84] S. Sangwongwanich, S. Suwankawin, S. Po-ngam, and S. Koonlaboon. "A Unified Speed Estimation Design Framework for Sensorless AC Motor Drives Based on Positive-Real Property". In: *2007 Power Conversion Conference - Nagoya.* Apr. 2007, pp. 1111–1118.

[85] L. Harnefors and M. Hinkkanen. "Complete Stability of Reduced-Order and Full-Order Observers for Sensorless IM Drives". In: *IEEE Transactions on Industrial Electronics* 55.3 (Mar. 2008), pp. 1319–1329.

[86] L. Harnefors. "Globally Stable Speed-Adaptive Observers for Sensorless Induction Motor Drives". In: *IEEE Trans. Ind. Electron.* 54.2 (2007), pp. 1243–1245.

[87] L. Harnefors and M. Hinkkanen. "Stabilization Methods for Sensorless Induction Motor Drives — A Survey". In: *IEEE Journal of Emerging and Selected Topics in Power Electronics* 2.2 (June 2014), pp. 132–142.

[88] Z. Qu, M. Hinkkanen, and L. Harnefors. "Gain Scheduling of a Full-Order Observer for Sensorless Induction Motor Drives". In: *IEEE Transactions on Industry Applications* 50.6 (Nov. 2014), pp. 3834–3845.

[89] B. Chen, W. Yao, F. Chen, and Z. Lu. "Parameter Sensitivity in Sensorless Induction Motor Drives with the Adaptive Full-Order Observer". In: *IEEE Trans. Ind. Electron.* 62.7 (2015), pp. 4307–4318.

[90] M. S. Zaky and M. K. Metwaly. "Sensorless Torque/Speed Control of Induction Motor Drives at Zero and Low Frequencies With Stator and Rotor Resistance Estimations". In: *IEEE Journal of Emerging and Selected Topics in Power Electronics* 4.4 (Dec. 2016), pp. 1416–1429.

[91] W. Sun et al. "Design Method of Adaptive Full Order Observer With or Without Estimated Flux Error in Speed Estimation Algorithm". In: *IEEE Transactions on Power Electronics* 31.3 (Mar. 2016), pp. 2609–2626.

[92] J. Chen and J. Huang. "Stable Simultaneous Stator and Rotor Resistances Identification for Speed Sensorless IM Drives: Review and New Results". In: *IEEE Transactions on Power Electronics* 33.10 (Oct. 2018), pp. 8695–8709.

[93] F. Kieferndorf et al. "ANPC-5L Technology Applied to Medium Voltage Variable Speed Drives Applications". In: *SPEEDAM 2010.* June 2010, pp. 1718–1725.

[94] T. Geyer. *Model Predictive Control of High Power Convertersand Industrial Drives.* en. Chichester, UK: John Wiley & Sons, Ltd, Nov. 2016.

[95] A. Veltman, D. W. J. Pulle, and R. W. D. Doncker. *Fundamentals of Electrical Drives.* Springer International Publishing, 2016.

[96] G. Shiny and M. R. Baiju. "A Space Vector Based Pulse Width Modulation Scheme for a 5-Level Induction Motor Drive". In: *2011 IEEE Ninth International Conference on Power Electronics and Drive Systems*. Dec. 2011, pp. 292–297.

[97] I. P.
bibinitperiod E. Society. *IEEE Standard Definitions for the Measurement of Electric Power Quantities Under Sinusoidal, Nonsinusoidal, Balanced, or Unbalanced Conditions*. en. Tech. rep. New York, NY, USA: IEEE, Mar. 2010.

[98] S. Bernet. "Recent Developments of High Power Converters for Industry and Traction Applications". In: *IEEE Transactions on Power Electronics* 15.6 (Nov. 2000), pp. 1102–1117.

[99] F. Endrejat and P. Pillay. "Resonance Overvoltages in Medium-Voltage Multilevel Drive Systems". In: *IEEE Transactions on Industry Applications* 45.4 (July 2009), pp. 1199–1209.

[100] "IEEE Recommended Practice for Specifying Electric Submersible Pump CableEthylene-Propylene Rubber Insulation". In: *IEEE Std 1018-2013 (Revison of IEEE Std 1018-2004)* (Apr. 2013), pp. 1–45.

[101] A. J. Schwab. *Elektroenergiesysteme*. de. 2. Auflage. Springer, 2009.

[102] C. R. Paul. *Analysis of Multiconductor Transmission Lines*. 2nd ed. Hoboken, N.J: Wiley-Interscience : IEEE Press, 2008.

[103] F. F. da Silva and C. Leth Bak. *Electromagnetic Transients in Power Cables*. Vol. 4. Power Systems. London: Springer London, Mar. 2013.

[104] A. I. Watson et al. "Tandem Motors". US7549849B2 (Sugar Land, TX). June 2009.

[105] A. Chen, R. B. Ummaneni, R. Nilssen, and A. Nysveen. "Review of Electrical Machine in Downhole Applications and the Advantages". In: *2008 13th International Power Electronics and Motion Control Conference*. Sept. 2008, pp. 799–803.

[106] T. R. Brinner, R. H. McCoy, and T. Kopecky. "Induction Versus Permanent-Magnet Motors for Electric Submersible Pump Field and Laboratory Comparisons". In: *IEEE Transactions on Industry Applications* 50.1 (Jan. 2014), pp. 174–181.

[107] C. Dirscherl and C. M. Hackl. "Dynamic Power Flow in Wind Turbine Systems with Doubly-Fed Induction Generator". In: *2016 IEEE International Energy Conference (ENERGYCON)*. Apr. 2016, pp. 1–6.

[108] R. D. Doncker, D. W. J. Pulle, and A. Veltman. *Advanced Electrical Drives*. Springer Netherlands, 2011.

[109] C. M. Hackl. *Non-Identifier Based Adaptive Control in Mechatronics*. en. Vol. 466. Lecture Notes in Control and Information Sciences. Cham: Springer International Publishing, 2017.

[110] C. F. Wagner. "Self-Excitation of Induction Motors". In: *Electrical Engineering* 58.2 (Feb. 1939), pp. 47–51.

[111] G. Ludyk. *Theoretische Regelungstechnik 1*. Springer-Lehrbuch. Berlin, Heidelberg: Springer Berlin Heidelberg, 1995.

[112] Y. A. Çengel and J. M. Cimbala. *Fluid Mechanics: Fundamentals and Applications*. Third edition. New York: McGraw Hill, 2014.

[113] P. Girdhar, O. Moniz, and S. Mackay. *Practical Centrifugal Pumps*. Elsevier, 2005.

[114] P. J. Pritchard. *Fox and McDonald's Introduction to Fluid Mechanics*. JOHN WILEY & SONS INC, Oct. 2011.

[115] S. L. Dixon. *Fluid Mechanics, Thermodynamics of Turbomachinery*. en. 5th edition. Amsterdam, Boston: Elsevier-Butterworth-Heinemann, 2005.

[116] C. Pfleiderer and H. Petermann. *Strömungsmaschinen*. de. 7., unveränd. Aufl. Klassiker der Technik. Berlin: Springer, 2005.

[117] W. Wesche. *Radiale Kreiselpumpen*. Springer Science + Business Media, 2012.

[118] B. Simeon. *Computational Flexible Multibody Dynamics*. en. Berlin, Heidelberg: Springer Berlin Heidelberg, 2013.

[119] F. Z. Peng and Jih-Sheng Lai. "Generalized Instantaneous Reactive Power Theory for Three-Phase Power Systems". In: *IEEE Transactions on Instrumentation and Measurement* 45.1 (Feb. 1996), pp. 293–297.

[120] T. Ohnishi, H. Miyazaki, and H. Okitsu. "High Efficiency Drive of an Induction Motor by Means of V/F Ratio Control". In: *Proceedings.14 Annual Conference of Industrial Electronics Society*. Vol. 3. Oct. 1988, pp. 780–785.

[121] J. Kullick and C. M. Hackl. "Generic Machine Identification and Maximum Efficiency Operation of Induction Machines". In: *arXiv:1812.02431 [cs]* (Dec. 2018). arXiv: 1812.02431 [cs].

[122] E. Levi, M. Sokola, A. Boglietti, and M. Pastorelli. "Iron Loss in Rotor-Flux-Oriented Induction Machines: Identification, Assessment of Detuning, and Compensation". In: *IEEE Transactions on Power Electronics* 11.5 (Sept. 1996), pp. 698–709.

[123] S. N. Vukosavic. *Electrical Machines*. Springer Science + Business Media, 2013.

[124] D. Schröder. *Elektrische Antriebe - Regelung von Antriebssystemen*. de. Berlin, Heidelberg: Springer Berlin Heidelberg, 2015.

[125] J. Adamy. *Nichtlineare Systeme und Regelungen*. de. Berlin, Heidelberg: Springer Berlin Heidelberg, 2014.

[126] E. Hering, R. Martin, and M. Stohrer. *Taschenbuch der Mathematik und Physik*. ger. 5. aktualis. u. erw. Aufl. Berlin: Springer, 2009.

[127] J. Kullick and C. M. Hackl. "Speed-Sensorless State Feedback Control of Induction Machines with LC Filter". en. In: *arXiv:1807.11799 [cs]* (July 2018). arXiv: 1807.11799 [cs].

[128] J. Lunze. *Regelungstechnik 2*. Vol. 53. Springer-Lehrbuch. Berlin, Heidelberg: Springer Berlin Heidelberg, 2014.

[129] G. Ludyk. *Theoretische Regelungstechnik 2*. Springer-Lehrbuch. Berlin, Heidelberg: Springer Berlin Heidelberg, 1995.

[130] J. Guzinski. "Closed Loop Control of AC Drive with LC Filter". In: *2008 13th Int. Power Electron. Motion Control Conf.* IEEE, Sept. 2008, pp. 994–1001.

[131] A. Tustin. "A Method of Analysing the Behaviour of Linear Systems in Terms of Time Series". In: *Journal of the Institution of Electrical Engineers - Part IIA: Automatic Regulators and Servo Mechanisms* 94.1 (May 1947), pp. 130–142.

[132] J. Lunze. *Regelungstechnik 1*. Vol. 53. Springer-Lehrbuch. Berlin, Heidelberg: Springer Berlin Heidelberg, 2014.

[133] C. C. D. Wit et al. "Observability Conditions of Induction Motors at Low Frequencies". In: *Proceedings of the 39th IEEE Conference on Decision and Control*. Vol. 3. Dec. 2000, 2044–2049 vol.3.

[134] L. Råde and B. Westergren. *Mathematics Handbook for Science and Engineering*. Vol. 1. Berlin, Heidelberg: Springer Berlin Heidelberg, 2004.

[135] P. Ioannou and J. Sun. *Robust Adaptive Control*. en. New York: Dover Publications, 2013.

[136] H. Bossel. *Modeling and Simulation*. en. Wiesbaden: Vieweg & Teubner, 2014.

[137] I. R. Bojoi, E. Armando, G. Pellegrino, and S. G. Rosu. "Self-Commissioning of Inverter Nonlinear Effects in AC Drives". In: *2012 IEEE International Energy Conference and Exhibition (ENERGYCON)*. Sept. 2012, pp. 213–218.

[138] J. Holtz. "Sensorless Control of Induction Motor Drives". In: *Proceedings of the IEEE* 90.8 (Aug. 2002), pp. 1359–1394.

[139] J. Holtz and Juntao Quan. "Drift- and Parameter-Compensated Flux Estimator for Persistent Zero-Stator-Frequency Operation of Sensorless-Controlled Induction Motors". In: *IEEE Transactions on Industry Applications* 39.4 (July 2003), pp. 1052–1060.

[140] J. Holtz. "Sensorless Vector Control of Induction Motors at Very Low Speed Using a Nonlinear Inverter Model and Parameter Identification". In: *IEEE Transactions on Industry Applications* 38.4 (July 2002), pp. 1087–1095.

[141] Jong-Woo Choi and Seung-Ki Sul. "Inverter Output Voltage Synthesis Using Novel Dead Time Compensation". In: *IEEE Transactions on Power Electronics* 11.2 (Mar. 1996), pp. 221–227.

[142] M. Hinkkanen, L. Harnefors, and J. Luomi. "Reduced-Order Flux Observers With Stator-Resistance Adaptation for Speed-Sensorless Induction Motor Drives". In: *IEEE Transactions on Power Electronics* 25.5 (May 2010), pp. 1173–1183.

[143] M. S. Zaky. "Stability Analysis of Speed and Stator Resistance Estimators for Sensorless Induction Motor Drives". In: *IEEE Transactions on Industrial Electronics* 59.2 (Feb. 2012), pp. 858–870.

[144] H. Unbehauen. *Regelungstechnik II*. Wiesbaden: Vieweg, 2007.

[145] R. Tóth, F. Felici, P. Heuberger, and P. Van den Hof. "Crucial Aspects of Zero-Order Hold LPV State-Space System Discretization". en. In: *IFAC Proceedings Volumes*. Vol. 41. 2008, pp. 4952–4957.

[146] P. Vaclavek, P. Blaha, and I. Herman. "AC Drive Observability Analysis". In: *IEEE Transactions on Industrial Electronics* 60.8 (Aug. 2013), pp. 3047–3059.

[147] C. Canudas de Wit and J.-J. Slotine. "Sliding Observers for Robot Manipulators". en. In: *IFAC Proceedings Volumes* 22.3 (June 1989), pp. 379–384.

[148] R. Hermann and A. Krener. "Nonlinear Controllability and Observability". In: *IEEE Transactions on Automatic Control* 22.5 (Oct. 1977), pp. 728–740.

[149] G. Fischer. *Lineare Algebra: eine Einführung für Studienanfänger*. de. 18. aktualisierte Auflage. Grundkurs Mathematik. Wiesbaden: Springer Spektrum, 2014.

List of Figures

List of Tables

List of Abbreviations

5L-ANPC five-level active neutral-point clamped

ADC analog-to-digital converter

BEMF back electromotive force

BEP best efficiency point

CT continuous-time

DT discrete-time

EPDM Ethylen-Propylen-Dien-Kautschuk

EMF electromotive force

ESP electric submersible pump

FEM finite element method

FFT fast Fourier transform

FOC field-oriented control

IGBT insulated-gate bipolar transistor

IM induction machine

KCL Kirchhoff's current law

KVL Kirchhoff's voltage law

LPF low-pass filter

LPV linear parameter-varying

LSP line-shaft pump

LTI linear time-invariant

LUT look-up table

LQR linear quadratic regulator

MRAS model reference adaptive system

MV medium voltage

PI proportional-integral

PUL per-unit-length

PWM pulse-width modulation

RTT Reynold's transport theorem

SCIM squirrel-cage induction machine

SPWM sinusoidal pulse-width modulation

SVM space vector modulation

THD total harmonic distortion

VSD variable speed drive

VSI voltage source inverter

ZOH zero-order hold

Appendix A

Additional topics related to the description of three-phase electric systems

This chapter deals with the description of three-phase electric systems using space vectors in matrix/vector notation.

A.1 Space vector theory using matrix/vector notation

Consider a three-phase electrical system with phases a, b, c, which are mutually shifted in space (e.g. the stator windings of an electrical machine) and/or time (phase lag of sinusoidal signals) by 120° (see Fig. A.1). Moreover, let $\boldsymbol{x}^{\mathrm{abc}} = (x^{\mathrm{a}}, x^{\mathrm{b}}, x^{\mathrm{c}})^{\top} \in \mathbb{R}^3$ denote the vector of phase voltages, currents or flux linkages, i.e. $x \in \{u, i, \psi\}$, stated in the stationary abc-reference frame.

A.1.1 Clarke transformation

The *Clarke transformation* is used to transform a vector $\boldsymbol{x}^{\mathrm{abc}}$ from the three-phase stationary abc-reference frame into the three-phase orthogonal and stationary $\alpha\beta\gamma$-reference frame ($\boldsymbol{x}^{\alpha\beta\gamma} = (x^{\alpha}, x^{\beta}, x^{\gamma})^{\top} \in \mathbb{R}^3$) and vice versa (see e.g. [109, Def. 14.7]), i.e.

$$\boldsymbol{x}^{\alpha\beta\gamma} = \boldsymbol{T}_{\mathrm{C}}(\kappa)\boldsymbol{x}^{\mathrm{abc}} \qquad \text{and} \qquad \boldsymbol{x}^{\mathrm{abc}} = \boldsymbol{T}_{\mathrm{C}}^{-1}(\kappa)\boldsymbol{x}^{\alpha\beta\gamma}, \tag{A.1}$$

where

$$\boldsymbol{T}_{\mathrm{C}}(\kappa) = \kappa \begin{bmatrix} 1 & -\frac{1}{2} & -\frac{1}{2} \\ 0 & \frac{\sqrt{3}}{2} & -\frac{\sqrt{3}}{2} \\ \frac{1}{\sqrt{2}} & \frac{1}{\sqrt{2}} & \frac{1}{\sqrt{2}} \end{bmatrix} \qquad \text{and} \qquad \boldsymbol{T}_{\mathrm{C}}^{-1}(\kappa) = \frac{1}{\kappa} \begin{bmatrix} \frac{2}{3} & 0 & \frac{\sqrt{2}}{3} \\ -\frac{1}{3} & \frac{1}{\sqrt{3}} & \frac{\sqrt{2}}{3} \\ -\frac{1}{3} & -\frac{1}{\sqrt{3}} & \frac{\sqrt{2}}{3} \end{bmatrix} \tag{A.2}$$

denote the Clarke transformation matrix and its inverse, respectively. The scaling factor κ determines whether the transformation is *amplitude invariant* ($\kappa = \frac{2}{3}$) or *power invariant* ($\kappa = \sqrt{2/3}$). For the amplitude invariant transformation, the amplitude of the a-component is equal to the amplitude of the α-component (see Fig. A.1), whereas for the power invariant transformation the

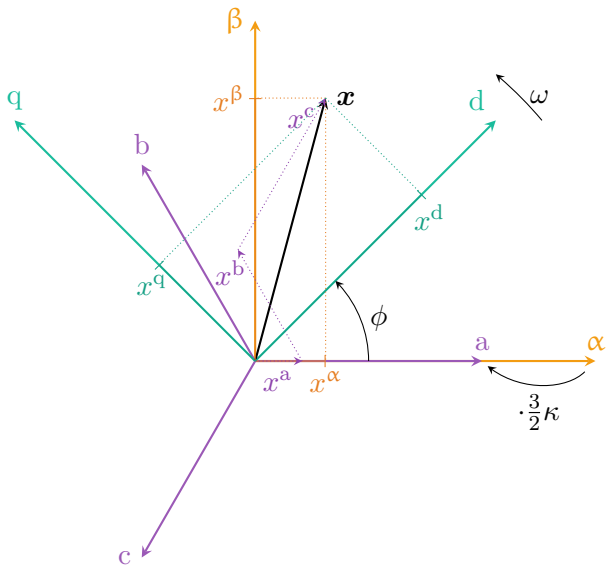

Figure A.1: *Space vector $\boldsymbol{x}$ of a three-phase electrical system in the stationary* abc*-reference frame, in the stationary and orthogonal* αβ*-reference frame and in the rotating and orthogonal* dq*-reference frame.*

following holds true for the calculation of the instantaneous active power

$$p = \boldsymbol{u}^{\mathrm{abc}\top}\boldsymbol{i}^{\mathrm{abc}} \overset{(A.1)}{=} \boldsymbol{u}^{\alpha\beta\gamma}\boldsymbol{T}_{\mathrm{C}}^{-1}(\kappa)^{\top}\boldsymbol{T}_{\mathrm{C}}^{-1}(\kappa)\boldsymbol{i}^{\alpha\beta\gamma} = \tfrac{2}{3\kappa^2}\boldsymbol{u}^{\alpha\beta\gamma}\boldsymbol{i}^{\alpha\beta\gamma} \overset{\kappa=\sqrt{\frac{2}{3}}}{=} \boldsymbol{u}^{\alpha\beta\gamma\top}\boldsymbol{i}^{\alpha\beta\gamma}. \tag{A.3}$$

The γ-component is also called *zero-sequence component*. It is zero for *balanced* (or symmetric) systems, i.e. when $x^{\mathrm{a}} + x^{\mathrm{b}} + x^{\mathrm{b}} = 0$ holds true. If the zero-sequence component is either zero or not of interest, the *reduced Clarke transformation* can be used instead, transforming a vector from the three-phase stationary abc-reference frame into the two-phase stationary and orthogonal αβ-reference frame ($\boldsymbol{x}^{\alpha\beta} = (x^\alpha, x^\beta)^\top \in \mathbb{R}^2$) , i.e.

$$\boldsymbol{x}^{\alpha\beta} = \boldsymbol{T}_{\mathrm{C,red}}(\kappa)\boldsymbol{x}^{\mathrm{abc}} \qquad \text{and} \qquad \boldsymbol{x}^{\mathrm{abc}} = \boldsymbol{T}_{\mathrm{C,red}}^{-1}(\kappa)\boldsymbol{x}^{\alpha\beta}, \tag{A.4}$$

where

$$\boldsymbol{T}_{\mathrm{C,red}}(\kappa) = \kappa\begin{bmatrix} 1 & -\frac{1}{2} & -\frac{1}{2} \\ 0 & \frac{\sqrt{3}}{2} & -\frac{\sqrt{3}}{2} \end{bmatrix} \qquad \text{and} \qquad \boldsymbol{T}_{\mathrm{C,red}}^{-1}(\kappa) = \frac{1}{\kappa}\begin{bmatrix} \frac{2}{3} & 0 \\ -\frac{1}{3} & \frac{1}{\sqrt{3}} \\ -\frac{1}{3} & -\frac{1}{\sqrt{3}} \end{bmatrix} \tag{A.5}$$

denote the reduced Clarke transformation matrix and its (pseudo) inverse.

A.1.2 Park transformation

The *Park transformation* is used to transform the vector $\boldsymbol{x}^{\mathrm{dq0}} = (x^{\mathrm{d}}, x^{\mathrm{q}}, x^0)^\top \in \mathbb{R}^3$ from the rotating and orthogonal dq0-reference frame into the stationary and orthogonal αβγ-reference frame and vice versa (see e.g. [109, Def. 14.11]), i.e.

$$\boldsymbol{x}^{\alpha\beta\gamma} = \boldsymbol{T}_{\mathrm{P3}}(\phi)\boldsymbol{x}^{\mathrm{dq0}} \qquad \text{and} \qquad \boldsymbol{x}^{\mathrm{dq0}} = \boldsymbol{T}_{\mathrm{P3}}^{-1}(\phi)\boldsymbol{x}^{\alpha\beta\gamma}, \tag{A.6}$$

where

$$\boldsymbol{T}_{\mathrm{P3}}(\phi)=\begin{bmatrix}\cos(\phi) & -\sin(\phi) & 0\\ \sin(\phi) & \cos(\phi) & 0\\ 0 & 0 & 1\end{bmatrix} \quad \text{and} \quad \boldsymbol{T}_{\mathrm{P3}}^{-1}(\phi)=\begin{bmatrix}\cos(\phi) & \sin(\phi) & 0\\ -\sin(\phi) & \cos(\phi) & 0\\ 0 & 0 & 1\end{bmatrix}=\boldsymbol{T}_{\mathrm{P3}}(-\phi)=\boldsymbol{T}_{\mathrm{P3}}^{\top}(\phi) \tag{A.7}$$

denote the Park transformation matrix and its inverse, respectively. The dq0-reference frame is rotated counter-clockwise with respect to the stationary $\alpha\beta\gamma$-reference frame by the Park transformation angle ϕ, whose derivative is the rotational speed $\omega=\frac{\mathrm{d}}{\mathrm{d}t}\phi$.

Likewise, a reduced transformation matrix can be stated, transforming the vector $\boldsymbol{x}^{\mathrm{dq}}=(x^{\mathrm{d}},x^{\mathrm{q}})^{\top}\in\mathbb{R}^2$ from the two-phase rotating dq-reference frame into the two-phase stationary $\alpha\beta$-reference frame, i.e.

$$\boldsymbol{x}^{\alpha\beta}=\boldsymbol{T}_{\mathrm{p}}(\phi)\boldsymbol{x}^{\mathrm{dq}} \qquad \text{and} \qquad \boldsymbol{x}^{\mathrm{dq}}=\boldsymbol{T}_{\mathrm{p}}^{-1}(\phi)\boldsymbol{x}^{\alpha\beta}, \tag{A.8}$$

where

$$\boldsymbol{T}_{\mathrm{p}}(\phi)=\begin{bmatrix}\cos(\phi) & -\sin(\phi)\\ \sin(\phi) & \cos(\phi)\end{bmatrix} \quad \text{and} \quad \boldsymbol{T}_{\mathrm{p}}^{-1}(\phi)=\begin{bmatrix}\cos(\phi) & \sin(\phi)\\ -\sin(\phi) & \cos(\phi)\end{bmatrix}=\boldsymbol{T}_{\mathrm{p}}(-\phi)=\boldsymbol{T}_{\mathrm{p}}^{\top}(\phi) \tag{A.9}$$

denote the reduced Park transformation matrix and its inverse.

Applying the (reduced) Park transformation on the derivative of the vector $\boldsymbol{x}^{\alpha\beta}$ yields

$$\begin{aligned}\boldsymbol{T}_{\mathrm{p}}^{-1}(\phi)\tfrac{\mathrm{d}}{\mathrm{d}t}\boldsymbol{x}^{\alpha\beta} &= \boldsymbol{T}_{\mathrm{p}}^{-1}(\phi)\tfrac{\mathrm{d}}{\mathrm{d}t}\boldsymbol{T}_{\mathrm{p}}(\phi)\boldsymbol{x}^{\mathrm{dq}}\\ &= \boldsymbol{T}_{\mathrm{p}}^{-1}(\phi)\omega\boldsymbol{J}\boldsymbol{T}_{\mathrm{p}}(\phi)\boldsymbol{x}^{\mathrm{dq}}+\boldsymbol{T}_{\mathrm{p}}^{-1}(\phi)\boldsymbol{T}_{\mathrm{p}}(\phi)\tfrac{\mathrm{d}}{\mathrm{d}t}\boldsymbol{x}^{\mathrm{dq}}\\ &= \omega\boldsymbol{J}\boldsymbol{x}^{\mathrm{dq}}+\tfrac{\mathrm{d}}{\mathrm{d}t}\boldsymbol{x}^{\mathrm{dq}},\end{aligned} \tag{A.10}$$

since $\boldsymbol{J}\boldsymbol{T}_{\mathrm{p}}(\phi)=\boldsymbol{T}_{\mathrm{p}}(\phi)\boldsymbol{J}$, and where $\boldsymbol{J}:=\boldsymbol{T}_{\mathrm{p}}(\frac{\pi}{2})$ describes a counter-clockwise rotation by 90°.

A.2 On the analogy between complex numbers and matrix/vector notation

Assume the following system

$$\tfrac{\mathrm{d}}{\mathrm{d}t}x=ax \tag{A.11}$$

with complex state $x\in\mathbb{C}$ and system coefficient $a\in\mathbb{C}$, respectively. Now, define $\boldsymbol{x}:=(x^i,x^j)^{\top}:=(\Re(x),\Im(x))^{\top}\in\mathbb{R}^2$ and $\bar{a}:=\Re(a),\tilde{a}:=\Im(a)\in\mathbb{R}$. It can be shown that the system (A.11) can be rewritten as

$$\tfrac{\mathrm{d}}{\mathrm{d}t}\boldsymbol{x}=\tfrac{\mathrm{d}}{\mathrm{d}t}\begin{pmatrix}x^i\\ x^j\end{pmatrix}=\begin{bmatrix}\bar{a} & -\tilde{a}\\ \tilde{a} & \bar{a}\end{bmatrix}\begin{pmatrix}x^i\\ x^j\end{pmatrix}=(\bar{a}\boldsymbol{I}_2+\tilde{a}\boldsymbol{J})\boldsymbol{x}. \tag{A.12}$$

Proof. Calculating

$$\tfrac{\mathrm{d}}{\mathrm{d}t}x=(\bar{a}+j\tilde{a})(\boldsymbol{x}^i+j\boldsymbol{x}^j)=\bar{a}\boldsymbol{x}^i-\tilde{a}\boldsymbol{x}^j+j(\bar{a}\boldsymbol{x}^j+\tilde{a}\boldsymbol{x}^i) \tag{A.13}$$

yields $\Re(\frac{\mathrm{d}}{\mathrm{d}t}x)=\bar{a}\boldsymbol{x}^i-\tilde{a}\boldsymbol{x}^j$ and $\Im(\frac{\mathrm{d}}{\mathrm{d}t}x)=\bar{a}\boldsymbol{x}^j+\tilde{a}\boldsymbol{x}^i$. □

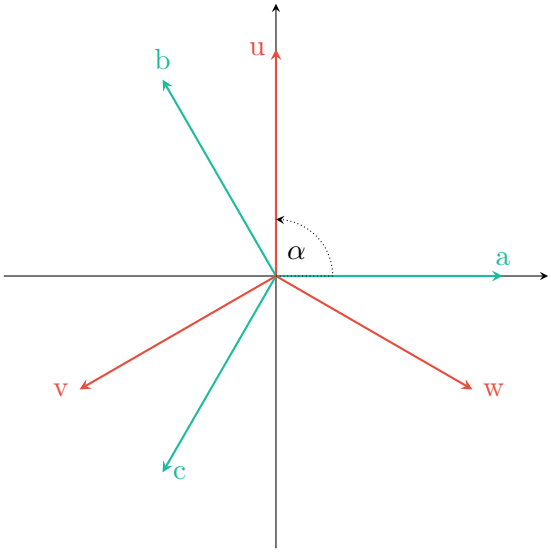

Figure A.2: *Rotation of a three-phase reference frame.*

A.3 Rotation of a three-phase reference frame on a 2D plane

Consider two three-phase coordinate systems abc and uvw that are shifted by the offset angle α (see Fig. A.2). Moreover, let $\boldsymbol{x}^{\mathrm{abc}} = (x^{\mathrm{a}}, x^{\mathrm{b}}, x^{\mathrm{c}})^\top$ and $\boldsymbol{x}^{\mathrm{uvw}} = (x^{\mathrm{u}}, x^{\mathrm{v}}, x^{\mathrm{w}})^\top$ denote the respective unit vectors. Then $\boldsymbol{x}^{\mathrm{abc}}$ can be expressed in terms of $\boldsymbol{x}^{\mathrm{uvw}}$ and α by

$$\begin{pmatrix} x^{\mathrm{a}} \\ x^{\mathrm{b}} \\ x^{\mathrm{c}} \end{pmatrix} = \begin{pmatrix} \cos(\alpha)x^{\mathrm{u}} + \cos(\alpha + \frac{2}{3}\pi)x^{\mathrm{v}} + \cos(\alpha + \frac{4}{3}\pi)x^{\mathrm{w}} \\ \cos(\alpha + \frac{4}{3}\pi)x^{\mathrm{u}} + \cos(\alpha)x^{\mathrm{v}} + \cos(\alpha + \frac{2}{3}\pi)x^{\mathrm{w}} \\ \cos(\alpha + \frac{2}{3}\pi)x^{\mathrm{u}} + \cos(\alpha + \frac{4}{3}\pi)x^{\mathrm{v}} + \cos(\alpha)x^{\mathrm{w}} \end{pmatrix} = [\cos(\alpha)\boldsymbol{I}_3 + \sin(\alpha)\boldsymbol{J}_3] \begin{pmatrix} x^{\mathrm{u}} \\ x^{\mathrm{v}} \\ x^{\mathrm{w}} \end{pmatrix} \tag{A.14}$$

where the trigonometric identity $\cos(\beta + \gamma) = \cos(\beta)\cos(\gamma) - \sin(\beta)\sin(\gamma)$ is used. Moreover, $\boldsymbol{I}_3$ denotes the identity matrix and

$$\boldsymbol{J}_3 := \frac{\sqrt{3}}{2} \begin{bmatrix} 0 & -1 & 1 \\ 1 & 0 & -1 \\ -1 & 1 & 0 \end{bmatrix} \tag{A.15}$$

is an auxiliary rotation matrix. However, since

$$\| \cos(\alpha)\boldsymbol{I}_3 + \sin(\alpha)\boldsymbol{J}_3 \| \neq 1 \quad \text{for} \quad \alpha \neq k\pi, k \in \mathbb{N} \tag{A.16}$$

the submatrix $\sin(\alpha)\boldsymbol{J}_3$ needs to be multiplied by $\frac{2}{3}$, yielding the rotation matrix

$$\boldsymbol{T}_{\mathrm{R}}(\alpha) := \cos(\alpha)\boldsymbol{I}_3 + \sin(\alpha)\tfrac{2}{3}\boldsymbol{J}_3. \tag{A.17}$$

Hence, for $\alpha = \frac{\pi}{2}$, the rotation matrix $\boldsymbol{J}_3^* := \boldsymbol{T}_{\mathrm{R}}(\alpha) = \frac{2}{3}\boldsymbol{J}_3$ is obtained.

A.4 Instantaneous power calculations

Given the three-phase voltages $\boldsymbol{u}^{\mathrm{abc}}$ and currents $\boldsymbol{i}^{\mathrm{abc}}$, and their amplitude invariant two-phase equivalents $\boldsymbol{u}^{\alpha\beta}$ and $\boldsymbol{i}^{\alpha\beta}$. Then the instantaneous active, reactive and apparent power terms can be

stated as (see e.g. [124, Sec. 24.2.2.3])

$$p = \boldsymbol{u}^{\mathrm{abc}\top}\boldsymbol{i}^{\mathrm{abc}} = \boldsymbol{u}^{\alpha\beta\top}\overbrace{\boldsymbol{T}_{\mathrm{C,red}}^{-1}(\tfrac{2}{3})^{\top}\boldsymbol{T}_{\mathrm{C,red}}^{-1}(\tfrac{2}{3})}^{=\frac{3}{2}\boldsymbol{I}_2}\boldsymbol{i}^{\alpha\beta} = \tfrac{3}{2}\boldsymbol{u}^{\alpha\beta\top}\boldsymbol{i}^{\alpha\beta}, \tag{A.18}$$

$$q = \boldsymbol{u}^{\mathrm{abc}\top}\boldsymbol{J}_3^{*}\,\boldsymbol{i}^{\mathrm{abc}} = \boldsymbol{u}^{\alpha\beta\top}\underbrace{\boldsymbol{T}_{\mathrm{C,red}}^{-1}(\tfrac{2}{3})^{\top}\boldsymbol{J}_3^{*}\boldsymbol{T}_{\mathrm{C,red}}^{-1}(\tfrac{2}{3})}_{=\frac{3}{2}\boldsymbol{J}}\boldsymbol{i}^{\alpha\beta} = \tfrac{3}{2}\boldsymbol{u}^{\alpha\beta\top}\boldsymbol{J}\,\boldsymbol{i}^{\alpha\beta} \quad \text{and} \tag{A.19}$$

$$s = \sqrt{p^2+q^2} = \tfrac{3}{2}\sqrt{(\boldsymbol{u}^{\alpha\beta\top}\boldsymbol{i}^{\alpha\beta})^2 + (\boldsymbol{u}^{\alpha\beta\top}\boldsymbol{J}\boldsymbol{i}^{\alpha\beta})^2} = \ldots = \tfrac{3}{2}\|\boldsymbol{u}^{\alpha\beta}\|\,\|\boldsymbol{i}^{\alpha\beta}\|, \tag{A.20}$$

where the calculation steps in the last equation follow intuitively by expanding and regrouping the square root term.

Appendix B

Testbench description

For the experimental results of Chs. 3 and 4, the testbench described in the following was used.

B.1 Basic drive setup

The basic experimental setup used for the machine identification is depicted in Fig. B.1 and consists of the following components (with ratings given in Tab. B.1):

1. **Induction machine (machine under test, `IM`):** The star-connected machine under test is connected to the electrical source `VSI1` and mechanically coupled with the prime mover `PM` (via an optional torque transducer `TS`). It is equipped with a rotational encoder, providing the angular velocity ω_m.

   → SEW DRE100L2 with Heidenhain ROD 486 (encoder)

2. **Permanent magnet synchronous machine (prime mover, `PM`):** A permanent magnet synchronous machine is employed as prime mover, keeping the test setup at a defined speed $\omega_\mathrm{m}^\star$. It is driven by a separate source `VSI2` and has a higher power rating than the induction machine.

   → SEW CMP80M with Heidenhain ROD 486 (encoder)

3. **Voltage source inverter (`VSI1`, `VSI2`):** The two-level VSIs are connected in back-to-back configuration, sharing a mutual DC-link capacitor at which the voltage u_dc is measured. Moreover the respective output currents $\boldsymbol{i}_\mathrm{s}^\mathrm{abc}$ at the inverter output terminals are measured. The pulse-width modulated gate signals are provided by the real-time system `RTS` and the inverter output voltages $\boldsymbol{u}_\mathrm{s}^\mathrm{abc}$ are reconstructed from the measured DC-link voltage and the (known) gate signal waveform.

   → 2 × SEW MOVIDRIVE MDX61B (with modified interface)

4. **[Optional] Torque transducer (`TS`):** A torque transducer is used to measure the shaft torque m_m measured between prime-mover `PM` and machine under test `IM`.

   → Lorenz DR-2212

5. **Real-time system (`RTS`):** The real-time system runs the control and identification routines and is interfaced with the physical test setup using various input / output (I/O) boards.

   → dSPACE Real-Time system

   - DS1007 - Processor board
   - DS5101 - PWM board (connected to `VSI1`, `VSI2`)
   - DS3002 - Encoder board (connected to `IM`, `PM`)
   - DS2001 - analog-to-digital converter (ADC) board (connected to `VSI1`, `VSI2`, `TS`)

6. **Host PC (`PC`):** The host PC is connected to the real-time system `RTS` via ethernet. It runs the required software to build real-time applications and provides online access while the application is running.

   → Custom-built workstation

   - Windows 10
   - MATLAB R2018b with dSPACE RCP/HiL Library
   - dSPACE ControlDesk 6.2

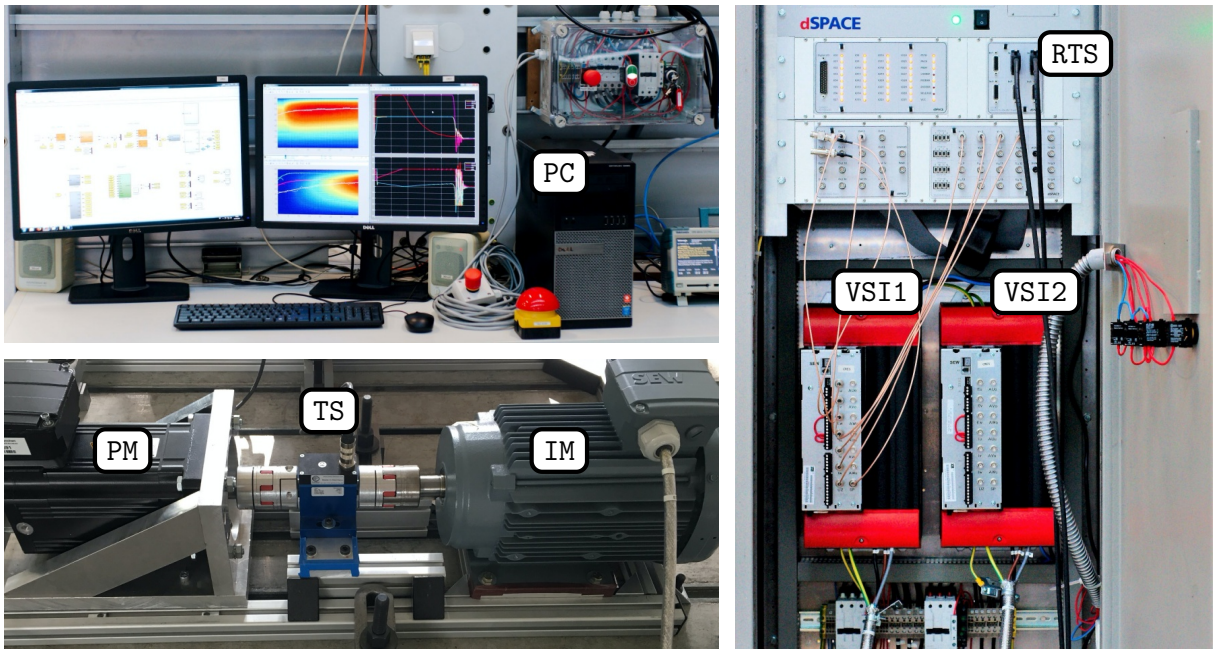

Figure B.1: *Experimental setup with induction machine under test `IM`, prime mover `PM`, torque sensor `TS`, inverters `VSI1` & `VSI2`, real-time system `RTS` and host computer `PC`.*

B.2 Testbench extension (LC filter)

For the control system evaluation, the basic testbench described in Sec. B.1 is extended by a custom-built LC filter and a measurement board (see Fig. B.2), equipped with additional current and voltage transducers so as to measure the stator phase currents $\boldsymbol{i}_{\mathrm{s}}^{\mathrm{abc}}$ and line-to-line voltages $\boldsymbol{u}_{\mathrm{s}}^{\mathrm{a\text{-}b\text{-}c}}$ (filter output), respectively. The electrical parameters of the LC filter are given in Tab. B.2.

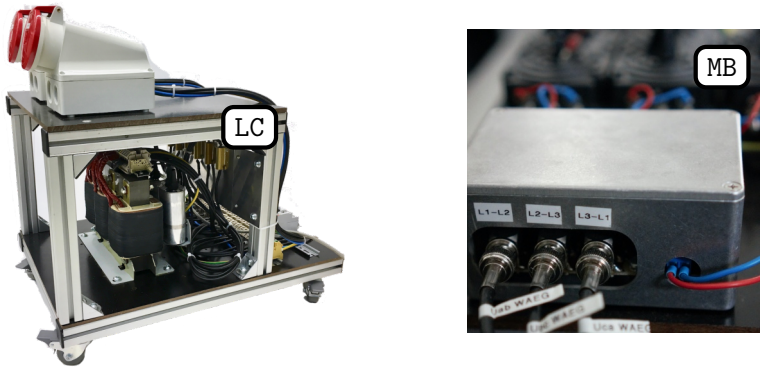

Figure B.2: *Extension of the experimental setup by a custom-built filter (`LC`) and a measurement board (`MB`).*

Table B.1: *Machine and inverter ratings of the laboratory equipment.*

	Parameter	Variable	Value	Unit
VSI	DC-link voltage	u_{dc}	565	V
	Switching frequency	f_{S}	8000	Hz
IM	Nominal speed	$\omega_{\mathrm{m,nom}}$	$2850/60 \cdot 2\pi$	$\mathrm{rad\,s^{-1}}$
	Nominal frequency	$\omega_{\mathrm{k,nom}}$	$50 \cdot 2\pi$	$\mathrm{rad\,s^{-1}}$
	Nominal torque	$m_{\mathrm{m,nom}}$	10.05	N m
	Nominal voltage (line-to-ground / peak)	$\hat{u}_{\mathrm{s,nom}}$	$400 \cdot \sqrt{2/3}$	V
	Nominal current (peak)	$\hat{i}_{\mathrm{s,nom}}$	$5.7 \cdot \sqrt{2}$	A
	Nominal flux (amplitude)	$\hat{\psi}_{\mathrm{r,nom}}$	1.2	Wb
	Nominal power factor	$\cos(\varphi_{\mathrm{nom}})$	0.93	
	Number of pole pairs	n_{p}	1	
	Stator resistance (20 °C)	R_{s}	2.4	Ω
	Rotor resistance (20 °C)	R_{r}	1.55	Ω
	Main inductance (linear)	L_{m}	$340 \cdot 10^{-3}$	H
	Stator leakage inductance (linear approx.)	$L_{\mathrm{s}\sigma}$	$16.5 \cdot 10^{-3}$	H
	Rotor leakage inductance (linear approx.)	$L_{\mathrm{r}\sigma}$	$16.5 \cdot 10^{-3}$	H
	Moment of inertia	Θ_{m}	$68.6 \cdot 10^{-4}$	$\mathrm{kg\,m^2}$
PM	Nominal speed	$\omega_{\mathrm{m,nom}}$	$6000/60 \cdot 2\pi$	$\mathrm{rad\,s^{-1}}$
	Nominal torque	$m_{\mathrm{m,nom}}$	18.7	N m
	Moment of inertia	Θ_{m}	$11.9 \cdot 10^{-4}$	$\mathrm{kg\,m^2}$

Table B.2: *LC filter ratings.*

	Parameter	Variable	Value	Unit
LC	Nominal voltage (line-to-ground / peak)	$\hat{u}_{\mathrm{f,nom}}$	$400 \cdot \sqrt{2/3}$	V
	Nominal current (peak)	$\hat{i}_{\mathrm{f,nom}}$	$7 \cdot \sqrt{2}$	A
	Filter resistance (20 °C)	R_{f}	$75 \cdot 10^{-3}$	Ω
	Filter inductance	L_{f}	$3.4 \cdot 10^{-3}$	H
	Filter capacitance	C_{f}	$28 \cdot 10^{-6}$	F
	Filter resonance frequency	f_{R1}	512	Hz

1*. **Induction machine (machine under test, `IM`):** The induction machine is now (electrically) connected to the output of the measurement board `MB`, instead of being directly connected to the inverter output. The mechanical connections, however, remain the same.

⋮

7. **LC filter (`LC`):** The input of the LC filter is connected to the output of `VSI1`, such that the measured inverter currents represent the filter input currents $\boldsymbol{i}_{\mathrm{f}}^{\mathrm{abc}}$ now, whereas the applied voltages at the inverter output become the filter input voltages $\boldsymbol{u}_{\mathrm{f}}^{\mathrm{abc}}$. The filter output, on the other hand, is connected to the input of the measurement board `MB`.

   → Custom-built

8. **Measurement board (`MB`):** A custom-built measurement board equipped with current and voltage transducers is employed in order to measure the `IM` currents $\boldsymbol{i}_{\mathrm{s}}^{\mathrm{abc}}$ and line-to-line voltages $\boldsymbol{u}_{\mathrm{s}}^{\text{a-b-c}}$ (filter output), respectively. Its inputs are connected to the outputs of the LC filter (`LC`), while its outputs are connected to the `IM` input terminals. The sensor data is processed by the DS2001 ADC boards of the dSPACE system (`RTS`).

   → Custom-built
   - LEM voltage transducer DVL 500
   - Sensitec current transducer CMS 3050ABA-KA

Appendix C

Additional topics related to the modeling chapter

This part of the appendix comprises additional topics regarding Ch. 2.

C.1 Pump calculations

In this section, analytic expressions for the impeller torque and head, respectively, are derived.

C.1.1 Impeller torque

Based on the conservation of momentum principle [114, p. 99], the load torque m_i is derived using Newton's second law, i.e. the rate of change of the angular momentum is equal to the resulting torque, which can be stated in terms of the control volume by the following equation

$$m_\mathrm{i} = \tfrac{\mathrm{d}}{\mathrm{d}t} \iiint_{\mathcal{V}} \rho\, r\, v(r) \mathrm{d}\mathcal{V}, \tag{C.1}$$

where the integral describes the total angular momentum occurring in the control volume $\mathcal{V}$ and $v_\perp$ is the tangential part of the absolute velocity v at radius r (see Fig. 2.17b). By applying Reynold's transport theorem (RTT; see e.g. [114, p. 103]), the equation above can be reformulated as

$$m_\mathrm{i} = \frac{\partial}{\partial t} \iiint_{\mathcal{V}} \rho\, r\, v_\perp(r) \mathrm{d}\mathcal{V} + \iint_{\partial\mathcal{V}} \rho\, r\, v_\perp(r) \boldsymbol{v}(r)^\top \mathcal{S}, \tag{C.2}$$

where the first integral describes the transient, and the second integral the steady-state part of the load torque, respectively. Since inlet and outlet surface of the impeller are not connected, the surface $\mathcal{S}$ is split into an inlet surface $\mathcal{S}_1$ (equal to $\partial\mathcal{V}_{in}$ in Fig. 2.17a) with normal vector pointing in $-r$ direction (by convention) and an outlet surface $\mathcal{S}_2$ (equal to $\partial\mathcal{V}_{out}$ in Fig. 2.17a) with normal vector pointing in $+r$ direction. Due to the dot product of the radially oriented infinitesimal surfaces and the absolute velocity, only the absolute value $v_\parallel(r)$ of the radial part of the velocity vector remains such that the impeller torque can be rewritten as

$$m_\mathrm{i} = \frac{\partial}{\partial t} \iiint_{\mathcal{V}} \rho r v_\perp(r) \mathrm{d}\mathcal{V} + \iint_{\partial\mathcal{V}_2} \rho r_2 v_\perp(r_2) v_\parallel(r_2) \mathrm{d}\mathcal{S}_2 - \iint_{\partial\mathcal{V}_1} \rho r_1 v_\perp(r_1) v_\parallel(r_1) \mathrm{d}\mathcal{S}_1, \tag{C.3}$$

Exploiting the cylindrical shape of the impeller, the volume flow can be defined as

$$Q_\mathrm{i} = 2\pi r h_\mathrm{i} v_\parallel, \tag{C.4}$$

where $v_\parallel$ is the radial component of the absolute velocity. Using basic trigonometry (see Fig. 2.17b), the tangential part $v_\perp$ of the absolute velocity can be expressed in terms of $v_\parallel$ and the angle β as

$$v_\perp(r) = \omega_\mathrm{i}\, r - v_\parallel(r)\cot(\beta(r)). \tag{C.5}$$

Invoking the infinitesimal volume $\mathrm{d}\mathcal{V} := r\mathrm{d}r\mathrm{d}\varphi\mathrm{d}z$ and the infinitesimal surfaces $\mathrm{d}\mathcal{S}_k := r_k\mathrm{d}\varphi\mathrm{d}\varphi$ for $k \in \{1, 2\}$ (both in cylindrical coordinates), and inserting (C.4) and (C.5) into (C.3) yields the impeller (load) torque as a function of rotational speed ω_i and volume flow Q_i, i.e.

$$m_\mathrm{i} = \underbrace{\vartheta \tfrac{\mathrm{d}}{\mathrm{d}t} Q_\mathrm{i} + \Theta_\mathrm{w} \tfrac{\mathrm{d}}{\mathrm{d}t}\omega_\mathrm{i}}_{\text{transient part}} + \underbrace{a_1 Q_\mathrm{i}^2 + a_2 Q_\mathrm{i}\omega_\mathrm{i}}_{\text{steady-state part}}, \tag{C.6}$$

with geometry dependent constants

$$\left.\begin{aligned} \vartheta &:= -\rho \int_{r_1}^{r_2} r\cot\beta(r)\mathrm{d}r, & \Theta_\mathrm{w} &:= 2\pi\rho h_\mathrm{i} \int_{r_1}^{r_2} r^3\mathrm{d}r, \\ a_1 &:= -\frac{\rho}{2\pi h_\mathrm{i}}(\cot\beta(r_2) - \cot\beta(r_1)) \quad \text{and} & a_2 &:= \rho(r_2^2 - r_1^2). \end{aligned}\right\} \tag{C.7}$$

The transient part of the torque is characterized by the constant ϑ describing the impact of flow variations on the load torque, and the constant Θ_w denoting the inertia of the fluid contained in the impeller. Moreover, the steady-state part of the load torque is characterized by the constants a_1 and a_2.

The derived torque equation is based on the change of the angular momentum inside the impeller. However, hydraulic friction between the rotating parts (impeller shrouds) and the liquid creates a drag opposing the rotation. This drag is called disk friction and causes additional power losses. Disk friction is modeled by an additional load torque component proportional to the rotational speed squared [22, Ch. 3.6.1], i.e. $m_\mathrm{df} = K_\mathrm{d}\omega_\mathrm{i}^2$, where K_d denotes the disk friction coefficient. The overall load torque of the impeller is hence given by

$$m_\mathrm{i} = \vartheta \tfrac{\mathrm{d}}{\mathrm{d}t} Q_\mathrm{i} + \Theta_\mathrm{w} \tfrac{\mathrm{d}}{\mathrm{d}t}\omega_\mathrm{i} + a_1 Q_\mathrm{i}^2 + a_2 Q_\mathrm{i}\omega_\mathrm{i} + a_3\omega_\mathrm{i}^2, \tag{C.8}$$

where, for conventional consistency, the constant $a_3 = K_\mathrm{d}$ accounting for disk friction was additionally introduced.

C.1.2 Impeller head

In analogy to the load torque derivation where the principle of conservation of momentum was used, the pressure—or head—created by the impeller can be derived using the conservation of energy principle (see e.g. [38, 112]). The total energy E_sys for a system of mass inside the control volume is given by [112]

$$E_\mathrm{sys} = \iiint_{\mathcal{V}} \rho\, e\, \mathrm{d}\mathcal{V} = W_\mathrm{t} + Q_\mathrm{t}, \tag{C.9}$$

which—according to the first law of thermodynamics—is equal to the sum of work W_t done on the system and heat Q_t (both in J) contained in the system. The variable e denotes the energy per unit mass. Taking the derivative of (C.9) and applying Reynold's transport theorem (RTT) as in (C.2) yields

$$\tfrac{\mathrm{d}}{\mathrm{d}t}E_\mathrm{sys} \overset{\text{(RTT)}}{=} \frac{\partial}{\partial t}\iiint_{\mathcal{V}} \rho\, e\, \mathrm{d}\mathcal{V} + \iint_{\partial\mathcal{V}} \rho\, e\, \boldsymbol{v}(r)^\top\, \mathrm{d}\boldsymbol{\mathcal{S}} \overset{\text{(C.9)}}{=} \tfrac{\mathrm{d}}{\mathrm{d}t}W_\mathrm{t} + \tfrac{\mathrm{d}}{\mathrm{d}t}Q_\mathrm{t}. \tag{C.10}$$

If it is assumed that the work done on the system is dominated by shaft and pressure work only [112, p. 203], the derivative of the total work then becomes

$$\tfrac{\mathrm{d}}{\mathrm{d}t}W_\mathrm{t} = \underbrace{\omega_\mathrm{i} m_\mathrm{i}}_{\text{shaft}} - \underbrace{\iint_{\partial\mathcal{V}} p\boldsymbol{v}(r)\cdot \mathrm{d}\boldsymbol{\mathcal{S}}}_{\text{pressure}}, \tag{C.11}$$

where p denotes the pressure and the derivative of the pressure work is negative by convention since work is done by the system [112, p. 204]. Moreover, if it is assumed that heat transfer across the system boundaries is negligible (see e.g. [112, p. 202]) since the fluid temperature is considered equal to the ambient temperature, i.e. $\frac{\mathrm{d}}{\mathrm{d}t}Q_\mathrm{t} \approx 0$ holds, Eq. (C.10) can be expressed as

$$\frac{\partial}{\partial t}\iiint_{\mathcal{V}} \rho e \mathrm{d}\mathcal{V} + \iint_{\partial\mathcal{V}} \rho e \boldsymbol{v}(r)^\top \mathrm{d}\boldsymbol{\mathcal{S}} \overset{\text{(C.11)}}{=} \omega_\mathrm{i} m_\mathrm{i} - \iint_{\partial\mathcal{V}} p\boldsymbol{v}(r)^\top \mathrm{d}\boldsymbol{\mathcal{S}}. \tag{C.12}$$

The total energy per unit mass is defined as (see [114, Ch. 6.4])

$$e = u + \tfrac{1}{2}v^2 + gz, \tag{C.13}$$

where u is the internal energy per unit mass, $\frac{1}{2}v^2$ is the kinetic energy per unit mass and gz is the potential energy per unit mass, with gravitational constant $g \approx 9.81\,\mathrm{m\,s^{-1}}$ and height z. Rearranging (C.12) and inserting (C.13) gives

$$\frac{\partial}{\partial t}\iiint_{\mathcal{V}} \rho\big(u + \tfrac{1}{2}v(r)^2 + gz\big)\mathrm{d}\mathcal{V} + \iint_{\partial\mathcal{V}} \rho\big(u + \frac{1}{2}v^2 + gz + \tfrac{1}{\rho}p\big)\boldsymbol{v}(r)^\top \mathrm{d}\boldsymbol{\mathcal{S}} = \omega_\mathrm{i} m_\mathrm{i}. \tag{C.14}$$

As in Section C.1.1, the surface integral is evaluated at the inlet and outlet surfaces, respectively. Moreover, the time derivative of the potential energy is zero, since the pump is assumed to be in a fixed position (height is not changing). Using $v^2 = v_\perp^2 + v_\parallel^2$ (see Fig. 2.17b) and invoking (C.4), (C.5) and (C.6), the integrals can be solved as follows

$$\underbrace{\frac{\partial}{\partial t}\iiint_{\mathcal{V}} \rho u \mathrm{d}\mathcal{V}}_{=\vartheta\frac{\mathrm{d}}{\mathrm{d}t}S} + \vartheta\tfrac{\mathrm{d}}{\mathrm{d}t}\omega_\mathrm{i} + \frac{\rho}{2\pi h_\mathrm{i}}\int_{r_1}^{r_2} \frac{1}{r\sin^2\beta(r)}\mathrm{d}r\,\tfrac{\mathrm{d}}{\mathrm{d}t}Q_\mathrm{i} + \rho g H_\mathrm{i} + \rho g H_\lambda = a_1\omega_\mathrm{i}Q_\mathrm{i} + a_2\omega_\mathrm{i}^2. \tag{C.15}$$

Since the fluid is assumed to be incompressible (see Assumption 8), the first term on the left-hand side can be referred to as the time rate of change of the fluid entropy S times the fluid temperature ϑ, which is neglected in the following [38] since it is assumed to change slowly, compared to the other system quantities. Based on Bernoulli's equation [22, p. 4], head H_i and head loss H_λ are defined as

$$H_\mathrm{i} := \frac{1}{2g}(v_\mathrm{o}^2 - v_\mathrm{i}^2) + \frac{1}{\rho g}(p_\mathrm{o} - p_\mathrm{i}) - (z_\mathrm{o} - z_\mathrm{i}), \qquad H_\lambda := \frac{1}{g}(u_\mathrm{o} - u_\mathrm{i}), \tag{C.16}$$

with velocities v_i and v_o, pressures p_i and p_o and vertical rise z_i and z_o evaluated at the inlet and outlet radii r_1 and r_2, respectively. Finally, the head equation can be stated as

$$H_\mathrm{i} = -\Gamma_\mathrm{w} \tfrac{\mathrm{d}}{\mathrm{d}t} Q_\mathrm{i} + \gamma \tfrac{\mathrm{d}}{\mathrm{d}t} \omega_\mathrm{i} + b_2^* \omega_\mathrm{i} Q_\mathrm{i} + b_3^* \omega_\mathrm{i}^2 - H_\lambda, \tag{C.17}$$

with geometry dependent but constant parameters

$$\Gamma_\mathrm{w} := \frac{1}{2\pi g h_\mathrm{i}} \int_{r_1}^{r_2} \frac{1}{r \sin^2 \beta(r)} \mathrm{d}r, \qquad \gamma := -\frac{\vartheta}{\rho g} = \frac{1}{g} \int_{r_1}^{r_2} r \cot \beta(r) \mathrm{d}r, \tag{C.18}$$

$$b_2^* := \frac{a_1}{\rho g} = -\frac{1}{2\pi g h_\mathrm{i}} (\cot \beta(r_2) - \cot \beta(r_1)) \qquad \text{and} \qquad b_3^* := \frac{a_2}{\rho g} = \frac{1}{g}(r_2^2 - r_1^2). \tag{C.19}$$

Again, Eq. (C.17) consists of a transient part and a steady-state part. The former is characterized by the (scaled) fluid inertia Γ_w and a constant γ which describes the impact of speed variations on the produced head. The steady-state part excluding losses is described by the constants b_2^* and b_3^* and is referred to as theoretical head.

Due to various fluid dynamical effects such as flow separation, secondary flow or recirculation, the output velocity distribution of the fluid is non-uniform as opposed to the mean streamline assumption (see Assumption 7). In fact, the tangential speed at the impeller outlet is reduced (on average) and does not achieve the theoretically calculated value in a real system. This lack of model accuracy is accounted for by introducing the so-called *slip factor* σ_s, an empirical constant describing the ratio of actual $v_\perp(r_2)$ over theoretical $v_\perp^*(r_2)$ output tangential velocity, i.e. $\sigma_\mathrm{s} := v_\perp(r_2)/v_\perp^*(r_2)$. Typically, the slip factor lies in the range of 0.9 [22, pp. 75 ff.]. Hydraulic losses such as hydraulic friction or shock losses further decrease the produced head (see e.g. [22]). Hydraulic friction occurs when fluid is flowing in close vicinity to solid materials and can be modeled by introducing the head loss $H_{\lambda,\mathrm{f}} = K_\mathrm{fi} Q_\mathrm{i}^2$, with material specific constant K_fi. Shock, or incidence, losses occur when the flow enters the impeller at an angle other than the blade angle and subsequently has to adjust its direction abruptly. At design conditions shock losses are zero. However, for off-design flow they can be modeled by $H_{\lambda,\mathrm{v}} = K_{\mathrm{s}1}(K_{\mathrm{s}2}\omega_\mathrm{i} - Q_\mathrm{i})^2$, where $K_{\mathrm{s}1}$ and $K_{\mathrm{s}2}$ are constants and $K_{\mathrm{s}2}\omega_\mathrm{i}$ is the design flow [36].

In conclusion, the overall impeller head *including* losses can be modeled as follows

$$H_\mathrm{i} = -\Gamma_\mathrm{w} \tfrac{\mathrm{d}}{\mathrm{d}t} Q_\mathrm{i} + \gamma \tfrac{\mathrm{d}}{\mathrm{d}t} \omega_\mathrm{i} + b_1 Q_\mathrm{i}^2 + b_2 \omega_\mathrm{i} Q_\mathrm{i} + b_3 \omega_\mathrm{i}^2, \tag{C.20}$$

with the new set of constants

$$b_1 := -K_\mathrm{fi} - K_{\mathrm{s}1}, \tag{C.21}$$

$$b_2 := 2K_{\mathrm{s}1}K_{\mathrm{s}2} - \frac{1}{2\pi g h_\mathrm{i}} (\sigma_\mathrm{s} \cot \beta(r_2) - \cot \beta(r_1)), \tag{C.22}$$

$$b_3 := \frac{1}{g}(\sigma_\mathrm{s} r_2^2 - r_1^2) - K_{\mathrm{s}1} K_{\mathrm{s}2}^2. \tag{C.23}$$

Finding analytical expressions for the derived coefficients is generally a complicated task, so that experimentally obtained pump curves are used to fit the parameters. These curves are typically provided by pump manufacturers.

C.2 Transformation of physical capacitances to line capacitances

The PUL model capacitances $\boldsymbol{C}_{\mathrm{c}}^{\prime\mathrm{abc}}$ used in the state-space description of the cable segments must be derived from the actual physical capacitances among conductors and between conductors and ground, respectively. Given a capacitive coupling network (as used in the π- and T-equivalent circuits depicted in Figs. C.2 and 2.9) with line-to-ground capacitances $C_{\mathrm{c}}^{\prime k\text{-}0}$ and line-to-line capacitances $C_{\mathrm{c}}^{\prime k\text{-}j}, C_{\mathrm{c}}^{\prime k\text{-}l}$, the model self capacitances $C_{\mathrm{c}}^{\prime kk}$ and mutual capacitances $C_{\mathrm{c}}^{\prime kj}$ for $j,k,l \in \{\mathrm{a},\mathrm{b},\mathrm{c}\}, k \neq j, k \neq l$ can be derived using circuit analysis of the network. In the following the derivation is conducted exemplarily for phase k. Figure C.1 illustrates the corresponding voltage meshes and current nodes that are used to derive the relation between model capacitances and physical capacitances. The line-to-line voltages are denoted by $u_{\mathrm{c}}^{k\text{-}j}$, the phase voltages by u_{c}^{k}, the line input and output currents by $i_{\mathrm{c_i}}^{k}$ and $i_{\mathrm{c_o}}^{k}$, respectively, the inter-phase currents by $i_{\mathrm{c}}^{k\text{-}j}$ and the voltage between the phase reference Y and ground by u_{c}^{0}.

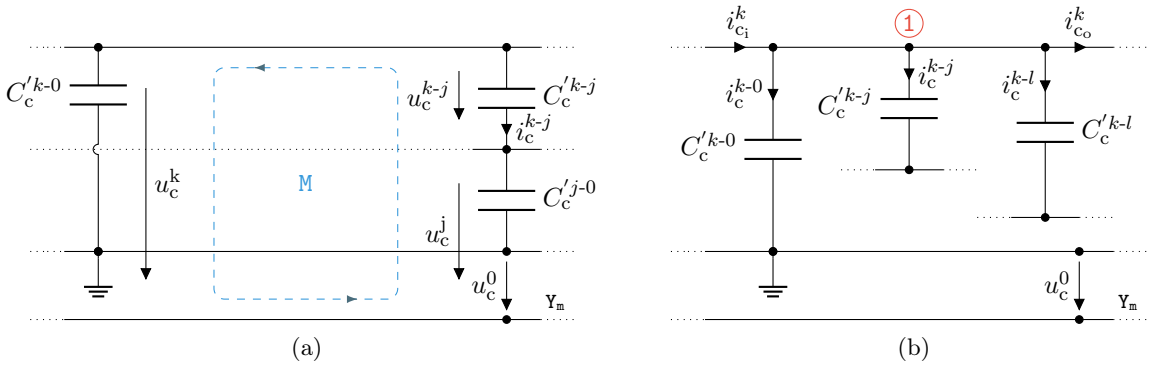

Figure C.1: *Isolated capacitance network of the π- and T-cable equivalent circuits: (a) Voltage mesh for phase k over phase j to ground, and (b) currents flowing from and to phase k.*

In (a) a voltage mesh (M) is drawn, comprising the voltages across the capacitances between phase k and ground, between phase j and ground and between phases k and j, respectively. Applying KVL yields

$$u_{\mathrm{c}}^{k\text{-}j} = u_{\mathrm{c}}^{k} - u_{\mathrm{c}}^{j}. \tag{C.24}$$

In (b) the currents associated with phase k are shown. The inter-phase currents can be stated as

$$i_{\mathrm{c}}^{k\text{-}j} = C_{\mathrm{c}}^{\prime k\text{-}j} \frac{\mathrm{d}}{\mathrm{d}t} u_{\mathrm{c}}^{k\text{-}j} \overset{(C.24)}{=} C_{\mathrm{c}}^{\prime k\text{-}j} \frac{\mathrm{d}}{\mathrm{d}t} u_{\mathrm{c}}^{k} - C_{\mathrm{c}}^{\prime k\text{-}j} \frac{\mathrm{d}}{\mathrm{d}t} u_{\mathrm{c}}^{j} \tag{C.25}$$

and, analogously,

$$i_{\mathrm{c}}^{k\text{-}l} = C_{\mathrm{c}}^{\prime k\text{-}l} \frac{\mathrm{d}}{\mathrm{d}t} u_{\mathrm{c}}^{k\text{-}l} = C_{\mathrm{c}}^{\prime k\text{-}l} \frac{\mathrm{d}}{\mathrm{d}t} u_{\mathrm{c}}^{k} - C_{\mathrm{c}}^{\prime k\text{-}l} \frac{\mathrm{d}}{\mathrm{d}t} u_{\mathrm{c}}^{l}. \tag{C.26}$$

Now, by applying KCL on node (1), the line-to-line voltages can be eliminated, i.e.

$$
\begin{aligned}
i_{\mathrm{c_i}}^{k} - i_{\mathrm{c_o}}^{k} &= i_{\mathrm{c}}^{k\text{-}0} + i_{\mathrm{c}}^{k\text{-}j} + i_{\mathrm{c}}^{k\text{-}l} \\
&\overset{(C.25),(C.26)}{=} C_{\mathrm{c}}^{\prime k\text{-}0}\left(\tfrac{\mathrm{d}}{\mathrm{d}t}u_{\mathrm{c}}^{k} - \tfrac{\mathrm{d}}{\mathrm{d}t}u_{\mathrm{c}}^{0}\right) + C_{\mathrm{c}}^{\prime k\text{-}j}\left(\tfrac{\mathrm{d}}{\mathrm{d}t}u_{\mathrm{c}}^{k} - \tfrac{\mathrm{d}}{\mathrm{d}t}u_{\mathrm{c}}^{j}\right) + C_{\mathrm{c}}^{\prime k\text{-}l}\left(\tfrac{\mathrm{d}}{\mathrm{d}t}u_{\mathrm{c}}^{k} - \tfrac{\mathrm{d}}{\mathrm{d}t}u_{\mathrm{c}}^{l}\right) \\
&= \left(C_{\mathrm{c}}^{\prime k\text{-}0} + C_{\mathrm{c}}^{\prime k\text{-}j} + C_{\mathrm{c}}^{\prime k\text{-}l}\right)\tfrac{\mathrm{d}}{\mathrm{d}t}u_{\mathrm{c}}^{k} - C_{\mathrm{c}}^{\prime k\text{-}j}\tfrac{\mathrm{d}}{\mathrm{d}t}u_{\mathrm{c}}^{j} - C_{\mathrm{c}}^{\prime k\text{-}l}\tfrac{\mathrm{d}}{\mathrm{d}t}u_{\mathrm{c}}^{l} - C_{\mathrm{c}}^{\prime k\text{-}0}\tfrac{\mathrm{d}}{\mathrm{d}t}u_{\mathrm{c}}^{0}.
\end{aligned}
\tag{C.27}
$$

It follows that the self capacitance is determined by $C_{\mathrm{c}}^{\prime kk} = C_{\mathrm{c}}^{\prime k\text{-}0} + C_{\mathrm{c}}^{\prime k\text{-}j} + C_{\mathrm{c}}^{\prime k\text{-}l}$, while the mutual capacitances are given by $C_{\mathrm{c}}^{\prime kj} = -C_{\mathrm{c}}^{\prime k\text{-}j}$ and $C_{\mathrm{c}}^{\prime kl} = -C_{\mathrm{c}}^{\prime k\text{-}l}$. Note that the zero voltage vector u_{c}^{0} will be eliminated by applying the reduced Clarke transformation.

C.3 Cable T-equivalent circuit

The equivalent circuit of the T-segment is shown in Fig. C.2, with input voltages $\boldsymbol{u}_{\mathrm{c},\tau_{\mathrm{i}}}^{\mathrm{abc}}$, input currents $\boldsymbol{i}_{\mathrm{c},\tau_{\mathrm{i}}}^{\mathrm{abc}}$, output voltages $\boldsymbol{u}_{\mathrm{c},\tau_{\mathrm{o}}}^{\mathrm{abc}}$, output currents $\boldsymbol{i}_{\mathrm{c},\tau_{\mathrm{o}}}^{\mathrm{abc}}$ and voltages across the capacitances $\boldsymbol{u}_{\mathrm{c},\tau}^{\mathrm{abc}}$. Moreover, the T-model parameters are given by

$$
\boldsymbol{R}_{\mathrm{c},\tau}^{\mathrm{abc}} = \mathrm{diag}(R_{\mathrm{c},\tau}^{\mathrm{a}}, R_{\mathrm{c},\tau}^{\mathrm{b}}, R_{\mathrm{c},\tau}^{\mathrm{c}}) = \frac{1}{4} l_{\mathrm{c}} \boldsymbol{R}_{\mathrm{c}}^{\prime\mathrm{abc}}, \quad \boldsymbol{L}_{\mathrm{c},\tau}^{\mathrm{abc}} = \frac{1}{4} l_{\mathrm{c}} \boldsymbol{L}_{\mathrm{c}}^{\prime\mathrm{abc}} \quad \text{and} \quad \boldsymbol{C}_{\mathrm{c},\tau}^{\mathrm{abc}} = \frac{1}{2} l_{\mathrm{c}} \boldsymbol{C}_{\mathrm{c}}^{\prime\mathrm{abc}}. \tag{C.28}
$$

Note that, for inductances and resistances, half of the respective values were considered on the input and the other half on the output of the T-segment.

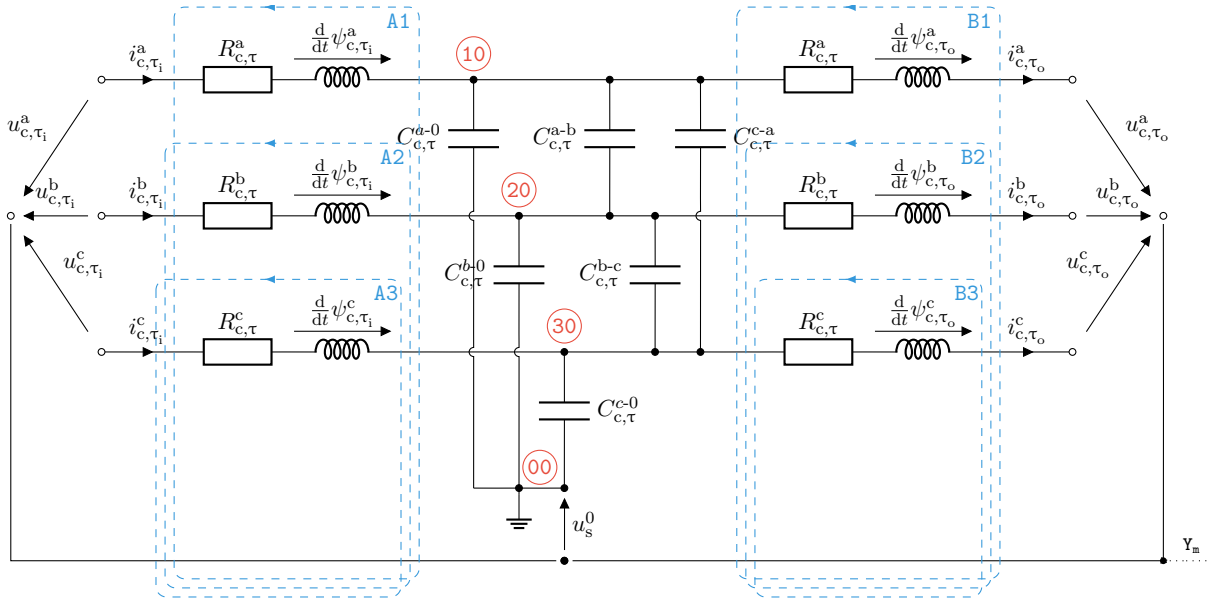

Figure C.2: *Equivalent circuit of the power cable T-segment.*

As for the π-segment, the state-space description can be derived using circuit analysis. For the T-model, evaluating meshes (A1) to (A3), meshes (B1) to (B3) and nodes (00) to (30) yields

$$\frac{\mathrm{d}}{\mathrm{d}t}\begin{pmatrix}\boldsymbol{i}_{\mathrm{c},\tau_\mathrm{i}}^{\mathrm{abc}}\\ \boldsymbol{u}_{\mathrm{c},\tau}^{\mathrm{abc}}\\ \boldsymbol{i}_{\mathrm{c},\tau_\mathrm{o}}^{\mathrm{abc}}\end{pmatrix} = \begin{bmatrix}-(\boldsymbol{L}_{\mathrm{c},\tau}^{\mathrm{abc}})^{-1}\boldsymbol{R}_{\mathrm{c},\tau}^{\mathrm{abc}} & -(\boldsymbol{L}_{\mathrm{c},\tau}^{\mathrm{abc}})^{-1} & \mathbf{0}_{3\times3}\\ (\boldsymbol{C}_{\mathrm{c},\tau}^{\mathrm{abc}})^{-1} & \mathbf{0}_{3\times3} & -(\boldsymbol{C}_{\mathrm{c},\tau}^{\mathrm{abc}})^{-1}\\ \mathbf{0}_{3\times3} & (\boldsymbol{L}_{\mathrm{c},\tau}^{\mathrm{abc}})^{-1} & -(\boldsymbol{L}_{\mathrm{c},\tau}^{\mathrm{abc}})^{-1}\boldsymbol{R}_{\mathrm{c},\tau}^{\mathrm{abc}}\end{bmatrix}\begin{pmatrix}\boldsymbol{i}_{\mathrm{c},\tau_\mathrm{i}}^{\mathrm{abc}}\\ \boldsymbol{u}_{\mathrm{c},\tau}^{\mathrm{abc}}\\ \boldsymbol{i}_{\mathrm{c},\tau_\mathrm{o}}^{\mathrm{abc}}\end{pmatrix} + \begin{bmatrix}(\boldsymbol{L}_{\mathrm{c},\tau}^{\mathrm{abc}})^{-1} & \mathbf{0}_{3\times3}\\ \mathbf{0}_{3\times3} & \mathbf{0}_{3\times3}\\ \mathbf{0}_{3\times3} & -(\boldsymbol{L}_{\mathrm{c},\tau}^{\mathrm{abc}})^{-1}\end{bmatrix}\begin{pmatrix}\boldsymbol{u}_{\mathrm{c},\tau_\mathrm{i}}^{\mathrm{abc}}\\ \boldsymbol{u}_{\mathrm{c},\tau_\mathrm{o}}^{\mathrm{abc}}\end{pmatrix} + \underbrace{\begin{pmatrix}(\boldsymbol{L}_{\mathrm{c},\tau}^{\mathrm{abc}})^{-1}\\ \mathbf{0}_{3\times3}\\ -(\boldsymbol{L}_{\mathrm{c},\tau}^{\mathrm{abc}})^{-1}\end{pmatrix}\mathbf{1}_3 u_\mathrm{s}^0}_{\circledast}, \tag{C.29}$$

where u_s^0 denotes the voltage between motor star point $\mathtt{Y}_\mathtt{m}$ and ground. Applying the reduced Clarke transformation as in (A.4) eliminates the term $\circledast$, i.e. $\boldsymbol{T}_{\mathrm{C,red}}\mathbf{1}_3 u_\mathrm{s}^0 = \mathbf{o}_2$, such that the state-space description of the T-segment in the $\alpha\beta$-reference frame can be stated as

$$\frac{\mathrm{d}}{\mathrm{d}t}\begin{pmatrix}\boldsymbol{i}_{\mathrm{c},\tau_\mathrm{i}}^{\alpha\beta}\\ \boldsymbol{u}_{\mathrm{c},\tau}^{\alpha\beta}\\ \boldsymbol{i}_{\mathrm{c},\tau_\mathrm{o}}^{\alpha\beta}\end{pmatrix} = \begin{bmatrix}-(\boldsymbol{L}_{\mathrm{c},\tau}^{\alpha\beta})^{-1}\boldsymbol{R}_{\mathrm{c},\tau}^{\alpha\beta} & -(\boldsymbol{L}_{\mathrm{c},\tau}^{\alpha\beta})^{-1} & \mathbf{0}_{2\times2}\\ (\boldsymbol{C}_{\mathrm{c},\tau}^{\alpha\beta})^{-1} & \mathbf{0}_{2\times2} & -(\boldsymbol{C}_{\mathrm{c},\tau}^{\alpha\beta})^{-1}\\ \mathbf{0}_{2\times2} & (\boldsymbol{L}_{\mathrm{c},\tau}^{\alpha\beta})^{-1} & -(\boldsymbol{L}_{\mathrm{c},\tau}^{\alpha\beta})^{-1}\boldsymbol{R}_{\mathrm{c},\tau}^{\alpha\beta}\end{bmatrix}\begin{pmatrix}\boldsymbol{i}_{\mathrm{c},\tau_\mathrm{i}}^{\alpha\beta}\\ \boldsymbol{u}_{\mathrm{c},\tau}^{\alpha\beta}\\ \boldsymbol{i}_{\mathrm{c},\tau_\mathrm{o}}^{\alpha\beta}\end{pmatrix} + \begin{bmatrix}(\boldsymbol{L}_{\mathrm{c},\tau}^{\alpha\beta})^{-1} & \mathbf{0}_{2\times2}\\ \mathbf{0}_{2\times2} & \mathbf{0}_{2\times2}\\ \mathbf{0}_{2\times2} & -(\boldsymbol{L}_{\mathrm{c},\tau}^{\alpha\beta})^{-1}\end{bmatrix}\begin{pmatrix}\boldsymbol{u}_{\mathrm{c},\tau_\mathrm{i}}^{\alpha\beta}\\ \boldsymbol{u}_{\mathrm{c},\tau_\mathrm{o}}^{\alpha\beta}\end{pmatrix}. \tag{C.30}$$

For the T-segment, the input voltage $\boldsymbol{u}_{\mathrm{c},\tau_\mathrm{i}}^{\alpha\beta}$ is equal to the filter output $\boldsymbol{u}_{\mathrm{f_o}}^{\alpha\beta}$ and the output voltage $\boldsymbol{u}_{\mathrm{f_o}}^{\alpha\beta}$ is equal to the stator voltage of the electrical machine.

Remark 27. *For flat-type cable layouts, the PUL inductances of the power cable are not identical for each phase, resulting in a non-diagonal inductance matrix. However, for the T-segment, the inductance matrix of the machine-side cable inductances needs to be added to the machine inductances, which significantly complicates the mathematical description of the induction machine. Therefore, it is recommended using the π-description here, since in this case scalar inductances can be used (for the fault-free case).*

Appendix D

Additional topics related to the efficiency optimization chapter

This part of the appendix comprises additional topics regarding Ch. 3.

D.1 Stator differential inductance maps

For synchronous machines, the stator flux linkages are functions of the stator currents only, provided that iron losses are negligible. On the contrary, for induction machines, the stator flux linkages (and rotor flux linkages alike) are functions of both, stator *and* rotor currents, i.e. $\boldsymbol{\psi}_\mathrm{s}^\mathrm{dq} = \boldsymbol{\psi}_\mathrm{s}^\mathrm{dq}(\boldsymbol{i}_\mathrm{s}^\mathrm{dq}, \boldsymbol{i}_\mathrm{r}^\mathrm{dq})$ and $\boldsymbol{\psi}_\mathrm{r}^\mathrm{dq} = \boldsymbol{\psi}_\mathrm{r}^\mathrm{dq}(\boldsymbol{i}_\mathrm{s}^\mathrm{dq}, \boldsymbol{i}_\mathrm{r}^\mathrm{dq})$. However, in steady-state, the rotor currents are fully determined by the stator currents, hence being functions of the stator currents themselves, i.e. $\boldsymbol{i}_\mathrm{r}^\mathrm{dq} = \boldsymbol{i}_\mathrm{r}^\mathrm{dq}(\boldsymbol{i}_\mathrm{s}^\mathrm{dq})$. Therefore, the *steady-state* stator flux linkages become functions of the stator currents only, i.e. $\boldsymbol{\psi}_\mathrm{s}^\mathrm{dq} = \boldsymbol{\psi}_\mathrm{s}^\mathrm{dq}(\boldsymbol{i}_\mathrm{s}^\mathrm{dq}, \boldsymbol{i}_\mathrm{r}^\mathrm{dq}(\boldsymbol{i}_\mathrm{s}^\mathrm{dq})) = \boldsymbol{\psi}_\mathrm{s}^\mathrm{dq}(\boldsymbol{i}_\mathrm{s}^\mathrm{dq})$. Defining the differential inductance as the partial derivative of flux linkage with respect to current, the differential inductance matrix can be stated as

$$\boldsymbol{L}_\mathrm{s}^\mathrm{dq} = \begin{bmatrix} L_\mathrm{s}^\mathrm{dd} & L_\mathrm{s}^\mathrm{dq} \\ L_\mathrm{s}^\mathrm{qd} & L_\mathrm{s}^\mathrm{qq} \end{bmatrix} := \frac{\partial \boldsymbol{\psi}_\mathrm{s}^\mathrm{dq}(\boldsymbol{i}_\mathrm{s}^\mathrm{dq})}{\partial \boldsymbol{i}_\mathrm{s}^\mathrm{dq}} = \begin{bmatrix} \frac{\partial \psi_\mathrm{s}^\mathrm{d}(\boldsymbol{i}_\mathrm{s}^\mathrm{dq})}{\partial i_\mathrm{s}^\mathrm{d}} & \frac{\partial \psi_\mathrm{s}^\mathrm{d}(\boldsymbol{i}_\mathrm{s}^\mathrm{dq})}{\partial i_\mathrm{s}^\mathrm{q}} \\ \frac{\partial \psi_\mathrm{s}^\mathrm{q}(\boldsymbol{i}_\mathrm{s}^\mathrm{dq})}{\partial i_\mathrm{s}^\mathrm{d}} & \frac{\partial \psi_\mathrm{s}^\mathrm{q}(\boldsymbol{i}_\mathrm{s}^\mathrm{dq})}{\partial i_\mathrm{s}^\mathrm{q}} \end{bmatrix}, \tag{D.1}$$

where $L_\mathrm{s}^\mathrm{dq} = L_\mathrm{s}^\mathrm{qd}$ holds (see e.g. [6]). The resulting differential inductance maps are shown in Fig. D.1. Note that, as the results are valid for steady-state conditions only, the inductance maps are plotted merely for illustrative purposes.

D.2 Power loss maps (decomposition of losses)

As no power is lost in a closed system, the steady-state active power measured at the (electrical) machine terminals comprises the useable electrical power which is converted into mechanical power and all power losses within the machine which are converted into heat. Irrespective of its composition, the *sum* of power losses p_λ is calculated as the difference between input and output power, independent of the direction of power flow, i.e. $p_\lambda = |\hat{p}_\mathrm{e} - p_\mathrm{m}|$. If the individual loss terms are to be quantified, the sum of losses can be written as

$$p_\lambda = p_\mathrm{cu,s} + p_\mathrm{cu,r} + p_\mathrm{fe} = \tfrac{3}{2} R_\mathrm{s}(\vartheta_\mathrm{s}) \|\boldsymbol{i}_\mathrm{s}^\mathrm{dq}\|^2 + \tfrac{3}{2} R_\mathrm{r}(\vartheta_\mathrm{r}) \|\boldsymbol{i}_\mathrm{r}^\mathrm{dq}\|^2 + \tfrac{3}{2} R_\mathrm{c}(\vartheta_\mathrm{c}) \|\boldsymbol{i}_\mathrm{c}^\mathrm{dq}\|^2, \tag{D.2}$$

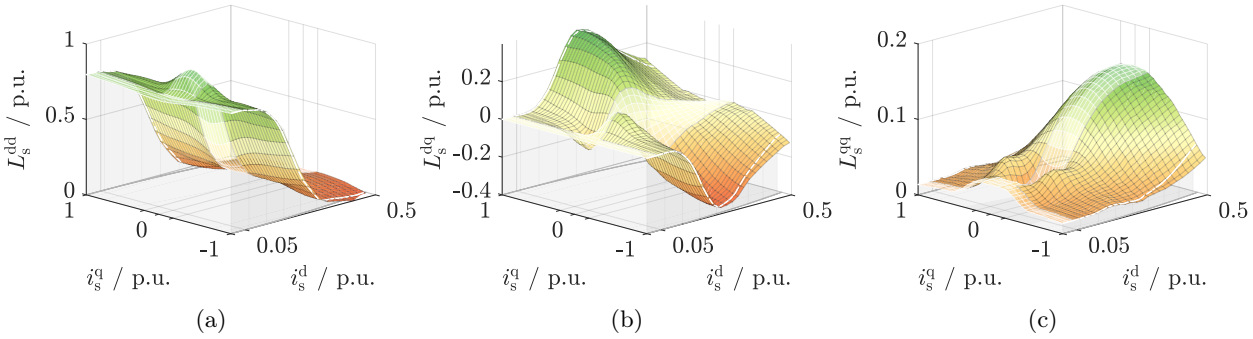

Figure D.1: *Machine maps (1. & 4. quadrant) recorded at* $\omega_\mathrm{m} = 0.5\,\omega_\mathrm{m,nom}$*: (a) stator* d*-inductance, (b) stator cross-coupling inductance and (c) stator* q*-inductance.*

where $p_\mathrm{cu,s}$, $p_\mathrm{cu,r}$ and p_fe denote the stator and rotor copper losses and the iron losses, respectively. While the stator copper losses can be estimated using the estimated stator resistance, i.e.

$$\hat{p}_\mathrm{cu,s} = \tfrac{3}{2}\hat{R}_\mathrm{s}\|\boldsymbol{i}_\mathrm{s}^\mathrm{dq}\|^2, \tag{D.3}$$

the like is not possible for the rotor and core losses, since neither current is measured. However, if the machine torque is measured, the rotor copper losses can be derived from the steady-state rotor voltage equation in (3.8) as

$$p_\mathrm{cu,r} = \tfrac{1}{n_\mathrm{p}}(\omega_\mathrm{k} - \omega_\mathrm{r})m_\mathrm{m,r}. \tag{D.4}$$

Note that the expression above is almost free of parameters and only depends on measured or known quantities, which makes it less prone to errors. An estimation of the core losses can be derived from the steady-state core voltage equation in (3.8) as

$$\hat{p}_\mathrm{fe} = \tfrac{1}{n_\mathrm{p}}\omega_\mathrm{k}(\hat{m}_\mathrm{m} - m_\mathrm{m,r}) \overset{(3.24)}{\approx} \tfrac{1}{n_\mathrm{p}}\omega_\mathrm{k}(m_\mathrm{m,s} - m_\mathrm{m,r}) \overset{(3.4)}{=} \tfrac{1}{n_\mathrm{p}}\omega_\mathrm{k}m_\mathrm{m,c}. \tag{D.5}$$

If the stator resistance is tracked and a good approximation of the stator-side torque can be calculated, a very precise decomposition of the individual power loss terms can be achieved. The power loss maps are shown in Fig. D.2. Apparently, for the given speed of $\omega_\mathrm{m} = 0.5\,\omega_\mathrm{m,nom}$, (a) stator and (b) rotor copper losses dominate the overall losses, whereas (c) iron losses appear to be negligible indeed.

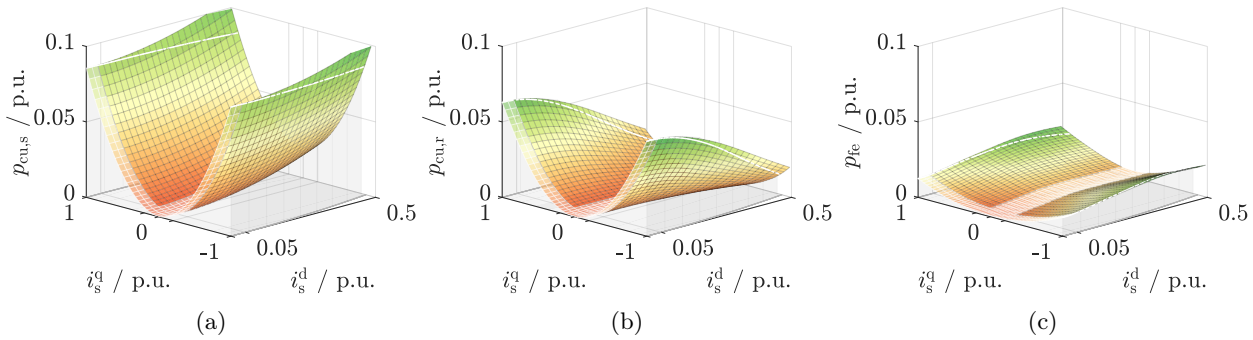

Figure D.2: *Machine maps (1. & 4. quadrant) recorded at* $\omega_\mathrm{m} = 0.5\,\omega_\mathrm{m,nom}$*: (a) Stator copper losses, (b) rotor copper losses and (c) iron losses.*

Appendix E

Additional topics related to the control chapter

This part of the appendix comprises additional topics regarding Ch. 4.

E.1 Exact discretization of a continuous-time plant with zero-order hold input

The general solution $\boldsymbol{x}(t)$ of some continuous-time LTI system

$$\tfrac{\mathrm{d}}{\mathrm{d}t}\boldsymbol{x}(t) = \boldsymbol{A}\boldsymbol{x}(t) + \boldsymbol{B}\boldsymbol{u}(t), \qquad \boldsymbol{x}(t_0) = x_0 \tag{E.1}$$

is given by (see [144, p. 170])

$$x(t) = \operatorname{expm}\left(\boldsymbol{A}(t-t_0)\right)\boldsymbol{x}(t_0) + \int_{t_0}^{t} \operatorname{expm}\left(\boldsymbol{A}(t-\tau)\right)\boldsymbol{B}\boldsymbol{u}(\tau)\mathrm{d}\tau, \quad t > t_0 \tag{E.2}$$

where expm(...) denotes the matrix exponential function. Assume now that the sampling occurs at time instant $k\,T_\mathrm{S}$, for $k \in \mathbb{N}$, and the input $\boldsymbol{u}(t)$ is considered constant over the interval $k\,T_\mathrm{S} \leq t \leq (k+1)T_\mathrm{S}$ (zero-order hold input). Then, the solution of (E.2) can be calculated explicitly (refer to [144, pp. 170, 171] for details) by

$$\boldsymbol{x}((k+1)T_\mathrm{S}) = \operatorname{expm}\left(\boldsymbol{A}T_\mathrm{S}\right)\boldsymbol{x}(kT_\mathrm{S}) + \left[\operatorname{expm}\left(\boldsymbol{A}T_\mathrm{S}\right) - \boldsymbol{I}_n\right]\boldsymbol{A}^{-1}\boldsymbol{B}\boldsymbol{u}(kT_\mathrm{S}) \tag{E.3}$$

Now, denoting $\boldsymbol{x}(kT_\mathrm{S})$ by $\boldsymbol{x}[k]$, and defining

$$\boldsymbol{\mathcal{A}} := \operatorname{expm}\left(\boldsymbol{A}T_\mathrm{S}\right), \qquad \boldsymbol{\mathcal{B}} := \left[\operatorname{expm}\left(\boldsymbol{A}T_\mathrm{S}\right) - \boldsymbol{I}_n\right]\boldsymbol{A}^{-1}\boldsymbol{B}, \tag{E.4}$$

the discrete-time equivalent of (E.1) can be stated as

$$\boldsymbol{x}[k+1] = \boldsymbol{\mathcal{A}}\boldsymbol{x}[k] + \boldsymbol{\mathcal{B}}\boldsymbol{u}[k]. \tag{E.5}$$

Solving (E.4) by calculating the matrix exponential $\operatorname{expm}\left(\boldsymbol{A}T_\mathrm{S}\right)\boldsymbol{x}(k\,T_\mathrm{S})$ yields what is called the *exact* discretization. However, as solving the matrix exponential and calculating the inverse of

the system matrix (required for $\boldsymbol{\mathcal{B}}$) is computationally expensive, the matrix exponential can be expressed using its series expansion [134, p. 90]

$$\operatorname{expm}(\boldsymbol{A}T_\mathrm{S}) = \boldsymbol{I}_n + \overbrace{\left[\sum_{i=1}^{\infty} \frac{T_\mathrm{S}^i}{i!}\boldsymbol{A}^{i-1}\right]}^{=:\boldsymbol{S}_\infty}\boldsymbol{A}. \tag{E.6}$$

Cutting-off the infinite series after some finite value N_δ yields an approximation which requires less computation effort, i.e.

$$\boldsymbol{\mathcal{A}} \approx \boldsymbol{I}_n + \overbrace{\left[\sum_{i=1}^{N_\delta} \frac{T_\mathrm{S}^i}{i!}\boldsymbol{A}^{i-1}\right]}^{=:\boldsymbol{S}_{N_\delta}}\boldsymbol{A} \qquad \text{and} \qquad \boldsymbol{\mathcal{B}} \approx \boldsymbol{S}_{N_\delta}\boldsymbol{B}, \tag{E.7}$$

where $\boldsymbol{S}_{N_\delta}$ is the discretization matrix. Note that $N_\delta = 1$ yields the simple *forward Euler* method, which is known to cause stability issues at lower sampling frequencies [145]. Therefore, it is recommended to choose at least $N_\delta \geq 2$. Note further that a finite discretization order results in residual terms

$$\tilde{\boldsymbol{\mathcal{A}}} \approx \overbrace{\left[\sum_{i=N_\delta+1}^{\infty} \frac{T_\mathrm{S}^i}{i!}\boldsymbol{A}^{i-1}\right]}^{=:\boldsymbol{R}_{N_\delta}}\boldsymbol{A} \qquad \text{and} \qquad \tilde{\boldsymbol{\mathcal{B}}} \approx \boldsymbol{R}_{N_\delta}\boldsymbol{B}. \tag{E.8}$$

with residual discretization matrix $\boldsymbol{R}_{N_\delta}$.

E.2 Approximation of the error difference equation of the speed-adaptive observer

In this section, the error difference equation for the speed adaptive observer $\hat{\mathfrak{S}}_{\mathrm{x},\hat{\omega}}$ [see (4.88)] is derived. For the error difference to be explicitly statable, the mutual parts of the actual and the estimated speed discrete-time system and input matrices need to be identified. It is shown in the following that under certain assumptions (see Ass. 22) the discrete-time system and input matrices can be stated as

$$\left.\begin{aligned}
\hat{\boldsymbol{\mathcal{A}}}_\mathrm{x}[k] &\approx \boldsymbol{\mathcal{A}}_\mathrm{x}[k] + \sum_{i=2}^{N_\delta} \tfrac{T_\mathrm{S}^i}{i!}\boldsymbol{R}_i(\omega_\mathrm{r}[k], \omega_\mathrm{k}[k], e_{\omega_\mathrm{r}}[k]) - T_\mathrm{S}\boldsymbol{A}_\mathrm{r}e_{\omega_\mathrm{r}}[k],\\
\hat{\boldsymbol{\mathcal{B}}}_\mathrm{x}^*[k] &\approx \boldsymbol{\mathcal{B}}_\mathrm{x}^*[k] + \sum_{i=3}^{N_\delta} \tfrac{T_\mathrm{S}^i}{i!}\boldsymbol{R}_{i-1}(\omega_\mathrm{r}[k], \omega_\mathrm{k}[k], e_{\omega_\mathrm{r}}[k])\boldsymbol{B}_\mathrm{x}
\end{aligned}\right\} \tag{E.9}$$

where

$$\boldsymbol{R}_i(\omega_\mathrm{r}, \omega_\mathrm{k}, e_{\omega_\mathrm{r}}) := \begin{cases} (\boldsymbol{A}_\mathrm{x}(\omega_\mathrm{r}, \omega_\mathrm{k}) - \boldsymbol{A}_\mathrm{r}e_{\omega_\mathrm{r}})^i - \boldsymbol{A}_\mathrm{x}^i(\omega_\mathrm{r}, \omega_\mathrm{k}) - (-\boldsymbol{A}_\mathrm{r}e_{\omega_\mathrm{r}})^i, & \text{for } i \geq 0\\ \boldsymbol{0}_{8\times 8} & \text{else,} \end{cases} \tag{E.10}$$

denotes the residual terms of $(\boldsymbol{A}_\mathrm{x}(\omega_\mathrm{r}, \omega_\mathrm{k}) - \boldsymbol{A}_\mathrm{r}e_{\omega_\mathrm{r}})^i$ after subtracting $\boldsymbol{A}_\mathrm{x}^i(\omega_\mathrm{r}, \omega_\mathrm{k})$ and $(-\boldsymbol{A}_\mathrm{r}e_{\omega_\mathrm{r}})^i$. It follows directly from (E.10) that, if e_{ω_r} tends to zero, the residual matrix $\boldsymbol{R}_i(\omega_\mathrm{r}, \omega_\mathrm{k}, e_{\omega_\mathrm{r}})$ tends to $\boldsymbol{0}_{8\times 8}$, i.e.

$$\forall\, i \geq 0: \quad \lim_{e_{\omega_\mathrm{r}} \to 0} \boldsymbol{R}_i(\omega_\mathrm{r}, \omega_\mathrm{k}, e_{\omega_\mathrm{r}}) = \boldsymbol{0}_{8\times 8}. \tag{E.11}$$

First, the approximation of the system matrix $\hat{\boldsymbol{\mathcal{A}}}_\mathrm{x}$ is derived. Rewriting (4.89) using the infinite series notation yields

$$\hat{\boldsymbol{\mathcal{A}}}_\mathrm{x}[k] = \boldsymbol{I}_8 + \sum_{i=1}^{N_\delta} \tfrac{T_\mathrm{S}^i}{i!} \boldsymbol{A}_\mathrm{x}^i(\hat{\omega}_\mathrm{r}[k], \omega_\mathrm{k}[k]) \overset{(4.86)}{=} \boldsymbol{I}_8 + \sum_{i=1}^{N_\delta} \tfrac{T_\mathrm{S}^i}{i!} (\boldsymbol{A}_\mathrm{x}(\omega_\mathrm{r}[k], \omega_\mathrm{k}[k]) - \boldsymbol{A}_\mathrm{r} e_{\omega_\mathrm{r}}[k])^i, \tag{E.12}$$

which can be further simplified to

$$\hat{\boldsymbol{\mathcal{A}}}_\mathrm{x}[k] \overset{(E.10)}{=} \underbrace{\boldsymbol{\mathcal{A}}_\mathrm{x}(\omega_\mathrm{r}[k], \omega_\mathrm{k}[k])}_{\text{mutual part}} + \underbrace{\sum_{i=2}^{N_\delta} \tfrac{T_\mathrm{S}^i}{i!} \boldsymbol{R}_i(\omega_\mathrm{r}[k], \omega_\mathrm{k}[k], e_{\omega_\mathrm{r}}[k])}_{\text{first residual part}} + \underbrace{\sum_{i=1}^{N_\delta} \tfrac{T_\mathrm{S}^i}{i!} (-\boldsymbol{A}_\mathrm{r} e_{\omega_\mathrm{r}}[k])^i}_{\text{second residual part}}, \tag{E.13}$$

In (E.13), the mutual part $\boldsymbol{\mathcal{A}}_\mathrm{x}$ can be identified. In addition, two residual terms appear in the equation, which are caused by the speed estimation error e_{ω_r}. Note that $\boldsymbol{R}_1(\omega_\mathrm{r}, \omega_\mathrm{k}, e_{\omega_\mathrm{r}}) = \boldsymbol{0}_{8\times 8}$, hence the starting index of the respective sum term is two. Note further that the higher the discretization order N_δ, the larger the residual term gets, which is counterintuitive at first sight, since a higher discretization order should intuitively improve the result instead of worsening it.

Neglecting the first residual part for now, the second part is inspected closer in the following. It can be shown that $\boldsymbol{A}_\mathrm{r}$ has the following properties

$$\boldsymbol{A}_\mathrm{r} = -\boldsymbol{A}_\mathrm{r}^3 = \boldsymbol{A}_\mathrm{r}^5 = \ldots = \boldsymbol{A}_\mathrm{r}^{2i+1}(-1)^i \qquad \text{for} \quad i = 0, 1, \ldots, \infty \tag{E.14}$$

$$\boldsymbol{A}_\mathrm{r}^2 = -\boldsymbol{A}_\mathrm{r}^4 = \boldsymbol{A}_\mathrm{r}^6 = \ldots = -\boldsymbol{A}_\mathrm{r}^{2i}(-1)^i \qquad \text{for} \quad i = 1, 2, \ldots, \infty. \tag{E.15}$$

Hence, the infinite series $\sum_{i=1}^{\infty} \frac{(T_\mathrm{S} e_{\omega_\mathrm{r}})^i}{i!}(-\boldsymbol{A}_\mathrm{r})^i$ can be written as

$$\begin{aligned}
\sum_{i=1}^{\infty} \tfrac{(T_\mathrm{S} e_{\omega_\mathrm{r}})^i}{i!}(-\boldsymbol{A}_\mathrm{r})^i &= \sum_{i=0}^{\infty} \tfrac{(T_\mathrm{S} e_{\omega_\mathrm{r}})^{2i+1}}{(2i+1)!}(-\boldsymbol{A}_\mathrm{r})^{2i+1} + \sum_{i=1}^{\infty} \tfrac{(T_\mathrm{S} e_{\omega_\mathrm{r}})^{2i}}{(2i)!}(-\boldsymbol{A}_\mathrm{r})^{2i} \\
&\overset{(E.14),(E.15)}{=} -\boldsymbol{A}_\mathrm{r} \sum_{i=0}^{\infty} \tfrac{(T_\mathrm{S} e_{\omega_\mathrm{r}})^{2i+1}}{(2i+1)!}(-1)^i - \boldsymbol{A}_\mathrm{r}^2 \sum_{i=1}^{\infty} \tfrac{(T_\mathrm{S} e_{\omega_\mathrm{r}})^{2i}}{(2i)!}(-1)^i \\
&= -\boldsymbol{A}_\mathrm{r} \sin(T_\mathrm{S} e_{\omega_\mathrm{r}}) - \boldsymbol{A}_\mathrm{r}^2(\cos(T_\mathrm{S} e_{\omega_\mathrm{r}}) - 1),
\end{aligned} \tag{E.16}$$

where the series expansion of the sine and cosine functions, respectively, were used [134, pp. 197, 198]. Since a finite discretization order of N_δ is used, the *Lagrange remainders* are non-zero and can be stated as (see [134, pp. 197, 198])

$$E_\mathrm{sin}(N_\delta) := \sin(T_\mathrm{S} e_{\omega_\mathrm{r}}) - \sum_{i=0}^{\alpha_1} \frac{(T_\mathrm{S} e_{\omega_\mathrm{r}})^{2i+1}}{(2i+1)!}(-1)^i \quad \text{and} \quad E_\mathrm{cos}(N_\delta) := \cos(T_\mathrm{S} e_{\omega_\mathrm{r}}) - \sum_{i=0}^{\alpha_2} \frac{(T_\mathrm{S} e_{\omega_\mathrm{r}})^{2i}}{(2i)!}(-1)^i$$

where $\alpha_1 = \lfloor \frac{1}{2}(N_\delta - 1) \rfloor$ and $\alpha_2 = \lfloor \frac{1}{2} N_\delta \rfloor$[1]. The absolute values of the remainders can be upper bounded by (see [134, pp. 197, 198])

$$|E_\mathrm{sin}(N_\delta)| \leq \left| \frac{(T_\mathrm{S} e_{\omega_\mathrm{r}})^{2(\alpha_1+1)+1}}{(2(\alpha_1+1)+1)!} \right| \qquad \text{and} \qquad |E_\mathrm{cos}(N_\delta)| \leq \left| \frac{(T_\mathrm{S} e_{\omega_\mathrm{r}})^{2(\alpha_2+1)}}{(2(\alpha_2+1))!} \right|.$$

[1] The mathematical *floor* operator $n = \lfloor x \rfloor$, rounds the real number $x \in \mathbb{R}$ down to the greatest integer $n \in \mathbb{N}$, less or equal x.

Concerning the given application, for a conservative choice of $T_\mathrm{S} = 1\,\mathrm{ms}, e_{\omega_\mathrm{r}} = 0.1\,\omega_{\mathrm{m,nom}} = 29.85\,\mathrm{rad\,s^{-1}}$, the errors are bounded by

$$\frac{|E_{\sin}(1)|}{|\sin(T_\mathrm{S} e_{\omega_\mathrm{r}})|} \leq 0.5\%, \qquad \frac{|E_{\sin}(2)|}{|\sin(T_\mathrm{S} e_{\omega_\mathrm{r}})|} \leq 0.5\%, \qquad \frac{|E_{\sin}(3)|}{|\sin(T_\mathrm{S} e_{\omega_\mathrm{r}})|} \leq 0.00003\%,$$
$$\frac{|E_{\cos}(1)|}{|\cos(T_\mathrm{S} e_{\omega_\mathrm{r}})|} \leq 0.05\%, \qquad \frac{|E_{\cos}(2)|}{|\cos(T_\mathrm{S} e_{\omega_\mathrm{r}})|} \leq 0.000004\%, \qquad \frac{|E_{\cos}(3)|}{|\cos(T_\mathrm{S} e_{\omega_\mathrm{r}})|} \leq 0.000004\%.$$

Hence, the approximation

$$\sum_{i=1}^{N_\delta} \tfrac{(T_\mathrm{S})^i}{i!}(-\boldsymbol{A}_\mathrm{r} e_{\omega_\mathrm{r}})^i \approx -\boldsymbol{A}_\mathrm{r}\sin(T_\mathrm{S} e_{\omega_\mathrm{r}}) - \boldsymbol{A}_\mathrm{r}^2(\cos(T_\mathrm{S} e_{\omega_\mathrm{r}}) - 1) \tag{E.17}$$

is sufficiently accurate for discretization orders of $N_\delta \geq 3$. Moreover, the small-angle approximation yields (for the values used above, the error is smaller than 0.05%)

$$\sin(T_\mathrm{S} e_{\omega_\mathrm{r}}) \approx T_\mathrm{S} e_{\omega_\mathrm{r}} \qquad \text{and} \qquad \cos(T_\mathrm{S} e_{\omega_\mathrm{r}}) \approx 1. \tag{E.18}$$

Using this result, the residual term can finally be simplified to

$$\sum_{i=1}^{N_\delta} \tfrac{(T_\mathrm{S})^i}{i!}(-\boldsymbol{A}_\mathrm{r} e_{\omega_\mathrm{r}})^i \approx -T_\mathrm{S}\boldsymbol{A}_\mathrm{r} e_{\omega_\mathrm{r}}, \tag{E.19}$$

which yields the approximated system matrix in (E.9).

Likewise, the mutual part between actual and estimated speed discrete-time *input* matrix must be identified. Rewriting the input matrix $\hat{\boldsymbol{\mathcal{B}}}_\mathrm{x}^*$ [defined in (4.89)] using the series expansion yields

$$\hat{\boldsymbol{\mathcal{B}}}_\mathrm{x}^*[k] = \Big(\sum_{i=1}^{N_\delta} \tfrac{T_\mathrm{S}^i}{i!}\boldsymbol{A}_\mathrm{x}^{i-1}(\hat{\omega}_\mathrm{r}[k], \omega_\mathrm{k}[k])\Big)\boldsymbol{B}_\mathrm{x} \overset{(4.86)}{=} \Big(\sum_{i=1}^{N_\delta} \tfrac{T_\mathrm{S}^i}{i!}(\boldsymbol{A}_\mathrm{x}(\omega_\mathrm{r}[k], \omega_\mathrm{k}[k]) - \boldsymbol{A}_\mathrm{r} e_{\omega_\mathrm{r}}[k])^{i-1}\Big)\boldsymbol{B}_\mathrm{x}, \tag{E.20}$$

which can be simplified to

$$\hat{\boldsymbol{\mathcal{B}}}_\mathrm{x}^*[k] \overset{(E.10)}{=} \underbrace{\boldsymbol{\mathcal{B}}_\mathrm{x}^*[k]}_{\text{mutual part}} + \underbrace{\Big(\sum_{i=3}^{N_\delta} \tfrac{T_\mathrm{S}^i}{i!}\boldsymbol{R}_{i-1}(\omega_\mathrm{r}[k], \omega_\mathrm{k}[k], e_{\omega_\mathrm{r}}[k])\Big)\boldsymbol{B}_\mathrm{x}}_{\text{first residual part}} + \underbrace{\Big(\sum_{i=1}^{N_\delta} \tfrac{T_\mathrm{S}^i}{i!}(-\boldsymbol{A}_\mathrm{r} e_{\omega_\mathrm{r}}[k])^i\Big)\boldsymbol{B}_\mathrm{x}}_{\text{second residual part}}. \tag{E.21}$$

It can be shown that for the given system $\boldsymbol{A}_\mathrm{r}^i\boldsymbol{B}_\mathrm{x} = \boldsymbol{0}_{8\times 2}$ holds true. Hence the second residual part is zero and the approximation in (E.9) is obtained.

Using the approximated matrices (E.9), the error difference equation can finally be stated as

$$\boldsymbol{e}_\mathrm{x}[k+1] \overset{(4.12),(4.88),(E.9)}{=} (\boldsymbol{\mathcal{A}}_\mathrm{x}[k] - \boldsymbol{\mathcal{L}}_\mathrm{x}\boldsymbol{\mathcal{C}}_\mathrm{x})\boldsymbol{e}_\mathrm{x}[k] + T_\mathrm{S}\boldsymbol{A}_\mathrm{r} e_{\omega_\mathrm{r}}[k]\hat{\boldsymbol{x}}_\mathrm{x}[k] + \boldsymbol{\epsilon}_1[k] + \boldsymbol{\epsilon}_2[k], \tag{E.22}$$

with discretization errors

$$\boldsymbol{\epsilon}_1[k] := \sum_{i=N_\delta+1}^{\infty} \frac{T_\mathrm{S}^i}{i!}\boldsymbol{A}_\mathrm{x}^i(\omega_\mathrm{r}[k], \omega_\mathrm{k}[k])\boldsymbol{x}_\mathrm{x}[k] + \sum_{i=N_\delta+1}^{\infty} \frac{T_\mathrm{S}^i}{i!}\boldsymbol{A}_\mathrm{x}^{i-1}(\omega_\mathrm{r}[k], \omega_\mathrm{k}[k])\boldsymbol{B}_\mathrm{x}\boldsymbol{u}_{\mathrm{f,zoh}}^{\mathrm{dq}}[k], \tag{E.23}$$

$$\boldsymbol{\epsilon}_2[k] := -\sum_{i=2}^{N_\delta} \tfrac{T_\mathrm{S}^i}{i!}\boldsymbol{R}_i(\omega_\mathrm{r}[k], \omega_\mathrm{k}[k], e_{\omega_\mathrm{r}}[k])\hat{\boldsymbol{x}}_\mathrm{x}[k] - \sum_{i=3}^{N_\delta} \tfrac{T_\mathrm{S}^i}{i!}\boldsymbol{R}_{i-1}(\omega_\mathrm{r}[k], \omega_\mathrm{k}[k], e_{\omega_\mathrm{r}}[k])\boldsymbol{B}_\mathrm{x}\boldsymbol{u}_{\mathrm{f,zoh}}^{\mathrm{dq}}[k] \tag{E.24}$$

Assumption 22 (Observer sampling time, discretization order and speed estimation error)**.** *The sampling time T_S and speed estimation error e_{ω_r} are assumed sufficiently small, while the discretization order N_δ is assumed high enough, such that the following approximations hold:*

$$\left.\begin{aligned} &\sum_{i=N_\delta+1}^{\infty} \frac{T_\mathrm{S}^i}{i!}\boldsymbol{A}_\mathrm{x}^i(\omega_\mathrm{r},\omega_\mathrm{k}) \approx \mathbf{0}_{8\times 8}, && \sum_{i=N_\delta+1}^{\infty} \frac{T_\mathrm{S}^i}{i!}\boldsymbol{A}_\mathrm{x}^{i-1}(\omega_\mathrm{r},\omega_\mathrm{k})\boldsymbol{B}_\mathrm{x} \approx \mathbf{0}_{8\times 2},\\ &\sum_{i=2}^{N_\delta} \frac{T_\mathrm{S}^i}{i!}\boldsymbol{R}_i(\omega_\mathrm{r},\omega_\mathrm{k},e_{\omega_\mathrm{r}}) \approx \mathbf{0}_{8\times 8}, && \sum_{i=3}^{N_\delta} \frac{T_\mathrm{S}^i}{i!}\boldsymbol{R}_{i-1}(\omega_\mathrm{r},\omega_\mathrm{k},e_{\omega_\mathrm{r}})\boldsymbol{B}_\mathrm{x} \approx \mathbf{0}_{8\times 2}. \end{aligned}\right\} \tag{E.25}$$

Due to Assumption 22, it follows that $\boldsymbol{\epsilon}_1[k] \approx 0$ and $\boldsymbol{\epsilon}_2[k] \approx 0$ and, hence, the error difference simplifies to

$$\boldsymbol{e}_\mathrm{x}[k+1] \overset{\text{Ass. } 22}{\approx} (\boldsymbol{\mathcal{A}}_\mathrm{x}[k] - \hat{\boldsymbol{\mathcal{L}}}_\mathrm{x}\boldsymbol{\mathcal{C}}_\mathrm{x})\boldsymbol{e}_\mathrm{x}[k] + T_\mathrm{S}\boldsymbol{A}_\mathrm{r}e_{\omega_\mathrm{r}}[k]\hat{\boldsymbol{x}}_\mathrm{x}[k]. \tag{E.26}$$

E.3 Discrete-time PI-controller with anti-windup

Let

$$\tilde{\Sigma}_\mathrm{pi}: \quad \begin{cases} \frac{\mathrm{d}}{\mathrm{d}t}\xi(t) = f_\mathrm{awu}(u)e(t), \\ u(t) = K_\mathrm{p}e(t) + K_\mathrm{i}\xi(t) \end{cases} \tag{E.27}$$

describe a generic PI controller with control error e, controller output u, integral error state ξ—where $\xi(0) = 0$—and gains K_p (proportional) and K_i (integral), respectively. In addition, the anti-windup decision function f_awu is given by

$$f_\mathrm{awu}(u) = \begin{cases} 1, & |u| < u_\mathrm{max} \\ 0, & \text{else,} \end{cases} \tag{E.28}$$

where u_max denotes the maximum output of the controller. The discrete-time equivalent is obtained by (i) transforming the linear (assuming constant f_awu) control system (E.27) to the frequency domain (s-domain), (ii) applying the bilinear transform (z-domain), and (iii) transforming back the result to the time domain [132, Sec. 14.2.1]. Performing steps (i)–(iii) yields the discrete-time description (details omitted here)

$$\tilde{\mathfrak{S}}_\mathrm{pi}: \quad \begin{cases} \xi[k] = f_\mathrm{awu}(u)\frac{T_\mathrm{S}}{2}e[k] + f_\mathrm{awu}(u)\frac{T_\mathrm{S}}{2}e[k-1] + \xi[k-1], \\ u[k] = K_\mathrm{p}e[k] + K_\mathrm{i}\xi[k], . \end{cases} \tag{E.29}$$

with $\xi[0] = 0$. The corresponding block diagram and its simplified version are shown in Fig. E.1.

E.4 Controllability of the continuous-time electric drive system (filter and induction machine)

Under the assumption of slowly varying parameters (Assumptions 17 and 18), controllability of the drive system can be shown for the continuous-time LPV system $\Sigma_\mathrm{x}(\omega_\mathrm{r},\omega_\mathrm{k})$ defined in (4.7) using *Kalman's controllability criterion* (KCC). The KCC states that the rank of the controllability matrix $\boldsymbol{S}_\mathrm{C} \in \mathbb{R}^{n\times p\cdot n}$ must be equal to the system order n (p denotes the number of inputs) [128,

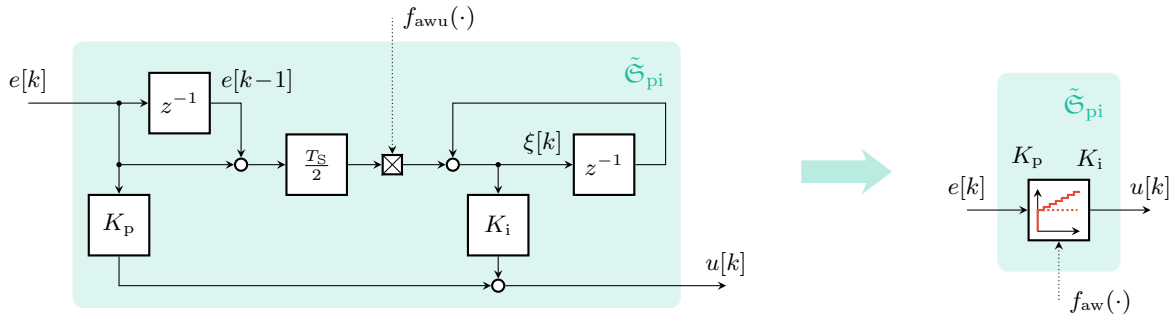

Figure E.1: *Detailed (left) and simplified (right) block diagrams of a generic discrete-time PI controller with anti-windup option.*

p. 66]. Hence, if it can be shown that any n columns of $\boldsymbol{S}_\mathrm{C}$ are linearly independent, the system is fully controllable.

The reduced controllability matrix

$$\boldsymbol{S}_\mathrm{C}^*[\Sigma_\mathrm{x}] := \begin{bmatrix}\boldsymbol{B}_\mathrm{x} & \boldsymbol{A}_\mathrm{x}\boldsymbol{B}_\mathrm{x} & \boldsymbol{A}_\mathrm{x}^2\boldsymbol{B}_\mathrm{x} & \boldsymbol{A}_\mathrm{x}^3\boldsymbol{B}_\mathrm{x}\end{bmatrix} \in \mathbb{R}^{8\times 8} \tag{E.30}$$

can be calculated for system Σ_x using symbol calculations in MATLAB®(Symbolic Math Toolbox), i.e.

$$\boldsymbol{S}_\mathrm{C}^*[\Sigma_\mathrm{x}] = \begin{bmatrix} \frac{1}{L_\mathrm{f}}\boldsymbol{I}_2 & * & * & * \\ \boldsymbol{0}_{2\times 2} & \frac{1}{C_\mathrm{f}L_\mathrm{f}}\boldsymbol{I}_2 & * & * \\ \boldsymbol{0}_{2\times 2} & \boldsymbol{0}_{2\times 2} & \frac{1}{C_\mathrm{f}L_\mathrm{f}\sigma L_\mathrm{s}}\boldsymbol{I}_2 - \frac{2\omega_\mathrm{k}}{C_\mathrm{f}L_\mathrm{f}}\boldsymbol{J} & * \\ \boldsymbol{0}_{2\times 2} & \boldsymbol{0}_{2\times 2} & \boldsymbol{0}_{2\times 2} & \frac{R_\mathrm{r}}{C_\mathrm{f}L_\mathrm{f}L_\mu}\boldsymbol{I}_2 \end{bmatrix} \tag{E.31}$$

where the off diagonal elements of the upper triangle matrix (marked by $*$) are not explicitly stated since they are not needed for the rank condition. If it can be shown that the determinant of $\boldsymbol{S}_\mathrm{C}^*[\Sigma_\mathrm{x}]$ is non-zero, the matrix has full rank and the system is controllable. Since $\boldsymbol{S}_\mathrm{C}^*[\Sigma_\mathrm{x}]$ has a triangular block structure, the determinant is given by

$$\begin{aligned}\det(\boldsymbol{S}_\mathrm{C}^*[\Sigma_\mathrm{x}]) &= \det\left(\tfrac{1}{L_\mathrm{f}}\boldsymbol{I}_2\right)\cdot\det\left(\tfrac{1}{C_\mathrm{f}L_\mathrm{f}}\boldsymbol{I}_2\right)\cdot\det\left(\tfrac{1}{C_\mathrm{f}L_\mathrm{f}\sigma L_\mathrm{s}}\boldsymbol{I}_2 - \frac{2\omega_\mathrm{k}}{C_\mathrm{f}L_\mathrm{f}}\boldsymbol{J}\right)\cdot\det\left(\tfrac{R_\mathrm{r}}{C_\mathrm{f}L_\mathrm{f}L_\mu}\boldsymbol{I}_2\right) \\ &= \tfrac{1}{L_\mathrm{f}^2}\cdot\tfrac{1}{(C_\mathrm{f}L_\mathrm{f})^2}\cdot\tfrac{1}{(C_\mathrm{f}L_\mathrm{f})^2}\left(\tfrac{1}{(\sigma L_\mathrm{s})^2}+4\omega_\mathrm{k}^2\right)\cdot\tfrac{R_\mathrm{r}^2}{(C_\mathrm{f}L_\mathrm{f}L_\mu)^2}\end{aligned} \tag{E.32}$$

which is always non-zero provided real positive parameters (and for any value of ω_k). Note that extending the system by additional integrators (integral-action) does not have an impact on controllability, which can be shown using *Hautus' criterion* [128, p. 215].

E.5 Weak observability of a continuous-time nonlinear system

Definition 1 (Weak observability)**.** *Let the system*

$$\Sigma: \quad \begin{cases} \frac{\mathrm{d}}{\mathrm{d}t}\boldsymbol{x} = \boldsymbol{f}(\boldsymbol{x},\boldsymbol{u}), & \boldsymbol{x}(t_0) = \boldsymbol{x}_0 \\ \quad \boldsymbol{y} = \boldsymbol{g}(\boldsymbol{x},\boldsymbol{u}) \end{cases}$$

be defined for $\boldsymbol{x} \in D_{\boldsymbol{x}} \subseteq \mathbb{R}^n$, $\boldsymbol{u} \in C_{\boldsymbol{u}} \subseteq C^{n-1}$ *and* $\boldsymbol{y} \in \mathbb{R}^r$, *where* $D_{\boldsymbol{x}}$ *is the domain of* $\boldsymbol{x}$, $C_{\boldsymbol{u}}$ *is the domain of* $\boldsymbol{u}$ *and* C^{n-1} *denotes the space of* $n-1$ *times continuously differentiable vector functions* $\boldsymbol{u}(\cdot)$. *If, for all* $\boldsymbol{x}_p \in \mathbb{R}^n$, *all initial states* $\boldsymbol{x}_0$ *in a local neighborhood*

$$U = \{\boldsymbol{x}_0 \in \mathbb{R}^n \,|\, \|\boldsymbol{x}_0 - \boldsymbol{x}_p\| < \rho\}$$

of $\boldsymbol{x}_p \in D_{\boldsymbol{x}}$ *are uniquely determinable by knowledge of* $\boldsymbol{u}(t)$ *and* $\boldsymbol{y}(t)$ *within the finite time interval* $[t_0, t_1 < \infty]$ *and for all* $\boldsymbol{u} \in C_{\boldsymbol{u}}$, *the system is called* weakly observable *[125, Sec. 7.1].*

In order to prove weak observability, the *observability matrix* is derived by calculating the $n-1$ derivatives of the output, i.e.

$$\left.\begin{aligned}
\boldsymbol{y} &= \boldsymbol{h}_0(\ldots) := \boldsymbol{g}(\boldsymbol{x}, \boldsymbol{u}) \\
\frac{\mathrm{d}}{\mathrm{d}t}\boldsymbol{y} &= \boldsymbol{h}_1(\ldots) := \frac{\partial \boldsymbol{g}}{\partial \boldsymbol{x}}\boldsymbol{f}(\boldsymbol{x}, \boldsymbol{u}) + \frac{\partial \boldsymbol{g}}{\partial \boldsymbol{u}}\frac{\mathrm{d}}{\mathrm{d}t}\boldsymbol{u} \\
\frac{\mathrm{d}^2}{\mathrm{d}t^2}\boldsymbol{y} &= \boldsymbol{h}_2(\ldots) := \frac{\partial \boldsymbol{h}_1}{\partial \boldsymbol{x}}\boldsymbol{f}(\boldsymbol{x}, \boldsymbol{u}) + \frac{\partial \boldsymbol{h}_1}{\partial \boldsymbol{u}}\frac{\mathrm{d}}{\mathrm{d}t}\boldsymbol{u} + \frac{\partial \boldsymbol{h}_1}{\partial (\frac{\mathrm{d}}{\mathrm{d}t}\boldsymbol{u})}\frac{\mathrm{d}^2}{\mathrm{d}t^2}\boldsymbol{u} \\
&\vdots \\
\frac{\mathrm{d}^{(n-1)}}{\mathrm{d}t^{(n-1)}}\boldsymbol{y} &= \boldsymbol{h}_{n-1}(\ldots) := \frac{\partial \boldsymbol{h}_{n-2}}{\partial \boldsymbol{x}}\boldsymbol{f}(\boldsymbol{x}, \boldsymbol{u}) + \sum_{i=1}^{n-1} \frac{\partial \boldsymbol{h}_{n-1}}{\partial (\frac{\mathrm{d}}{\mathrm{d}t})^{i-1}\boldsymbol{u}}(\tfrac{\mathrm{d}}{\mathrm{d}t})^i \boldsymbol{u}
\end{aligned}\right\}. \tag{E.33}$$

and partially deriving the resulting vector of output derivatives with respect to $\boldsymbol{x}$, i.e. calculating its *Jacobian* [125].

Definition 2 (Observability matrix)**.** *The* observability matrix $\boldsymbol{S}_{\mathrm{O}}[\Sigma] \in \mathbb{R}^{(r \cdot n) \times n}$ *of system* Σ *is defined as*

$$\boldsymbol{S}_{\mathrm{O}}[\Sigma] := \frac{\partial}{\partial \boldsymbol{x}} \begin{pmatrix} \boldsymbol{h}_0(\boldsymbol{x}, \boldsymbol{u}) \\ \boldsymbol{h}_1(\boldsymbol{x}, \boldsymbol{u}, \frac{\mathrm{d}}{\mathrm{d}t}\boldsymbol{u}) \\ \boldsymbol{h}_2(\boldsymbol{x}, \boldsymbol{u}, \frac{\mathrm{d}}{\mathrm{d}t}\boldsymbol{u}, (\frac{\mathrm{d}}{\mathrm{d}t})^2\boldsymbol{u}) \\ \vdots \\ \boldsymbol{h}_{n-1}(\boldsymbol{x}, \boldsymbol{u}, \frac{\mathrm{d}}{\mathrm{d}t}\boldsymbol{u}, (\frac{\mathrm{d}}{\mathrm{d}t})^2\boldsymbol{u}, \ldots, (\frac{\mathrm{d}}{\mathrm{d}t})^{n-1}\boldsymbol{u}) \end{pmatrix}. \tag{E.34}$$

Note that the definition in [125] only treats scalar outputs, whereas in the definition above $\boldsymbol{y}$ is an r-dimensional vector. Note further, that the definition is closely related to those in [133, 146, 147], where, however, piecewise constant inputs are assumed, such that the derivative of the outputs can be written in terms of *Lie* derivatives.

The so-called *observability rank condition* for proving weak observability of a nonlinear system was first presented in [148] and can be stated as follows for the defined observability matrix [125].

Theorem 1 (Observability rank condition)**.** *A system* Σ *is weakly observable if the rank of the observability matrix* $\boldsymbol{S}_{\mathrm{O}}[\Sigma]$ *is equal to the number of states* n, *i.e.*

$$\operatorname{rank} \boldsymbol{S}_{\mathrm{O}}[\Sigma] = n \quad \Longrightarrow \quad \Sigma \text{ weakly observable.} \tag{E.35}$$

Remark 28. *For the given system* Σ_{x} *[defined in (4.7)], those parts of the output derivatives which are multiplied with the input or any of its derivatives do not depend on the states. Therefore, the observability matrix can be written in terms of Lie derivatives, as in the case where a piecewise constant input is assumed.*

E.6 Remark on the discrete-time LQR observer gain calculation using MATLAB

Calculating the discrete-time observer gains can be performed using either `lqrd(...)` or `dlqr(...)`, provided by the Control System Toolbox of MATLAB®.

However, in contrast to the controller design case, the *dual* system is considered for the observer design. The question arises, whether the discretized continuous-time dual system

$$\check{\boldsymbol{x}}_{\mathrm{x}}[k+1] = \underbrace{\left(\boldsymbol{I}_8 + \check{\boldsymbol{S}}_\infty (\boldsymbol{A}_{\mathrm{x}} - \boldsymbol{L}_{\mathrm{x}}\boldsymbol{C}_{\mathrm{x}})^\top\right)}_{=:\check{\boldsymbol{M}}} \check{\boldsymbol{x}}_{\mathrm{x}}[k] \tag{E.36}$$

with discretization matrix

$$\check{\boldsymbol{S}}_\infty \approx (\mathrm{expm}(\boldsymbol{A}_{\mathrm{x}}^\top T_{\mathrm{S}}) - \boldsymbol{I}_8)(\boldsymbol{A}_{\mathrm{x}}^\top)^{-1}, \tag{E.37}$$

or the discrete-time dual system

$$\check{\boldsymbol{x}}_{\mathrm{x}}[k+1] = \underbrace{\left(\boldsymbol{I}_8 + (\boldsymbol{A}_{\mathrm{x}} - \boldsymbol{L}_{\mathrm{x}}\boldsymbol{C}_{\mathrm{x}})^\top \boldsymbol{S}_\infty^\top\right)}_{=:\boldsymbol{M}^\top} \check{\boldsymbol{x}}_{\mathrm{x}}[k] \tag{E.38}$$

should be used for gain calculation. The first case (E.36) is realized using the `lqrd(...)` function with input matrices $\boldsymbol{A}_{\mathrm{x}}^\top$ and $\boldsymbol{C}_{\mathrm{x}}^\top$, yielding $\boldsymbol{L}_{\mathrm{x}}$. The second case (E.38), in turn, is realized by using the `dlqr(...)` function with input matrices $\boldsymbol{I}_8 + \boldsymbol{A}_{\mathrm{x}}^\top \boldsymbol{S}_\infty^\top$ and $\boldsymbol{C}_{\mathrm{x}}^\top$, and calculating $\boldsymbol{L}_{\mathrm{x}} = \boldsymbol{S}_\infty^{-1}\boldsymbol{\mathcal{L}}_{\mathrm{x}}$.

It can be shown, that $\boldsymbol{S}_\infty^\top = \check{\boldsymbol{S}}_\infty$ holds true[2], and, although

$$\check{\boldsymbol{M}} = \boldsymbol{I}_8 + \boldsymbol{S}_\infty^\top (\boldsymbol{A}_{\mathrm{x}} - \boldsymbol{L}_{\mathrm{x}}\boldsymbol{C}_{\mathrm{x}})^\top \neq \boldsymbol{I}_8 + (\boldsymbol{A}_{\mathrm{x}} - \boldsymbol{L}_{\mathrm{x}}\boldsymbol{C}_{\mathrm{x}})^\top \boldsymbol{S}_\infty^\top = \boldsymbol{M}^\top, \tag{E.39}$$

their eigenvalues are equal, as both matrices are *similar*[3] since

$$\boldsymbol{S}_\infty^\top \boldsymbol{M}^\top = \check{\boldsymbol{M}} \boldsymbol{S}_\infty^\top \tag{E.40}$$

holds true. It follows that both system representations (E.36) and (E.38) may be used, since the corresponding closed-loop eigenvalues are identical. Note that calculating the observer gains using the `dlqr(...)` function with input matrices $\boldsymbol{I}_8 + \boldsymbol{A}_{\mathrm{x}}^\top \boldsymbol{S}_\infty^\top = \boldsymbol{\mathcal{A}}_{\mathrm{x}}^\top$ and $(\boldsymbol{C}_{\mathrm{x}}\boldsymbol{S}_\infty)^\top$ yields the same closed-loop eigenvalues as `lqrd(...)` with inputs $\boldsymbol{A}_{\mathrm{x}}^\top$ and $\boldsymbol{C}_{\mathrm{x}}^\top$.

---

[2] The matrix $\boldsymbol{S}_\infty^\top$ is given by

$$\boldsymbol{S}_\infty^\top = \left[(\mathrm{expm}(\boldsymbol{A}_{\mathrm{x}} T_{\mathrm{S}}) - \boldsymbol{I}_8)\boldsymbol{A}_{\mathrm{x}}^{-1}\right]^\top = (\boldsymbol{A}_{\mathrm{x}}^{-1})^\top (\mathrm{expm}(\boldsymbol{A}_{\mathrm{x}}^\top T_{\mathrm{S}}) - \boldsymbol{I}_8).$$

If it can be shown that $(\boldsymbol{A}_{\mathrm{x}}^{-1})^\top$ and $\mathrm{expm}(\boldsymbol{A}_{\mathrm{x}}^\top T_{\mathrm{S}})$ commute, it follows that $\boldsymbol{S}_\infty^\top = \check{\boldsymbol{S}}_\infty$ must hold true [compare (E.37)]. Using the series expansion of the matrix exponential yields

$$\mathrm{expm}(\boldsymbol{A}_{\mathrm{x}}^\top T_{\mathrm{S}}) = \left[\boldsymbol{I}_n + T_{\mathrm{S}}\boldsymbol{A}_{\mathrm{x}}^\top + \frac{T_{\mathrm{S}}^2}{2}(\boldsymbol{A}_{\mathrm{x}}^\top)^2 + \ldots\right].$$

Clearly, it does not matter, whether $(\boldsymbol{A}_{\mathrm{x}}^\top)^{-1}$ is multiplied from the left or from the right, hence the matrices do in fact commute and $\boldsymbol{S}_\infty^\top = \check{\boldsymbol{S}}_\infty$ holds true. □

[3] Two matrices $\boldsymbol{A}$ and $\boldsymbol{B}$ are called *similar*, if there exists a *regular* matrix $\boldsymbol{S}$, such that $\boldsymbol{B} = \boldsymbol{S}\boldsymbol{A}\boldsymbol{S}^{-1}$ holds true [149, p. 160]. It follows that $\boldsymbol{S}\boldsymbol{A} = \boldsymbol{B}\boldsymbol{S}$ holds true as well.